PACIFIC EARTHQUAKE ENGINEERING
RESEARCH CENTER

Seismic Demands for Nondeteriorating Frame Structures and Their Dependence on Ground Motions

Ricardo Medina

and

Helmut Krawinkler

John A. Blume Earthquake Engineering Center
Department of Civil and Environmental Engineering
Stanford University

PEER 2003/15
MAY 2004

Seismic Demands for Nondeteriorating Frame Structures and Their Dependence on Ground Motions

Ricardo Antonio Medina

and

Helmut Krawinkler

John A. Blume Earthquake Engineering Center
Department of Civil & Environmental Engineering
Stanford University

PEER Report 2003/15
Pacific Earthquake Engineering Research Center
College of Engineering
University of California, Berkeley

May 2004

ABSTRACT

The objective of this study is to improve the understanding of behavior patterns and the quantification of seismic demands for nondeteriorating regular frames subjected to ordinary ground motions. In this study, the term *ordinary* refers to ground motions that are recorded at distances greater than 13 km from the fault rupture, that do not exhibit pulse-type characteristics, and that are recorded on stiff soil sites. Engineering demand parameters (EDPs) of interest include roof and story drifts, local deformations, absolute floor accelerations and velocities, story shears and overturning moments, and energy terms, which are obtained by means of nonlinear time history analyses. Since nondeteriorating frames are used, the EDPs of primary interest are those that correlate best with structural, nonstructural, and contents damage at performance levels related to dollar losses and downtime. A relational database management system is used to perform statistical evaluation of EDPs and to establish relationships between structural and ground motion parameters. The primary intensity measure used, IM, is the spectral acceleration at the first mode of the structure, $S_a(T_1)$.

The emphasis of this study is on quantification of EDPs for performance evaluation but includes a discussion of issues related to the design of components that need to be protected to avoid brittle failure in the response, e.g., columns in a moment-resisting frame. An exploration of probabilistic evaluation of EDPs is summarized, in which EDP hazard curves are developed and based on numerical integration procedures and closed-form solutions. The use of global collapse fragility functions (for a frame in which P-delta causes dynamic instability in the response) along with an IM hazard curve to estimate the mean annual frequency of collapse is explored and illustrated in an example.

This study has provided much insight into the inelastic dynamic response characteristics of moment-resisting frames and the statistical properties of important engineering demand parameters. The data from the extensive nonlinear analyses of various frames with variations in their properties are stored in a database management system and can be exploited to obtain comprehensive statistical information on other EDPs of interest in the performance evaluation of frame structures.

ACKNOWLEDGMENTS

This work was supported in part by the Pacific Earthquake Engineering Research Center through the Earthquake Engineering Research Centers Program of the National Science Foundation under award number EEC-9701568. The work reported herein is part of the PEER mission to develop and disseminate technologies to support performance-based earthquake engineering.

This report was originally published as the Ph.D. dissertation of the first author. The financial support provided by PEER is gratefully acknowledged. The authors would like to thank Professors C. Allin Cornell, Gregory G. Deierlein, and Eduardo Miranda, who provided constructive feedback on the manuscript. Several graduate students, present and former, at the Stanford University John A. Blume Earthquake Engineering Center, have provided assistance and valuable input. In particular, the help provided by Luis F. Ibarra, Farzin Zareian, and Fatemeh Jalayer is much appreciated.

CONTENTS

LIST OF FIGURES

LIST OF TABLES

1 Introduction

1.1 MOTIVATION FOR THIS STUDY

Recent earthquake events in the U.S. have shown that the vast majority of structural systems designed according to current code-compliant seismic design measures have been able to fulfill the two basic performance targets addressed in codes: life safety and collapse prevention. However, design and evaluation methodologies in codes and guidelines rely mostly on limited historical data, empirical knowledge, and past experience, and are not transparent or explicit enough to allow engineers to make a ***reliable*** assessment of the seismic performance of a system. On the other hand, there is a huge stock of existing buildings that are designed according to outdated seismic design guidelines. These buildings need reliable performance evaluation procedures that allow the implementation of effective and economical retrofit strategies to improve their seismic performance.

In the past, emphasis in design and evaluation has been placed on structural components. However, damage to nonstructural components and contents constitutes a significant portion of the associated dollar losses of buildings after a seismic event. This last statement implies that performance targets other than life safety and collapse prevention, such as direct dollar losses and downtime (business interruption), deserve much consideration. Therefore, there is a need to improve seismic design and evaluation methods in order to achieve a more efficient use of resources and provide enhanced seismic protection of property and lives.

At this time it seems to be widely accepted in the earthquake engineering community that performance-based earthquake engineering (PBEE) can be used to establish measures of acceptable performance and to develop design and evaluation procedures that take into account different performance objectives. Targets for performance objectives include collapse prevention, life safety, direct dollar losses, and downtime. This implies a socio-economic assessment to decide whether the seismic performance is cost effective and suitable to the owner(s) and society. However, the implementation of PBEE poses a spectrum of challenges. For instance, there is a need for interdisciplinary research in which structural engineers work together with the industry and researchers in other fields (e.g., earth and social sciences) to formulate a methodology that can be translated into terms that the decision makers are able to understand and adopt. Additional challenges include the evaluation of nonstructural and contents damage, the incorporation of all the relevant uncertainties that are inherit in the design and evaluation process, and the education of the engineering community.

Research efforts developed by the Pacific Earthquake Engineering Research (PEER) Center have formalized a performance assessment methodology that includes the aleatory and epistemic uncertainties inherent in the process (Krawinkler, 2002). The general framework can be summarized in the following equation, in which a Decision Variable (DV) is related to a ground motion Intensity Measure (IM), an Engineering Demand Parameter (EDP) and a Damage Measure (DM):

$$\nu(DV) = \iiint G(DV \mid DM)\, dG(DM \mid EDP)\, dG(EDP \mid IM)\, d\lambda(IM) \qquad (1.1)$$

This equation is obtained based on the total probability theorem where ν(DV) is the mean annual frequency of exceedance of a specific value of DV. In this context, DV relates to collapse, loss of lives, direct dollar losses, and business interruption. G(DV|DM) is the probability of exceeding a certain value of DV conditioned on DM (fragility function of DV given DM). The DMs correspond to damage states associated with repairs to structural, nonstructural components, or contents. dG(DM/EDP) is the derivate of the conditional probability of a damage state being exceeded given a value of the EDP. EDPs of interest are story drifts, story ductilities, floor acceleration, etc. The term dG(EDP/IM) is the derivative of the conditional probability of exceeding a value of an EDP given the IM. IM is a ground motion intensity measure, such as peak ground acceleration, spectral acceleration at the first-mode period, and others. Finally, the expression dλ(IM) corresponds to the derivate of the seismic hazard curve based on IM.

In order to fully implement the aforementioned performance assessment methodology, there is the need to carry out probabilistic evaluation of EDPs that can be related to DVs on which quantitative seismic performance assessment can be based. This process of probabilistic seismic demand analysis requires careful selection of sets of ground motions that represent the intensity, frequency, and duration characteristics of interest at the various hazard levels at which performance is to be evaluated. In the context of this performance assessment framework, it is important to note that the choice of EDPs depends on the performance target and that the emphasis should be on the complete structural, nonstructural, and content system and not on a component.

1.2 OBJECTIVES AND OUTLINE

The global objective of this study is to understand and quantify, with statistical measures, the force, deformation, and energy demands imposed by ground motions of general characteristics, magnitudes, and distances on regular frames with different configurations and structural properties. The specific objectives summarized as follows are:

- To develop a database management system for seismic demand evaluation;
- To evaluate demand patterns as a function of the properties of moment-resisting frames and ground motions
- To identify relevant ground motion and structural response parameters and to establish relationships between these parameters that take into account the aleatory uncertainty in the results;
- To evaluate the sensitivity of demands to variations in structural properties, analysis models and methods; and
- To quantify central values and dispersion of EDPs (given an IM) of particular concern for nonstructural and content systems, e.g., floor accelerations, story drifts.

This study focuses on the development of IM-EDP relationships based on simulations by means of nonlinear time history analyses of two-dimensional, nondeteriorating regular moment-resisting frame structures subjected to ordinary ground motions. Generic frames are used and the EDPs of interest are those that correlate best with DVs corresponding to direct dollar losses and downtime.

The issues identified here are elaborated in the following chapters. Chapter 2 presents a global perspective on seismic demand evaluation issues and the implementation of a database management system to identify behavior patterns and quantify IM-EDP relationships for moment-resisting frames. Discussions on different models, variations in structural properties, relevant EDPs, analysis tools, and statistical methods are also included. This chapter contains an example on the flexibility and versatility of the database to quantify the efficiency of different IMs.

Chapter 3 discusses the use of the spectral acceleration at the fundamental period as the basic IM in this study. A description of the properties of the set of ordinary ground motions used in this study and the evaluation of the dependence of elastic and inelastic single-degree-of-freedom (SDOF) demands on magnitude and distance is investigated. A limited evaluation of the magnitude and distance dependence of the response of multi-degree-of-freedom (MDOF) systems on spectral shape is also presented.

Chapter 4 presents a comprehensive evaluation of story drifts, story ductilities, beam plastic rotations, absolute floor accelerations, and velocities for various levels of inelastic behavior. Quantification of central values of EDPs and their associated aleatory uncertainties as well as the identification of behavior patterns are carried out for a family of generic regular frames with different number of stories and fundamental period. Beam-hinge models with peak-oriented (modified Clough) hysteretic behavior at plastic hinge locations are utilized. The study of the distribution of EDPs over the height as a function of the structural system and the level of inelastic behavior is also included in order to provide information on the distribution of damage in the structure. Simplified equations to predict median MDOF deformation demands based on baseline SDOF elastic spectral information are presented.

Chapter 5 deals with the statistical evaluation of energy demands for the family of generic frames used in Chapter 4. Energy demands include total dissipated energy (input energy at the end of the response), hysteretic energy dissipated, and the normalized hysteretic energy at plastic hinge locations. A definition of strong motion duration that identifies the interval of the response that is most relevant for demand evaluation and damage assessment is discussed as well as the evaluation of the distribution of energy demands over the height. Comparisons are made with the energy demands experienced by SDOF systems. Relationships between strong ground motion duration, relative intensity, and structural systems are investigated.

Chapter 6 summarizes seismic demand evaluation of strength parameters relevant for the design of columns that form part of a moment-resisting frame. Demand evaluation is carried out for the base case regular frames used in Chapters 4 and 5. Global demands such as story shear strength and story overturning moments are evaluated. This chapter includes statistical information on the column strength required to avoid plastic hinging in columns, which is another important issue relevant for design. A discussion on the factors that contribute to large column moment demands is addressed. Moments at the midheight of columns are evaluated, since they become important quantities to assess the demands imposed on column-splice locations in steel structures. For reinforced concrete structures, moments at the midheight of columns are important when precast concrete columns are used and also at rebar splice locations in conventional reinforced concrete columns. A comparison of strength demands from dynamic results with demands obtained from the pushover analysis technique is carried out. Since plastic hinging is expected at the bottom of the first-story columns, this chapter also provides statistical information related to the maximum plastic rotation demands at the base of the first-story columns.

Chapter 7 summarizes a sensitivity study on seismic demands for variations in structural properties. The following variations are investigated: hysteretic behavior (peak-oriented, pinching and bilinear), strain hardening in the moment-rotation relationship at the component level (0% and 3%), structure P-delta effects (where the use of the pushover analysis for the assessment of potential instability problems in frames due to P-delta is illustrated), additional strength and stiffness provided by elements that do not form part of the moment-resisting frame, story shear strength distribution based on different design load patterns (parabolic, triangular, and uniform, including random overstrength), beam moments due to gravity loads, and different "failure" mechanisms (beam-hinge and column-hinge models).

In Chapter 8 the utilization of a one-bay generic frame for seismic demand evaluation is assessed by correlating its response with that of a "real" structure (represented by the SAC LA9-M1 model, Gupta and Krawinkler, 1999). This correlation is performed based on deformation EDPs such as the maximum roof and story drift angles.

Chapter 9 deals with illustrations of probabilistic evaluation of EDPs by developing hazard curves for the maximum roof and the maximum story drift angle over the height. A brief discussion on the use of closed-form solutions and numerical integration to develop EDP hazard curves is presented. The evaluation of the mean annual frequency of collapse for a P-delta sensitive frame is illustrated by means of developing a global collapse fragility curve (probability of global collapse given the IM).

Chapter 10 summarizes the main conclusions drawn in this study and identifies future research directions. Two appendices are included. Appendix A presents a summary of the main properties and static behavior of the base case generic frame models used in this study. A brief discussion on modeling issues to avoid spurious damping forces and moments is included. This issue is relevant when performing nonlinear time history analyses because when spurious damping forces (or moments) are present, static equilibrium is not satisfied at all times during the analysis. Appendix B presents a comprehensive list of EDPs that are stored in the relational database and are relevant for seismic demand evaluation of frame models.

2 Seismic Demand Evaluation Using a Database Management System

2.1 VARIABLES IN SEISMIC DEMAND EVALUATION

Seismic demand evaluation of structural systems is a broad subject that involves the study of relationships between ground motion parameters, base-line SDOF information and MDOF response. This process involves a wide variety of variables ranging from ground motion to structural response parameters, and it has to incorporate many factors such as local site conditions, local seismicity, structural configuration, structural properties, hazard level of interest, modeling assumptions and others. This study focuses on the seismic demand evaluation of multi-story frames based on simulations by means of nonlinear time history analyses using recorded ground motions. Therefore, variations in ground motion characteristics as well as structural properties become critical aspects of this problem.

Figure 2.1 depicts an overview of some of the most important variables involved in a general seismic demand evaluation study. The problem is complex, and although several studies have been carried out to understand and quantify seismic demands and their associated uncertainties (Shome and Cornell, 1999; Krawinkler and Gupta, 1998), much more research needs to be devoted to this subject. The purpose of this work is to provide an in-depth understanding of several important variables and of their effect on the structural response of regular frame systems. The variables considered are shaded in Figure 2.1 and include:

- Different hysteretic behavior at the component level (bilinear, peak-oriented, pinching);
- Strain-hardening effects;
- Stiffness distribution over the height;
- Strength distribution over the height (including random overstrength);
- Failure mechanism; and
- Contribution of “secondary” systems to the lateral strength and stiffness

- Structure P-delta effects; and
- Gravity load effects

The relationships between ground motions and structural response parameters are evaluated for the aforementioned variables in Chapters 4 to 7.

2.2 THE NEED FOR A DATABASE MANAGEMENT SYSTEM

As discussed in the previous section, the seismic demand evaluation process involves the study of relationships between ground motion parameters, baseline SDOF information and MDOF response. Owing to the large number of variables involved in this process, a relational database management system is a viable and effective way to accomplish the aforementioned objectives. It allows both versatility and flexibility in data manipulation, which permits the fulfillment of different data needs according to the goal of interest. For example, a relational database can be used to analyze the following aspects of the seismic demand evaluation problem:

- The sufficiency and efficiency of different intensity measures (IMs). In this context, an efficient IM is defined as one that results in a relatively small dispersion of EDP given IM, while a sufficient IM is defined as one for which the EDP given IM is conditionally independent of ground motion parameters such as magnitude and distance;
- The relationship between demand parameters and IMs in different formats, for instance, constant R (strength-reduction factor) and constant ductility approaches;
- The effect of different structural configurations and types; and
- The relationships between the response of SDOF and MDOF systems.

A relational database is utilized in this project to carry out the different demand evaluation studies. A general description of the database is provided in Section 2.9.

2.3 GROUND MOTION PARAMETERS

As it is shown in Figure 2.1, the focus of this study is on the dynamic response of regular frames subjected to ordinary ground motions (the set of ordinary ground motions used in this project is described in Chapter 3). The relational database utilized in this study includes information on relevant ground motion parameters necessary to relate ground motion characteristics, such as intensity and frequency content, to structural response. Ground motion parameters and characteristics stored in the database include:

- Moment magnitude
- Closest distance to the fault rupture zone
- Site class
- Peak values (PGA, PGV, and PGD)
- Record duration
- Strong ground motion duration
- Cut-off frequencies
- Fault mechanism

Spectral response quantities, i.e., spectral acceleration, velocity and displacement for a SDOF system with 5% mass proportional damping are also stored in the database.

2.4 STRUCTURAL SYSTEMS

This study focuses on the seismic demand evaluation of nondeteriorating regular-moment-resisting-frame systems. Nonlinear behavior at the component level is modeled by using rotational springs to represent the global cyclic response under the action of earthquake loads. Three different hysteretic models are used: peak-oriented, bilinear, and pinching. Figure 2.2 presents a description of the hysteretic rules of these models. Although engineering demand parameters for these three types of hysteretic models are stored in the database, the emphasis of this work is placed on the peak-oriented hysteretic model, which has stiffness-degrading properties that resemble those exhibited by many reinforced concrete components. The sensitivity of demands to different types of hysteretic models is discussed in Chapter 7.

In reality, structures are complex three-dimensional systems that are subjected to complex seismic excitations in different planes. Although it would be ideal to perform seismic demand studies by considering three-dimensional effects in the ground motion excitation and the structural system, improved models and a better understanding of structural behavior are required to accomplish this objective. In addition, three-dimensional models become a critical issue for structural systems with severe irregularities in plan where a simplified two-dimensional model would not capture the most important dynamic response characteristics of the system. Since this study focuses on seismic demand evaluation of regular frames, two-dimensional models are used. For regular structures, the properties of a complex three-dimensional system can be condensed into a simplified two-dimensional model that is adequate to capture the global response (deformation, strength, and energy demands) of the real system. As shown by Seneviratna and Krawinkler (1997) for regular frames, simplified procedures can be developed to estimate local response parameters, e.g., beam rotations, from a global parameter such as the roof drift angle. In the development of these procedures, special attention should be given to the uncertainty introduced by modeling assumptions, which can be particularly important for the case of local response parameters.

The objective of this study is to carry out demand evaluation of relevant EDPs for damage assessment. Therefore, the need for generality of the results, and hence, of the conclusions becomes a critical issue. The structural frame models are not intended to represent a specific structure, for which the results from the analyses are a function of a particular system. Instead, regular frames are modeled by using two-dimensional generic one-bay frames for which the sensitivity of results to different strength and stiffness properties can be readily evaluated. However, the latter statement implies that two-dimensional generic frames are able to capture the behavior of more complex two-dimensional configurations. In order to assess the effectiveness of using a one-bay generic frame to represent the behavior of a multi-bay frame, a limited study was performed using the SAC LA9-M1 model (Gupta and Krawinkler, 1999). The results show that in general one-bay generic frames are adequate to capture the global behavior of a multi-bay frame. This study is discussed in detail in Chapter 8.

In this research study, the demand parameters of interest are those that correlate best with structural, nonstructural, and contents damage at performance levels related to direct dollar losses and downtime. At these performance levels, severe cyclic deterioration is not expected; thus, nondeteriorating models are deemed to be appropriate to model the cyclic load-deformation behavior of structural components. Cyclic deterioration issues, which are outside the scope of this report, are addressed in a parallel research study (Ibarra et al. 2002).

2.4.1 Base Case Regular Frame Models Used in This Study

The core of the analysis and evaluation is performed by using a family of one-bay frames denoted as base case regular frames. These base cases consist of frames with number of stories, N, equal to 3, 6, 9, 12, 15, and 18, and fundamental periods, T_1, of 0.1N and 0.2N, which are considered to be reasonable bounds for reinforced concrete and steel-moment-resisting frames, respectively (Figures 2.3 and 2.4). The main characteristics of this family of structures are as follows:

- The frames are two dimensional;
- The same mass is used at all floor levels;
- One-bay frames have constant story height equal to 12′ and beam span equal to 24′;
- Centerline dimensions are used for beam and column elements;
- The same moment of inertia is assigned to the columns in a story and the beam above them;
- Relative stiffnesses are tuned so that the first mode is a straight line (a spring is added at the bottom of the first-story columns to achieve a uniform distribution of moments of inertia over the height, see Appendix A);
- Absolute stiffnesses of beams and columns are tuned such that T_1 = 0.1N or 0.2N;
- Beam-hinge models (plastification occurs at the ends of the beams and the bottom of the first-story columns; see Figure 2.5);
- Frames are designed so that simultaneous yielding is attained under a parabolic (NEHRP, k=2) load pattern;
- Hysteretic behavior at the component level is modeled by using a peak-oriented model with 3% strain hardening in the moment-rotation relationship;
- Cyclic deterioration is ignored;
- The effect of gravity load moments on plastic hinge formation is not included;
- Global (structure) P-delta is included (member P-delta is ignored); see Section 7.4;
- Axial deformations and M-P-V interaction are not considered;
- The effect of soil-foundation-structure interaction is neglected; and
- For the nonlinear time history analyses, 5% Rayleigh damping is assigned to the first mode and the mode at which the cumulative mass participation exceeds 95%.

Static and modal properties of this family of frames are detailed in Appendix A.

2.4.2 Variations to the Basic Regular Frames

The base cases used in this report are modified to study the sensitivity of response parameters and patterns of behavior to structural properties. The main variations to the base cases include:

- Different hysteretic behavior (peak-oriented, pinching and bilinear);
- Strain hardening in the moment-rotation relationship at the component level (0% and 3%);
- Structure P-delta effects (where the use of the pushover analysis is illustrated in order to assess potential stability problems in frames due to P-delta);
- Additional strength and stiffness provided by elements that do not form part of the moment-resisting frame;
- Story strength distribution based on different design load patterns (parabolic, triangular, and uniform, including random overstrength);
- Beam moments due to gravity loads; and
- Various “failure” mechanisms (beam-hinge and column-hinge models).

A summary of the results for these modified generic frame models is presented in Chapter 7.

2.5 EDPS RELEVANT FOR THE PERFORMANCE ASSESSMENT OF REGULAR FRAMES

The main EDPs evaluated in this report are those that correlate best with decision variables such as direct dollar losses and length of downtime (since cyclic deterioration is not studied in this project, the limit state of collapse is not of concern except for cases where structure P-delta alone causes dynamic instability of the response). Because regular frames are the lateral-load-resisting system of interest in this study, the most relevant EDPs should be those that encompass structural, nonstructural, and contents damage and correlate best to the performance assessment of this type of system. A comprehensive list of EDPs obtained from nonlinear time history analyses that are included in the database is presented in Appendix B. However, throughout this report, the discussion of seismic demand evaluation issues is limited to a small number of EDPs. The following EDPs are the primary ones used for seismic demand evaluation of regular frames:

- For structural damage: roof drift, story drifts, story ductilities, plastic beam rotations, story shears, story overturning moments, input energy, and hysteretic and damping energy
- For nonstructural damage: story drifts, absolute floor acceleration, and velocities

- For contents damage: floor accelerations and velocities

2.6 TIME HISTORY ANALYSES AND REPRESENTATION OF RESULTS

The basic analysis approach used in this project consists of performing nonlinear time history analyses for a given structure and ground motion, using the DRAIN-2DX computer program (DRAIN-2DX, 1993). Although DRAIN-2DX has several limitations (e.g., it does not update the geometric stiffness matrix in a time history analysis, it does not incorporate member P-delta, and it does not take into account large displacement effects), it is deemed to be an appropriate analytical tool for this project since the limit states of primary interest are those of direct losses and business interruption, where very large displacements are not of primary concern (except for cases in which structure P-delta effects become important and a state of dynamic instability is approached). A pilot study was performed with the OpenSees program (OpenSees, 2002), using a large displacement option, which did disclose that large displacement effects do not significantly affect the response even when dynamic instability is approached (Adam and Krawinkler, 2003).

The control parameter used to "scale" the ground motion intensity for a given structure strength, or to "scale" the structure strength for a given ground motion intensity, is the parameter $[S_a(T_1)/g]/\gamma$, where $S_a(T_1)$ is the 5% damped spectral acceleration at the fundamental period of the structure (without P-delta effects), and γ is base shear coefficient, i.e., $\gamma = V_y/W$, with V_y being the yield base shear (without P-delta effects). The parameter $[S_a(T_1)/g]/\gamma$ represents the ductility-dependent strength reduction factor (often denoted as R_μ), which, in the context of present codes, is equal to the conventional R factor if no overstrength is present. This parameter identifies the intensity of the ground motion (using $S_a(T_1)$ as the ground motion intensity measure) relative to the structure base shear strength. Unless (1) gravity moments are a significant portion of the plastic moment capacity of the beams, (2) there are considerable changes in axial loads due to overturning moments as compared to the gravity axial loads in columns, (3) large displacement effects become important (the latter case has not been encountered in this study), the use of $[S_a(T_1)/g]/\gamma$ as a relative intensity measure can be viewed two ways: either keeping the ground motion intensity constant while decreasing the base shear strength of the structure (the R-factor perspective), or keeping the base shear strength constant while increasing the intensity of the ground motion (the [Incremental Dynamic Analysis] IDA perspective, Vamvatsikos and Cornell, 2002).

In the analysis process for a given structure and a given ground motion, the value of $[S_a(T_1)/g]/\gamma$ is increased (in the actual execution of analyses, $S_a(T_1)$ is kept constant and γ is decreased) in small increments of 0.25 until either a value of 15 is reached or dynamic instability is imminent. For each increment, a dynamic analysis is performed and all EDPs listed in Appendix B are stored in the relational database to allow flexibility of data manipulation in different formats and domains. The basic graphical communication scheme for a given structure and a set of 40 ground motions is as shown in Figure 2.6. The relative intensity $[S_a(T_1)/g]/\gamma$ usually is plotted on the vertical axis, and the selected EDP is plotted on the horizontal axis, either without normalization (IDA domain, for which $S_a(T_1)$ is plotted on the vertical axis) or normalized by an appropriate ground motion parameter (such as spectral displacement, $S_d(T_1)$, divided by structure height, H, if the EDP is a drift angle). In the latter representation, a vertical line implies that the value of the EDP increases linearly with the ground motion intensity level $S_a(T_1)/g$ (or with the inverse of the base shear strength, $1/\gamma$).

A list of parameters is shown in the second line of the title of each graph to characterize the structural system under consideration. A description of these parameters is shown next:

- Number of stories, N = 3, 6, 9, 12, 15, and 18.
- Fundamental period, T_1 = 0.1N and 0.2N.
- Percent of critical damping, ξ (assigned to the first mode and the mode at which the total mass participation exceeds 95%).
- Base shear strength, $\gamma = V_y/W$ (when applicable, e.g., Figure 2.6(b)).
- Hysteretic behavior: peak-oriented, bilinear, and pinching. Rotational spring elements with the aforementioned hysteretic rules were incorporated in DRAIN-2DX (Krawinkler et al., 1999).
- Elastic first-story stability coefficient, θ ($\theta = P\delta_{s1} / V_1 h_1$, where P is the axial load in the first-story columns, δ_{s1} and V_1 are the first-story drift and shear force, respectively, and h_1 is the first-story height. P is the dead load plus a live load equal to 40% of the dead load).
- "Failure" mechanism (BH-beam hinge and CH-column hinge).

- Stiffness pattern (K_1-straight line first mode).
- Strength design load pattern (S_1-parabolic, S_2-triangular, S_3-uniform).
- Ground motion record set.

The same data as in Figure 2.6(a), but in the IDA domain, are shown in Figure 2.6(b). Representation in the IDA domain implies that the strength of the structure, i.e., γ, is given. For the example shown, γ is equal to 0.10. The EDP on the horizontal axis, in this case the maximum story drift angle over the height, is presented in the non-normalized domain. Such a representation pertains to a structure of specified base shear strength, and permits inspection of absolute (non-normalized) EDPs. The inherent assumption is that the ground motions, whose intensities are incremented as shown on the vertical axis, are representative for the full range of intensities ($S_a(T_1)$) for which the data are shown. This assumption becomes very questionable for large $S_a(T_1)$ values (see Chapter 3).

Graphs of the type presented in Figure 2.6, which include statistical measures of the type summarized in Section 2.7, constitute the departure point for the evaluation of demand parameters. IDA curves can be derived directly from graphs of the type represented in Figure 2.6(a) by assigning a given value of γ to the structure and multiplying the normalized EDP values by $S_d(T_1)/H = S_a(T_1)T_1^2/(4\pi^2H)$. For instance, if $S_a(T_1)$ is given by the UBC 1997 ground motion spectrum for site class D, seismic zone 4, for the family of generic structures used in this project the previous relationship becomes:

$$S_d(T_1)/H = 0.748\frac{T_1^2}{N} \quad \text{for } 0.12 \text{ sec} \le T_1 \le 0.58 \text{ sec} \tag{2.1}$$

and

$$S_d(T_1)/H = 0.0435\frac{T_1}{N} \quad \text{for } T_1 > 0.58 \text{ sec} \tag{2.2}$$

Thus, the latter two equations can be used to estimate absolute values of the EDPs if the system is subjected to a ground motion hazard level represented by the UBC 1997 site class D ground motion spectrum.

2.7 STATISTICAL EVALUATION OF ENGINEERING DEMAND PARAMETERS

2.7.1 Counted and Computed Statistics

Throughout this study, unless otherwise specified, a lognormal distribution is assumed for the different EDPs given IM ($S_a(T_1)$ is used as the primary intensity measure). There are two basic approaches that can be utilized to provide central values and measures of dispersion once a lognormal distribution is assumed (in this report, dispersion refers to the standard deviation of the natural logarithm of the values). The first approach is computed statistics, for which the median of the EDP (the EDP is denoted as *x*) is estimated by computing the geometric mean of the data:

$$\breve{x} = \exp(\overline{\ln x}) \qquad (2.3)$$

where $\overline{\ln x}$ is the mean of the natural logarithm of the data.

The standard deviation of the natural log of the values is computed by:

$$\sigma_{\ln x} = \sqrt{\sum_{i=1}^{n} \frac{(\ln x_i - \overline{lnx})^2}{n-1}} \qquad (2.4)$$

The second approach is denoted as counted statistics, where values are sorted from smallest to largest. For a set of 40 data points, the average between the 20th and 21th sorted values becomes the median, the average between the 6th and 7th sorted is the 16th percentile, and the 84th percentile is the average between the 33th and 34th sorted values. In this case, the standard deviation of the natural logarithm of the values is estimated by using either the 16th or the 84th percentile (see Figure 2.7, in which a statistical evaluation of the response of an N = 12, T_1 = 1.2 s system is illustrated). If the 84th percentile is used, x_{84}, the standard deviation of the natural logarithm of the values is given by:

$$\sigma_{\ln x} = \ln(\frac{x_{84}}{\breve{x}}) \qquad (2.5)$$

Figure 2.7(b) shows the standard deviation of the natural logarithm of the normalized maximum roof drift angle for a wide range of relative intensities. When the response is elastic (or slightly inelastic, $[S_a(T_1)/g)]/\gamma$ in the order of 1.0), a small dispersion is caused by higher modes. As the relative intensity increases, the dispersion also increases. For large relative intensities, the dispersion is larger, for it is caused by both higher modes and period-elongation effects. It can be seen in Figure 2.7(b) that differences between the curve based on the 16th percentile and the one based on the 84^{th} percentile are not significant. In general, this pattern is observed for the complete family of structures and various EDPs, so dispersion values in this study are reported based upon 84^{th} percentiles.

As stated above, in this study the standard deviation of the natural logarithm of the data is used as the primary measure of dispersion, which is close to the coefficient of variation (C.O.V.) for values smaller than 0.30.

Figure 2.8 illustrates the differences between computed and counted statistical values. The statistical results depicted in Figure 2.8(a) are counted statistics, while the ones shown in Figure 2.8(b) are computed statistics. The differences between counted and computed statistics generally are found to be small. Because counted statistics allow a more consistent and complete statistical evaluation of results when data points are missing (e.g., "collapse" cases due to P-delta effects), counted statistics are used throughout this study in the evaluation of the seismic response of regular frames. An example of missing data is shown in Figure 2.9, in which less than 50% of the responses to individual ground motion records "survive" relative intensities greater than 7.

2.7.2 "Vertical" and "Horizontal" Statistics

Statistical information necessary to understand and quantify the behavior of structural systems can be presented in different formats depending upon the objective. For instance, if the issue is damage assessment, for which it is important to evaluate the distribution, central value and/or dispersion of an EDP given an IM, "horizontal" statistics are computed (Figure 2.10(a)). However, if the issue is conceptual design where the designer desires to find the global strength required to limit the value of an EDP to a certain quantity, "vertical" statistics are required (Figure 2.10(b)). "Vertical" statistics are also used to quantify the ground motion intensity (or relative intensity) at which a system approaches the "collapse" limit state given a ground motion input. The terms "horizontal" and "vertical" are relative, so the previous information presupposes that EDPs are plotted on the horizontal axis and the IM (or relative intensity) on the vertical axis. Most of the work involved in this project is concerned with damage/loss evaluation, so the focus is on horizontal statistics. However, the relational database has data on IM-EDP relationships stored at closely spaced points to allow the calculation of both “horizontal and vertical statistics by linear interpolation between data points.

2.7.3 Number of Records Required To Provide a Specified Confidence Level in the Statistical Results

Statistical results are used to characterize the sample of a given population by providing representative parameters such as a central value and a measure of dispersion. However, there are confidence levels associated with the aforementioned results. For example, in this study, the distribution of an EDP given an IM provides an estimate of central value for the EDP and a measure of dispersion, which is due to the uncertainty in the frequency content of the ground motions. However, there is uncertainty associated with these estimates that is indirectly quantified as a function of the number of data points evaluated. This quantification can be expressed in the form of confidence levels, for which a value such as the median of the data points is estimated within a given confidence band. In this study, the bulk of the seismic demand evaluation is performed using 40 ordinary ground motions, which provides estimates of the median that are within a one-sigma confidence band of 10% as long as the standard deviation of the natural logarithm of the EDP given IM is less than $0.1\sqrt{N} = 0.63$, where N is the number of records.

2.8 DATABASE MANAGEMENT SYSTEM FOR SEISMIC DEMAND EVALUATION

As discussed in the previous sections, the number of variables involved in the seismic demand evaluation process requires the use of a data management system that provides both versatility and flexibility in the evaluation of results. For this purpose, a Microsoft Access relational database has been used in this study. The entity-relationship model for the database is presented in Figure 2.11 (an entity-relationship model constitutes a graphical representation conventionally used to illustrate the organization of a relational database). The different entities shown in the diagram correspond to physical tables in the database. The lines joining the entities describe the different relationships between them. In this case, the database is organized in different tables, where the ground motion properties, structural properties, and EDPs described in Sections 2.3–2.5 are stored:

- Ground motion properties: Tables describing ground motion properties such as moment magnitude, closest distance to the fault rupture plane, peak values (PGA, PGV, PGD), record length, strong motion duration, cut-off frequencies, fault mechanism and site class;
- Elastic spectral values: Tables including spectral acceleration, velocity, and displacements for a SDOF oscillator with 5% damping;
- Structural properties: Tables describing the different models used for seismic demand evaluation analyses. Each table has a set of attributes that correspond to the properties of the models;
- Structural response: Tables where response information (EDPs) is stored. Response tables are subdivided into:
  - Global response parameters: story deformations and ductilities, residual drifts, floor accelerations and velocities, story shears, story overturning moments, damping energy dissipated and input energy;
  - Local response parameters for spring elements: total and plastic rotations, cumulative plastic rotation ranges, number of inelastic excursions, residual rotations, moments, and hysteretic energy dissipated; and
  - Response parameters for elastic columns: moments, shears, and axial loads.

Relationships across tables allow the calculation of relationships among seismic demand variables and the extraction of information in a format useful for the statistical evaluation of EDPs similar to the results presented in Figure 2.6. For most of the seismic demand evaluation carried out throughout this study, information is usually retrieved by performing cross-tab queries involving the various tables described in the previous paragraph.

2.8.1 Versatility and Flexibility of the Database

The relational database can be utilized to evaluate IM-EDP relationships such as the ones illustrated in Figure 2.6. In this figure, normalized IM and normalized EDP values are calculated in a format useful for statistical evaluation by using the database. The normalization values help in relating MDOF properties and responses to SDOF baseline information such as elastic spectral values. The flexibility of the database can be further illustrated with the following example, which deals with the issue of testing the efficiency of two different IMs. As it is discussed in

Chapter 3, an improvement in the efficiency of IMs is desirable in order to decrease the uncertainty in the predictions and reduce the number of ground motions needed for statistical evaluation of results. Therefore, testing the efficiency of an IM is an important issue in the performance assessment methodology discussed in Chapter 1.

Figure 2.12 shows IM-EDP relationships for two different types of IM. The "conventional" IM ($S_a(T_1)$) and a "candidate" IM ($S_a(T_1) * \sqrt{\frac{S_a(2T_1)}{S_a(T_1)}}$) proposed in Cordova et. al., 2000. IM-EDP information for the conventional IM is shown in part (a), while part (b) shows the results for the candidate IM. Results for part (a) are readily obtained from the database because the analyses are carried out using the spectral acceleration at the first mode as the primary intensity measure. Since data are stored in the database at closely spaced points, it is not necessary to redo the nonlinear time history analyses to test the efficiency of the candidate IM. Instead, values for the conventional IM (given in "stripes") can be rescaled using the relational database and then linear interpolation can be used to obtain "stripes" for the candidate IM and compute statistical values of EDP given IM. A comparison of the medians and dispersions for the results presented in Figure 2.12 is illustrated in Figure 2.13.

In order to compare medians and measures of dispersion, an approximate procedure is implemented (a direct comparision cannot be readily made since different quantities are plotted in the vertical axes of Figure 2.12). In this procedure, the median $\sqrt{\frac{S_a(2T_1)}{S_a(T_1)}}$ value, which is equal to 0.69 for the set of 40 ground motions, is used to scale the vertical coordinates of the IDAs shown in Figure 2.12(b), i.e., for a given maximum story drift value, the vertical coordinate becomes $\left(\frac{1}{0.69}\right) * S_a(T_1) * \sqrt{\frac{S_a(2T_1)}{S_a(T_1)}}$. The median curve for the candidate IM obtained from the scaled IDAs is then compared to the median curve for the conventional IM (Figure 2.13(a)). Figure 2.13(b) shows a plot of the dispersion corresponding to Figure 2.12(a) and the scaled version of Figure 2.12(b). A more rigorous procedure used to assess the efficiency of the candidate IM as compared to the conventional IM is presented in Cordova et. al., 2000.

The information presented in Figure 2.13 becomes the basis for assessing the efficiency of both IMs at different relative intensities. For this particular case, IM testing becomes a trivial issue if the database management system is used.

2.8.2 Capabilities for Expansion

The relational database used in this study is organized in such a way that it is relatively easy to include additional information. For instance, if different types of ground motions are evaluated (e.g., near-fault, soft soil), it is necessary to add tables similar to the existing one for ordinary ground motions. Their spectral values can be added to the existing table in which spectral quantities are stored. If a different structural system is utilized, e.g., structural walls, it is necessary to add tables with response parameters corresponding to the EDPs of the new models. The user will have the flexibility to add information in any format he/she desires as long as the new relationships are compatible with the ones previously established.

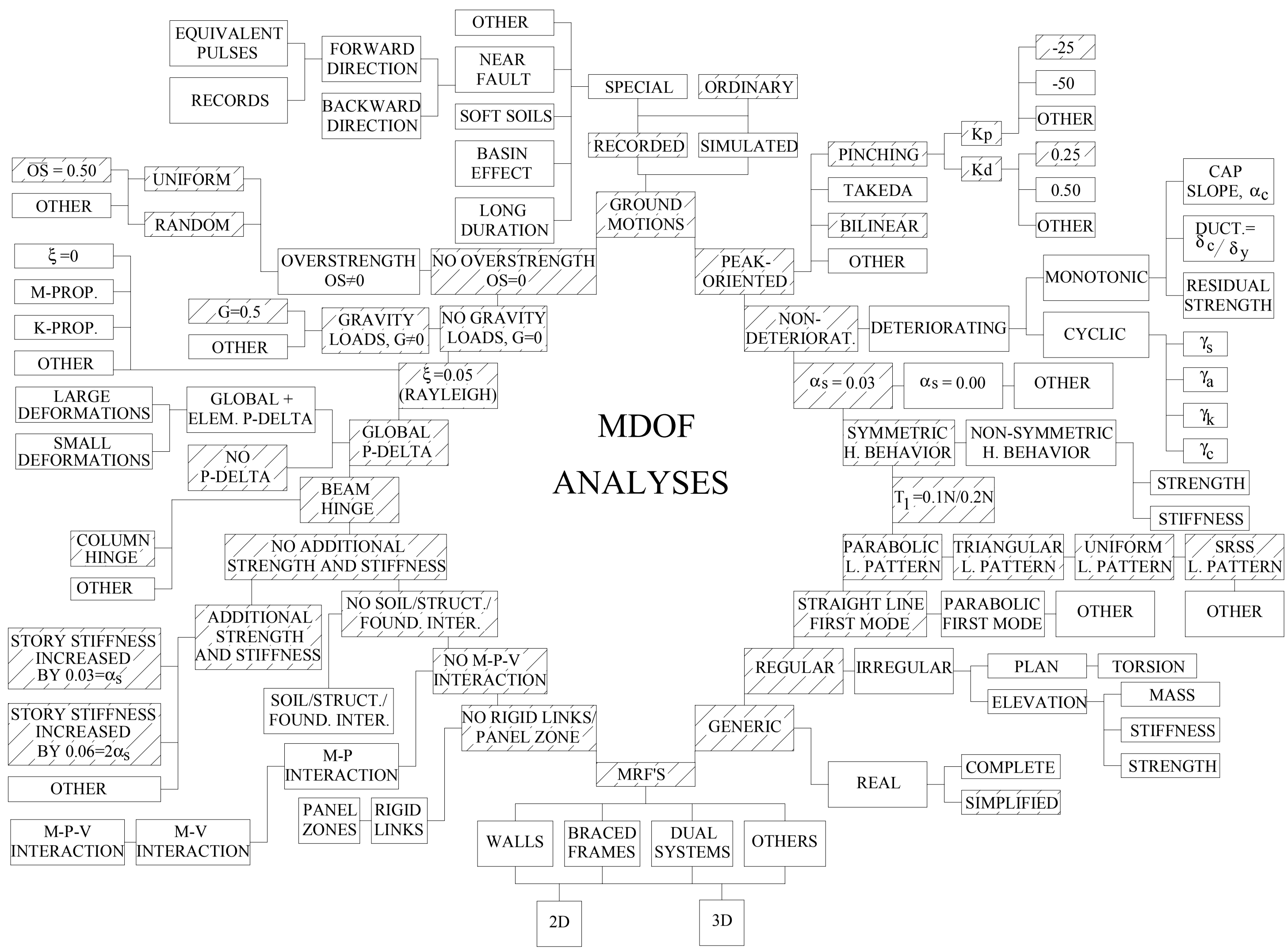

Figure 2.1 Variables in Seismic Demand Evaluation

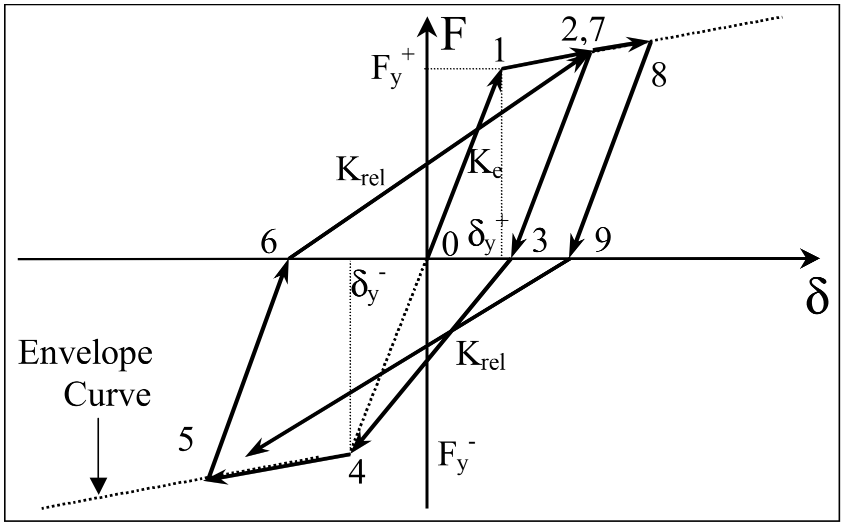

(a) Peak-Oriented Model

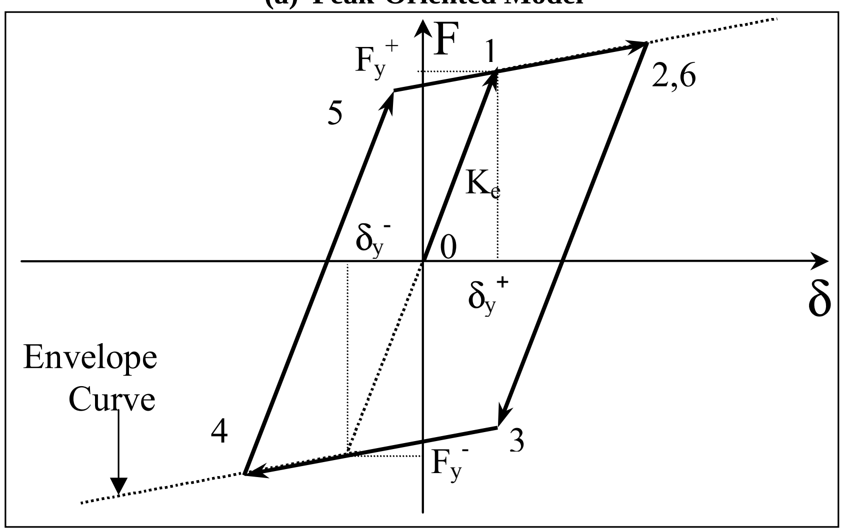

(b) Bilinear Model

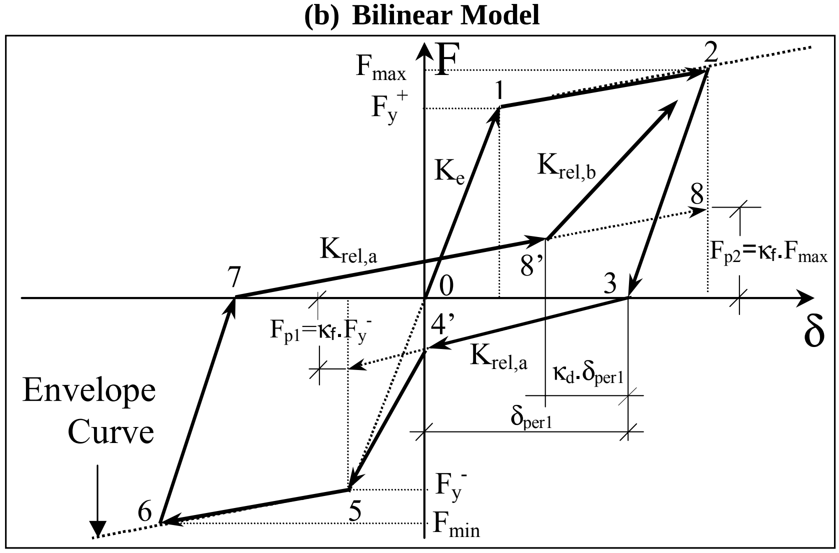

(c) Pinching Model

Figure 2.2 General Load-Deformation Behavior of Various Hysteretic Models

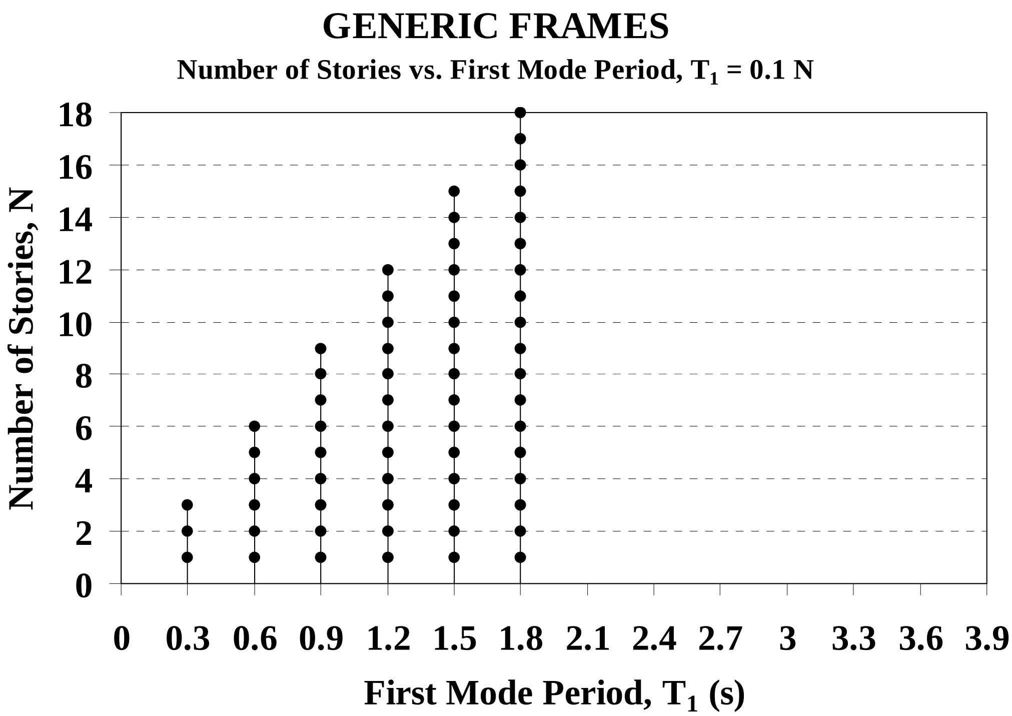

(a) $T_1 = 0.1N$

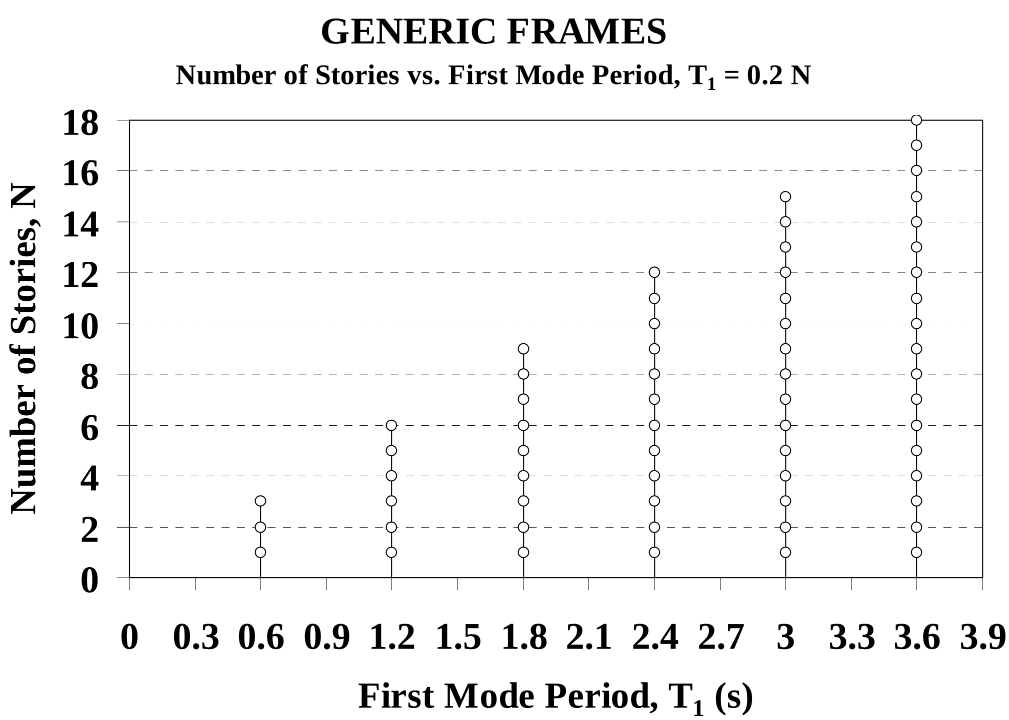

(b) $T_1 = 0.2N$

Figure 2.3 Family of Generic Frames, Stiff and Flexible Frames

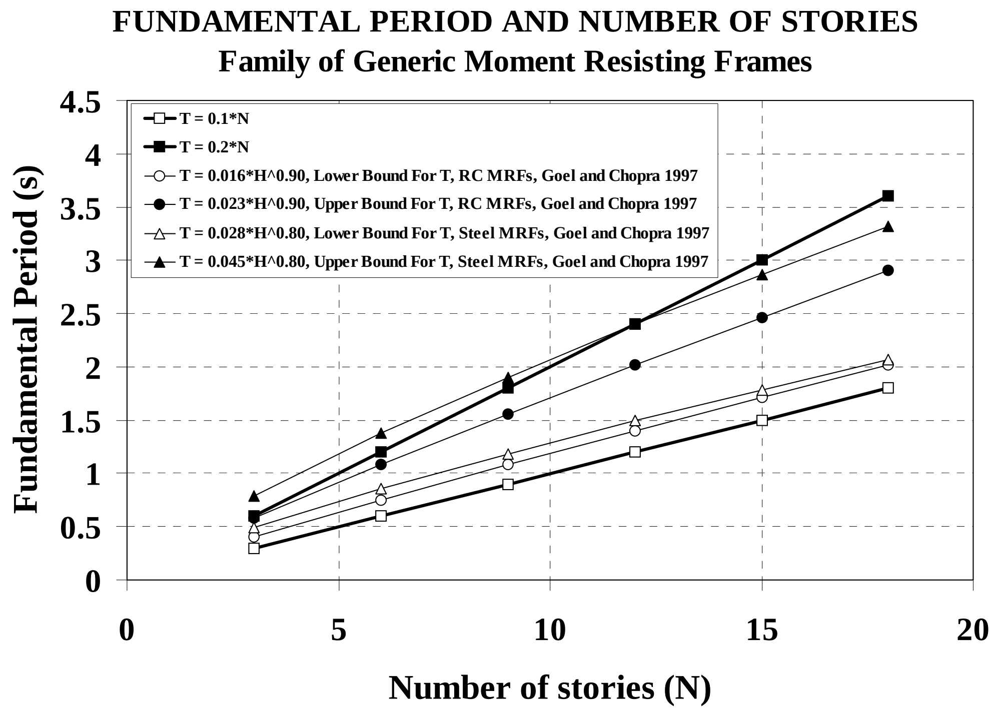

Figure 2.4 Relationship between Fundamental Period and Number of Stories

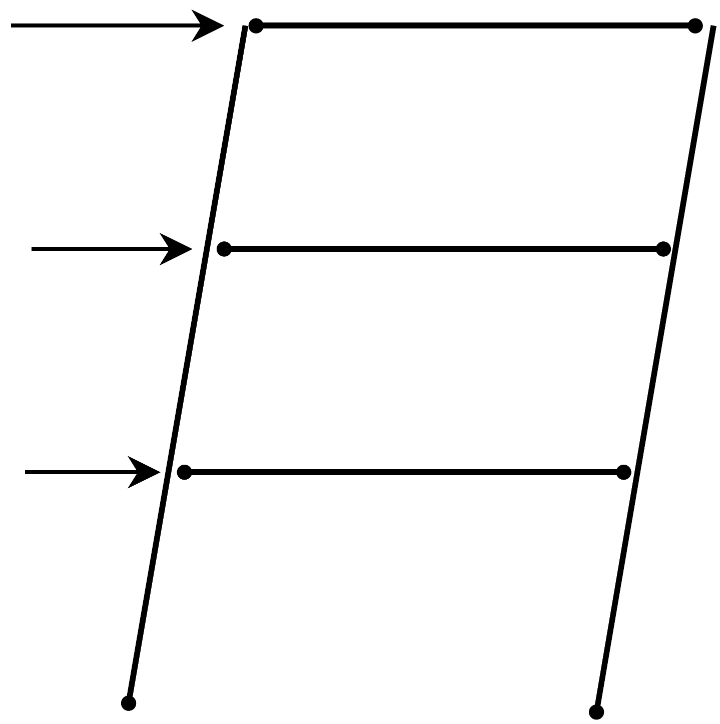

Figure 2.5 Beam-Hinge Mechanism

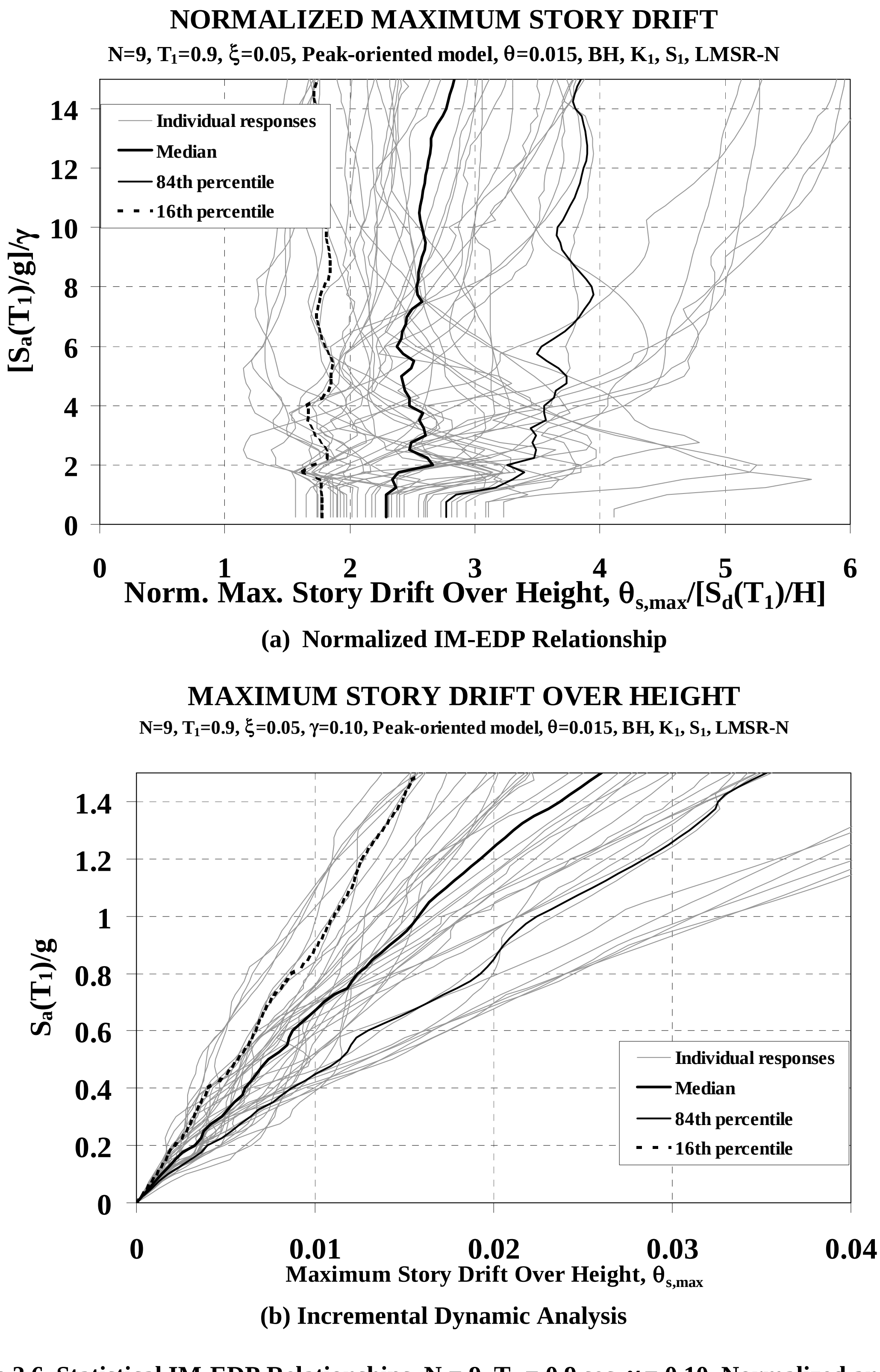

(a) Normalized IM-EDP Relationship

(b) Incremental Dynamic Analysis

Figure 2.6 Statistical IM-EDP Relationships, N = 9, T_1 = 0.9 sec, γ = 0.10, Normalized and Non-Normalized Domain

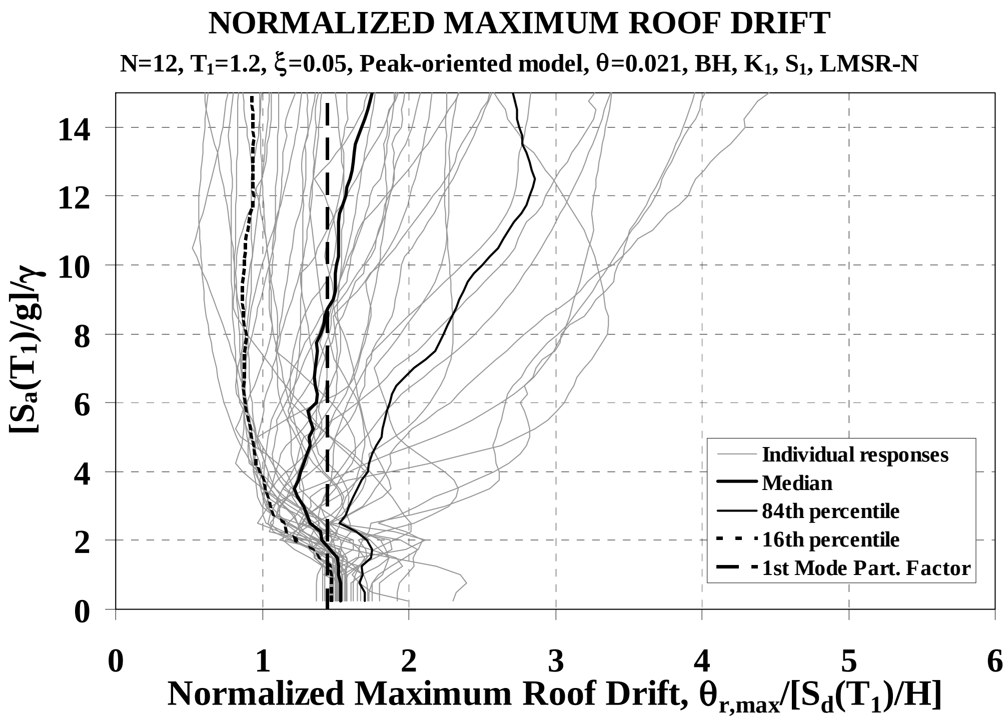

(a) Statistical Values and Individual Responses

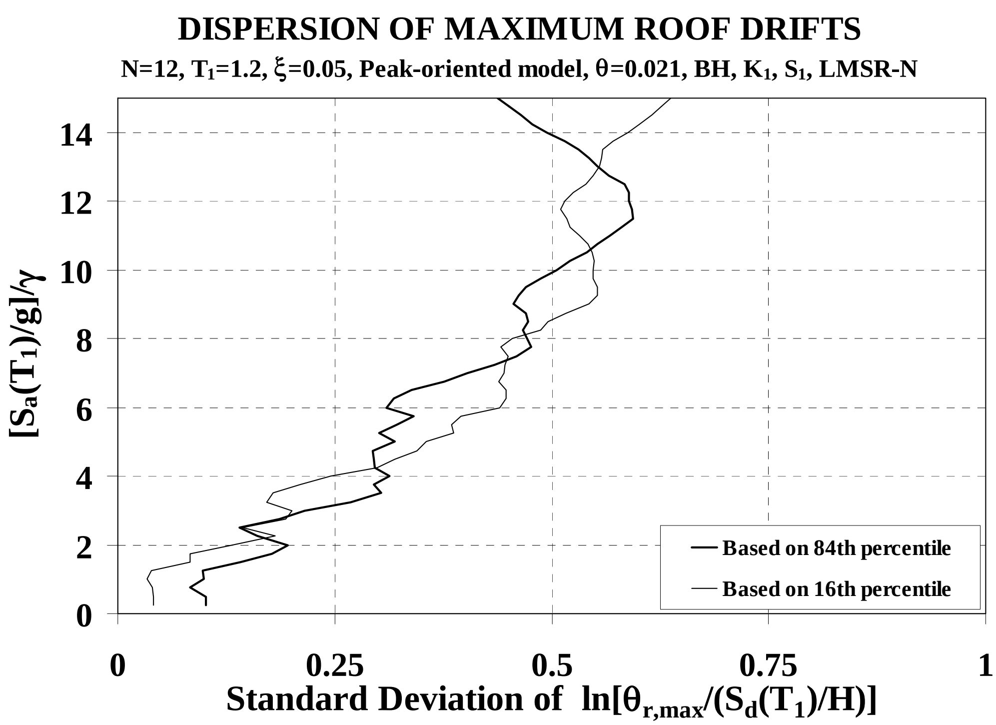

(b) Computed Dispersion Based on the 84th and 16th Percentiles

Figure 2.7 Normalized Maximum Roof Drift Angle, N = 12, T_1 = 1.2 sec

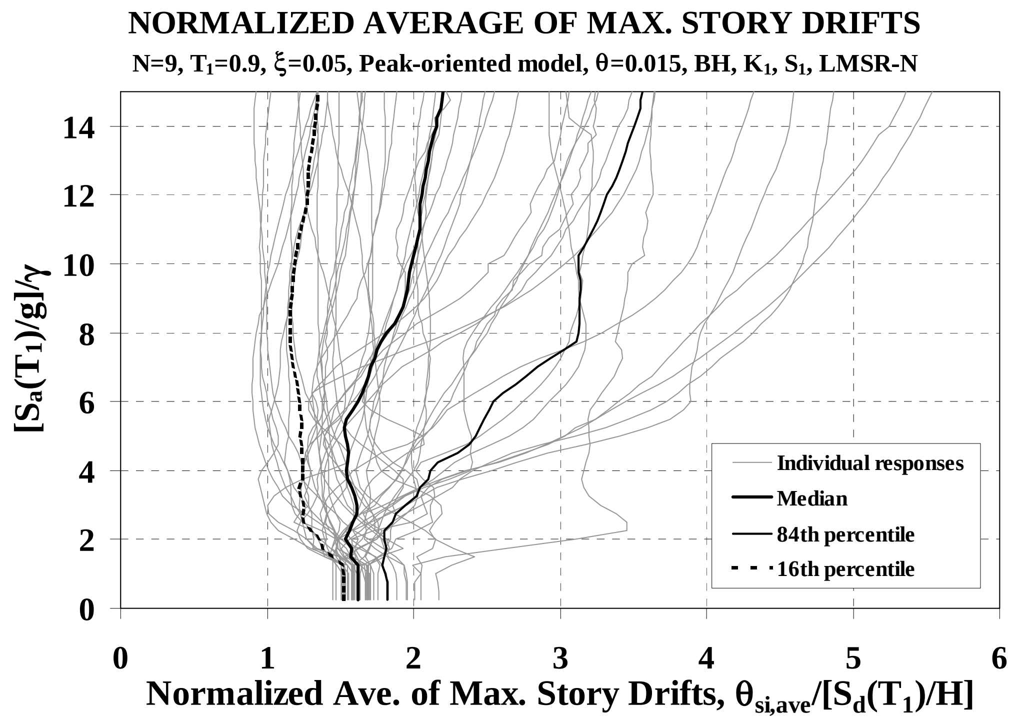

(a) Counted Statistics

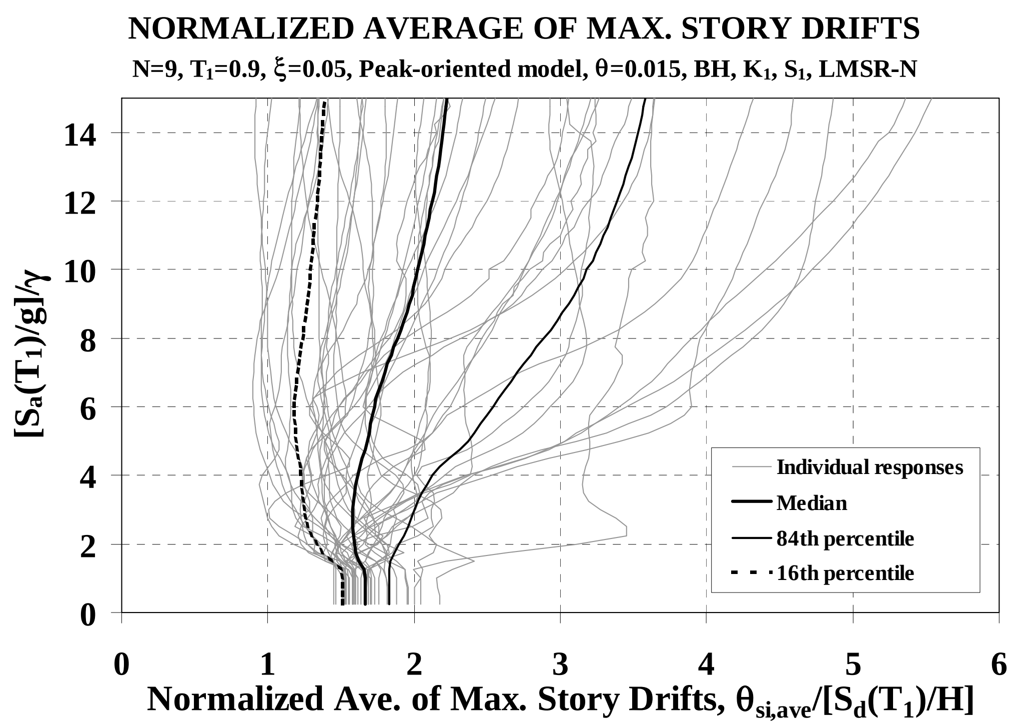

(b) Computed Statistics

Figure 2.8 Normalized Average of the Maximum Story Drift Angles, N = 9, T_1 = 0.9 sec, Counted and Computed Statistics

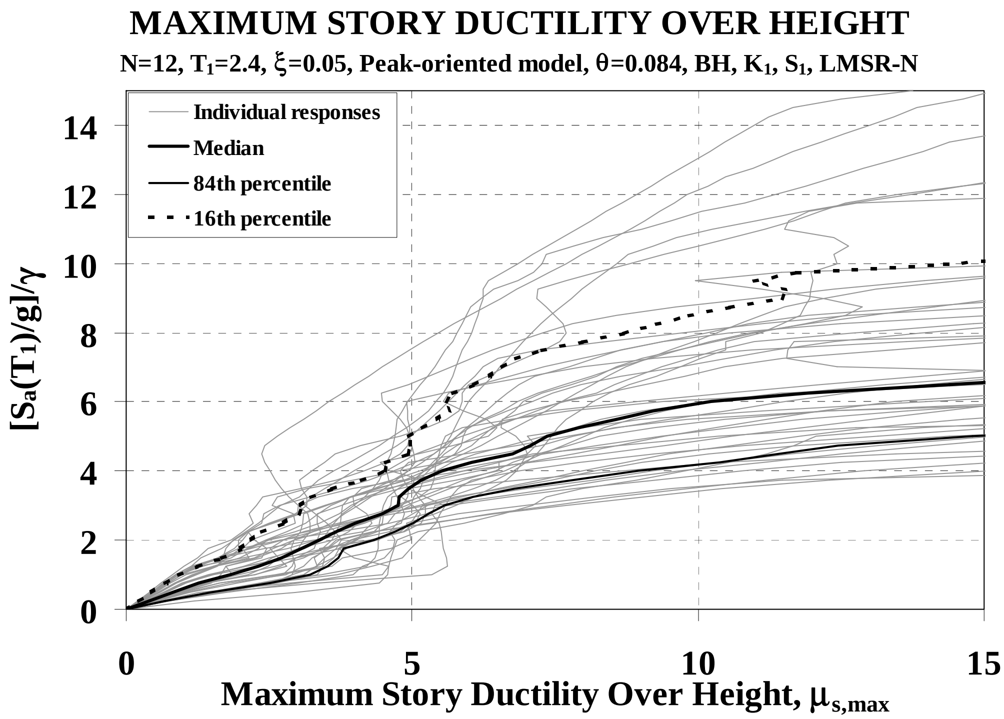

Figure 2.9 "Collapse" (Dynamic Instability) due to Structural P-delta Effects, N = 12, T_1 = 2.4 sec

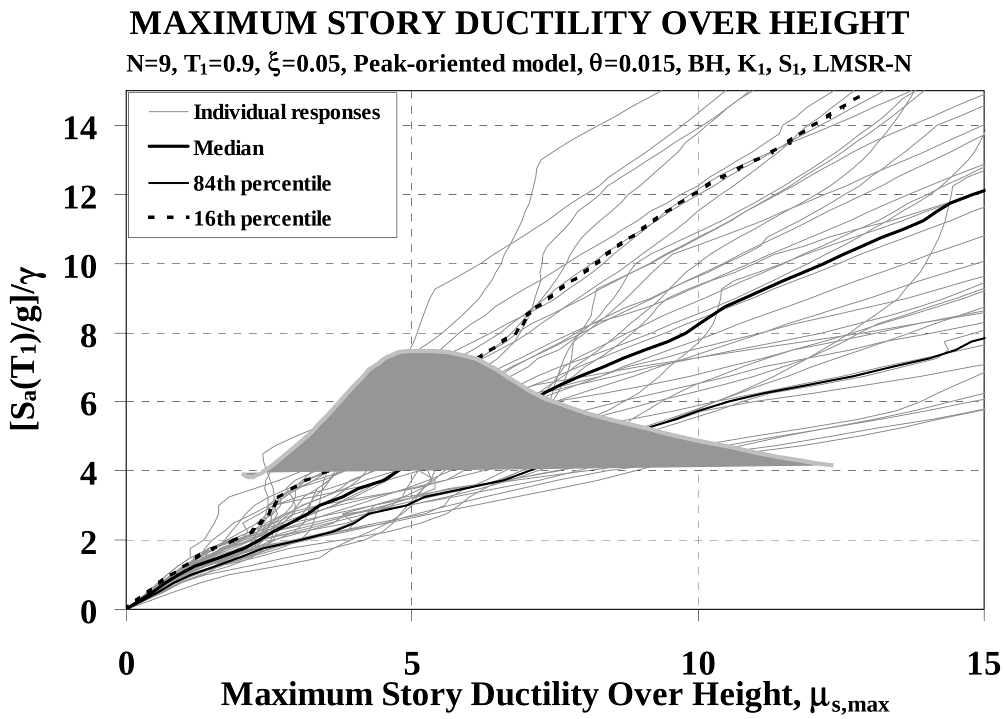

(a) "Horizontal" Statistics, Maximum Story Ductility Given Relative Intensity

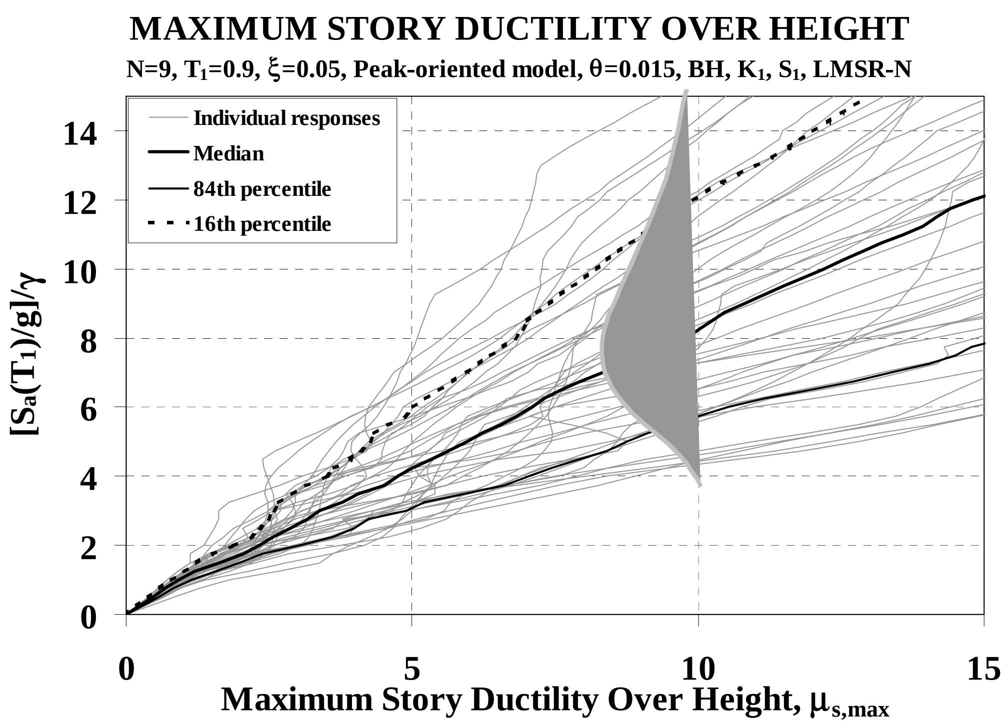

(b) Vertical Statistics, Relative Intensity Given Max. Story Ductility

Figure 2.10 Statistical IM-EDP Relationships, N = 9, T_1 = 0.9 sec, "Horizontal" and "Vertical" Statistics

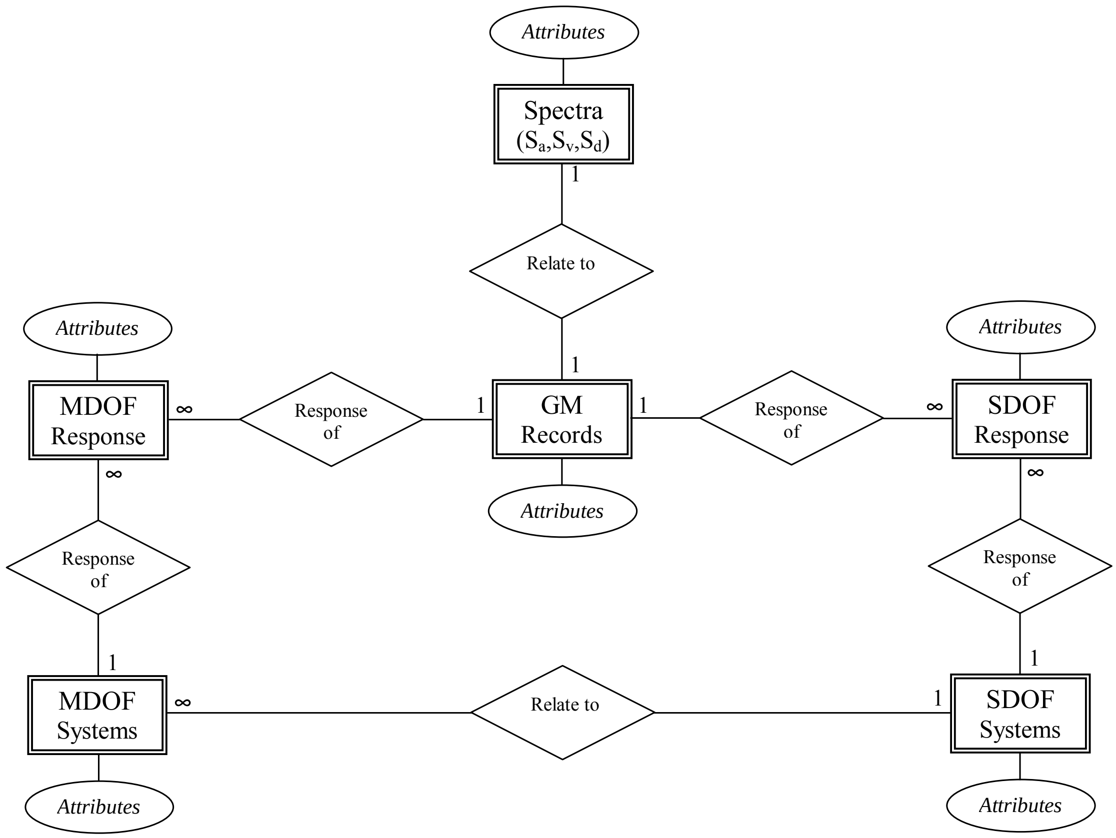

Figure 2.11 Database Entity-Relationship Model

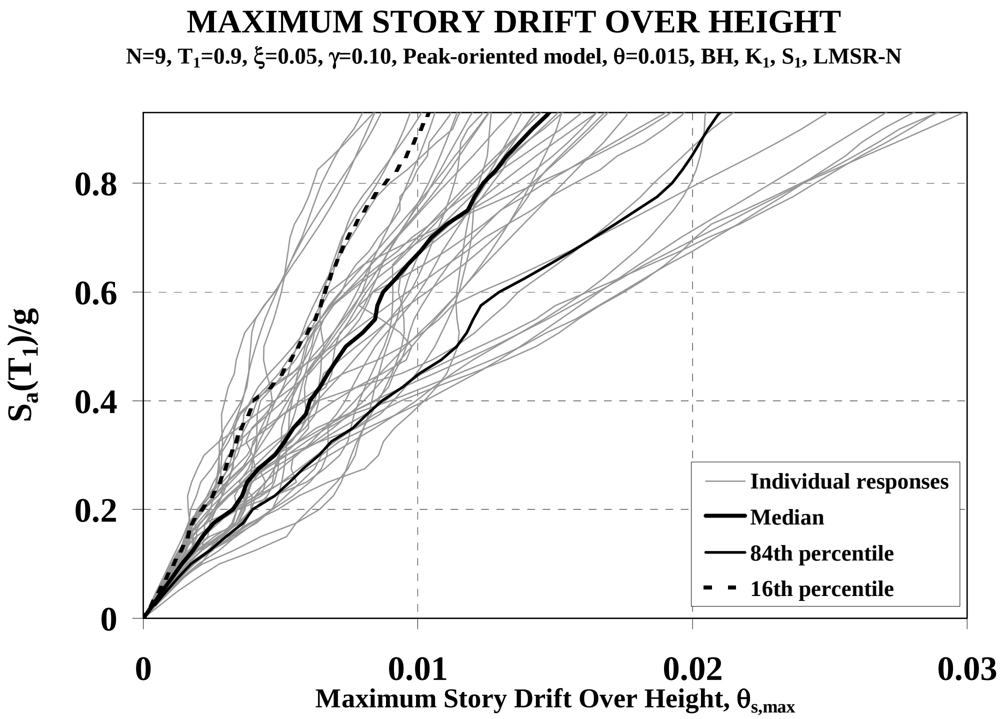

(a) “Conventional” IM

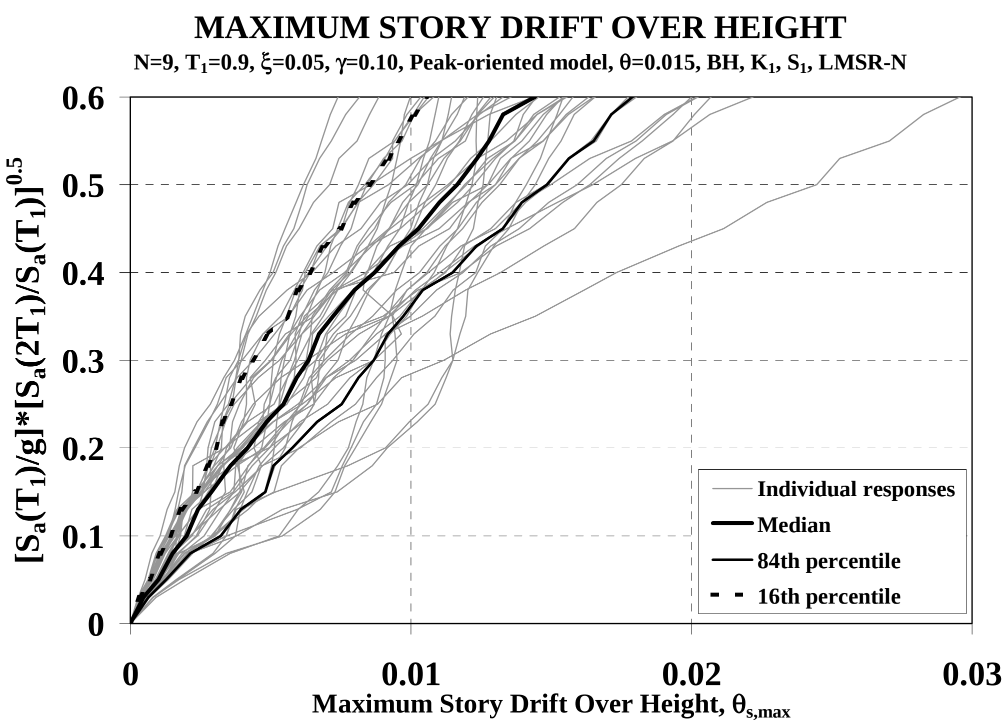

(b) “Candidate” IM

Figure 2.12 Testing the Efficiency of IMs Using the Relational Database; All Records, N = 9, T_1 = 0.9 sec

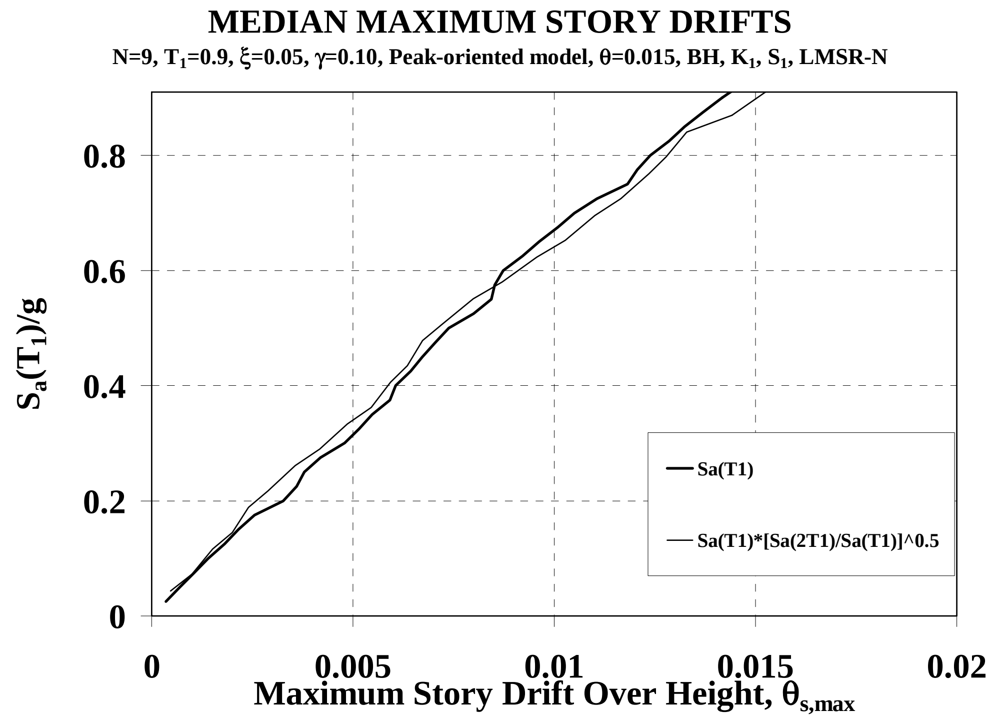

(a) Median EDP given IM

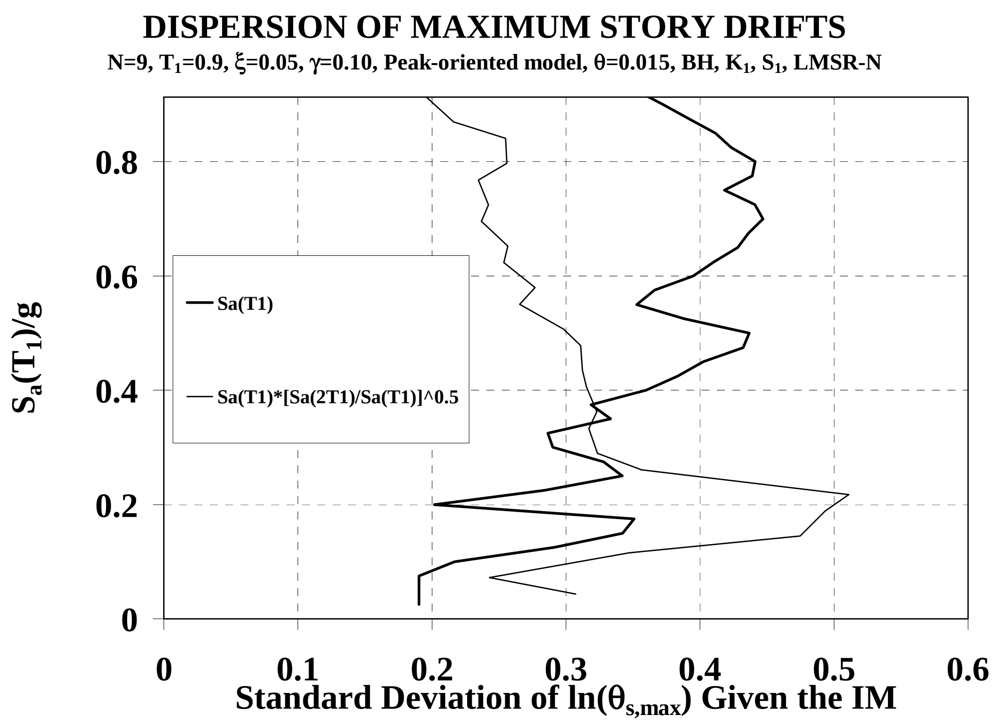

(b) Dispersion of EDP given IM

Figure 2.13 Testing the Efficiency of IMs Using the Relational Database, Median IM-EDP Relationships and Their Associated Dispersions, "Conventional" and "Candidate" IMs, N = 9, T_1 = 0.9 sec

3 Ground Motion Selection

3.1 INTRODUCTION

Ideally, assessment of demands and their uncertainties necessitates the availability of sets of acceleration time histories that represent the seismic hazard at different return periods, and describe intensity, frequency content, and duration with sufficient comprehensiveness so that central values and measures of dispersion of the demand parameters can be determined with confidence and efficiency. At this time there is no established procedure to select such sets of ground motions. However, rigorous demand prediction necessitates inelastic time history analyses, which means that records have to be selected (or generated) for the aforementioned purpose. This chapter deals with issues related to ground motion selection and its effect on the seismic demand evaluation of elastic and inelastic systems.

The accepted ground motion selection process is to perform hazard analysis on selected ground motion parameters and use the hazard information for record selection and uncertainty propagation. This process implies that the selected ground motion parameters should be capable of capturing all intensity, frequency content, and duration information that significantly affect the elastic and inelastic response of complex soil-structure systems. No single parameter is ideally suited for this purpose, and, unfortunately, the best choice of parameters depends, sometimes weakly and sometimes strongly, on the structural system and the performance level to be evaluated. This issue, which implies a search for better (more efficient) intensity measures leading to demand predictions with smaller dispersion, is one of the basic challenges of performance-based earthquake engineering. Several research efforts on this issue are in progress (Luco and Cornell, 2002; Bray et al., 2001), but at the time this study is performed, it is too early to advocate any of the alternatives under investigation.

In this research study, it is assumed that the spectral acceleration (S_a) (more specifically, the pseudo-spectral acceleration) is the primary ground motion parameter (Intensity Measure, IM), and that all other parameters that affect the seismic demands can be accounted for in the dispersion of the demand predictions. A distinction is made, however, between near-fault ground motions and ground motions recorded more than about 15 km from the fault rupture zone, for there is evidence that near-fault ground motions have distinctly different frequency and duration characteristics, particularly if they are in the forward direction of the fault rupture (Somerville, 1997). Ground motions recorded more than about 15 km from the fault rupture zone are denoted in this study as ordinary ground motions, and they are of the type on which most of the present seismic design criteria are based.

3.2 SPECTRAL ACCELERATION AS THE PRIMARY INTENSITY MEASURE

As discussed in Section 3.1, spectral acceleration (S_a) is the primary intensity measure used in this study. Hazard information on S_a is readily available, but the commitment to a single intensity measure presupposes that the computed seismic demands for MDOF systems are well correlated with this selected measure. At present time, a good choice for S_a appears to be the spectral acceleration at the first-mode period of the structure ($S_a(T_1)$), especially for systems with responses dominated by the first mode (Shome and Cornell, 1999). However, the use of $S_a(T_1)$ as the IM of interest implies that the frequency content of the ground motion cannot be considered explicitly and that the fundamental period of the structure is known. Since the frequency content depends on magnitude and distance (the extent of this dependence is the subject of the next section), biases in the evaluation of demands may be introduced by the record selection unless the records are carefully selected in narrow magnitude and distance bins that represent the disaggregated hazard at the return period(s) of interest. Even records in relatively narrow bins show a large dispersion in frequency content, as is illustrated in Figure 3.1, where 20 records with moment magnitudes between 6.5 and 7.0 and distances between 13km and 30km are used. In this example, the 20 records have an identical spectral acceleration at the period of 0.5 sec. As the figure shows, the dispersion in spectral accelerations is large for all other periods, even those very close to 0.5 sec. The consequence is that response predictions for all structures, except for an elastic SDOF system with a period of 0.5 sec, will exhibit significant scatter. The amount of scatter depends on the importance of higher mode effects (scatter for $T < 0.5$ sec) and on the extent of inelasticity, which leads to “period elongation” (scatter for $T > 0.5$ sec). This compounds the problem of ground motion selection and the assessment of uncertainties based on a single scalar intensity measure such as S_a.

3.3 ORDINARY GROUND MOTIONS

The issue of magnitude and distance dependence (or lack thereof) of ground motion characteristics (in addition to that captured by a conventional hazard analysis on spectral accelerations) is important in the context of demand assessment based on a single intensity measure, in particular for the now widely used Incremental Dynamic Analysis (IDA) (Vamvatsikos and Cornell, 2002) in which it is assumed that the same ground motions can be used to evaluate seismic demands over a wide range of hazard levels. This assumption is inherent in the process of incrementing the intensity of the same ground motion to obtain relationships between an intensity measure (e.g., first-mode spectral acceleration) and a demand parameter (e.g., story drift). When IDAs are used for specific site assessment purposes, this process can be justified if the ground motion frequency content (described by the shape of the spectrum) is not sensitive to magnitude and distance or if the structural response is not sensitive to the frequency content of the ground motions. If cumulative damage is of concern, then duration enters and insensitivity of this parameter to magnitude and distance has to be assumed as well (unless duration becomes part of the intensity measure).

In order to assess the sensitivity of ground motion characteristics (i.e., frequency content [spectral shape]) of ordinary ground motions to magnitude and distance, 80 recorded ground motions from Californian earthquakes of moment magnitude between 5.8 and 6.9 and closest distance to the fault rupture between 13km and 60km are studied. These ground motions were recorded on NEHRP site class D (FEMA368, 2000). Qualitatively, conclusions drawn from the seismic demand evaluation using this set of ground motions are expected to hold true also for stiffer soils and rock (soft-soil effects are not addressed in this seismic demand evaluation study). The records are selected from the PEER Center Ground Motion Database (http://peer.berkeley.edu/smcat/) and are classified into four magnitude-distance bins for the purpose of performing statistical evaluation within the four bins and regression analysis incorporating all records. The record bins are designated as follows:

- Large Magnitude-Short Distance Bin, LMSR, ($6.5 < M_w < 7.0$, $13 \text{ km} < R < 30 \text{ km}$),
- Large Magnitude-Long Distance Bin, LMLR, ($6.5 < M_w < 7.0$, $30 \text{ km} \leq R \leq 60 \text{ km}$),

- Small Magnitude-Short Distance Bin, SMSR, ($5.8 < M_w \leq 6.5$, 13 km < R < 30 km), and
- Small Magnitude-Long Distance Bin, SMLR, ($5.8 < M_w \leq 6.5$, 30 km ≤ R ≤ 60 km).

Additional criteria used in the selection of this set of 80 ordinary ground motions are summarized below:

- High-pass frequency, $f_{HP} \leq 0.20$ Hz
- Fault mechanism included: strike-slip, reverse-slip, and reverse-oblique
- For each station, a horizontal component of the record is randomly selected to avoid biases in the selection process
- No aftershocks are included

Figure 3.2 shows the magnitude-distance distribution of the aforementioned set of 80 ordinary ground motions, and Tables 3.1 to 3.4 list the most important properties for each one of the selected records.

The set of 80 ordinary ground motion records has strong motion duration characteristics that are not sensitive to magnitude and distance, as shown in Figure 3.3. In this context, strong motion duration is defined as the time it takes for the cumulative energy of the ground motion record to grow from 5% to 95% of its value at the end of the history (Trifunac and Brady, 1975). Therefore, ground motion frequency content (spectral shape) becomes the most relevant ground motion characteristic of interest when investigating the sensitivity of ground motion properties to magnitude and distance when S_a is used as the intensity measure. The dependence of a cumulative damage parameter such as normalized hysteretic energy, which is understood to be correlated to an “effective” strong motion duration, on magnitude and distance is studied in Section 3.3.2.

A statistical evaluation of the bins of records shows that bin-to-bin variations in spectral shapes are noticeable but not very strong. This is illustrated with the data plotted in Figures 3.4–3.6, which are obtained by scaling all ground motions to a common spectral acceleration at preselected periods (T_1 = 0.3s, 0.9s and 1.8s) and computing statistical measures for each of the four bins. In this chapter, a log-normal distribution is assumed for all response parameters of interest. The term *median* refers to the *geometric mean* of the data points (the exponential of the average of the natural log of the data points) and the term *dispersion* denotes the standard deviation of the natural log of the values (which is close to the COV for values smaller than 0.30), unless it is otherwise specified. The median spectral shapes for the four bins are comparable (Figures 3.4(a)–3.6(a)), and so are the measures of dispersion (Figures 3.4(b)–3.6(b)). For the latter purpose, the standard deviation of the natural log of $S_a(T)/S_a(T_1)$ is plotted against T/T_1. It is noted that the dispersion is rather insensitive to the magnitude-distance combination (bin) but is large at all periods $T \neq T_1$. It may be concluded that the effect of frequency content on the prediction of demands is dominated by the dispersion of spectral values rather than the median shape of the spectrum. The conclusion is that within the range of magnitude and distance covered by the four bins used in this study, the magnitude-distance dependence of the spectral shapes does not have a dominating effect.

This is not to say that a magnitude and distance dependence of spectral shapes does not exist in the range of these magnitude-distance bins. The dependence of median (or mean) spectra on magnitude and distance has been established through regression analysis in many studies. For instance, one can take the well-known Abrahamson-Silva (A-S) attenuation relationships (Abrahamson and Silva, 1997), develop scenario spectra for specific magnitude and distance combinations, define (within a preselected period range) the spectral shape by the relationship $S_a = CT^b$, and compute the exponent b (which is a measure of the rate of decay of the spectrum) by regressing $\ln(S_a) = C_0 + b*\ln(T)$ within the selected period range. Results obtained from this process are shown in Table 3.5 for Geometrix site class A-B and C-D (denoted as A-S (A-B) and A-S (C-D), respectively), using period ranges of 0.4 to 3.0 sec for soil types (A-B) and 0.6 to 3.0 sec for soil types (C-D). These period ranges are selected as representative for the "constant velocity range," which ideally should have an exponent of b = 1.0. The results are presented for two distances (R = 20 km and 35 km) and magnitudes ranging from 5.5 to 7.0. For this range, the magnitude dependence of b (i.e., of the spectral shape) is much stronger than the distance dependence. The same observation (magnitude dependence much stronger than distance dependence) applies when a larger distance range (15 km $\leq$ R$\leq$ 60 km) is used.

Compatible results are obtained when the 80 records of the four magnitude-distance bins are combined. Spectral values for a given period are regressed using the attenuation relationship $\ln(S_a) = C_0 + C_1M + C_2\ln(R)$, and the exponent b is subsequently regressed from $\ln(S_a) = C +$

b*ln(T). The least-squares method is used for the regression analyses. The corresponding values for b are also shown in Table 3.5 in the column denoted O.G.M. (Ordinary Ground Motions). Ideally, the values of b should be identical to those for Abrahamson-Silva, but they clearly are not because of the differences in the data sets used in the two cases. The differences are noticeable but are outweighed by the similarities in patterns. As for the case of the Abrahamson-Silva results, for the given magnitude-distance ranges, the magnitude dependence of b (i.e., of spectral shape) is much stronger than the distance dependence. This latter point is illustrated in Figure 3.7. Figure 3.7(a) shows the magnitude dependence of spectral shape for the set of 80 ordinary ground motions, where regressed spectra for R = 20 km are scaled to the same spectral acceleration at 1.0 sec. Figure 3.7(b) illustrates the distance dependence of spectral shape for the set of ordinary ground motions, where regressed spectra for $M_w = 6.7$ are scaled to the same spectral acceleration at 1.0 sec. The following alternative form of the regression equation was also used with the set of 80 ordinary ground motions: $\ln(S_a) = C_0 + C_1M + C_2M^2 + C_3\ln(R)$. However, the regressed spectral values (with their corresponding errors and residuals) were not sensitive to the type of regression equation utilized. The results are encouraging insofar that the selection of independent data sets (Abrahamson-Silva and O.G.M.) has led to compatible and consistent patterns.

The similarity of spectral shapes (and absolute spectral values) from different data sets can be evaluated also from the graph presented in Figure 3.8, which compares a scenario spectrum obtained from the Abrahamson-Silva attenuation relationship with the corresponding scenario spectrum obtained from regression analysis of the 80 records. Clearly, the spectra are not identical, but they are comparable and are expected to lead to qualitatively and quantitatively compatible conclusions on seismic demands. For inelastic SDOF systems, this is illustrated in the following section.

3.3.1 Effect of Magnitude and Distance Dependence of the Spectral Shape in the Demand Evaluation of SDOF Systems

3.1.1.1 Normalized displacement demands

Magnitude and distance dependence of spectral shapes is a moot issue unless it is reflected in the demand evaluation. In the SDOF domain the effects can be evaluated by considering inelastic systems, which exhibit period elongation and hence incorporate the effects of spectral shape and its dispersion at periods greater than the period associated with the intensity measure S_a. A widely used measure of inelastic SDOF response is the ratio of displacements of the inelastic and elastic systems, δ_{in}/δ_{el}, which is also equal to μ/R (in this case, $R = F_e/F_y = mS_a/F_y$). This measure is relevant for evaluating the dependence of demands on spectral shapes because δ_{el} depends only on the intensity measure S_a. For the four magnitude-distance bins, plots of median values and measures of dispersion of the ratio δ_{in}/δ_{el} versus period are presented in Figure 3.9 and Figure 3.10 for a bilinear model with 3% strain-hardening and strength reduction factors of R = 4 and 8, respectively. Except for very short-period systems (T = 0.3 sec), the median values for the four bins are similar and show no clear pattern among bins. The dispersion is large, particularly for short-period systems, and its effect on demands is judged to be as important as the relatively small differences in the median. The same observations are valid for the case of a pinching hysteretic model. Figures 3.11 and 3.12 show the median and dispersion of the ratio δ_{in}/δ_{el} versus period for the four magnitude-distance bins using a pinching hysteretic model with 3% strain-hardening, $\kappa_f = \kappa_d = 0.25$, and strength reduction factors of R = 4 and 8, respectively. The hysteretic properties and rules of the pinching model are illustrated in Figure 2.2(c).

A simplified approach to quantify differences in the ratio δ_{in}/δ_{el} among bins is to normalize the median δ_{in}/δ_{el} values for a magnitude-distance bin by the median δ_{in}/δ_{el} values for the full set of 80 ordinary ground motions. In this way, it is possible to evaluate how large the median of one magnitude-distance bin is as compared to the median of the set of 80 records, and hence, quantify differences among bins. This normalization is shown in Figures 3.13 and 3.14 for the bilinear models used in Figure 3.11. From the graphs, it can be noted that the median δ_{in}/δ_{el} values for a given magnitude-distance range (bin) are generally within 10% of the median values for the complete set of 80 records for R = 4 and 8, respectively (except in the short-period range, T = 0.3 sec, where the large magnitude bins LMSR and LMLR provide higher δ_{in}/δ_{el} values).

The results presented in the previous paragraphs were obtained for constant strength reduction factors (R). Magnitude and distance dependence of spectral shape can also be evaluated in the constant-ductility domain. In order to do so, conventional R-μ-T relationships (for constant ductility ratio, $\mu = \delta_{max}/\delta_y$) are developed for each of the four magnitude-distance bins. R-μ-T relationships are suitable for the aforementioned purpose because both R and μ are normalized quantities (independent of the intensity of the ground motion), so the effect of spectral shape (frequency content) on the response of inelastic SDOF systems can be directly assessed. Median R-μ-T relationships for $\mu = 4$ and 8, and their corresponding dispersions, are shown in Figures 3.15 and 3.16 for a bilinear model with strain hardening equal to 3%. It can be seen from the graphs that there are no clear differences among medians (or dispersions), except for the case of $\mu = 8$ (Figure 3.16 (a)), where medium-long-period systems subjected to the LMSR record set exhibit median R-values that are slightly smaller than the ones corresponding to the other three magnitude-distance ranges. The conclusion appears to be that in the constant-ductility domain, the four magnitude-distance bins selected in this study possess similar frequency content characteristics, which translates into consistent statistical evaluation (median and dispersions) of SDOF strength reduction factors required to achieve a target ductility ratio, given a structural period, T.

Perhaps a better evaluation of magnitude and distance dependence can be obtained by carrying out regressions of a demand parameter, such as ductility ratio μ, against magnitude and distance. Regression analyses with the full set of 80 records are considered to be relevant since they are not based on arbitrary decisions regarding the limits for the different magnitude-distance bins. Two regression methods were utilized: the least-squares method and the maximum-likelihood method. Both methods yielded similar results, so the least-squares method is used next for illustration.

For this record set, magnitude dependence has been shown to have a stronger effect than distance dependence; thus, examples of magnitude dependence of μ, using the 80 records of the four bins, are presented in Figures 3.17 and 3.18 (three different forms of regression equations are used and are listed in the legend of the plots). The results are for a bilinear system with strain hardening equal to 3%, periods equal to 0.9 sec and 3.6 sec, and a strength reduction factor of R = 8. In these plots, a dependence of μ on magnitude is noted, but the dependence is sensitive to the type of regression equation used, particularly if the relationships are extrapolated beyond the range of data points. An inspection shows clearly that the residuals of the data points are large, and that the patterns are not as evident as the slopes of the regressed lines seem to indicate.

3.3.1.2 Normalized maximum absolute acceleration demands

The dependence of normalized maximum absolute acceleration demands on magnitude and distance is also investigated. Maximum absolute acceleration normalized by the intensity measure S_a is deemed to be a relevant demand parameter to evaluate the sensitivity of ground motion frequency content to magnitude and distance, because it is able to capture the effects of spectral shape and its dispersion on the inelastic response of SDOF systems. For a slightly damped inelastic SDOF system with a strain-hardening ratio α and a maximum restoring force F_{max}, maximum absolute accelerations are expected to be close to $(F_{max}/W)g$, which is equal to $(S_a/R)[(1+(\mu-1)\alpha]$, or approximately equal to $(S_a/R)[(1+(R\text{-}1)\alpha]$ (for medium-long-period systems). The above relationships suggest that maximum absolute acceleration demands are not expected to be sensitive to the choice of magnitude-distance ranges (bins) since for a given R factor, the maximum absolute acceleration is a function of the ductility demand, which for this record set has been shown to be insentitive to magnitude and distance (Section 3.3.1). The latter statement is illustrated in Figures 3.19–3.21, where median normalized maximum absolute accelerations (and their corresponding dispersions) are plotted for a given R factor and periods of 0.3 sec, 0.9 sec, and 1.8 sec. Results are presented for a bilinear hysteretic model with 3% strain hardening (consistent results are obtained when using a pinching hysteretic model with $\kappa_f = \kappa_d = 0.25$ [not shown]). Differences in the median are small among sets of records and their corresponding dispersions are also relatively small (differences are still minor, but more noticeable in the short-period range). Therefore, for this record set, SDOF normalized absolute acceleration demands are slightly dependent on magnitude and distance, which is important for MDOF demand evaluation since absolute floor acceleration demands are considered relevant demand parameters for nonstructural and content damage (Section 4.4).

3.3.2 Magnitude and Distance Dependence of Cumulative Damage Parameters in the Demand Evaluation of SDOF Systems

The dependence of cumulative damage parameters on magnitude and distance is relevant for ground motion selection especially when assessment of structural damage is of concern. Damage is caused mainly by inelastic (plastic) excursions and its accumulation as the number of excursions increases. The longer the strong motion duration, the more cumulative damage is inflicted on the system. As discussed in Section 3.3, for the set of 80 ordinary ground motions used in this study, strong motion duration (defined as the time it takes for the cumulative energy of the ground motion record to grow from 5% to 95% of its value at the end of the history) is only weakly dependent on magnitude and distance. However, since cumulative damage is understood to be correlated to strong motion duration, it is necessary to investigate whether the mild dependence of strong motion duration on magnitude and distance is indeed reflected in a cumulative demand parameter such as the normalized hysteretic energy (NHE = Hysteretic Energy Dissipated/[$F_y\delta_y$]). NHE is considered to be a suitable parameter for cumulative damage evaluation since it is a function of both the structural system and the ground motion duration and has been used traditionally as an "index" for cumulative damage assessment.

In order to investigate the dependence of SDOF NHE demands on magnitude and distance for the set of 80 ordinary ground motions used in this study, NHE values are calculated for different periods (T = 0.3 sec, 0.9 sec, and 1.8 sec) as a function of the strength reduction factor R. A bilinear hysteretic model with 3% strain hardening is used (similar patterns are observed when using a pinching hysteretic model with $\kappa_f = \kappa_d = 0.25$ [not shown]). Figures 3.22–3.24 show the relationship between NHE and R for the four different bins and the aforementioned hysteretic models. Differences in the median values of NHE for a given R are noticeable, especially for T = 0.3 sec. In addition, the values of dispersion are rather large (0.45 to 0.75). Thus, the effects of magnitude and distance on the normalized hysteretic energy demands for SDOF systems are notable in the medians, but are expected to be dominated by the dispersions rather than the differences in the medians.

Since the total duration of the record is used for the time history analyses utilizing the set of 80 ordinary ground motions, it is fair to argue that NHE demands are only relevant for a bilinear hysteretic model, where NHE is directly related to the number of plastic excursions (cumulative damage). For a stiffness-degrading hysteretic model, e.g., pinching model, NHE demands are sensitive to the total duration of the record; thus, NHE is not necessarily a representative cumulative damage parameter unless it is computed for an "effective" strong motion duration of the record, which depends on both the ground motion and the structural system (Section 5.4).

An alternative way of assessing the magnitude and distance dependence of NHE demands for SDOF systems is through regression analyses. NHE demands are regressed as a function of magnitude and distance for different periods. As in the case of the ductility demands, both the least-squares and the maximum-likelihood methods are used for the regression analyses. Both methods yield similar results, and regressed lines obtained using the least-squares method are shown for illustration.

Examples of magnitude dependence of NHE, using the 80 records of the four bins, are presented in Figures 3.25 and 3.26 (the different regression equations used to fit the data are shown in the legend of the plots). The results are for a bilinear system with strain hardening equal to 3%, periods equal to 0.9 sec and 3.6 sec, and a strength reduction factor of R = 8. In these plots, a dependence of NHE on magnitude is noted, but the dependence is sensitive to the type of regression equation used, especially when the relationships are extrapolated beyond the range of data points. The residuals of the data points are large, and the patterns are not as evident as the slopes of the regressed lines seem to indicate. An example of distance dependence of NHE is shown in Figure 3.27 for the bilinear model used in Figures 3.25 and 3.26. From Figure 3.27, it can be seen that there is a mild dependence of NHE demands on distance; however, as in the case of the magnitude dependence of NHE demands, the residuals of the data points are large and the pattern is not as clear as the slope of the regressed lines shows.

3.3.3 Magnitude and Distance Dependence of Normalized Displacements in the Demand Evaluation of MDOF Systems

Magnitude and distance dependence of seismic demand parameters should be reflected not only in the response of SDOF models but also in the response of MDOF models. In addition, inelastic SDOF systems allow us to study the effect of period elongation but not the effect of higher modes in the seismic response. Therefore, MDOF systems provide us with the means to assess the sensitivity of ground motion spectral shape to magnitude and distance both to the "right" ($T > T_1$) and to the "left" ($T < T_1$) of the fundamental period (T_1) when $S_a(T_1)$ is used as the intensity measure of interest.

A pilot study was performed to evaluate the sensitivity of maximum story ductility demands over the height to magnitude and distance for a two-dimensional MDOF frame model subjected to ordinary ground motions. The model used for this purpose is an 18-story beam-hinge model with a fundamental period of 1.8 sec. An 18-story model was chosen because its response exhibits significant higher mode effects. Plastification is limited to the beam ends and the bottom of the first-story columns. The hysteretic behavior at plastic hinge locations corresponds to a bilinear hysteretic model with 3% strain hardening. This frame is subjected to the set of 80 ordinary ground motions, and statistics for each magnitude-distance bin are computed for a given strength reduction factor R. In this context, maximum story ductility over the height is defined as the maximum ratio of story drift normalized by a story yield drift computed from a pushover analysis. The strength reduction factor R is defined as $[S_a(T_1)/g]/\gamma$, where $S_a(T_1)$ is the 5% damped spectral acceleration at the fundamental period of the structure, and γ is the base shear coefficient, i.e., $\gamma = V_y/W$, with V_y being the yield base shear strength. Figure 3.28 shows median R-μ relationships for the 18-story frame subjected to the four magnitude-distance bins and the dispersion of maximum story ductility values associated with a given R-factor. R-μ relationships such as the ones illustrated in Figure 3.28(a) are equivalent to an Incremental Dynamic Analysis in which the intensity of the ground motion ($S_a(T_1)$) is increased (increase in R-factor) and the value of the demand parameter of interest is recorded (maximum story ductility over the height) for a given ground motion intensity level. Computing statistics for a given R-factor is equivalent to computing statistics for cases in which all records are scaled to the same $S_a(T_1)$.

Figure 3.28(a) shows that the median maximum story ductility demands of the 18-story frame subjected to the four magnitude-distance bins exhibit differences that vary with the R-factors. For this case of a MDOF system, the assumption of magnitude and distance independence of the response becomes questionable, particularly for highly inelastic systems. For large R-values the median maximum ductility demands are highest for the LMSR set of ground motions while the dispersions of maximum ductility demands are comparable for all bins (except the SMLR set of ground motions which exhibits larger dispersions).A comparison with SDOF system responses indicates that both period-elongation effects and higher mode effects take on a larger importance for the LMSR record bin than for the other three bins. These results, and others not shown, provide evidence that for the range of ordinary ground motions evaluated in this study ($5.8 \leq M_w \leq 6.9$ and 13 km < R ≤ 60 km), the records in the LMSR bin (Table 3.1) impose somewhat higher demands than the records in the other three bins if spectral accelerations of the first-mode period ($Sa(T_1)$) are used as the IM, i.e., all records are scaled to a common $Sa(T_1)$. Thus, there are good reasons to place emphasis on the LMSR record set.

3.3.4 Conclusions on the Magnitude and Distance Dependence of the SDOF and MDOF Responses to Ordinary Ground Motions

Based on the observations discussed in Sections 3.3.1, 3.3.2, and 3.3.3, and in view of the many large uncertainties in demand evaluation, there appears to be justification to de-emphasize magnitude and distance dependence of seismic demand parameters given S_a. This argument has its limitations. Foremost, it applies only to ground motions outside the near-fault and soft-soil regions. It also applies only to the limited magnitude and distance range used in the selection of the 80 ground motion record set. There are very few data points available for magnitude > 7, and an extrapolation to this range is not intended.

Considering that in the western U.S. most of the damage of relevance to seismic performance assessment is caused by larger earthquakes (particularly if R > 10 km [non-near-fault range]), there appear to be good reasons to de-emphasize records of the type contained in three (LMLR, SMSR, and SMLR) of the four bins discussed previously and to focus on LMSR records. This also is an argument for the validity of IDAs (Incremental Dynamic Analyses), in which the same ground motion is incremented in intensity to predict the intensity dependence of demand parameters — except in ranges in which the hazard is dominated by near-fault ground motions. The latter is likely to be the case for long return-period hazards, especially for sites located in the proximity of major faults.

3.3.5 LMSR vs. LMSR-N Record Sets

Because of the mild dependence of spectral shape on magnitude and distance and the need for a larger set of records (20 records were found to be insufficient in some cases to develop consistent statistical information), the boundaries of the LMSR bin are expanded to cover the range of $6.5 \leq M_w < 7$ and 13km < R < 40km. This new set, denoted as LMSR-N, contains 40 records and is the record set used to carry out the seismic demand evaluation summarized in this dissertation. The magnitude-distance pairs for this set of records are shown boxed in Figure 3.29, and their corresponding properties are summarized in Table 3.6 (the gray dots in Figure 3.29 represent two ground motion records that are not part of the original set of 80, NR94lv6 and NR94stn). Figure 3.30(a) shows the median acceleration spectra for both the LMSR and LMSR-N bins, when the S_a values are normalized by the spectral acceleration at a period of one second. From the figure it can be seen that both record sets have comparable spectral shape characteristics. Their dispersions (in terms of the standard deviation of the natural log of $S_a(T)/S_a(1.0s)$) are also comparable as can be observed in Figure 3.30(b). A slight increase in dispersion is noted by the addition of 20 records to the LMSR bin for periods greater than one second. In some cases, an increase in dispersion is expected since the LMSR-N bin covers larger magnitude and distance ranges than the LMSR bin. However, the conclusion is that expanding the boundaries of the LMSR bin (to obtain the LMSR-N bin) does not cause a significant variation in the frequency content of the ground motions as compared to the original record set. This statement implies that statistical seismic demand evaluation based on the LMSR-N record set should yield patterns of behavior similar to the ones obtained by using the LMSR records, with the additional advantage that more consistent statistical information can be derived by increasing the number of records from 20 to 40.

As stated in the preceding paragraph, similarities in spectral shapes between the LMSR and the LMSR-N bin are expected to yield consistent patterns of behavior. As an example, Figure 3.31(a) shows median R-μ-T relationships for a SDOF system with bilinear hysteretic behavior and strain hardening equal to 3%. Median strength reduction factors, R, are shown for $\mu = 4$. No clear differences between bins are observed, which is consistent with the fact that the frequency content characteristics of both record sets are comparable. The dispersions in R-factors exhibit consistent values, as seen in Figure 3.34(b).

Similarities in spectral shape between the LMSR and the LMSR-N bins are also reflected in the statistical seismic demand evaluation of MDOF systems. The seismic demand evaluation of two-dimensional, MDOF frame systems subjected to both record sets is discussed in Section 4.2.

Therefore, in this research study, the LMSR-N record set is used to carry out the seismic demand evaluation of systems subjected to ordinary ground motions.

Table 3.1 LMSR Ground Motion Records

Record ID	Event	Year	Mw	Station	R (km)	NEHRP Site	Mechanism	fHP (Hz)	fLP (Hz)	PGA (g)	PGV (cm/s)	PGD (cm)	D (s)	Rec. Length (s)
LP89agw	Loma Prieta	1989	6.9	Agnews State Hospital	28.2	D	reverse-oblique	0.20	30.0	0.172	26.0	12.6	18.4	40.0
LP89cap	Loma Prieta	1989	6.9	Capitola	14.5	D	reverse-oblique	0.20	40.0	0.443	29.3	5.5	13.2	40.0
LP89g03	Loma Prieta	1989	6.9	Gilroy Array #3	14.4	D	reverse-oblique	0.10	40.0	0.367	44.7	19.3	11.4	39.9
LP89g04	Loma Prieta	1989	6.9	Gilroy Array #4	16.1	D	reverse-oblique	0.20	30.0	0.212	37.9	10.1	14.8	40.0
LP89gmr	Loma Prieta	1989	6.9	Gilroy Array #7	24.2	D	reverse-oblique	0.20	40.0	0.226	16.4	2.5	11.5	40.0
LP89hch	Loma Prieta	1989	6.9	Hollister City Hall	28.2	D	reverse-oblique	0.10	29.0	0.247	38.5	17.8	17.4	39.1
LP89hda	Loma Prieta	1989	6.9	Hollister Differential Array	25.8	D	reverse-oblique	0.10	33.0	0.279	35.6	13.1	13.2	39.6
LP89svl	Loma Prieta	1989	6.9	Sunnyvale - Colton Ave.	28.8	D	reverse-oblique	0.10	40.0	0.207	37.3	19.1	21.2	39.3
NR94cnp	Northridge	1994	6.7	Canoga Park - Topanga Can.	15.8	D	reverse-slip	0.05	30.0	0.420	60.8	20.2	10.4	25.0
NR94far	Northridge	1994	6.7	LA - N Faring Rd.	23.9	D	reverse-slip	0.13	30.0	0.273	15.8	3.3	8.8	30.0
NR94fle	Northridge	1994	6.7	LA - Fletcher Dr.	29.5	D	reverse-slip	0.15	30.0	0.240	26.2	3.6	11.8	30.0
NR94glp	Northridge	1994	6.7	Glendale - Las Palmas	25.4	D	reverse-slip	0.10	30.0	0.206	7.4	1.8	11.5	30.0
NR94hol	Northridge	1994	6.7	LA - Holywood Stor FF	25.5	D	reverse-slip	0.20	23.0	0.231	18.3	4.8	12.0	40.0
NR94nya	Northridge	1994	6.7	La Crescenta-New York	22.3	D	reverse-slip	0.10	0.3	0.159	11.3	3.0	11.0	30.0
NR94stc	Northridge	1994	6.7	Northridge - 17645 Saticoy St.	13.3	D	reverse-slip	0.10	30.0	0.368	28.9	8.4	15.7	30.0
SF71pel	San Fernando	1971	6.6	LA - Hollywood Stor Lot	21.2	D	reverse-slip	0.20	35.0	0.174	14.9	6.3	11.2	28.0
SH87bra	Superstition Hills	1987	6.7	Brawley	18.2	D	strike-slip	0.10	23.0	0.156	13.9	5.4	13.5	22.1
SH87icc	Superstition Hills	1987	6.7	El Centro Imp. Co. Cent	13.9	D	strike-slip	0.10	40.0	0.358	46.4	17.5	16.1	40.0
SH87pls	Superstition Hills	1987	6.7	Plaster City	21.0	D	strike-slip	0.20	18.0	0.186	20.6	5.4	11.3	22.2
SH87wsm	Superstition Hills	1987	6.7	Westmorland Fire Station	13.3	D	strike-slip	0.10	35.0	0.172	23.5	13.0	19.6	40.0

Table 3.2 LMLR Ground Motion Records

Record ID	Event	Year	Mw	Station	R (km)	NEHRP Site	Mechanism	fHP (Hz)	fLP (Hz)	PGA (g)	PGV (cm/s)	PGD (cm)	D (s)	Rec. Length (s)
BM68elc	Borrego Mountain	1968	6.8	El Centro Array #9	46.0	D	strike-slip	0.20	12.8	0.057	13.2	10.0	28.7	40.0
LP89a2e	Loma Prieta	1989	6.9	APEEL 2E Hayward Muir Sch	57.4	D	reverse-oblique	0.20	30.0	0.171	13.7	3.9	12.8	40.0
LP89fms	Loma Prieta	1989	6.9	Fremont - Emerson Court	43.4	D	reverse-oblique	0.10	32.0	0.141	12.9	8.4	17.9	39.7
LP89hvr	Loma Prieta	1989	6.9	Halls Valley	31.6	D	reverse-oblique	0.20	22.0	0.134	15.4	3.3	16.2	40.0
LP89sjw	Loma Prieta	1989	6.9	Salinas - John & Work	32.6	D	reverse-oblique	0.10	28.0	0.112	15.7	7.9	20.3	40.0
LP89slc	Loma Prieta	1989	6.9	Palo Alto - SLAC Lab.	36.3	D	reverse-oblique	0.20	33.0	0.194	37.5	10.0	12.5	39.6
NR94bad	Northridge	1994	6.7	Covina - W. Badillo	56.1	D	reverse-slip	0.20	30.0	0.100	5.8	1.2	17.4	35.0
NR94cas	Northridge	1994	6.7	Compton - Castlegate St.	49.6	D	reverse-slip	0.20	30.0	0.136	7.1	2.2	23.4	39.8
NR94cen	Northridge	1994	6.7	LA - Centinela St.	30.9	D	reverse-slip	0.20	30.0	0.322	22.9	5.5	12.4	30.0
NR94del	Northridge	1994	6.7	Lakewood - Del Amo Blvd.	59.3	D	reverse-slip	0.13	30.0	0.137	11.2	2.0	20.8	35.4
NR94dwn	Northridge	1994	6.7	Downey - Co. Maint. Bldg.	47.6	D	reverse-slip	0.20	23.0	0.158	13.8	2.3	17.3	40.0
NR94jab	Northridge	1994	6.7	Bell Gardens - Jaboneria	46.6	D	reverse-slip	0.13	30.0	0.068	7.6	2.5	20.1	35.0
NR94lh1	Northridge	1994	6.7	Lake Hughes #1	36.3	D	reverse-slip	0.12	23.0	0.087	9.4	3.7	13.9	32.0
NR94loa	Northridge	1994	6.7	Lawndale - Osage Ave.	42.4	D	reverse-slip	0.13	30.0	0.152	8.0	2.6	23.3	40.0
NR94lv2	Northridge	1994	6.7	Leona Valley #2	37.7	D	reverse-slip	0.20	23.0	0.063	7.2	1.6	12.5	32.0
NR94php	Northridge	1994	6.7	Palmdale - Hwy 14 & Palmdale	43.6	D	reverse-slip	0.20	46.0	0.067	16.9	8.0	18.2	60.0
NR94pic	Northridge	1994	6.7	LA - Pico & Sentous	32.7	D	reverse-slip	0.20	46.0	0.186	14.3	2.4	14.8	40.0
NR94sor	Northridge	1994	6.7	West Covina - S. Orange Ave.	54.1	D	reverse-slip	0.20	30.0	0.063	5.9	1.3	19.3	36.5
NR94sse	Northridge	1994	6.7	Terminal Island - S. Seaside	60.0	D	reverse-slip	0.13	30.0	0.194	12.1	2.3	13.4	35.0
NR94ver	Northridge	1994	6.7	LA - E Vernon Ave.	39.3	D	reverse-slip	0.10	30.0	0.153	10.1	1.8	15.9	30.0

Table 3.3 SMSR Ground Motion Records

Record ID	Event	Year	Mw	Station	R (km)	NEHRP Site	Mechanism	fHP (Hz)	fLP (Hz)	PGA (g)	PGV (cm/s)	PGD (cm)	D (s)	Rec. Length (s)
IV79cal	Imperial Valley	1979	6.5	Calipatria Fire Station	23.8	D	strike-slip	0.10	40.0	0.078	13.3	6.2	23.3	39.5
IV79chi	Imperial Valley	1979	6.5	Chihuahua	28.7	D	strike-slip	0.05		0.270	24.9	9.1	20.1	40.0
IV79e01	Imperial Valley	1979	6.5	El Centro Array #1	15.5	D	strike-slip	0.10	40.0	0.139	16.0	10.0	8.9	39.5
IV79e12	Imperial Valley	1979	6.5	El Centro Array #12	18.2	D	strike-slip	0.10	40.0	0.116	21.8	12.1	19.4	39.0
IV79e13	Imperial Valley	1979	6.5	El Centro Array #13	21.9	D	strike-slip	0.20	40.0	0.139	13.0	5.8	21.2	39.5
IV79qkp	Imperial Valley	1979	6.5	Cucapah	23.6	D	strike-slip	0.05		0.309	36.3	10.4	15.7	40.0
IV79wsm	Imperial Valley	1979	6.5	Westmorland Fire Station	15.1	D	strike-slip	0.10	40.0	0.110	21.9	10.0	25.2	40.0
LV80kod	Livermore	1980	5.8	San Ramon - Eastman Kodak	17.6	D	strike-slip	0.20	20.0	0.076	6.1	1.7	27.3	40.0
LV80srm	Livermore	1980	5.8	San Ramon Fire Station	21.7	D	strike-slip	0.20	15.0	0.040	4.0	1.2	14.2	21.0
MH84agw	Morgan Hill	1984	6.2	Agnews State Hospital	29.4	D	strike-slip	0.20	13.0	0.032	5.5	2.1	40.3	59.9
MH84g02	Morgan Hill	1984	6.2	Gilroy Array #2	15.1	D	strike-slip	0.20	31.0	0.162	5.1	1.4	16.4	30.0
MH84g03	Morgan Hill	1984	6.2	Gilroy Array #3	14.6	D	strike-slip	0.10	37.0	0.194	11.2	2.4	16.0	40.0
MH84gmr	Morgan Hill	1984	6.2	Gilroy Array #7	14.0	D	strike-slip	0.10	30.0	0.113	6.0	1.8	10.7	30.0
PM73phn	Point Mugu	1973	5.8	Port Hueneme	25.0*	D	reverse-slip	0.20	25.0	0.112	14.8	2.6	10.8	23.2
PS86psa	N. Palm Springs	1986	6.0	Palm Springs Airport	16.6	D	strike-slip	0.20	60.0	0.187	12.2	2.1	15.6	30.0
WN87cas	Whittier Narrows	1987	6.0	Compton - Castlegate St.	16.9	D	reverse	0.09	25.0	0.332	27.1	5.0	8.0	31.2
WN87cat	Whittier Narrows	1987	6.0	Carson - Catskill Ave.	28.1	D	reverse	0.18	25.0	0.042	3.8	0.8	20.6	32.9
WN87flo	Whittier Narrows	1987	6.0	Brea - S Flower Ave.	17.9	D	reverse	0.16	25.0	0.115	7.1	1.2	9.4	27.6
WN87w70	Whittier Narrows	1987	6.0	LA - W 70th St.	16.3	D	reverse	0.20	25.0	0.151	8.7	1.5	11.2	31.9
WN87wat	Whittier Narrows	1987	6.0	Carson - Water St.	24.5	D	reverse	0.20	25.0	0.104	9.0	1.9	15.2	29.7

* Hypocentral distance

Table 3.4 SMLR Ground Motion Records

Record ID	Event	Year	Mw	Station	R (km)	NEHRP Site	Mechanism	fHP (Hz)	fLP (Hz)	PGA (g)	PGV (cm/s)	PGD (cm)	D (s)	Rec. Length (s)
BO42elc	Borrego	1942	6.5	El Centro Array #9	49.0*	D		0.10	15.0	0.068	3.9	1.4	29.5	40.0
CO83c05	Coalinga	1983	6.4	Parkfield - Cholame 5W	47.3	D	reverse-oblique	0.20	22.0	0.131	10.0	1.3	14.6	40.0
CO83c08	Coalinga	1983	6.4	Parkfield - Cholame 8W	50.7	D	reverse-oblique	0.20	23.0	0.098	8.6	1.5	15.0	32.0
IV79cc4	Imperial Valley	1979	6.5	Coachella Canal #4	49.3	D	strike-slip	0.20	40.0	0.128	15.6	3.0	10.0	28.5
IV79cmp	Imperial Valley	1979	6.5	Compuertas	32.6	D	strike-slip	0.20		0.186	13.9	2.9	21.7	36.0
IV79dlt	Imperial Valley	1979	6.5	Delta	43.6	D	strike-slip	0.05		0.238	26.0	12.1	51.1	99.9
IV79nil	Imperial Valley	1979	6.5	Niland Fire Station	35.9	D	strike-slip	0.10	30.0	0.109	11.9	6.9	21.7	40.0
IV79pls	Imperial Valley	1979	6.5	Plaster City	31.7	D	strike-slip	0.10	40.0	0.057	5.4	1.9	10.7	18.7
IV79vct	Imperial Valley	1979	6.5	Victoria	54.1	D	strike-slip	0.20		0.167	8.3	1.1	17.1	40.0
LV80stp	Livermore	1980	5.8	Tracy - Sewage Treatment Plar	37.3	D	strike-slip	0.08	15.0	0.073	7.6	1.8	20.2	33.0
MH84cap	Morgan Hill	1984	6.2	Capitola	38.1	D	strike-slip	0.20	30.0	0.099	4.9	0.6	17.2	36.0
MH84hch	Morgan Hill	1984	6.2	Hollister City Hall	32.5	D	strike-slip	0.20	19.0	0.071	7.4	1.6	21.4	28.3
MH84sjb	Morgan Hill	1984	6.2	San Juan Bautista	30.3	C	strike-slip	0.10	21.0	0.036	4.4	1.5	19.0	28.0
PS86h06	N. Palm Springs	1986	6.0	San Jacinto Valley Cemetery	39.6	D	strike-slip	0.20	31.0	0.063	4.4	1.2	17.0	40.0
PS86ino	N. Palm Springs	1986	6.0	Indio	39.6	D	strike-slip	0.10	35.0	0.064	6.6	2.2	18.6	30.0
WN87bir	Whittier Narrows	1987	6.0	Downey - Birchdale	56.8	D	reverse	0.15	25.0	0.299	37.8	5.0	3.8	28.6
WN87cts	Whittier Narrows	1987	6.0	LA - Century City CC South	31.3	D	reverse	0.20	25.0	0.051	3.5	0.6	20.2	40.0
WN87har	Whittier Narrows	1987	6.0	LB - Harbor Admin FF	34.2	D	reverse	0.25	25.0	0.071	7.3	0.9	24.9	40.0
WN87sse	Whittier Narrows	1987	6.0	Terminal Island - S. Seaside	35.7	D	reverse	0.20	25.0	0.042	3.9	1.0	16.3	22.9
WN87stc	Whittier Narrows	1987	6.0	Northridge - Saticoy St.	39.8	D	reverse	0.20	25.0	0.118	5.1	0.8	19.8	40.0

* Hypocentral distance

Table 3.5 Exponent b in Expression $S_a = CT^b$ for Regressed Spectral Shapes (A-S = Abrahamson-Silva, O.G.M. = Set of 80 Ordinary Ground Motions)

		0.4s-3.0s	0.6s- 3.0s	
		A-S (A-B)	A-S (C-D)	O.G.M.
R=20 km	M_w=5.5	1.51	1.48	1.64
	M_w=6.0	1.35	1.30	1.46
	M_w=6.2	1.29	1.24	1.38
	M_w=6.5	1.22	1.16	1.27
	M_w=6.7	1.18	1.11	1.20
	M_w=6.8	1.16	1.08	1.16
	M_w=7.0	1.12	1.04	1.09
R=35 km	M_w=5.5	1.43	1.45	1.77
	M_w=6.0	1.27	1.27	1.59
	M_w=6.2	1.22	1.21	1.51
	M_w=6.5	1.14	1.13	1.40
	M_w=6.7	1.10	1.07	1.33
	M_w=6.8	1.08	1.05	1.29
	M_w=7.0	1.04	1.00	1.21

Table 3.6 LMSR-N Ground Motion Records

Record ID	Event	Year	Mw	Station	R (km)	NEHRP Site	Mechanism	fHP (Hz)	fLP (Hz)	PGA (g)	PGV (cm/s)	PGD (cm)	D (s)	Rec. Length (s)
IV79cal	Imperial Valley	1979	6.5	Calipatria Fire Station	23.8	D	strike-slip	0.10	40	0.078	13.3	6.2	23.3	39.5
IV79chi	Imperial Valley	1979	6.5	Chihuahua	28.7	D	strike-slip	0.05		0.270	24.9	9.1	20.1	40.0
IV79cmp	Imperial Valley	1979	6.5	Compuertas	32.6	D	strike-slip	0.20		0.186	13.9	2.9	21.7	36.0
IV79e01	Imperial Valley	1979	6.5	El Centro Array #1	15.5	D	strike-slip	0.10	40.0	0.139	16.0	10.0	8.9	39.5
IV79e12	Imperial Valley	1979	6.5	El Centro Array #12	18.2	D	strike-slip	0.10	40.0	0.116	21.8	12.1	19.4	39.0
IV79e13	Imperial Valley	1979	6.5	El Centro Array #13	21.9	D	strike-slip	0.20	40.0	0.139	13.0	5.8	21.2	39.5
IV79nil	Imperial Valley	1979	6.5	Niland Fire Station	35.9	D	strike-slip	0.10	30.0	0.109	11.9	6.9	21.7	40.0
IV79pls	Imperial Valley	1979	6.5	Plaster City	31.7	D	strike-slip	0.10	40.0	0.057	5.4	1.9	10.7	18.7
IV79qkp	Imperial Valley	1979	6.5	Cucapah	23.6	D	strike-slip	0.05		0.309	36.3	10.4	15.7	40.0
IV79wsm	Imperial Valley	1979	6.5	Westmorland Fire Station	15.1	D	strike-slip	0.10	40.0	0.110	21.9	10.0	25.2	40.0
LP89agw	Loma Prieta	1989	6.9	Agnews State Hospital	28.2	D	reverse-oblique	0.20	30.0	0.172	26.0	12.6	18.4	40.0
LP89cap	Loma Prieta	1989	6.9	Capitola	14.5	D	reverse-oblique	0.20	40.0	0.443	29.3	5.5	13.2	40.0
LP89g03	Loma Prieta	1989	6.9	Gilroy Array #3	14.4	D	reverse-oblique	0.10	40.0	0.367	44.7	19.3	11.4	39.9
LP89g04	Loma Prieta	1989	6.9	Gilroy Array #4	16.1	D	reverse-oblique	0.20	30.0	0.212	37.9	10.1	14.8	39.9
LP89gmr	Loma Prieta	1989	6.9	Gilroy Array #7	24.2	D	reverse-oblique	0.20	40.0	0.226	16.4	2.5	11.5	39.9
LP89hch	Loma Prieta	1989	6.9	Hollister City Hall	28.2	D	reverse-oblique	0.10	29.0	0.247	38.5	17.8	17.4	39.1
LP89hda	Loma Prieta	1989	6.9	Hollister Differential Array	25.8	D	reverse-oblique	0.10	33.0	0.279	35.6	13.1	13.2	39.6
LP89hvr	Loma Prieta	1989	6.9	Halls Valley	31.6	D	reverse-oblique	0.20	22.0	0.134	15.4	3.3	16.2	39.9
LP89sjw	Loma Prieta	1989	6.9	Salinas - John & Work	32.6	D	reverse-oblique	0.10	28.0	0.112	15.7	7.9	20.3	39.9
LP89slc	Loma Prieta	1989	6.9	Palo Alto - SLAC Lab.	36.3	D	reverse-oblique	0.20	33.0	0.194	37.5	10.0	12.5	39.6
LP89svl	Loma Prieta	1989	6.9	Sunnyvale - Colton Ave.	28.8	D	reverse-oblique	0.10	40.0	0.207	37.3	19.1	21.2	39.2
NR94cen	Northridge	1994	6.7	LA - Centinela St.	30.9	D	reverse-slip	0.20	30.0	0.322	22.9	5.5	12.4	30.0
NR94cnp	Northridge	1994	6.7	Canoga Park - Topanga Can.	15.8	D	reverse-slip	0.05	30.0	0.420	60.8	20.2	10.4	25.0
NR94far	Northridge	1994	6.7	LA - N Faring Rd.	23.9	D	reverse-slip	0.13	30.0	0.273	15.8	3.3	8.8	30.0
NR94fle	Northridge	1994	6.7	LA - Fletcher Dr.	29.5	D	reverse-slip	0.15	30.0	0.240	26.2	3.6	11.8	30.0
NR94glp	Northridge	1994	6.7	Glendale - Las Palmas	25.4	D	reverse-slip	0.10	30.0	0.206	7.4	1.8	11.5	30.0
NR94hol	Northridge	1994	6.7	LA - Holywood Stor FF	25.5	D	reverse-slip	0.20	23.0	0.231	18.3	4.8	12.0	40.0
NR94lh1	Northridge	1994	6.7	Lake Hughes #1 #	36.3	D	reverse-slip	0.12	23.0	0.087	9.4	3.7	13.9	32.0
NR94lv2	Northridge	1994	6.7	Leona Valley #2 #	37.7	D	reverse-slip	0.20	23.0	0.063	7.2	1.6	12.5	32.0
NR94lv6	Northridge	1994	6.7	Leona Valley #6	38.5	D	reverse-slip	0.20	23.0	0.178	14.4	2.1	10.4	32.0
NR94nya	Northridge	1994	6.7	La Crescenta-New York	22.3	D	reverse-slip	0.10	0.3	0.159	11.3	3.0	11.0	30.0
NR94pic	Northridge	1994	6.7	LA - Pico & Sentous	32.7	D	reverse-slip	0.20	46.0	0.186	14.3	2.4	14.8	40.0
NR94stc	Northridge	1994	6.7	Northridge - 17645 Saticoy St.	13.3	D	reverse-slip	0.10	30.0	0.368	28.9	8.4	15.7	30.0
NR94stn	Northridge	1994	6.7	LA - Saturn St	30.0	D	reverse-slip	0.10	30.0	0.474	34.6	6.6	11.6	31.6
NR94ver	Northridge	1994	6.7	LA - E Vernon Ave	39.3	D	reverse-slip	0.10	30.0	0.153	10.1	1.8	15.9	30.0
SF71pel	San Fernando	1971	6.6	LA - Hollywood Stor Lot	21.2	D	reverse-slip	0.20	35.0	0.174	14.9	6.3	11.2	28.0
SH87bra	Superstition Hills	1987	6.7	Brawley	18.2	D	strike-slip	0.10	23.0	0.156	13.9	5.4	13.5	22.1
SH87icc	Superstition Hills	1987	6.7	El Centro Imp. Co. Cent	13.9	D	strike-slip	0.10	40.0	0.358	46.4	17.5	16.1	40.0
SH87pls	Superstition Hills	1987	6.7	Plaster City	21.0	D	strike-slip	0.20	18.0	0.186	20.6	5.4	11.3	22.2
SH87wsm	Superstition Hills	1987	6.7	Westmorland Fire Station	13.3	D	strike-slip	0.10	35.0	0.172	23.5	13.0	19.6	40.0

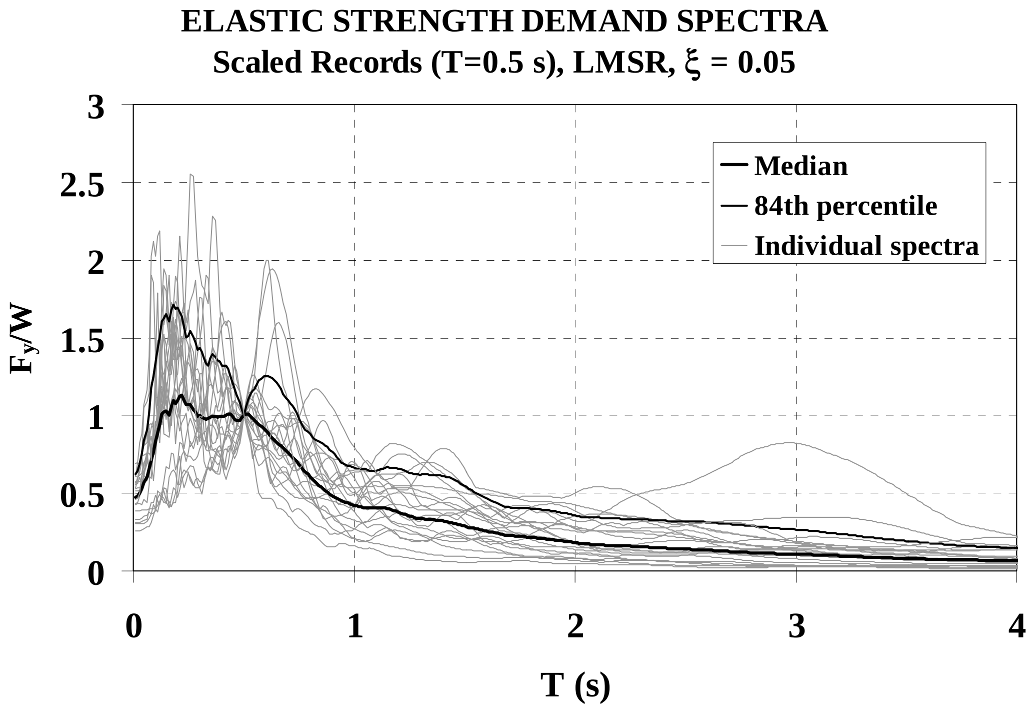

Figure 3.1 Spectra of Ordinary Ground Motions Scaled to the Same Spectral Acceleration at T = 0.5 sec

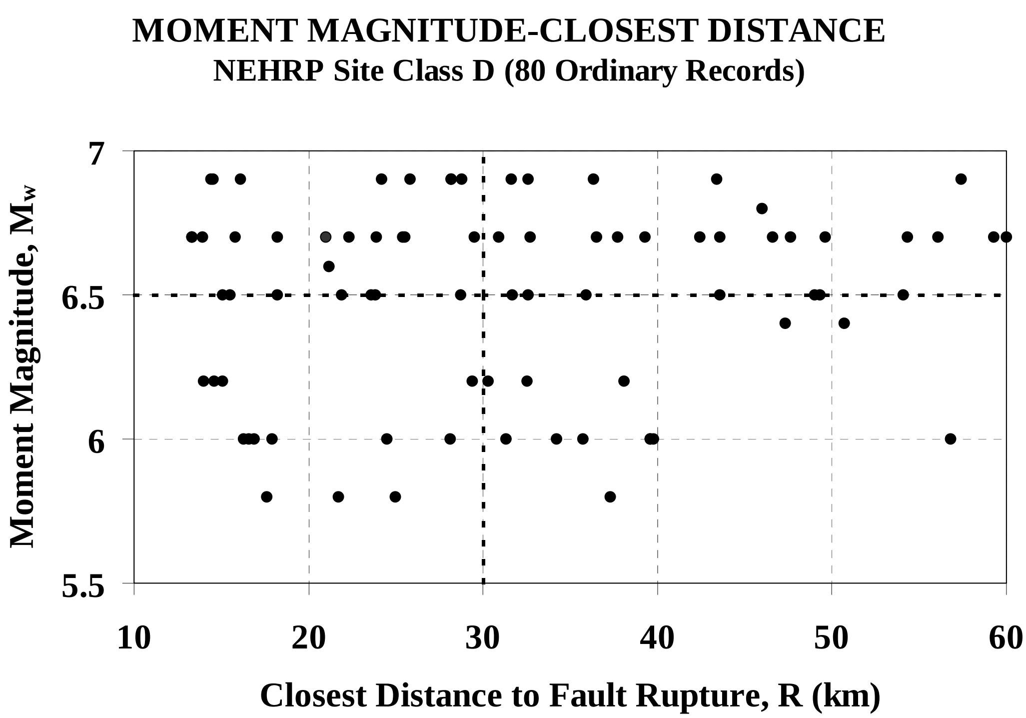

Figure 3.2 Magnitude-Distance Distribution of Set of 80 Ordinary Ground Motions

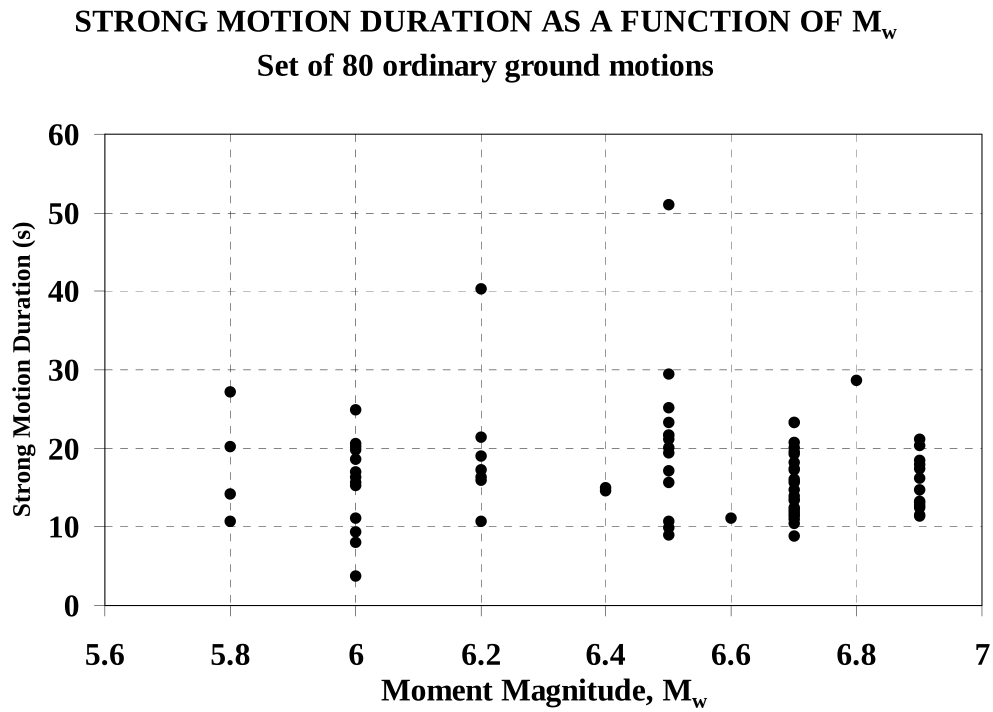

(a) Strong Motion Duration as a Function of Magnitude

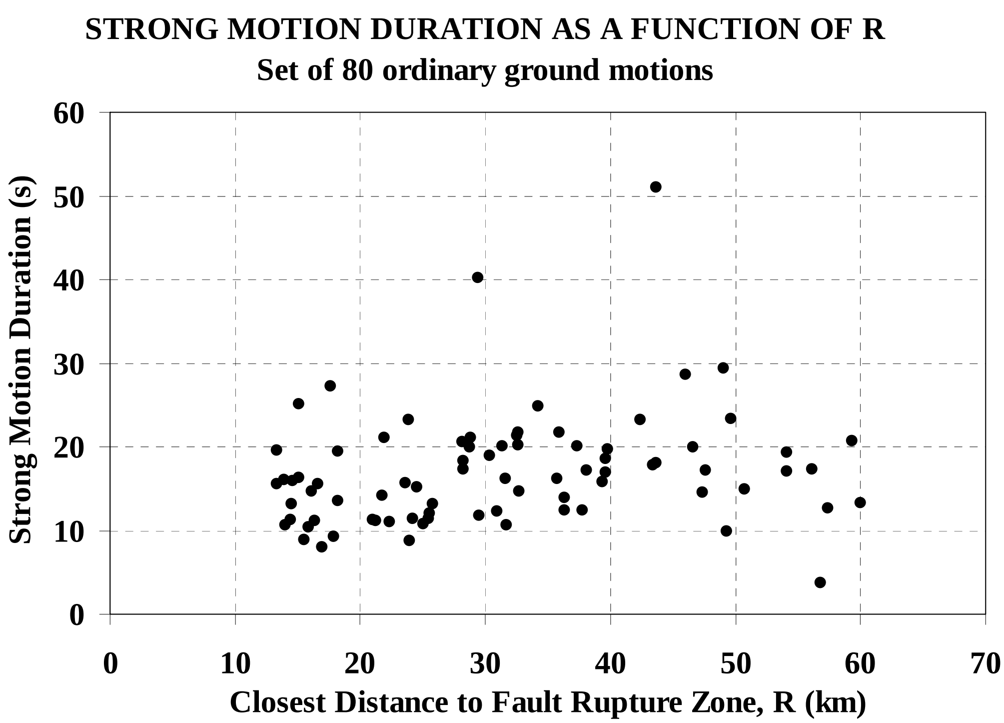

(b) Strong Motion Duration as a Function of Distance

Figure 3.3 Strong Motion Duration as a Function of Magnitude and Distance (O.G.M. Record Set)

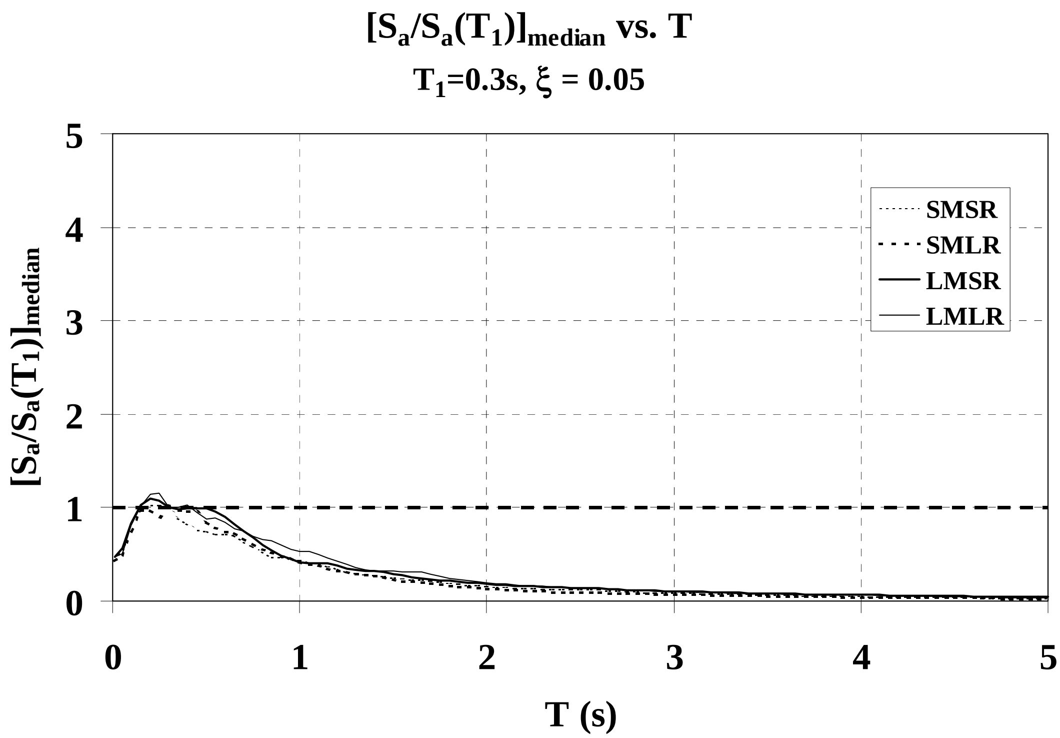

(a) Median of Scaled Spectra

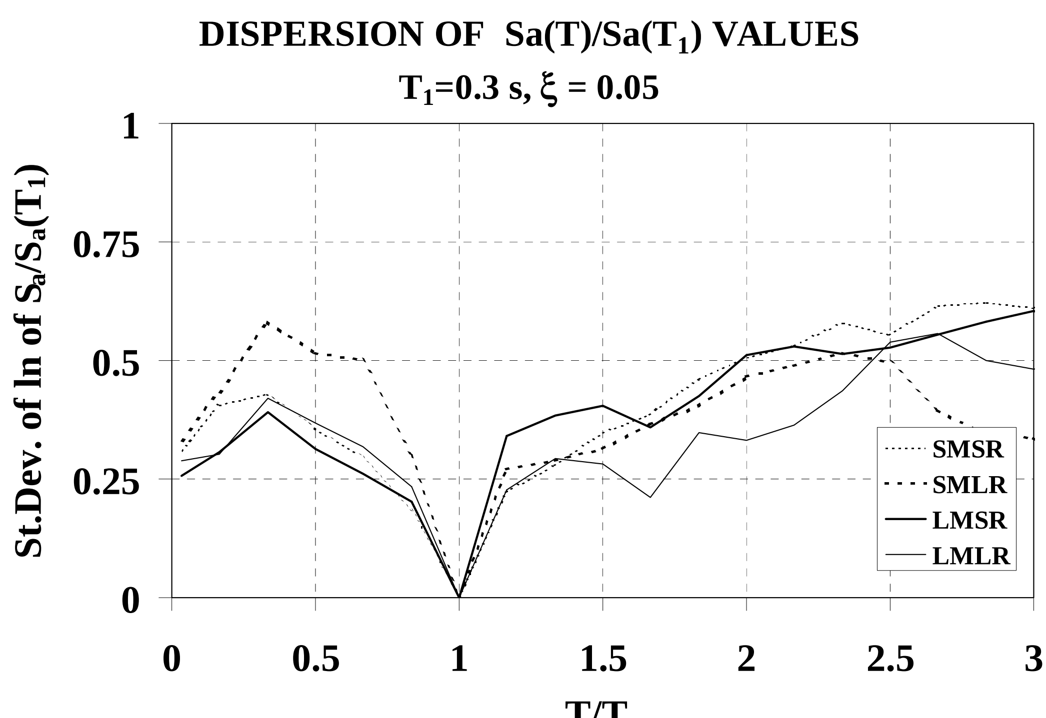

(b) Dispersion of $S_a(T)/S_a(T_1)$ Values

Figure 3.4 Statistical Evaluation of Spectral Shape for Four M-R Bins (Normalized at T_1 = 0.3 sec)

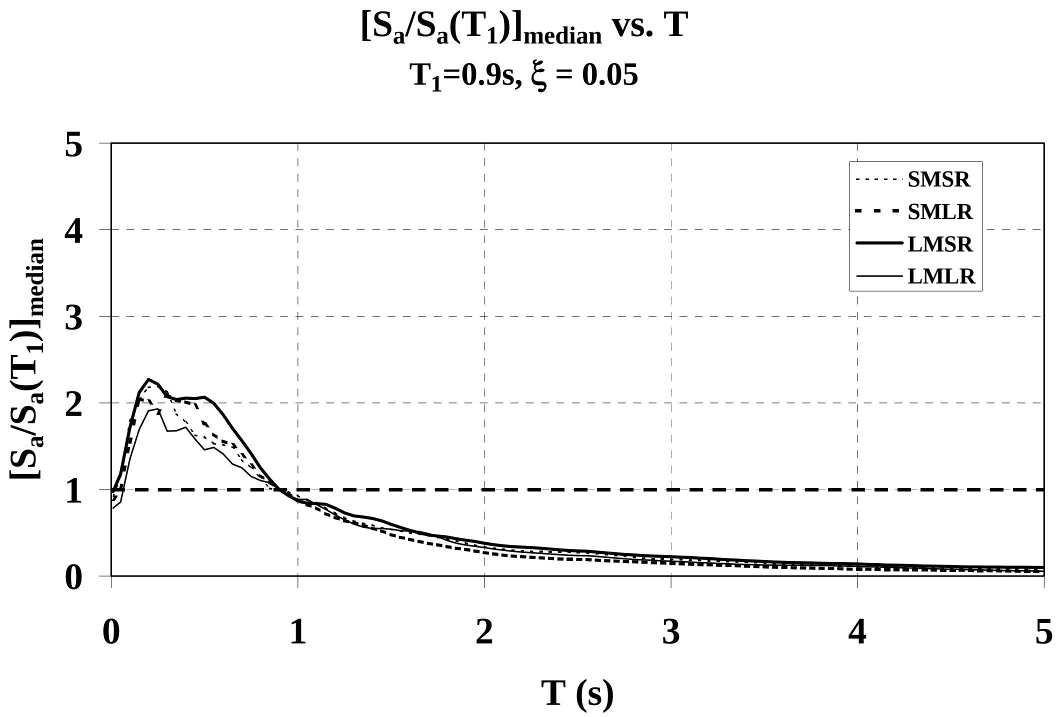

(a) Median of Scaled Spectra

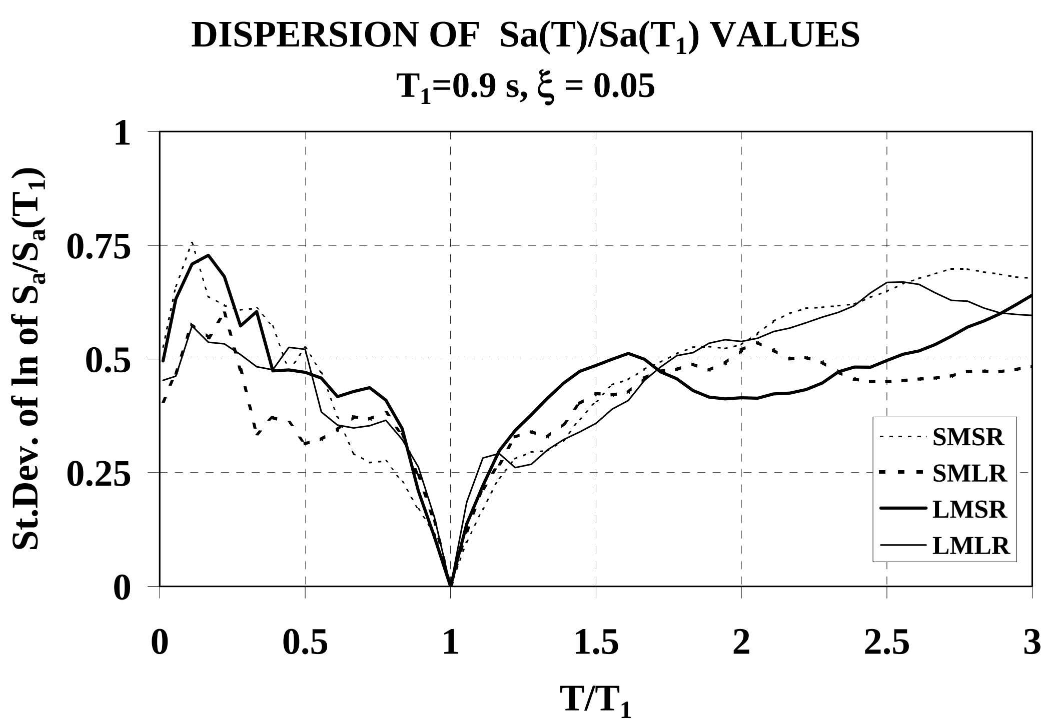

(b) Dispersion of $S_a(T)/S_a(T_1)$ Values

Figure 3.5 Statistical Evaluation of Spectral Shape for Four M-R Bins (Normalized at T_1 = 0.9 sec)

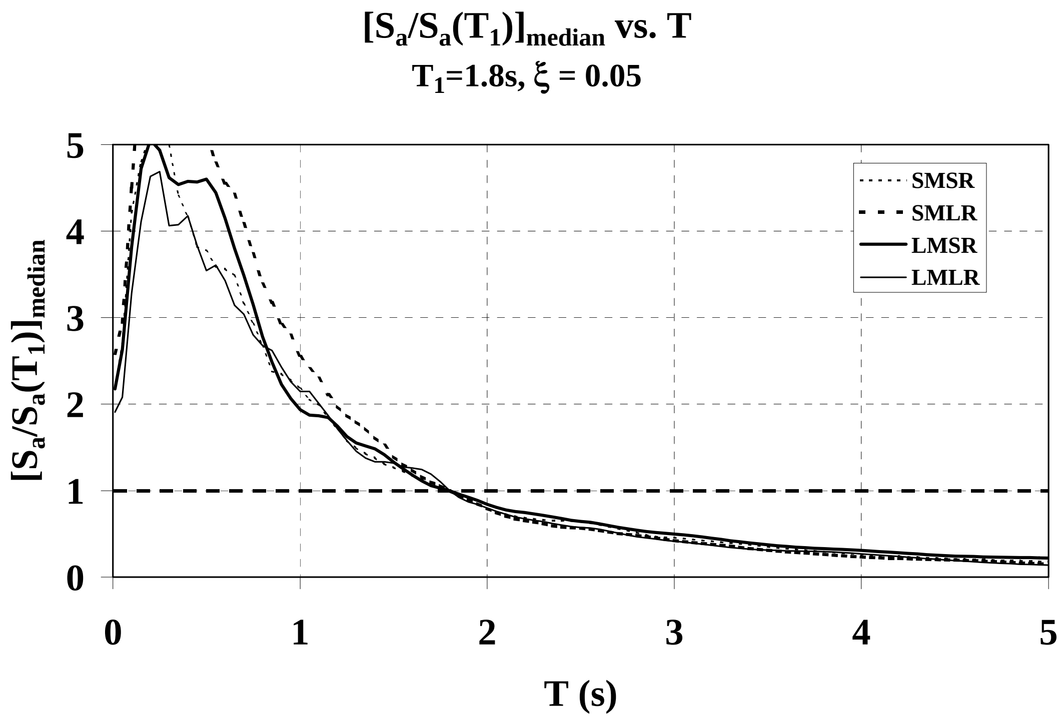

(a) Median of Scaled Spectra

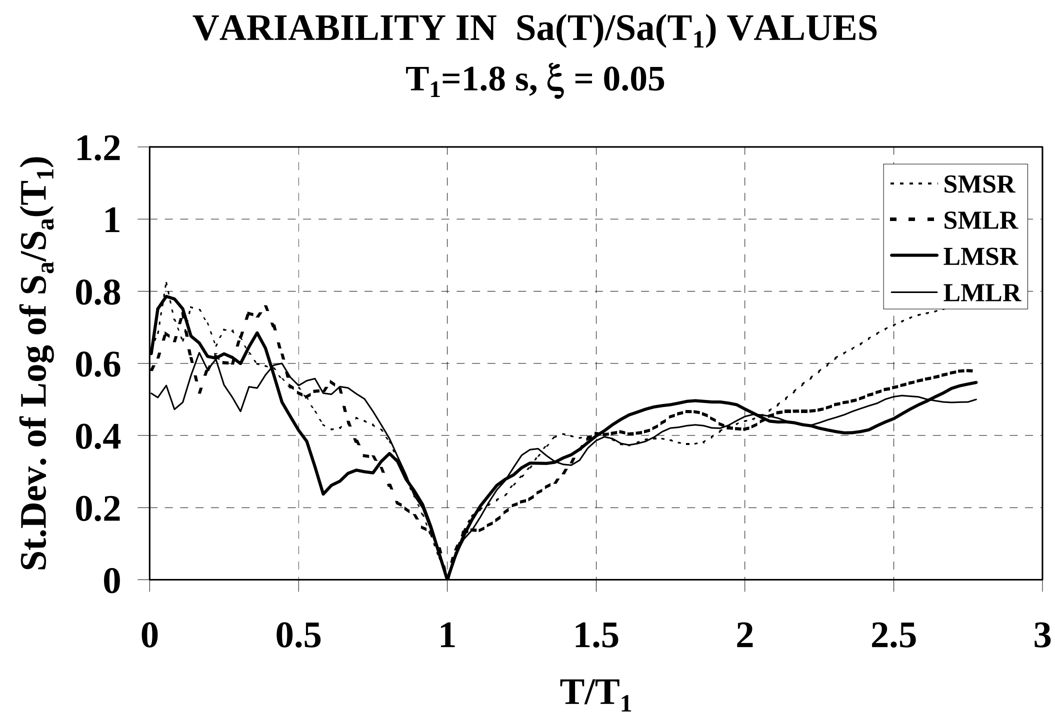

(b) Dispersion of $S_a(T)/S_a(T_1)$ Values

Figure 3.6 Statistical Evaluation of Spectral Shape for Four M-R Bins (Normalized at T_1 = 1.8 sec)

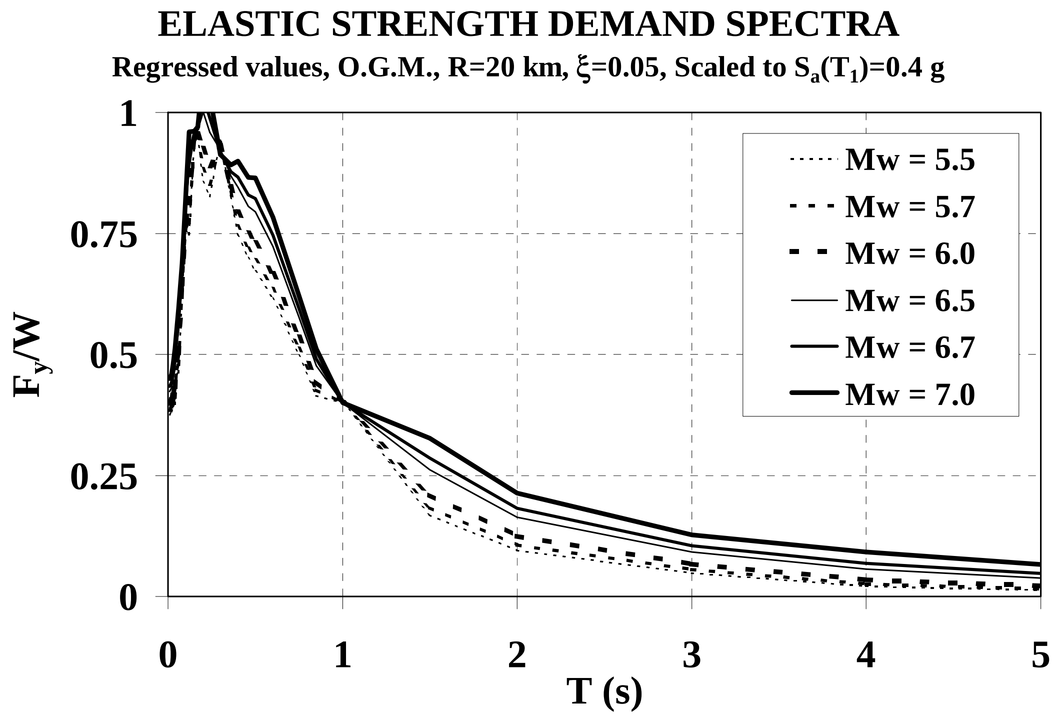

(a) Magnitude Dependence of Spectral Shape for a Given R = 20 km

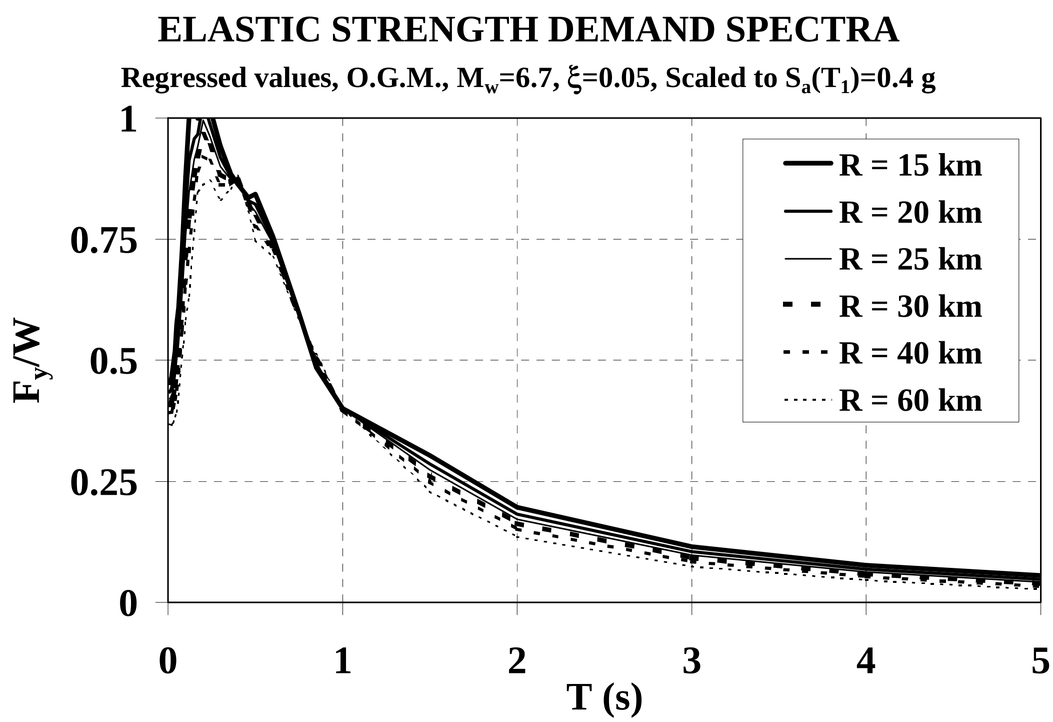

(b) Distance Dependence of Spectral Shape for a Given M_w = 6.7

Figure 3.7 Regression Analysis, M and R Dependence of Spectral Shape (O.G.M. Record Set)

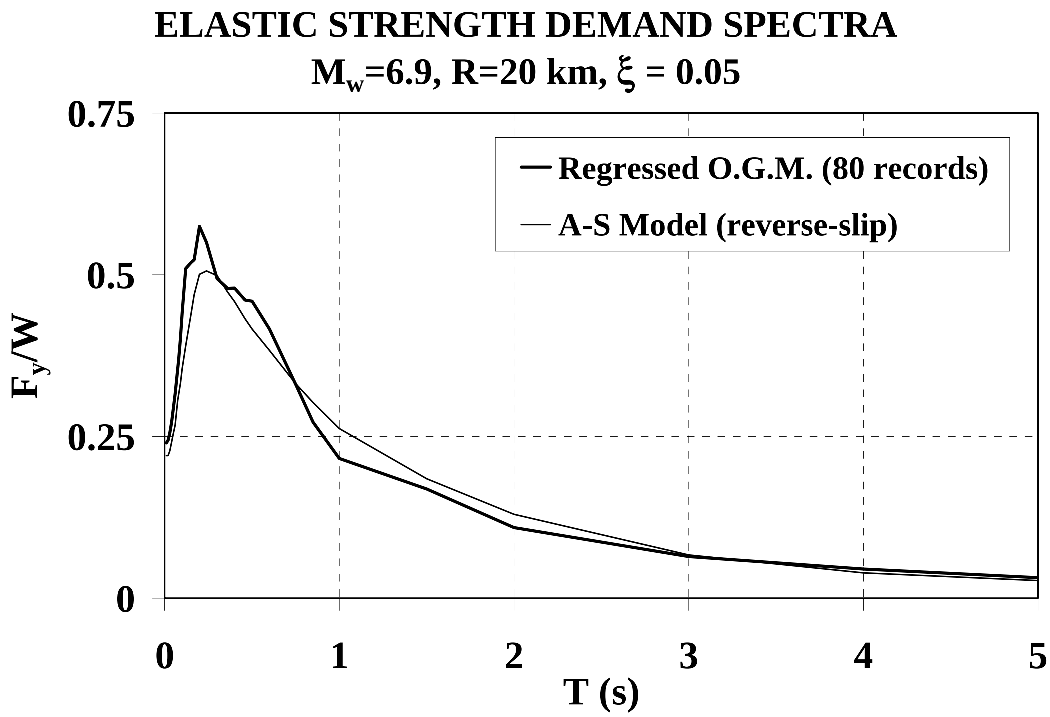

Figure 3.8 Regressed Spectra for M_w = 6.9 and R = 20 km (Abrahamson-Silva and O.G.M. Record Set)

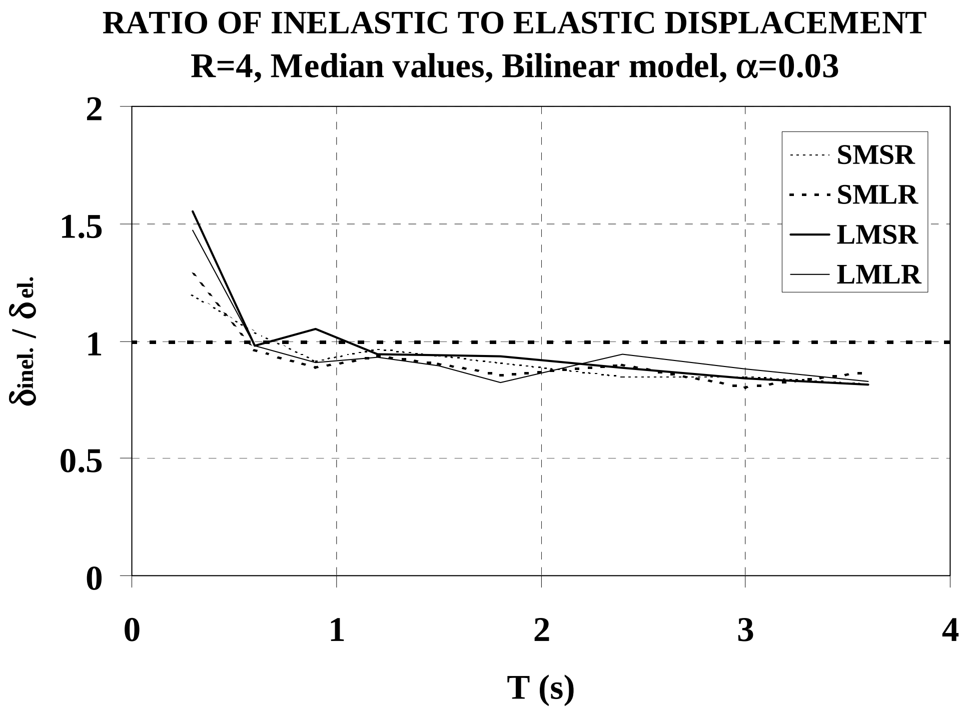

(a) Median of Ratio δ_{in}/δ_{el}

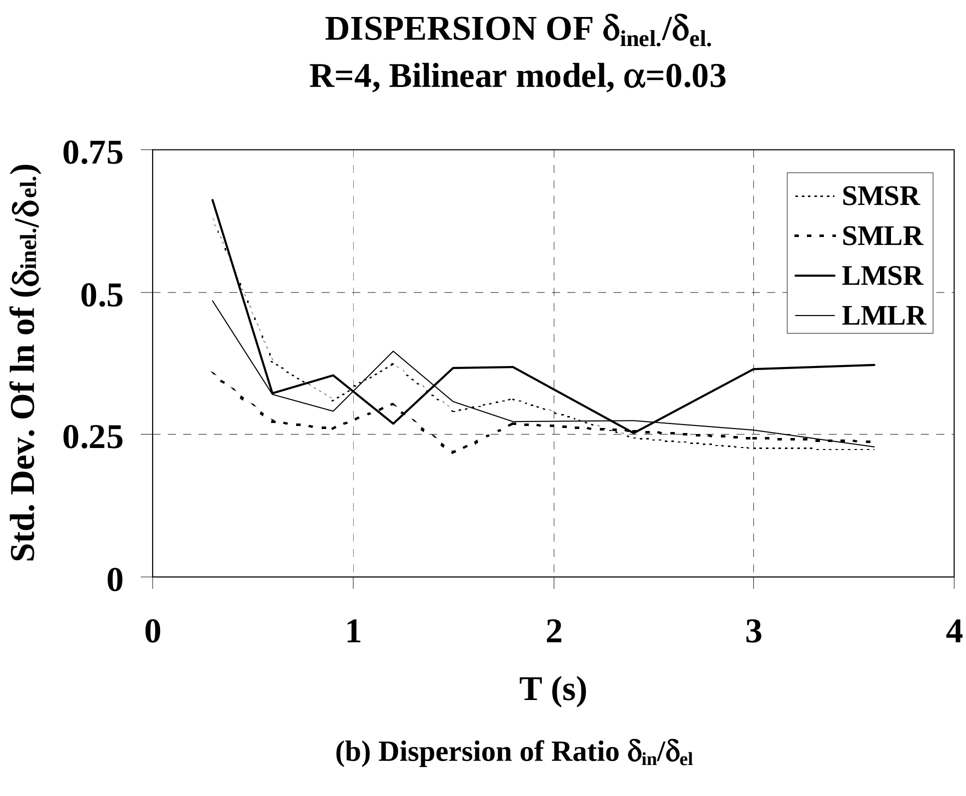

(b) Dispersion of Ratio δ_{in}/δ_{el}

Figure 3.9 Ratio of Inelastic to Elastic Displacement, Four M-R Bins, R = 4, Bilinear Model

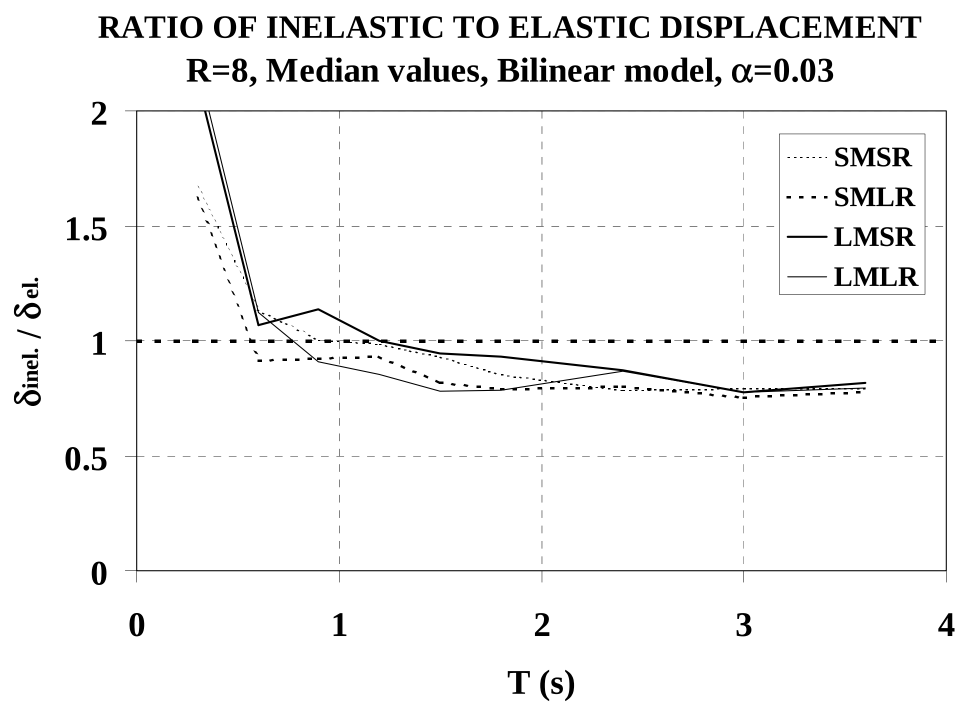

(a) Median of Ratio δ_{in}/δ_{el}

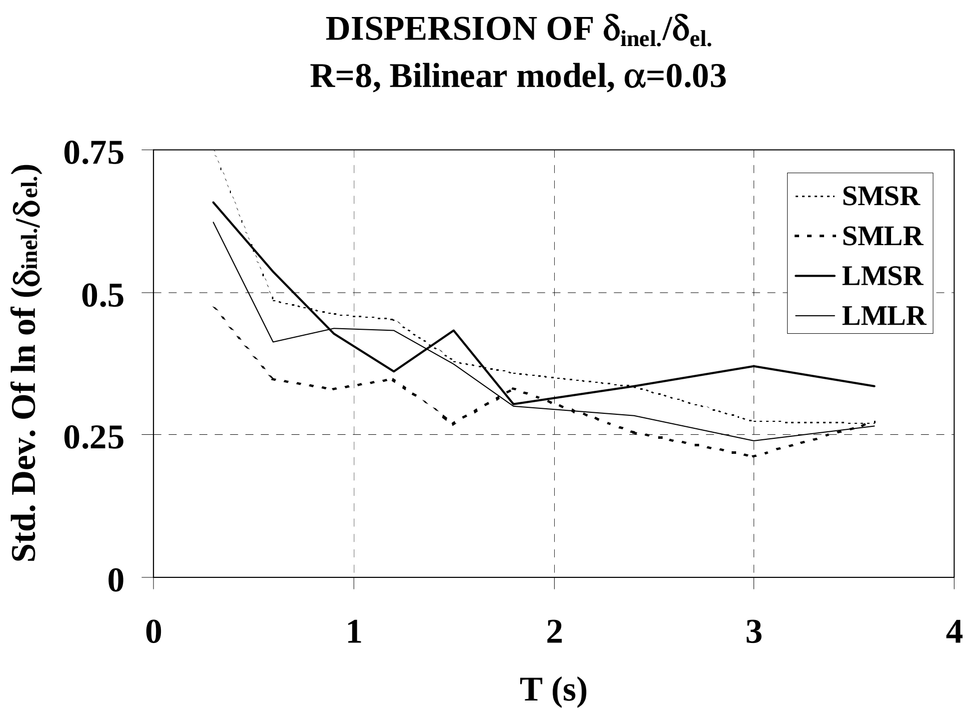

(b) Dispersion of Ratio δ_{in}/δ_{el}

Figure 3.10 Ratio of Inelastic to Elastic Displacement, Four M-R Bins, R = 8, Bilinear Model

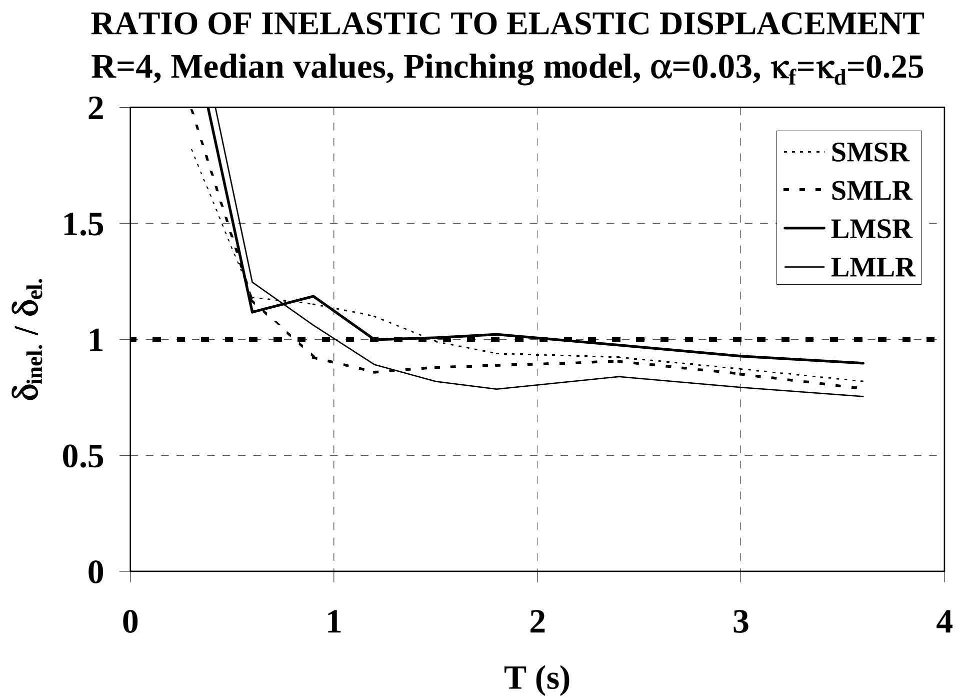

(a) Median of Ratio δ_{in}/δ_{el}

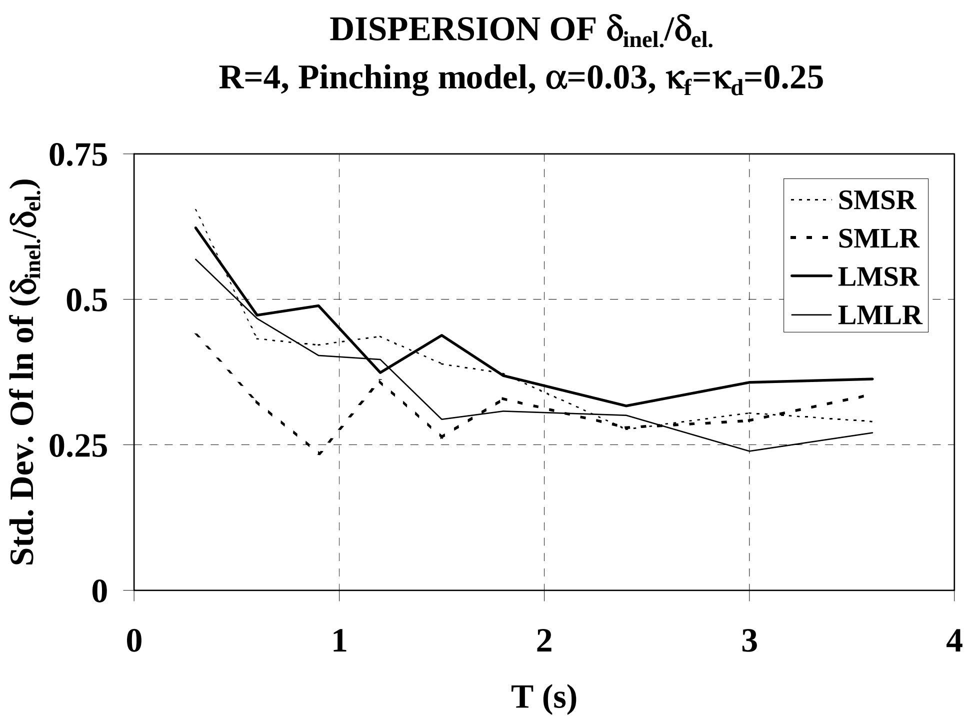

(b) Dispersion of Ratio δ_{in}/δ_{el}

Figure 3.11 Ratio of Inelastic to Elastic Displacement, Four M-R Bins, R = 4, Pinching Model

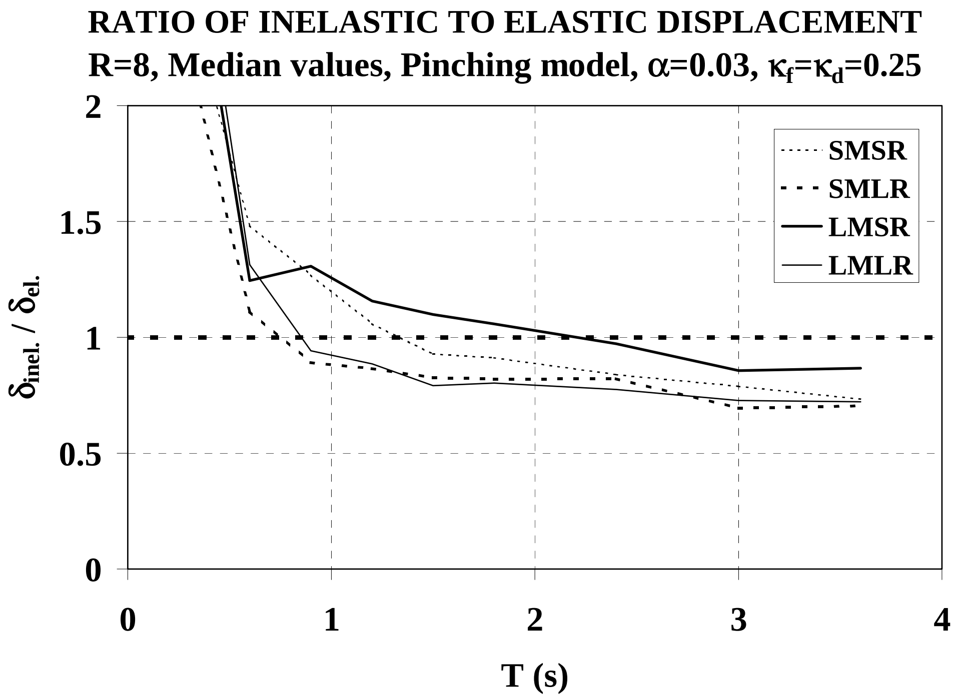

(a) Median of Ratio δ_{in}/δ_{el}

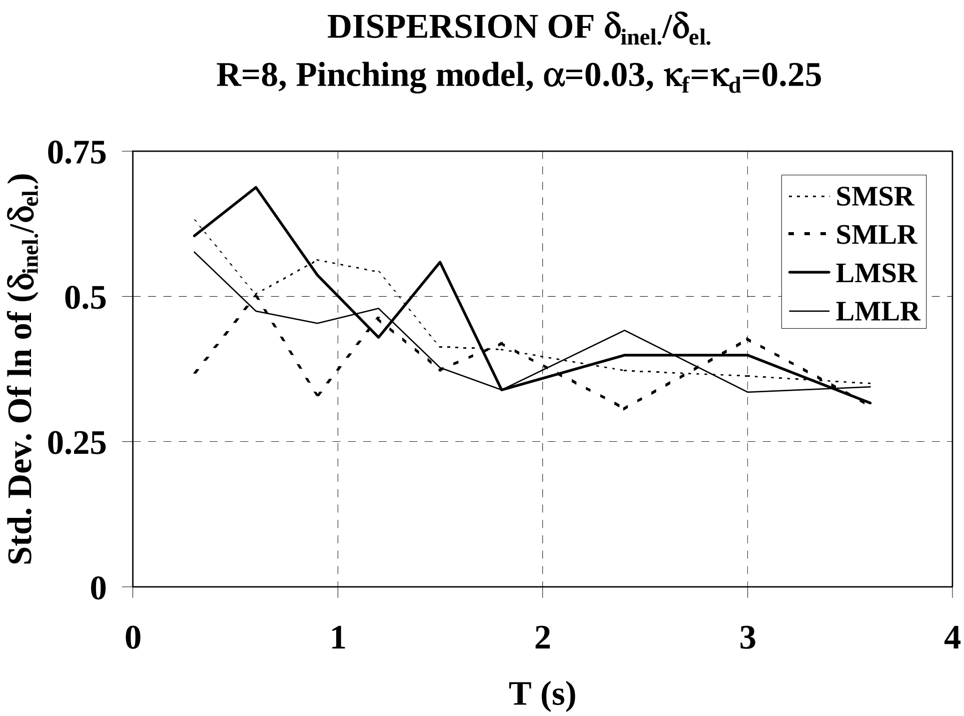

(b) Dispersion of Ratio δ_{in}/δ_{el}

Figure 3.12 Ratio of Inelastic to Elastic Displacement, Four M-R Bins, R = 8, Pinching Model

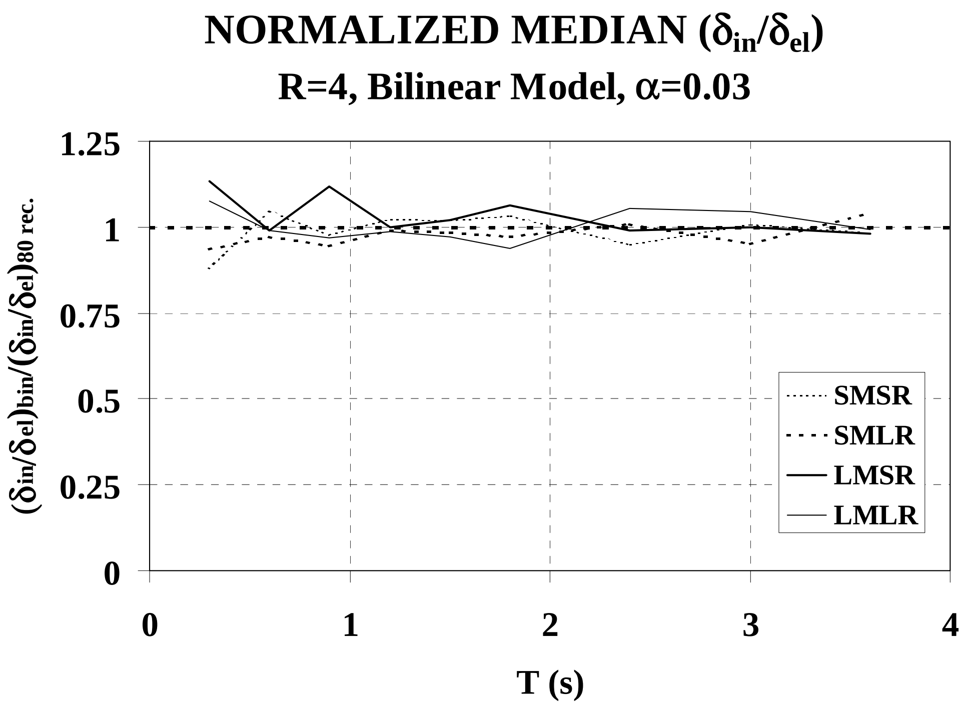

Figure 3.13 Normalized Median of the Ratio δ_{in}/δ_{el} , Four M-R Bins, R = 4, Bilinear Model

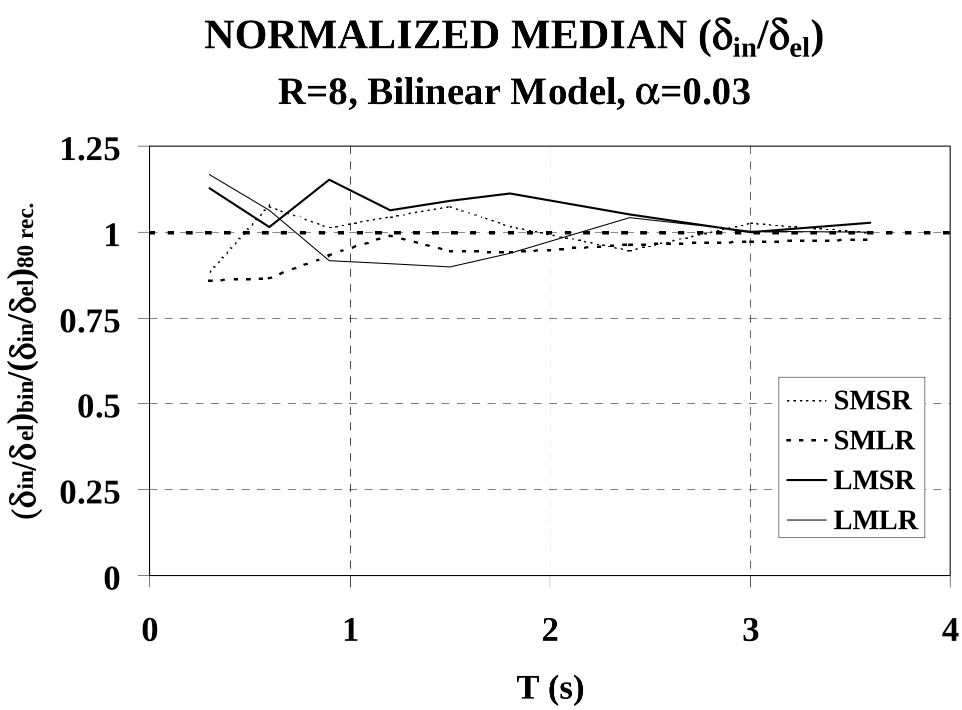

Figure 3.14 Normalized Median of the Ratio δ_{in}/δ_{el} , Four M-R Bins, R = 8, Bilinear Model

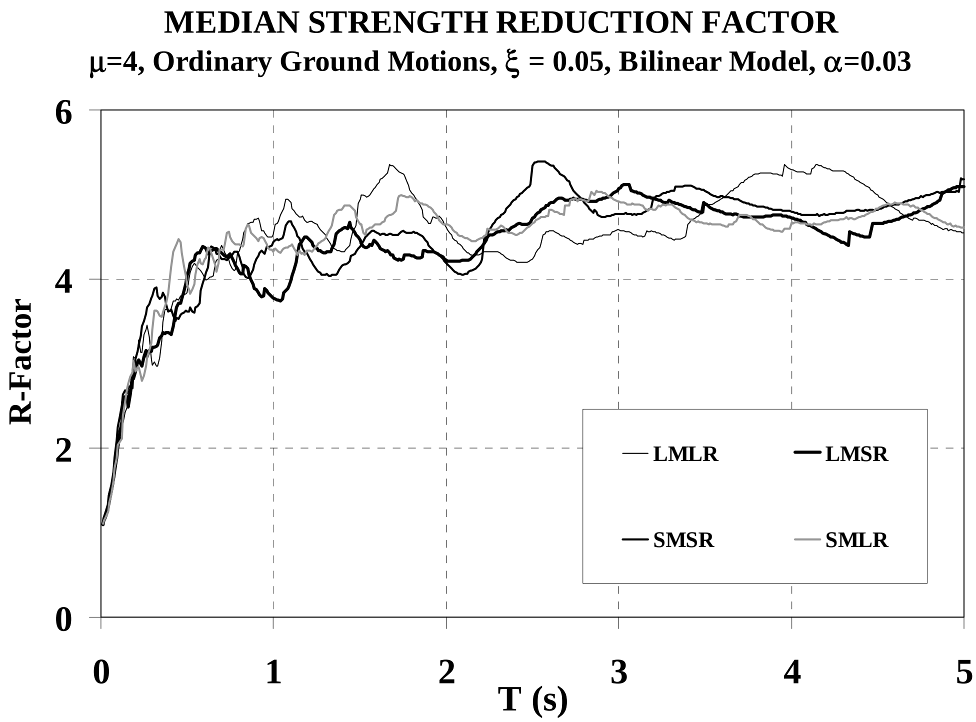

(a) Median R-μ-T Relationships

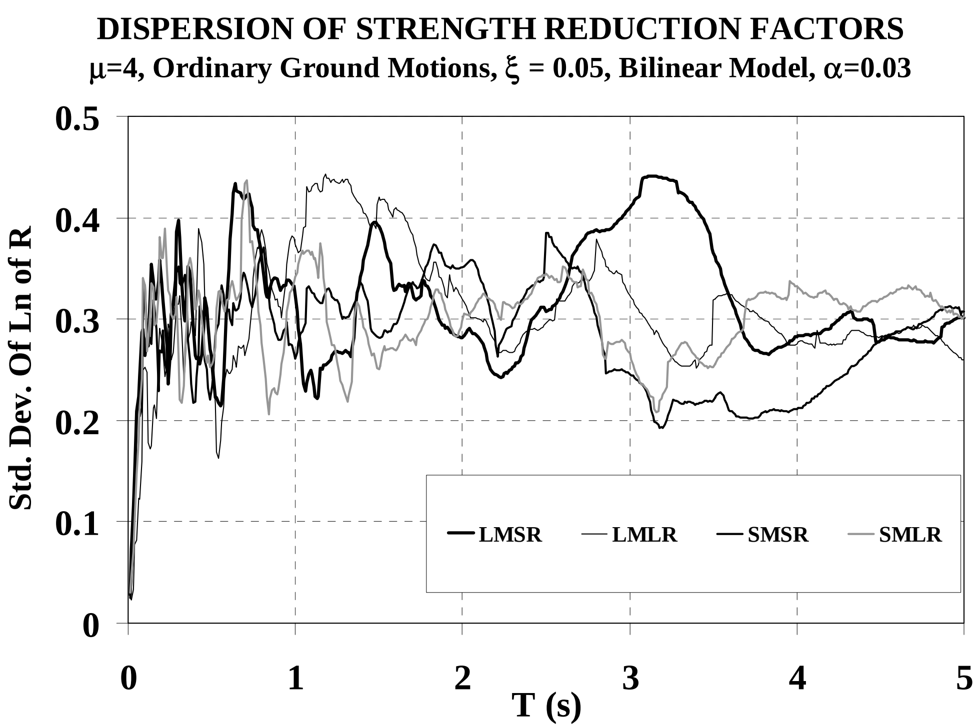

(b) Dispersion of R-Factors

Figure 3.15 Statistics on R-μ-T Relationships, Four M-R Bins, μ = 4, Bilinear Model

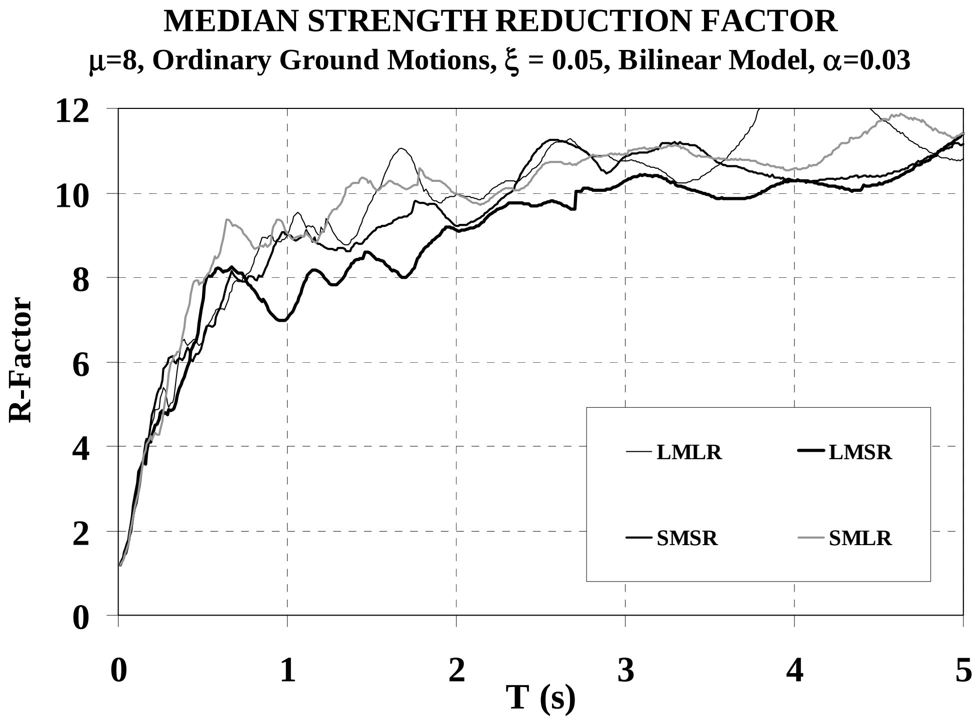

(a) Median R-μ-T Relationships

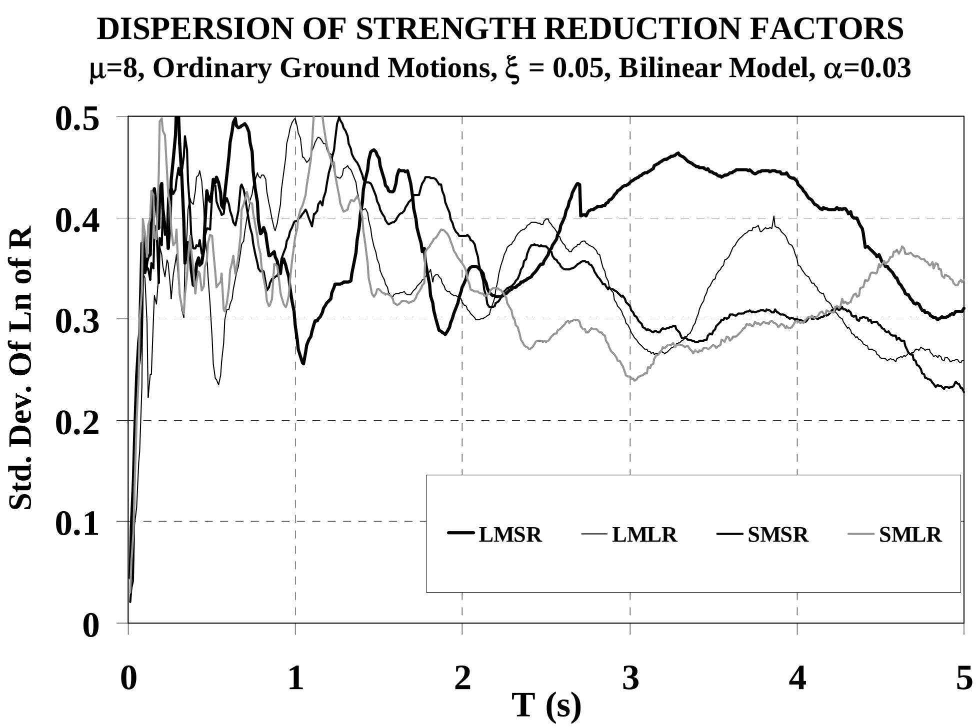

(b) Dispersion of R-Factors

Figure 3.16 Statistics on R-μ-T Relationships, Four M-R Bins, μ = 8, Bilinear Model

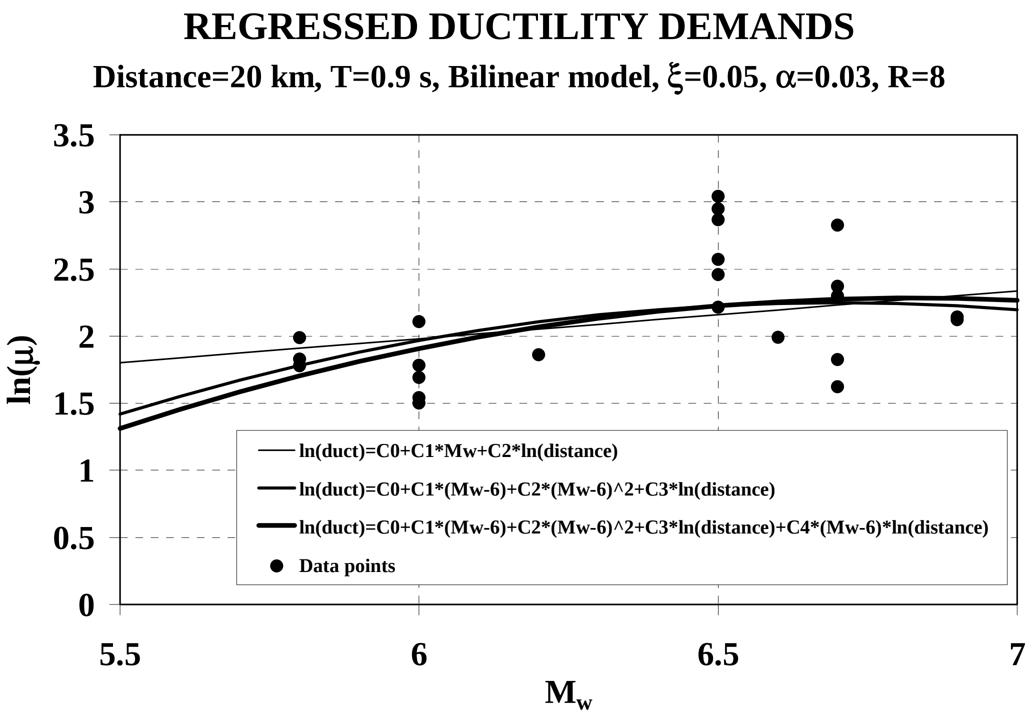

Figure 3.17 .Regressed Ductility Demands for R = 8, as a Function of Magnitude (O.G.M. Record Set), T = 0.9 sec

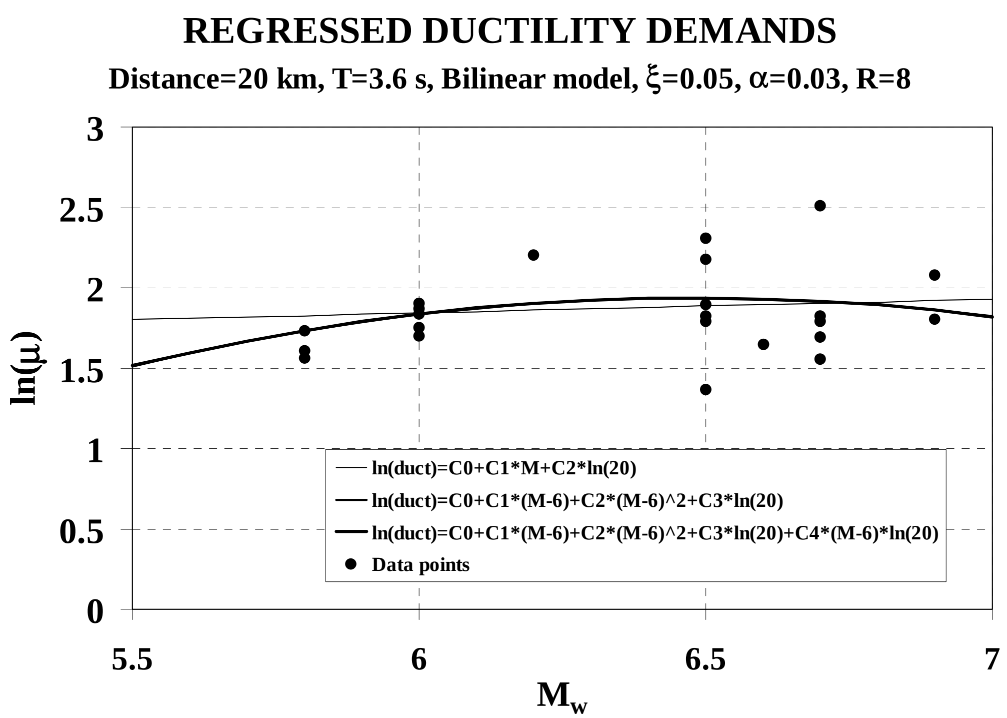

Figure 3.18 Regressed Ductility Demands for R = 8, as a Function of Magnitude (O.G.M. Record Set), T = 3.6 sec

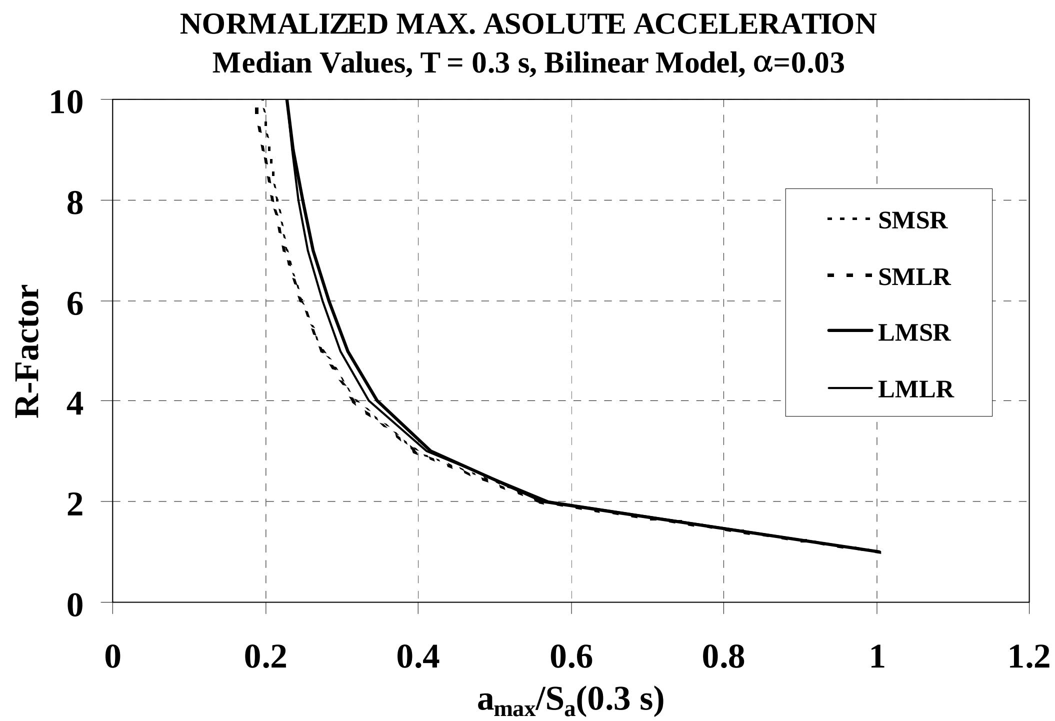

(a) Median Normalized Maximum Absolute Acceleration Demands

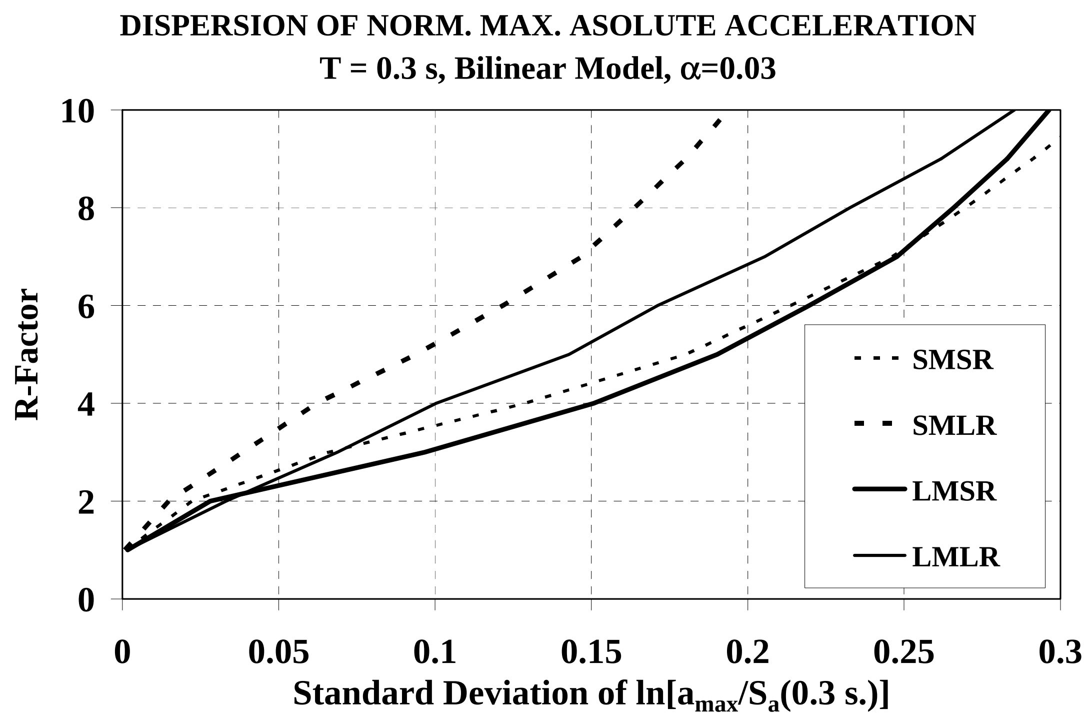

(b) Dispersion of Normalized Maximum Absolute Acceleration Demands

Figure 3.19 Statistics on the Normalized Maximum Absolute Acceleration, Four M-R Bins, Bilinear Model, T = 0.3 sec

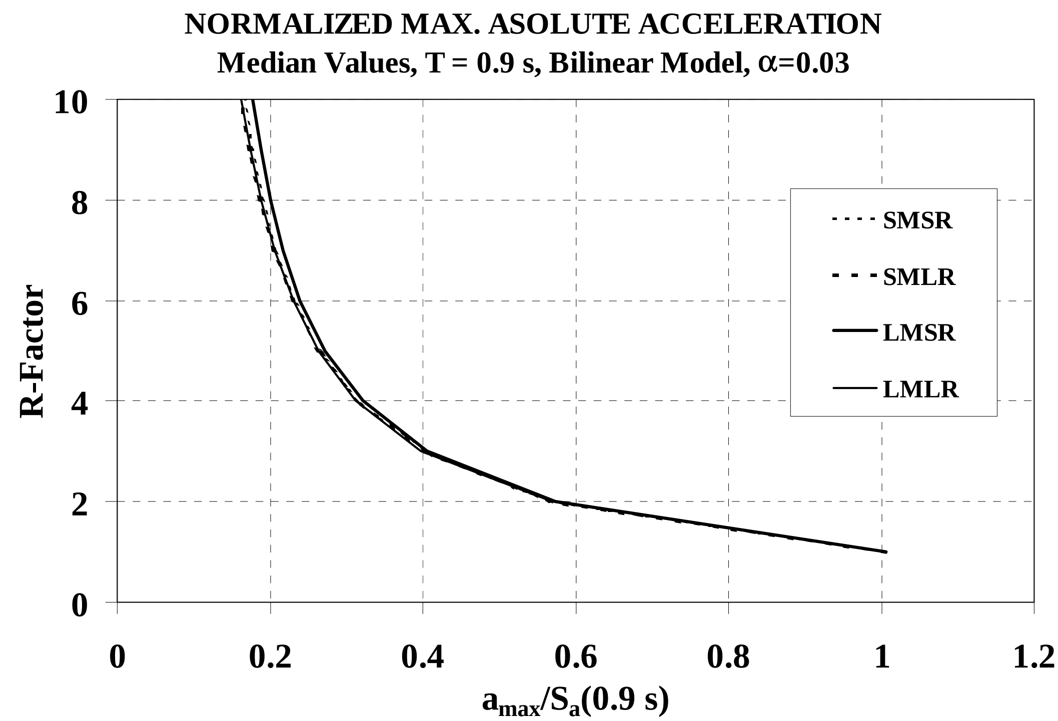

(a) Median Normalized Maximum Absolute Acceleration Demands

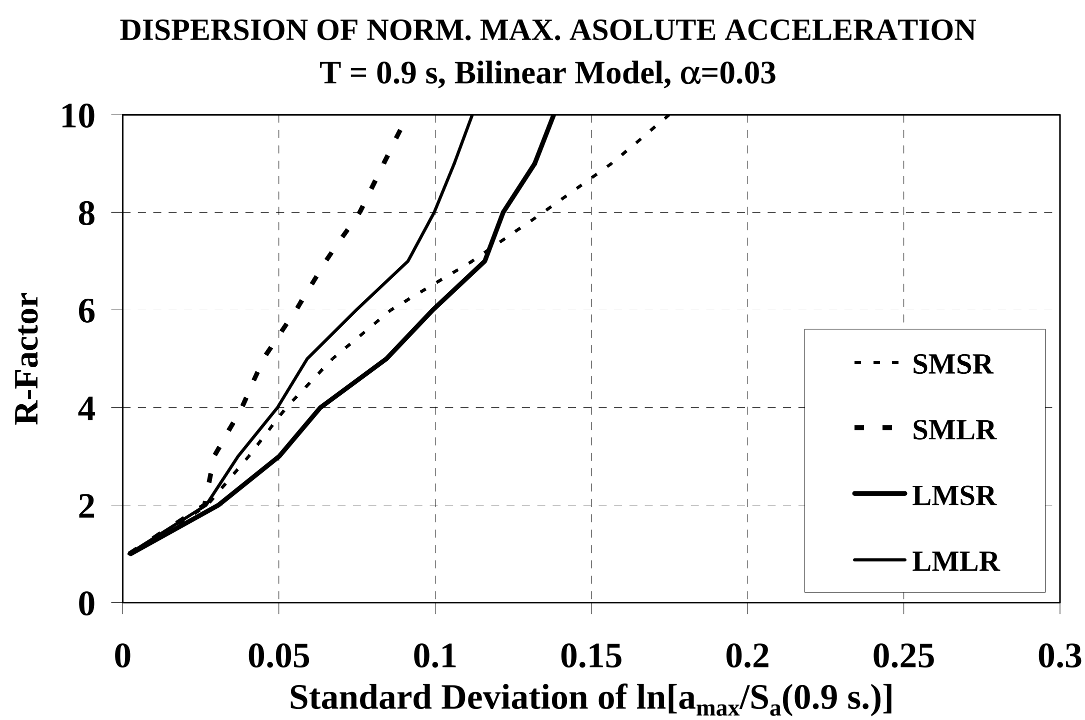

(b) Dispersion of Normalized Absolute Acceleration Demands

Figure 3.20 Statistics on the Normalized Maximum Absolute Acceleration, Four M-R Bins, Bilinear Model, T = 0.9 sec

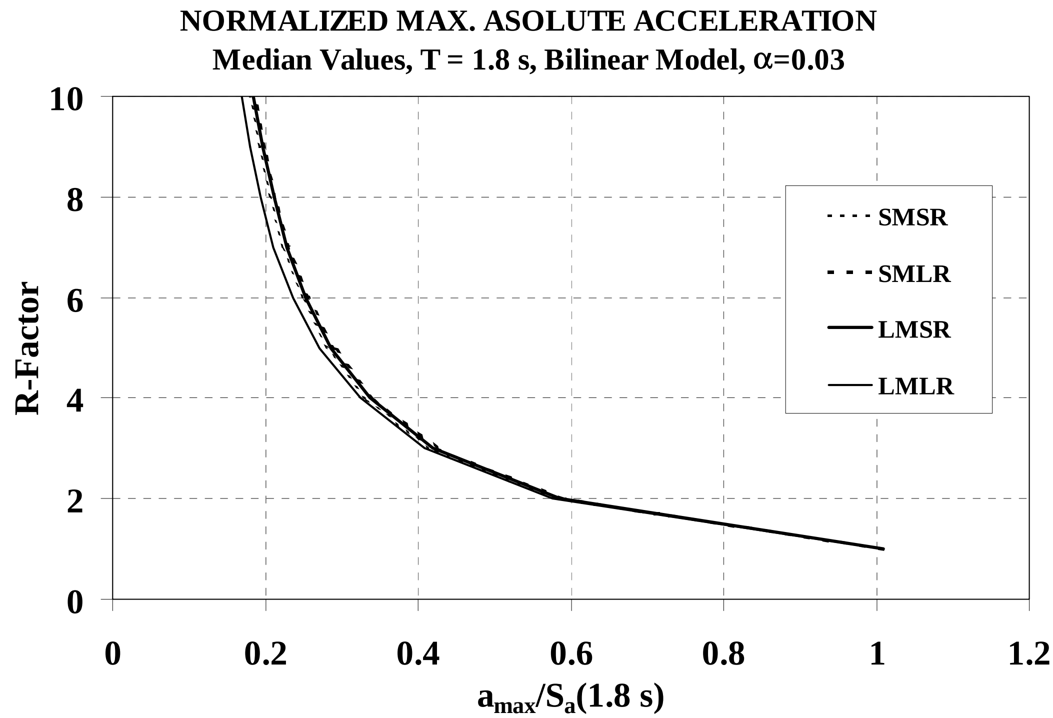

(a) Median Normalized Maximum Absolute Acceleration Demands

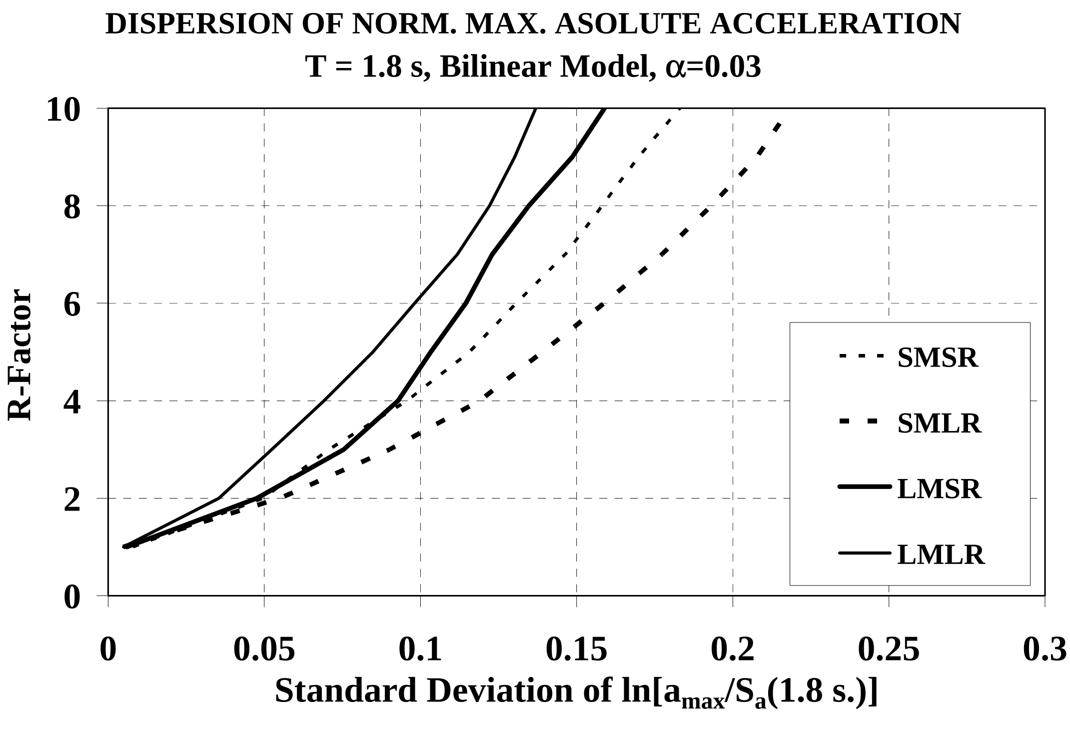

(b) Dispersion of Normalized Maximum Absolute Acceleration Demands

Figure 3.21 Statistics on the Normalized Maximum Absolute Acceleration, Four M-R Bins, Bilinear Model, T = 1.8 sec

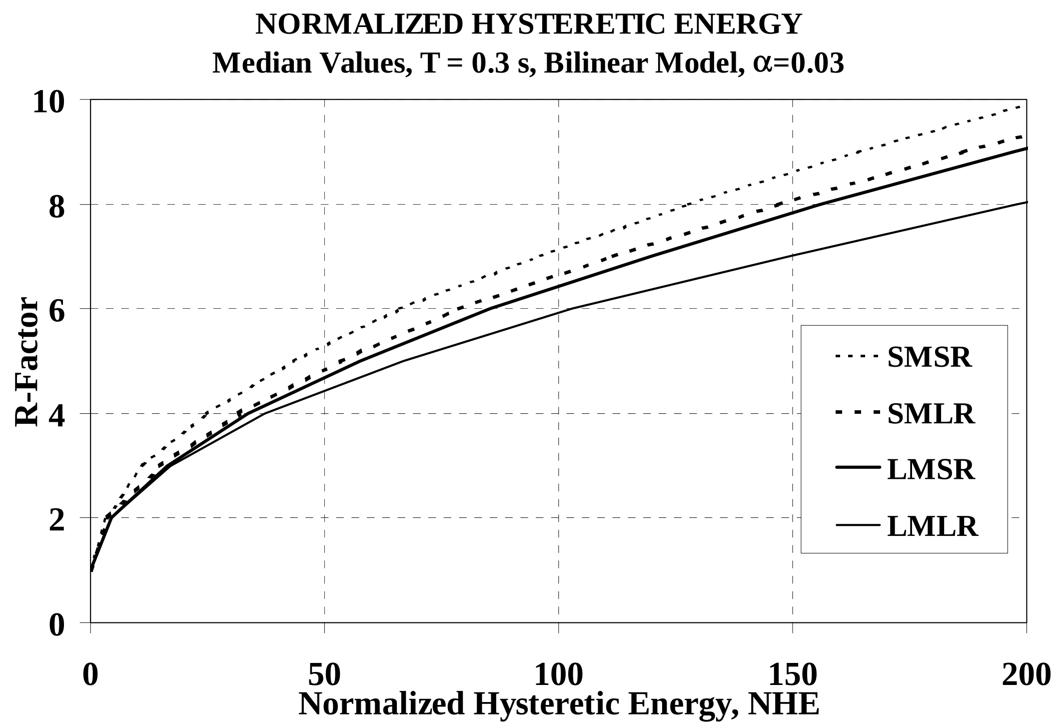

(a) Median Normalized Hysteretic Energy Demands

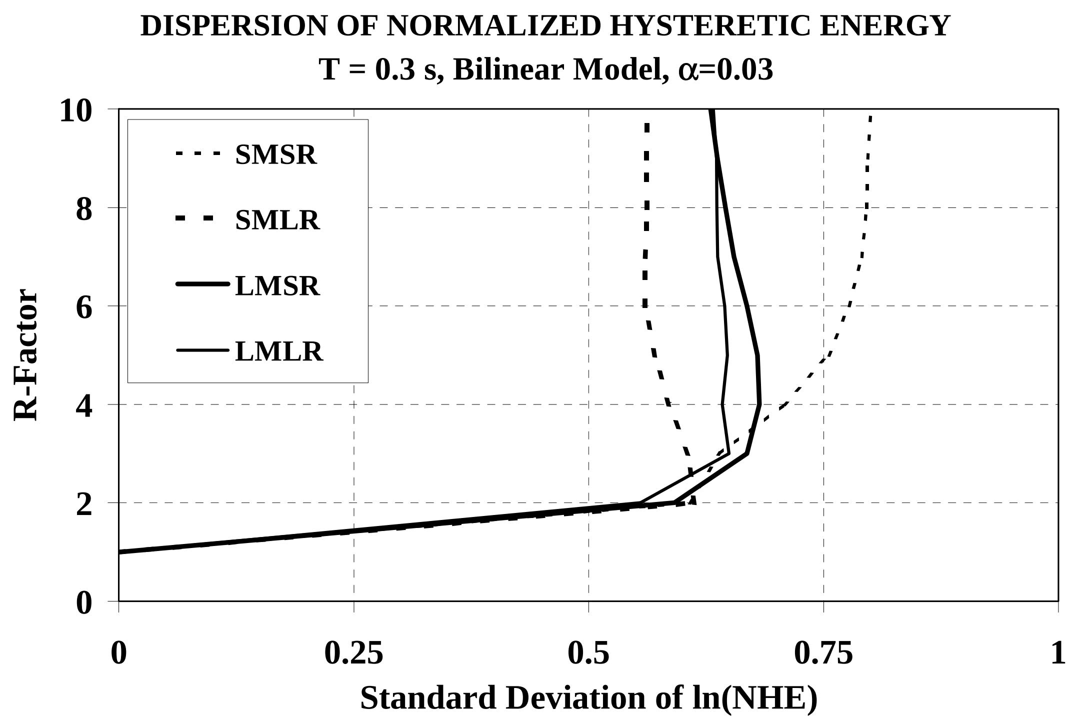

(b) Dispersion of Normalized Hysteretic Energy Demands

Figure 3.22 Statistics on the Normalized Hysteretic Energy, Four M-R Bins, Bilinear Model, T = 0.3 sec

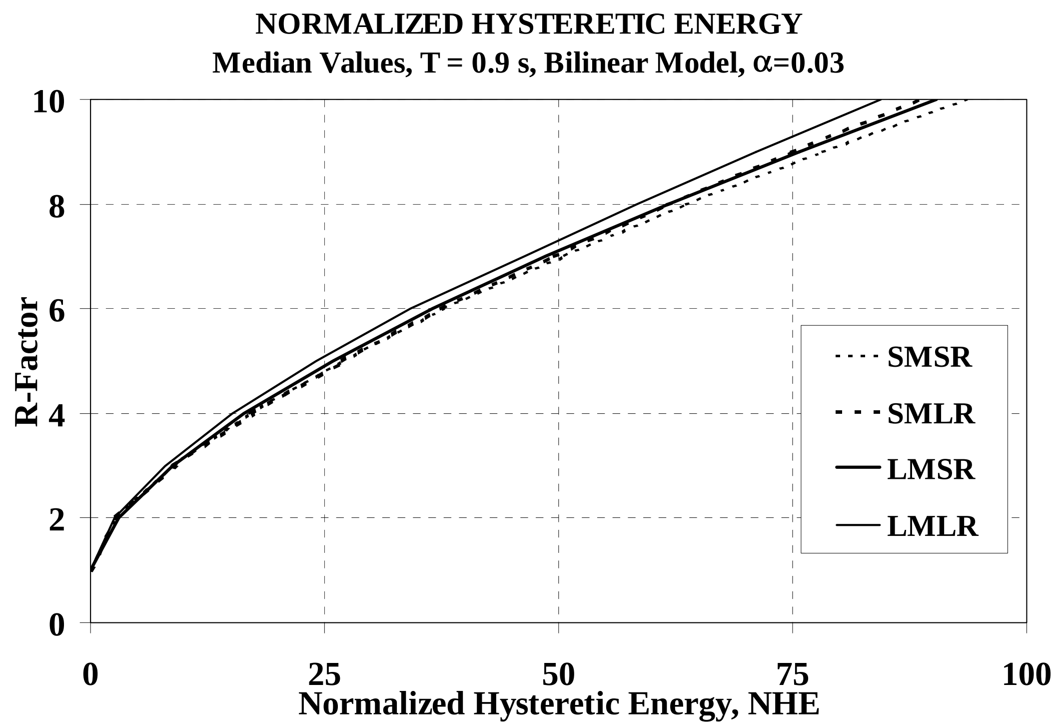

(a) Median Normalized Hysteretic Energy Demands

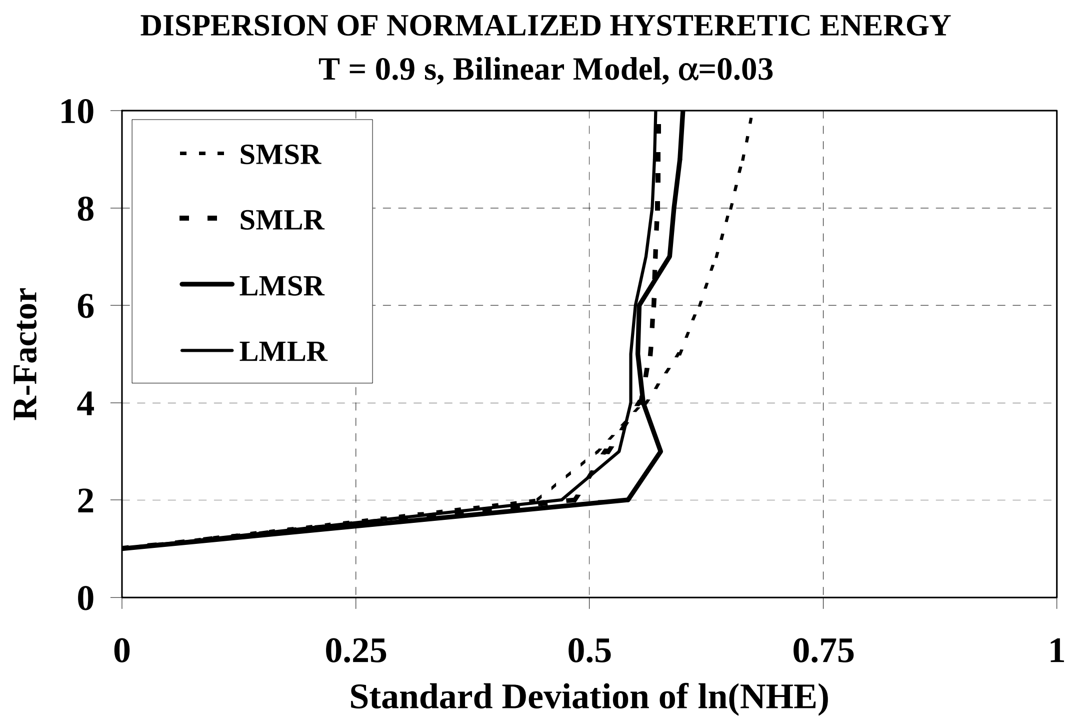

(b) Dispersion of Normalized Hysteretic Energy Demands

Figure 3.23 Statistics on the Normalized Hysteretic Energy, Four M-R Bins, Bilinear Model, T = 0.9 sec

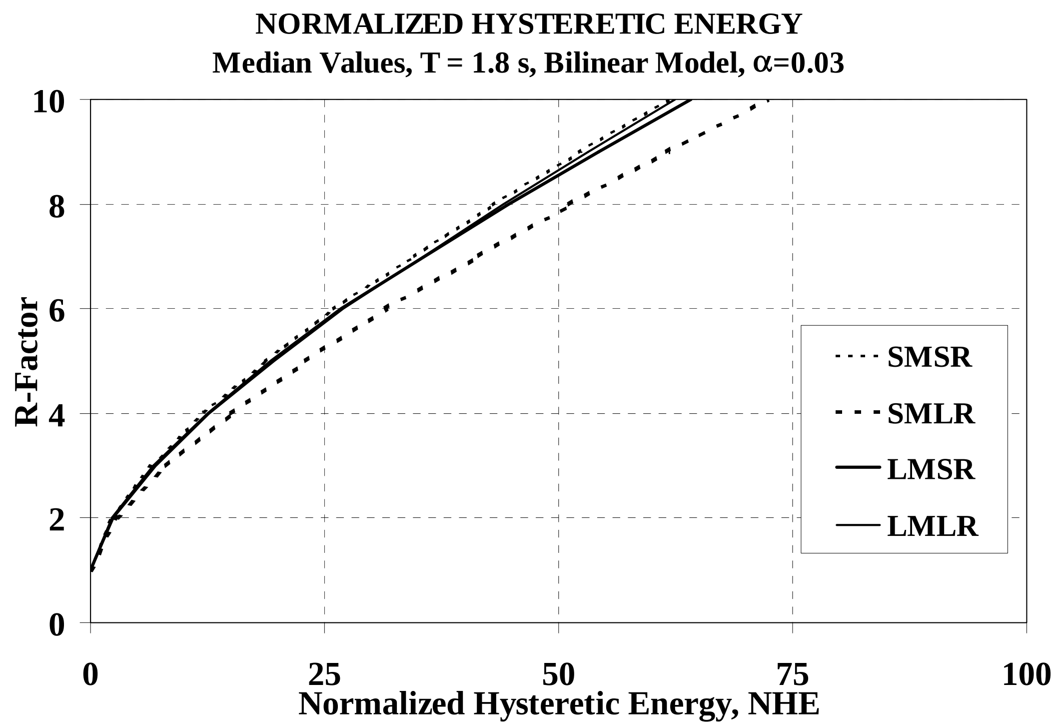

(a) Median Normalized Hysteretic Energy Demands

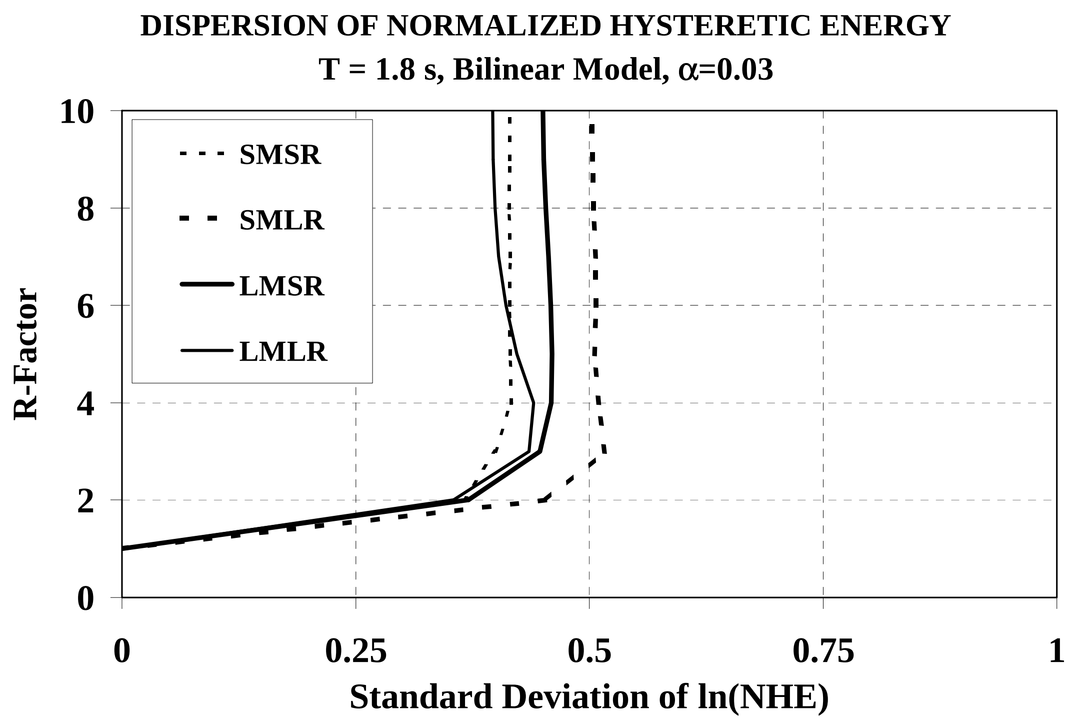

(b) Dispersion of Normalized Hysteretic Energy Demands

Figure 3.24 Statistics on the Normalized Hysteretic Energy, Four M-R Bins, Bilinear Model, T = 1.8 sec

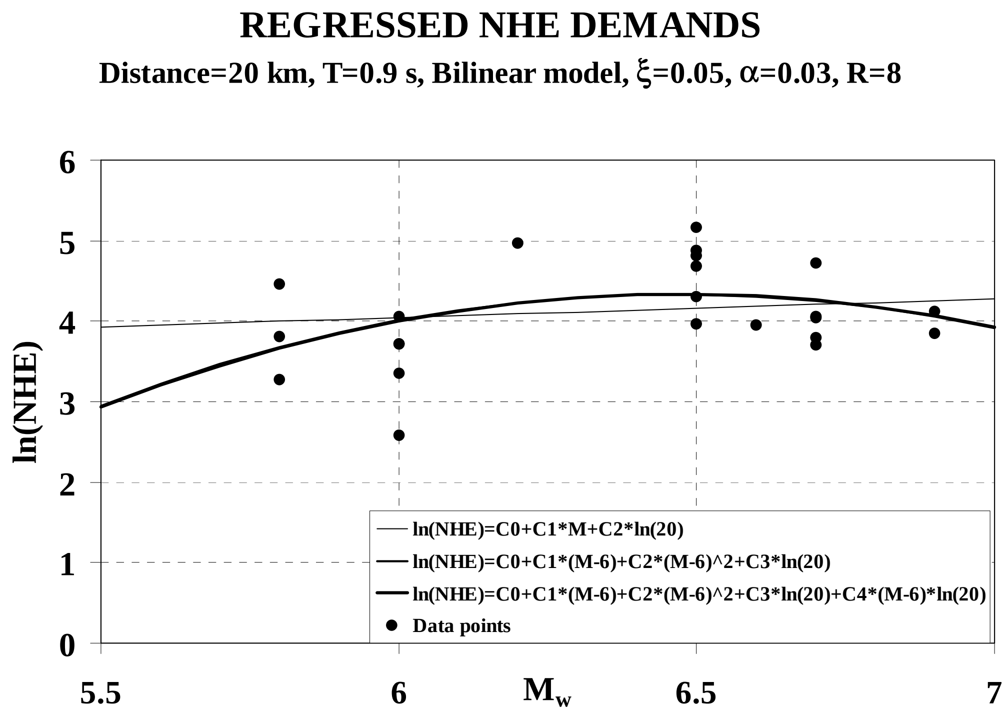

Figure 3.25 Regressed NHE Demands as a Function of Magnitude (O.G.M. Record Set), T = 0.9 sec

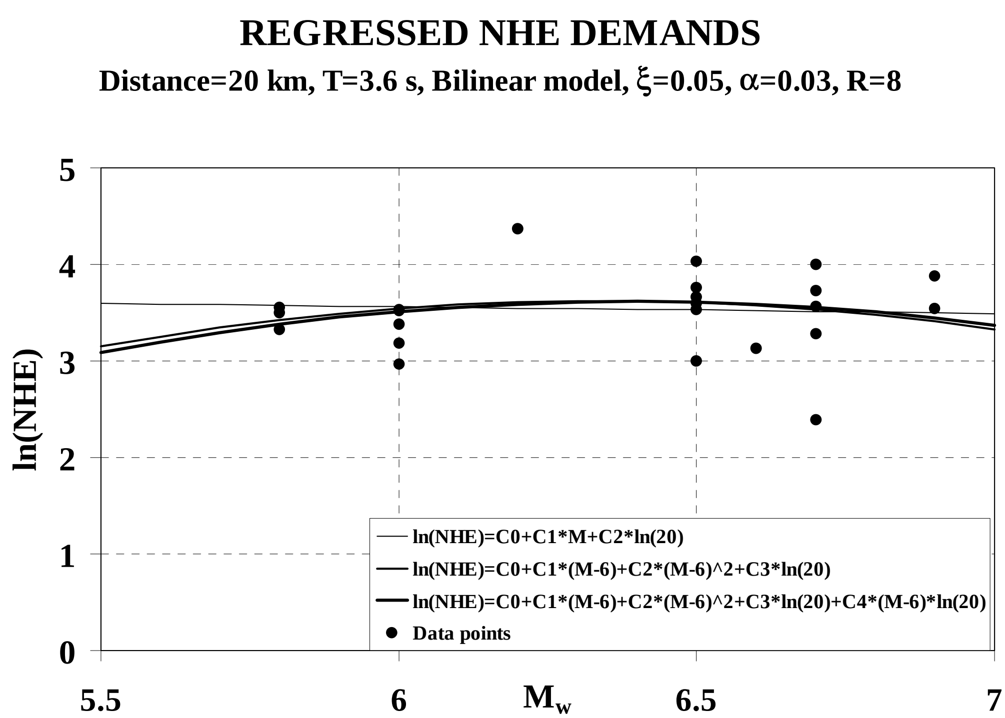

Figure 3.26 Regressed NHE Demands as a Function of Magnitude (O.G.M. Record Set), T = 3.6 sec

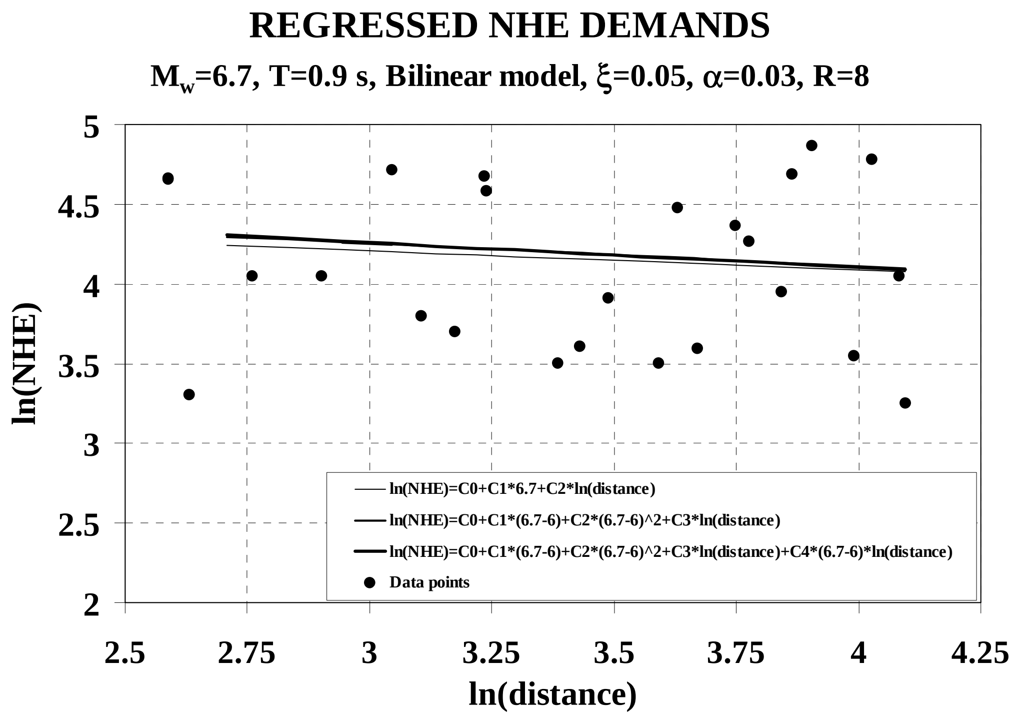

Figure 3.27 Regressed NHE Demands as a Function of Distance (O.G.M. Record Set), T = 0.9 sec

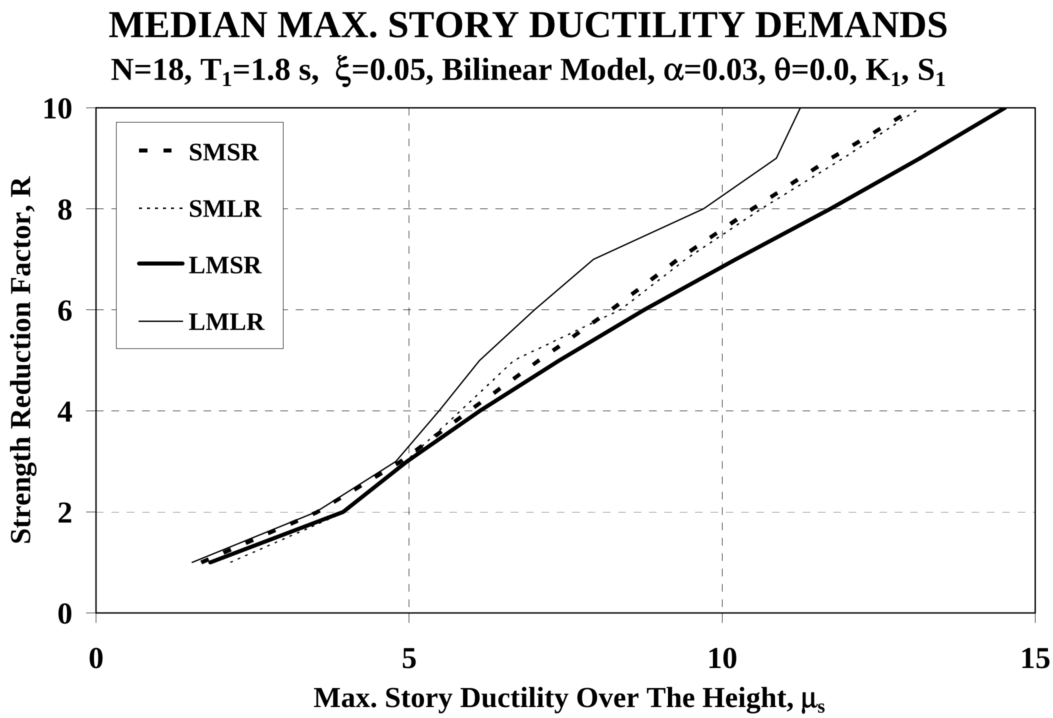

(a) Median Maximum Story Ductility over the Height

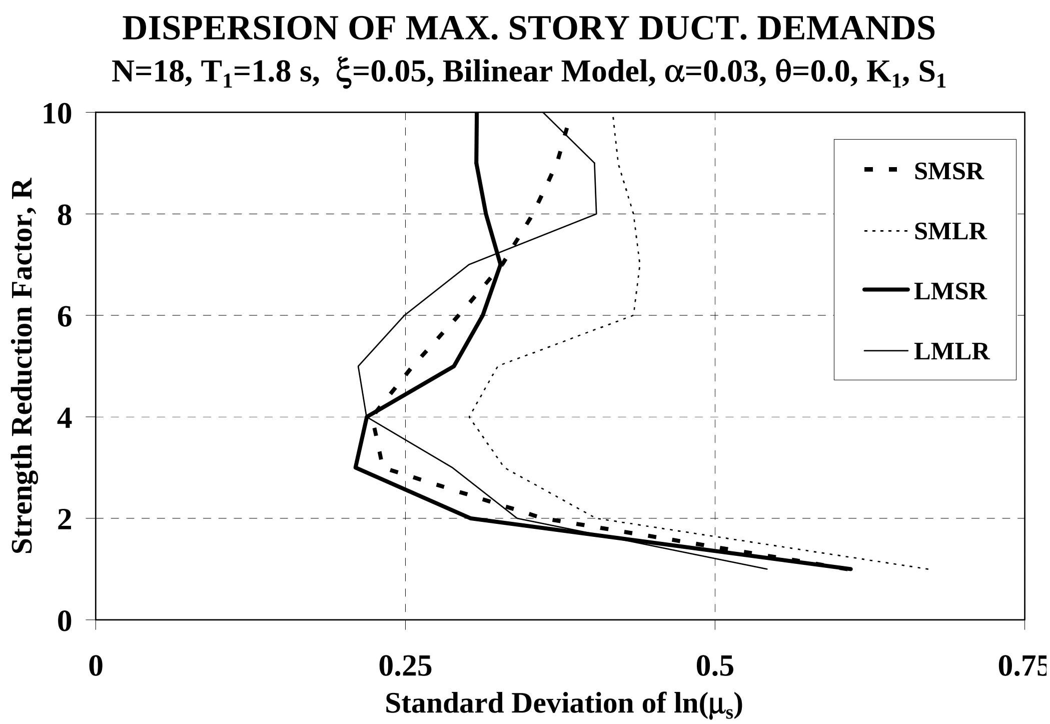

(b) Dispersion of the Maximum Story Ductility Over the Height

Figure 3.28 Statistics on the Maximum Story Ductility over the Height, Four M-R Bins, Bilinear Model, MDOF Case

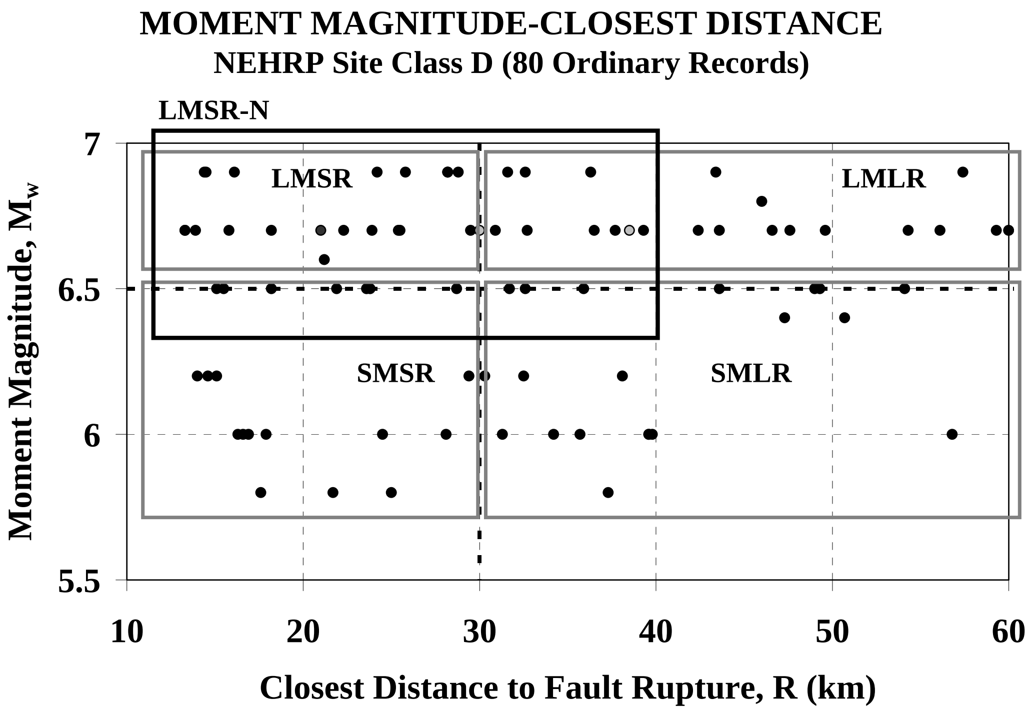

Figure 3.29 LMSR-N Record Set (Magnitude-Distance Pairs)

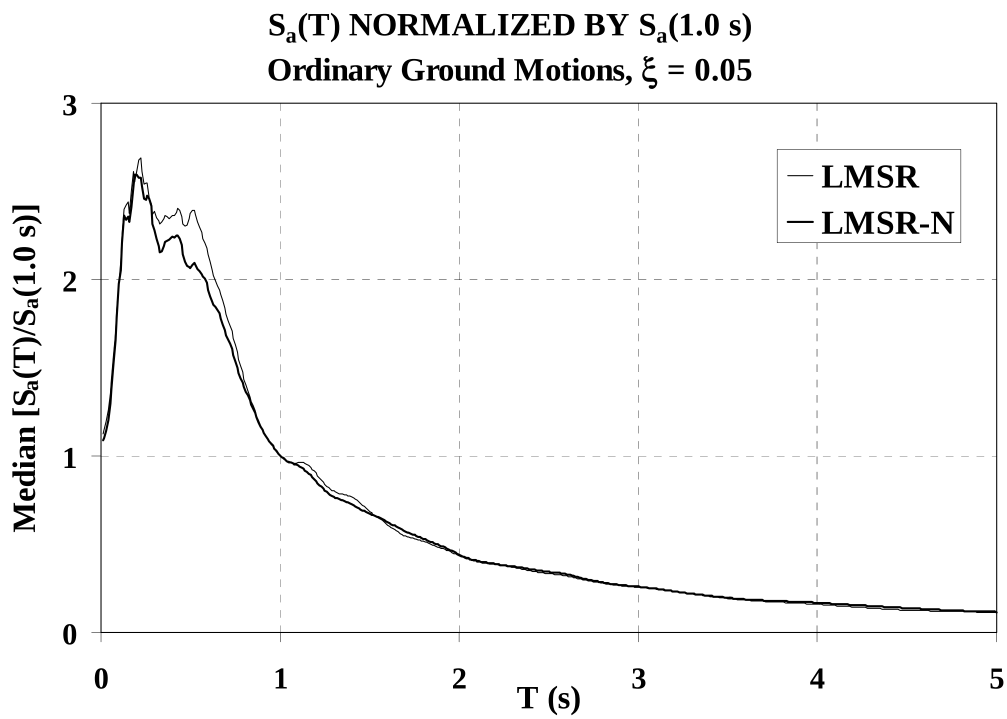

(a) Median $S_a(T)/S_a(1.0\text{ s})$ Ratios

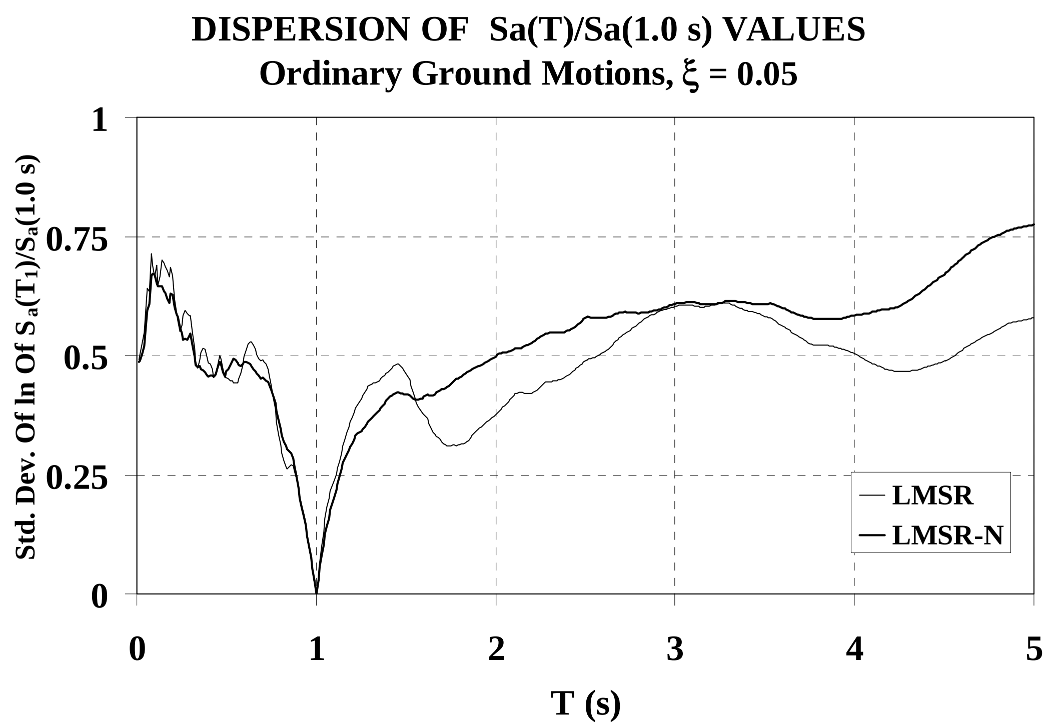

(b) Dispersion of $S_a(T)/S_a(1.0\text{ s})$ Ratios

Figure 3.30 Statistics on Normalized Elastic Spectral Acceleration Demands (LMSR vs. LMSR-N Bin)

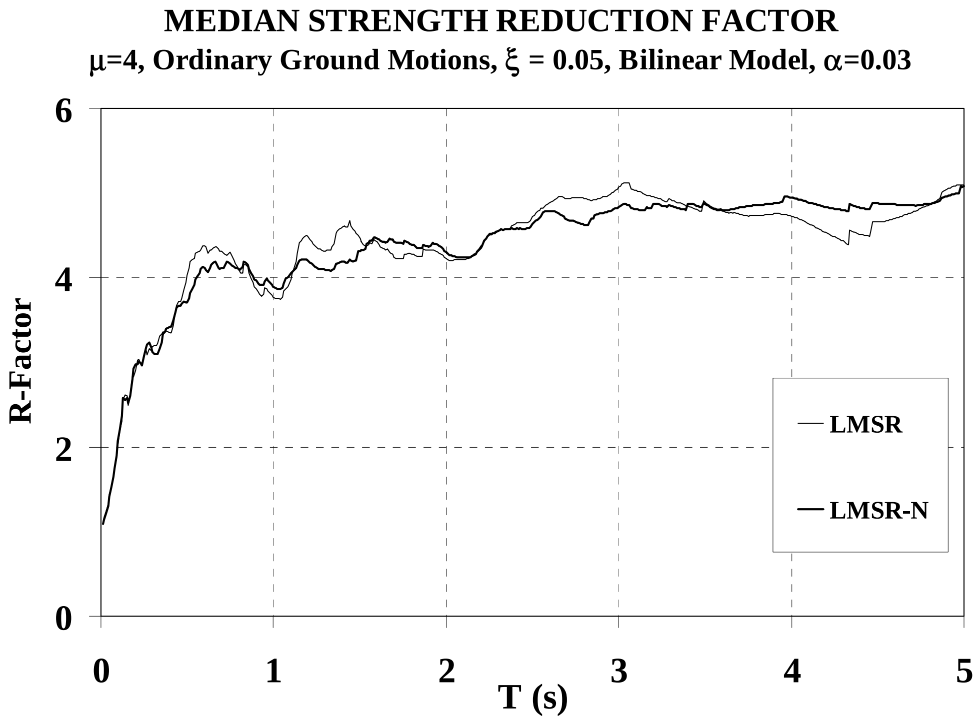

(a) Median R-μ-T Relationships

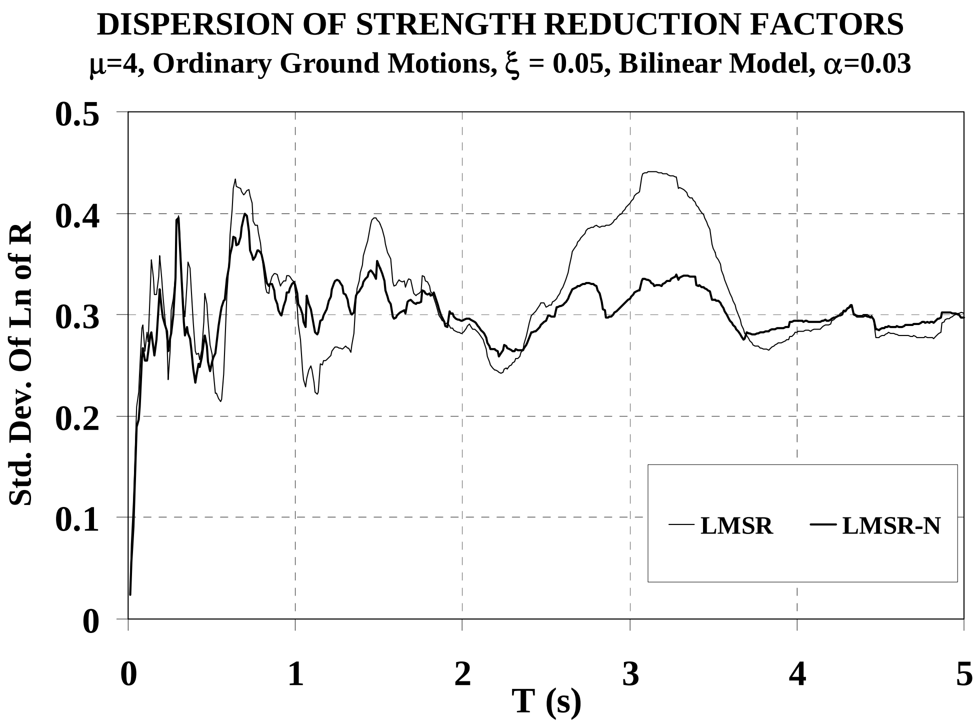

(b) Dispersion of R-factors

Figure 3.31 Statistics on R-μ-T Relationships, LMSR vs. LMSR-N Bin, μ = 4, Bilinear Model

4 Evaluation of EDPs for Regular Frames: Deformation, Acceleration, and Velocity Demands

4.1 INTRODUCTION

In a performance evaluation context, quantification of demand parameters implies the statistical evaluation of EDPs as a function of IMs and the study of the sensitivity of these relationships to different structural characteristics and ground motion intensity, frequency content and duration. The purpose of this chapter is to evaluate deformation, acceleration and velocity demands for nondeteriorating regular frames subjected to ordinary ground motions. The dependence of the aforementioned demands on fundamental period, number of stories, and ground motion intensity level is studied as well as the variation of their associated uncertainties with the level of inelastic behavior.

The main EDPs evaluated in this study are those that correlate best with decision variables related to direct dollar losses and downtime. Therefore, hysteretic models that do not include cyclic deterioration are considered to be useful for the aforementioned purpose. If the limit state of collapse is of concern, cyclic deterioration must be included in the analyses. Moreover, ordinary ground motions are used to represent the ground motion hazard corresponding to the limit states of direct losses and downtime (not "long" return-period hazards that are expected to cause deterioration in structural response). Ground motions in the near-field region are expected to dominate the hazard corresponding to the limit state of collapse ("long" return-period hazard). Relationships between EDPs and IMs are established, with the primary IM of interest being the spectral acceleration at the first mode of the structure $S_a(T_1)$. As discussed in Chapter 3, although $S_a(T_1)$ is not considered to be the "ideal" IM (the most efficient and sufficient one for most applications), it was shown to be an adequate IM for ordinary ground motions.

Since regular frames are the lateral-load-resisting system of interest in this study, the most relevant EDPs should be those that correlate best with the performance assessment of this type of system. Roof drift, story drifts, plastic hinge rotations, absolute floor accelerations, and absolute floor velocities are investigated. The statistical evaluation of the aforementioned EDPs and their relationships to $S_a(T_1)$ are presented in the following sections as well as the variation of their associated uncertainties with the relative intensity level. The regular frames used are generic one-bay beam-hinge models with concentrated plasticity modeled by using peak-oriented hysteretic rules with 3% strain hardening. The story shear strength pattern is tuned so that simultaneous yielding is attained under a parabolic load pattern (NEHRP, k =2). These frames form the base case family of structures described in Chapter 2. Seismic demands for variations in structural properties are the focus of Chapter 7.

4.2 DEMAND EVALUATION USING THE LMSR-N GROUND MOTION SET

In Chapter 3 it was stated that *within certain limitations,* there are reasons to de-emphasize records from the LMLR, SMLR, and SMSR magnitude-distance bins and carry out the seismic demand evaluation of response parameters (given $S_a(T_1)$) using records from the LMSR bin. However, as discussed in Section 3.3.5, for SDOF systems, the expansion in the boundaries of the LMSR bin to the LMSR-N (to include 20 more records) does not introduce any significant modification in the frequency content (spectral shape) of the ground motion set, while allowing a more consistent statistical evaluation of the results. A limited study was performed with various EDPs to assess whether this conclusion is reflected in the seismic demand evaluation of MDOF systems. Representative results are shown in Figure 4.1, where the relationship between the normalized average of maximum story drift angles and the normalized spectral acceleration at the first mode is illustrated for a nine-story frame with T_1 = 0.9 sec. Figure 4.1(a) shows the statistical evaluation for the LMSR data set and Figure 4.1(b) for the LMSR-N set. Within the range of primary interest (approximately $[S_a(T_1)/g]/\gamma < 8$) there is no significant difference between the two analyses (medians, 16th and 84th percentiles). This observation is in agreement with the conclusion obtained in Section 3.3.5. The LMSR-N data set (with 40 records) is thus used for the seismic demand evaluation of MDOF frames, for it provides more reliable statistical information than the LMSR bin.

4.3 EVALUATION OF DEFORMATION DEMANDS RELEVANT FOR PERFORMANCE ASSESSMENT

Several research efforts have focused on the evaluation of deformation demands for both SDOF and MDOF systems in which displacement demands from nonlinear time history analyses have been quantified as a function of a normalized strength or ground motion intensity level (Seneviratna and Krawinkler, 1997; Gupta and Krawinkler, 1999; Miranda, 1999; Fajfar, 2000). The objective of this work is to achieve a better understanding of the global seismic behavior of regular frames while providing statistical data useful for a probabilistic evaluation of relevant EDPs as a function of a ground motion IM (in this study, the IM of interest is the spectral acceleration at the first mode of the system). For a given system, this information can be further utilized in conjunction with (1) IM hazard information to quantify the EDP hazard and (2) fragility functions that quantify the relationship between EDPs and different levels of damage to make a probabilistic assessment of a specific damage state (Krawinkler, 2002). An illustration of this process is presented in Section 9.2.

Since the performance targets of interest are those related to direct losses and downtime, it is necessary to focus on deformation parameters that relate to both structural and nonstructural damage for relatively “small” ductility levels where cyclic deterioration effects are not critical. In this context, the primary EDPs of interest are:

Maximum roof drifts,

Average of the maximum story drift angles,

Maximum story drift angle over the height,

Average of the maximum story ductilities (story ductility is defined as the story drift normalized by the story yield drift obtained from a pushover analysis),

Maximum story ductility over the height,

Residual drifts, and

Maximum beam plastic rotations

The maximum roof drift is a global deformation measure that relates to both structural and nonstructural damage. It has been used to relate MDOF to SDOF elastic spectral information (Seneviratna and Krawinkler, 1997; Miranda, 1998). The maximum story drift (or ductility) over the height is relevant for structural damage (if damage is dominated by the maximum story deformation over the height). It is also a measure of damage to nonstructural components, e.g., partitions, which are sensitive to relative deformations between floors. The average of the maximum drifts (or ductilities) over the height is a good measure of structural damage if damage is about linearly proportional to drift (or ductility). Residual story drifts are also important for performance assessment; in particular, after a seismic event when the structural stability of the system is judged by the residual floor deformations. Maximum beam plastic rotations are also studied to provide information related to damage to structural components of a system.

4.3.1 Maximum Roof Drift Demands

As stated earlier in Section 4.3, the maximum roof drift angle, $\theta_{r,max}$, from a nonlinear time history analysis is as a global parameter that can be used to relate MDOF response to SDOF elastic spectral information. Simplified procedures have been suggested to estimate local demand parameters, e.g., beam plastic rotations, based on elastic SDOF displacements (Gupta and Krawinkler, 1999). The process involves the use of empirical factors obtained from the statistical evaluation of demands to relate: SDOF elastic displacements to elastic roof displacements, elastic roof displacements to inelastic roof displacements, inelastic roof drift angles to story drift angles, story drift angles to plastic story drift angles, and plastic story drift angles to beam plastic rotations. Gupta and Krawinkler (1999) illustrate this process for the family of steel frames analyzed in the SAC Joint Venture project. In the context of performance evaluation, $\theta_{r,max}$ has also been used as the target displacement for nonlinear static (pushover) analyses (FEMA 356, 2000).

In order to quantify relationships between the maximum roof drift angle and ground motion intensity, nonlinear time history analyses are performed with the base case family of generic frames described in Section 2.4.1 subjected to the LMSR-N set of ground motions. The objective is to relate $S_a(T_1)/g$ to $\theta_{r,max}$ (IM-EDP relationships) and study the sensitivity of these relationships to strength, fundamental period, and number of stories. Representative results for this specific IM-EDP relationship are shown in Figures 4.2(a) and 4.2(b). Since nondeteriorating systems are used, results for large $[S_a(T_1)/g]/\gamma$ values (causing large story ductility ratios) are of academic value. Although $[S_a(T_1)/g]/\gamma$ represents the conventional R-factor (strength reduction factor) when overstrength is not present, a better measure of the level of inelastic behavior is given by the maximum story ductility ratios. Information regarding the maximum story ductility ratios for the base case family of generic structures is provided in Section 4.3.9.

Figure 4.2 shows that for small relative intensities ($[S_a(T_1)/g]/\gamma$ in the order of 1.0), the median normalized elastic roof drift angle is approximately equal to the first-mode participation factor, PF_1. In this case, PF_1 is defined as the first-mode participation factor obtained when the first-mode shape is normalized to be equal to one at the roof. Thus, the median elastic roof drift angle is dominated by the first mode, and its dispersion (given $S_a(T_1)/g$) is caused mainly by higher mode effects. As the relative intensity increases, the normalized $\theta_{r,max}$ remains approximately constant implying a linear increase in $\theta_{r,max}$ with $S_a(T_1)/g$. For the flexible frame (T_1 = 1.8 sec) and large relative intensities, a small increase in relative intensity causes a large increase in the normalized $\theta_{r,max}$. This behavior is attributed to the structure P-delta effect, which causes the response to approach dynamic instability at large relative intensities. In both Figures 4.2(a) and 4.2(b) the dispersion in the results is significant, especially at large relative intensity levels, which shows the limitations of using a simple IM such as $S_a(T_1)/g$.

The fact that in the range of interest the median normalized maximum roof drift is approximately equal to the first-mode participation factor, indicates that $PF_1 {*} S_d(T_1)$ often provides an estimate of the median maximum roof displacement. However, Figure 4.2(b) demonstrates that this estimate is not applicable to relative large relative intensity levels for which P-delta effects compromise the dynamic stability of flexible systems. In the following paragraphs it will be seen that estimating the median maximum roof displacement based on $PF_1 {*} S_d(T_1)$ does not apply to inelastic short-period regular frames either.

Figure 4.3 illustrates the median normalized $\theta_{r,max}$ demands ($\theta_{r,max}/[S_d(T_1)/H]$), given $[S_a(T_1)/g]/\gamma$, for the base case family of generic frames. Results are presented for the stiff (T_1 = 0.1N) and flexible (T_1 = 0.2N) frames. Median values are reported because they provide general patterns of behavior. $\theta_{r,max}/[S_d(T_1)/H]$ (which for elastic behavior is close to the first-mode participation factor) decreases up to a relative intensity of approximately $[S_a(T_1)/g]/\gamma = 4$, which implies that in this range, as the relative intensity increases, the inelastic roof displacement is less than the elastic one. This behavior is not observed for the T_1 = 0.3 sec frame because for relatively weak short-period systems, the ratio of inelastic to elastic displacement is much greater than unity (see Figure 4.4). As the relative intensity increases above about 4.0, the normalized $\theta_{r,max}$ increases for all systems. Flexible frames for which P-delta effects cause a negative postyield stiffness in the response exhibit large $\theta_{r,max}/[S_d(T_1)/H]$ values. A small increase in the relative intensity causes a large increase in the maximum roof drift demands, implying that the system is approaching dynamic instability. The relative intensity at which dynamic instability is imminent decreases with an increase in the fundamental period. A more detailed discussion on the effect of structure P-delta on the response of regular frames is presented in Chapter 7.

The relationship between the median of the maximum roof drift, relative intensity level and fundamental period is presented in Figure 4.5. Figure 4.5(a) shows the variation of median $\theta_{r,max}/[S_d(T_1)/H]$ values with period for different number of stories and $[S_a(T_1)/g]/\gamma$ = 0.25, 1.0, and 2.0, while Figure 4.5(b) is presented for $[S_a(T_1)/g]/\gamma$ = 4.0, 6.0, and 8.0. In the median, $\theta_{r,max}/[S_d(T_1)/H]$ is a well-contained quantity except for large relative intensities ($[S_a(T_1)/g]/\gamma$ = 4.0, 6.0, and 8.0) when the system has a short period (T_1 = 0.3 s) or is sensitive to P-delta effects (N = 12, T_1 = 2.4 sec; N = 15, T_1 = 3.0 sec; N = 18, T_1 = 3.6 sec). Note that in Figure 4.5(b) some values are not reported for two of the frames, N = 15, T_1 = 3.0 sec, and N = 18, T_1 = 3.6 sec, because at large relative intensities the structures experience dynamic instability due to P-delta effects with more than 50% of the ground motion records. Given the period (T_1 = 0.6 sec, 1.2 sec or 1.8 sec), frames with different number of stories have similar median $\theta_{r,max}/[S_d(T_1)/H]$ values. This implies that regular frames with the same period and different number of stories experience similar roof displacements unless the flexible frames become P-delta sensitive.

An alternative for evaluating the relationship between the normalized $\theta_{r,max}$, the relative intensity, the fundamental period and the number of stories is illustrated in Figure 4.6. Figure 4.6(a) presents information for the stiff frames (T_1 = 0.1N) and Figure 4.6(b) for the flexible frames (T_1 = 0.2N). The first-mode participation factors are shown with individual squares. As discussed before, except for relatively weak short-period frames and P-delta sensitive frames, the median $\theta_{r,max}/[S_d(T_1)/H]$ values are approximately equal to the first-mode participation factor regardless of the number of stories and the fundamental period. This result coincides with observations presented in Seneviratna and Krawinkler (1997) and suggests that for ordinary ground motions, and levels of inelastic behavior for which cyclic deterioration effects are negligible, the maximum roof drift of regular frames is dominated by the first mode (except for P-delta-sensitive frames).

The dispersion of $\theta_{r,max}/[S_d(T_1)/H]$ values as a function of the relative intensity level is shown in Figure 4.7. For the range of primary interest, the dispersion tends to increase with the level of inelastic behavior except for the short-period frame (T_1 = 0.3 sec). The large dispersion experienced by short-period systems for relative small $[S_a(T_1)/g]/\gamma$ values is due to the "erratic" individual spectral shapes observed in the short-period range of many of the recorded ground motions. This dispersion of $\theta_{r,max}/[S_d(T_1)/H$ follows similar trends to the dispersion observed for the ratio of the inelastic to the elastic displacement in SDOF systems (Figures 3.9(b) to 3.12(b)). P-delta sensitive frames exhibit a large increase in dispersion for a small increase in relative intensity once they approach dynamic instability in the response. These observations are relevant within the probabilistic seismic performance assessment methodology discussed in Chapter 9, when closed-form solutions assuming a constant dispersion are implemented.

4.3.2 Normalized Average of the Maximum Story Drift Angle Demands

The average of the maximum story drift angles, $\theta_{si,ave}$, is equivalent to the maximum roof drift angle if all maximum story drift angles occur simultaneously. In order to investigate the relationship between $S_a(T_1)/g$ and $\theta_{si,ave}$, plots of the type shown in Figures 4.8 to 4.11 are utilized. Note the similarities in patterns of these relationships with the ones observed for the normalized maximum roof drift angle (Figures 4.2, 4.3, 4.5, and 4.7). These similarities imply that the average of the maximum story drifts and the maximum roof drift are well correlated. This observation is further studied in Section 4.3.4 where ratios of $\theta_{si,ave}/\theta_{r,max}$ are evaluated for different relative intensities, periods, and number of stories.

Figure 4.9 presents median $\theta_{si,ave}/[S_d(T_1)/H]$, given $[S_a(T_1)/g]/\gamma$, for the T_1 = 0.1N and the T_1 = 0.2N frames. Patterns of behavior observed for $\theta_{r,max}/[S_d(T_1)/H]$ (Figure 4.3) also apply in this case. However, median $\theta_{si,ave}/[S_d(T_1)/H]$ values are slightly larger due to the influence of higher modes in the response. Figure 4.10 presents a graphical representation of the dependence of $\theta_{si,ave}/[S_d(T_1)/H]$ on the relative intensity, fundamental period, and number of stories. For small relative intensities (see Figure 4.10(a)) it can be observed that $\theta_{si,ave}/[S_d(T_1)/H]$ increases approximately linearly proportional to the fundamental period. Furthermore, in cases where there are overlapping periods (N = 3, N = 6, and T_1 = 0.6 sec; N = 6, N = 12, and T_1 = 1.2 sec; N = 9, N = 18, and T_1 = 1.8 sec), similar median $\theta_{si,ave}/[S_d(T_1)/H]$ imply that the flexible (T_1 = 0.2N) frames experience $\theta_{si,ave}$ demands that are twice as large as those experienced by the stiff (T_1 = 0.1N) frames. Figure 4.10(b) conveys a different message. As in the case of the normalized maximum roof drift, for $[S_a(T_1)/g]/\gamma$ = 4, 6, and 8, median $\theta_{si,ave}/[S_d(T_1)/H]$ values do not vary considerably as a function of the fundamental period except for frames with short periods (T_1 = 0.3 sec) and significant P-delta effects.

The dispersion of $\theta_{si,ave}/[S_d(T_1)/H]$ values as a function of $[S_a(T_1)/g]/\gamma$ is illustrated in Figure 4.11. It can be observed that the variation of the dispersion with the relative intensity follows patterns similar to the variation of the dispersion of $\theta_{r,max}/[S_d(T_1)/H]$. However, in the elastic range, some frames exhibit a dispersion of $\theta_{si,ave}/[S_d(T_1)/H]$ much larger than the dispersion of $\theta_{r,max}/[S_d(T_1)/H]$ due to the influence of higher modes in the response.

For specific cases, e.g., T_1 = 3.0 sec, N = 15, a decrease in dispersion with respect to the dispersion in the elastic range is observed up to a value of $[S_a(T_1)/g]/\gamma$ = 2. This behavior is a consequence of the different frequency content of the ground motion records. Even when records are carefully selected to minimize the magnitude-distance dependence of spectral shapes, differences in frequency content (i.e., valleys or humps) to the right of the fundamental period cause the IM-EDP relationships to have different shapes, as shown in Figure 4.12 where IDAs for a system with T_1 = 3.0 sec, N = 15 and γ = 01.0 are presented. Values for the standard deviation of the natural log of $\theta_{si,ave}$ (denoted as σ in the plots) are also shown for $S_a(T_1)$ = 0.025 g, 0.30 g, and 0.40 g. The response for two individual ground motions is highlighted and their corresponding elastic acceleration spectra (scaled to $S_a(3.0s)$ = 0.2 g) are shown in Figure 4.12(b). While for the NR94cen record $\theta_{si,ave}$ increases almost linearly proportional to $S_a(T_1)$, for the IV79cmp record the value of $\theta_{si,ave}$ increases up to a value and then stabilizes to later increase rapidly due to structure P-delta effects. This stabilization in $\theta_{si,ave}$ coincides with the transition of the maximum story drift from the top story to the bottom one (Section 4.3.7), which in the case of the NR94cen occurs for larger intensity values (not shown in the plot). This behavior is mostly caused by the hump in the elastic acceleration spectra of the IV79cmp record to the right of 3.0 sec. Thus, when the behavior is elastic, for most records $\theta_{si,ave}$ increases linearly proportional to $S_a(T_1)$ and large dispersion values are caused by higher mode effects. As the system becomes inelastic, differences in spectral shapes cause some of the IDAs to stabilize causing the dispersion to decrease. Large dispersion values are observed for larger intensities due to the presence of severe P-delta effects.

In general, values of dispersion are similar to those obtained for the normalized maximum roof drift except in the elastic range where the average of the maximum story drifts exhibits larger dispersions because of the influence of higher modes.

4.3.3 Normalized Maximum Story Drift Angle Demands

The maximum story drift angle over the height, $\theta_{s,max}$, is a relevant EDP for damage assessment and collapse evaluation of frames when collapse is attained in an incremental fashion due to the presence of severe P-delta effects. In order to evaluate the relationship between $\theta_{s,max}$ and $S_a(T_1)/g$, plots of the type shown in Figure 4.13 are developed. It can be seen that patterns are not as clear as the ones observed in Figures 4.2 and 4.8 for $\theta_{r,max}$ and $\theta_{si,ave}$, respectively. Moreover, the dispersion of $\theta_{s,max}/[S_d(T_1)/H]$ values is greater than the one observed for $\theta_{r,max}/[S_d(T_1)/H]$ and $\theta_{si,ave}/[S_d(T_1)/H]$. Figure 4.13(a) shows a large dispersion for small relative intensity levels. This result is more evident in Figure 4.13(b) in which the effect of higher modes is more pronounced at small relative intensities. For the T_1 = 1.8 sec frame, the decrease in $\theta_{s,max}/[S_d(T_1)/H]$ with an increase in relative intensity (in the range $2 \leq [S_a(T_1)/g]/\gamma \leq 4$) coincides with the transition of the maximum story drift over the height from top to bottom (see Section 4.3.7) as the level of inelastic behavior increases (behavior similar to the one observed in Figure 4.12(a) for the IV79cmp record). The rapid increase in $\theta_{s,max}/[S_d(T_1)/H]$ for a relatively small increase in relative intensity is caused by P-delta effects.

Figure 4.14 shows median $\theta_{s,max}/[S_d(T_1)/H]$ values for various frames and relative intensities. For $T_1 \geq 0.6$ sec, there is an increase in median $\theta_{s,max}/[S_d(T_1)/H]$ with the fundamental period. Moreover, median $\theta_{s,max}/[S_d(T_1)/H]$ values tend to increase with the relative intensity, except for tall frames (N > 9), for which a rapid decrease in median $\theta_{s,max}/[S_d(T_1)/H]$ values is observed for

$2 \leq [S_a(T_1)/g]/\gamma \leq 6$, which is consistent with the observations presented in the previous paragraph regarding Figure 4.13.

Figure 4.15 shows relationships between the normalized maximum story drift angle over the height, fundamental period, and number of stories, for relative intensities from 0.25 to 8.0. As discussed before, median $\theta_{s,max}/[S_d(T_1)/H]$ values increase with the level of intensity and fundamental period. Differences of more than a factor of 4 are observed in Figure 4.15(a) between normalized maximum story drift values corresponding to periods of 0.6 sec and 3.6 sec. Two additional observations can be made: first, for both small (Figure 4.15(a)) and large relative intensities (Figure 4.15(b)) and a given fundamental period (0.6 sec, 1.2 sec, and 1.8 sec), the stiffer frame ($T_1 = 0.1N$) experiences median $\theta_{s,max}/[S_d(T_1)/H]$ values that are 20% to 60% larger than those obtained for the flexible frame ($T_1 = 0.2N$). Thus, there is a clear dependence of $\theta_{s,max}/[S_d(T_1)/H]$ on the number of stories. A weaker dependence is observed for $\theta_{r,max}/[S_d(T_1)/H]$ and $\theta_{si,ave}/[S_d(T_1)/H]$ (Figures 4.5 and 4.10). Differences in median $\theta_{s,max}/[S_d(T_1)/H]$ for the stiff and flexible frames increase with the value of the fundamental period. For the same strength, T_1 and $S_a(T_1)$, even when the median maximum $\theta_{r,max}$ and $\theta_{si,ave}$ differ approximately by a factor of 2 between the $T_1 = 0.1N$ and 0.2N frames, the median maximum story drift angles differ by a factor of less than 2 and approach each other as the fundamental period of the frames increases. For a given relative intensity, median $\theta_{s,max}/[S_d(T_1)/H]$ values tend to increase with the fundamental period (except in the short-period range, e.g., $T_1 = 0.3$ sec). Therefore, it is evident that the maximum story drift over the height is highly influenced by higher mode and P-delta effects, which is also reflected in the assessment of dispersions discussed in the next paragraph.

The dispersion of $\theta_{s,max}/[S_d(T_1)/H]$ values as a function of $[S_a(T_1)/g]/\gamma$ is shown in Figure 4.16. It can be observed that in both graphs the dispersion increases with period (except in the short-period range). In some cases, values for the standard deviation of the natural log of the maximum story drift angle data are as high as 1.0 when the models experience small levels of inelastic behavior. This observation suggests that the maximum story drift over the height is quite sensitive to the effect of the higher modes in the response particularly at small relative intensities. The variation of the dispersion with the relative intensity follows patterns similar to the ones observed for the average of the maximum story drift angles (Figure 4.11).

4.3.4 Ratio of the Average of the Maximum Story Drift Angles to the Maximum Roof Drift Angle

The ratio of the average of maximum story drift angles to the maximum roof drift angle, $\theta_{si,ave}/\theta_{r,max}$, is considered relevant for seismic performance assessment, since it serves a dual purpose. First, statistical information on this ratio provides means to relate the maximum roof drift from nonlinear time history analyses (which in some cases can be estimated from SDOF baseline information, Section 4.3.1) to an EDP ($\theta_{si,ave}$) relevant for damage assessment if damage is linearly proportional to drift. Second, the ratio $\theta_{si,ave}/\theta_{r,max}$ could be used to estimate the target displacement currently prescribed in nonlinear static (pushover) analysis procedures (FEMA 356, 2000).

Median $\theta_{si,ave}/\theta_{r,max}$ values demonstrate that $\theta_{si,ave}$ is close to $\theta_{r,max}$ regardless of the level of inelastic behavior except for P-delta sensitive frames (see Figure 4.17). For the stiff ($T_1 = 0.1N$) frames, this ratio remains rather constant with the relative intensity. The flexible ($T_1 = 0.2N$) frames exhibit slightly larger median $\theta_{si,ave}/\theta_{r,max}$ values and small variations with the relative intensity. For instance, for small relative intensities, median $\theta_{si,ave}/\theta_{r,max}$ are slightly larger because of the presence of higher mode effects for which the maximum story drift occurs at the top of the system.

Figure 4.18 shows the variation in median values of $\theta_{si,ave}/\theta_{r,max}$ with fundamental period, number of stories and relative intensity level. The median of this ratio increases with the value of the fundamental period, for the contribution of higher modes to the response increases with T_1. For the case of the 3 story frames (T_1 = 0.3 sec and 0.6 sec) the ratio $\theta_{si,ave}/\theta_{r,max}$ is close to 1.0. This result is expected, since the response of short-period structures is dominated by the first mode, so the systems deflect primarily in a straight line. For a given fundamental period and different number of stories (T_1 = 0.6 sec, 1.2 sec, 1.8 sec) differences in median $\theta_{si,ave}/\theta_{r,max}$ are negligible for small relative intensity levels (Figure 4.18(a)), and they are in the order of 15% for large relative intensity levels (Figure 4.18(b)).

For the range of relative intensity levels of interest in this study, $\theta_{si,ave}/\theta_{r,max}$ is a stable parameter that is weakly dependent on the intensity level. Given the fundamental period, this ratio is also weakly dependent on the number of stories. However, it seems to be a noticeable dependence on the fundamental period. A simple least-squares regression of the data corresponding to systems *without severe P-delta effects* (systems with severe P-delta effects are those for which the global pushover shows a negative postyield stiffness) is performed to obtain to following median $\theta_{si,ave}/\theta_{r,max}$ estimate (correlation coefficient, r = 0.89):

$$\frac{\theta_{si,ave}}{\theta_{r,\max}} = 1 + 0.13T_1 \text{ , for } [S_a(T_1)/g]/\gamma \leq 8 \text{ and } 0.3 \text{ sec} \leq T_1 \leq 3.6 \text{ sec} \qquad (4.1)$$

The dispersion of the ratio $\theta_{si,ave}/\theta_{r,max}$ is reported in Figure 4.19. Relatively small values of dispersion are encountered in all cases (except for those where P-delta effects jeopardize the dynamic stability of the system), with an increase in the dispersion observed at small relative intensity levels for flexible frames. Relatively small dispersions suggest that the ratio $\theta_{si,ave}/\theta_{r,max}$ is not severely influenced by the frequency content of the ground motions.

4.3.5 Ratio of the Maximum Story Drift Angle over the Height to the Maximum Roof Drift Angle

Past studies have shown that the estimation of maximum story drift over the height is associated with large dispersions, while the estimation of maximum roof drift angles depicts smaller dispersions. Sources of uncertainty are found in the frequency content of the ground motion, structural properties, and modeling assumptions. This section addresses central values and the dispersion of this ratio as a function of both ground motion frequency content and structural properties. The ratio $\theta_{s,max}/\theta_{r,max}$ also provides information related to the concentration of maximum story drift in a single story. This information is useful for loss estimation and performance levels in which global instability is of concern.

Median values of $\theta_{s,max}/\theta_{r,max}$ exhibit patterns that are not as uniform as the ones observed for $\theta_{si,ave}/\theta_{r,max}$, which is illustrated in Figure 4.20. $\theta_{s,max}/\theta_{r,max}$ values are maximum for $2 \leq [S_a(T_1)/g]/\gamma \leq 4$ and decrease with a further increase in relative intensity (except for P-delta sensitive frames). These patterns are similar to the ones observed for the maximum story drift angle (Section 4.3.3).

Median values of $\theta_{s,max}/\theta_{r,max}$ are evaluated for various fundamental periods, number of stories and relative intensity levels. Figure 4.21 demonstrates that the ratio of maximum story drift angle over the height to the maximum roof drift angle increases with both the fundamental period and the number of stories. Median values are considerable larger for this ratio than for the ratio of $\theta_{si,ave}/\theta_{r,max}$ (Figure 4.18). Values as high as 4 are observed even for relatively small intensity levels. For the short-period frame (T_1 = 0.3 sec), median ratios are close to 1.0, for the response is basically dominated by the first mode and the structures deflect in a straight line even for large levels of intensity. For a given fundamental period (T_1 = 0.6 sec, 1.2 sec, 1.8 sec) stiffer frames (T_1 = 0.1N) experience median $\theta_{s,max}/\theta_{r,max}$ values 20% to 50% larger than those of the flexible frames (T_1 = 0.2N). These observations are in agreement with the fact that the maximum story drift over the height is sensitive to higher mode effects, and suggests that, given the period, the ratio $\theta_{s,max}/\theta_{r,max}$ is strongly influenced by the number of stories. This dependence on the number of stories is illustrated in Figure 4.22. In order to quantify these effects, simple least-squares regressions are carried out for systems that *do not experience severe P-delta effects*, yielding the following estimates of the median $\theta_{s,max}/\theta_{r,max}$ (correlation coefficient, r = 0.93 for Eq. 4.2 and 0.94 for Eq. 4.3):

$$\frac{\theta_{s,\max}}{\theta_{r,\max}} = 0.67 + 1.1T_1 \quad \text{for } [S_a(T_1)/g]/\gamma \leq 8,\ 3 \leq N \leq 18 \text{ and } T_1 = 0.1N \qquad (4.2)$$

$$\frac{\theta_{s,\max}}{\theta_{r,\max}} = 0.46 + 0.9T_1 \quad \text{for } [S_a(T_1)/g]/\gamma \leq 4,\ 3 \leq N \leq 18 \text{ and } T_1 = 0.2N \qquad (4.3)$$

The dispersion of the ratio $\theta_{s,max}/\theta_{r,max}$ is depicted in Figure 4.23. Small values of dispersion (less than 0.25) are observed in most cases for $[S_a(T_1)/g]/\gamma > 2$. However, for slight levels of inelastic behavior, the dispersion can be as high as 1.0. These large values of dispersion follow patterns similar to the ones observed for the dispersion in the maximum story drift over the height discussed in Section 4.3.3.

4.3.6 Estimation of Peak Drift Parameters for Regular Frames

Based on the information presented in Sections 4.3.1 to 4.3.5, peak story drift parameters ($\theta_{si,ave}$ and $\theta_{s,max}$) can be estimated based on elastic SDOF spectral information by using a procedure similar to the one developed by Seneviratna and Krawinkler (1997) and Gupta and Krawinkler (1999). This simple procedure is applicable to structures that are not in the short-period range (T_1

$\geq$ 0.6 sec) and that do not experience severe P-delta effects (i.e., drift demands in the region in which a negative postyield slope exists). A nonlinear static (pushover) analysis technique is recommended to assess whether a system is sensitive to P-delta effects (see Section 7.4). Furthermore, the relationships presented below are given for regular frame structures subjected to ordinary ground motions. Frame models with a smooth strength and stiffness distribution over the height in which a beam-hinge mechanism develops are utilized. For conditions similar to the ones specified in this section, *median* maximum story drift parameters can be estimated as follows:

- $\theta_{r,max} = PF_1 * S_d(T_1)/H$, where PF_1 is the first-mode participation factor and H is the total height of the frame;
- $\theta_{si,ave} = (1.0 + 0.13T_1) * \theta_{r,max}$, where T_1 is the fundamental period of the system;
- $\theta_{s,max} = (0.67 + 1.1T_1) * \theta_{r,max}$, for stiff frames ($T_1$ close to 0.1N), $[S_a(T_1)/g]/\gamma \leq 8$; and
- $\theta_{s,max} = (0.46 + 0.9T_1) * \theta_{r,max}$, for flexible frames ($T_1$ close to 0.2N), $[S_a(T_1)/g]/\gamma \leq 4$.

The above relationships are based on median values that are obtained from Equations 4.1, 4.2, and 4.3. The variability associated with $\theta_{r,max}$, $\theta_{si,ave}$, and $\theta_{s,max}$ can be obtained from the information on dispersion values presented in previous sections of this chapter.

4.3.7 Normalized Maximum Story Drift Profiles

Most of the content of this chapter has focused on the evaluation of a single EDP (e.g., maximum roof drift angle) and ratios of EDPs (e.g., maximum story drift angle over the height normalized by the maximum roof drift angle) as a function of an intensity measure, with the purpose of understanding behavior, providing relevant statistical data on IM-EDP relationships, and relating these EDPs to both structural and nonstructural damage. The distribution of story drifts over the height provides additional information relevant for understanding and quantifying behavior. Moreover, rigorous seismic performance assessment is incomplete without a description of the distribution of damage over the height of the structure. Since maximum story drift angles are considered relevant EDPs for structural and nonstructural damage evaluation, information provided by maximum story drift angle profiles also becomes useful for performance assessment.

Basic graphical representations used to analyze the distribution of normalized maximum story drift angles over the height are given in Figures 4.24–4.26 for structures with 3, 9, and 18 stories. The three-story structures exhibit a uniform distribution of maximum story drift angles over the height, indicating that the structures deflect essentially in a straight-line mode. For the 9 and 18 story frames, the distribution of story drift angles over the height is clearly influenced by the ground motion intensity level. For elastic behavior, the maximum story drift angles occur at the upper portion of the frames, which is in part a consequence of designing the structures so that their first mode is a straight line. For small levels of inelastic behavior, maximum story drifts concentrate at the top stories because the story strengths are tuned based on a predefined load pattern, which implies much weaker beams at the top stories. As the intensity level increases, the maximum story drift angle migrates from the top story to the bottom one. This migration is especially important for P-delta sensitive systems ($N = 18$, $T_1 = 3.6$ sec) where there is no median value reported for $[S_a(T_1)/g]/\gamma = 4$ because at this relative intensity the system exhibits first-story drift amplifications that cause dynamic instability with more than 50% of the records.

Figures 4.27–4.30 show the distribution of normalized maximum story drift over the height for frames with $T_1 = 0.6$ sec, 1.2 sec, and 1.8 sec, different number of stories, and relative intensity levels causing a response that varies from elastic ($[S_a(T_1)/g]/\gamma = 0.25$) to highly inelastic ($[S_a(T_1)/g]/\gamma = 8.0$) behavior. It can be observed that the distribution of story drifts over the height is similar for systems with the same fundamental period and different number of stories, regardless of the level of intensity.

The standard deviation of the natural log of the normalized maximum story drift angles over the height is shown in Figures 4.27(b)–4.30(b). In the elastic range (Figure 4.27(b)), the variability is largest at the top story where the maximum drift angle over the height occurs. It is important to highlight that for $[S_a(T_1)/g]/\gamma \leq 4.0$ the dispersion in the bottom portion of the structure is not very large (much smaller than 0.50). For larger relative intensities, the dispersion is more uniformly distributed over the height without a clear dependence on the fundamental period or the number of stories, but showing a clear tendency to increase with an increase in relative intensity.

In order to obtain an estimate of absolute maximum story drift angle profiles, Equation 2.2 is used along with the normalized profiles shown in Figure 4.29. The resulting median maximum story drift angles over the height are shown in Figure 4.31.

The distributions of maximum story drifts over the height observed in the results presented in this section are based on the base case family of generic systems for which the story shear strengths are tuned to a specific predefined load pattern, and the global stiffness is based on a straight-line first mode. The sensitivity of these distributions to the design story shear strength pattern and the presence of overstrength is discussed in Chapter 7.

4.3.8 Normalized Residual Story Drift Demands

Residual story drift demands provide an indication of potential stability problems after an earthquake event. Residual drifts are not necessarily reliable indicators of damage, since responses with larger inelastic deformations can exhibit residual values smaller than those observed in responses with smaller inelastic deformations. In order to address whether the aforementioned statement is applicable to the family of generic frames used in this study and the LMSR-N ground motion set, a limited evaluation of residual story drift demands is performed. Residual story drift demands are evaluated as a function of $S_d(T_1)/H$ to allow a direct comparison to previously presented results for maximum story drift angles.

Figures 4.32 and 4.33 show the distribution of median normalized residual story drift angles over the height, $\theta_{si,res}$ and their associated dispersions for frames with T_1 = 0.6 sec, 1.2 sec, and 1.8 sec, different number of stories, and $[S_a(T_1)/g]/\gamma = 2$ and 4. It can be observed that the distribution of median $\theta_{si,res}$ over the height is similar for systems with the same fundamental period and number of stories, for both relative intensities. As the relative intensity increases, the residual story drift angles also increase and their distribution over the height follows patterns similar to the ones observed for the distribution of maximum story drift angles. For instance, as the level of intensity increases, maximum story drift demands migrate from top to bottom, and residual story drifts do the same.

The dispersion of $\theta_{si,res}$ over the height is large and nonuniform; thus, estimates of residual story drift angles are very sensitive to the frequency content of the ground motions. However, caution and good judgment must be used when interpreting dispersion values that involve parameters with central values close to zero, for small central values can produce large dispersions. Although there are similarities between the distribution over the height of median $\theta_{si,res}$ and $\theta_{si,max}$ demands, $\theta_{si,res}$ cannot be considered a reliable indicator of structural damage. Damage is assumed to be related to the distribution of maximum story drift angles and the large dispersion in residual story drift angles implies that $\theta_{si,res}$ is not very well correlated to $\theta_{si,max}$. This last statement is illustrated in Figure 4.34 where median ratios of $\theta_{si,res}/\theta_{si,max}$ and their corresponding dispersions are presented for $[S_a(T_1)/g]/\gamma = 4$.

For the family of structures used in this project, which have hysteretic behavior represented by a stiffness-degrading, peak-oriented model, and the LMSR-N set of ordinary ground motions, residual story drift angles have not demonstrated to be reliable EDPs for damage evaluation. However, they can be used as indicators of potential stability problems for frames that have experienced severe levels of ground motion shaking.

4.3.9 Story Ductility Demands

Maximum story drifts are global EDPs related to damage to structural and nonstructural components; however, they do not quantify directly the level of inelastic behavior that a system experiences when subjected to seismic excitations. A relevant global EDP used to quantify this level of inelasticity is the story ductility demand, μ_s. However, the definition of ductility is based upon a normalization value that corresponds to an estimate of the yield deformation, which is not a well-defined property for the majority of materials, especially those with stiffness-degrading properties, e.g., reinforced concrete. In this chapter, story ductility is defined as the maximum story drift normalized by the story yield drift obtained from a pushover analysis. For the base case family of frames used in this project, simultaneous yielding is achieved under a parabolic load pattern (FEMA 368, 2000), so story yield drift values are well-defined quantities. As in the case of maximum story drift angles, the maximum story ductility over the height, $\mu_{s,max}$ and the average of the story ductilities over the height, $\mu_{si,ave}$, are considered relevant EDP for structural damage assessment. $\mu_{si,ave}$ is most relevant if damage is about linearly proportional to the story ductility, while $\mu_{s,max}$ is important if damage is dominated by the maximum story ductility over the height. In this section, story ductilities (along with their corresponding profiles) and their associated record-to-record variability are studied.

Basic graphical representations for $\mu_{si,ave}$ and $\mu_{s,max}$ are shown in Figure 4.35 for the N = 9, T_1 = 0.9 sec frame. These results are equivalent to incremental dynamic analyses where the strength of the structure is kept constant while the intensity of the ground motion is increased. This information can be interpreted as MDOF R-μ relationships. A summary of these MDOF R-μ relationship plots is given in Figure 4.36 and 4.37. $\mu_{s,max}$, given the relative intensity, tends to increase with period (except for T_1 = 0.3 sec for which a small increase in relative intensity causes a large increase in ductility values because the inelastic displacement is larger than the elastic one), while this pattern is not as clear for $\mu_{si,ave}$. Given the relative intensity, the dependence of $\mu_{si,ave}$ values on the fundamental period is less noticeable at small to medium relative intensities. However, a clear dependence is evident for short-period and P-delta sensitive frames.

Median story ductility values as a function of the fundamental period, number of stories and relative intensity are shown in Figure 4.38. The average of the story ductilities is a more stable parameter than the maximum story ductility, since for small and medium intensities ($[S_a(T_1)/g]/\gamma < 6$), the median $\mu_{si,ave}$ remains rather constant as the fundamental period increases. For larger relative intensities, $\mu_{si,ave}$ tends to decrease with period while $\mu_{s,max}$ increases with period, indicating that as the period increases, the ratio of $\mu_{s,max}$ to $\mu_{si,ave}$ also increases. Thus, the maximum story ductility concentrates in a few stories. For the primary relative intensity range of interest in this study, the median $\mu_{si,ave}$ can be conservatively estimated by the value of $[S_a(T_1)/g]/\gamma$.

For a given relative intensity level and fundamental period, the effect of the number of stories is observed in the median maximum story ductility over the height, where for any given period, the stiffer (taller) frames experience maximum story ductility demands higher than those of the flexible (shorter) ones. These differences in maximum story ductility demands increase with the fundamental period, and are consistent with observations discussed for the normalized maximum story drift angle over the height. For instance, if all records are scaled to the same spectral acceleration at the first-mode period, given the same period and strength, the maximum story drift experienced by the flexible frame is greater than that of the stiff frame. The maximum differences are usually less than a factor of 2 and decrease as the period and the relative intensity increase. At the same time, the story yield drift of the stiffer frame is one half the story yield drift of the flexible one, so for long periods and large relative intensities, the stiffer frame experiences larger story ductilities.

The dispersion of the average of the story ductilities is shown in Figure 4.39. For the cases presented, its pattern of variation and its absolute value are similar to those of the normalized average of maximum story drifts (Section 4.3.7). The same observation applies for the dispersion of maximum story ductility demands over the height.

Story ductility profiles provide information related to the distribution of structural damage over the height, for the story ductility is a measure of the degree of inelastic behavior experienced by components (in this case beams and the bottom of the first-story columns). Since the story shear strength of regular frames is tuned to a specified load distribution, story ductility distributions are expected to follow the same patterns observed for the normalized maximum story drifts for which the maximum value over the height migrates from top to bottom as the intensity level increases. This pattern of behavior is illustrated in Figures 4.40 to 4.43, in which median story ductility profiles for frames with T_1 = 0.6 sec, 1.2 sec, and 1.8 sec, different number of stories, and different relative intensities are presented. The variation of story ductilities over the height implies that structures designed according to current design guidelines will experience a highly nonuniform distribution of structural damage over the height.

4.3.10 Maximum Beam Plastic Rotations

Local EDPs such as the maximum plastic element rotation are useful as damage measures at the component level. For the family of generic frames used in this project, which are designed based on the strong-column, weak-beam concept, the distribution of plastic rotations at the beam ends over the height constitutes basic information to assess the distribution of structural damage. Plastic rotation demands at the base of the first-story columns are also of interest because of the high axial load demands experienced by first-story columns due to gravity load and overturning moments, which can potentially reduce the bending capacity of a column significantly. Plastic rotation demands at the base of the first-story columns are evaluated in Chapter 6, where issues regarding column strength are investigated. The objective of this section is to provide additional statistical information related to the distribution of maximum beam plastic rotations over the height of regular frames and its correlation with the distribution of maximum story drift angles over the height. Correlations between maximum story drift angles and maximum plastic element deformations have been studied by Gupta and Krawinkler (1999), who developed a procedure to estimate maximum plastic element deformation demands from maximum story drift demands.

Another EDP conventionally used as an indicator of structural damage is the cumulative plastic rotation, for those cases in which cumulative plastic rotations can be related to the energy dissipation in a component. The dependence of energy demands on the frequency content and duration of the ground motions is studied in Chapter 5 where issues related to strong ground motion duration effects are addressed.

For the family of generic frames utilized in this study, normalized maximum beam plastic rotation profiles follow patterns similar to those of the normalized maximum story drift angle profiles. However, the dispersion of maximum beam plastic rotations, $\theta_{pbi,max}$, is larger than that of the maximum story drift angles, $\theta_{si,max}$ (as in the case of the normalized maximum residual drift demands, caution must be exercised when interpreting large dispersion values based on quantities with central values near zero). These observations are illustrated in Figure 4.44 where normalized maximum beam plastic rotation profiles are shown for $[S_a(T_1)/g]/\gamma = 4$ and systems with T_1 = 0.6 sec, 1.2 sec, and 1.8 sec. Figure 4.44 can be studied along with Figure 4.29 to assess differences between $\theta_{pbi,max}$ and $\theta_{si,max}$ profiles.

The similarities in patterns between $\theta_{pbi,max}$ and $\theta_{si,max}$ discussed in the previous paragraph suggest that maximum story drift angle demands are well correlated with the maximum beam plastic rotations. In order to investigate this correlation, the N = 9, T_1 = 1.8 sec system used in Figure 4.44 is utilized for illustration. For this system $[S_a(T_1)/g]/\gamma = 4$ and the normalized base shear strength, γ, is equal to 0.09 when the spectral acceleration at the first mode is given by the UBC 1997 ground motion spectrum for site class D. Figure 4.45 shows the distribution over the height of median maximum story drift angles, the median maximum story drift angles minus story yield drift angles (estimate of maximum plastic story drifts), and maximum beam plastic rotations. Values for story drifts are plotted at the story level, while values for the beam plastic rotations are plotted at the floor level. Note the good correlation between the median maximum beam plastic rotations and the estimate of the maximum plastic story drift. These results imply that maximum beam plastic rotations can be estimated from maximum story drift angles (when plastic column deformations are not significant) by approximating the maximum plastic story rotations. Therefore, if maximum beam plastic rotations are EDPs relevant for structural damage evaluation of beams, maximum story drift angles can provide basic information to assess the structural integrity of beam elements that are part of regular moment-resisting frames.

4.4 EVALUATION OF ABSOLUTE FLOOR ACCELERATION AND VELOCITY DEMANDS

Absolute floor acceleration and velocity demands are EDPs that can be used to assess the performance of nonstructural components and equipment, which by virtue of their configuration or anchorage (or lack thereof) are sensitive to large floor accelerations and velocities. For instance, maximum absolute floor accelerations (and velocities) can be used to develop floor acceleration spectra. These floor spectra are useful to design and assess the performance of nonstructural and contents systems resting on or attached to floors and ceilings. The objective of this section is to understand and quantify acceleration and velocity demands imposed by ordinary ground motions on regular frames of different characteristics. Statistical information relevant for performance assessment is also provided. As in the case of the deformation demands evaluated in Section 4.3, peak values and average values as well as the distribution of maximum absolute floor accelerations and velocities over the height of the structures are studied.

4.4.1 Absolute Floor Acceleration Demands

In the context of probabilistic seismic performance evaluation, relationships between EDPs and IMs are established in order to combine them with fragility curves to make a probabilistic assessment of a damage measure and/or a decision variable. Hence, the normalized maximum absolute floor accelerations over the height and the normalized average of maximum absolute floor accelerations are EDPs of interest whose relationships with an IM, $S_a(T_1)$, are investigated.

In this study, the term "floor acceleration" corresponds to the horizontal component of acceleration. Since the results presented in this section are obtained with the objective of providing general patterns of behavior, normalized absolute acceleration values are used. The basic parameter to describe the level of intensity is $[S_a(T_1)/g]/\gamma$; however, there are several parameters that could be used to normalize maximum absolute acceleration values. One of them is $S_a(T_1)$, while another option is the PGA. An advantage of using PGA as a normalization value is that it provides values for the amplification of floor acceleration demands with respect to the maximum ground acceleration (in current seismic code provisions/recommendations in the United States this ratio increases proportionally to the height of the structure). Furthermore, as Figure 4.46(a) indicates, the maximum absolute floor acceleration correlates well with the PGA except for the case of the elastic short-period frame (T_1 = 0.3 sec). Figure 4.46 shows the dispersion of normalized maximum absolute accelerations for different frames with $T_1 = 0.1N$ and the full range of relative intensities, once they are normalized by both PGA and $S_a(T_1)$. In most cases, especially at medium to large relative intensities, smaller dispersions are observed when PGA is used as the normalization parameter, which implies that in this case PGA is a more efficient IM. These patterns are consistent with the ones observed for the flexible frames ($T_1 = 0.2N$). Elastic short-period systems (in this case, T_1 = 0.3 sec) correlate better with $S_a(T_1)$ because their response is dominated by the first mode (see Figure 4.52); thus, the maximum absolute floor acceleration occurs at the top of the structure and is much larger than the PGA. For the reasons identified in this paragraph, in this study the PGA is used as the IM of interest to understand and quantify the relationships between $a_{f,max}$, relative intensity, number of stories and fundamental period.

Basic information used to evaluate normalized maximum absolute floor accelerations over the height, $a_{f,max}$/PGA, and the normalized average of maximum floor accelerations, $a_{fi,ave}$/PGA is shown in Figure 4.47 for the N = 9, T_1 = 0.9 sec frame. Maximum absolute floor accelerations are computed from the second-floor level and above. There are three distinct regions in the plot, which are common to all frames used in this study. The first region corresponds to the elastic range in which normalized $a_{f,max}$ values remain constant regardless of the relative intensity. In the second region, normalized $a_{f,max}$ values decrease rapidly with the relative intensity. The third region corresponds to the stabilization of the normalized maximum absolute floor acceleration for very large values of the relative intensity. In the third region, higher modes have a significant contribution to the dynamic behavior of the system, and the first mode does not dominate the response. Therefore, $a_{f,max}$ values do not decrease inversely proportional to the relative intensity as is the case for a slightly damped inelastic SDOF system with no strain hardening,α,; i.e., in this case maximum absolute accelerations are expected to be close to $(F_{max}/W)g$ (where F_{max} is the maximum resisting force experienced by the SDOF system), which is equal to S_a/R or $(S_a/R)[(1+(\mu-1)\alpha]$ when α has a nonzero value (μ represents the displacement ductility factor). If the SDOF has a medium-to-long period, its maximum absolute floor acceleration is approximately equal to $(S_a/R)[(1+(R-1)\alpha]$. Patterns of behavior similar to the ones described in this paragraph for the N = 9, T_1 = 0.9 sec frame were observed by Rodriguez et al. (2000) when evaluating floor accelerations for structural walls.

Information of the type presented in Figure 4.47 can be summarized as shown in Figures 4.48 and 4.49 for the complete family of generic frames. It is observed that for a given period, both the median of $a_{fi,ave}$/PGA and $a_{f,max}$/PGA decrease with the relative intensity; however, for large relative intensity values (Figures 4.48(b) and 4.49(b)) the median normalized floor accelerations stabilize and are only weakly dependent on the level of inelastic behavior. This observation is in agreement with the behavior depicted in Figure 4.47 for the N = 9, T_1 = 0.9 sec frame for large intensity values. In the median, given the period, differences between values of $a_{f,max}$/PGA for the T_1 = 0.1N and T_1 = 0.2N frames are noticeable (as large as 50%) for small relative intensities (Figure 4.49(a)). However, the influence of the number of stories on the median maximum absolute floor acceleration decreases with increasing relative intensity. For any given period, median $a_{fi,ave}$/PGA demands are weakly dependent on the number of stories. Moreover, flexible frames experience de-amplification of median absolute floor acceleration demands with respect to the PGA for large relative intensity values ($[S_a(T_1)/g]/\gamma > 4$) and $T_1 > 0.6$ sec.

The median normalized acceleration response spectrum of the LMSR-N ground motion set is plotted in both Figures 4.48 and 4.49 for R (strength-reduction factor) = 1 and 4 respectively. For elastic behavior (R = 1) differences between the LMSR-N median spectrum and median normalized absolute acceleration demands corresponding to $[S_a(T_1)/g]/\gamma = 0.25$ are mainly the result of the influence of higher modes in the response. For a given relative intensity, higher mode and period-elongation effects also cause the correlation between normalized absolute floor acceleration demands and SDOF elastic spectral demands to diminish with increasing period.

The decrease in normalized absolute floor accelerations with an increase in relative intensity is not inversely proportional to the R factor, and hence, the level of inelastic behavior. For elastic responses, $a_{fi,ave}$/PGA exhibits better correlation with the elastic spectral demands than $a_{f,max}$/PGA. Thus, $a_{fi,ave}$/PGA is slightly affected by concentrations of maximum floor acceleration demands in a single story and provides a better global measure of floor acceleration demands.

The dispersion associated with the values shown in Figures 4.48 and 4.49 are shown in Figures 4.50 and 4.51 for the T_1 = 0.1N and 0.2N frames as a function of the relative intensity level. The dispersion in the normalized absolute floor acceleration demands is small at all relative intensity levels and periods, which implies that for this family of generic frames, amplifications in maximum absolute floor accelerations with respect to the PGA are not very sensitive to the frequency content of ordinary ground motions.

Figures 4.52 to 4.55 show median normalized maximum absolute floor acceleration profiles for different relative intensity levels and frames with periods T_1 = 0.6 sec, 1.2 sec, and 1.8 sec. It can be seen that $a_{f,max}$ migrates from the top story (for elastic and low levels of inelastic behavior) to the bottom stories (for highly inelastic systems). Moreover, as the system becomes more inelastic, the maximum absolute floor accelerations, $a_{fi,max}$, stabilize and remain rather constant over the height of the frame. This general pattern has been observed for the complete family of generic frames. The fact that the T_1 = 0.6 sec elastic frames exhibit median floor acceleration amplifications greater than 2 at the top story (Figure 4.52) also explains why for stiff, elastic systems, $S_a(T_1)$ is a more efficient IM than PGA. For elastic behavior, a short-period system experiences floor acceleration amplifications nearly proportional to its height because the system deflects primarily in the first mode. Thus, its behavior resembles that of an elastic SDOF structure in which $S_a(T_1)$ becomes a relevant ground motion intensity measure. However, as the relative intensity increases and the system becomes more inelastic, it experiences period-elongation effects with a dynamic response controlled by a combination of modes. Maximum absolute floor accelerations become smaller than the PGA, while their distribution is rather constant over the height of the frame due to yielding and subsequent plastification in beams. For this family of generic frames simultaneous yielding is very likely to occur for large relative intensities.

Given the fundamental period, the influence of the number of stories on the distribution of maximum absolute floor accelerations over the height decreases with an increase in the level of inelastic behavior. This observation is in agreement with the results presented in Figure 4.49. The information presented in Figures 4.52 to 4.55 has relevant implications in the design of acceleration-sensitive components because current seismic design guidelines in the United States assume amplification of floor accelerations proportional to height regardless of the level of inelastic behavior, fundamental period, and number of stories.

A typical distribution of the dispersion of normalized maximum absolute floor accelerations is shown in Figure 4.56, which corresponds to the median profiles presented in Figure 4.52 ($[S_a(T_1)/g]/\gamma = 0.25$) and Figure 4.55 ($[S_a(T_1)/g]/\gamma = 8$). It can be seen that values of the standard deviation of the natural log of $a_{fi,max}$/PGA are generally smaller than 0.30; thus, as previously discussed, normalized maximum absolute floor accelerations are not very sensitive to the frequency content of ordinary ground motions (given PGA as the IM of interest).

4.4.2 Absolute Floor Velocity Demands

Similar to the evaluation of deformation and acceleration demands, maximum absolute floor velocities as well as the average of the maximum absolute floor velocities over the height are the two primary EDPs of interests. For instance, absolute floor velocities, $v_{f,max}$, are important to evaluate the dynamic behavior of nonstructural components and equipment that have the potential to overturn because of strong floor shaking. The normalization parameter utilized is the PGV, which provides a direct measure of the absolute floor velocity amplification with respect to the ground velocity. PGV is a ground motion intensity measure that provides a relatively small dispersion (in the order of 0.3) for the elastic behavior of all frames. The dispersion of absolute floor acceleration values normalized by PGV decreases with an increase in the level of inelastic behavior.

A typical graphical representation of the variation of the normalized maximum absolute floor velocity over the height is presented in Figure 4.57 for the N = 9, T_1 = 0.9 sec frame. Patterns are similar to the ones observed for both $a_{fi,ave}$/PGA and $a_{f,max}$/PGA. As the level of inelastic behavior increases, there is a rapid decrease in normalized maximum absolute floor velocities followed by a region where $v_{fi,ave}$/PGA and $v_{f,max}$/PGA stabilize.

A comprehensive assessment of the relationships between absolute floor velocities, the relative intensity level, fundamental period, and number of stories is presented in Figures 4.58 and 4.59. These figures, which depict statistical information on $v_{fi,ave}$/PGV and $v_{f,max}$/PGV, demonstrate that patterns of behavior between these EDPs and those of $a_{fi,ave}$/PGA and $a_{f,max}$/PGA are very similar. It can be observed that for a given period, the medians of $v_{fi,ave}$/PGV and $v_{f,max}$/PGV decrease with the level of intensity; however, for large relative intensity values (Figures 4.58(b) and 4.59(b)) the median normalized floor velocities remain rather constant and independent of the level of inelastic behavior. This observation is in agreement with the behavior depicted in Figure 4.57 for the N = 9, T_1 = 0.9 sec frame for large relative intensities. In the median, given the period, differences between values of $v_{f,max}$/PGV (and $v_{fi,ave}$/PGV) for the T_1 = 0.1N and T_1 = 0.2N frames are within 10% indicating that for these cases maximum absolute floor velocity demands are controlled by the fundamental period and are not severely influenced by the number of stories.

Figures 4.58(a) and 4.59(a) portray the median normalized elastic absolute velocity spectrum of the LMSR-N ground motion set along with median normalized absolute floor velocities. For elastic behavior differences between the LMSR-N median spectrum and median normalized maximum absolute velocity demands corresponding to $[S_a(T_1)/g]/\gamma = 0.25$ are the result of the influence of higher modes in the response. It can be observed that for this relative intensity, the influence of higher modes increase with an increase in the fundamental period.

Dispersions associated with the values shown in Figures 4.58 and 4.59 are presented in Figures 4.60 and 4.61 for the T_1 = 0.1N and 0.2N frames as a function of the relative intensity level. The relatively small values of dispersion suggest that for the cases studied in this section, normalized maximum absolute floor velocities are only weakly dependent on the frequency content of ordinary ground motions.

Median normalized maximum absolute floor velocity profiles are shown in Figures 4.62 to 4.65 for various relative intensity levels and systems with T_1 = 0.6 sec, 1.2 sec, and 1.8 sec. In most cases the maximum absolute floor velocity occurs at the top floor. For instance, even when $S_a(T_1)/g]/\gamma = 8.0$ (Figure 4.65), maximum demands occur at both top and bottom except for the $T_1 = 1.8$ sec systems (the first value in each curve corresponds to the ground floor). This pattern is different from the one observed for the case of maximum absolute floor accelerations, in which at large relative intensities the maximum absolute floor acceleration demands occur at the bottom of the structure. Another important observation is that in the elastic range maximum absolute floor velocities increase with height regardless of the fundamental period and the number of stories. This last statement agrees with the notion that for the range of period of consideration 0.6 sec to 1.8 sec, the response of the structure resembles that of an elastic SDOF system in the "constant velocity" region of the spectrum. The dispersion of the normalized maximum absolute floor velocities over the height is small (with smaller values observed at the bottom stories, Figure 4.66). Thus, as it has been previously discussed, this parameter is weakly dependent on the frequency content of ordinary ground motions.

4.5 SUMMARY

The conclusions presented in this section are based on seismic demand analyses for regular, two-dimensional frames with fundamental periods ranging from 0.3 sec to 3.6 sec and number of stories from 3 to 18. Frames are designed according to the strong-column, weak-beam philosophy and plastic hinging is modeled by using a peak-oriented model that does not include cyclic deterioration. 5% Rayleigh damping is used in all cases. The following conclusions are based on the response of the basic family of generic frames used in this study subjected to records with frequency content characteristics similar to those of the LMSR-N set. Generalization of the results for different types of structural systems and ground motion frequency content is not intended. A summary of the most salient conclusions and observations made in this chapter is presented next:

- The use of a simple scalar intensity measure such as $S_a(T_1)$ can in some cases (depending upon the EDP of interest) yield large dispersions of the EDP given IM.

Deformation demands

- Except for inelastic short-period systems (for which the inelastic deformations are much larger than the elastic ones) and frames that are sensitive to P-delta effects (which cause large amplifications of drift demands at medium to large relative intensities), the median normalized maximum roof drift angle, $\theta_{r,max}/S_d(T_1)$, in which $S_d(T_1)$ is the elastic spectral displacement at the first-mode period, is approximately equal to the first-mode participation factor, PF_1. This implies that both the elastic and inelastic roof displacements are dominated by the first-mode (PF_1 is obtained using a first-mode shape which is normalized to be equal to one at the roof level). $\theta_{r,max}/S_d(T_1)$ is a stable quantity associated with a small dispersion especially for the range of relative intensities of interest in this study, $[S_a(T_1)/g]/\gamma < 8$. Large dispersions are observed for inelastic short-period systems and flexible frames with significant P-delta effects.

- The normalized average of maximum story drift angles, $\theta_{si,ave}/S_d(T_1)$, shows trends similar to that of the maximum roof drift angle. Its dispersion is also comparable to that of the normalized maximum roof drift angle except at low levels of inelastic behavior ($[S_a(T_1)/g]/\gamma < 2$) in which higher modes cause larger dispersions. The ratio $\theta_{si,ave}/\theta_{r,max}$ is a very stable parameter which is weakly dependent on the fundamental period. For a given fundamental period and relative intensity, the median $\theta_{si,ave}/\theta_{r,max}$ is not sensitive to the number of stories. The dispersion associated with this ratio is very small (in the order of 0.15), which implies that this parameter is weakly dependent on the frequency content of the ground motions. A simplified relationship to obtain median estimates of $\theta_{si,ave}/\theta_{r,max}$ as a function of the fundamental period is presented in Section 4.3.4.
- Median normalized maximum story drift angles over the height, $\theta_{s,max}/S_d(T_1)$, exceed the median roof drift by a percentage that increases with period, i.e., the median of the ratio $\theta_{s,max}/\theta_{r,max}$ increases with period. For a given period and relative intensity, higher mode effects cause systems with larger number of stories to experience larger median $\theta_{s,max}/\theta_{r,max}$, and hence, a less uniform distribution of maximum story drift angles over the height. The dispersion of this ratio is relatively small (less than 0.25) except for $[S_a(T_1)/g]/\gamma < 2$ at which higher mode effects cause the dispersion to increase. Simplified relationships to estimate the median $\theta_{s,max}/\theta_{r,max}$ as a function of the fundamental period and the number of stories are given in Section 4.3.5.
- Maximum story drift angle demands concentrate at the top stories for elastic behavior as well as relatively low levels of inelastic behavior. As the level of inelastic behavior increases, maximum story drift angle demands migrate toward the bottom stories. The large top-story

drifts at small levels of inelastic deformation are due to the fact that the beam strength at the top floors is tuned to the NEHRP k = 2 load pattern. For real frame structures, in which gravity loads tend to control beam sizes at the top floors, smaller maximum story drifts in the top stories are expected. P-delta sensitive systems experience large $\theta_{s,max}$ demands at high levels of inelastic behavior because of the concentration of maximum drifts at the bottom stories. For relative intensities of less than 2.0, a significant dependence of this EDP on the frequency content of the ground motions is reflected in the fact that the dispersion of $\theta_{s,max}$ given $S_a(T_1)$ is much larger than the dispersion of $\theta_{r,max}$ and $\theta_{si,ave}$ given $S_a(T_1)$.

- Based on the results of this study, residual story drifts are not reliable indicators of damage, since their quantification is associated with very large dispersions.
- The average of the story ductilities over the height, $\mu_{si,ave}$, is a global indicator of the degree of inelastic behavior of the system and can be conservatively estimated by the value of $[S_a(T_1)/g]/\gamma$ (except for short-period structures and systems where large ductility demands are obtained due to the presence of severe P-delta effects).
- Given the relative intensity, maximum story ductility demands increase with the fundamental period. Moreover, for a given period, stiff frames (T_1 = 0.1N) experience larger maximum story ductility demands primarily due to the influence of higher mode effects in their response.
- Maximum story drift and maximum beam plastic rotation profiles follow similar patterns as a function of the relative intensity. Maximum beam plastic rotations can be estimated from the maximum plastic story drifts.

Floor acceleration and velocity demands

- PGA and PGV are used to normalize floor acceleration and velocity demands because they provide a direct measure of the amplification (or de-amplification) of floor demands relative to the ground floor. Moreover, except for the T_1 = 0.3 sec frame, absolute floor acceleration demands correlate better with PGA rather than $S_a(T_1)$ because of inelastic effects and the influence of higher modes in the response. PGV is a ground motion intensity measure that provides a relatively small dispersion (in the order of 0.3) for the elastic behavior of all frames. The dispersion of absolute floor acceleration values normalized by PGV decreases with an increase in the level of inelastic behavior.

- The amplification of floor accelerations and velocities with respect to maximum ground motion parameters, e.g., PGA and PGV, respectively, decreases with relative intensity until it becomes rather constant with increasing levels of inelastic behavior. This trend is not observed in the SDOF system for which the maximum acceleration demands are approximately inversely proportional to the strength reduction factor, i.e., relative intensity level.
- Given the fundamental period and the relative intensity, for relatively low levels of inelastic behavior, frames with larger number of stories exhibit larger maximum absolute floor accelerations. As the relative intensity increases, maximum absolute floor acceleration demands become weakly dependent on the number of stories. On the other hand, maximum absolute floor velocity demands are weakly dependent on the number of stories for all relative intensity levels.
- Except for short-period systems, maximum absolute floor accelerations concentrate at the top floors for elastic systems and systems with relative small levels of inelastic behavior. Maximum absolute floor acceleration demands migrate to the bottom floors with an increase in the relative intensity. For short-period systems, maximum absolute floor accelerations occur at the top floor regardless of the level of inelastic behavior. This information has relevant implications in the design of acceleration-sensitive components because current seismic design guidelines assume amplification of floor accelerations proportional to height regardless of the level of inelastic behavior, fundamental period, and number of stories. Maximum absolute floor velocity demands also tend to concentrate at the top of the structures regardless of the structural period and the level of inelastic behavior.
- The amplification of absolute floor acceleration and velocity demands with respect to PGA and PGV, respectively, is not very sensitive to the frequency content of ordinary ground motions, which is demonstrated by the relatively small dispersion of the ratios $a_{f,max}$/PGA and $v_{f,max}$/PGV.

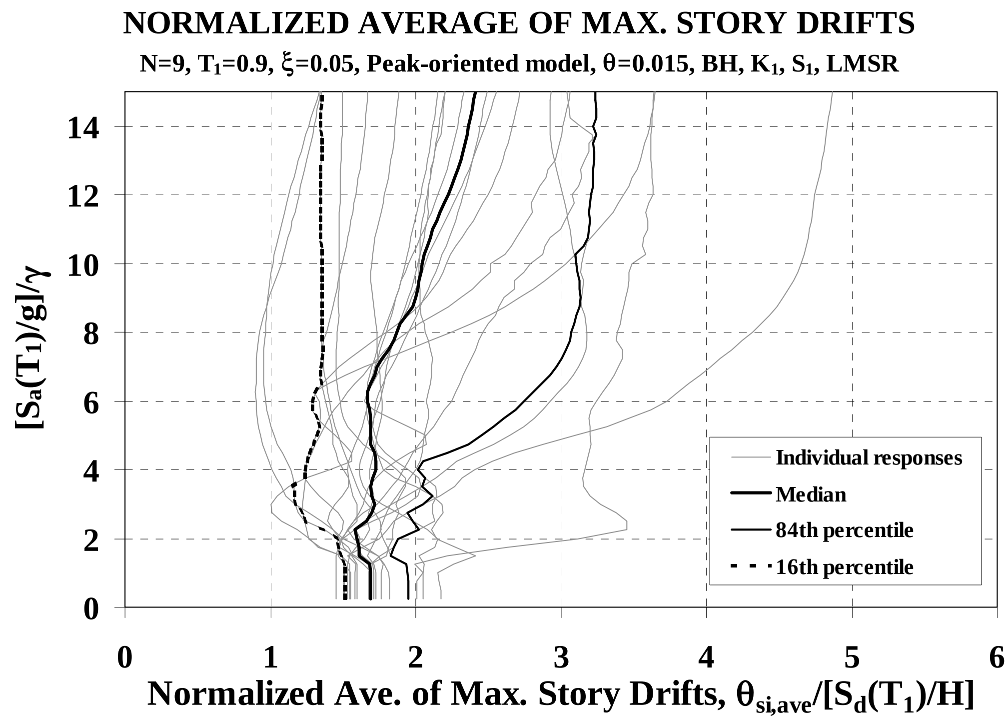

(a) LMSR Ground Motion Bin (20 records)

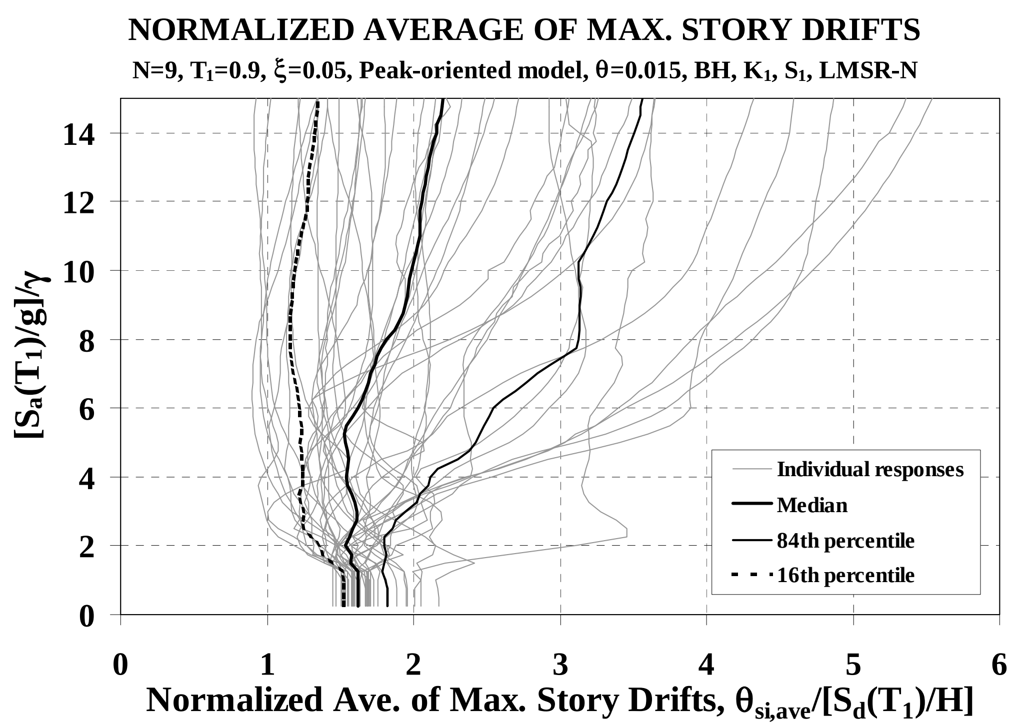

(b) LMSR-N Ground Motion Bin (40 records)

Figure 4.1 Normalized Average of the Maximum Story Drifts, $T_1 = 0.9$ sec, N = 9

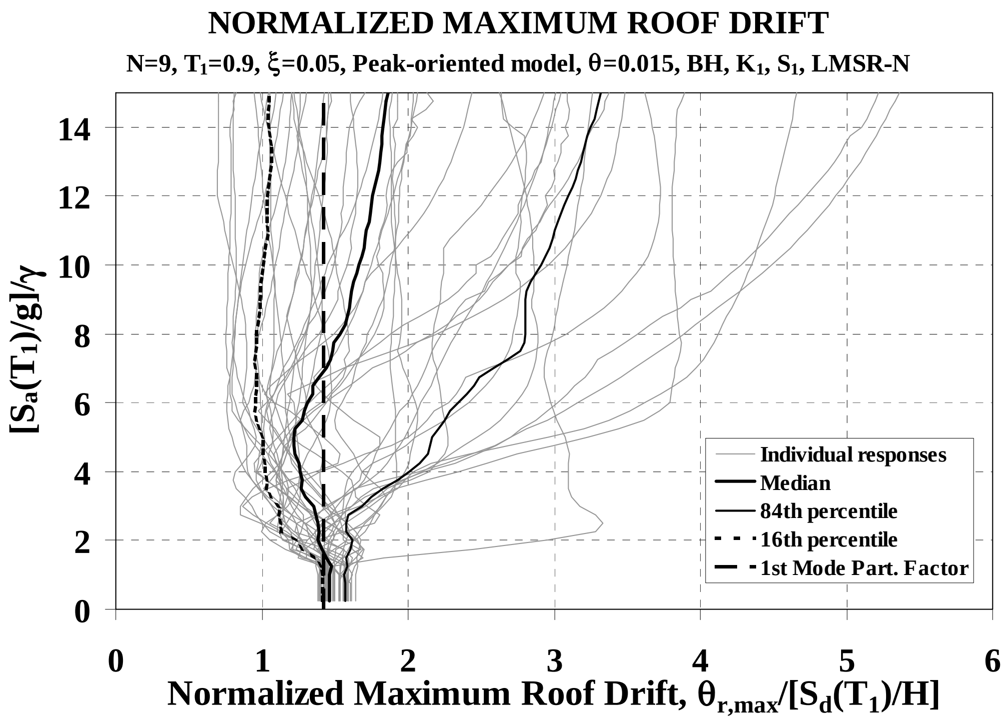

(a) T_1 = 0.9 sec

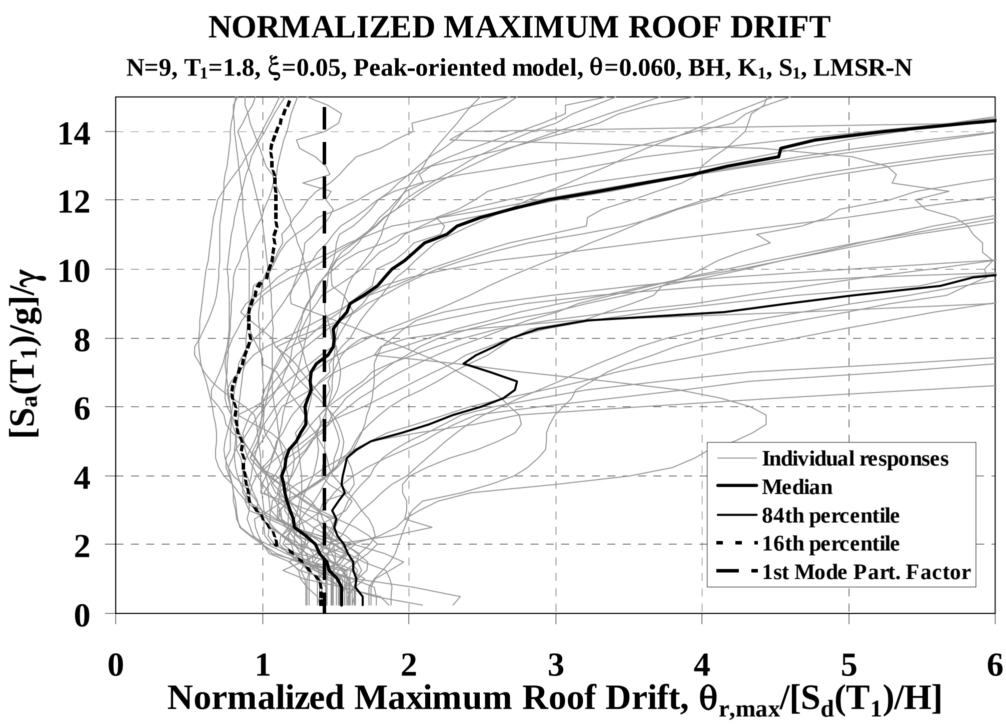

(b) T_1 = 1.8 sec

Figure 4.2 Normalized Maximum Roof Drift Demands, N = 9

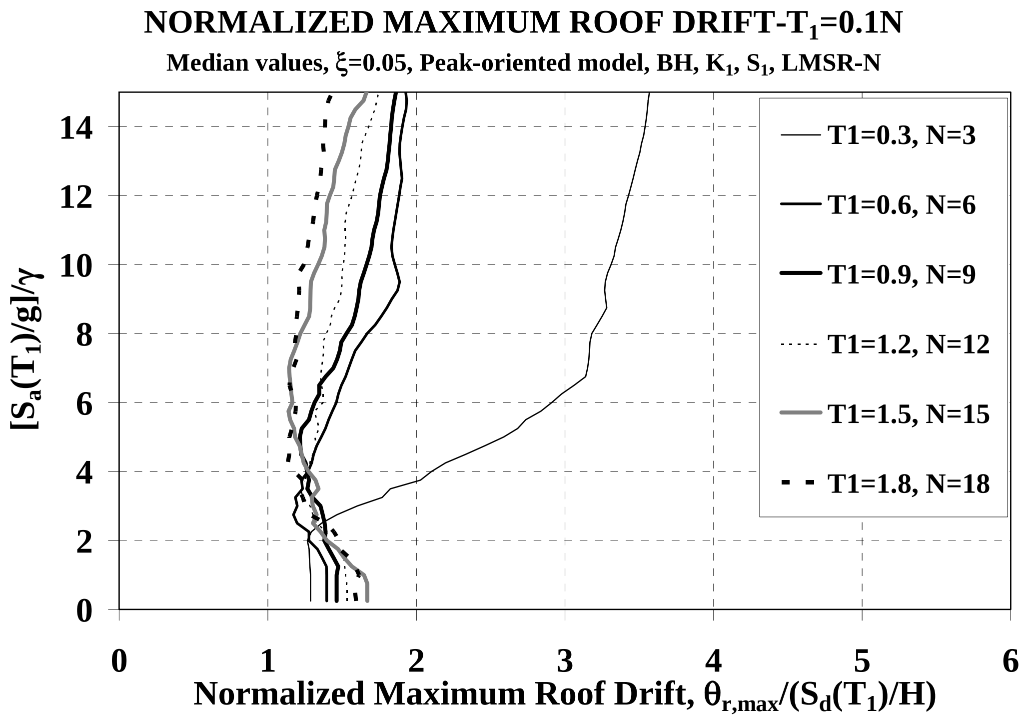

(a) T_1 = 0.1N

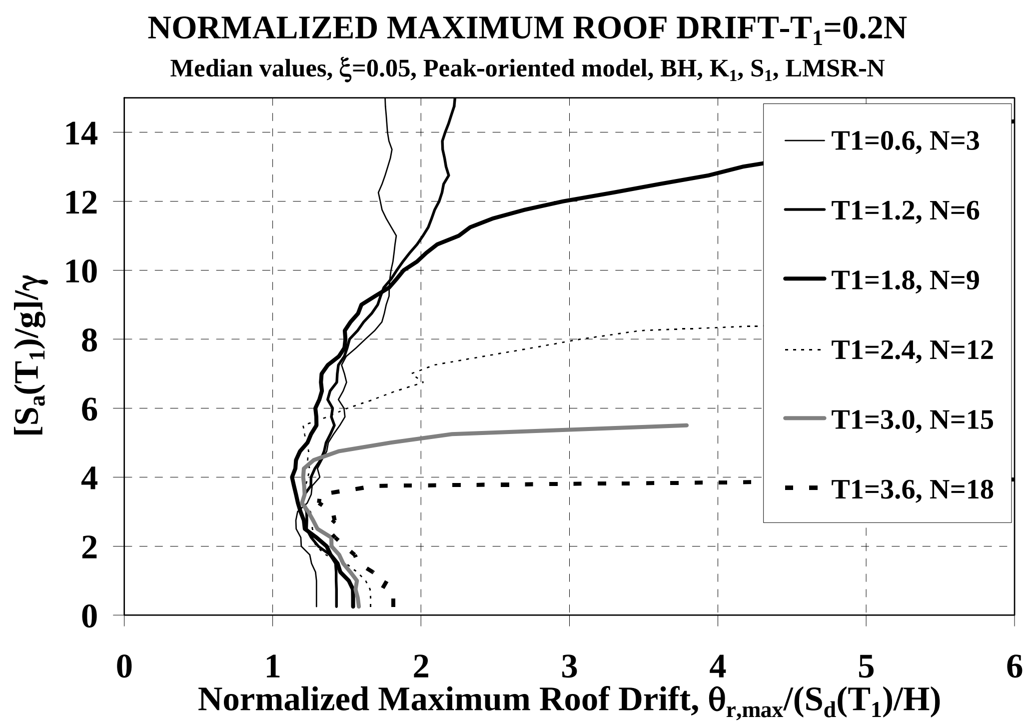

(b) T_1 = 0.2N

Figure 4.3 Median Normalized Maximum Roof Drift, Stiff and Flexible Frames

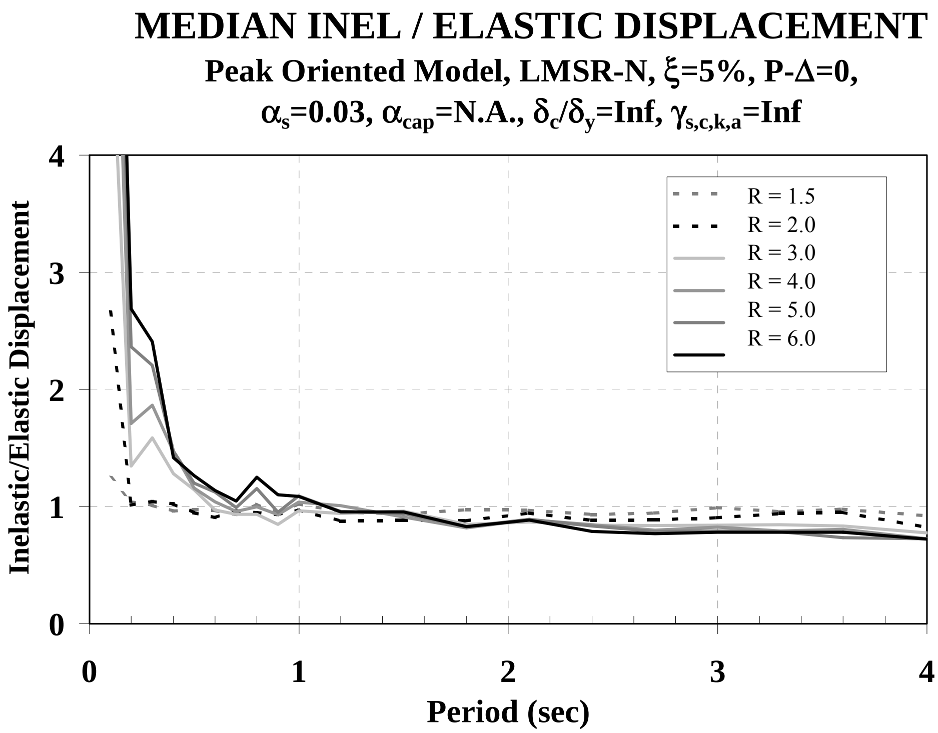

Figure 4.4 Ratio of Inelastic to Elastic Displacement, SDOF Systems, Various R-Factors

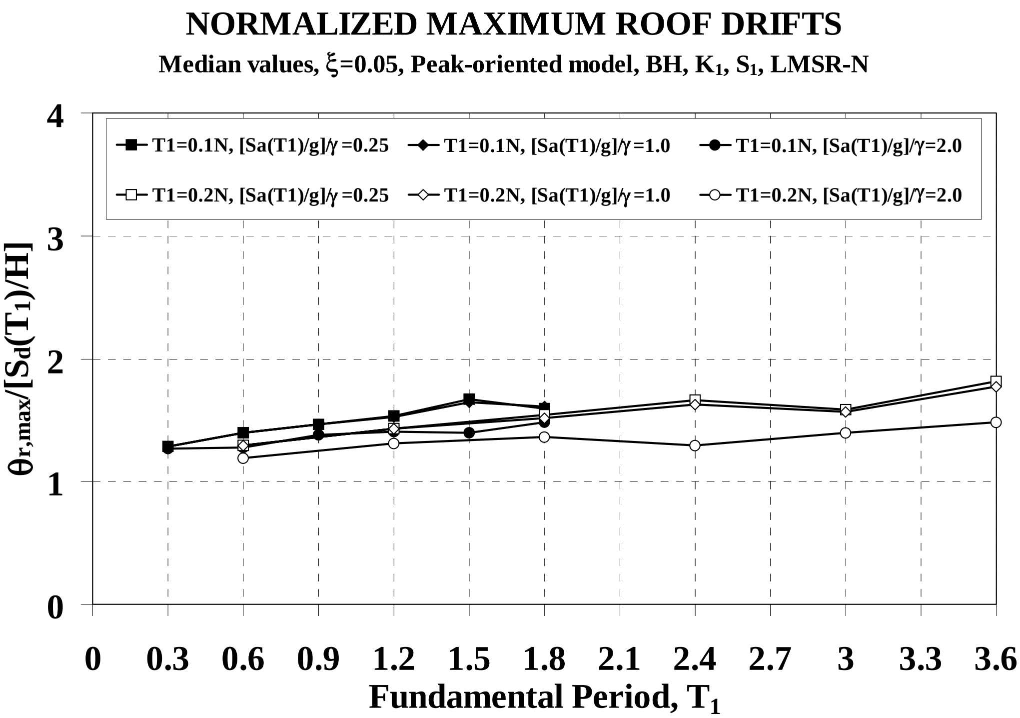

(a) $[S_a(T_1)/g]/\gamma$ = 0.25, 1.0, 2.0

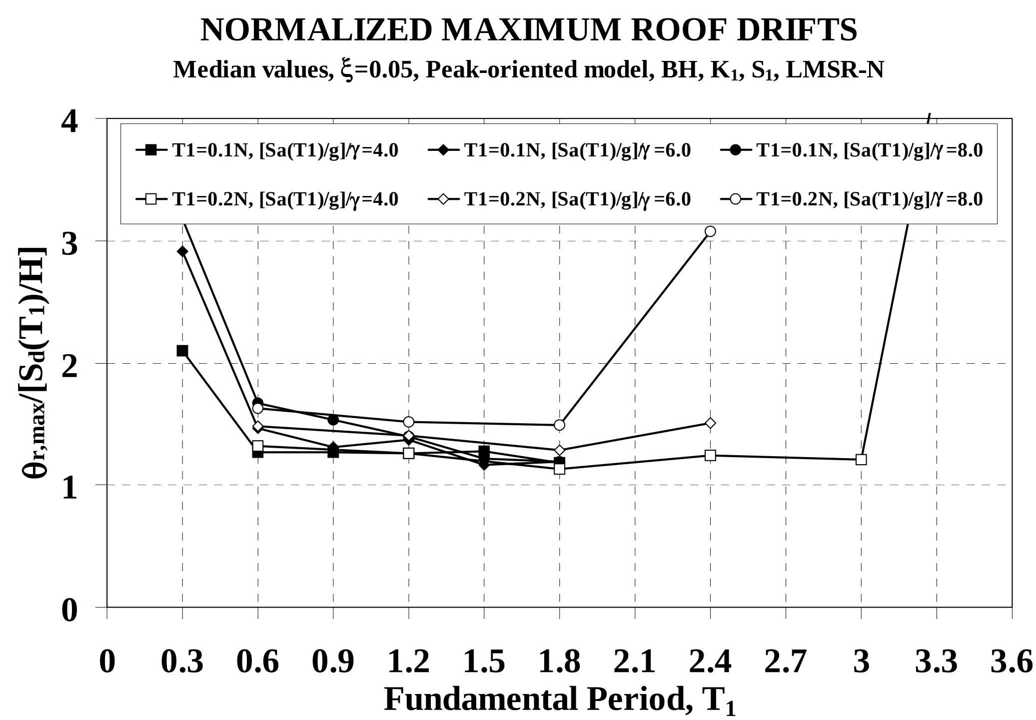

(b) $[S_a(T_1)/g]/\gamma$ = 4.0, 6.0, 8.0

Figure 4.5 Dependence of the Median Normalized Maximum Roof Drift on T_1, All Frames, Various Relative Intensities

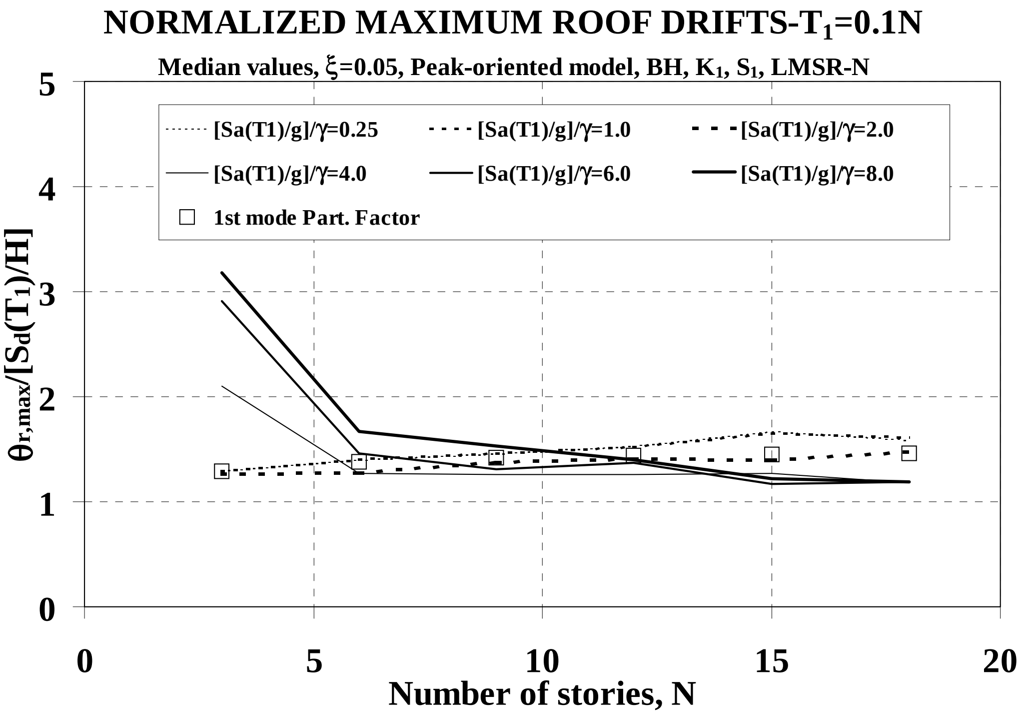

(a) $T_1 = 0.1N$

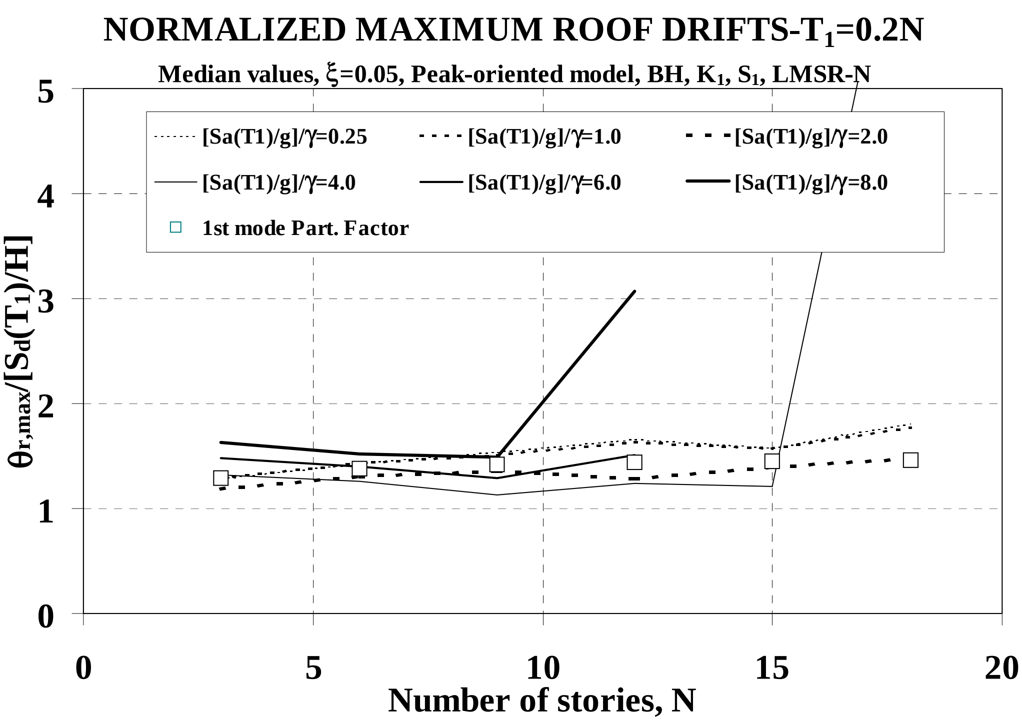

(b) $T_1 = 0.2N$

Figure 4.6 Dependence of the Median Normalized Maximum Roof Drift on N, Stiff and Flexible Frames

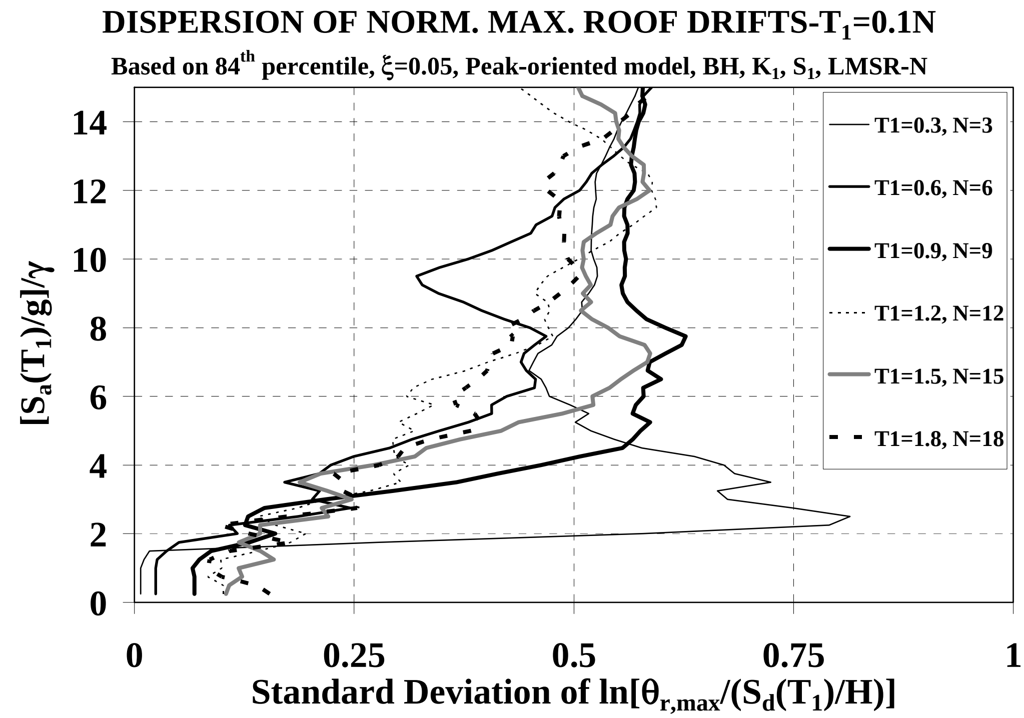

(a) $T_1 = 0.1N$

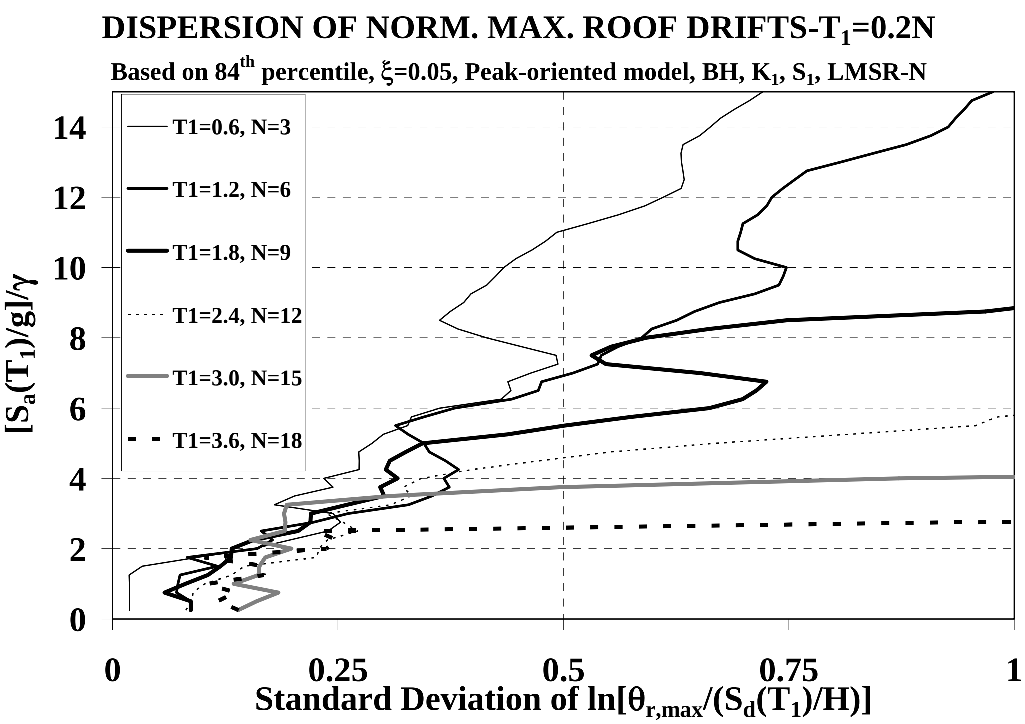

(b) $T_1 = 0.2N$

Figure 4.7 Dispersion of the Normalized Maximum Roof Drifts, Stiff and Flexible Frames

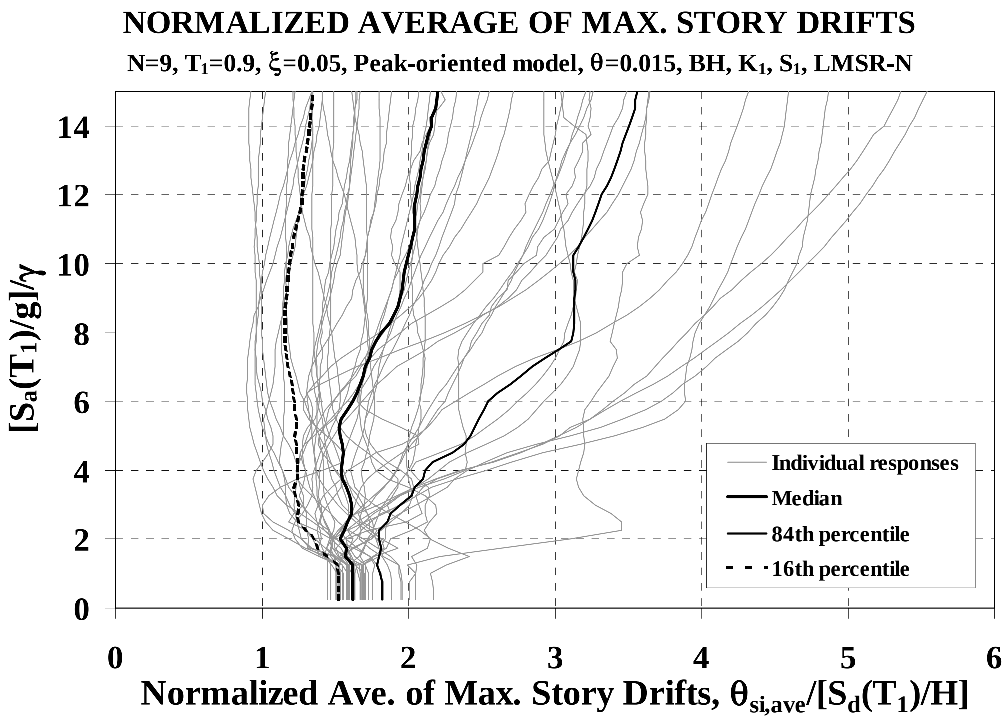

(a) T_1 = 0.9 sec

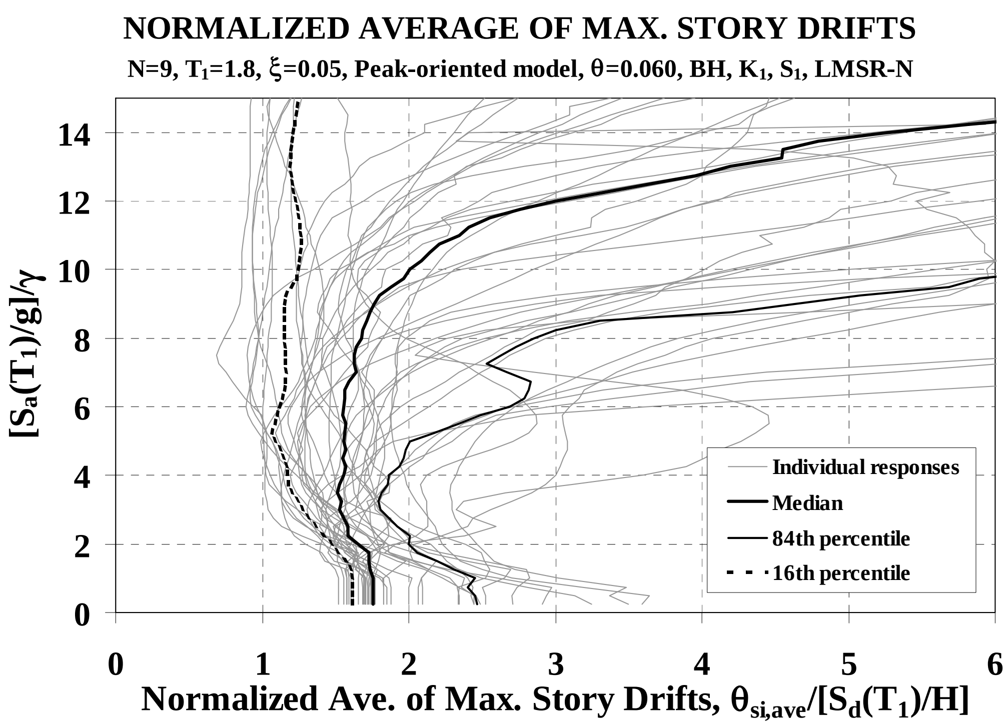

(b) T_1 = 1.8 sec

Figure 4.8 Normalized Average of the Maximum Story Drift Angles, N = 9

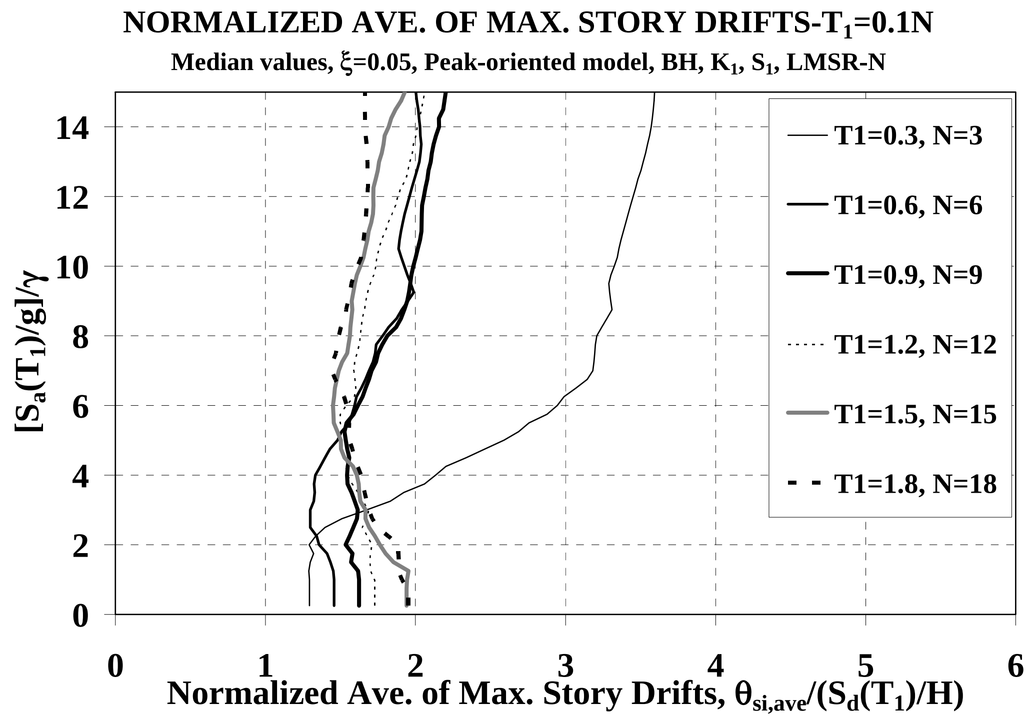

(a) $T_1 = 0.1N$

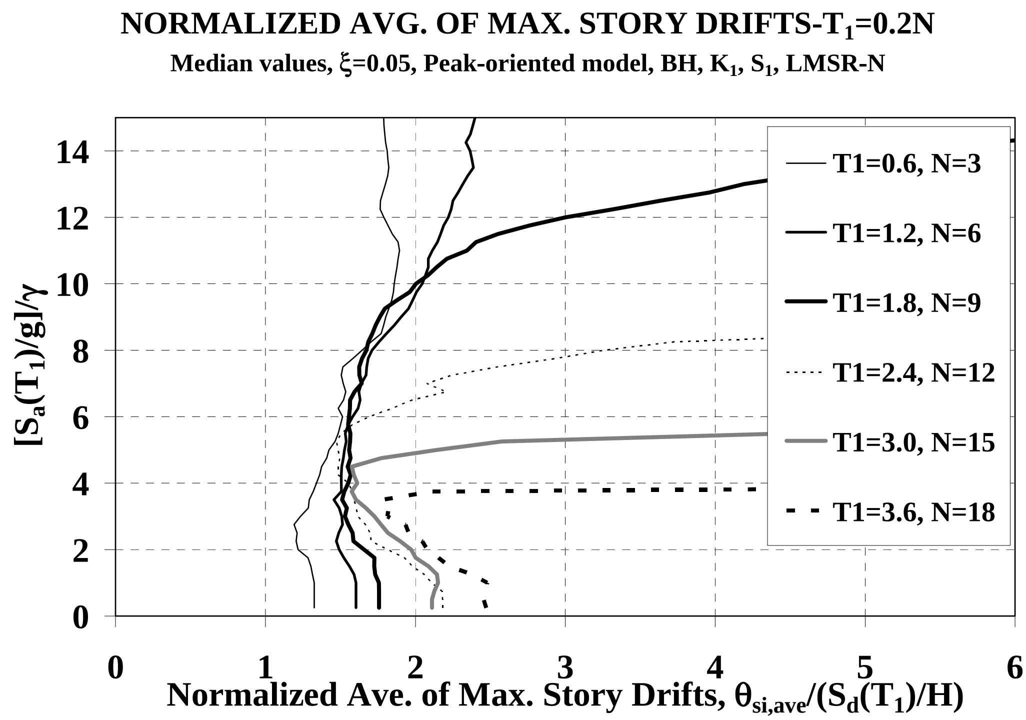

(b) $T_1 = 0.2N$

Figure 4.9 Median Normalized Average of the Maximum Story Drift Angles, Stiff and Flexible Frames

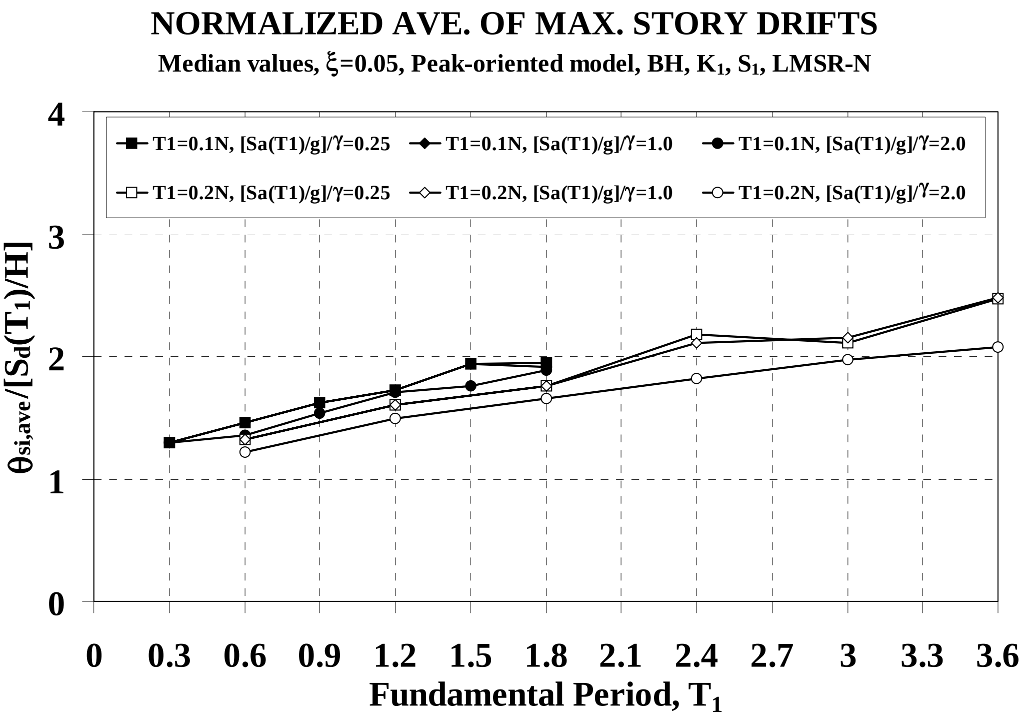

(a) $[S_a(T_1)/g]/\gamma$ = 0.25, 1.0, 2.0

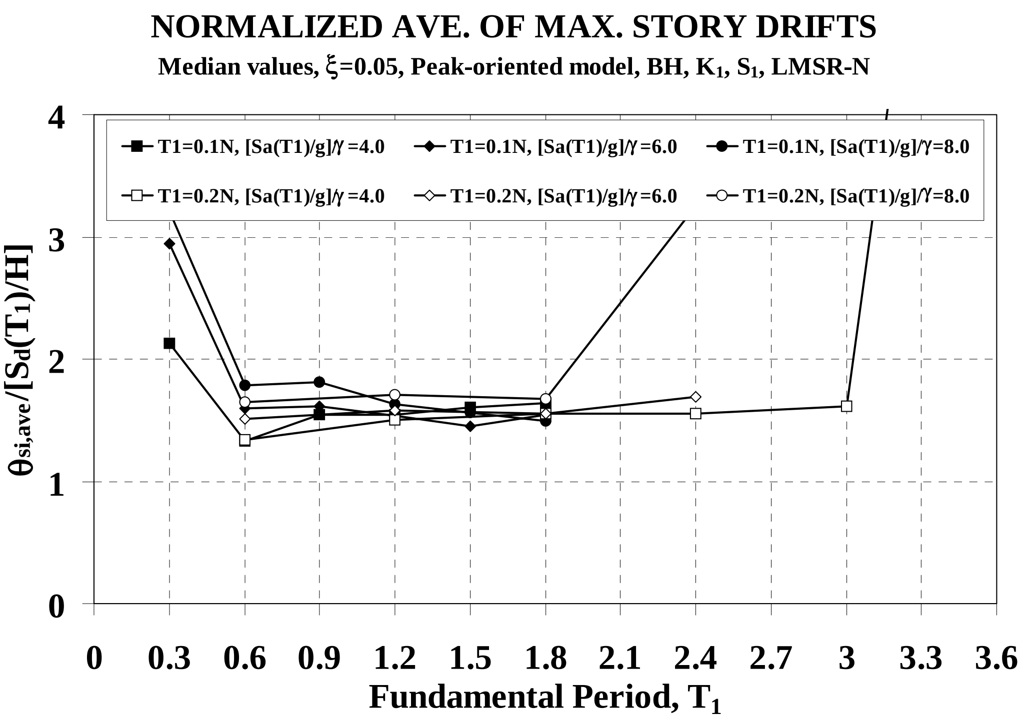

(b) $[S_a(T_1)/g]/\gamma$ = 4.0, 6.0, 8.0

Figure 4.10 Dependence of the Median Normalized Average of the Maximum Story Drift Angles on T_1, All Frames, Various Relative Intensities

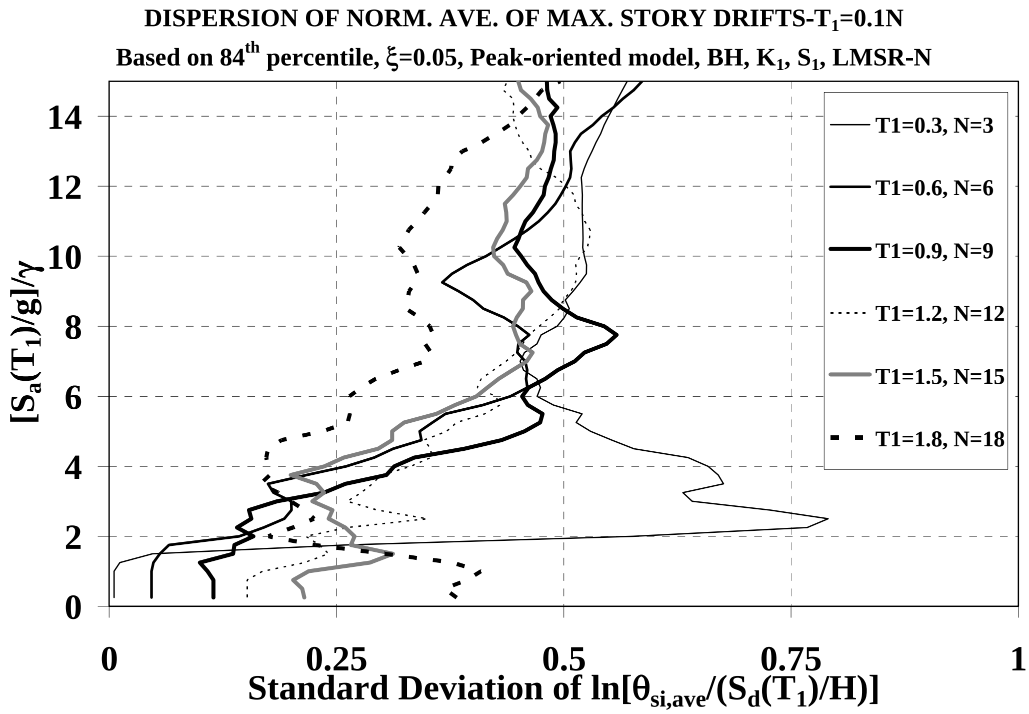

(a) $T_1 = 0.1N$

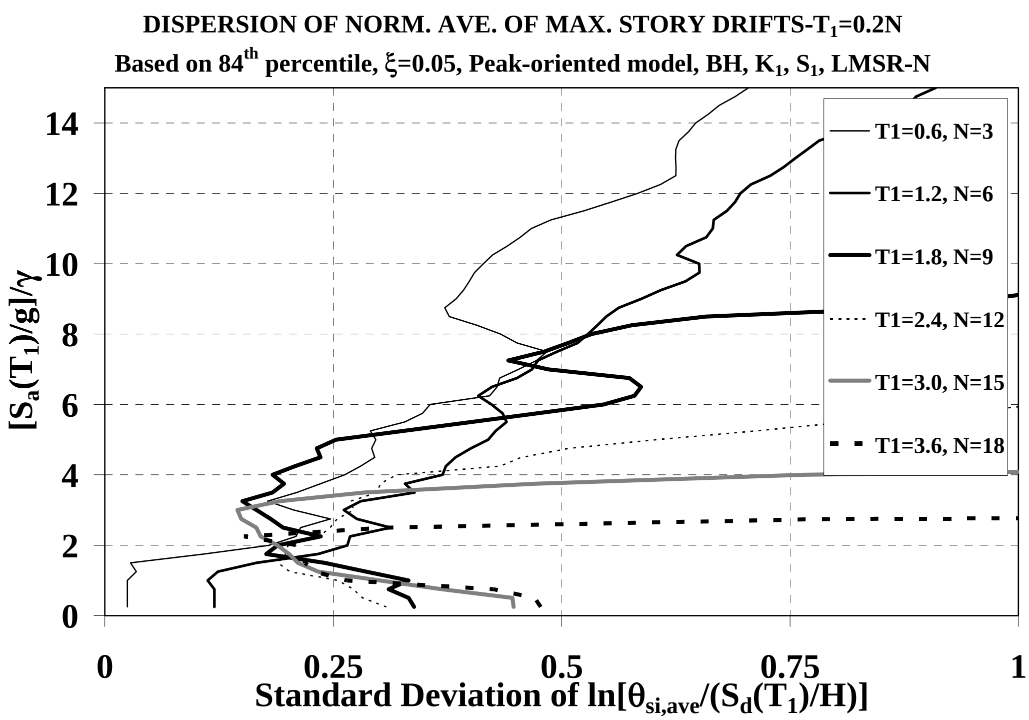

(b) $T_1 = 0.2N$

Figure 4.11 Dispersion of the Normalized Average of the Maximum Story Drift Angles, Stiff and Flexible Frames

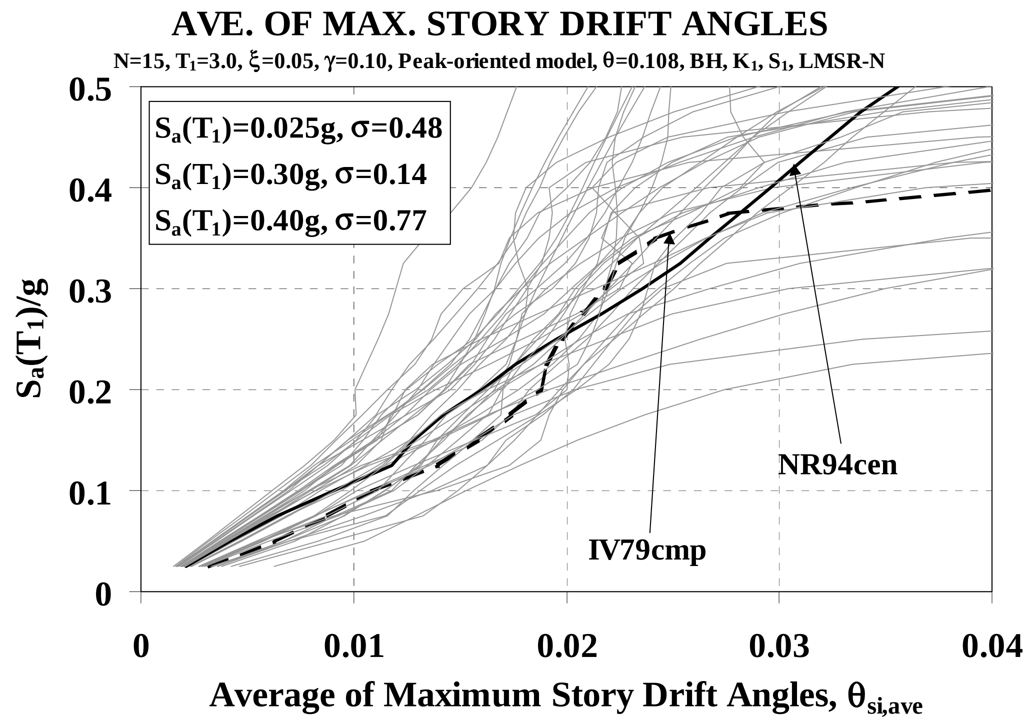

(a) Incremental Dynamic Analysis, N = 15, T_1 = 3.0 sec

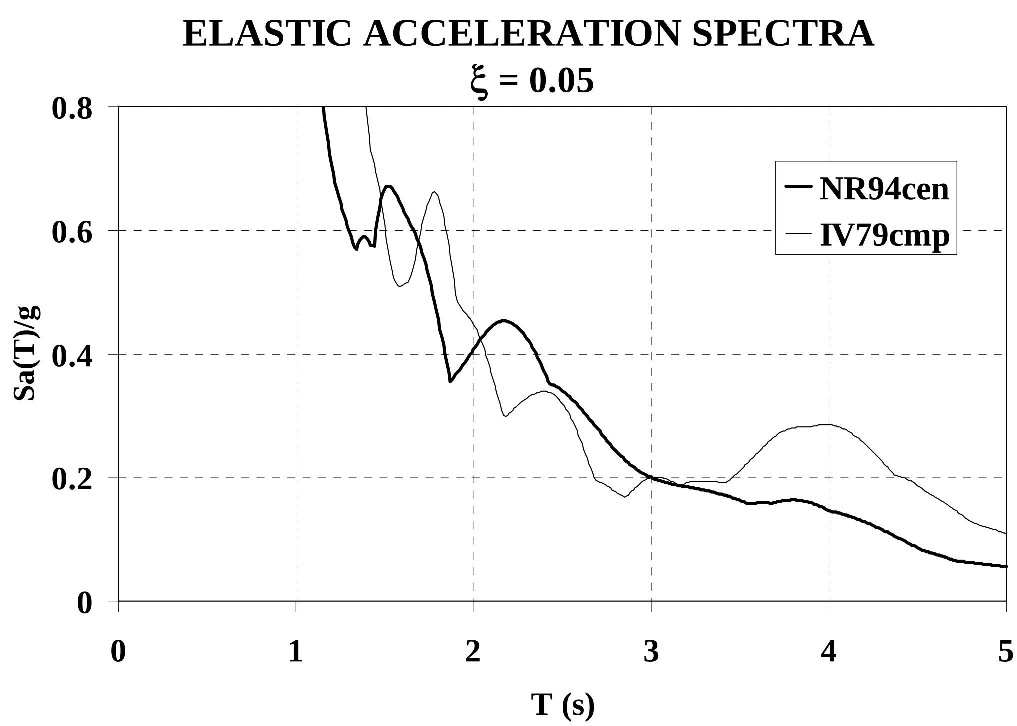

(b) Elastic Acceleration Spectra, NR94cen and IV79cmp records

Figure 4.12 Effect of the Ground Motion Frequency Content in the Dispersion of $\theta_{si,ave}$ Values

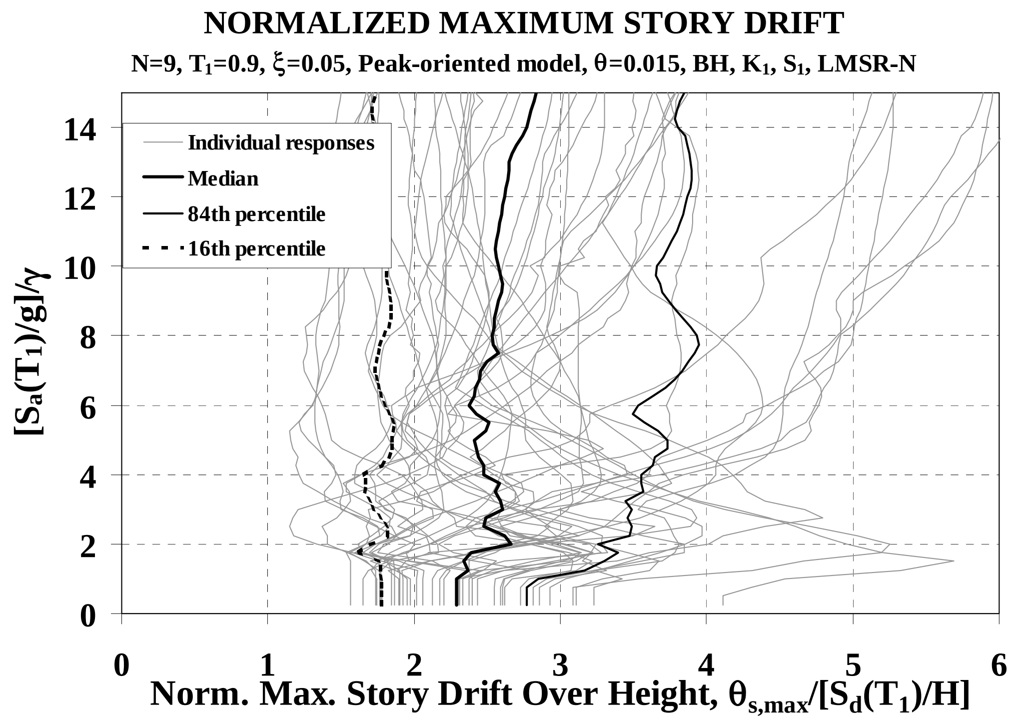

(a) T_1 = 0.9 sec

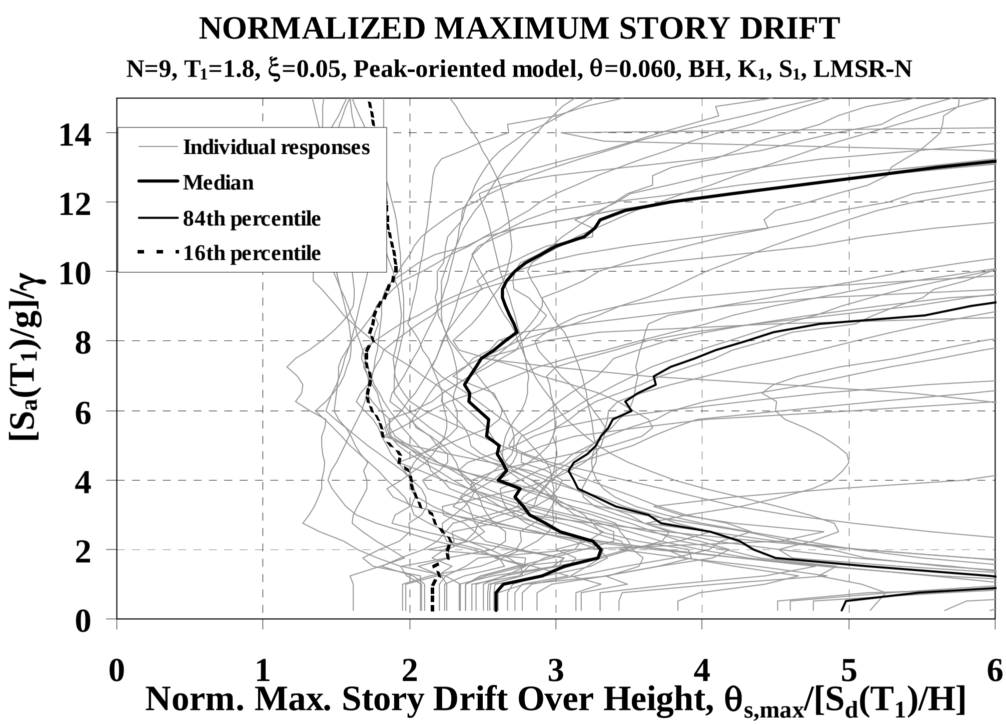

(b) T_1 = 1.8 sec

Figure 4.13 Normalized Maximum Story Drift Angles over the Height, N = 9

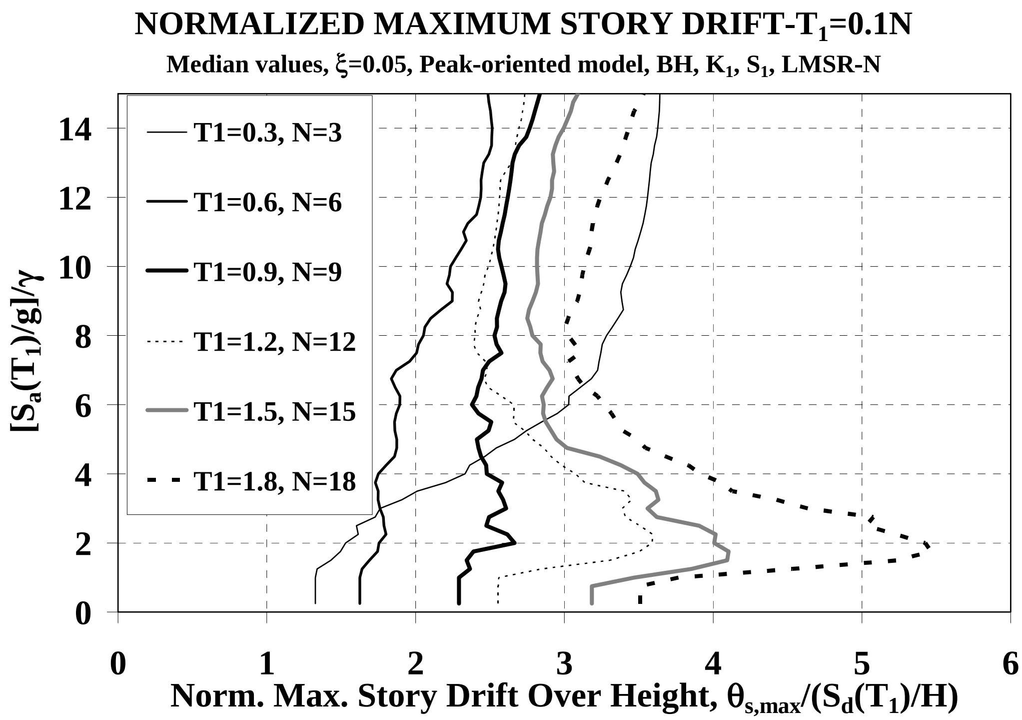

(a) $T_1 = 0.1N$

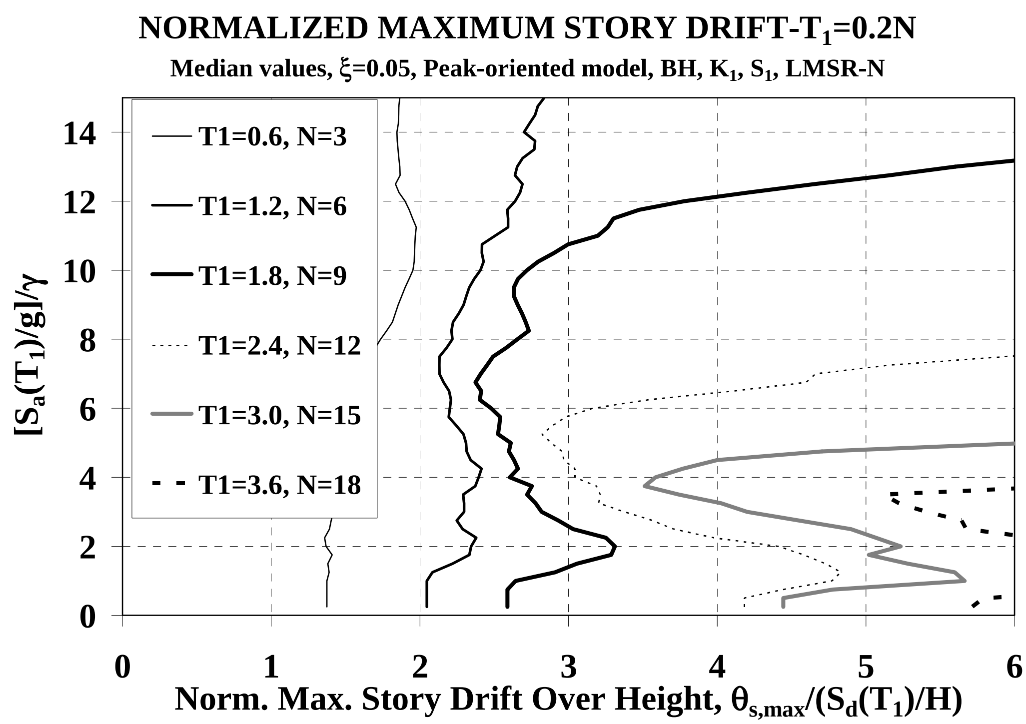

(b) $T_1 = 0.2N$

Figure 4.14 Median Normalized Maximum Story Drift Angle over the Height, Stiff and Flexible Frames

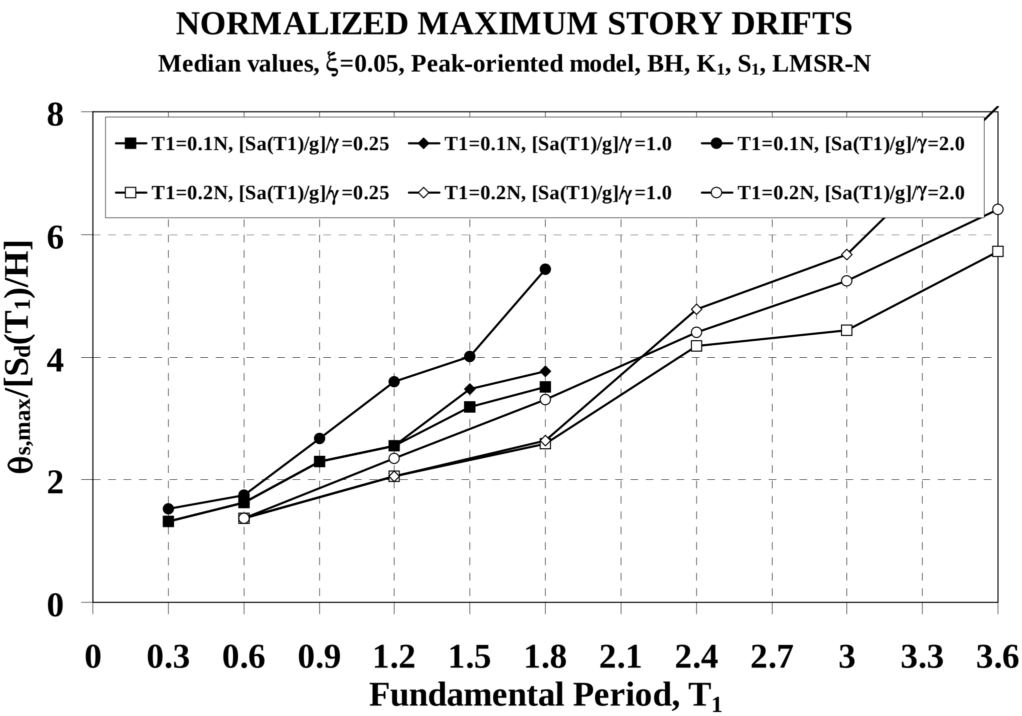

(a) $[S_a(T_1)/g]/\gamma$ = 0.25, 1.0, 2.0

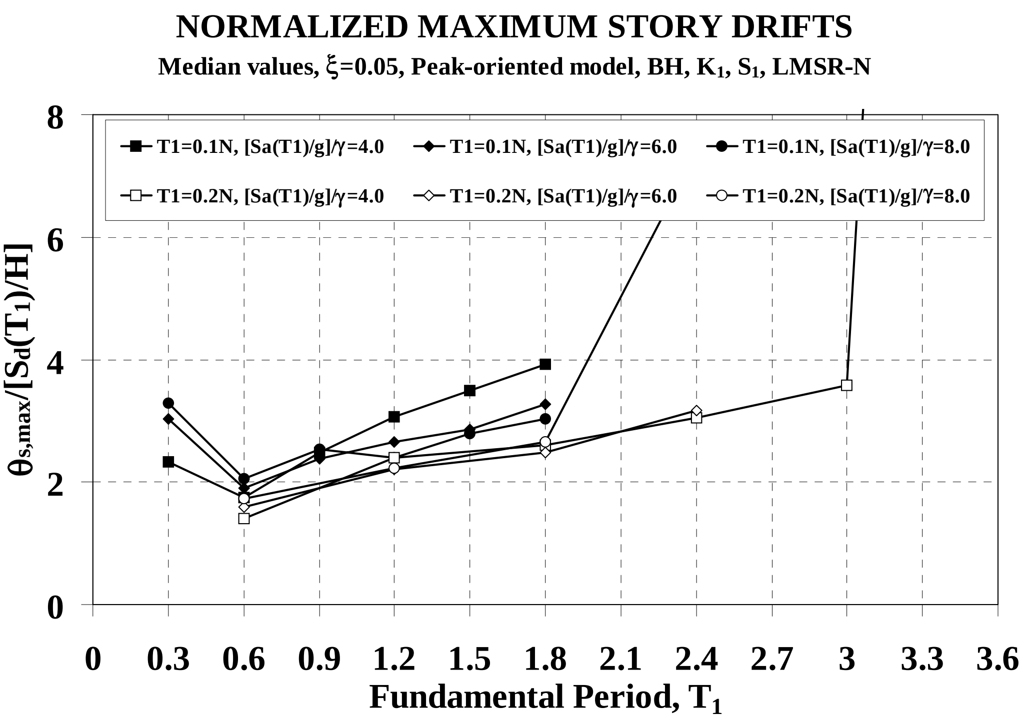

(b) $[S_a(T_1)/g]/\gamma$ = 4.0, 6.0, 8.0

Figure 4.15 Dependence of the Median Normalized Maximum Story Drift Angle over the Height on T_1, All Frames, Various Relative Intensities

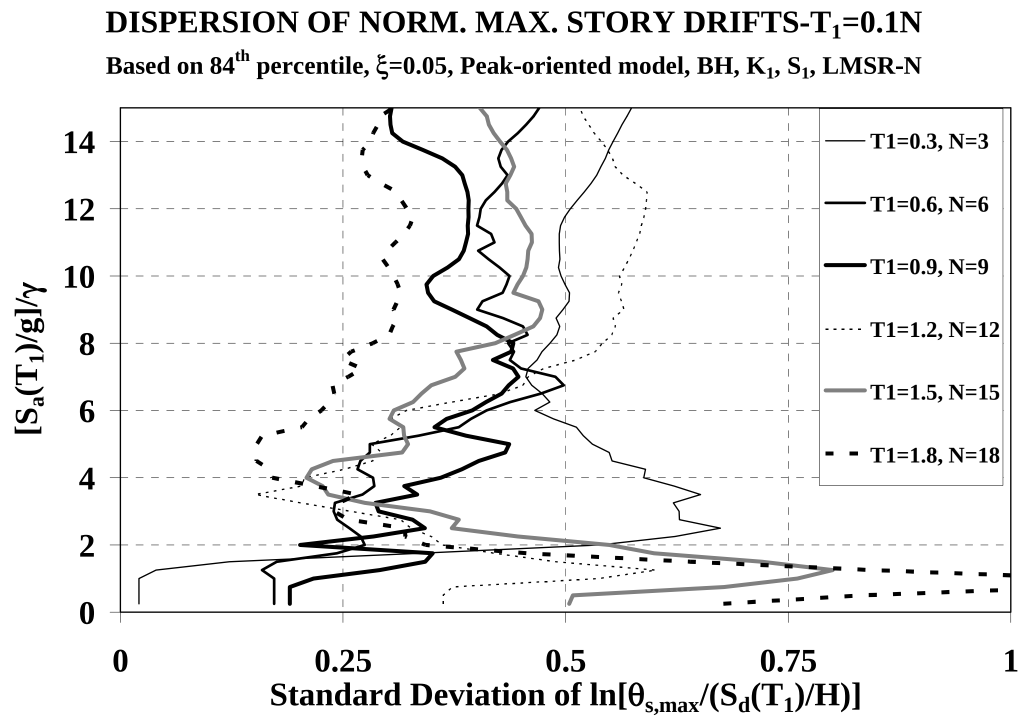

(a) $T_1 = 0.1N$

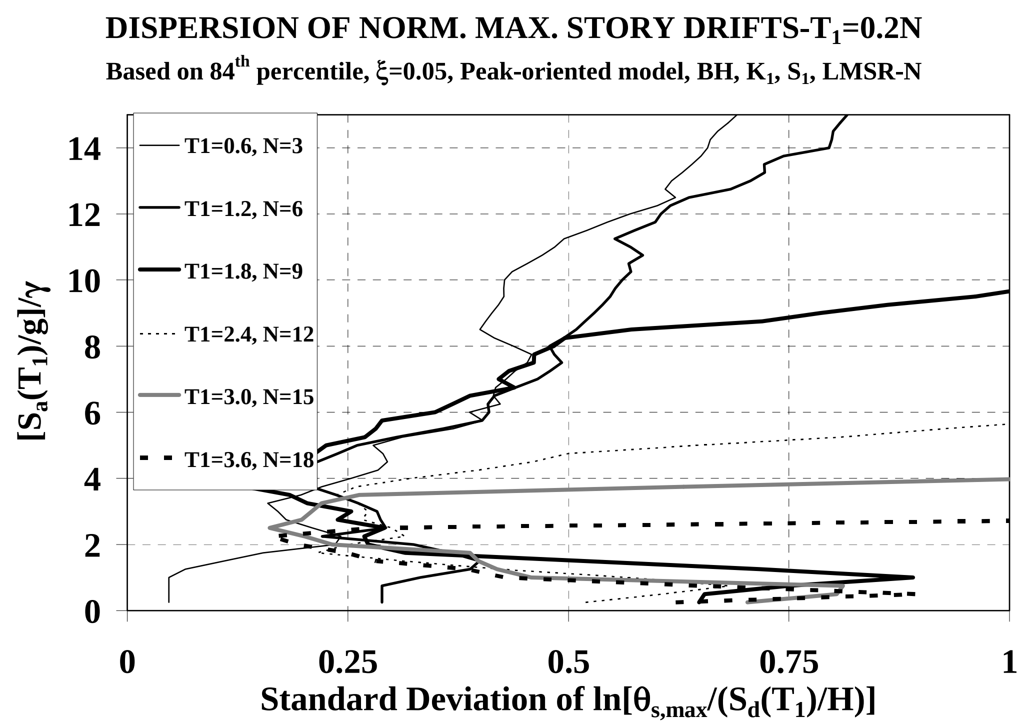

(b) $T_1 = 0.2N$

Figure 4.16 Dispersion of the Normalized Maximum Story Drift Angle over the Height, Stiff and Flexible Frames

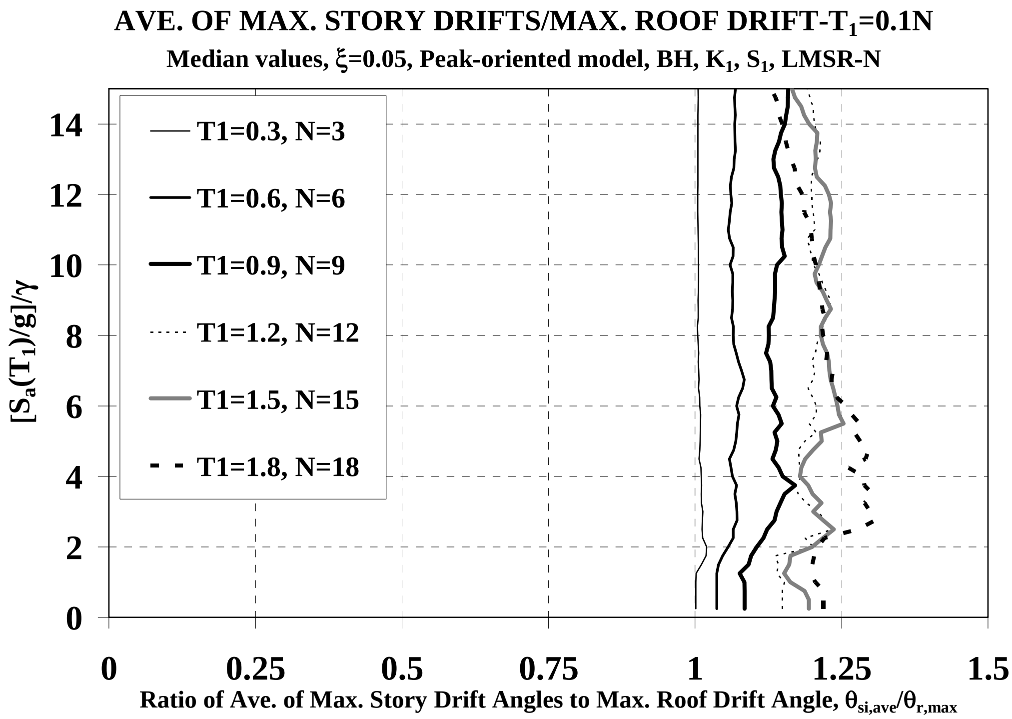

(a) T_1 = 0.1N

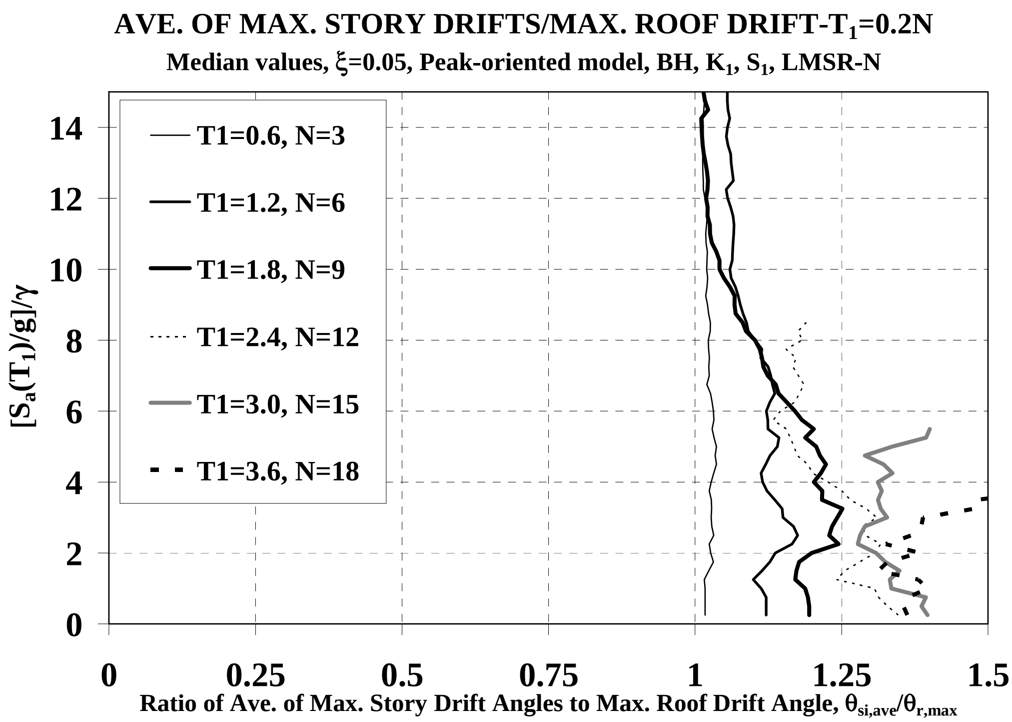

(b) T_1 = 0.2 N

Figure 4.17 Median Ratio of the Average of the Maximum Story Drift Angles to the Maximum Roof Drift Angle, Stiff and Flexible Frames

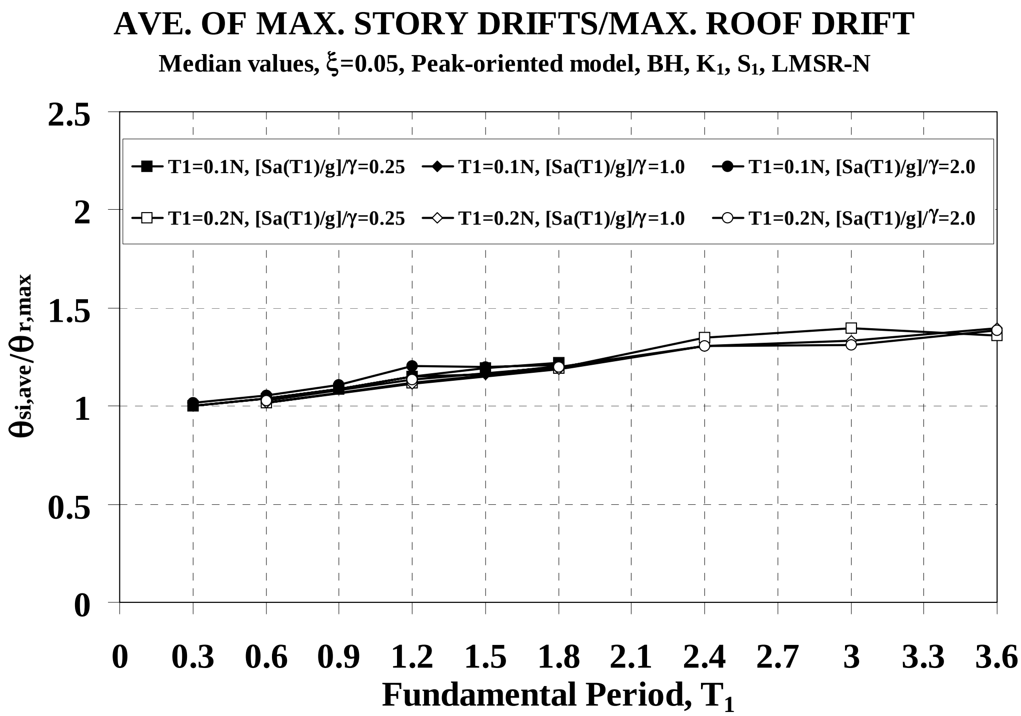

(a) $[S_a(T_1)/g]/\gamma$ = 0.25, 1.0, 2.0

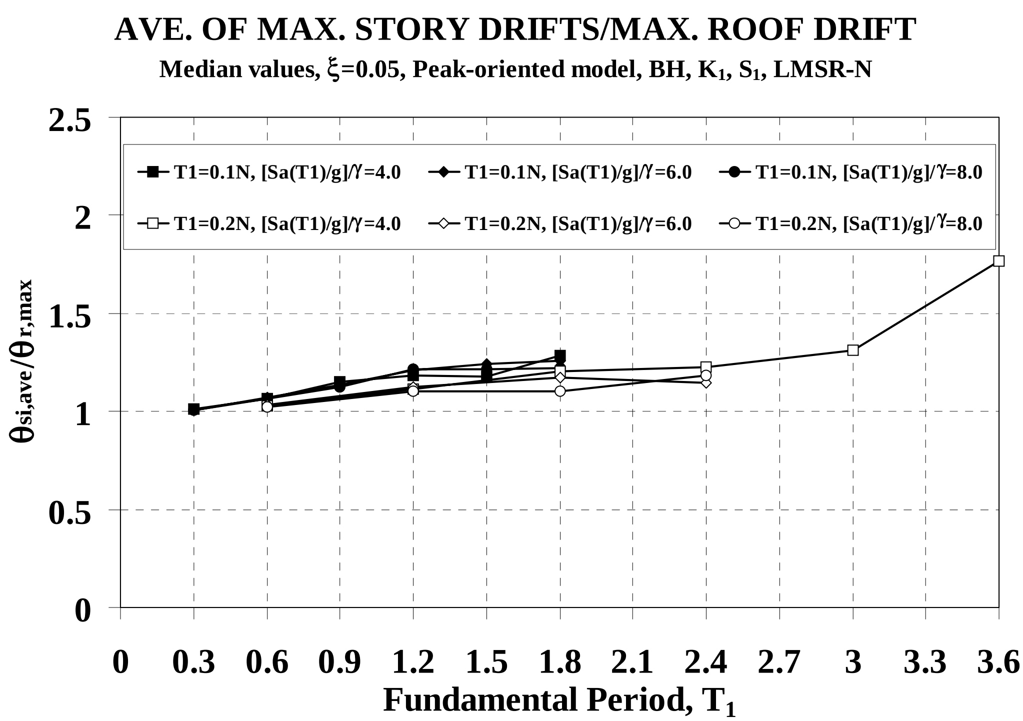

(b) $[S_a(T_1)/g]/\gamma$ = 4.0, 6.0, 8.0

Figure 4.18 Median Ratio of the Average of the Maximum Story Drift Angles to the Maximum Roof Drift Angle, All frames, Various Relative Intensities

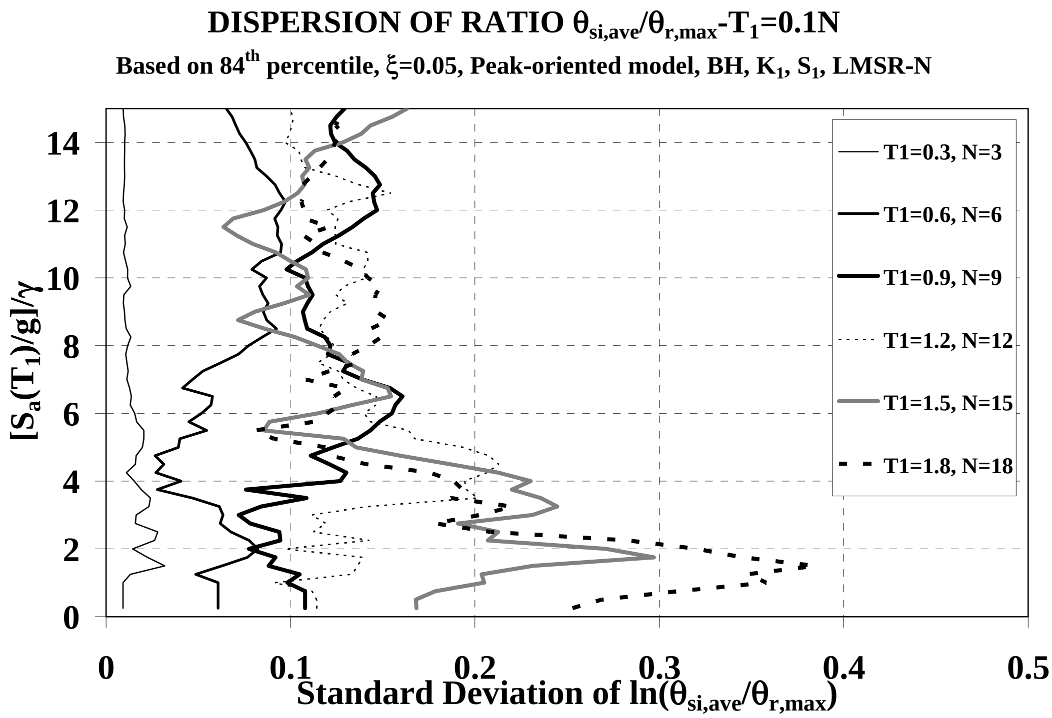

(a) T_1 = 0.1N

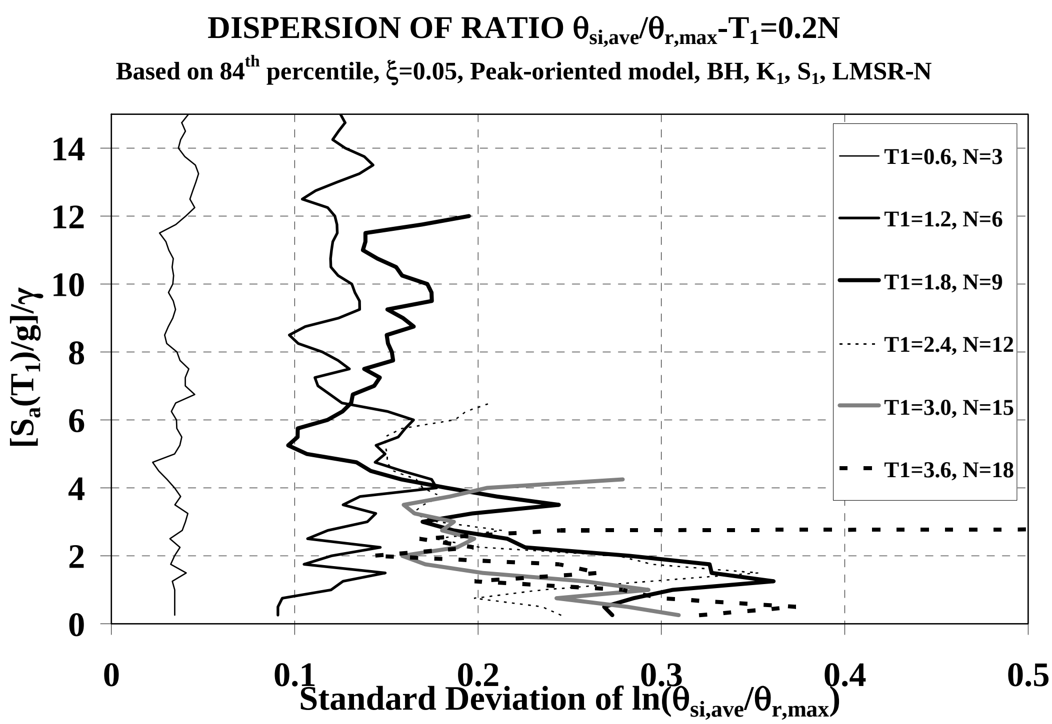

(b) T_1 = 0.2N

Figure 4.19 Dispersion of the Ratio of the Average of the Maximum Story Drift Angles to the Maximum Roof Drift Angle, Stiff and Flexible Frames

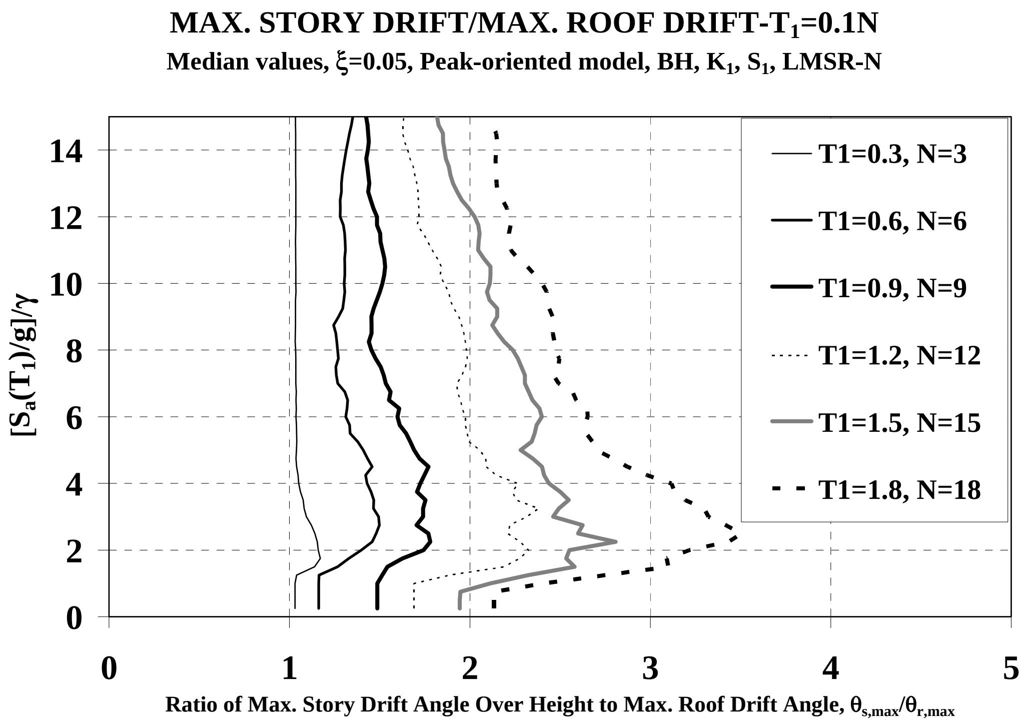

(a) $T_1 = 0.1N$

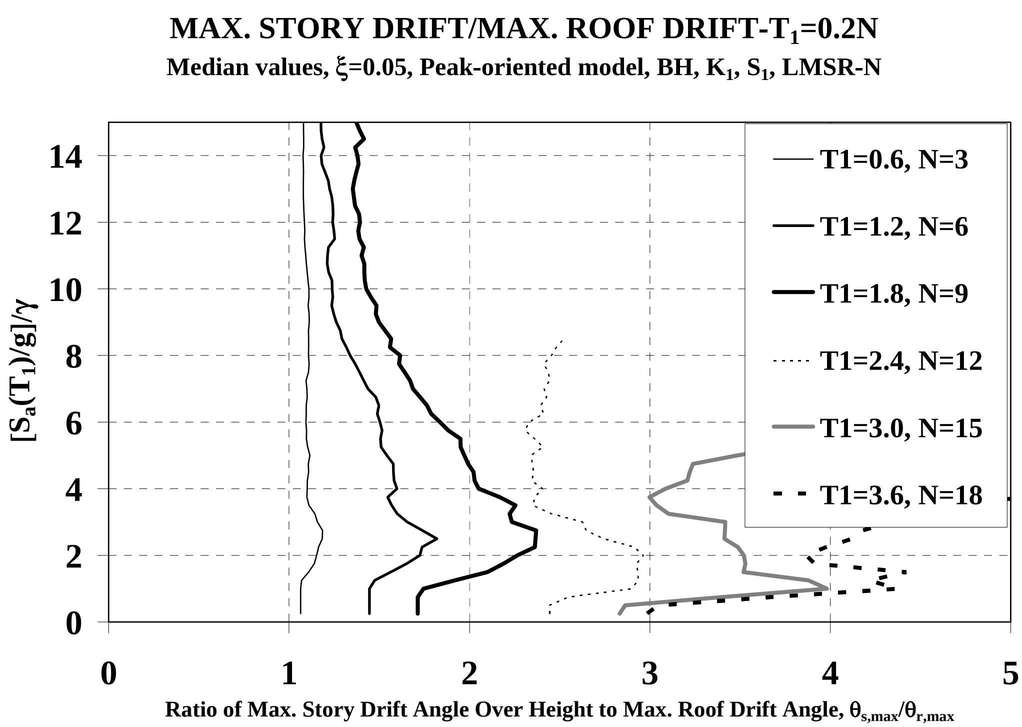

(b) $T_1 = 0.2N$

Figure 4.20 Median Ratio of the Maximum Story Drift Angle over Height to the Maximum Roof Drift Angle, Stiff and Flexible Frames

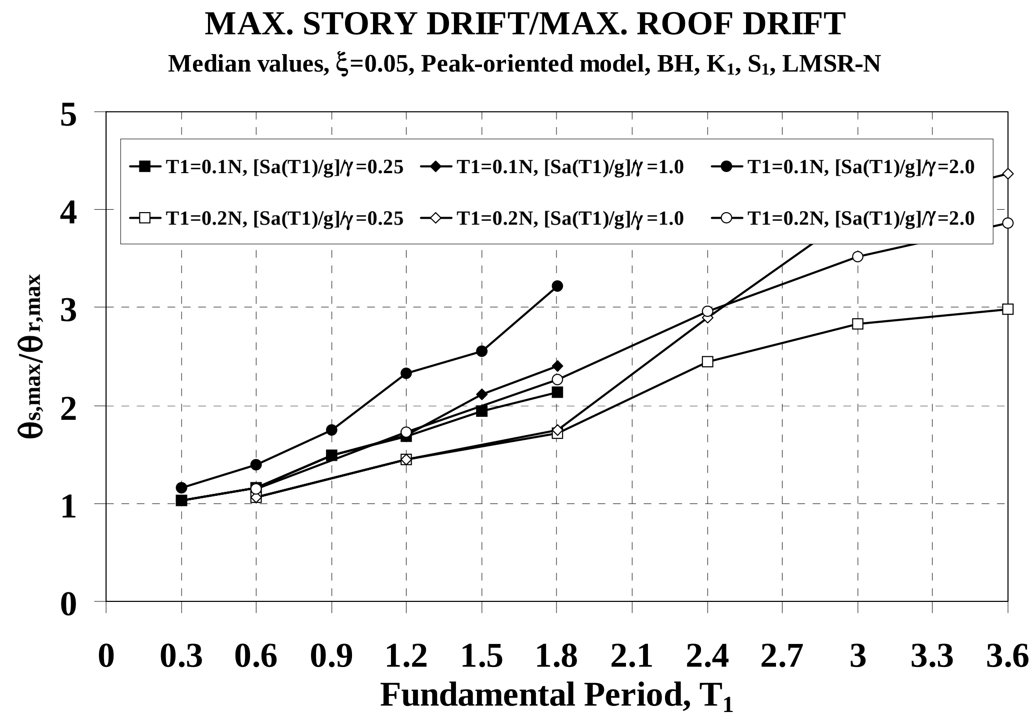

(a) $[S_a(T_1)/g]/\gamma$ = 0.25, 1.0, 2.0

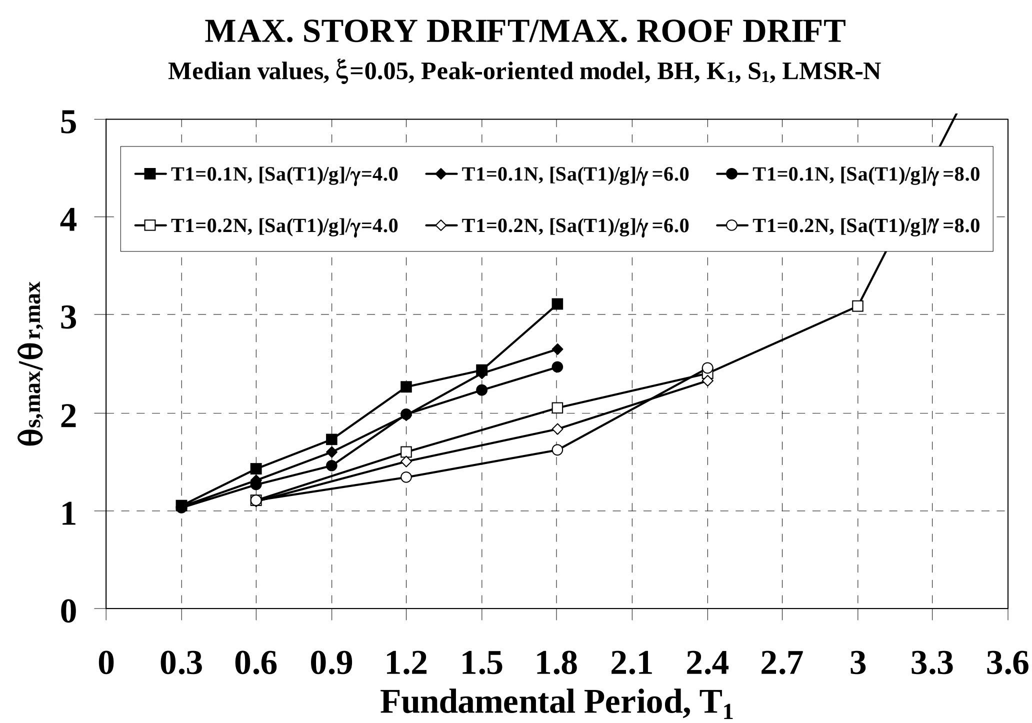

(b) $[S_a(T_1)/g]/\gamma$ = 4.0, 6.0, 8.0

Figure 4.21 Dependence of the Median Ratio of the Maximum Story Drift Angle over the Height to the Maximum Roof Drift Angle on T_1, All Frames, Various Relative Intensities

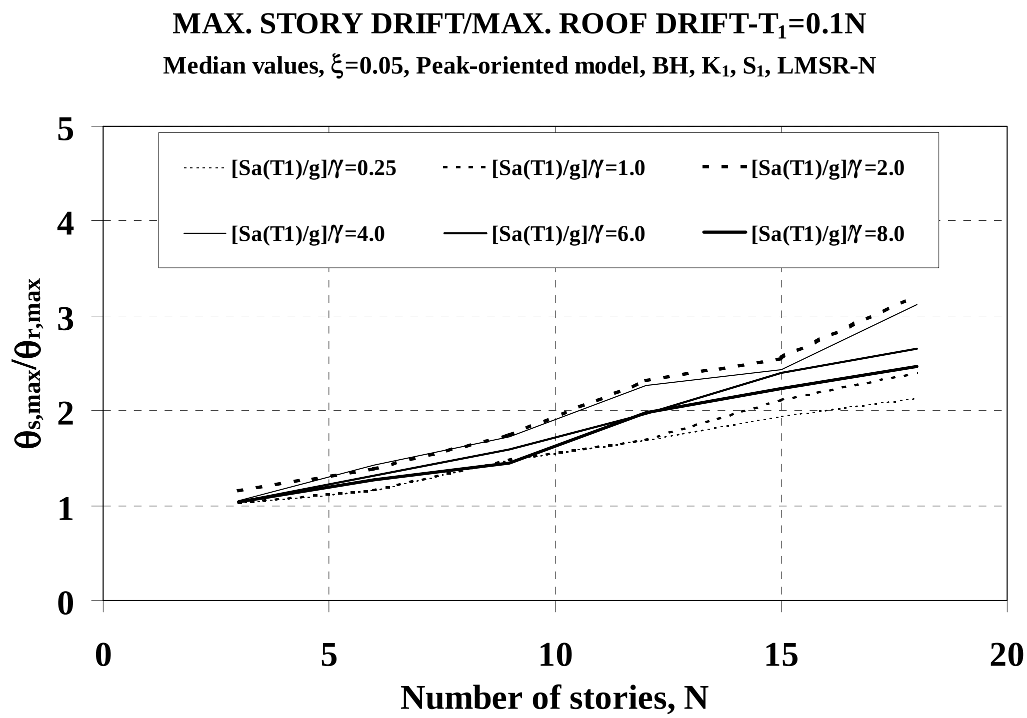

(a) T_1 = 0.1N

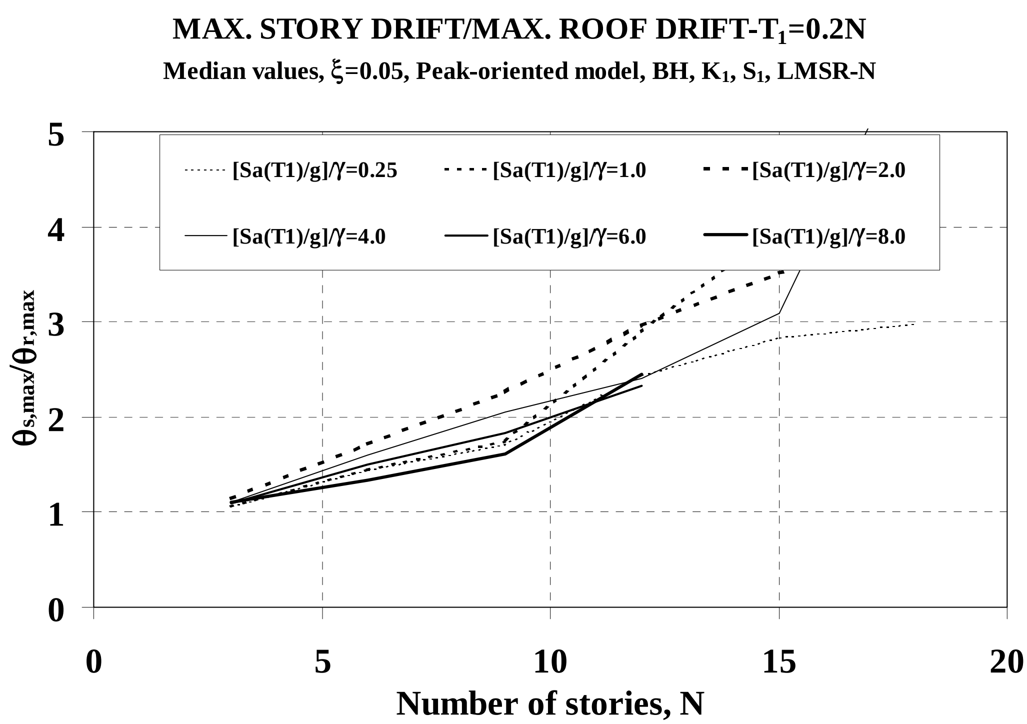

(b) T_1 = 0.2N

Figure 4.22 Dependence of the Median Ratio of the Maximum Story Drift Angle over Height to the Maximum Roof Drift Angle on N, Stiff and Flexible Frames

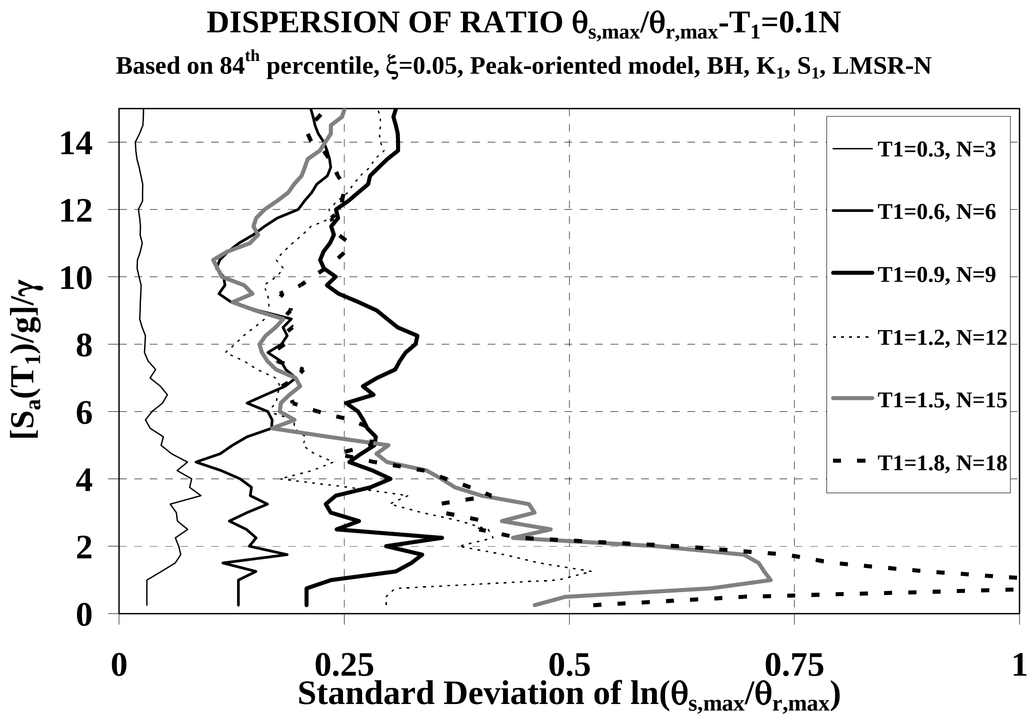

(a) $T_1 = 0.1N$

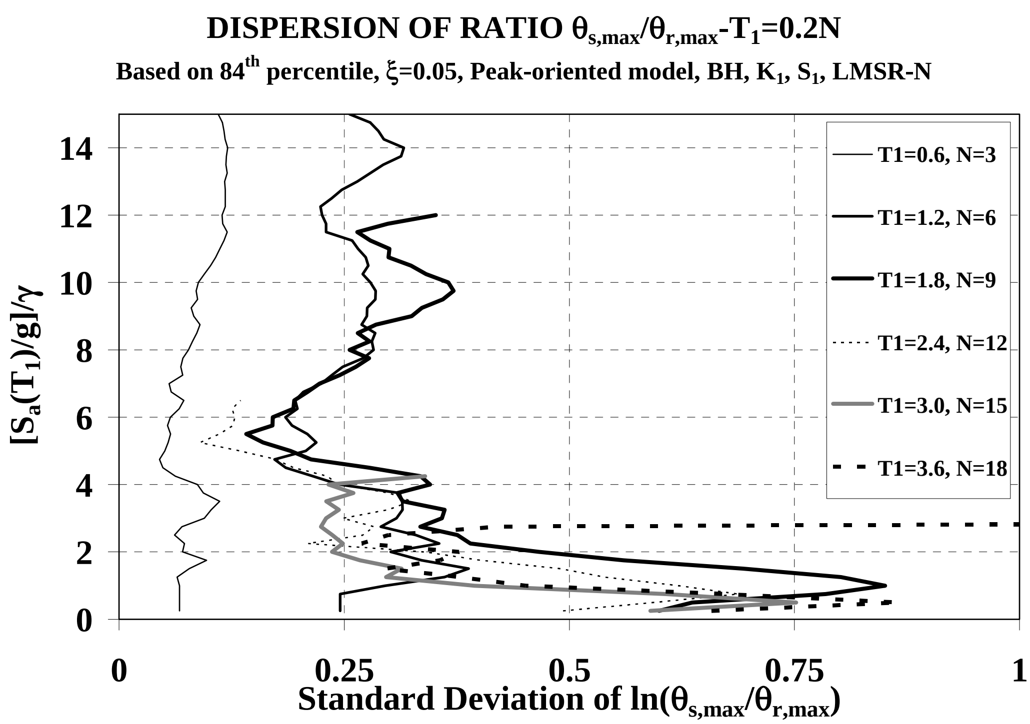

(b) $T_1 = 0.2\ N$

Figure 4.23 Dispersion of the Ratio of the Maximum Story Drift Angle over the Height to the Maximum Roof Drift Angle, Stiff and Flexible Frames

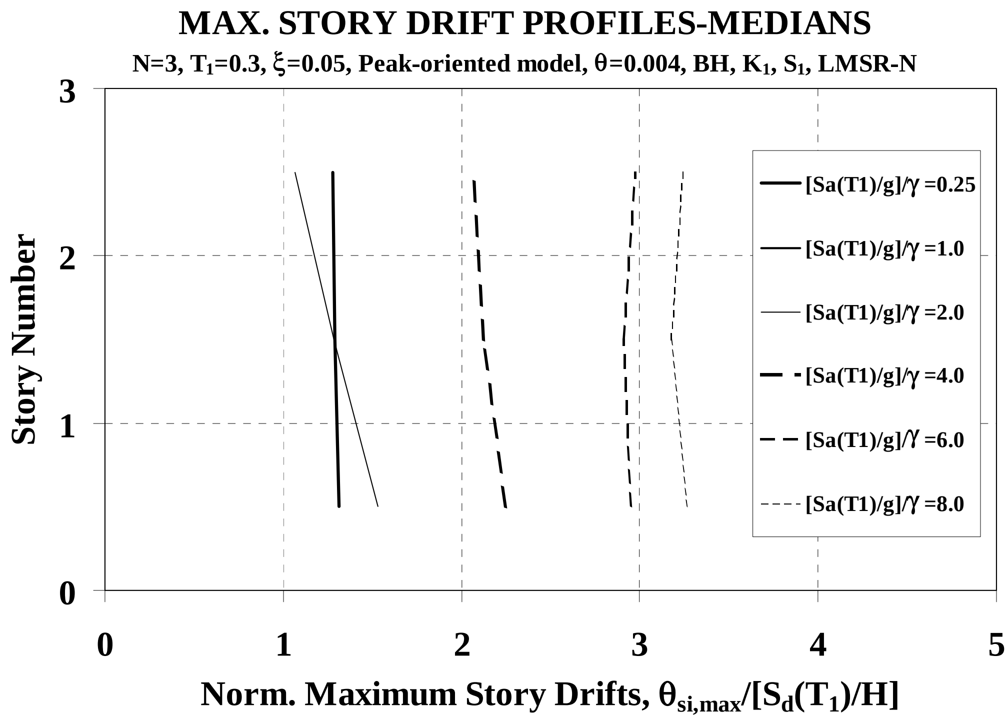

(a) T_1 = 0. 3 sec

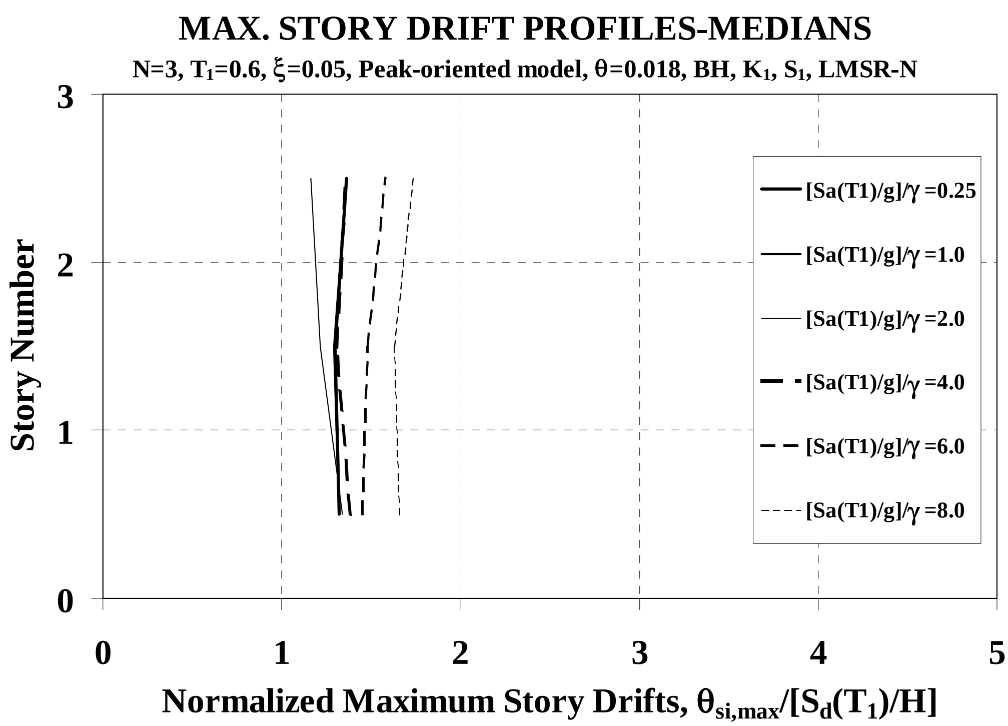

(b) T_1 = 0.6 sec

Figure 4.24 Distribution over the Height of Normalized Maximum Story Drift Angles, N = 3

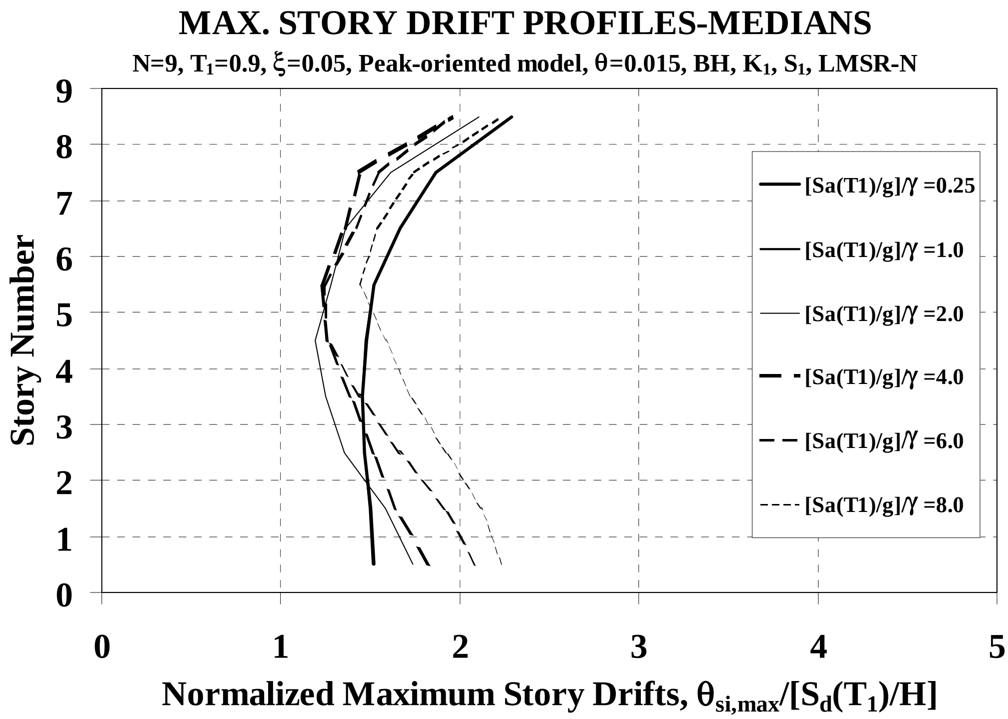

(a) T_1 = 0.9 sec

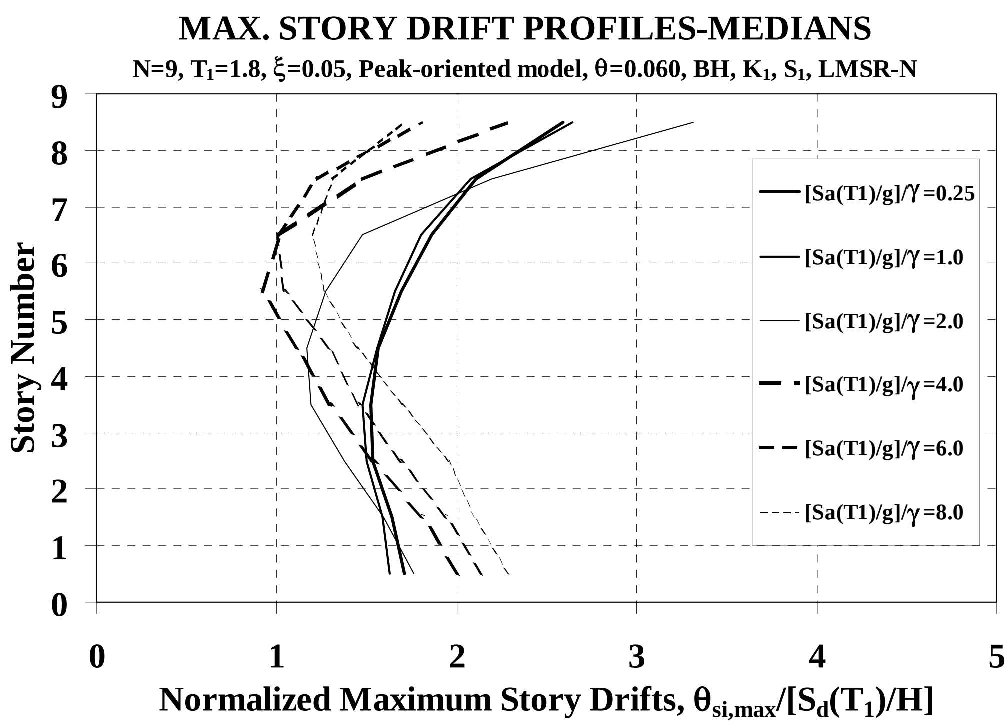

(b) T_1 = 1.8 sec

Figure 4.25 Distribution over the Height of Normalized Maximum Story Drift Angles, N = 9

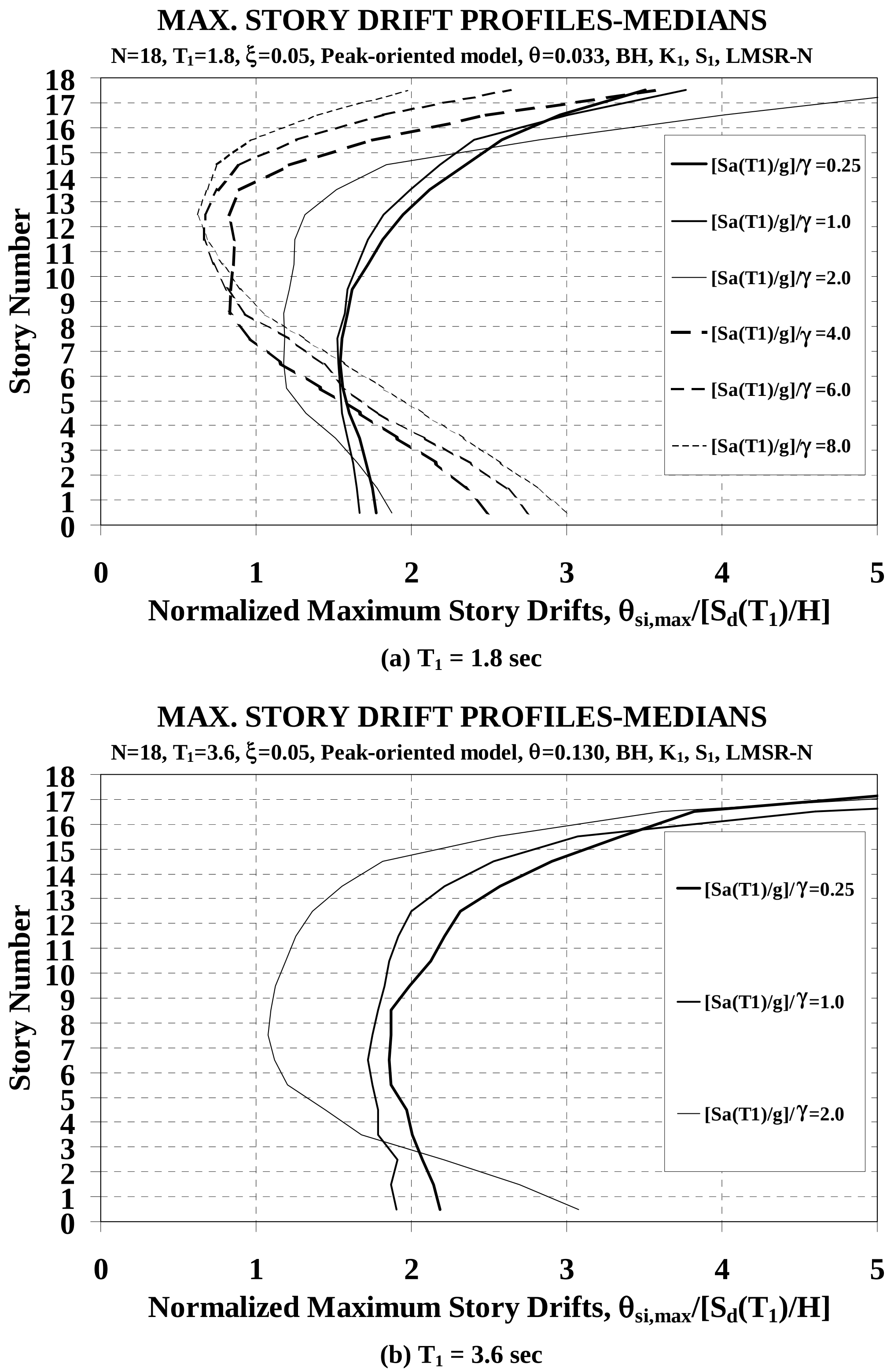

Figure 4.26 Distribution over the Height of Normalized Maximum Story Drift Angles, N = 18

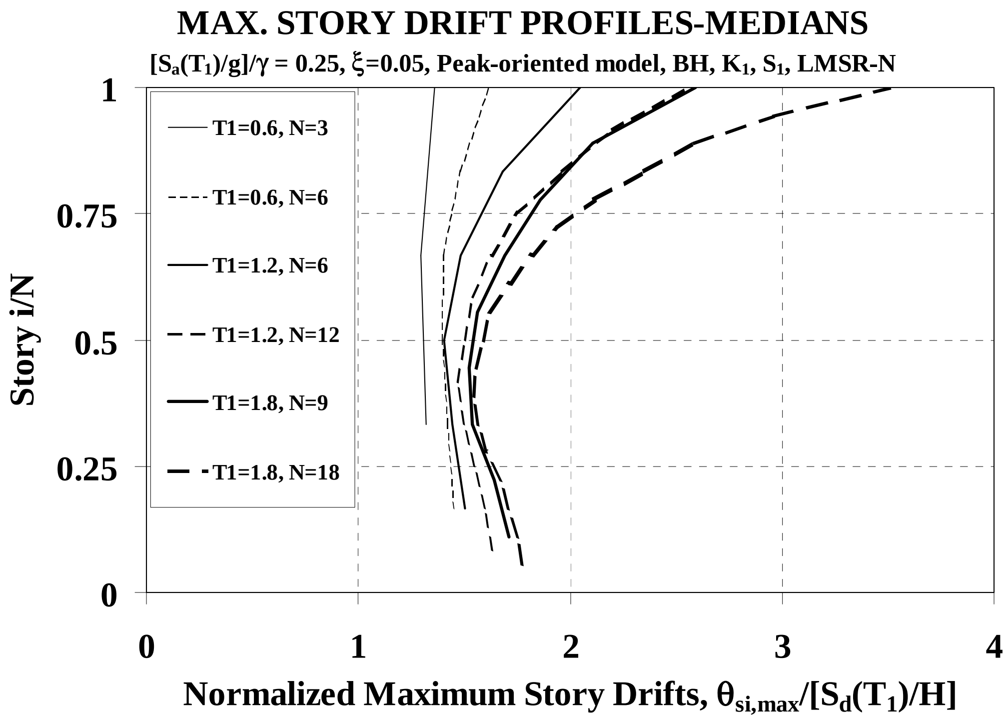

(a) Median Values

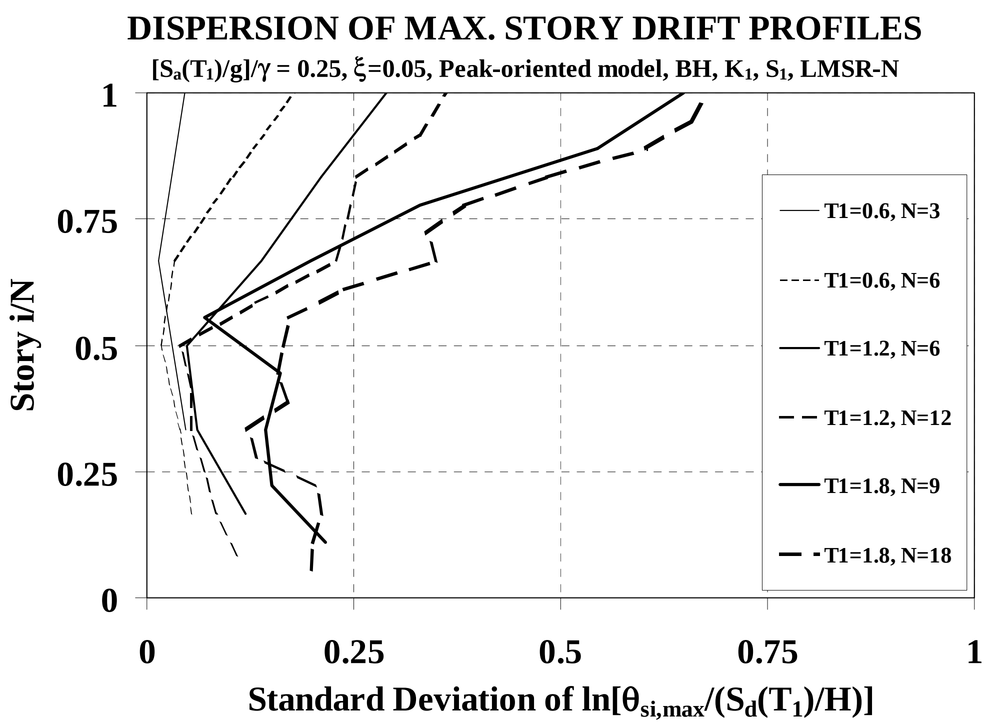

(b) Dispersion

Figure 4.27 Distribution over the Height of Normalized Maximum Story Drift Angles, $[S_a(T_1)/g]/\gamma = 0.25$

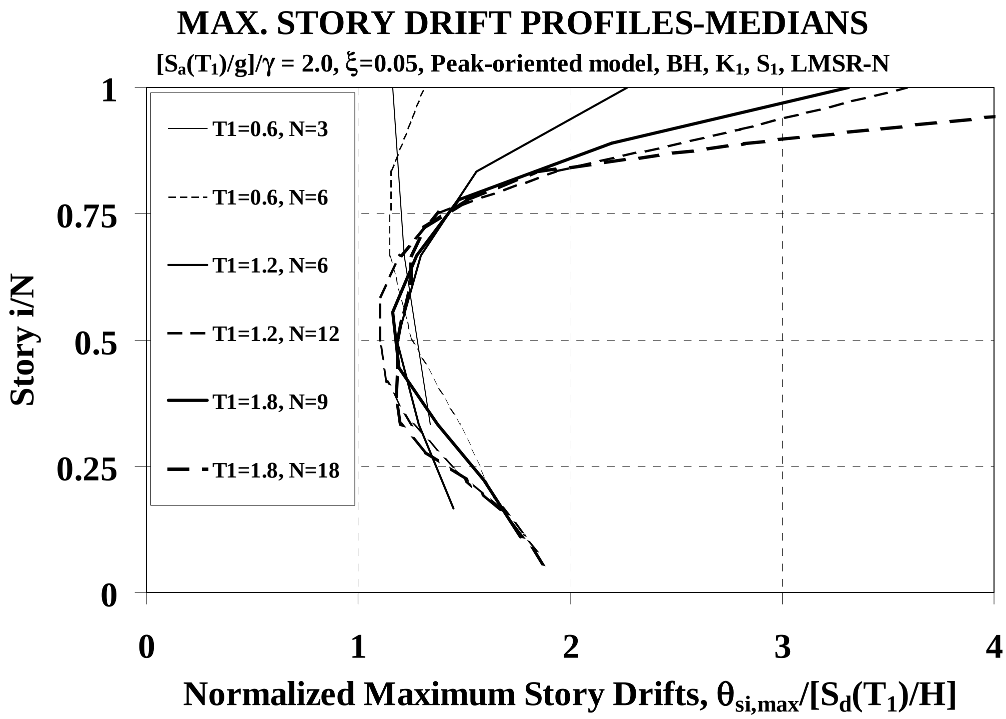

(a) Median Values

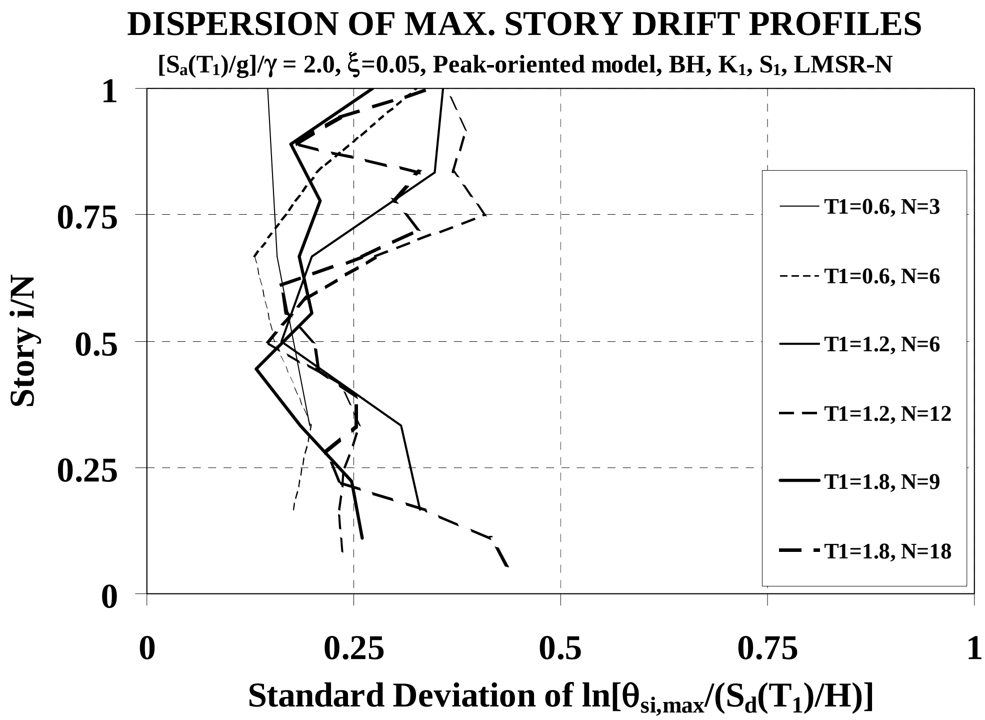

(b) Dispersion

Figure 4.28 Distribution over the Height of Normalized Maximum Story Drift Angles, $[S_a(T_1)/g]/\gamma = 2.0$

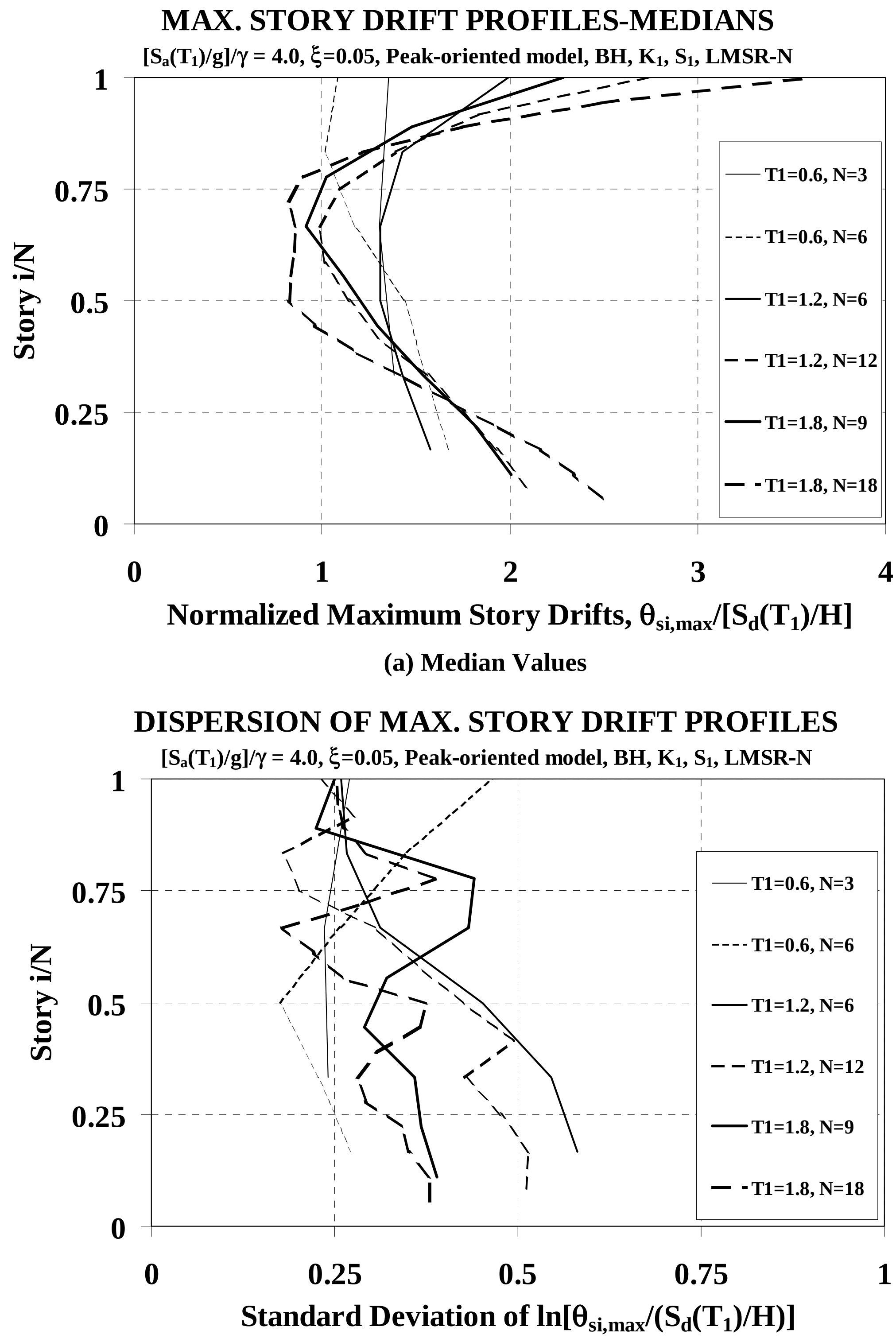

(a) Median Values

(b) Dispersion

Figure 4.29 Distribution over the Height of Normalized Maximum Story Drift Angles, $[S_a(T_1)/g]/\gamma = 4.0$

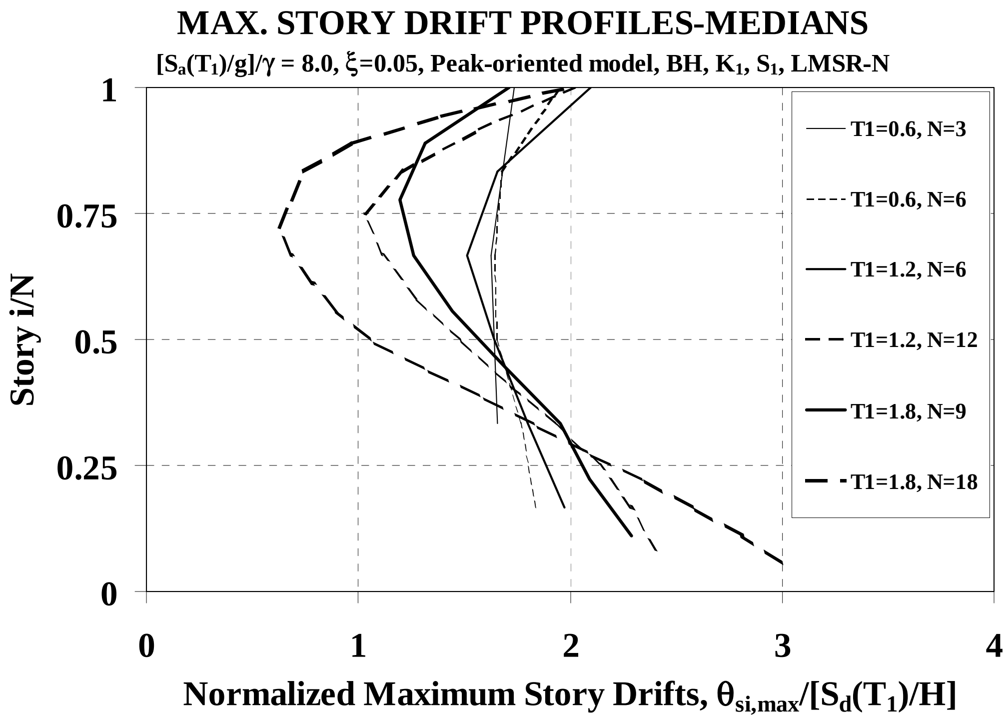

(a) Median Values

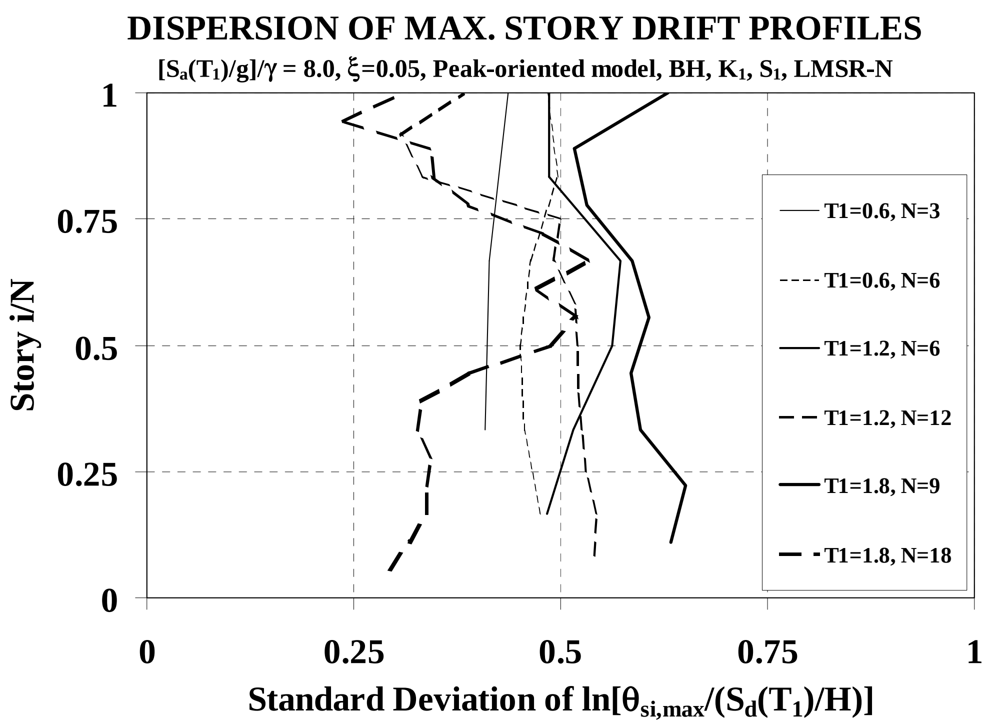

(b) Dispersion

Figure 4.30 Distribution over the Height of Normalized Maximum Story Drift Angles, $[S_a(T_1)/g]/\gamma = 8.0$

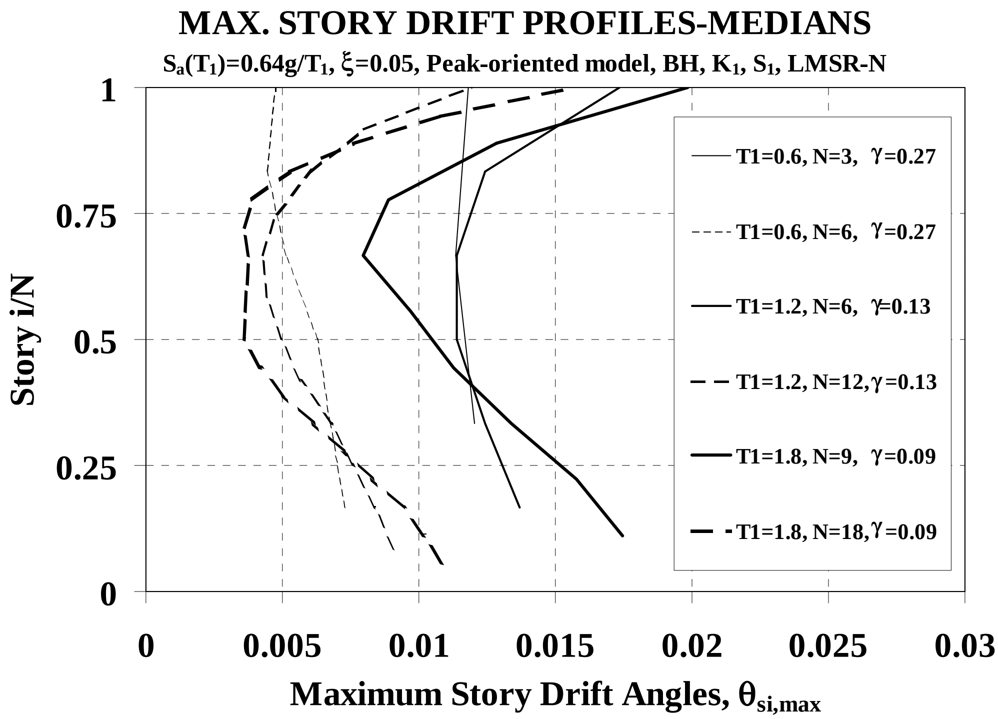

Figure 4.31 Absolute Values for the Maximum Story Drift Angles over the Height (Based on UBC 1997 Ground Motion Spectrum for Site Class D)

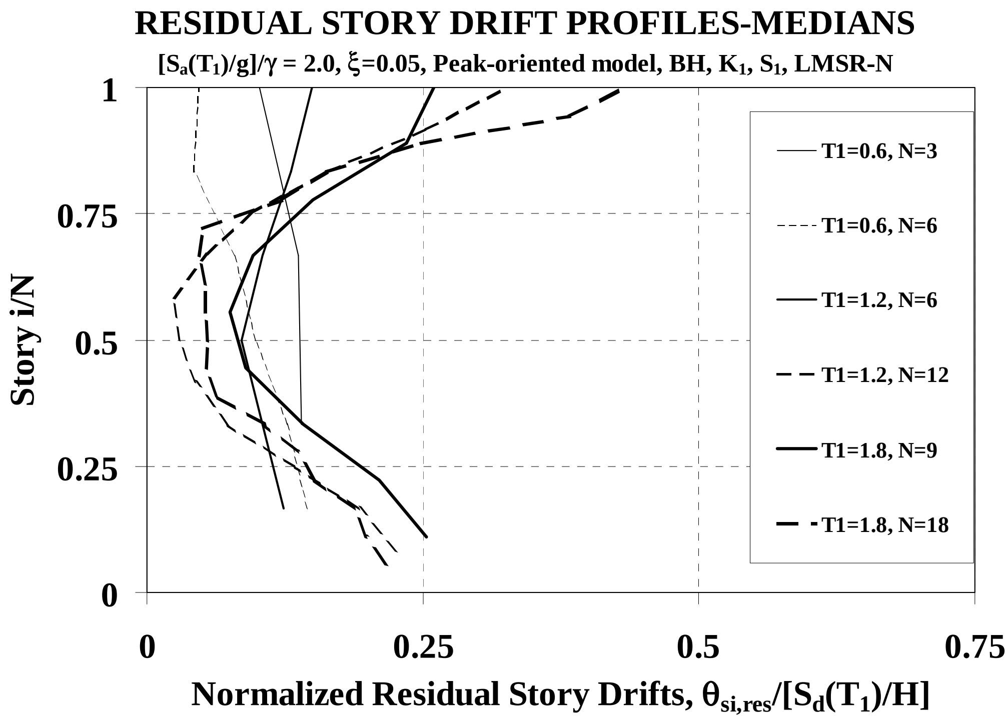

(a) Median Values

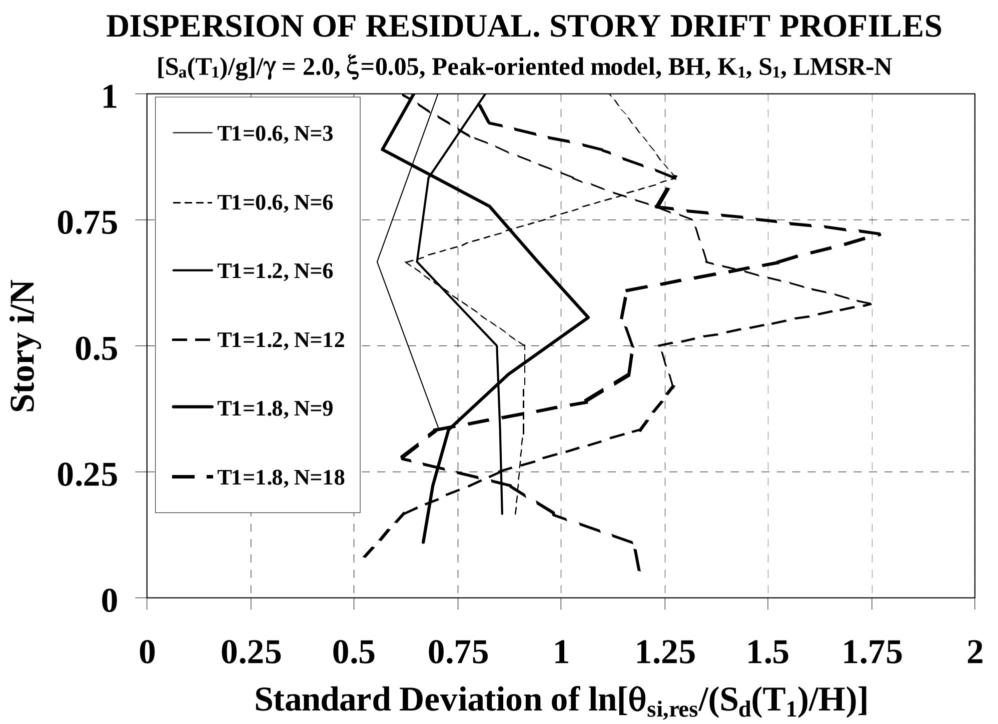

(b) Dispersion

Figure 4.32 Distribution over the Height of Normalized Residual Story Drift Angles, $[S_a(T_1)/g]/\gamma = 2.0$

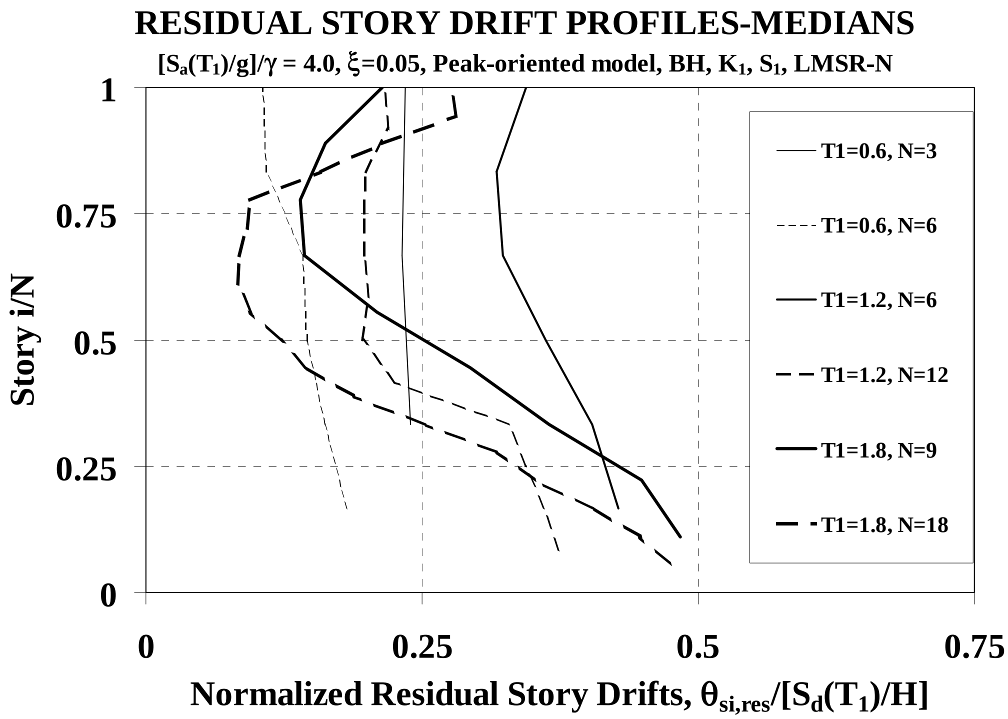

(a) Median Values

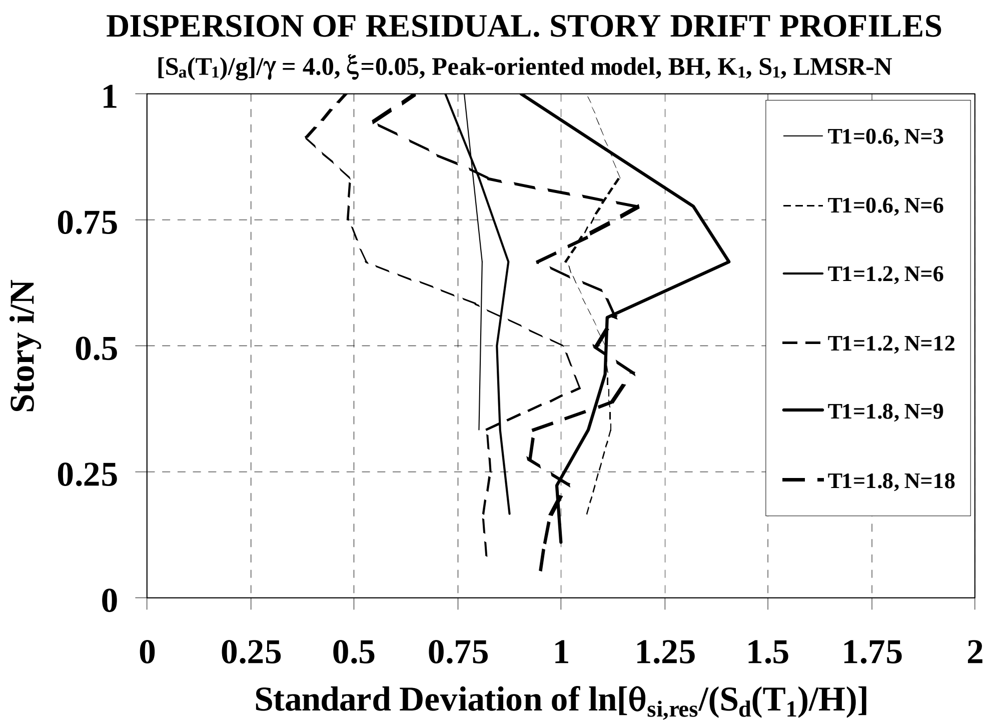

(b) Dispersion

Figure 4.33 Distribution over the Height of Normalized Residual Story Drift Angles, $[S_a(T_1)/g]/\gamma = 4.0$

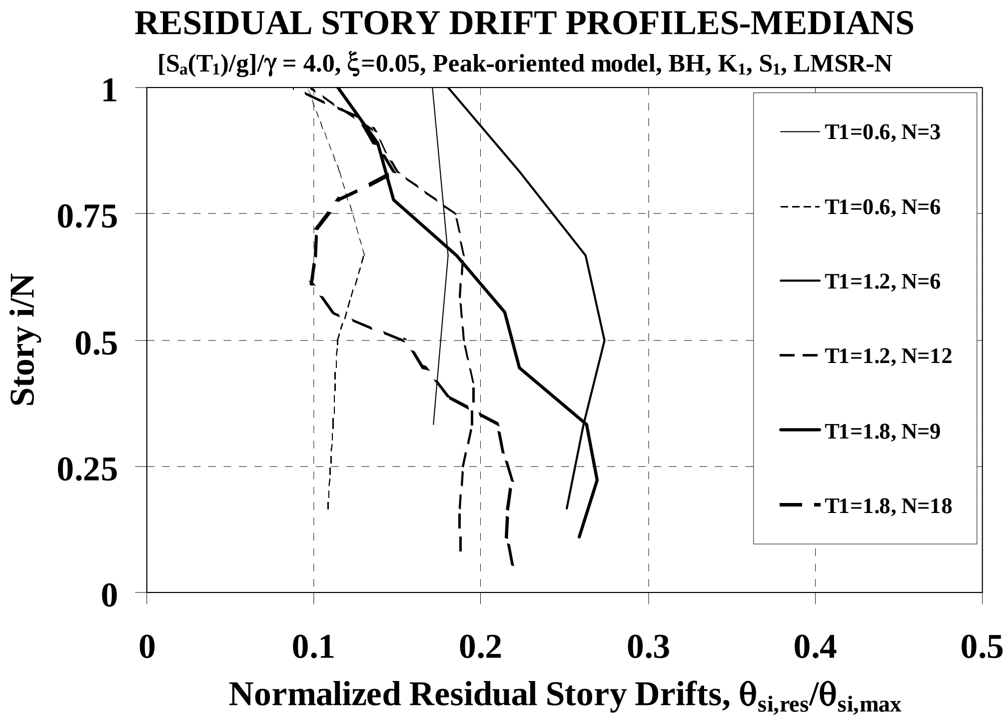

(a) Median Values

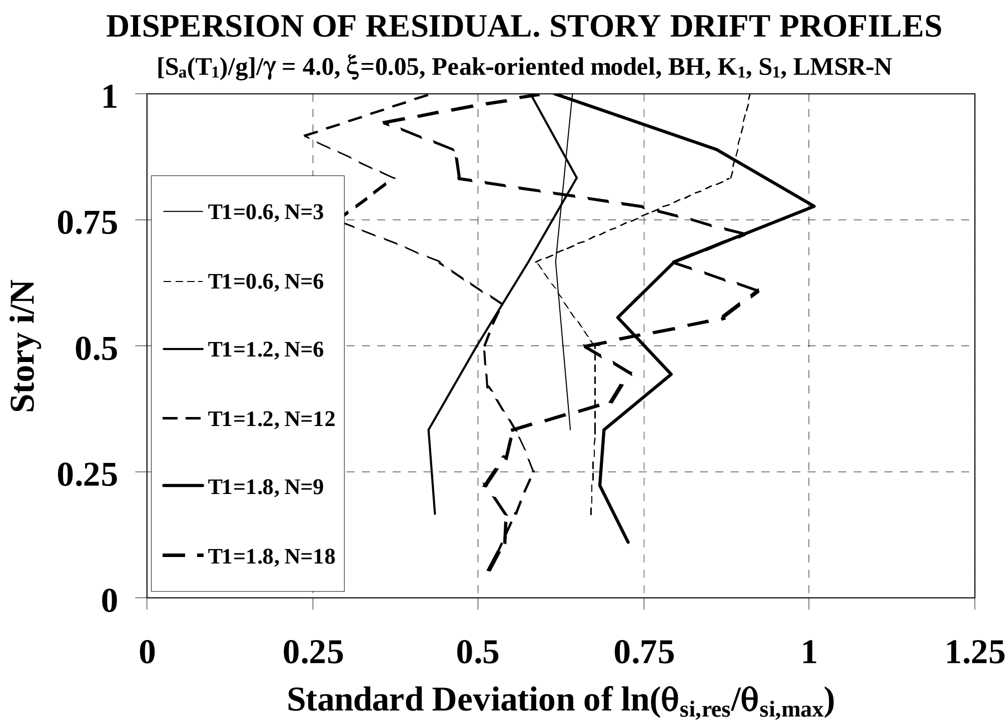

(b) Dispersion

Figure 4.34 Distribution over the Height of Residual Story Drift Angles Normalized by the Maximum Story Drift Angles, $[S_a(T_1)/g]/\gamma = 4.0$

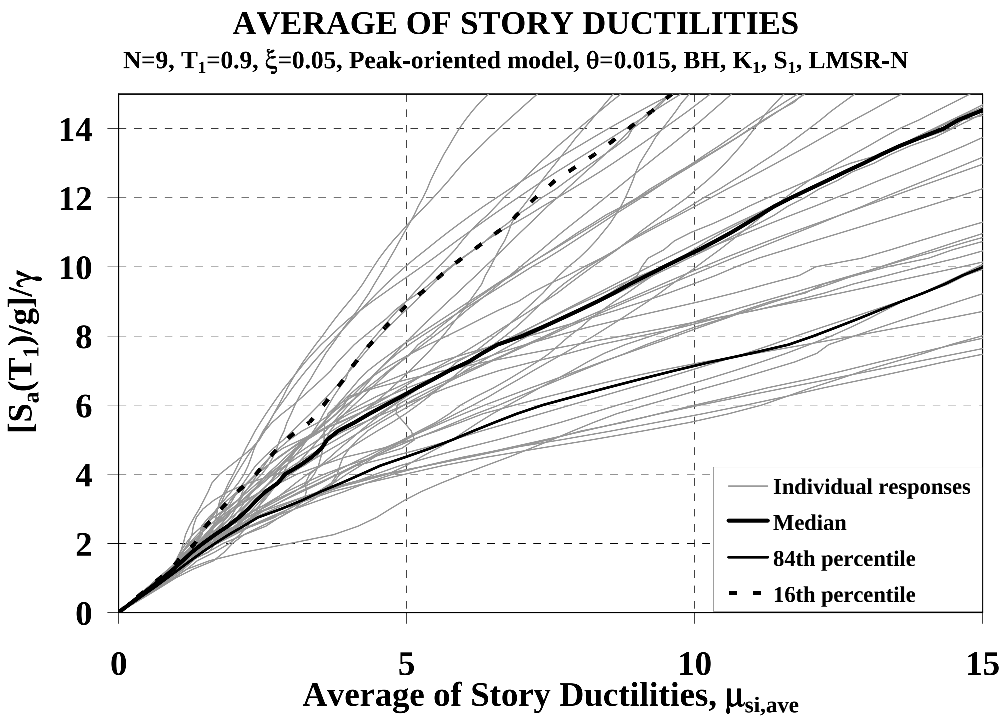

(a) Average of the Story Ductility Demands

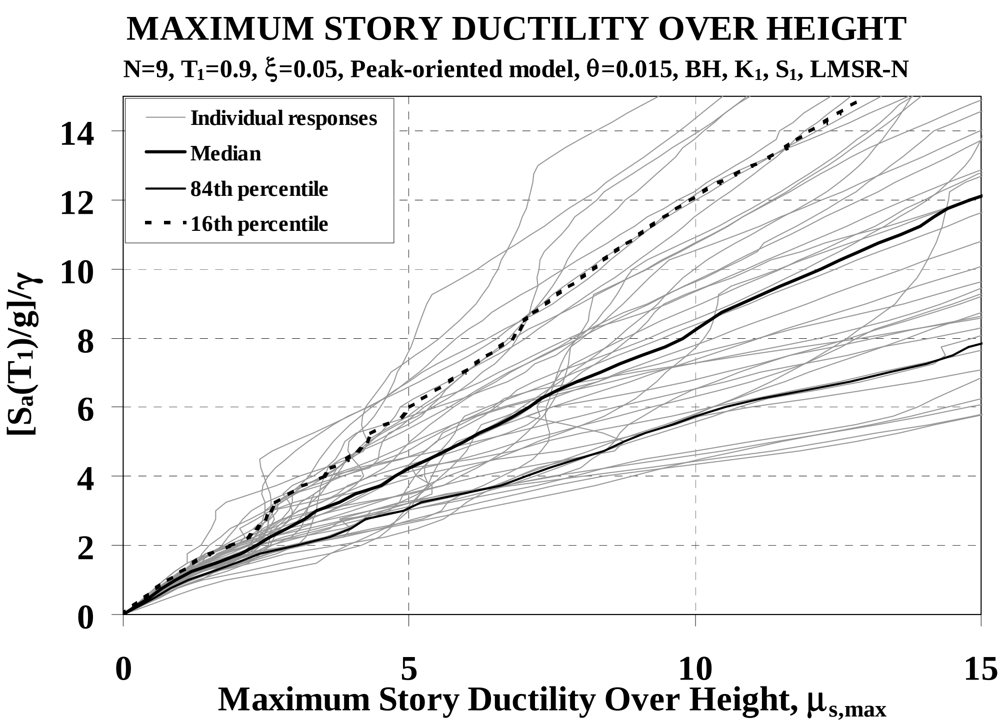

(b) Maximum Story Ductility Demands Over the Height

Figure 4.35 Variation of Story Ductility Demands with Relative Intensity, N = 9, T_1 = 0.9 sec

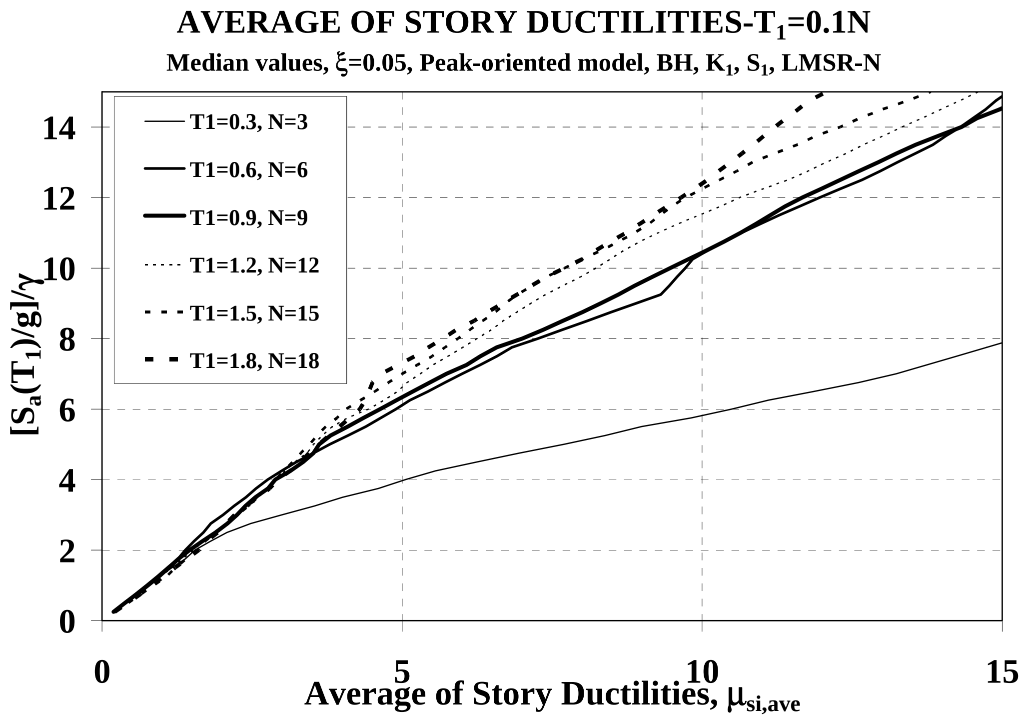

(a) $T_1 = 0.1N$

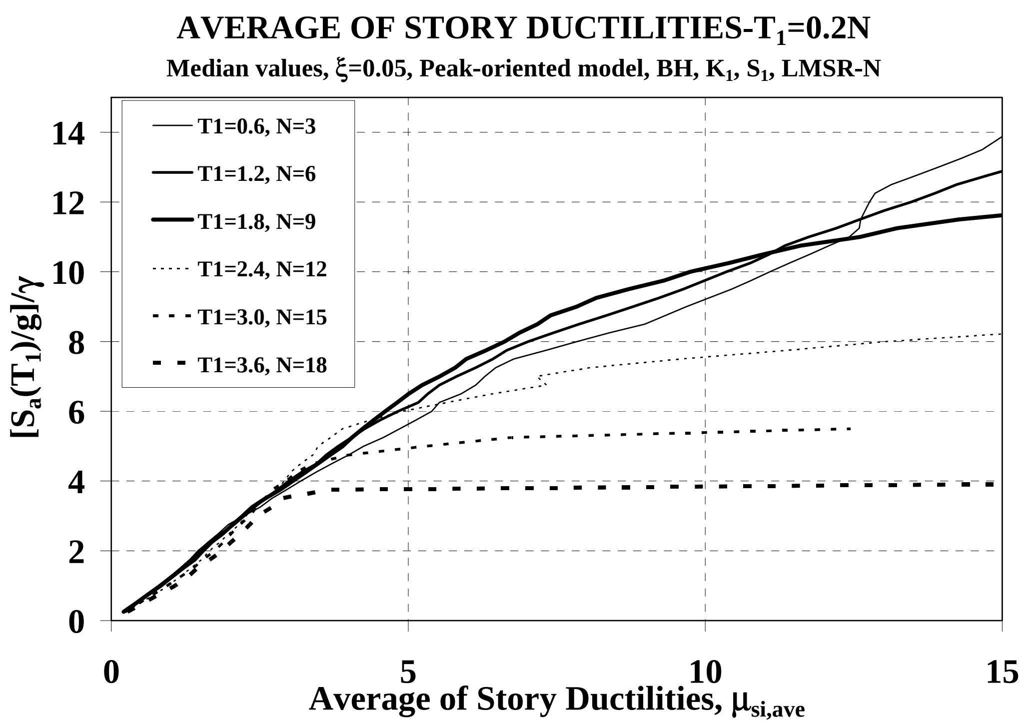

(b) $T_1 = 0.2N$

Figure 4.36 Median Average of the Story Ductilities, Stiff and Flexible Frames

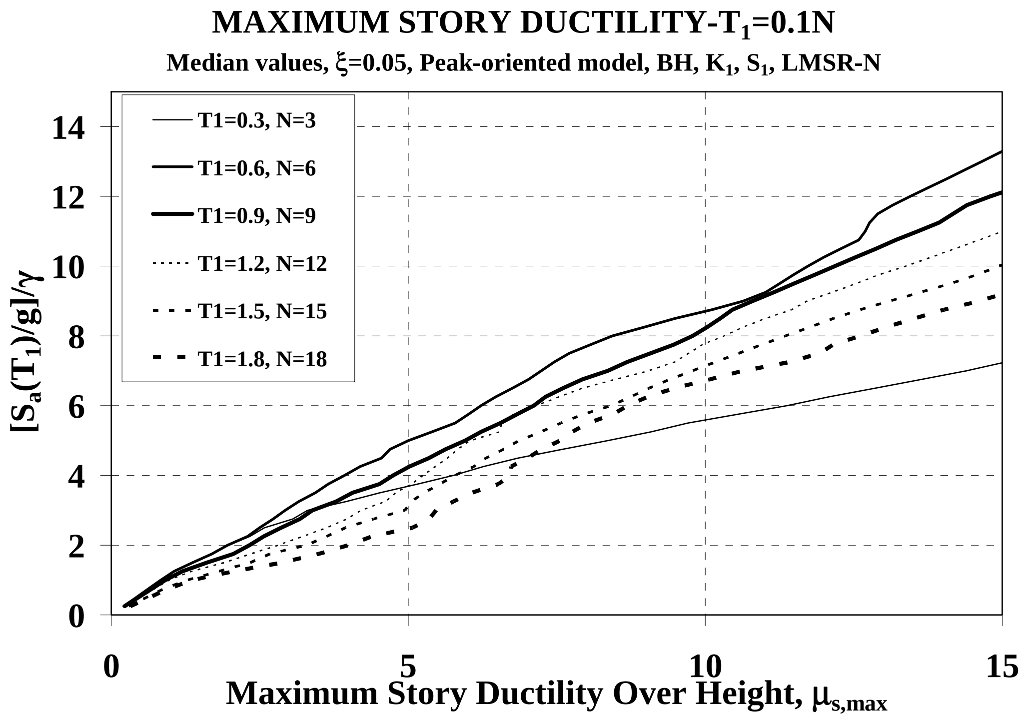

(a) T_1 = 0.1N

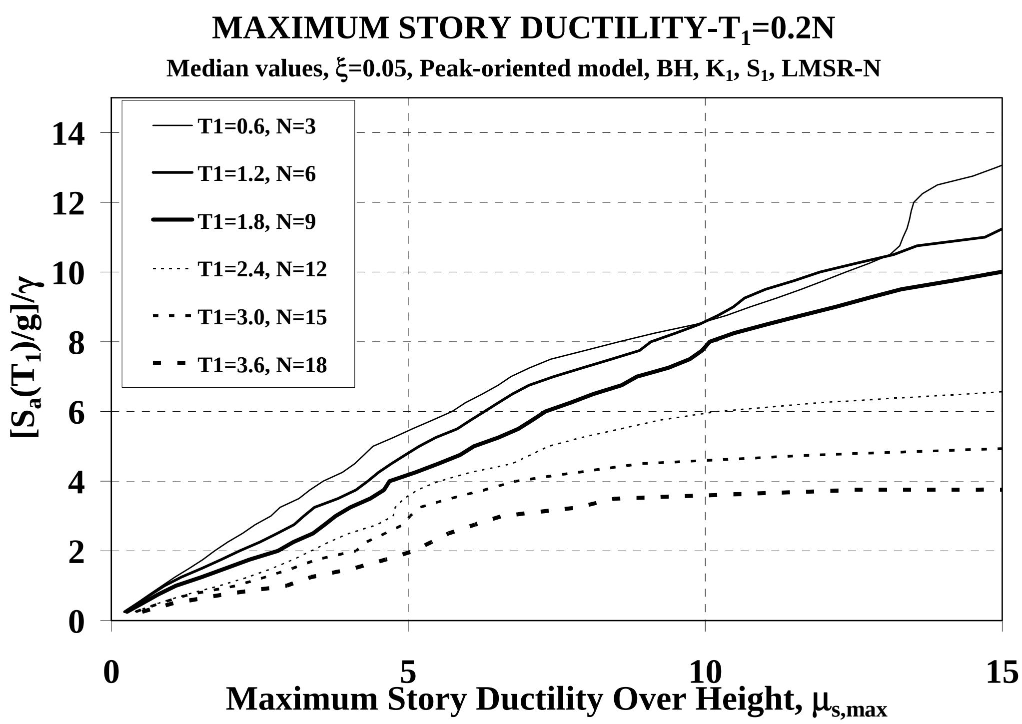

(b) T_1 = 0.2N

Figure 4.37 Median Maximum Story Ductility over Height, Stiff and Flexible Frames

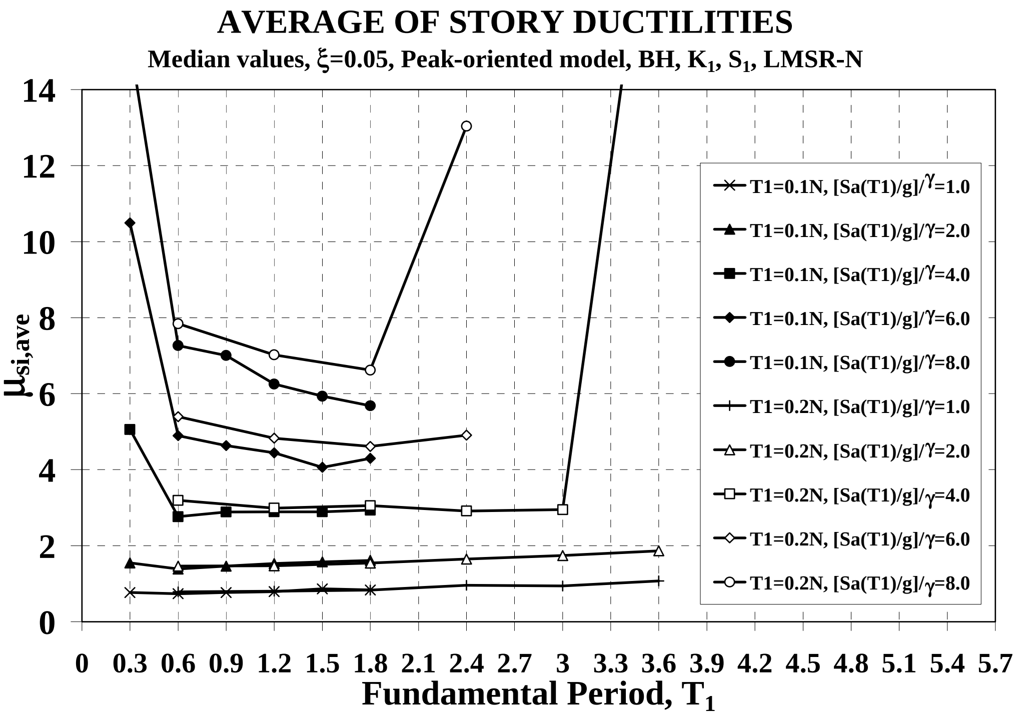

(a) Median Average of the Story Ductilities

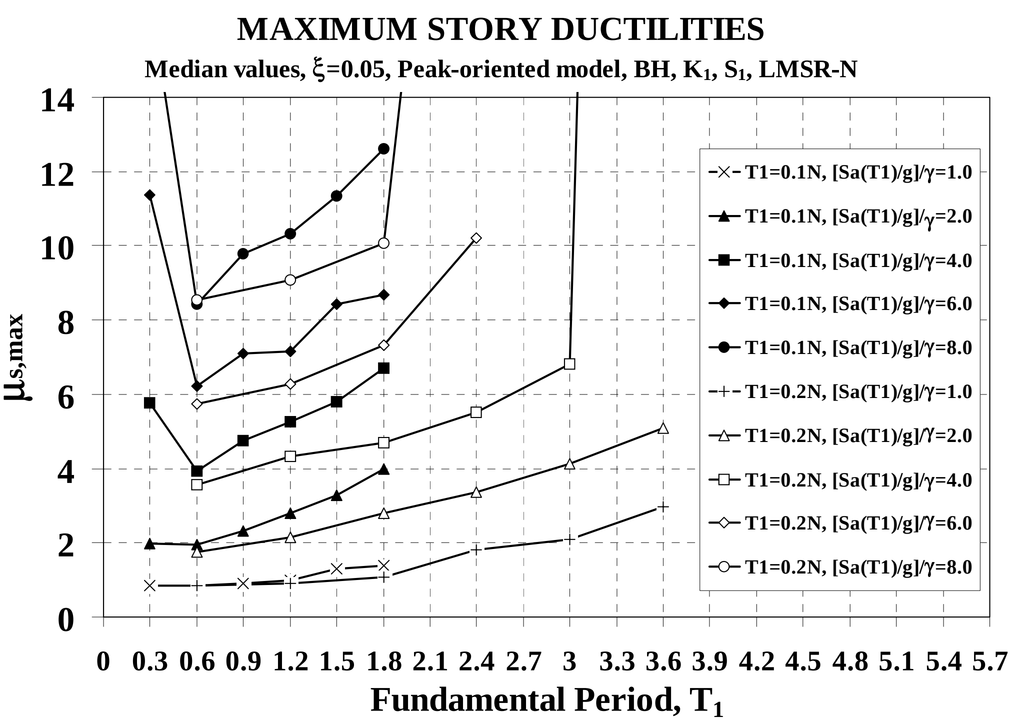

(b) Median Maximum Story Ductilities over the Height

Figure 4.38 Median Story Ductility Demands, All Frames, Various Relative Intensities

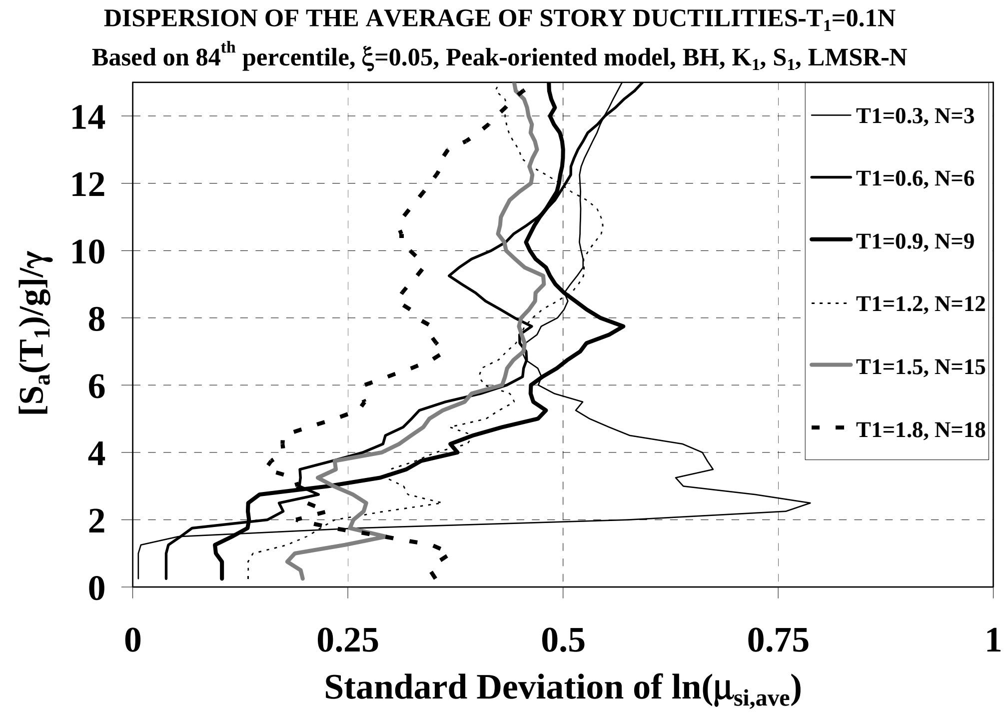

(a) T_1 = 0.1N

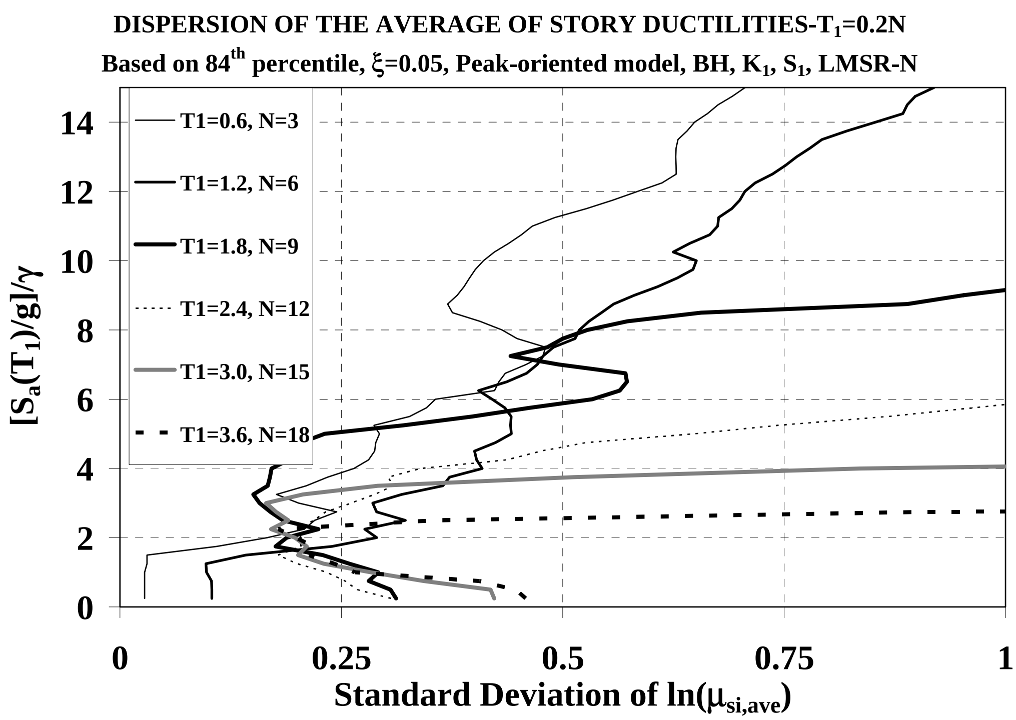

(b) T_1 = 0.2N

Figure 4.39 Dispersion of the Average of the Story Ductilities, Stiff and Flexible Frames

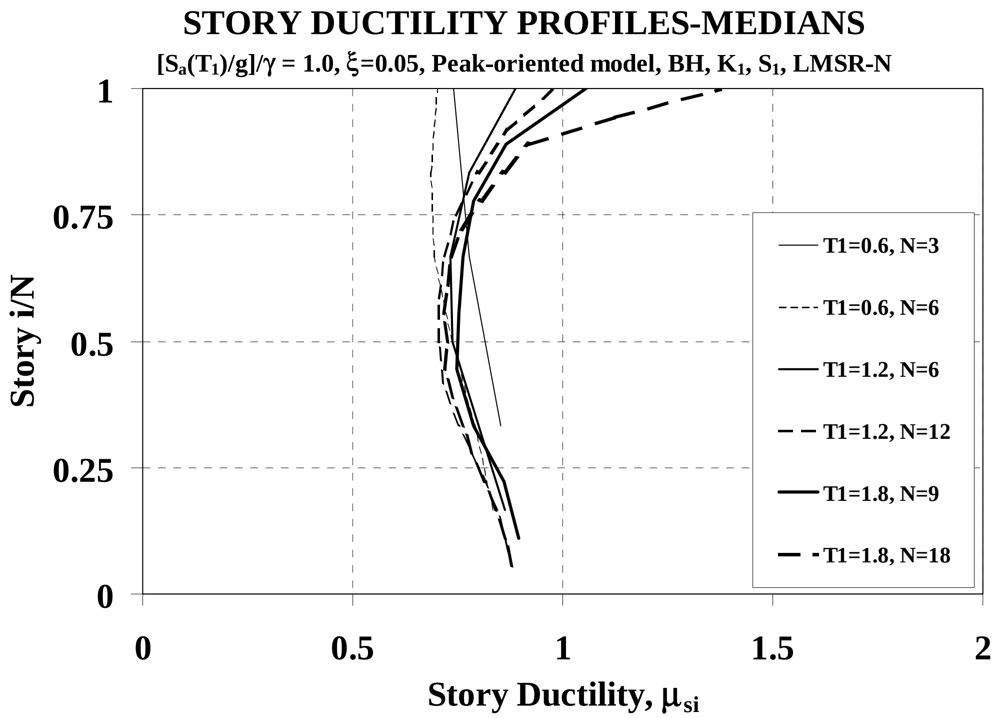

Figure 4.40 Distribution of Story Ductilities over the Height, $[S_a(T_1)/g]/\gamma = 1.0$

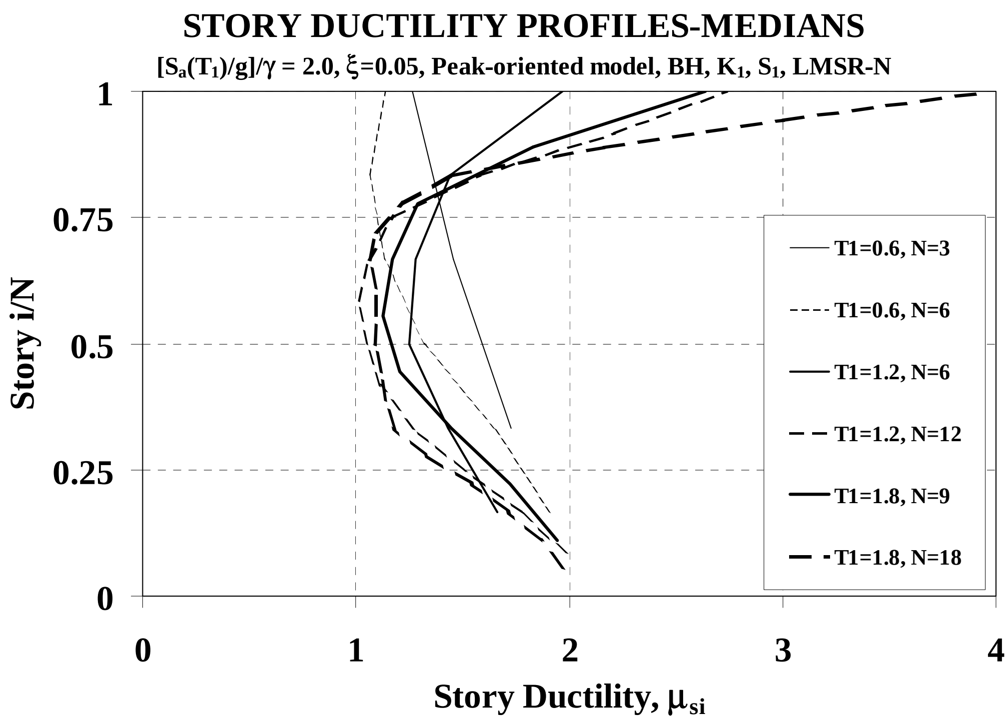

Figure 4.41 Distribution of Story Ductilities over the Height, $[S_a(T_1)/g]/\gamma = 2.0$

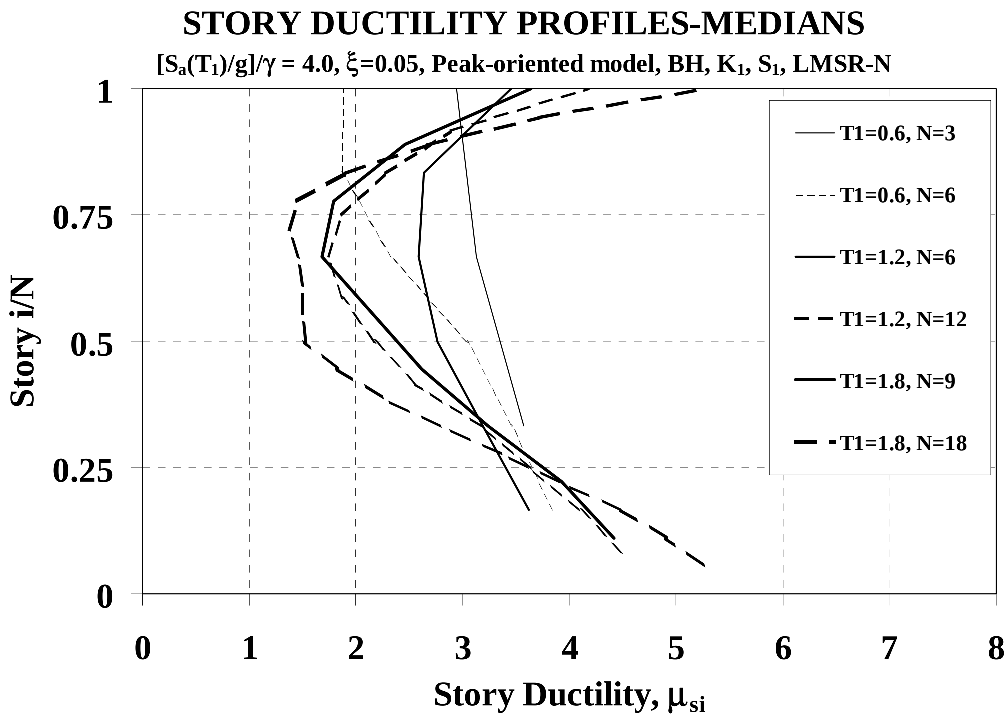

Figure 4.42 Distribution of Story Ductilities over the Height, $[S_a(T_1)/g]/\gamma = 4.0$

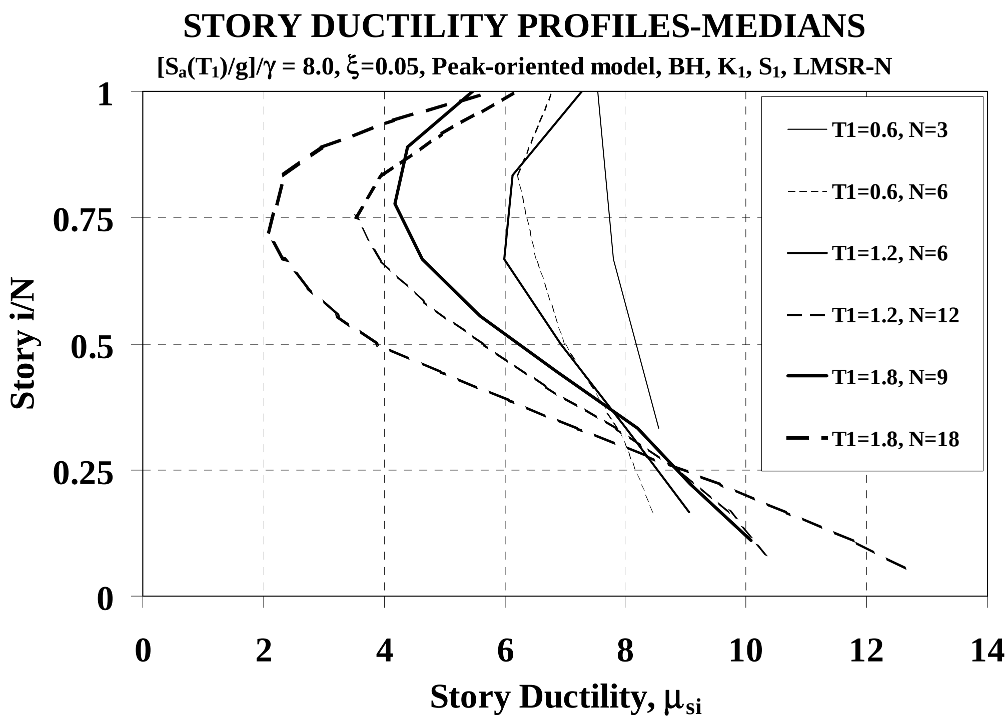

Figure 4.43 Distribution of Story Ductilities over the Height, $[S_a(T_1)/g]/\gamma = 8.0$

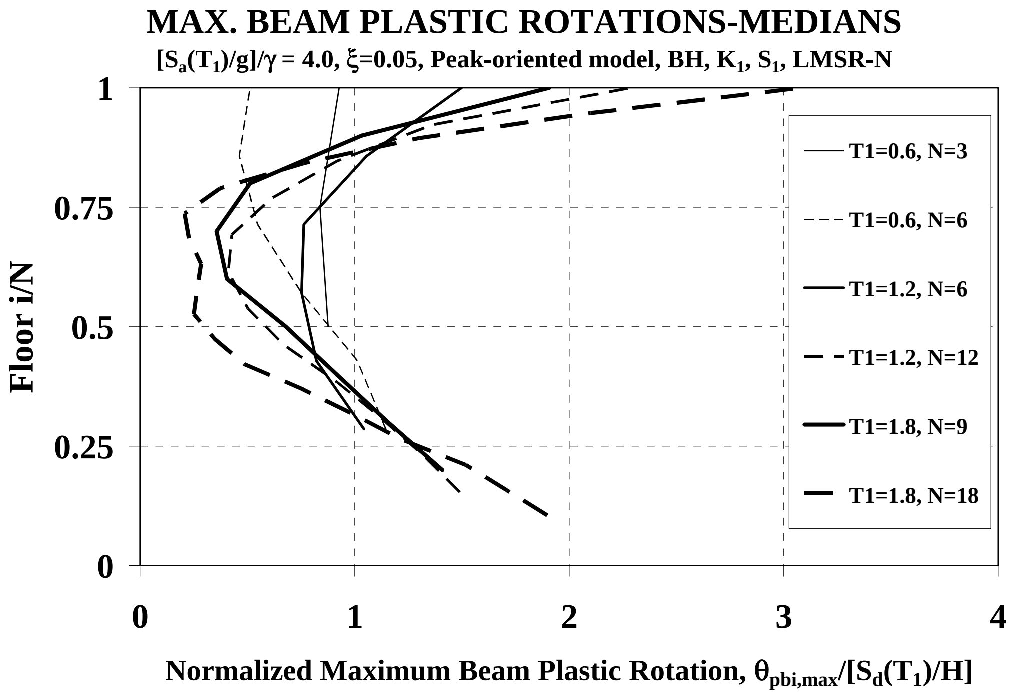

(a) Median Values

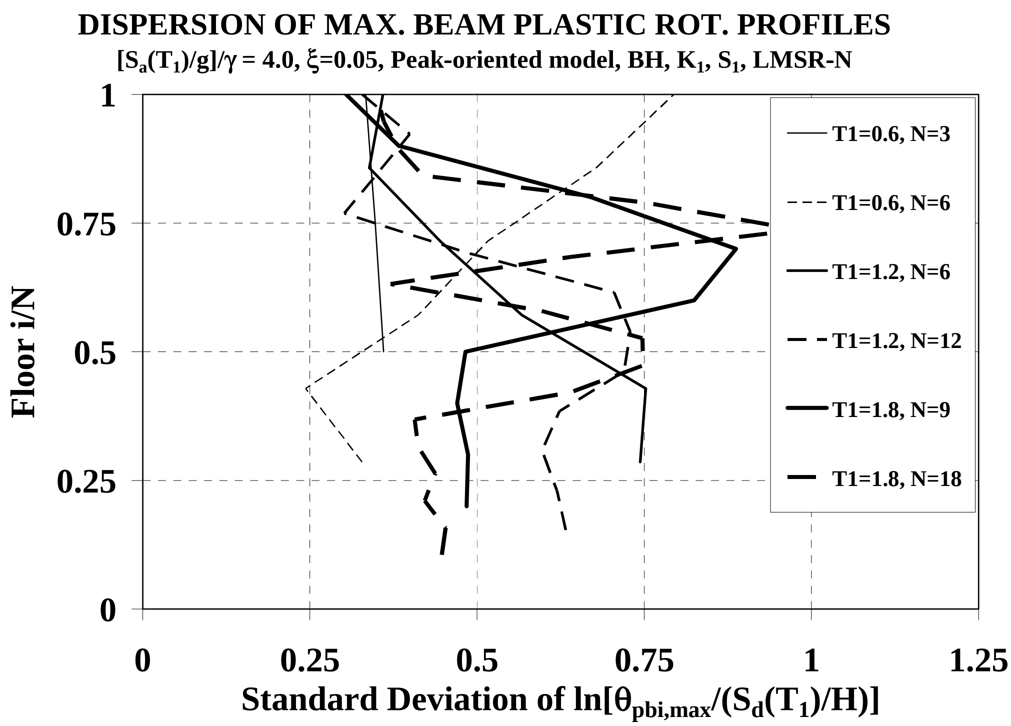

(b) Dispersion

Figure 4.44 Distribution of Normalized Maximum Beam Plastic Rotations over the Height, $[S_a(T_1)/g]/\gamma = 4.0$

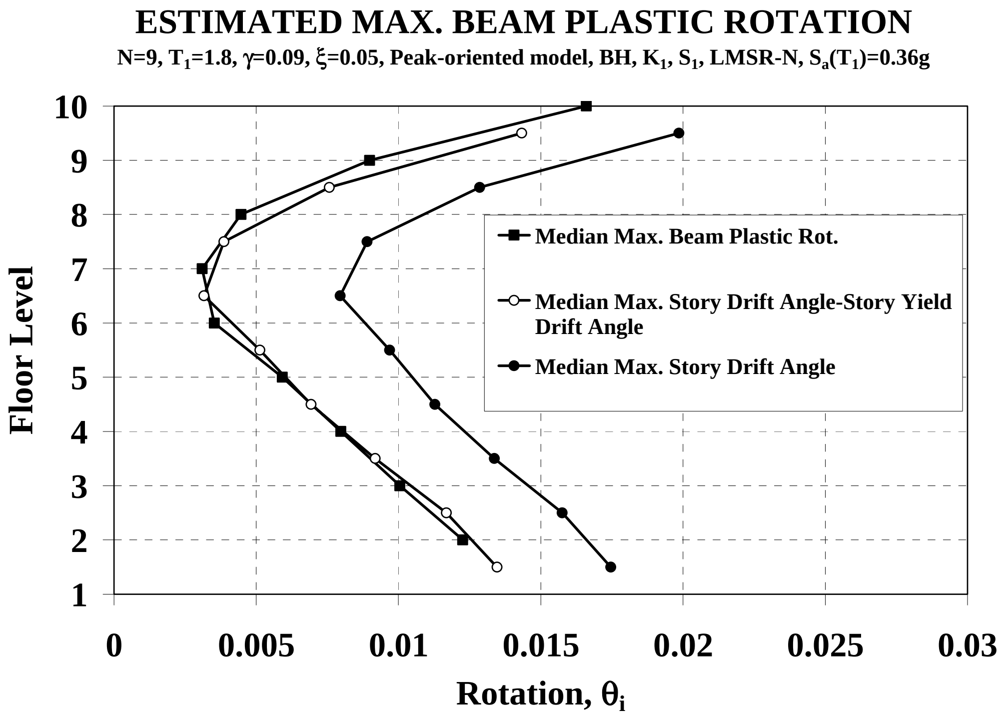

Figure 4.45 Estimation of Maximum Beam Plastic Rotations, N = 9, T_1 = 1.8 sec

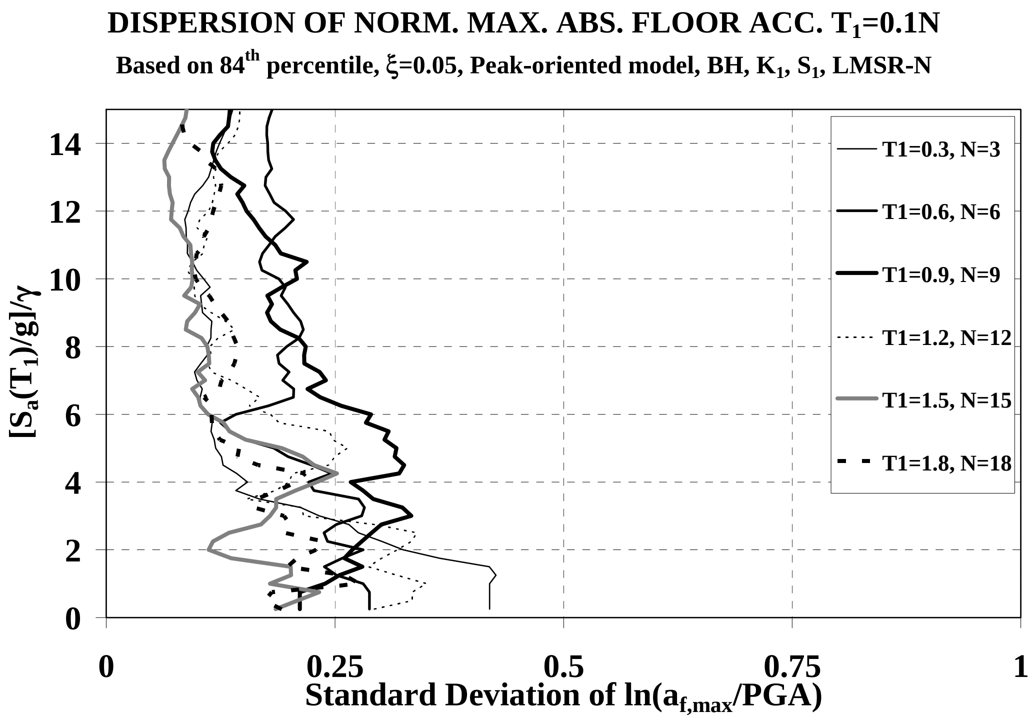

(a) Maximum Absolute Floor Acceleration Normalized with Respect to PGA

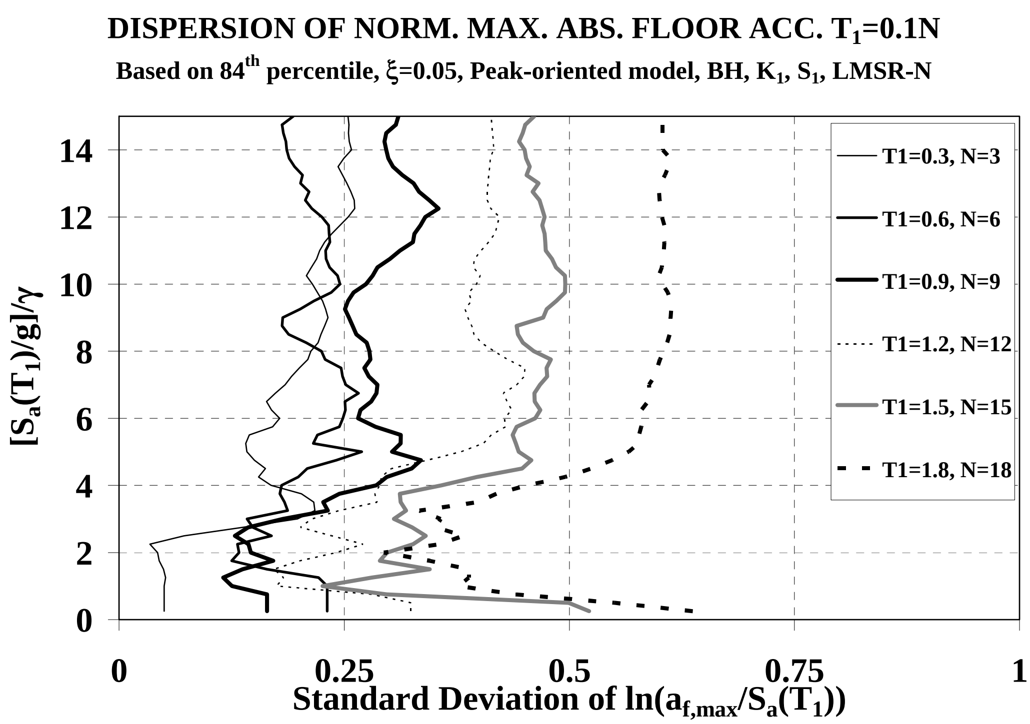

(b) Maximum Absolute Floor Acceleration Normalized With Respect to $S_a(T_1)$

Figure 4.46 Dispersion of Normalized Maximum Absolute Floor Acceleration Demands, T_1 = 0.1N Frames

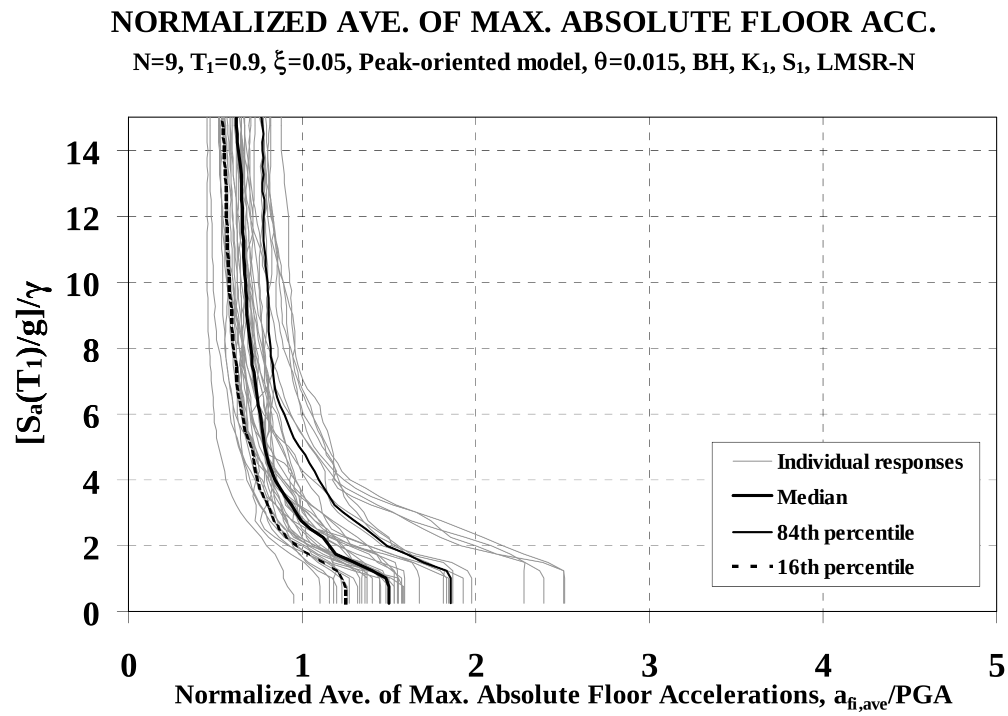

(a) Normalized Average of the Maximum Absolute Floor Accelerations

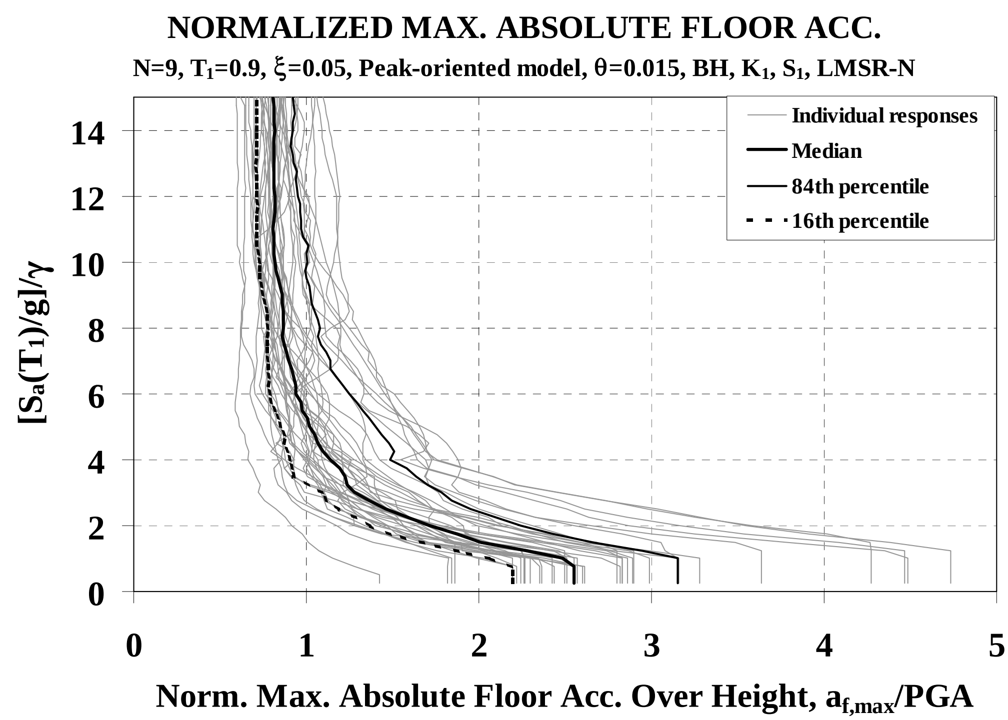

(b) Normalized Maximum Absolute Floor Acceleration over Height

Figure 4.47 Variation of Maximum Absolute Floor Acceleration Demands with Relative Intensity, N = 9, T_1 = 0.9 sec

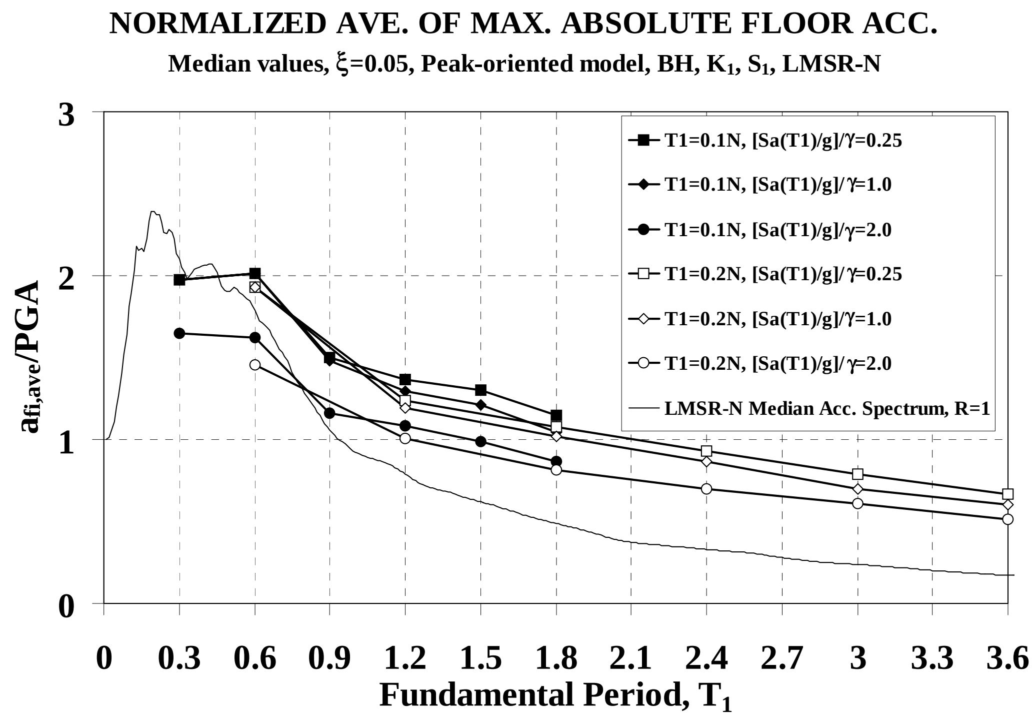

(a) $[S_a(T_1)/g]/\gamma$ = 0.25, 1.0, 2.0

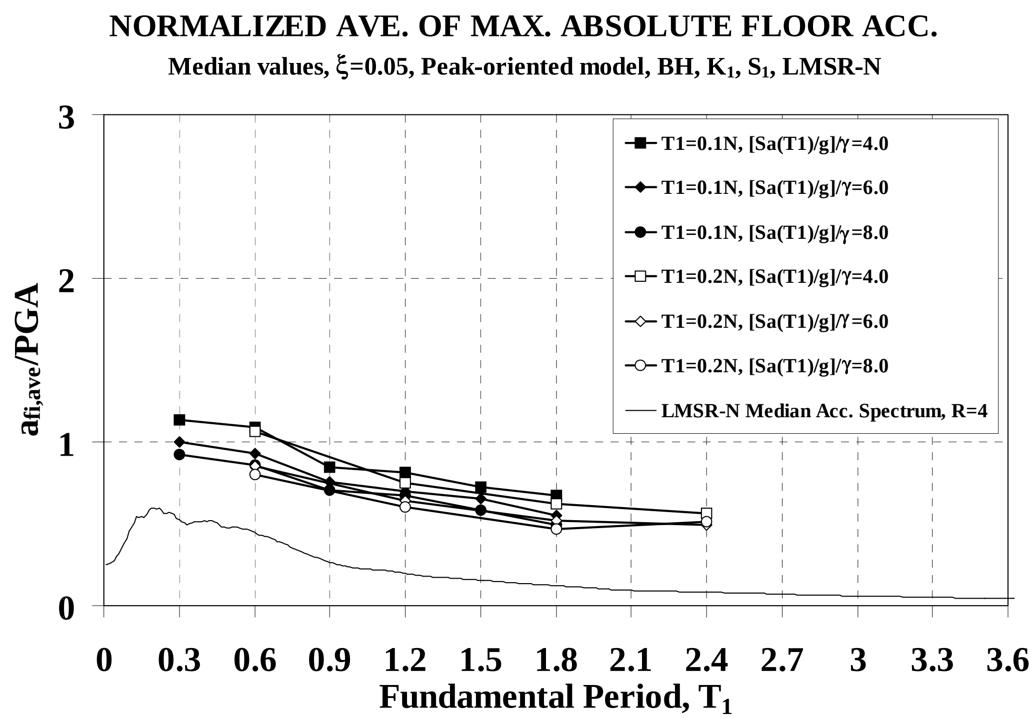

(b) $[S_a(T_1)/g]/\gamma$ = 4.0, 6.0, 8.0

Figure 4.48 Dependence of the Median Normalized Average of the Maximum Absolute Floor Accelerations on T_1, All Frames, Various Relative Intensities

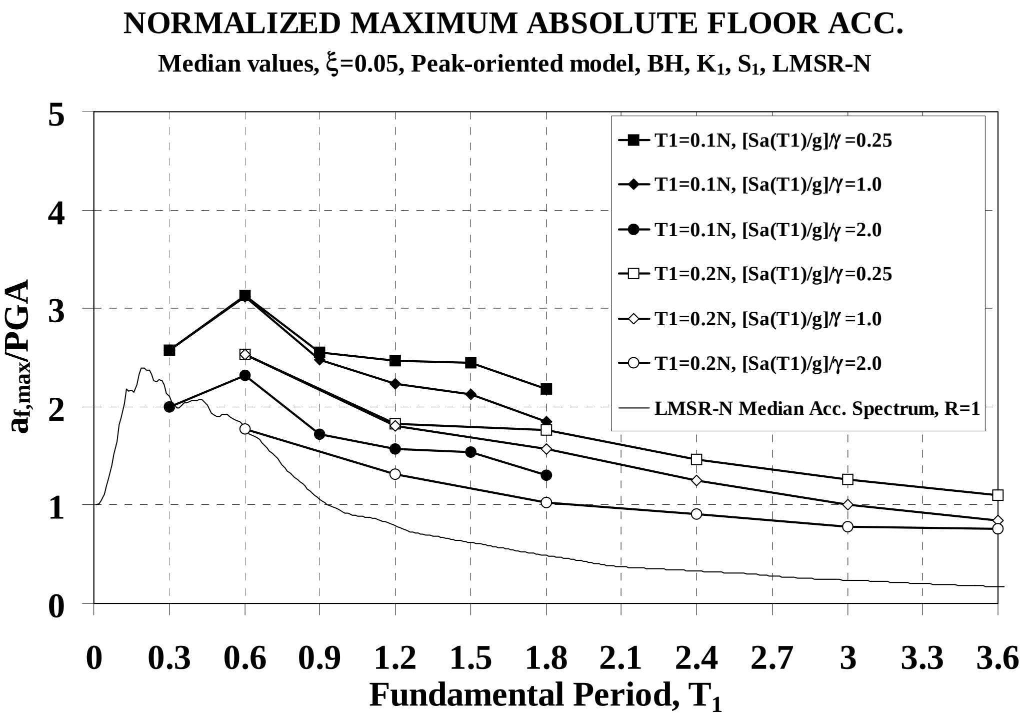

(a) $[S_a(T_1)/g]/\gamma$ = 0.25, 1.0, 2.0

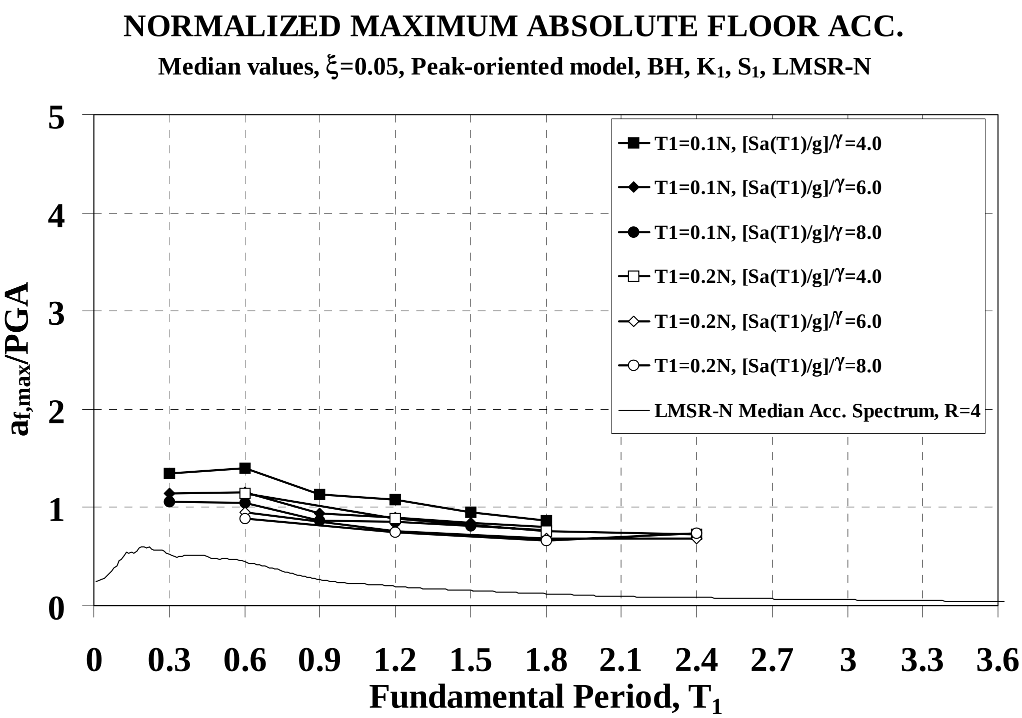

(b) $[S_a(T_1)/g]/\gamma$ = 4.0, 6.0, 8.0

Figure 4.49 Dependence of the Median Normalized Maximum Absolute Floor Acceleration over the Height on T_1, All Frames, Various Relative Intensities

DISPERSION OF NORM. AVE. OF MAX. ABS. FLOOR ACC. T_1=0.1N
Based on 84th percentile, ξ=0.05, Peak-oriented model, BH, K_1, S_1, LMSR-N

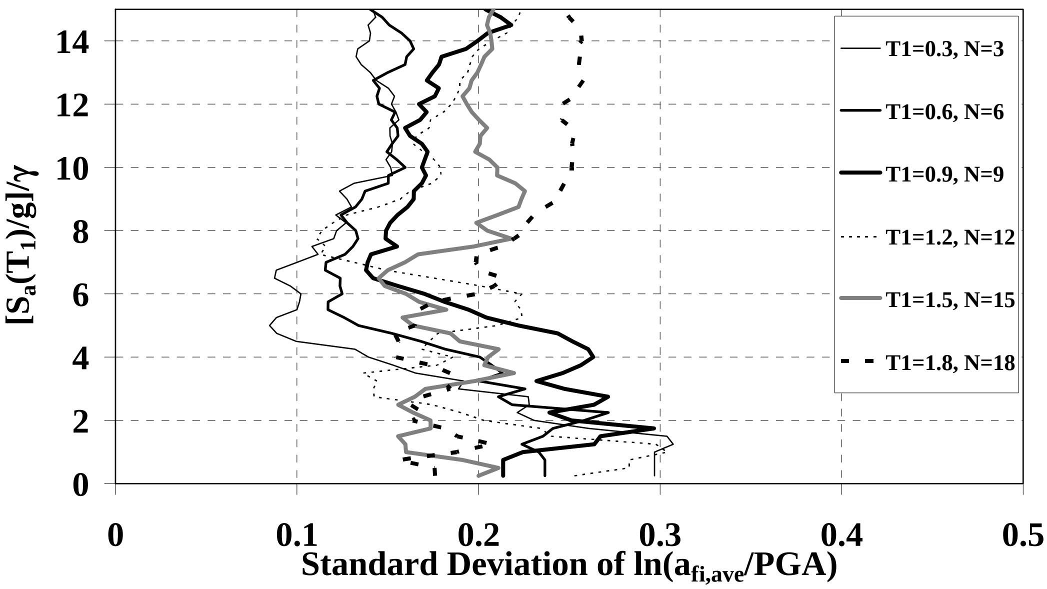

(a) T_1 = 0.1N

DISPERSION OF NORM. AVE. OF MAX. ABS. FLOOR ACC. T_1=0.2N
Based on 84th percentile, ξ=0.05, Peak-oriented model, BH, K_1, S_1, LMSR-N

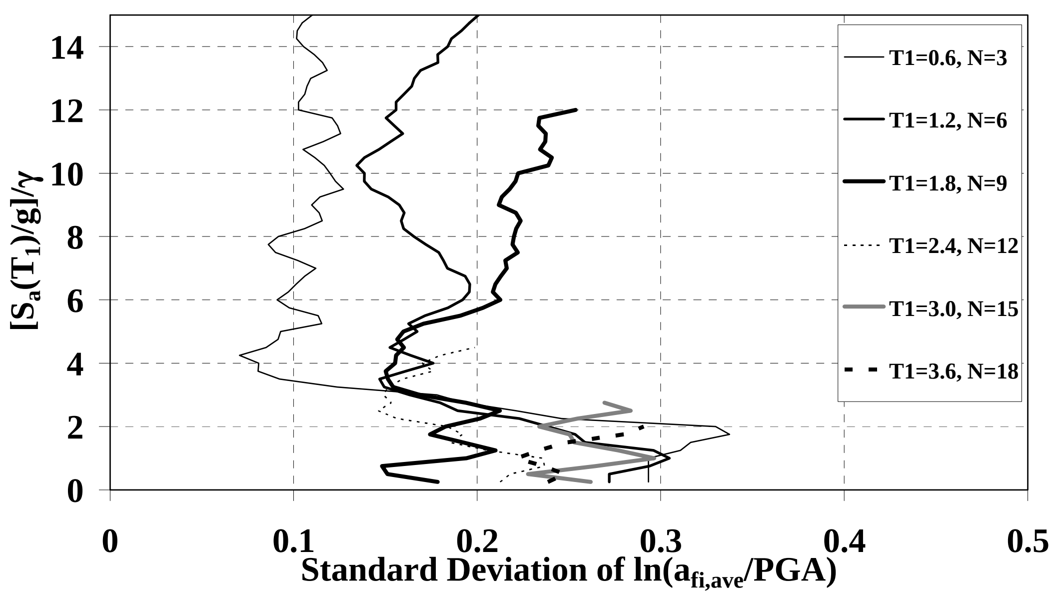

(b) T_1 = 0.2N

Figure 4.50 Dispersion of the Normalized Average of the Maximum Absolute Floor Accelerations, Stiff and Flexible Frames

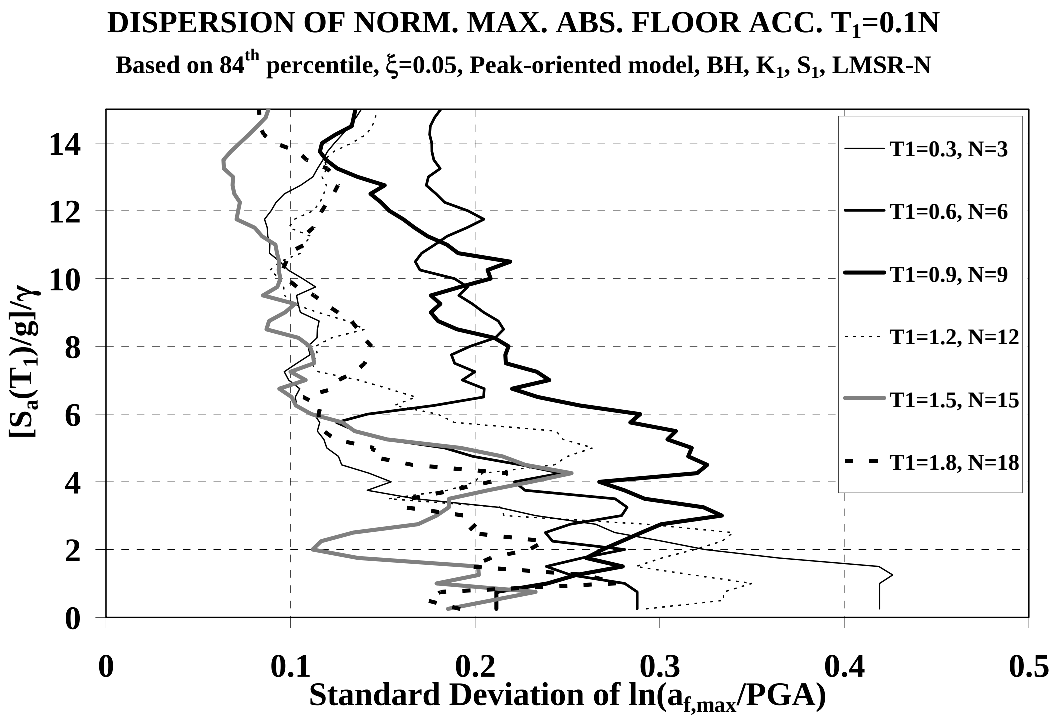

(a) T_1 = 0.1N

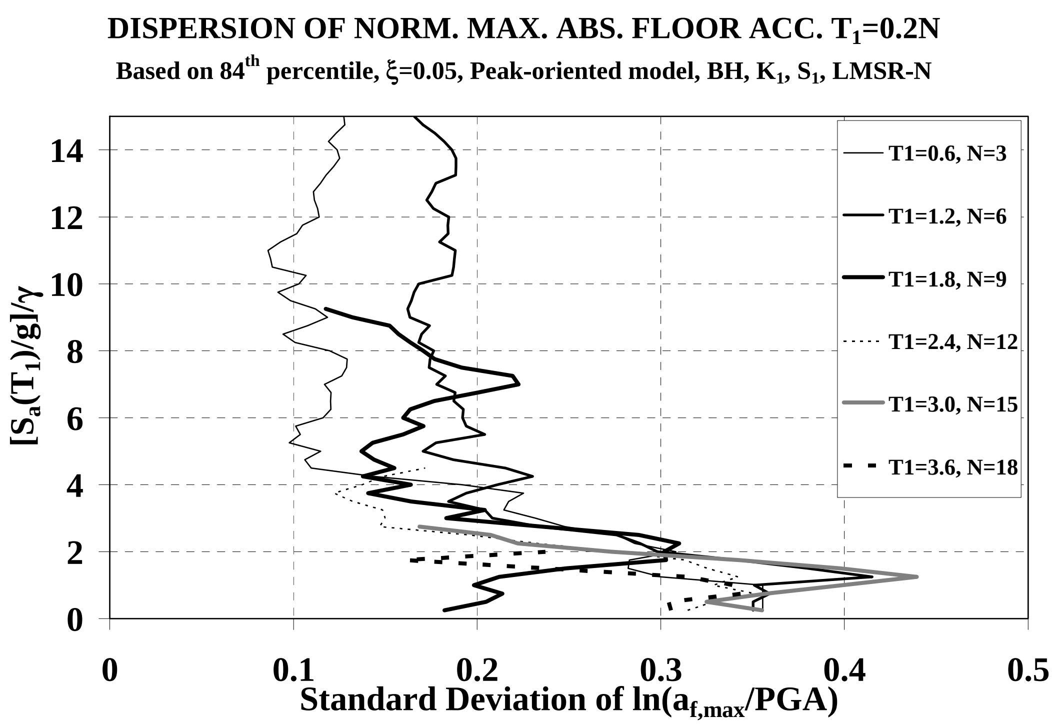

(b) T_1 = 0.2N

Figure 4.51 Dispersion of the Normalized Maximum Absolute Floor Acceleration over the Height, Stiff and Flexible Frames

MAX. ABSOLUTE FLOOR ACC. PROFILES-MEDIANS

[Sa(T1)/g]/γ = 0.25, ξ=0.05, Peak-oriented model, BH, K1, S1, LMSR-N

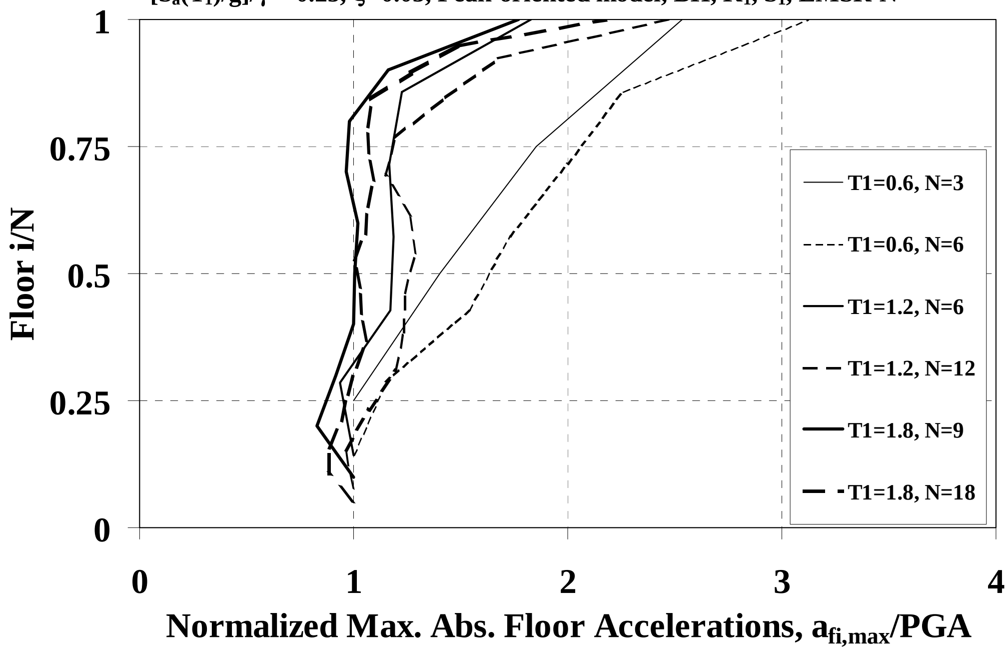

Figure 4.52 Distribution of Normalized Maximum Absolute Floor Accelerations over the Height, $[S_a(T_1)/g]/\gamma = 0.25$

MAX. ABSOLUTE FLOOR ACC. PROFILES-MEDIANS

[Sa(T1)/g]/γ = 2.0, ξ=0.05, Peak-oriented model, BH, K1, S1, LMSR-N

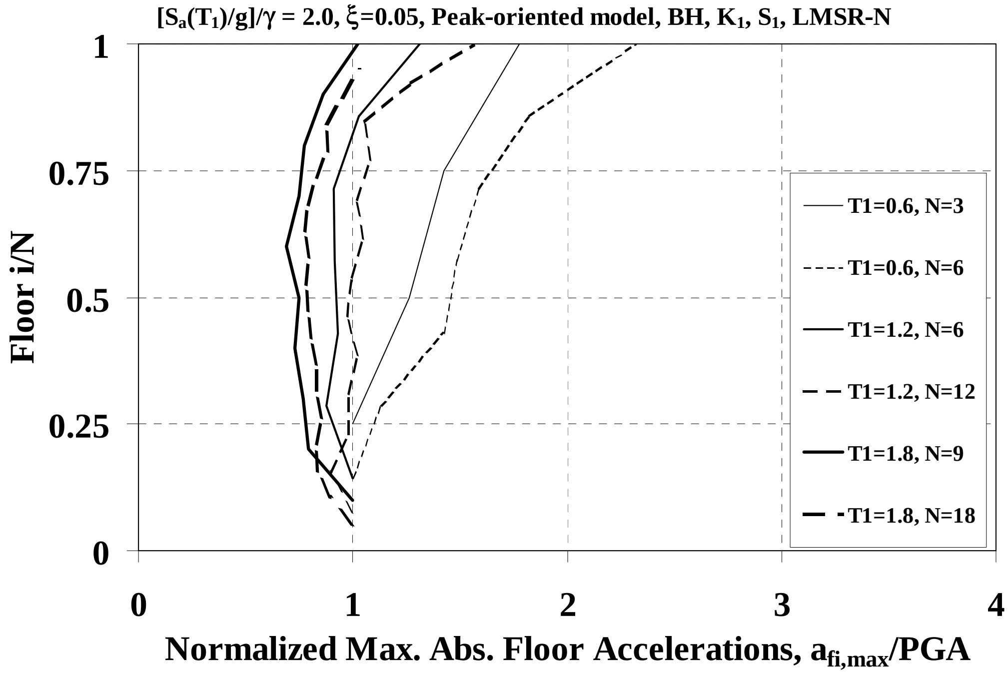

Figure 4.53 Distribution of Normalized Maximum Absolute Floor Accelerations over the Height, $[S_a(T_1)/g]/\gamma = 2.0$

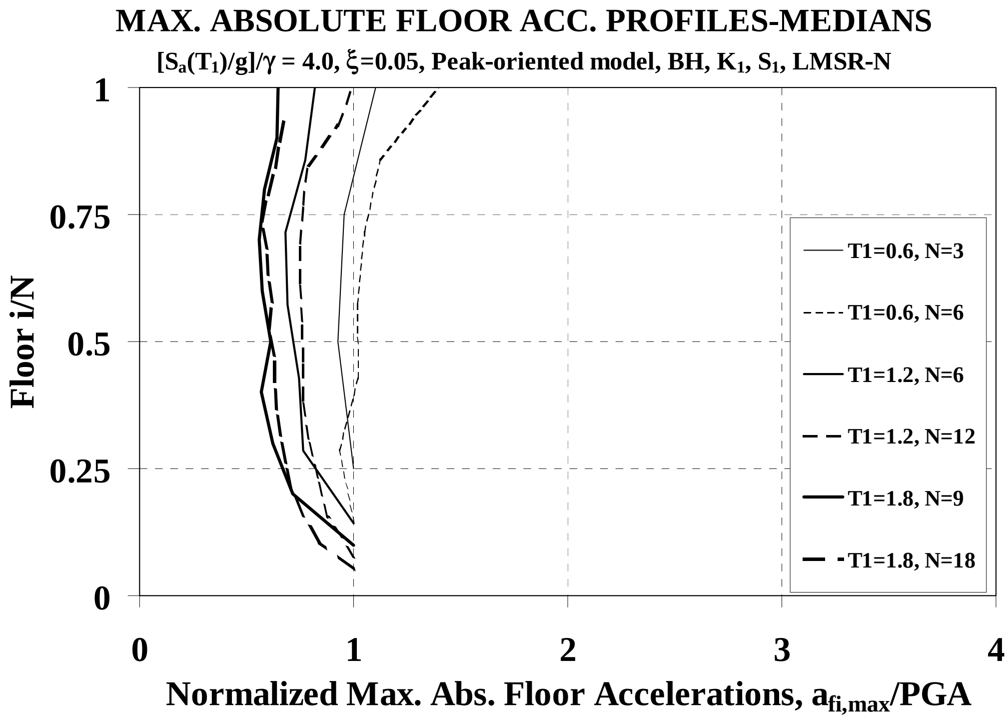

Figure 4.54 Distribution of Normalized Maximum Absolute Floor Accelerations over the Height, $[S_a(T_1)/g]/\gamma = 4.0$

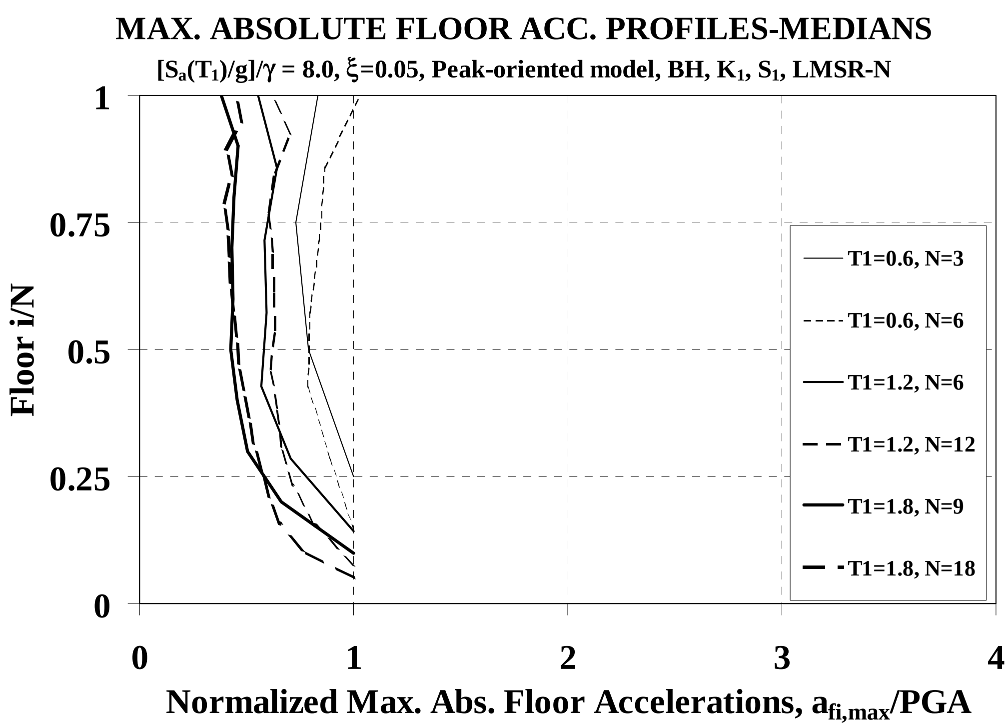

Figure 4.55 Distribution of Normalized Maximum Absolute Floor Accelerations over the Height, $[S_a(T_1)/g]/\gamma = 8.0$

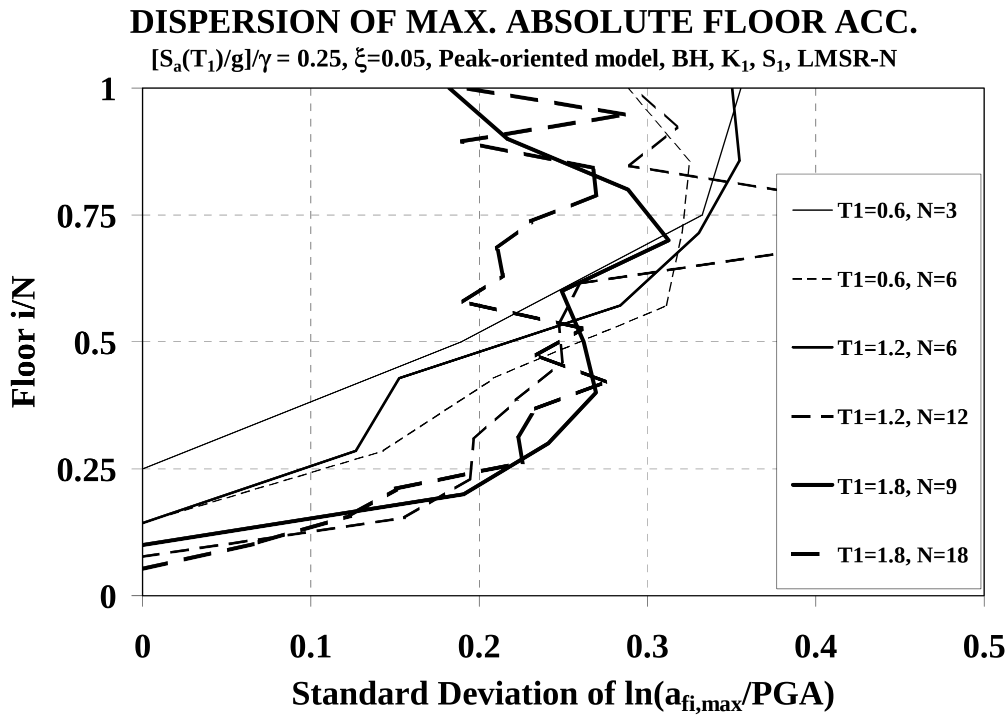

(a) $[S_a(T_1)/g]/\gamma = 0.25$

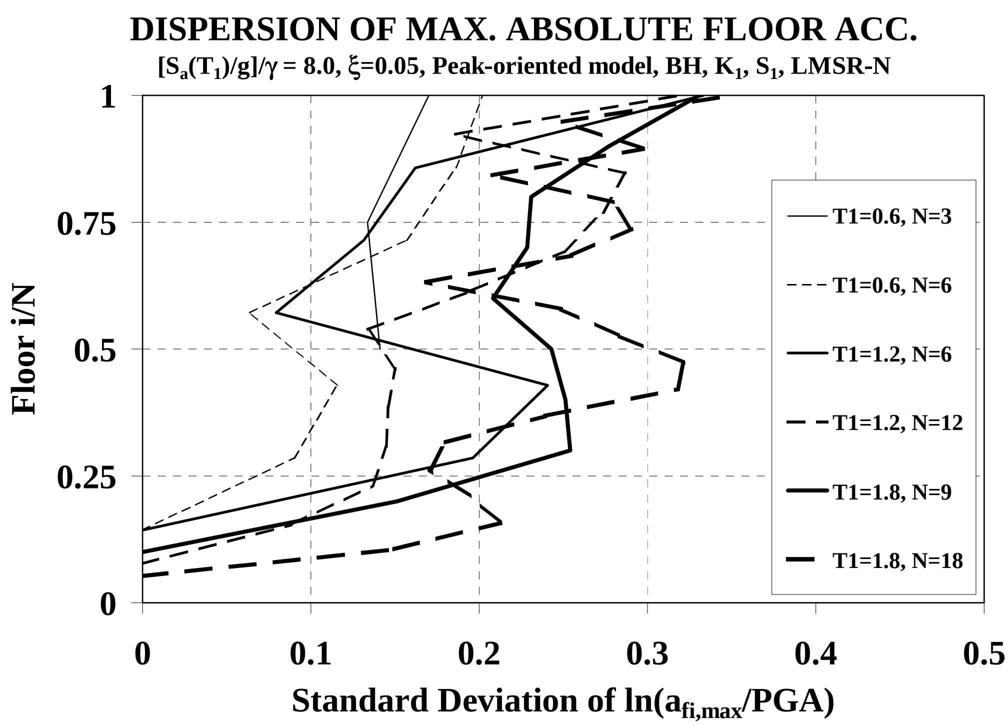

(b) $[S_a(T_1)/g]/\gamma = 8.0$

Figure 4.56 Dispersion of Maximum Absolute Floor Accelerations over the Height

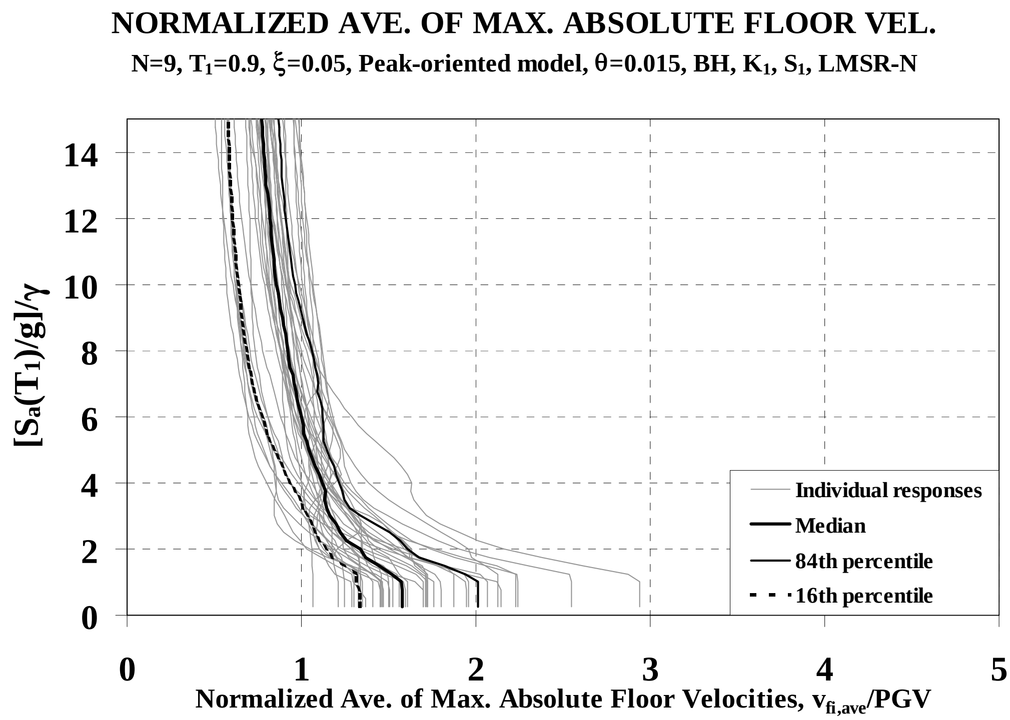

(a) Normalized Average of the Maximum Absolute Floor Velocities

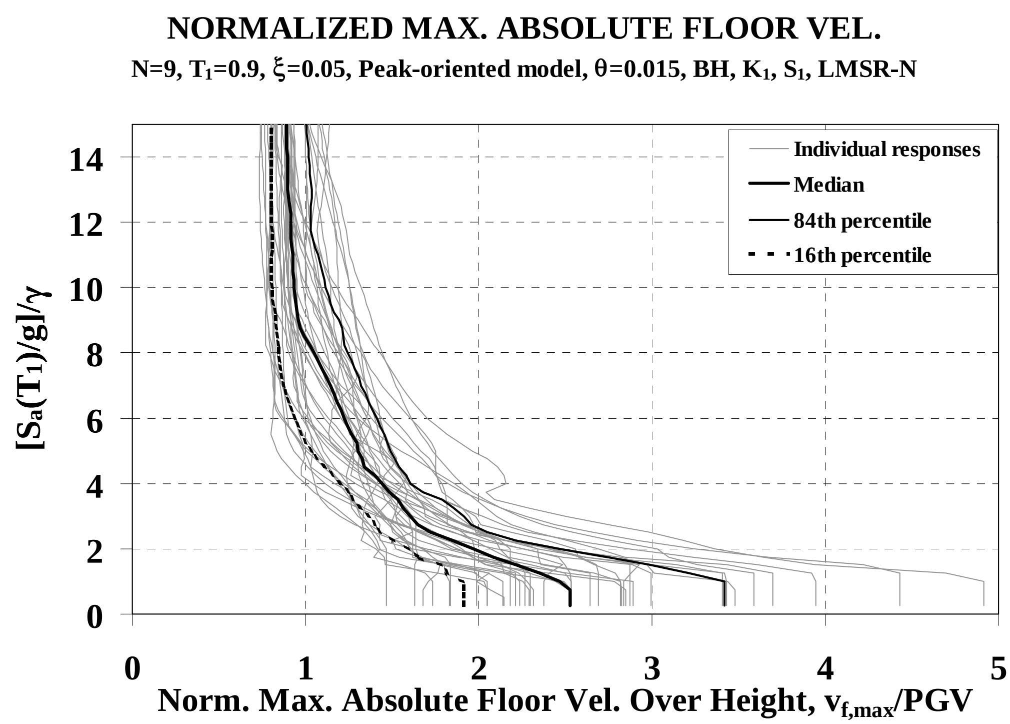

(b) Normalized Maximum Absolute Floor Velocity over the Height

Figure 4.57 Variation of Maximum Absolute Floor Velocity Demands with Relative Intensity, N = 9, T_1 = 0.9 sec

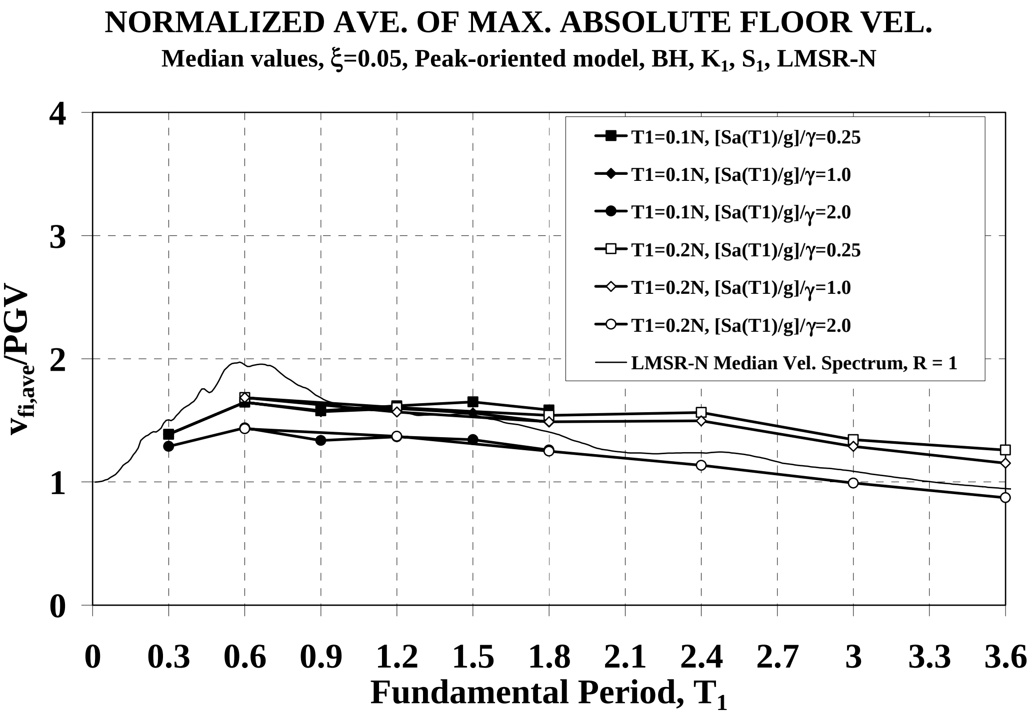

(a) $[S_a(T_1)/g]/\gamma$ = 0.25, 1.0, 2.0

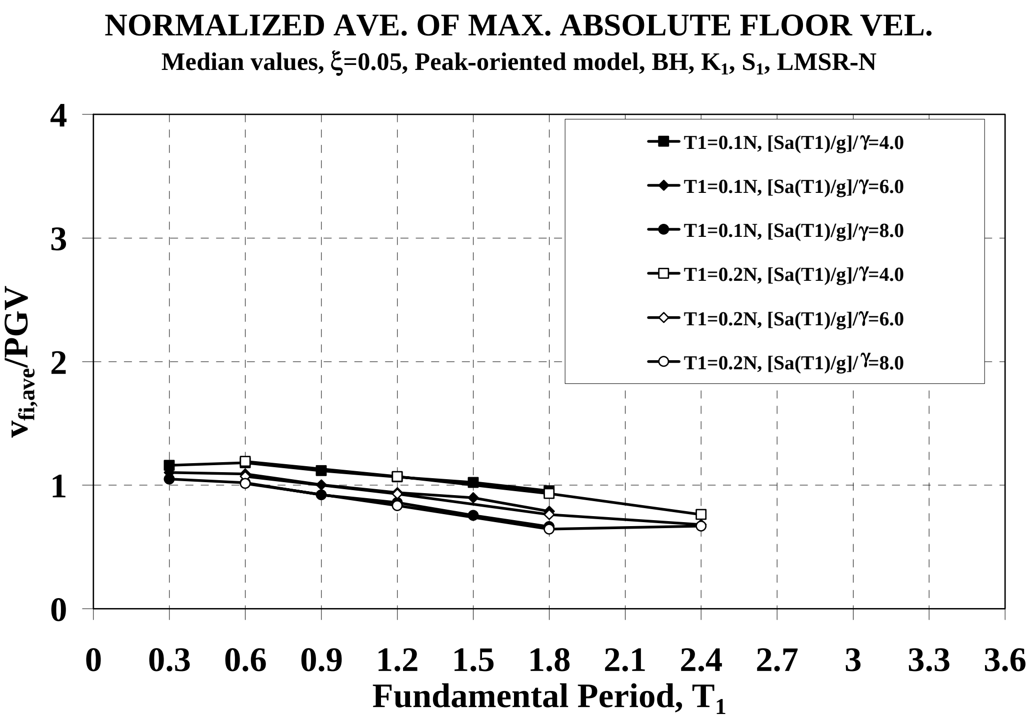

(b) $[S_a(T_1)/g]/\gamma$ = 4.0, 6.0, 8.0

Figure 4.58 Dependence of the Median Normalized Average of the Maximum Absolute Floor Velocities on T_1, All Frames, Various Relative Intensities

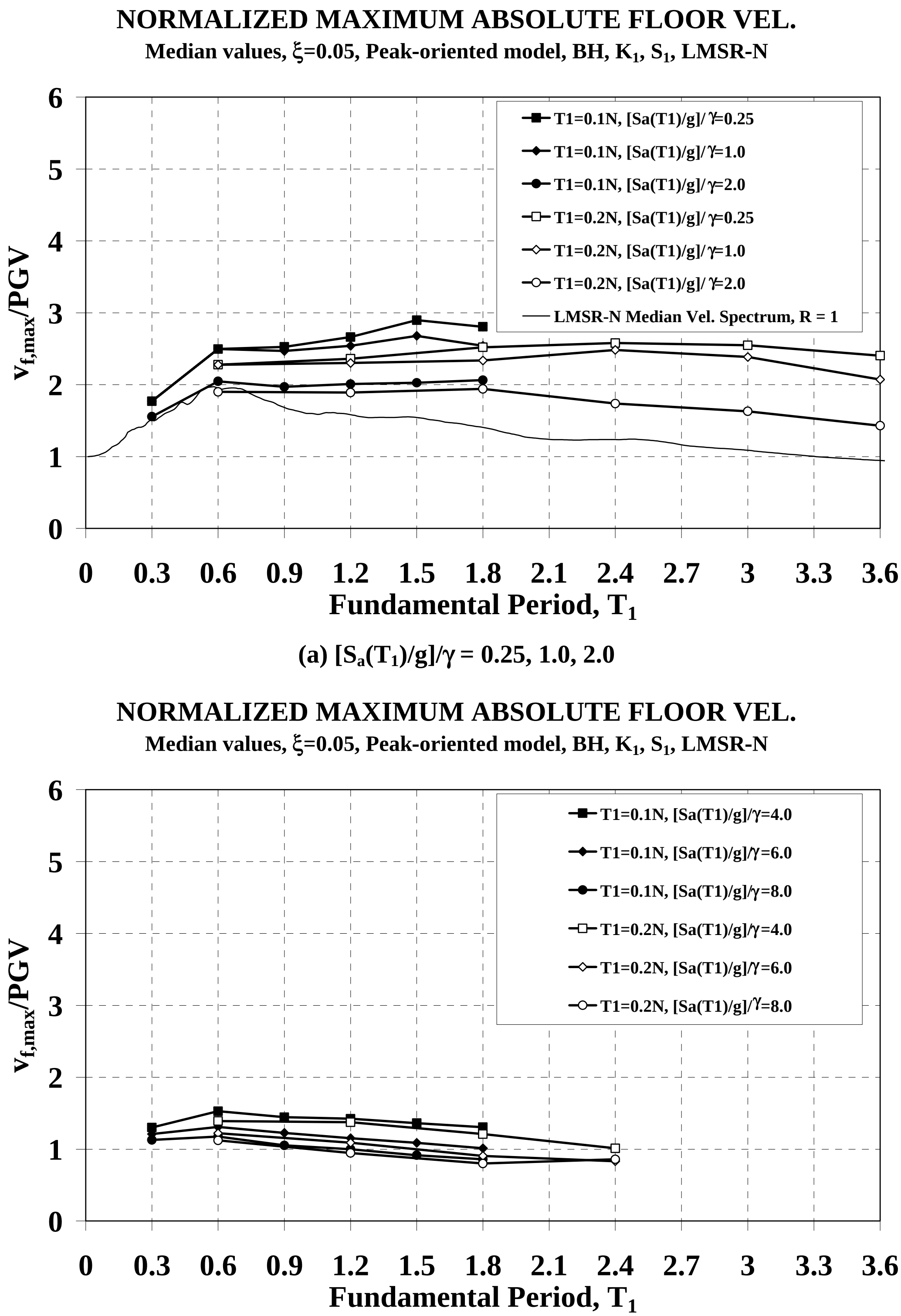

(a) $[S_a(T_1)/g]/\gamma$ = 0.25, 1.0, 2.0

(b) $[S_a(T_1)/g]/\gamma$ = 4.0, 6.0, 8.0

Figure 4.59 Dependence of the Median Normalized Maximum Absolute Floor Velocity over the Height on T_1, All Frames, Various Relative Intensities

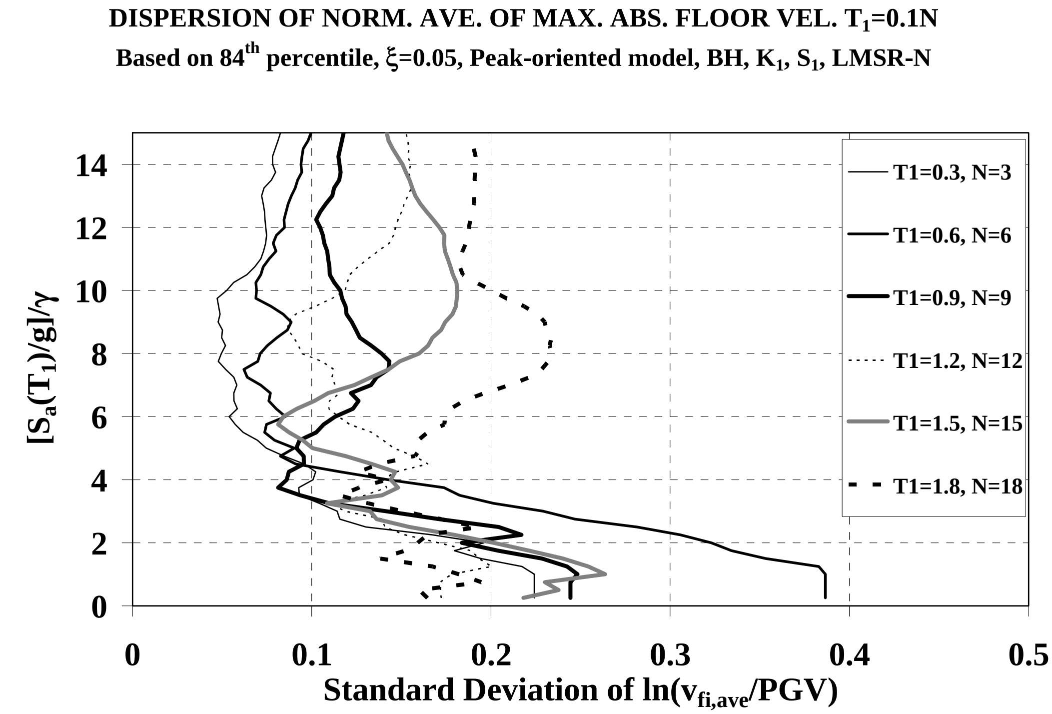

(a) T_1 = 0.1N

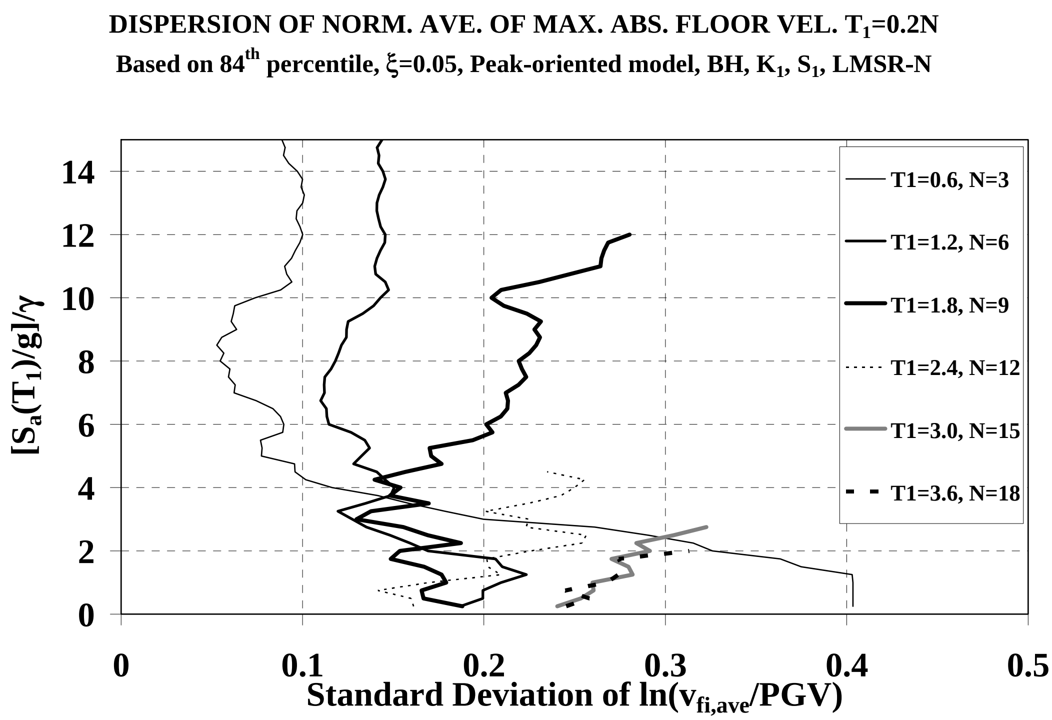

(b) T_1 = 0.2N

Figure 4.60 Dispersion of the Normalized Average of the Maximum Absolute Floor Velocities, Stiff and Flexible Frames

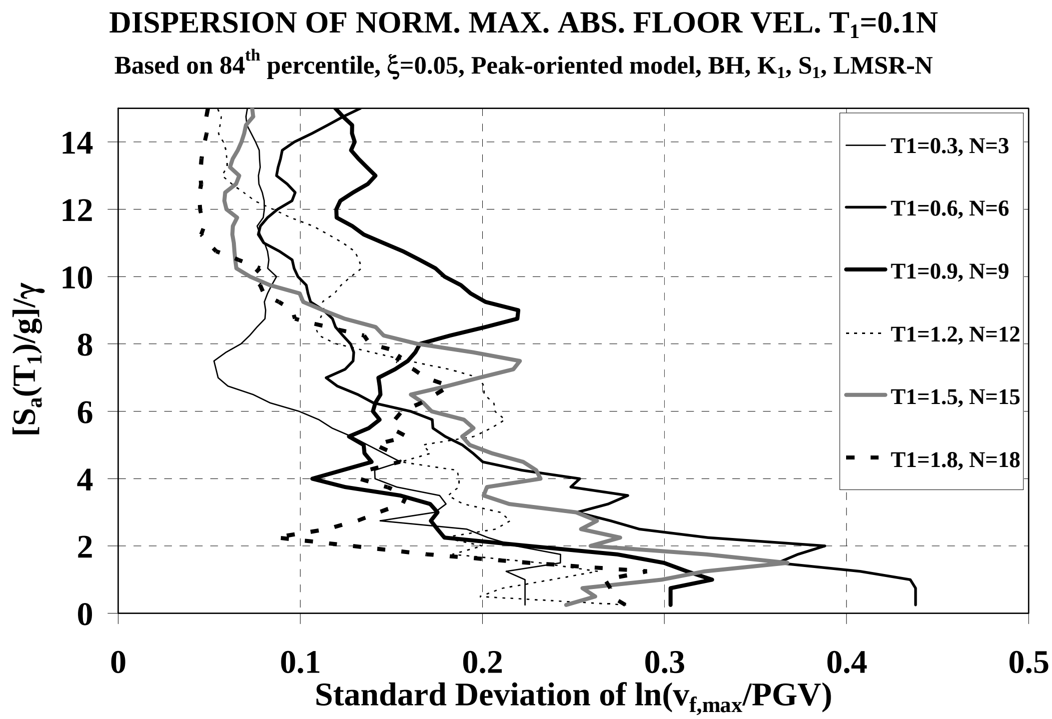

(a) T_1 = 0.1N

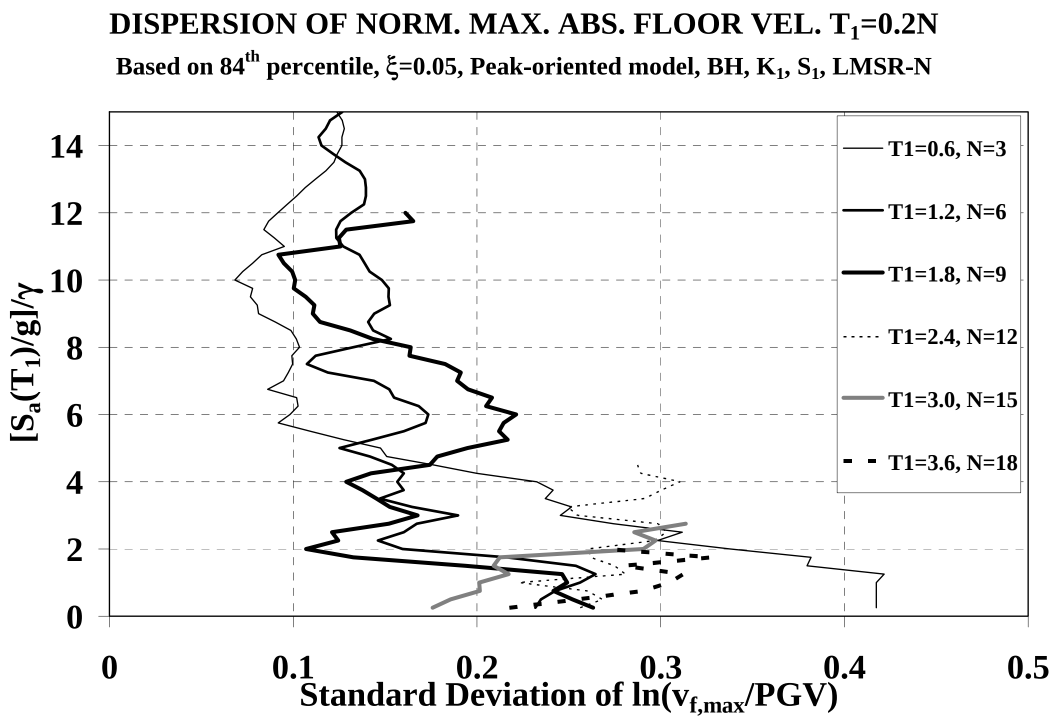

(b) T_1 = 0.2N

Figure 4.61 Dispersion of the Normalized Maximum Absolute Floor Velocity over the Height, Stiff and Flexible Frames

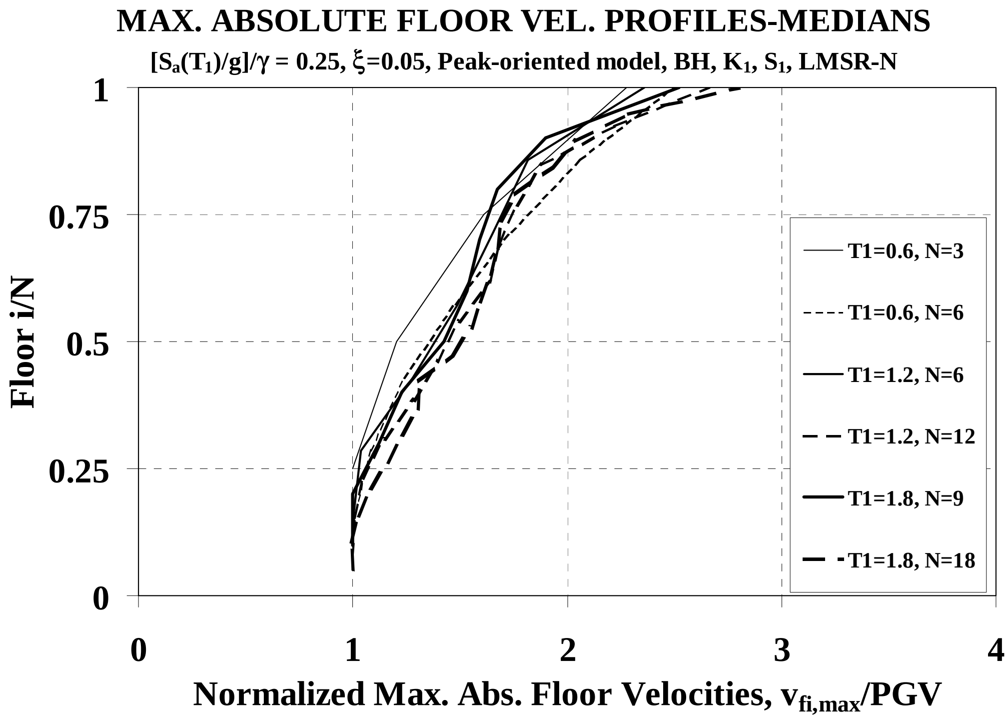

Figure 4.62 Distribution of Normalized Maximum Absolute Floor Velocities over the Height, $[S_a(T_1)/g]/\gamma = 0.25$

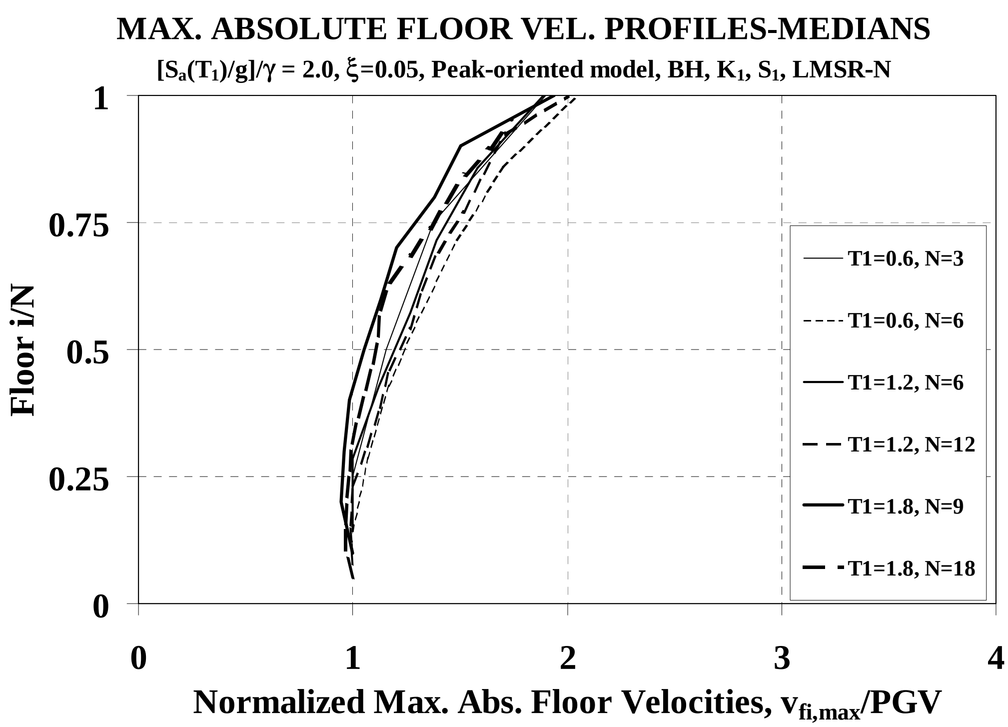

Figure 4.63 Distribution of Normalized Maximum Absolute Floor Velocities over the Height, $[S_a(T_1)/g]/\gamma = 2.0$

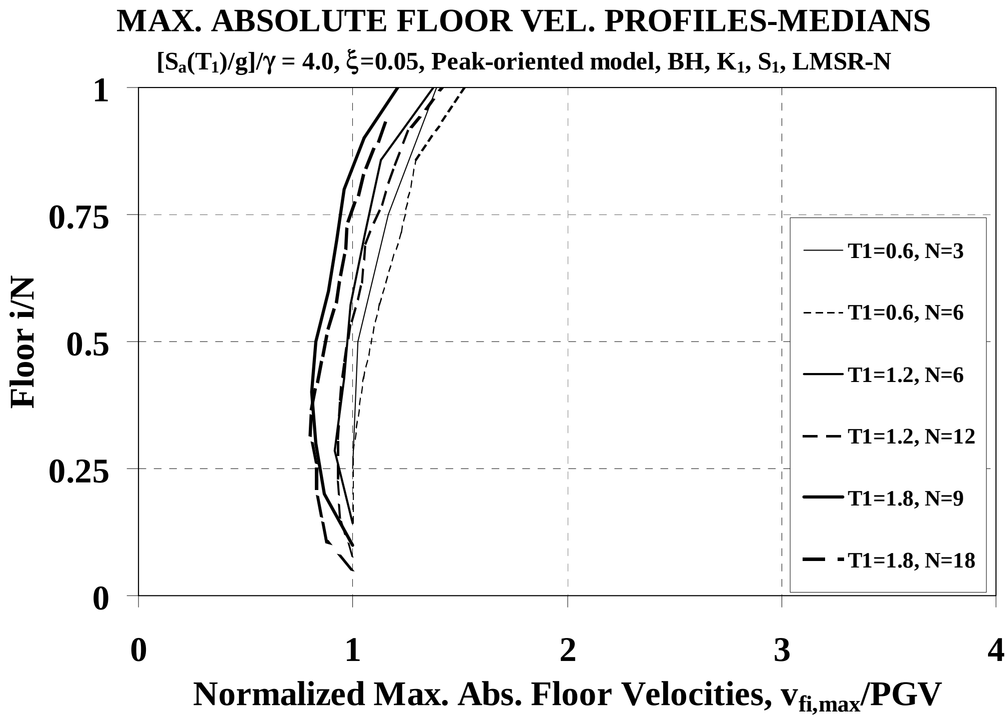

Figure 4.64 Distribution of Normalized Maximum Absolute Floor Velocities over the Height, $[S_a(T_1)/g]/\gamma = 4.0$

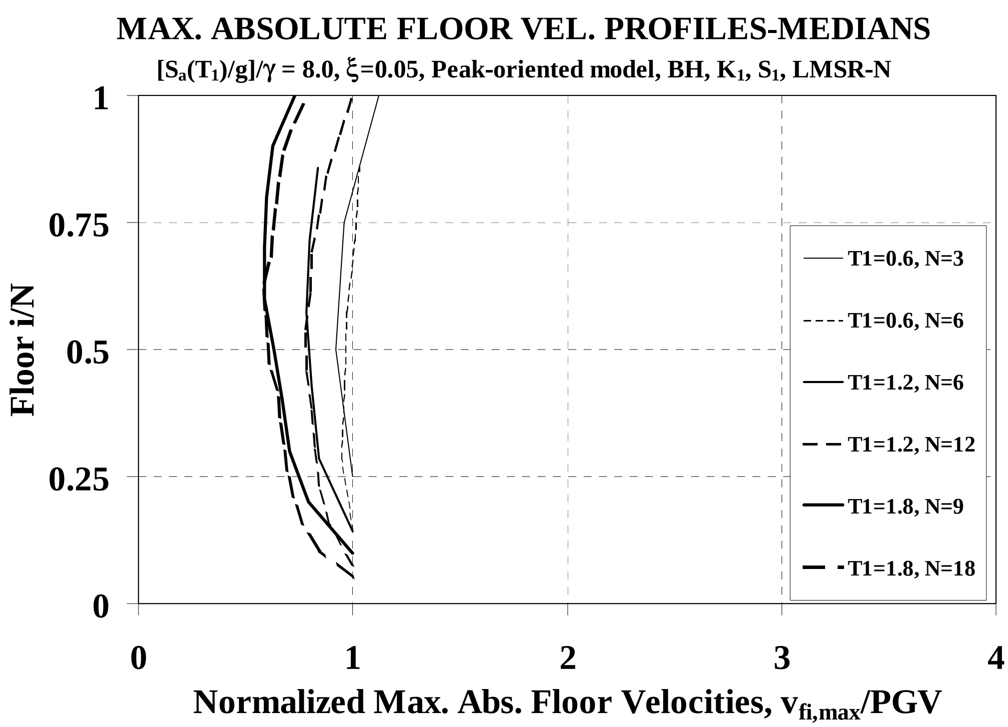

Figure 4.65 Distribution of Normalized Maximum Absolute Floor Velocities over the Height, $[S_a(T_1)/g]/\gamma = 8.0$

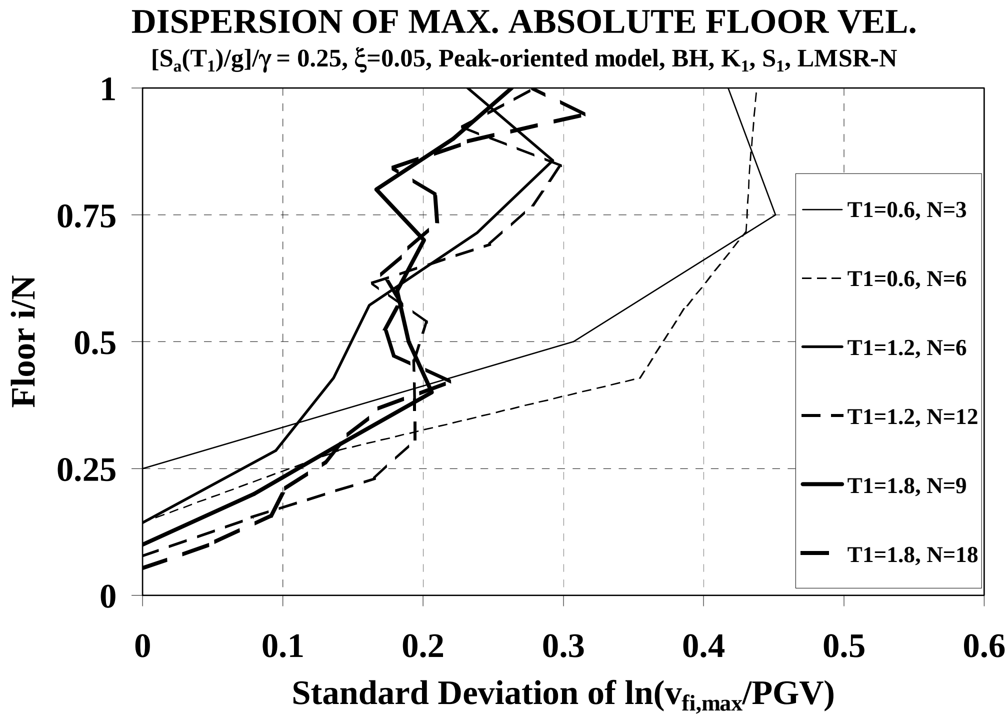

(a) $[S_a(T_1)/g]/\gamma = 0.25$

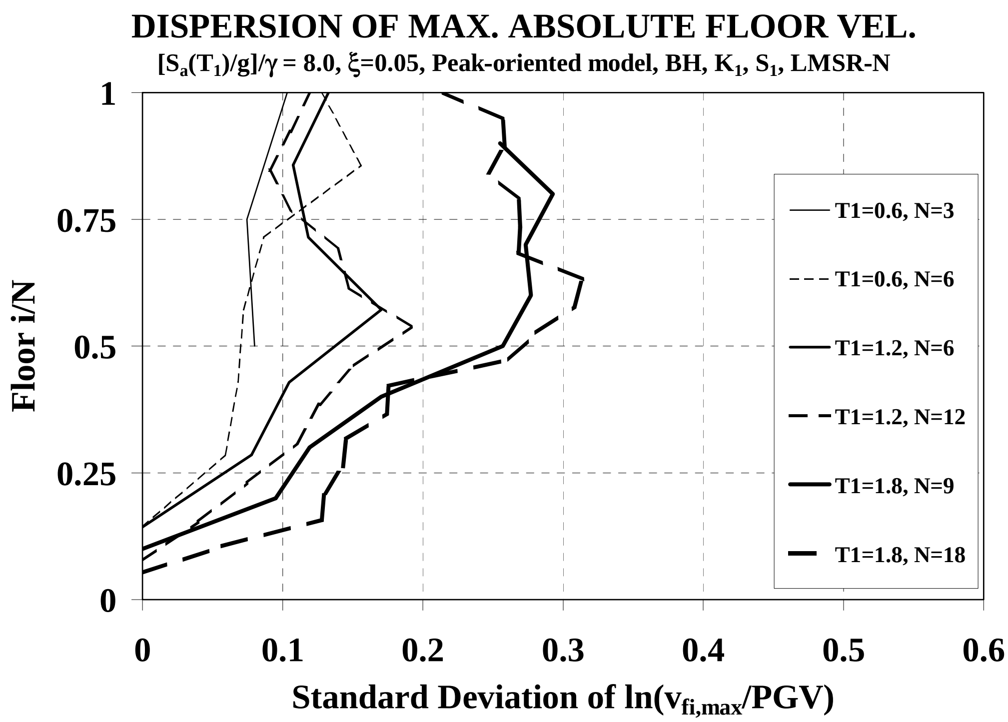

(b) $[S_a(T_1)/g]/\gamma = 8.0$

Figure 4.66 Dispersion of Maximum Absolute Floor Velocities over the Height

5 Evaluation of Energy Demands for Regular Frames

5.1 INTRODUCTION

Engineering demand parameters that account for the cumulative nature of the seismic response of structural systems, e.g., energy demands, are considered important because they relate to damage to structural components. Several research studies have quantified energy demands and suggested design philosophies based on energy considerations (Uang and Bertero, 1988; Bertero and Teran, 1993; Chai and Fajfar, 2000). However, additional knowledge and an improved understanding of both energy demands and capacities are needed for a robust and reliable implementation of damage assessment and conceptual design procedures based on energy considerations rather than displacements or forces. The purpose of this chapter is to provide a better understanding of the energy demands experienced by nondeteriorating regular frame structures subjected to ordinary ground motions. Global (i.e., total dissipated energy, hysteretic energy dissipated) and local (i.e., component normalized hysteretic energy) demands are evaluated by means of statistical measures. A definition of strong motion duration that is a function of both the structural response and the ground motion record is utilized in the evaluation of the distribution of energy demands over the height of the structure.

5.2 GLOBAL ENERGY DEMANDS

In this section, two basic global energy EDPs are evaluated: the total dissipated energy (TDE) and the total hysteretic energy dissipated (HE). The TDE is equal to the sum of the energy dissipated by damping (damping energy dissipated, DE) and the HE. The TDE is approximately equal to the input energy at the end of the record (IE_{end}) because at this instant of time there is little kinetic energy in the system. Previous research studies (Nassar and Krawinkler, 1991; Seneviratna and Krawinkler, 1997) have indicated that the ratio of HE to TDE is a stable parameter and that estimates of the TDE per unit mass is not very sensitive to the level of inelastic behavior. In order to assess whether these observations are applicable to the base case family of generic frame structures used in this study, a statistical evaluation of the TDE per unit mass as well as the ratio of HE to TDE is performed.

5.2.1 TDE Demands

Figure 5.1 depicts the dependence on fundamental period of the median TDE per unit mass for the generic frames. Except for the short-period frame model (T_1 = 0.3 sec) and models that are sensitive to P-delta effects, the median TDE per unit mass tends to decrease with an increase in the fundamental period. Moreover, the median TDE per unit mass is not very sensitive to the level of inelastic behavior. This observation is in agreement with results obtained by Nassar and Krawinkler (1991) for SDOF systems. Short-period frame models exhibit larger median TDE per unit mass as the level of inelastic behavior increases because they are subjected to a rapid increase in the number of inelastic cycles. This is important for stiffness-degrading hysteretic models in which hysteretic energy is dissipated throughout the duration of the ground motion, i.e., even for relatively small cycles at the end of the record. For P-delta sensitive models, the TDE per unit mass tends to increase very rapidly with an increase in the relative intensity once dynamic instability is approached.

5.2.2 HE Demands

The ratio of the hysteretic energy dissipated, HE, to the total dissipated energy, TDE, provides a measure of the percentage of the input energy of the system that is dissipated by yielding of its members. The results for median ratios of HE/TDE for the base case family of generic frame structures used in this study are shown in Figure 5.2. It can be observed that the median of HE/TDE is similar for both the flexible and stiff frames. Its value increases with the relative intensity up to $[S_a(T_1)/g]/\gamma = 4.0$ and remains rather constant (approximately equal to 0.70) for larger relative intensities. This result implies that for the generic frames and the LMSR-N set of ground motions, for relative intensities greater than 4.0, approximately 70% of the input energy of the system is dissipated by yielding of its members, while 30% percent of the energy is dissipated by damping. The distribution over the height of the normalized hysteretic energy dissipated by the frame structures is discussed in Section 5.3. Figure 5.3 presents the standard deviation of the natural log of HE/TDE for the stiff and flexible frames. The dispersion in this ratio is very small except for small relative intensities for which the median ratio HE/TDE can be close to zero causing the dispersion to be large.

The variation of median HE/TDE demands with the fundamental period of the frame systems is illustrated in Figure 5.4. It can be seen that for $4.0 \le [S_a(T_1)/g]/\gamma \le 8.0$, the median of HE/TDE is weakly dependent on the fundamental period (and hence, number of stories) as well as the relative intensity, except for P-delta sensitive structures (N = 12, T_1 = 2.4 sec, N = 15, T_1 = 3.0 sec and N = 18, T_1 = 3.6 sec) for which it tends to increase with period. For the small relative intensity of $[S_a(T_1)/g]/\gamma = 1.0$, structures with $T_1 \ge 2.4$ sec experience yielding and dissipate approximately 20% of the input energy by hysteretic action because of the influence of higher modes in the response.

Figure 5.5 presents median HE/TDE demands for SDOF systems with P-delta slopes equal to the elastic first-story stability coefficient of the generic frame structures. For instance, a SDOF system labeled "T1 = 0.1N, R = 4" in Figure 5.5 represents a SDOF model with a strength-reduction factor (relative intensity) of 4 and a negative P-delta slope with an absolute value equal to the elastic first-story stability coefficient of the T_1 = 0.1N frames (full mass participation is assumed). The median HE/TDE ratio for SDOF systems is weakly dependent on the level of inelasticity for medium to large relative intensities. This behavior is consistent with the one observed for the case of frame structures (Figure 5.4). For SDOF systems, as the period increases, the median ratio HE/TDE is rather stable for all relative intensity levels even for P-delta-sensitive systems. This behavior is not observed for inelastic frame structures (Figure 5.4) because higher modes of vibration increase the hysteretic energy dissipation at small relative intensities, and P-delta effects are more pronounced for the generic frames, i.e., the absolute value of the effective P-delta slope in the inelastic range is greater than that obtained based on the elastic first-story stability coefficient. However, in most cases, behavior patterns are sufficiently consistent between SDOF and MDOF systems to make an estimate of HE/TDE ratios for frames that are not P-delta sensitive from the HE/TDE ratios of the corresponding SDOF systems. This is illustrated in Figure 5.6 in which median ratios of HE/TDE for the generic frames normalized by the HE/TDE of the SDOF systems are presented.

5.3 LOCAL ENERGY DEMANDS

Energy demands imposed on the components of a system provide information on the distribution of damage over the height of a structure. The normalized hysteretic energy (NHE) is one measure of "local" damage. It is equal to the total hysteretic energy dissipated by the component divided by the yield moment (or force) times the yield rotation (or displacement). Thus, the NHE is a multiple of twice the value of the strain energy at yield. For an elastoplastic system, the NHE is equal to the sum of the plastic excursions normalized by the yield rotation (or displacement). The sum of plastic excursions has been used as a measure of structural damage to components (Krawinkler and Zoheri, 1983).

In Krawinkler et al. (2000), arguments are made to use only the energy dissipated in the prepeak segment of the response history as a measure of cumulative damage. This segment terminates when the later of the maximum positive and negative deformation peaks occurs. The excursions occurring after the prepeak segment will do little cumulative damage and they will not cause a further increase in maximum deformations.

Figures 5.7 and 5.8 show a response history (Figure 5.7) and the corresponding hysteretic response of a peak-oriented model with 3% strain hardening (Figure 5.8). The time associated with the end of the prepeak segment can be used to define the end of the strong motion portion of the response. Strong motion duration, D_{sm}, is defined in this study as the difference between the time when the prepeak segment of the response ends (t_{pp} in Figure 5.7) and the time of first yielding (t_y in Figure 5.7). For times greater than t_{pp} (postpeak segment), although stiffness-degrading models can experience deformations close to the maximum deformations, the energy dissipation is relatively small. This is illustrated in Figure 5.8 in which the response for $t > t_{pp}$ is portrayed with thin black lines. Thus, the relevant damage is expected to occur during the duration of strong motion defined by D_{sm}. The response in the interval corresponding to D_{sm} is represented by thick black lines in Figures 5.7 and 5.8.

Based on the arguments made, the normalized hysteretic energy in the prepeak segment of the response is used as the basic energy parameter for evaluation of the distribution of structural damage over the height. NHE demands are calculated per floor based on the hysteretic energy dissipated at the ends of beams. At the first floor, it is based on the hysteretic energy dissipated at the bottom of the first-story columns. Figure 5.9 shows median NHE demands over the height for the N = 9, T_1 = 1.8 sec frame structure. Total NHE, NHE_{total}, and NHE in the prepeak segment of the response, NHE_{pp}, are presented. Both the NHE_{total} and NHE_{pp} distributions are similar, with the NHE_{pp} values being smaller by a percentage that decreases with an increase in relative intensity. The NHE profiles look similar in shape to the story drift profiles (Figure 4.25(b)), but the top stories have relatively larger values because these stories experience more inelastic excursions due to higher mode effects.

Figures 5.10–5.12 present the distribution of median NHE_{pp} over the height for the 3-, 9-, and 18-story frames. In all cases, there is a systematic increase in median NHE_{pp} demands with the relative intensity. The largest increase is observed in Figure 5.10(a) for the T_1 = 0.3 sec structure due to the large ductility levels (see Section 4.3.9) and the large number of cycles experienced by short-period structures. Both the 9- and 18-story frames exhibit the largest median NHE_{pp} at the top and second floors, whereas small demands are observed in the middle stories (the 18-story frame with T_1 = 3.6 sec does not have median values for relative intensities of 4 or greater because dynamic instability occurs at a relative intensity less than 4). A more uniform distribution of median NHE_{pp} demands is observed for the 3-story frames.

5.4 STRONG MOTION DURATION

In this section the relationship between the duration of strong motion, $D_{sm,}$ and the relative intensity is explored for the base case family of generic frame structures. As discussed in Section 5.3, D_{sm} is important within the context of damage assessment because of its relationship to structural damage. The main assumption is that structural damage is controlled by the hysteretic energy dissipated in the prepeak segment of the response, which is also the hysteretic energy dissipated during the duration of strong motion (Figure 5.7).

The definition of D_{sm} used in Section 5.3, which is illustrated in Figure 5.7, is applicable to the components of a system (more specifically, to the rotational springs used in the frame models). In this section, a global measure of D_{sm} is used. It is defined as the duration between the earliest time of first yielding, t_y, and the longest t_{pp} among all the components of the structure (t_y and t_{pp} are illustrated in Figure 5.7).

The variation of median D_{sm} with the relative intensity for the base case family of generic frames is shown in Figure 5.13. Median D_{sm} values tend to increase with the relative intensity. A more rapid increase is observed for the flexible frames (Figure 5.13(b)), especially structures that are sensitive to P-delta effects (flexible frames with N = 12, 15, and 18). P-delta effects cause the system to experience large deformations and approach the onset of dynamic instability with an increase in relative intensity. As the system experiences larger deformation demands and approaches dynamic instability, its response tends to drift toward one side, so t_{pp} and hence D_{sm} increases. The dispersion associated with the median D_{sm} values shown in Figure 5.13 is presented in Figure 5.14. Except for small relative intensities, the measure of dispersion fluctuates around 0.5 and shows no clear pattern with relative intensity. The large values of dispersion observed for $[S_a(T_1)/g]/\gamma \leq 2.0$ are due to the fact that in this relative intensity range not all ground motion records cause yielding in the systems, while some other systems experience very small inelastic deformation. Thus, small median values of D_{sm} are likely, which potentially increases the estimate of dispersion.

The variation of median D_{sm} values with fundamental period is presented in Figure 5.15. There is a pronounced increase of median D_{sm} with period and relative intensity, particularly for P-delta sensitive-frames. For systems in which P-delta effects are not significant, for a given fundamental period, there is weak dependence of median D_{sm} values on the number of stories. Thus, except for short-period and long, flexible frames, given the relative intensity, fundamental period rather than stiffness controls the duration of strong motion.

5.5 SUMMARY

This chapter focuses on the evaluation of energy demands for the base case family of generic frames subjected to the set of 40 LMSR-N ordinary ground motions. Global (total dissipated and hysteretic energy) as well as local (normalized hysteretic energy) demands are evaluated. A definition of strong motion duration that accounts for the interval of the response relevant for damage assessment is discussed. The relationship between strong motion duration and relative intensity is studied. A summary of specific issues addressed in this chapter is presented below:

- Except for short-period frame structures and systems that are sensitive to P-delta effects, the median TDE per unit mass decreases with an increase in the fundamental period and it is not very sensitive to the level of inelastic behavior. As the relative intensity increases, short-period models exhibit larger median TDE per unit mass because they are subjected to a rapid increase in the number of inelastic cycles. This is particularly important for stiffness-degrading systems in which hysteretic energy is dissipated throughout the duration of the ground motion, i.e., even for relatively small cycles at the end of the record.

- The ratio of hysteretic energy (HE) to total dissipated energy (TDE) for generic frame structures can be estimated using "equivalent" SDOF systems, except for long, flexible frames. For the frames used in this study the median ratio HE/TDE is associated with small dispersions and increases with the relative intensity up to $[S_a(T_1)/g]/\gamma = 4.0$. Except for P-delta-sensitive frames, for $[S_a(T_1)/g]/\gamma > 4.0$ the median ratio HE/TDE is about 0.70, which implies that in this relative intensity range, most of the input energy is dissipated by inelastic deformations.
- The evaluation of energy demands for damage assessment necessitates the quantification of engineering demand parameters such as the normalized hysteretic energy, NHE, for the interval of the response associated with most of the damage experienced by the elements of the system. This issue is particularly important for stiffness-degrading systems in which a large amount of energy can be dissipated in small hysteretic loops without inducing significant additional structural damage to the component. Thus, energy demand evaluation based on the total energy dissipated by a component may provide a misleading picture of its real damage state.
- A definition of strong motion duration that identifies the interval of the response that is most relevant for damage assessment is discussed. The strong motion duration tends to increase with fundamental period and relative intensity with a rapid increase observed for P-delta-sensitive frames. Except for short-period and long, flexible frames, given the relative intensity, fundamental period rather than stiffness controls the duration of strong motion.
- Median NHE demands over the height are larger at the top floor and at the bottom floors (except for the N = 3 frames in which a more uniform distribution over the height is observed). As is the case with the drift demands evaluated in Chapter 4, the shape of the median NHE profiles are a result of the criteria utilized to design the base case family of generic frames. For instance, NHE demands are large at the top floor because a relatively weak beam is used. A "weak" beam is the result of tuning the strength of the structure so that simultaneous yielding is attained under a parabolic load pattern.

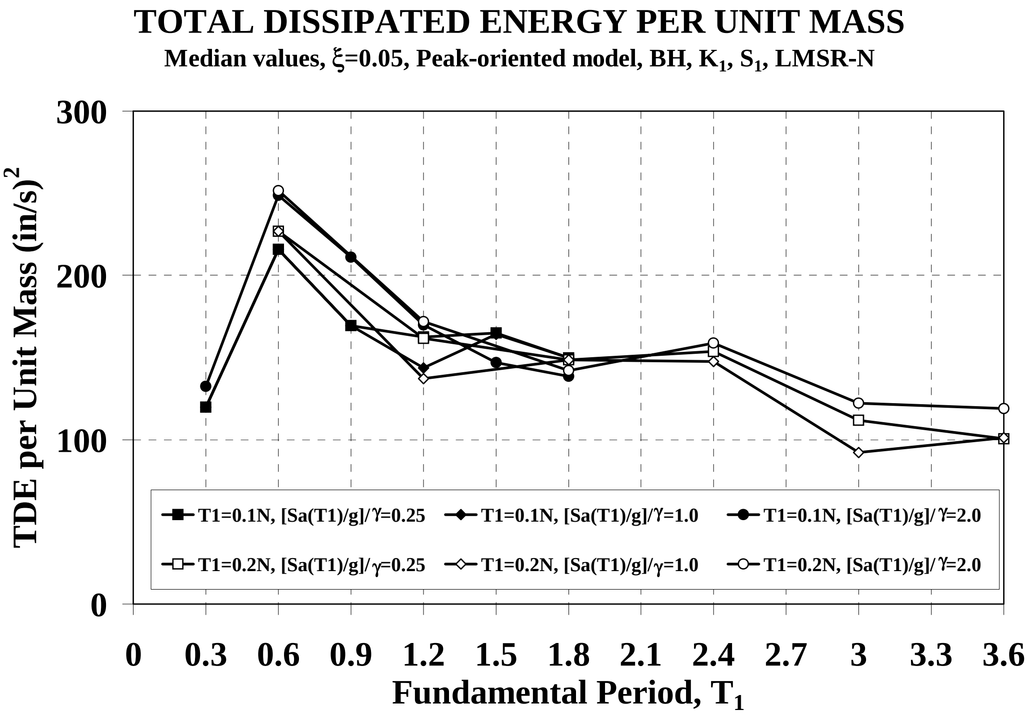

(a) $[S_a(T_1)/g]/\gamma$ = 0.25, 1.0, 2.0

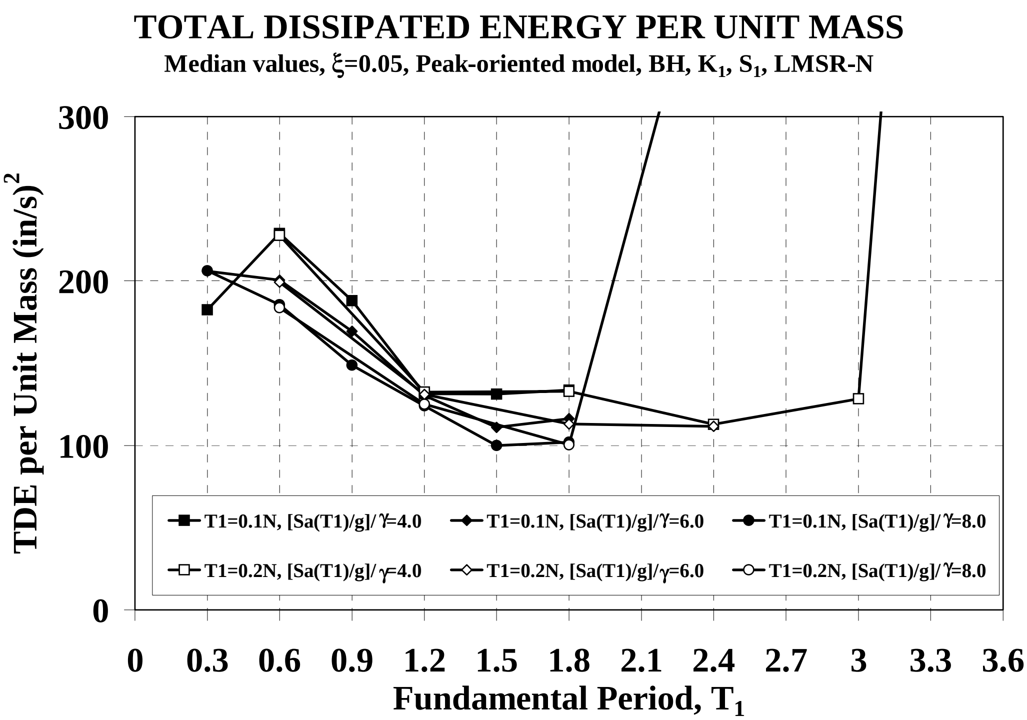

(b) $[S_a(T_1)/g]/\gamma$ = 4.0, 6.0, 8.0

Figure 5.1 Dependence on the Fundamental Period of the Median TDE per Unit Mass, All Frames, Various Relative Intensities

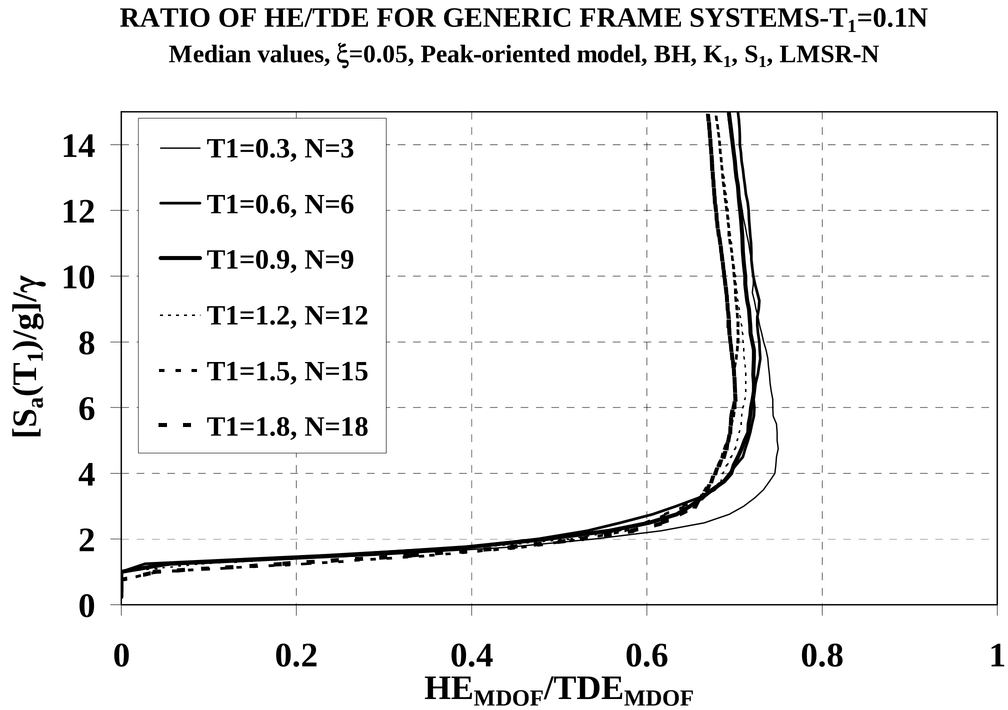

(a) $T_1 = 0.1N$

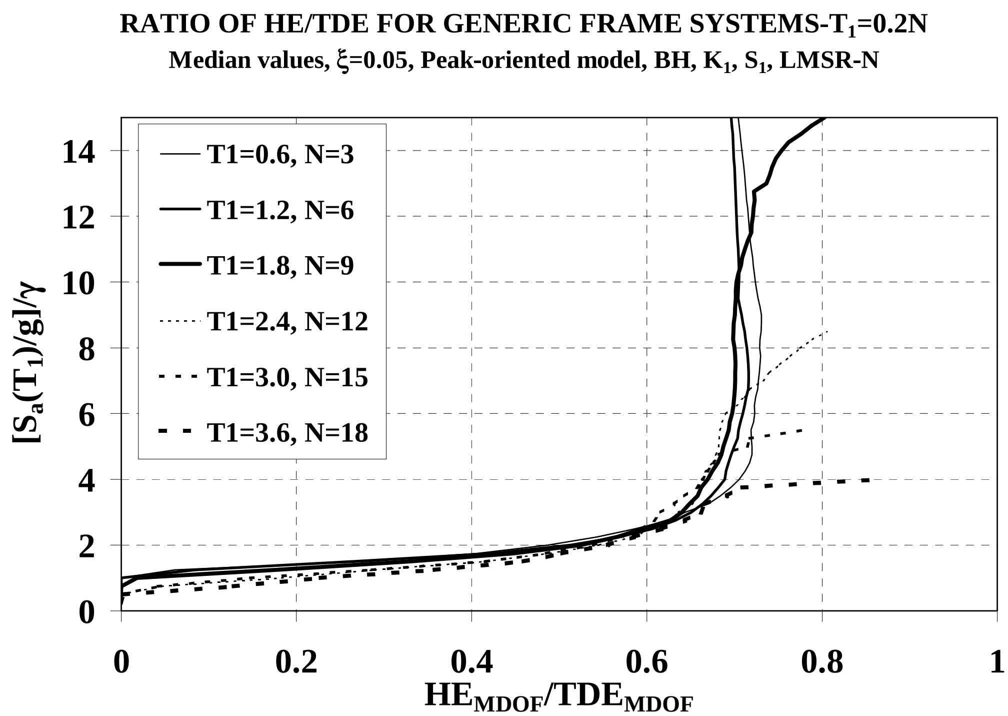

(b) $T_1 = 0.2N$

Figure 5.2 Median Ratio of HE to TDE, Stiff and Flexible Frames

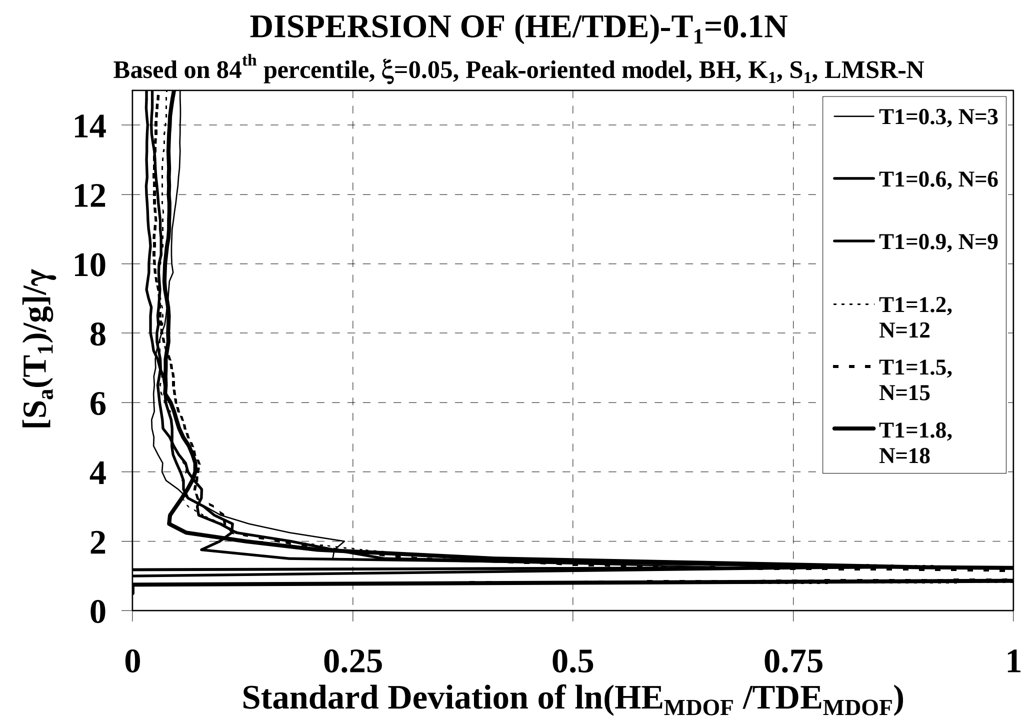

(a) $T_1 = 0.1N$

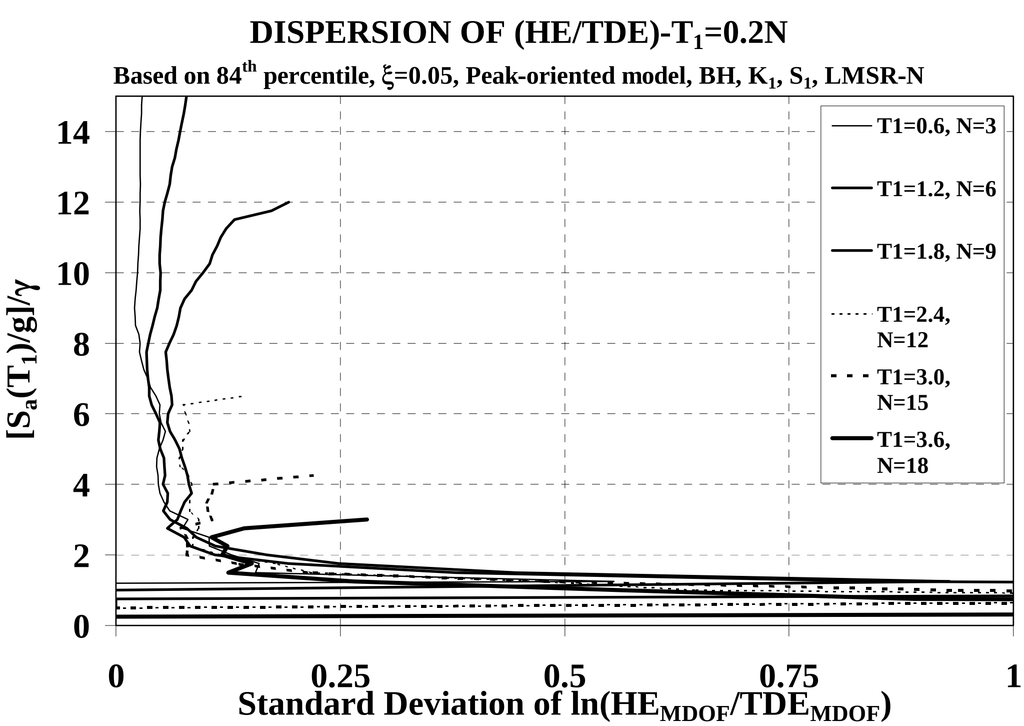

(b) $T_1 = 0.2N$

Figure 5.3 Dispersion of the Ratio of HE to TDE, Stiff and Flexible Frames

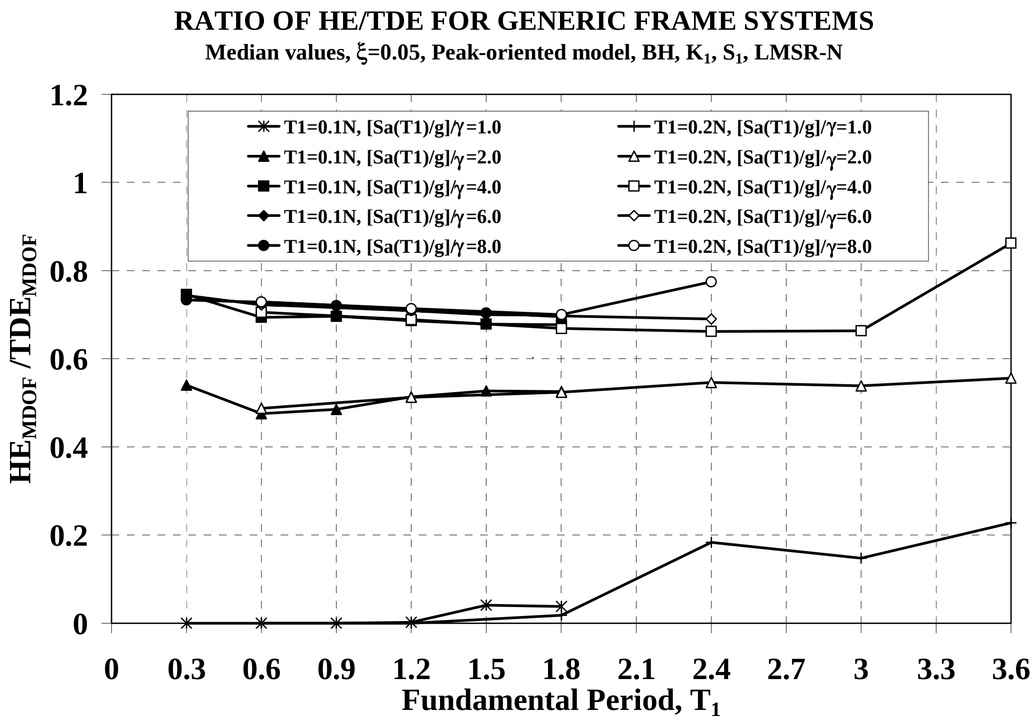

Figure 5.4 Dependence on the Fundamental Period of the Median Ratio of HE to TDE, All Frames, Various Relative Intensities

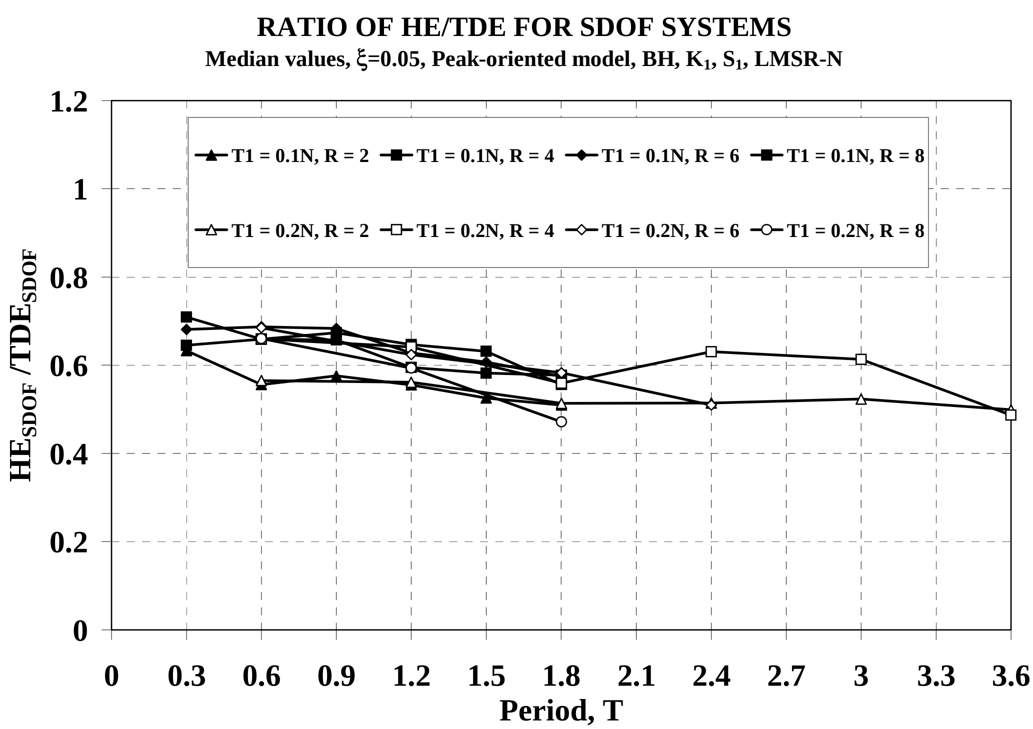

Figure 5.5 Dependence on Period of the Median Ratio of HE to TDE, SDOF Systems, Various Strength-Reduction Factors (R-Factors)

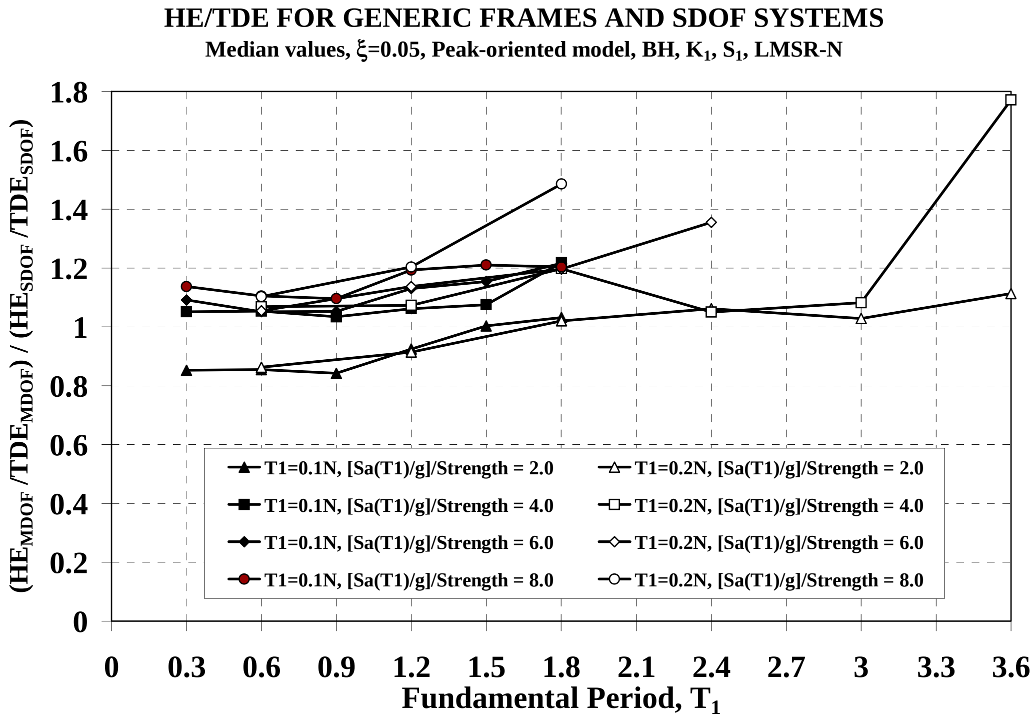

Figure 5.6 Dependence on the Fundamental Period of the Median Ratio of HE/TDE for Generic Frames to HE/TDE for SDOF Systems, Various Relative Intensities, Stiff and Flexible Frames

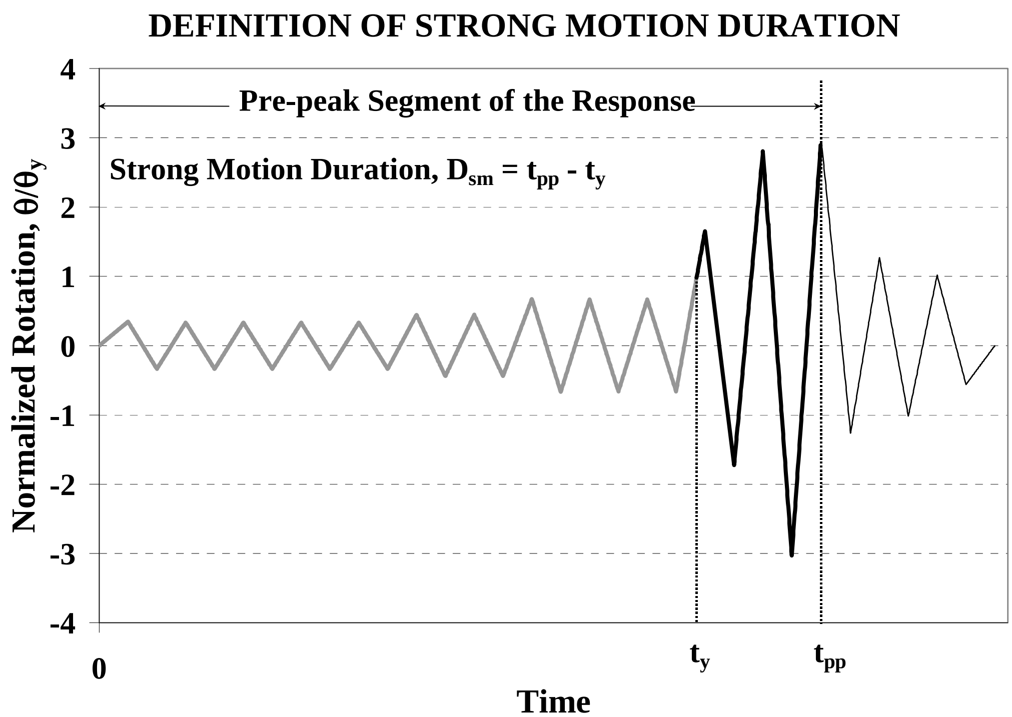

Figure 5.7 Definition of Strong Motion Duration and Prepeak Portion of the Response

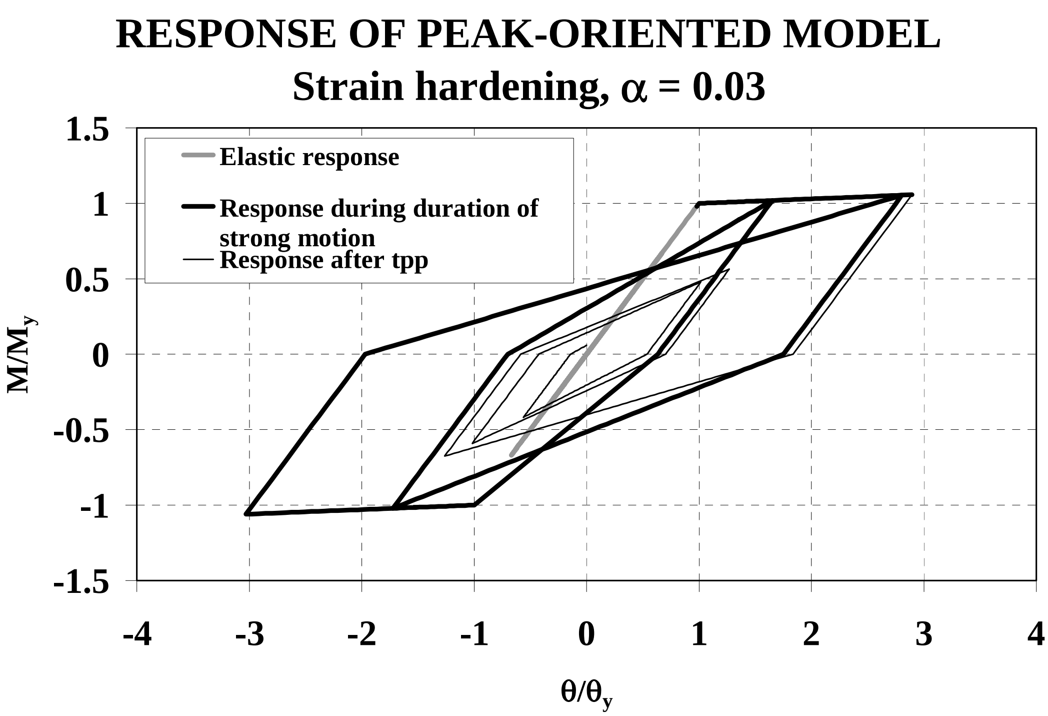

Figure 5.8 Hysteretic Response of Peak-Oriented Model Corresponding to Figure 5.7

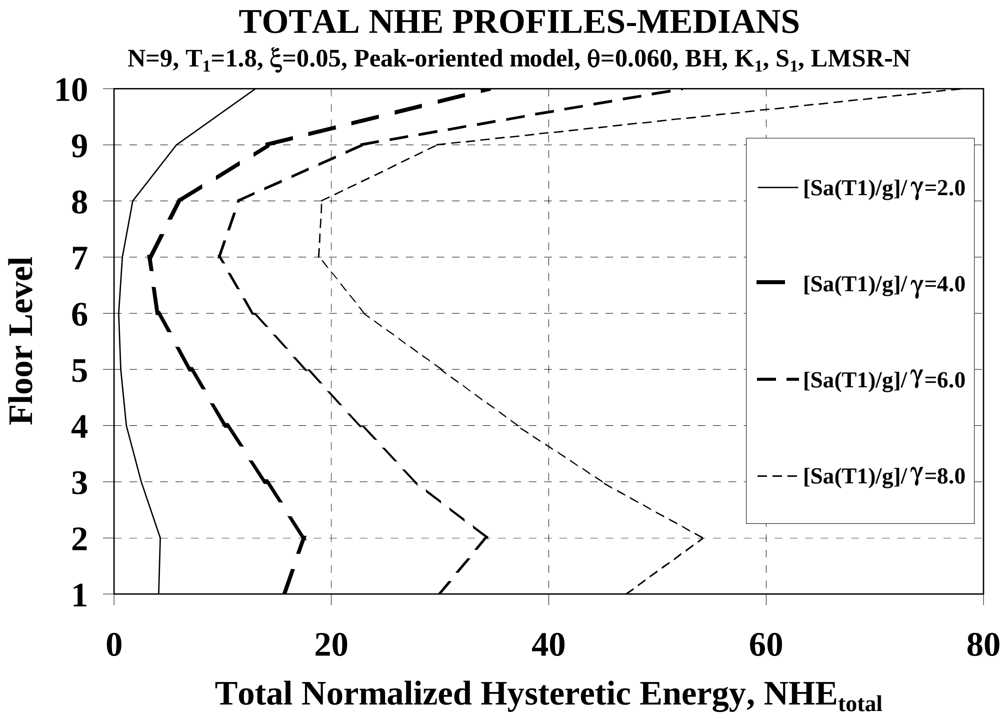

(a) Total Normalized Hysteretic Energy

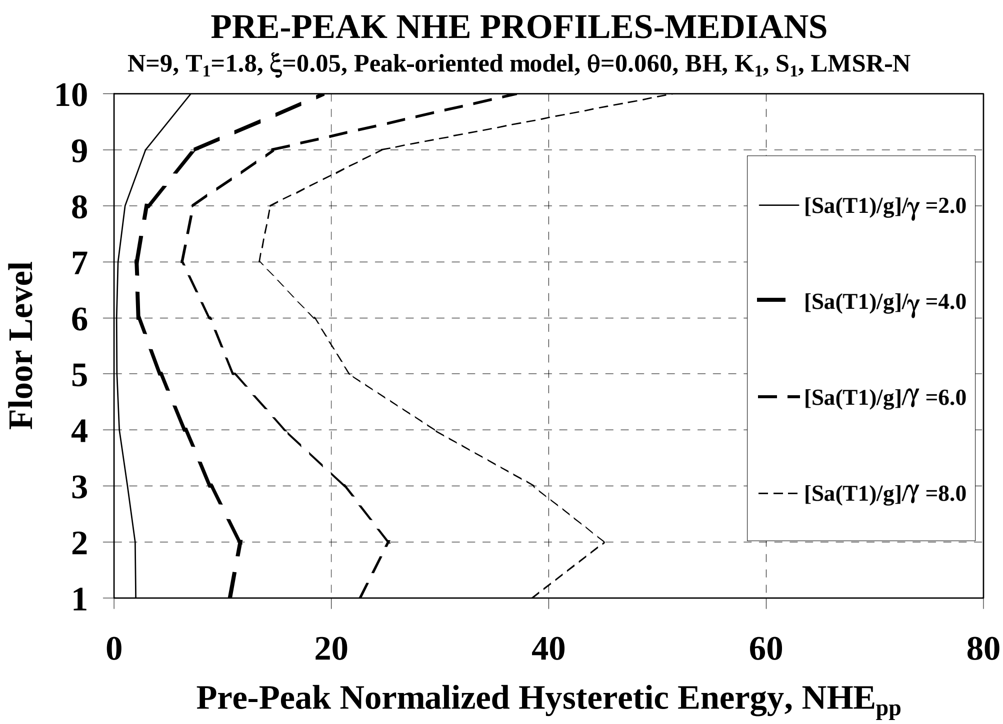

(b) Normalized Hysteretic Energy in the Prepeak Segment of the Response

Figure 5.9 Distribution over the Height of Median Normalized Hysteretic Energy Demands, N = 9, T_1 = 1.8 sec

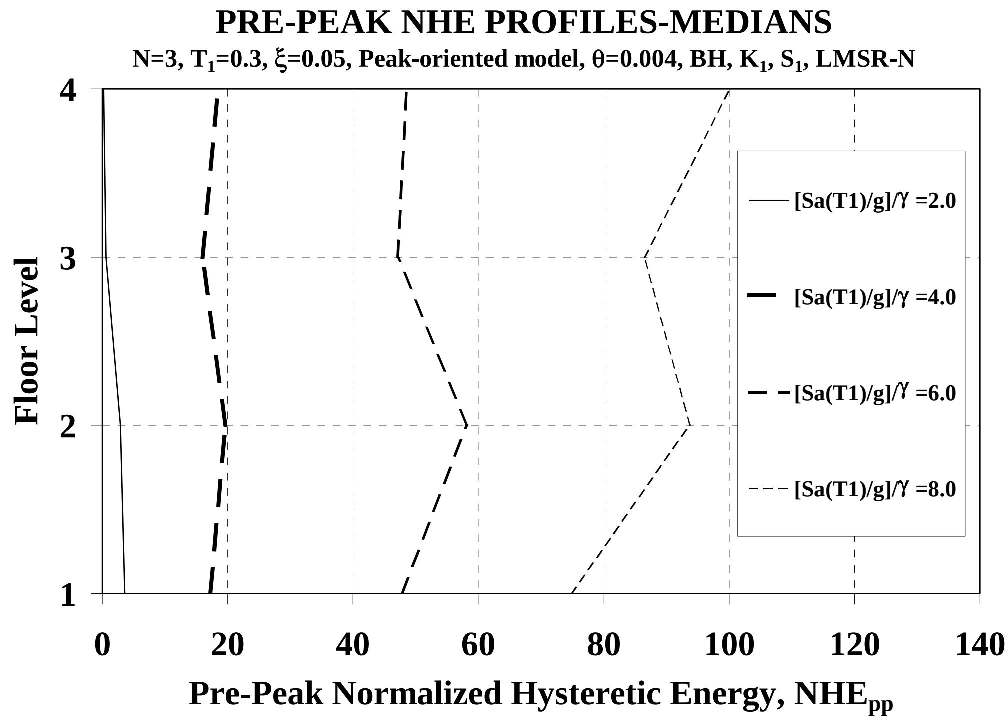

(a) T_1 = 0.3 sec

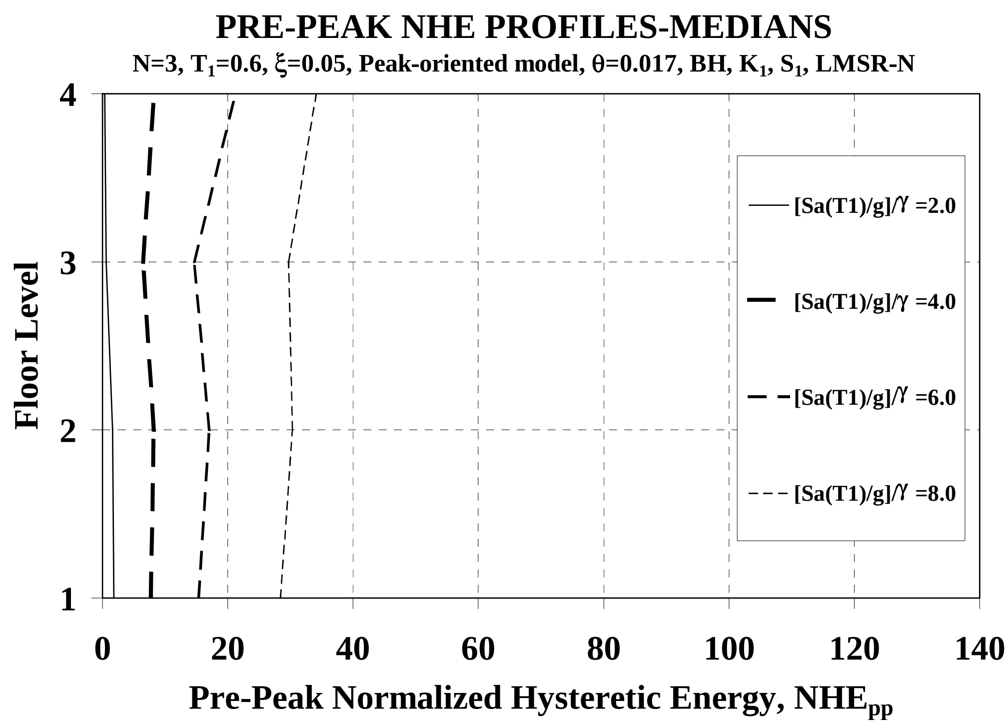

(b) T_1 = 0.6 sec

Figure 5.10 Distribution over the Height of the Normalized Hysteretic Energy Dissipated per Floor in the Prepeak Segment of the Response, Various Relative Intensities, N = 3

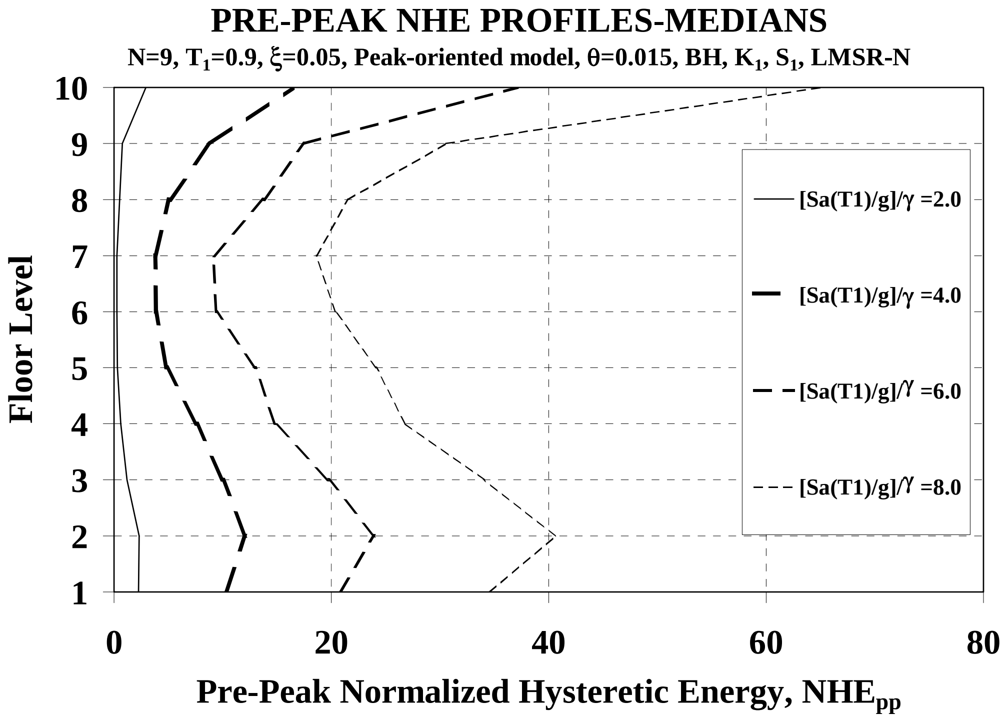

(a) T_1 = 0.9 sec

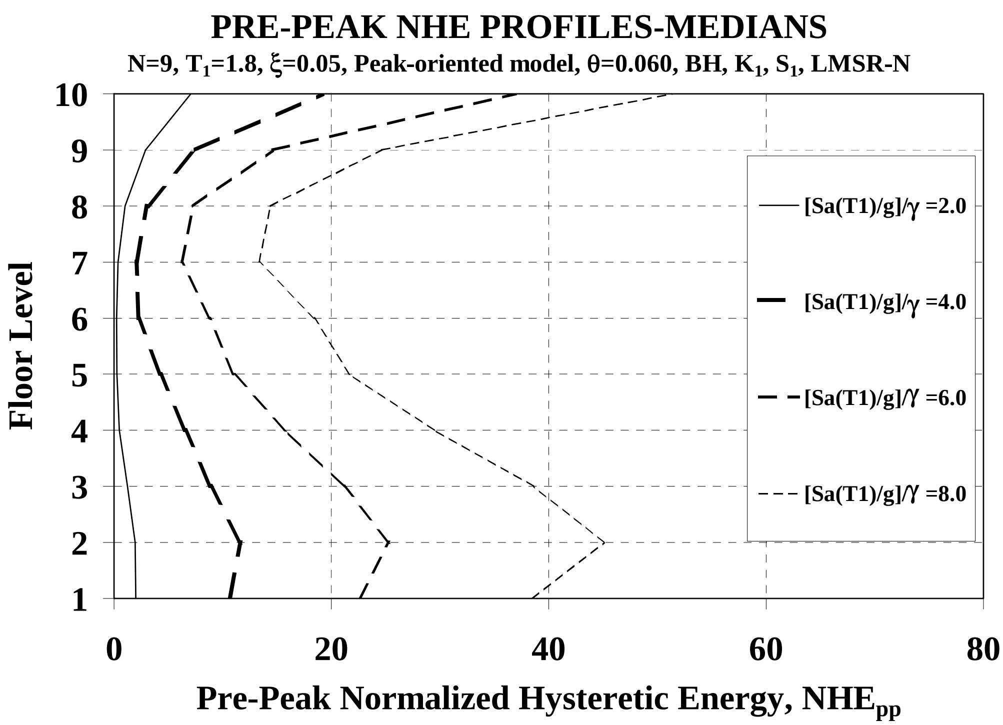

(b) T_1 = 1.8 sec

Figure 5.11 Distribution over the Height of the Normalized Hysteretic Energy Dissipated per Floor in the Prepeak Segment of the Response, Various Relative Intensities, N = 9

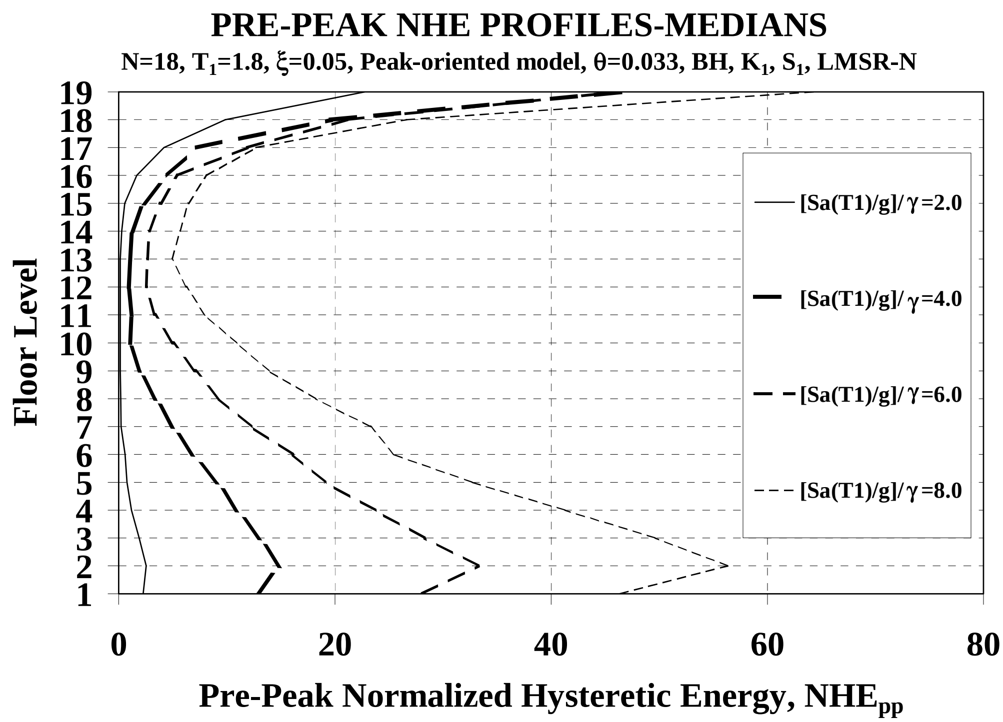

(a) T_1 = 1.8 sec

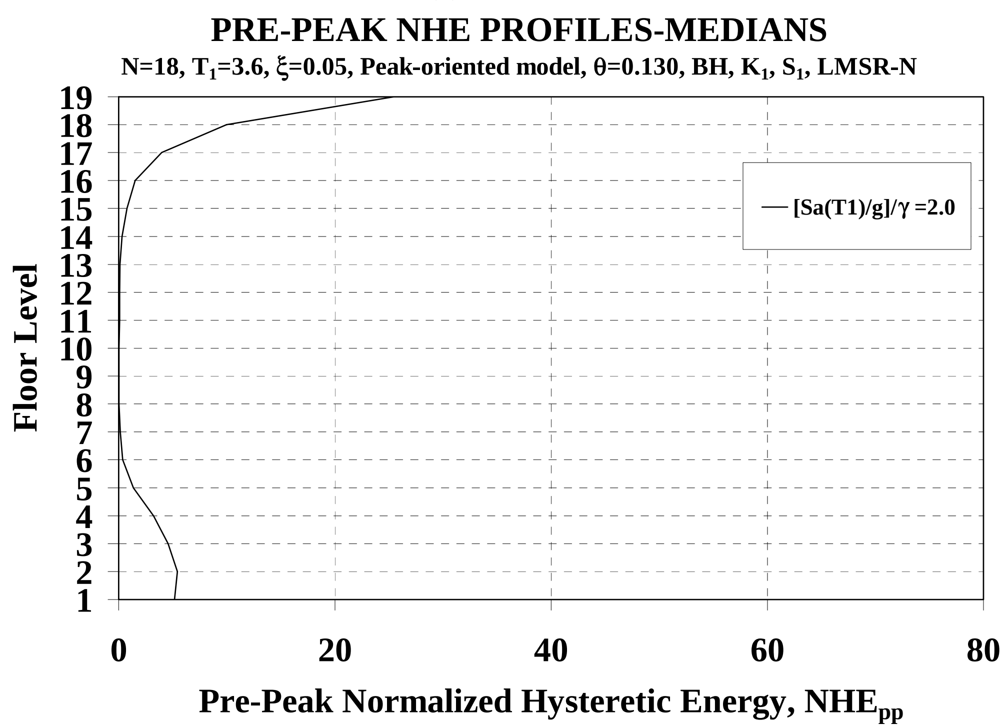

(b) T_1 = 3.6 sec

Figure 5.12 Distribution over the Height of the Normalized Hysteretic Energy Dissipated per Floor in the Prepeak Segment of the Response, Various Relative Intensities, N = 18

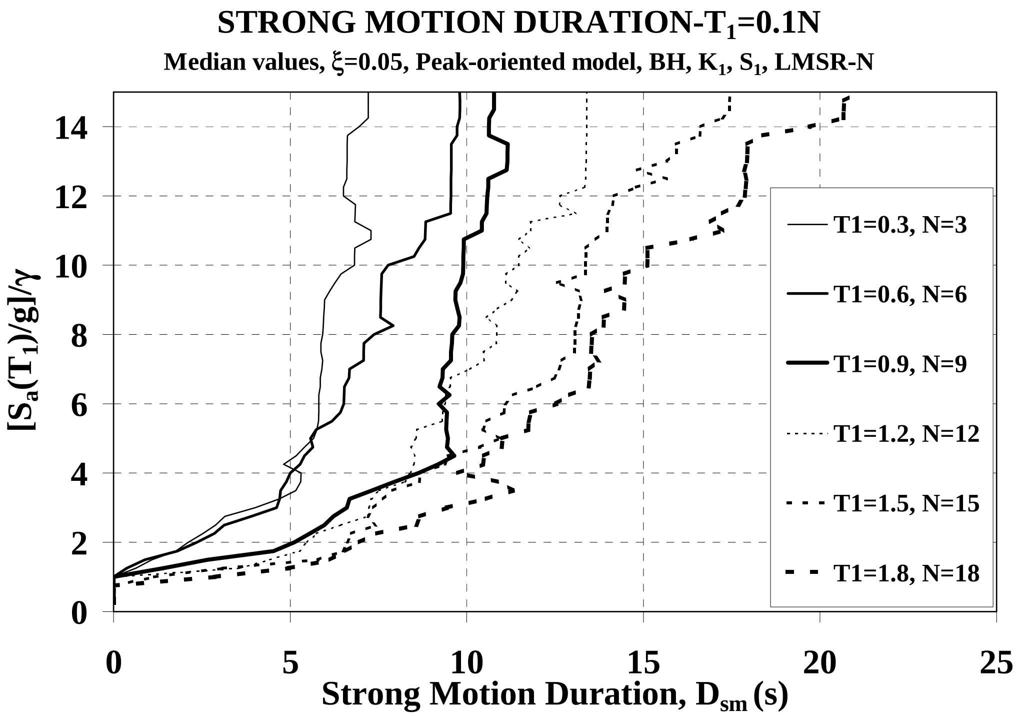

(a) $T_1 = 0.1N$

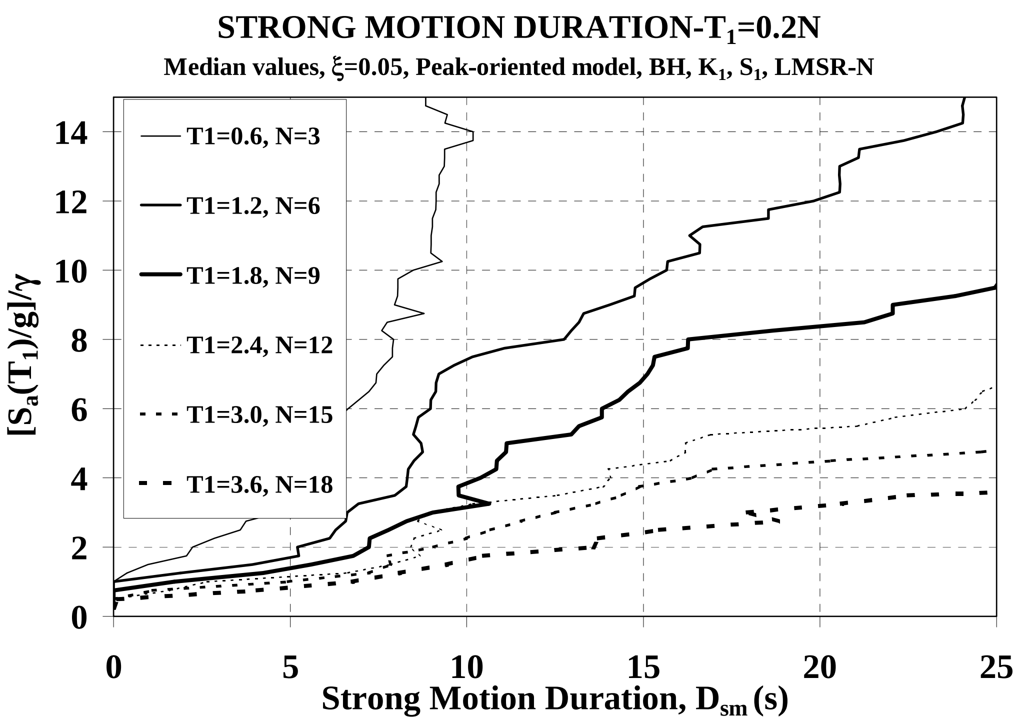

(b) $T_1 = 0.2N$

Figure 5.13 Median Strong Motion Duration, Stiff and Flexible Frames

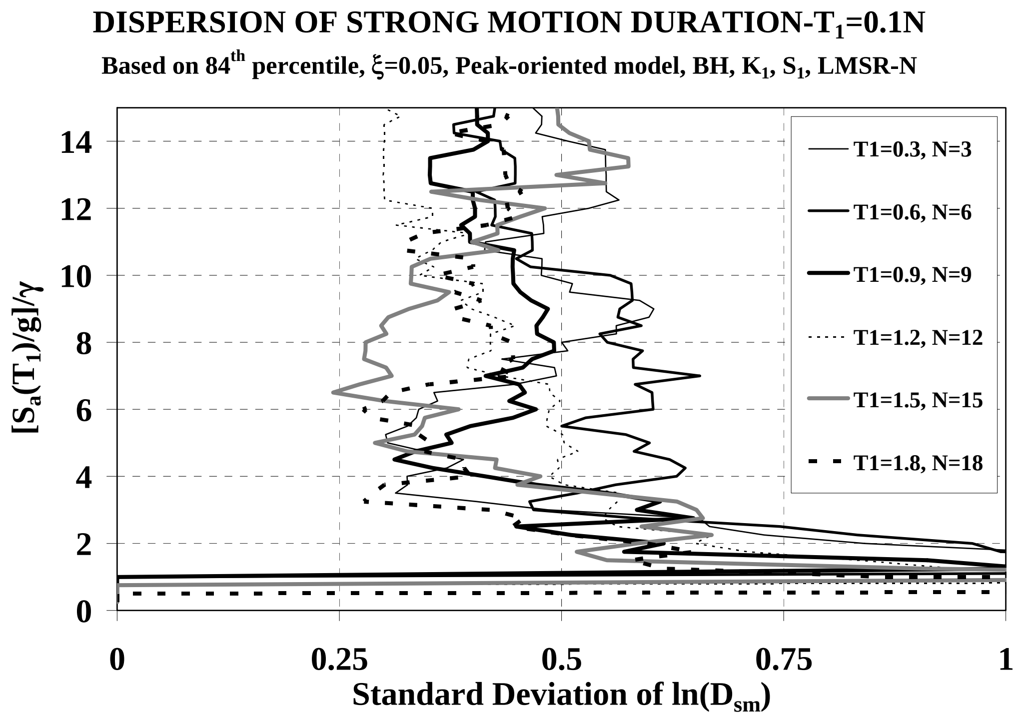

(a) T_1 = 0.1N

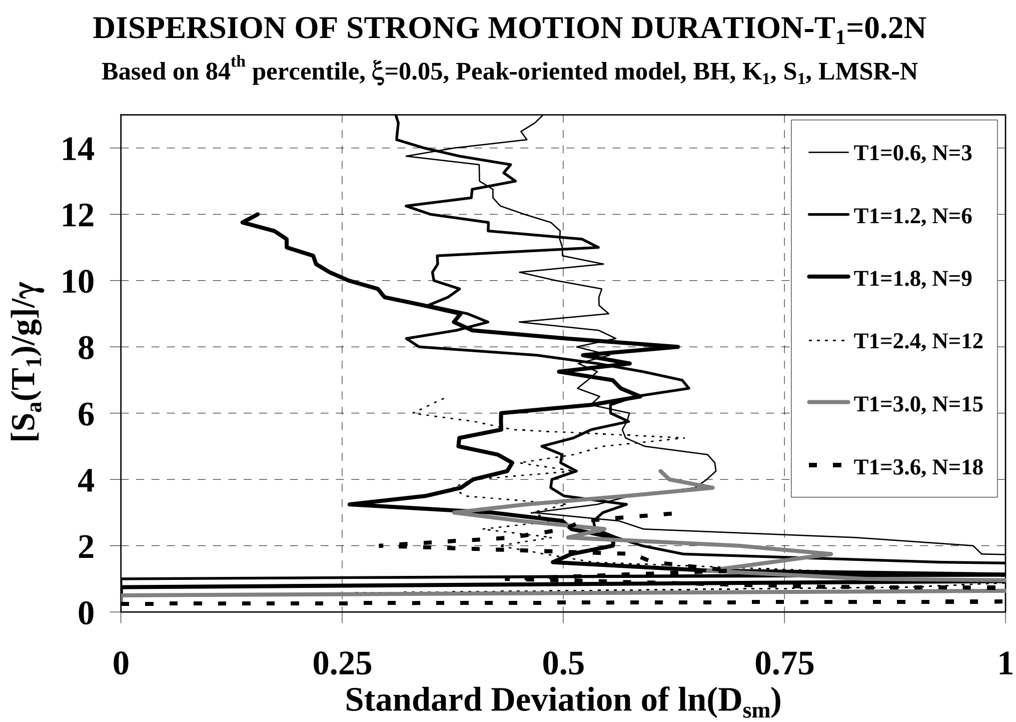

(b) T_1 = 0.2N

Figure 5.14 Dispersion of Strong Motion Duration Values, Stiff and Flexible Frames

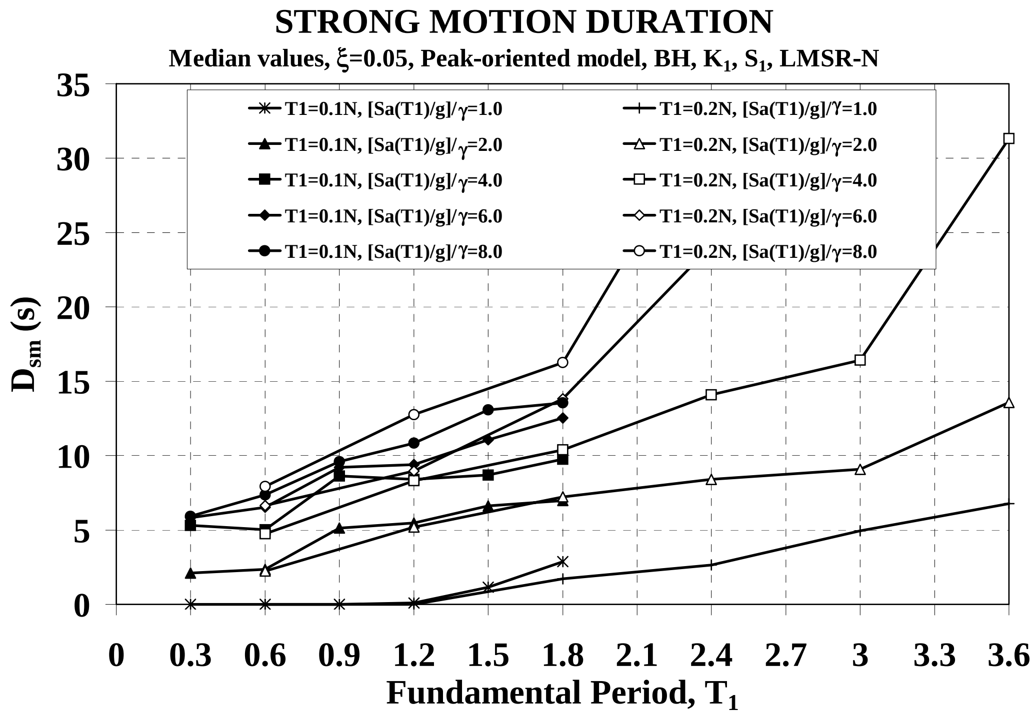

Figure 5.15 Dependence of Median Strong Motion Duration Values on the Fundamental Period, Various Relative Intensities, Stiff and Flexible Frames

6 Strength Demand Issues Relevant for Design

6.1 INTRODUCTION

Displacement-based methods of design are effective as long as the system has enough deformation (ductility) capacity to accommodate the demands imposed by earthquakes and enough strength to avoid brittle failure of components that are a critical part of the load path. Columns are critical elements in the gravity load path, so they have to be designed with sufficient strength to avoid brittle failure. Thus, the evaluation of strength demands becomes an important issue, for it provides information relevant for the design of critical elements, e.g., columns in a frame. This chapter deals with the evaluation of global and local strength demands. Global demands include story shear strength and story overturning moments, and local demands include column moments.

Story shear forces are relevant (particularly for reinforced concrete elements), for they relate to the sum of the shear forces in individual columns. Story overturning moments are important, since they can be translated into column compressive and tensile axial force demands, especially for the exterior columns of a frame. Axial loads can significantly affect the moment (and shear) capacity of a column, and hence, compromise the ability of a system to withstand the demands imposed by earthquakes. High tensile demands in columns located at the bottom story may also cause potential uplift problems in the foundation.

For the type of frames used in this project, which are designed according to the strong-column, weak-beam philosophy, columns can experience large moment demands leading to potential hinging in a real structure, which can lead to undesirable failure mechanisms. Columns must also be designed to accommodate plastic rotations, especially columns located at the base of a frame, which due to their boundary conditions, shear force and moment demands experience changes in the moment diagram leading to plastification at the bottom. Sufficient ductility must be provided in these cases.

This chapter focuses on the study of regular frames subjected to ordinary ground motions. Regular frames correspond to the basic cases described in Appendix A. The main objective is to provide a better understanding of the strength demands imposed by earthquakes and assess whether the pushover analysis technique is effective in detecting potential overload in columns. In order to evaluate strength demands, it is important to model damping effects properly (as discussed in Appendix A) to ensure that both dynamic and static equilibrium are satisfied at every time step in the solution.

6.2 GLOBAL STRENGTH DEMANDS

6.2.1 Story Shear Force Demands

Current seismic design methods are based on an estimate of the elastic story shear demand, which is then decreased based on a "strength reduction factor" (which is implicitly related to the ductility level) to estimate design story shear strengths. Quantification of the relationship between design story shear strength and the dynamic story shear demands becomes a relevant design issue because of the amplification of the static story shear strength due to redistribution of forces in the inelastic range of the response. In this context, story shear is defined as the sum of the shear forces experienced by columns in a story. In a static analysis it is equivalent to the sum of the horizontal loads applied to the building above the story under consideration.

Figure 6.1 presents information on the variation of median normalized maximum base shear demands with relative intensity, fundamental period, and number of stories. Maximum dynamic base shear forces are normalized by the static shear forces computed from a pushover analysis. The static shear forces are calculated at a global (roof) drift equal to the median global drift, given the relative intensity, corresponding to the median maximum dynamic base shear, given the same relative intensity. The median ratio of the dynamic base shear demands to the static base shear predicted by the pushover analysis increases with the relative intensity. The one exception is the short-period model in which higher modes are not significant and the ratio is independent of the relative intensity. For $T_1 \geq 0.6$ sec, given the relative intensity, the dynamic amplification of static base shear forces is not dependent on the fundamental period except for models that are sensitive to P-delta effects. Furthermore, given the fundamental period, models with different number of stories experience similar dynamic base shear amplifications.

In the inelastic range, differences between the dynamic story shears and the static one are due to the redistribution of forces that occur during a dynamic analysis. A displacement-controlled pushover analysis is unable to capture this redistribution, since the applied load pattern is fixed regardless of the level of deformation.

6.2.2 Story Overturning Moments

Story overturning moments (OTMs) discussed in this section correspond to the story overturning moments obtained from the axial force demands experienced by the columns in a given story, and *do not* include the moments in the columns. This definition of story overturning moments allows a direct comparison with the simplified story overturning moment capacity obtained from $\Sigma 2M_{pi}/L$ of the shear forces experienced by the beams times the distance between the two columns in the generic single-bay frames. For the base case of the family of regular single-bay frames used in this study, simultaneous plastic hinges occurs at the end of the beams, so $\Sigma 2M_{pi}/L$ is a reasonable estimate of the accumulated axial forces due to the maximum beam shear forces when simultaneous yielding occurs and strain-hardening and redistribution effects are ignored.

An important issue relevant for design is to determine whether the simplified $\Sigma 2M_{pi}/L$ estimate of maximum column axial loads needs to be de-amplified or amplified. Arguments in favor of de-amplification factors suggest that due to dynamic effects simultaneous yielding in all stories is unlikely to occur and strain-hardening effects are counteracted by the redistribution of forces, so there is no need for an amplification factor. However, for the basic regular frames used in this study, which have their story shear strengths tuned to a parabolic load pattern, time history analyses disclosed that simultaneous yielding is likely to occur, and story overturning moments are larger than the ones predicted by the $\Sigma 2M_{pi}/L$ estimate.

Median story overturning moments are shown in Figure 6.2 for frames with $N = 9$, $T_1 = 0.9$ sec and 1.8 sec along with story overturning moments computed based on the sum of plastic moments in beams. Story OTM values are normalized by the design base shear strength ($V_y = \gamma W$) multiplied by the total height of the frame, H. Thus, the normalized value at the first-story indicates the location of the resultant of the lateral loads corresponding to the design base shear strength (lever arm) that would produce the same overturning moment at the base. It can be seen that for the $T_1 = 0.9$ sec frame, for $[S_a(T_1)/g]/\gamma \geq 2$, median story OTM demands are greater than or equal to the overturning moments based on the sum of plastic moments in beams. For $[S_a(T_1)/g]/\gamma = 2$ and 4, the $T_1 = 1.8$ sec frame exhibits story OTM amplifications with respect to $\Sigma 2M_{pi}/L$ that occur at the top and mid-stories whereas small de-amplifications are observed at the bottom stories due to the presence of significant higher modes in the response. However, for $[S_a(T_1)/g]/\gamma \geq 6$ an amplification of median story OTMs with respect to $\Sigma 2M_{pi}/L$ is observed over the full height of the structure.

Figure 6.3 presents data on the OTM amplification and de-amplification with respect to $\Sigma 2M_{pi}/L$ at the base of the frames and its variation with the relative intensity level, period, and number of stories. Figure 6.3(a) depicts median results for the $T_1 = 0.1N$ frames and Figure 6.3(b) for the $T_1 = 0.2N$ frames. The amplification of OTM at the base with respect to $\Sigma 2M_{pi}/L$ tends to increase with the relative intensity and decrease with an increase in the fundamental period. For instance, when $[S_a(T_1)/g]/\gamma$ is relatively small and T_1 is long, the maximum OTM at the base can be less than the one computed based on $\Sigma 2M_{pi}/L$. This behavior is observed because for small relative intensities, higher modes translates into redistribution of forces that cause floor loads to act in opposite directions, hence reducing the maximum story overturning moment at the base with respect to $\Sigma 2M_{pi}/L$.

The largest amplifications of dynamic OTM at the base with respect to $\Sigma 2M_{pi}/L$ are observed in the short-period range ($T_1 = 0.3$ sec) because simultaneous yielding occurs and this type of frame experiences larger story ductility demands and therefore greater strain-hardening effects.

6.3 LOCAL STRENGTH DEMANDS

6.3.1 Moments at the Ends of Columns

Current seismic design practice establishes that at any given connection the sum of the moment capacity of the columns should be greater than the sum of the moment capacity of the beams (or panel zone in the case of steel, AISC Seismic Provisions, 1997). For reinforced concrete members framing into a joint, $\Sigma M_c > (6/5)\Sigma M_g$ (ACI 318-99, Section 21.4.2.2), where ΣM_c is the sum of the moment capacity of the columns framing into the joint and ΣM_g is the sum of the moment capacity of the beams.

The regular frames used in this study are designed so that columns are infinitely strong (except at the bottom of the first story), which permits a direct assessment of the required strength to avoid plastic hinging in columns. Figure 6.4 shows the maximum "strong column factor" (SCF) over the height for the N = 9 frames. The maximum SCF, $(2M_c/M_{p,b})_{s,max}$, is the ratio of the maximum moment demand of a column in a connection normalized by one half the plastic moment of the beam framing into the joint (a factor of one half is used to replicate the condition of an interior joint [except at the top floor where a factor of one is utilized]). In the range of primary interest, $[S_a(T_1)/g]/\gamma$ up to about 8, median SCFs in the order of 3 or more are obtained. Thus, for frames designed according to the strong-column, weak-beam philosophy, the potential for column plastic hinging exists even when the sum of the moment capacity of the columns framing into a joint is as high as 3 to 4 times the sum of the moment capacity of the beams.

Figure 6.5 presents median values of the maximum SCF over the height for all frames for various relative intensity levels. It can be observed that there is a linear increase in the median maximum SCF with the intensity level, which is also observed in Figure 6.5 for the N = 9 frames. Except for the short-period frame (T_1 = 0.3 sec), for any given relative intensity, the median maximum SCF increases with the value of the fundamental period due to the presence of higher mode effects in the response (this issue will be further discussed in the following paragraphs). Given the period and the relative intensity level, differences in the number of stories do not have a significant effect on the median maximum SCF, so its value is dominated by the fundamental period rather than the number of stories.

The distribution of the maximum SCF over the height is important, for it provides insight into the mechanism that causes elastic columns to experience such large moment demands. Figures 6.6–6.9 show median maximum SCF profiles for frames with T_1 = 0.6 sec, 1.2 sec, and 1.8 sec. It can be seen that the maximum SCF occurs near the top of the frame for small levels of inelastic behavior, but as the relative intensity level increases, the distribution over the height of SCFs is rather uniform. It is important to note that even for $[S_a(T_1)/g]/\gamma = 1$, there are median maximum SCF greater than one for frames with N = 9, 12, 15 and 18. For $[S_a(T_1)/g]/\gamma = 2$ all systems show median maximum SCF greater than one. For a given intensity level and a given period, even when the maximum SCF over the height is similar for both the stiff and the flexible frame, the distribution of SCFs over the height is more uniform for the flexible frame because the stiffer frame (more stories) experiences larger higher mode effects.

In order to understand the seismic behavior that leads to large values of SCF in the family of regular frames used in this study, the N = 9, $T_1 = 1.8$ sec frame subjected to the LP89agw ground motion is used for illustration. The intensity level of interest is $[S_a(T_1)/g]/\gamma = 6$ and the maximum SCF factor, which occurs at the 4^{th} floor level is 3.24. Figure 6.10 depicts the variation with time of the 4^{th} floor SCF for this case. In several instances during the time history SCFs greater than 2 are observed and the maximum (3.24) occurs at approximately 15 sec. Figure 6.11 shows the deformed shape of the frame at 15 sec, normalized by the roof displacement, as well as the deformed shape from a pushover analysis (based on a parabolic load pattern) at the same roof drift angle. The deformed shape from the time history analysis at 15 sec shows global bending which is not dominated by the first mode. At this instant in time the response is a combination of the first and second modes. Thus, the second mode causes global bending that leads to redistribution of forces, and hence, the movement of the point of inflection in the columns causing some of them to bend in a single curvature mode as observed in Figure 6.12. Figure 6.12 shows the maximum moments at the end of the 3^{rd} and 4^{th} story columns normalized by the plastic moment of the beam at the 4^{th} floor at t = 15 sec. Both the 3^{rd} and 4^{th} story columns are in single curvature (moments at top and bottom have equal signs) due to the presence of the second mode in the response, causing large moment demands at the ends of the column. These observations are in agreement with results presented in Nakashima and Sawaizumi (2002) and Bondy (1996).

Both Figure 6.11 and Figure 6.12 show the results from a pushover analysis in which the roof drift angle is the same as the roof drift angle the structure experiences under the LP89agw ground motion at 15 sec. Neither the deformed shape nor the column moment diagrams from the pushover analysis are able to capture the behavior of the frame at the given roof drift angle. This result is not surprising because the displacement-controlled pushover analysis is based on a fixed load pattern, and the effect of the second mode in the response and the corresponding redistribution of forces are not captured.

6.3.2 Moments at the Midheights of Columns

Moments at the midheights of columns are important in steel structures due to the presence of column splices near the middle of a column. For the case of reinforced concrete structures, they are important when precast concrete columns are used and also at rebar splice locations in conventional reinforced concrete columns. Section 6.3.1 shows that the effect of the second mode and redistribution of forces cause the inflection point in columns to move from near the midheight of a column (for elastic behavior) to one of its ends, and in some cases, causes the column to undergo single curvature. Therefore, potentially large moment demands are expected at the midheights of columns, which, combined with the high column axial force demands due to OTM (Section 6.2.2), can cause splices to experience large states of stress.

Figures 6.13–6.16 show median profiles of the maximum moment at the center of a column, $M_{c,mid}$, normalized by one half the average of the plastic moments of the beams in the floors that bound that particular story (for the bottom story it is normalized by one half the plastic moment of the second floor beam). As in the case of the SCFs, the factor of one half is used to replicate the condition of an interior joint. For the basic family of regular frames used in this study, values of M_p of the beams that bound a story are similar, since the strength of the system is tuned to a parabolic load pattern. Results are shown for frames with T_1 = 0.6 sec, 1.2 sec, and 1.8 sec. and different levels of inelastic behavior. Normalized $M_{c,mid}$ values increase strongly with the relative intensity level, and their distribution over the height is similar to the one observed for the maximum SCFs (Figures 6.6-6.9) especially at levels where both quantities (SCF and the normalized $M_{c,mid}$) are maximum. This last observation is expected, since there is a correlation between the maximum column moment at one end (which is used to compute the SCF) and the maximum moment at the midheight of the column due to changes in the moment diagram, which in some cases exhibits a condition of single curvature (Figure 6.12).

The results shown in Figures 6.13–6.16 demonstrate that for the type of regular frames used in this study, which are subjected to ordinary ground motions, the assumption of small column moments near the center of the column is not valid once the system undergoes large levels of inelastic deformation. The moment diagram of a column changes as forces redistribute, forcing the point of inflection of some columns to move toward one end and in some cases cause the column to bend in single curvature.

6.3.3 Plastic Rotations at the Bottoms of the First-Story Columns

The objective of this section is to provide statistical information on the magnitude of column plastic rotation demands at the bottom of the first story and the uncertainties associated with them for the family of generic frames used in this study. Basic statistical data on maximum plastic rotation demands at the bottoms of the first-story columns are presented in Figures 6.17 and 6.18 for the $T_1 = 0.1N$ and $T_1 = 0.2N$ frames, respectively. The maximum plastic rotation at the bottom of the columns, $\theta_{pc1,max}$, is normalized by the column yield rotation at the base. It can be observed that for a given relative intensity level, median normalized $\theta_{pc1,max}$ demands increase with the fundamental period of the system. For the case of P-delta-sensitive systems ($T_1 = 0.2N$ and N = 12, 15, and 18) a small increase in intensity causes a large increase in normalized $\theta_{pc1,max}$ demands because of the amplification of the first-story drift. In addition, the median values shown in Figures 6.17(a) and 6.18(a) suggest that the bases of the columns are expected to undergo severe levels of inelastic deformation, so they must be designed with sufficient ductility capacity. It is important to note that the dispersion associated with the normalized $\theta_{pc1,max}$ demands is large (greater than 0.5), especially for small relative intensity levels due to the fact that in this range, the first-story columns remain elastic (zero plastic rotation) or experience small levels of inelastic behavior when the model is subjected to some of the ground motion records.

A comprehensive assessment of median normalized $\theta_{pc1,max}$ demands can be obtained from the data presented in Figure 6.19. It can be seen that for a given relative intensity level, the median normalized $\theta_{pc1,max}$ demands increase with the value of the fundamental period, except in the short-period range where larger demands are observed. The fact that the short-period frame (T_1 = 0.3 sec) experiences large demands is in agreement with observations presented in Chapter 4 that for a given relative intensity the short-period frame undergoes larger ductility demands. Another relevant observation is that given the period, taller structures experience larger median normalized $\theta_{pc1,max}$ demands, which is also in agreement with results discussed in Chapter 4 where the same behavior was observed for the maximum story ductility demands (Figure 4.38). In these cases, higher mode effects cause the taller structures to experience larger levels of inelastic behavior.

6.4 SUMMARY

The results presented in this section are for nondeteriorating regular moment-resisting frames, modeled based on centerline dimensions, whose story strengths are tuned to a parabolic load pattern and which are subjected to ordinary ground motions. The main emphasis is on strength demands that could jeopardize the integrity of the columns in frames, leading to potential brittle modes of failure. A summary of the main conclusion drawn from this chapter is presented next:

- For inelastic structures, amplification of the maximum dynamic base shear force with respect to the static base shear strength occurs because of redistribution of loads during a dynamic analysis and tends to increase with the relative intensity. The one exception is the short-period model (T1 = 0.3 sec) in which higher mode effects are not significant and the ratio of dynamic to static shear force is weakly dependent on the relative intensity. For T1 > 0.6 sec, given the relative intensity, the dynamic amplification of static base shear forces is weakly dependent on the fundamental period except for flexible frames sensitive to P-delta effects. Moreover, given the fundamental period, frames with different number of stories experience similar dynamic base shear amplifications. For the range of inelastic behavior of interest in this study, in which ductility levels are not so large that they cause significant cyclic deterioration in the components of the structural system, amplification of median static story strength demands in the order of 50% can be expected.
- For regular frame structures with story shear strengths tuned to a code-specified load pattern, simultaneous yielding in all stories is likely to occur during their nonlinear dynamic response, and a reduction of the story overturning moments based on $\Sigma 2M_{pi}/L$ is not justified, especially at medium and large relative intensity levels.
- The amplification of OTM at the base with respect to $\Sigma 2M_{pi}/L$ tends to increase with the relative intensity and decrease with the fundamental period. This behavior is observed because as the period becomes longer, higher modes translate into redistribution of forces

that cause floor loads to act in opposite directions, hence reducing the maximum story overturning moment at the base with respect to $\Sigma 2M_{pi}/L$.

- The largest amplifications of dynamic OTM at the base with respect to $\Sigma 2M_{pi}/L$ are observed in the short-period range (T_1 = 0.3 sec) because simultaneous yielding occurs and this type of frame experiences larger story ductility demands and therefore greater strain-hardening effects.
- Higher modes (particularly the second mode) and dynamic redistribution of forces cause the point of inflection in some columns to move from near the midheight of a column (for elastic behavior) to one of its ends, which in some cases produces a condition of single curvature in a column. This behavior is not appropriately captured by a pushover analysis based on a predefined load pattern since the effects of higher modes and dynamic redistribution are not incorporated.
- Large moments at the end of columns translate into strong column factors (SCFs) that increase almost linearly with the level of inelastic behavior. Except for the short-period frame, T_1 = 0.3 sec, which exhibits larger SCFs, SCFs increase with increasing fundamental period. Median strong column factors of 3 and larger are observed in the range of intensity levels of interest for nondeteriorating frames. Thus, the potential of plastic hinging in columns is high for regular frames designed according to the strong-column, weak-beam requirements of current code provisions, which in the United States require strong column factors greater than or equal to 1.0 for steel, and 1.2 for reinforced concrete frames.
- For low levels of inelastic behavior and frames with $N \geq 6$, maximum SCFs occur at the top stories, whereas at high levels of inelastic behavior maximum SCFs remain rather constant over the height.
- The behavior pattern that leads to large SCF in the dynamic response of regular frames also leads to large moments at the midheights of columns. These large moments are important especially for steel structures where splices are located near the center of columns in a story. A design based on the assumption of a point of inflection near the midheight of the column is not appropriate once the structure experiences large levels of inelastic behavior.
- The distribution over the height of normalized maximum moments at the midheight of a column follows patterns similar to those of the maximum SCFs, especially in portions of the structure where SCFs are the largest.

- Plastic rotations at the bases of the first-story columns can be very large. These large demands are due to the amplification of displacements experienced by short-period structures and the concentration of the amplification of the maximum story ductility at the bottom story due to structure P-delta effects for long-period structures.
- Median normalized $\theta_{pc1,max}$ demands tend to increase linearly with the level of inelastic behavior except for the T_1 = 0.3 sec and the P-delta-sensitive frames where they tend to increase at a higher rate. For $T_1 \geq 0.6$ sec median $\theta_{pc1,max}$ demands increase with increasing period, and for a fixed period taller frames experience larger demands due to the presence of higher mode effects.
- Dispersions in normalized $\theta_{pc1,max}$ are large, in the order of 0.5 or more especially for small intensity levels where some ordinary records do not cause the first-story columns to undergo inelastic deformations, and for P-delta-sensitive frames where the dispersion grows once the systems approach the onset of dynamic instability.

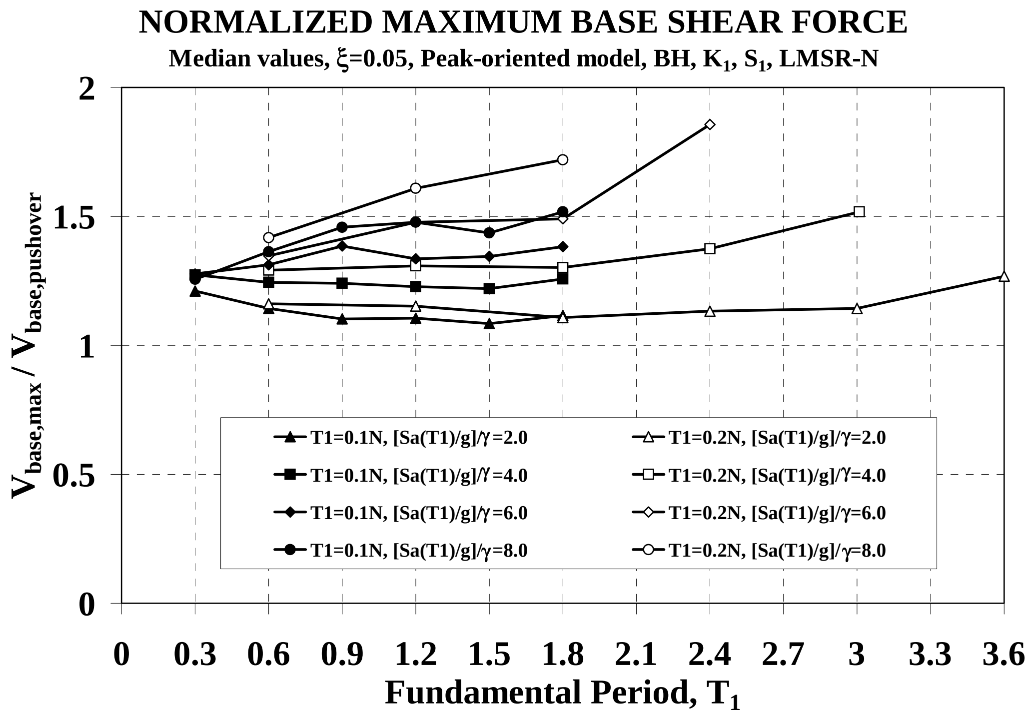

Figure 6.1 Dynamic Base Shear Amplification, All Frames, Various Relative Intensities

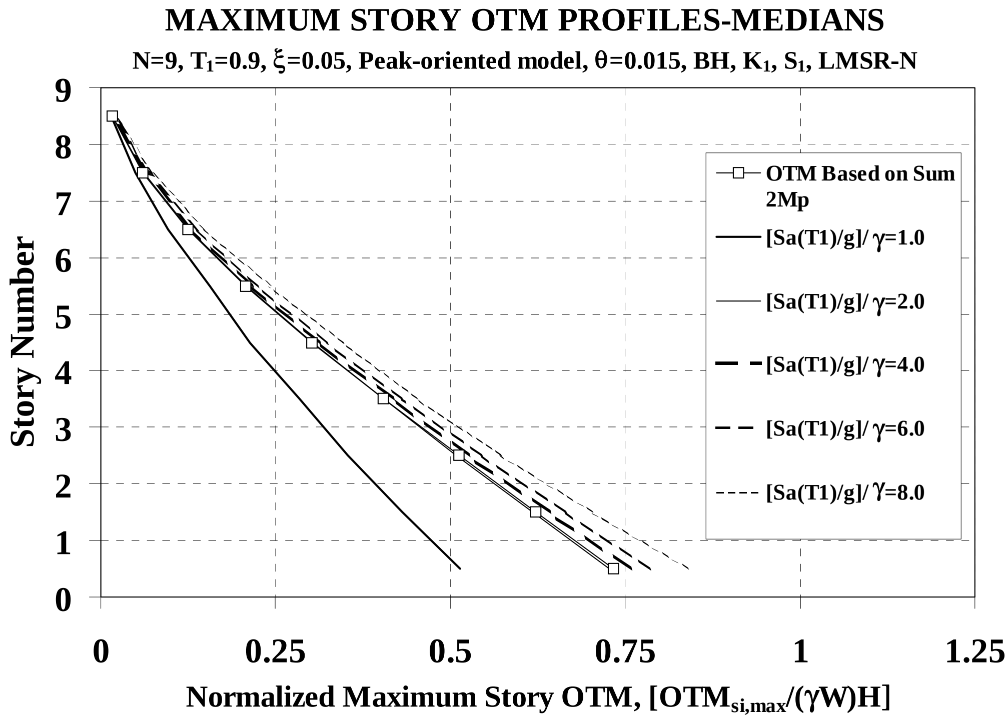

(a) T_1 = 0.9 sec

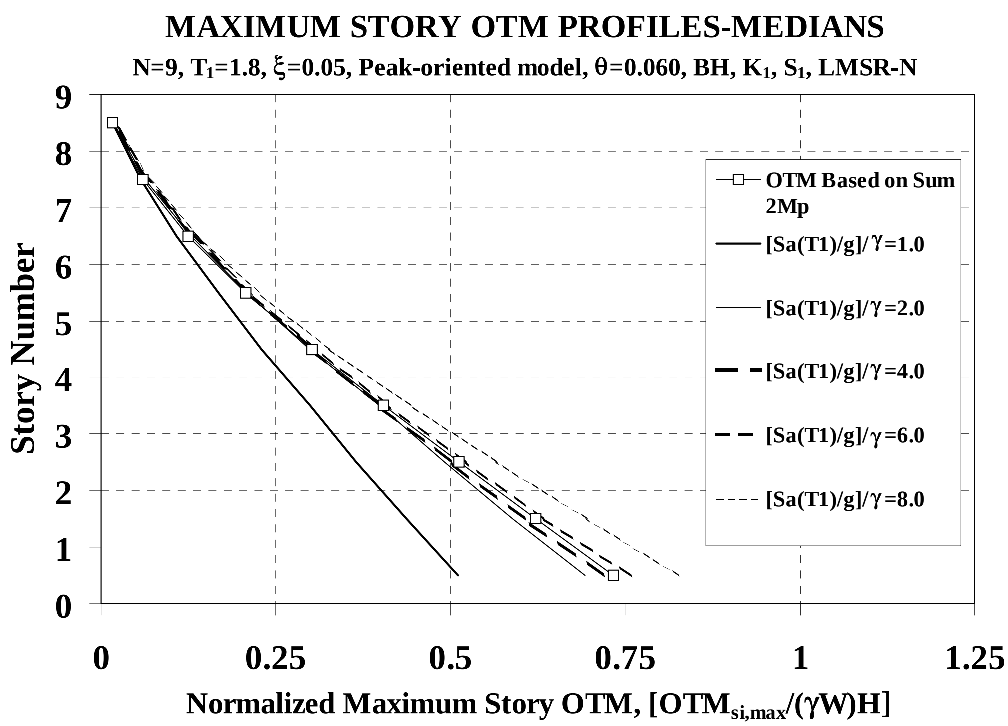

(b) T_1 = 1.8 sec

Figure 6.2 Normalized Maximum Story Overturning Moments, N = 9, Various Relative Intensities

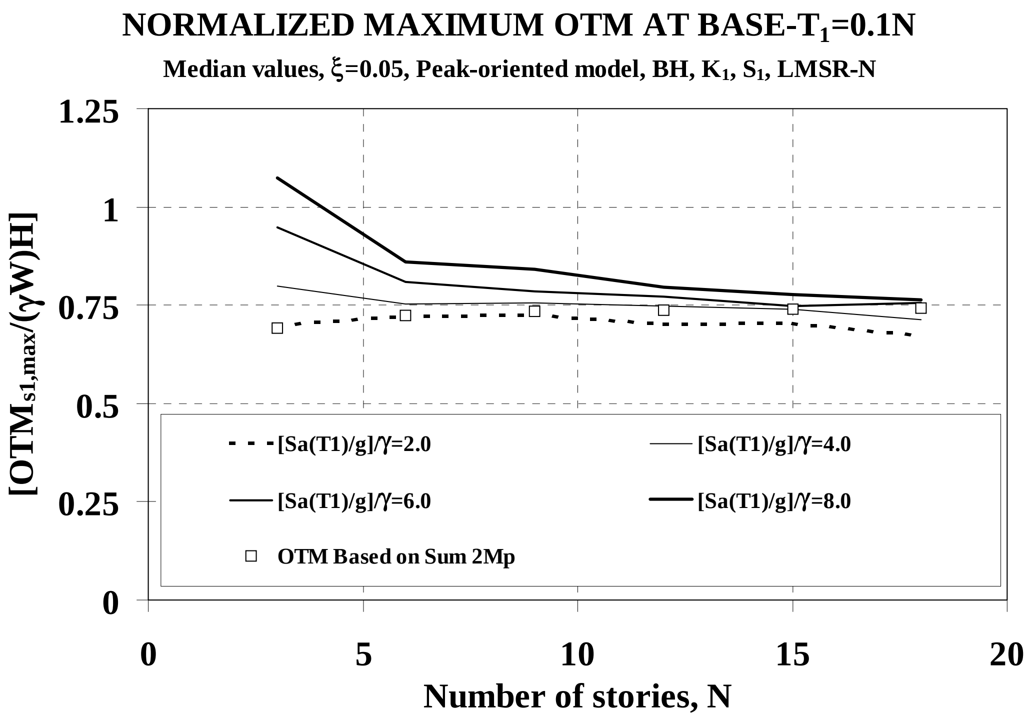

(a) $T_1 = 0.1N$

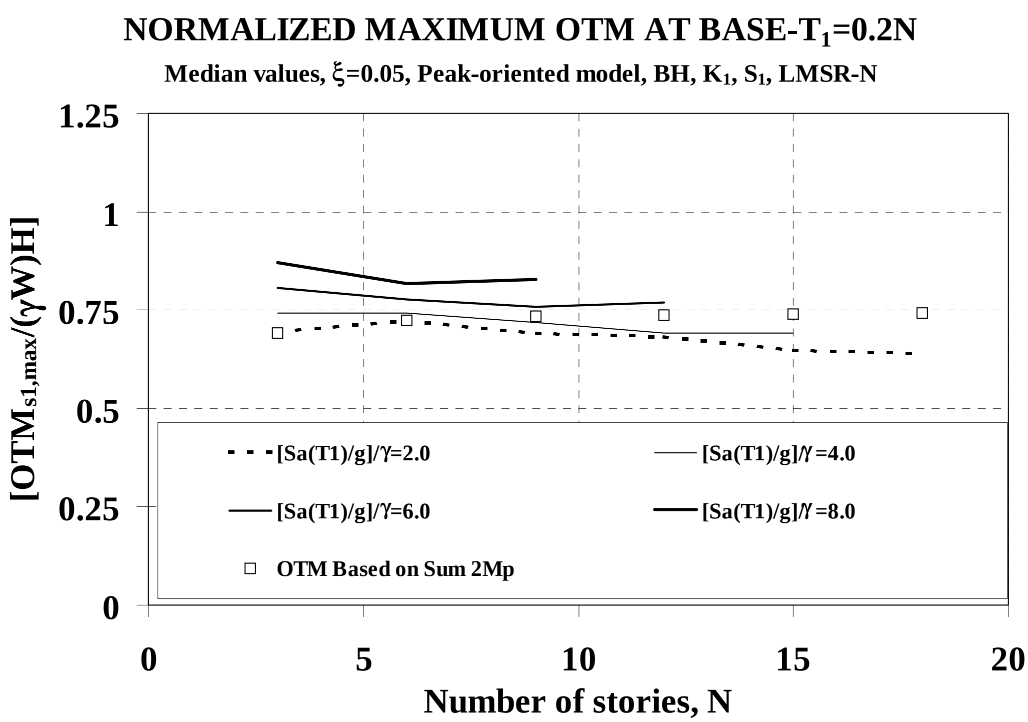

(b) $T_1 = 0.2N$

Figure 6.3 Normalized Maximum OTM at the Base, Stiff and Flexible Frames, Various Stiffnesses

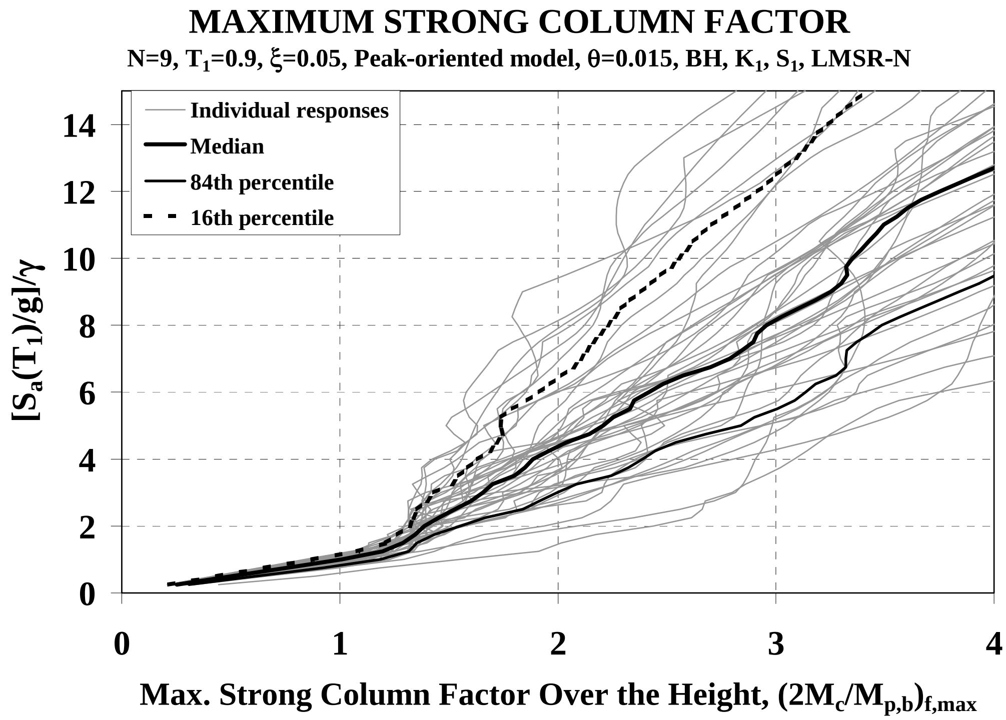

(a) $T_1 = 0.9$ sec

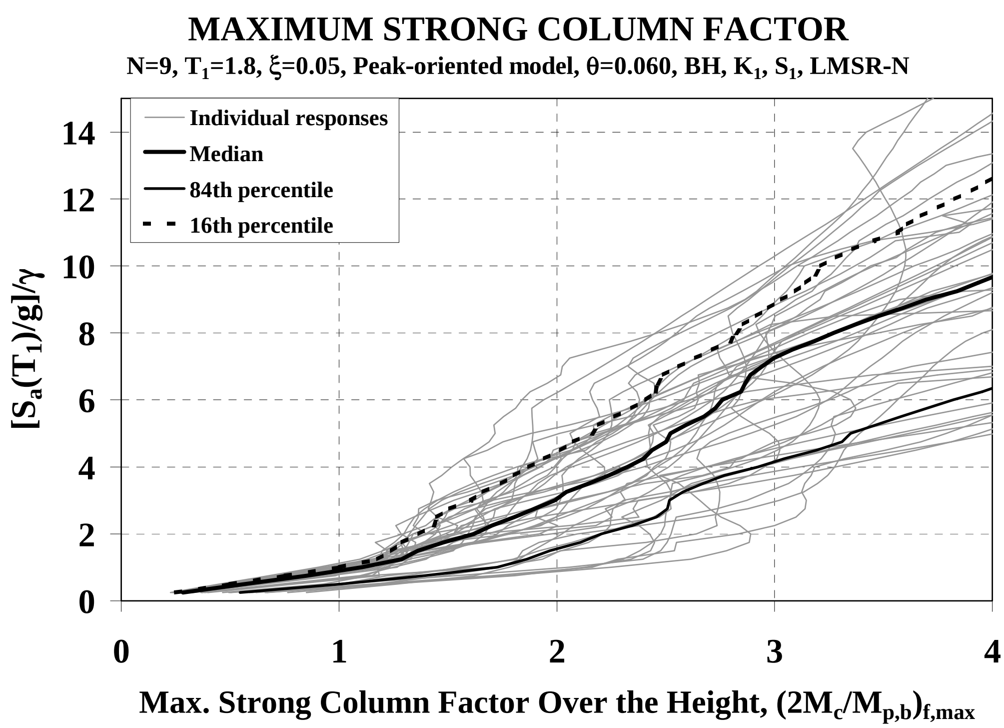

(b) $T_1 = 1.8$ sec

Figure 6.4 Maximum Strong Column Factor over the Height, N = 9

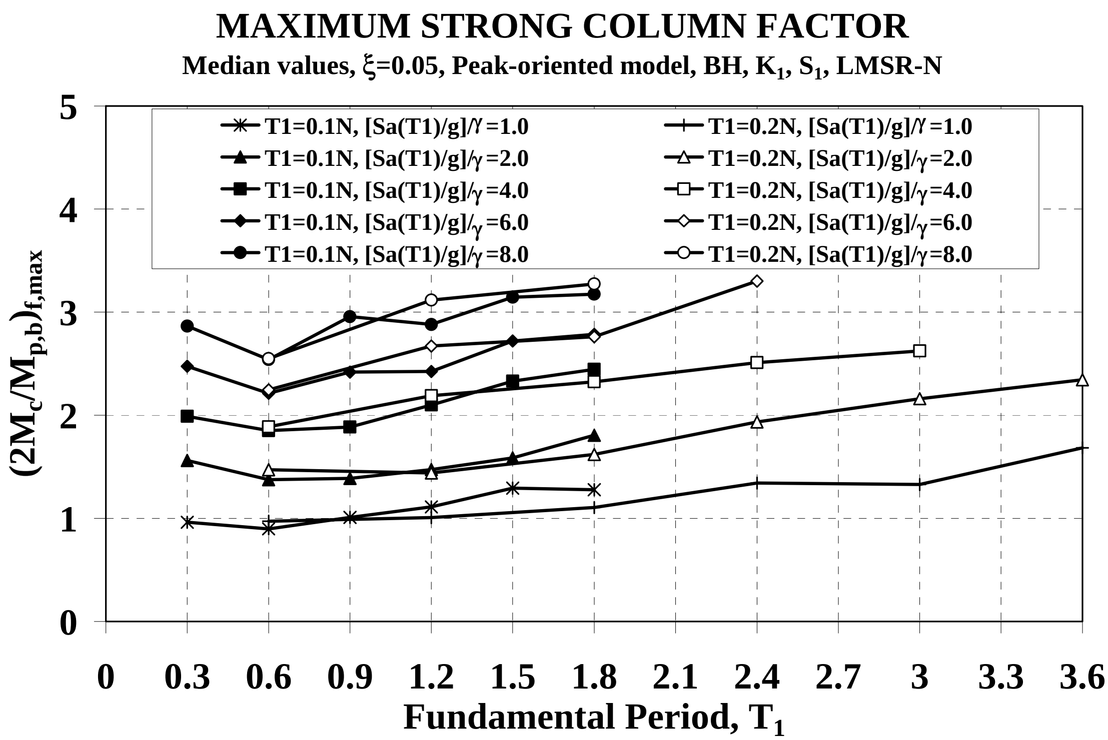

Figure 6.5 Maximum Strong Column Factor over the Height, All Frames, Various Relative Intensities

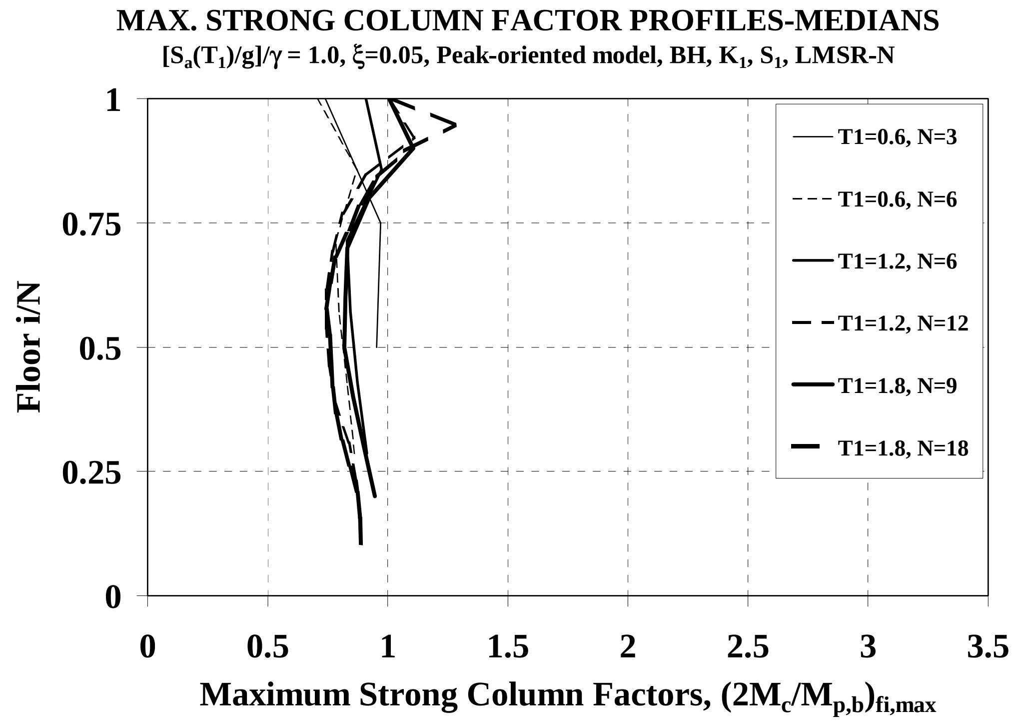

Figure 6.6 Distribution of Maximum Strong Column Factors over the Height, $[S_a(T_1)/g]/\gamma = 1.0$

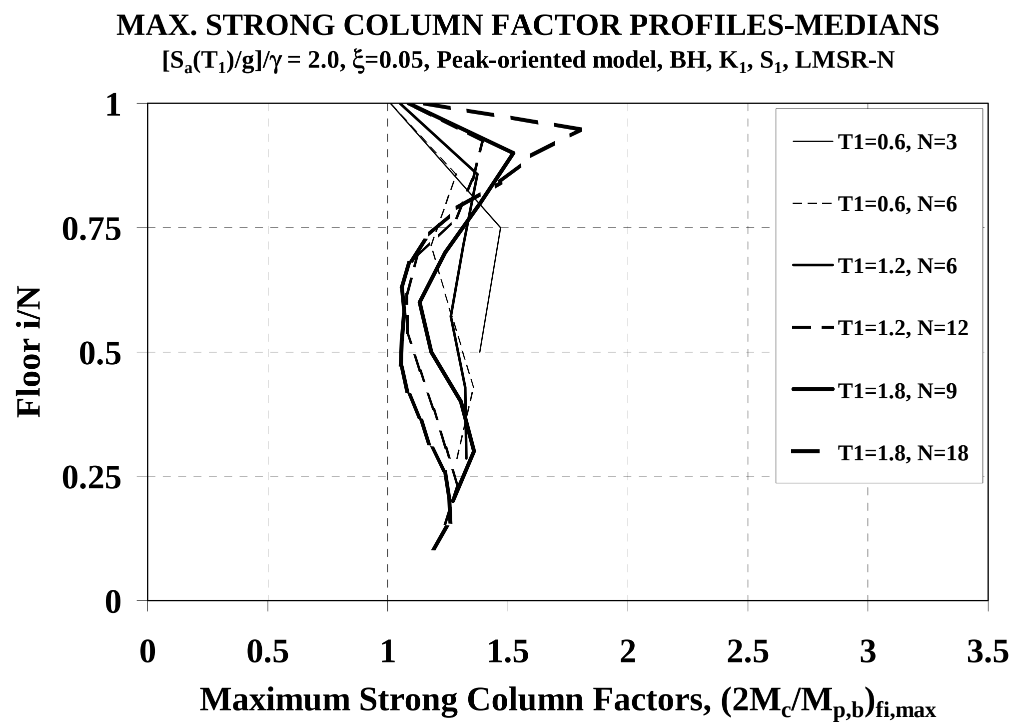

Figure 6.7 Distribution of Maximum Strong Column Factors over the Height, $[S_a(T_1)/g]/\gamma = 2.0$

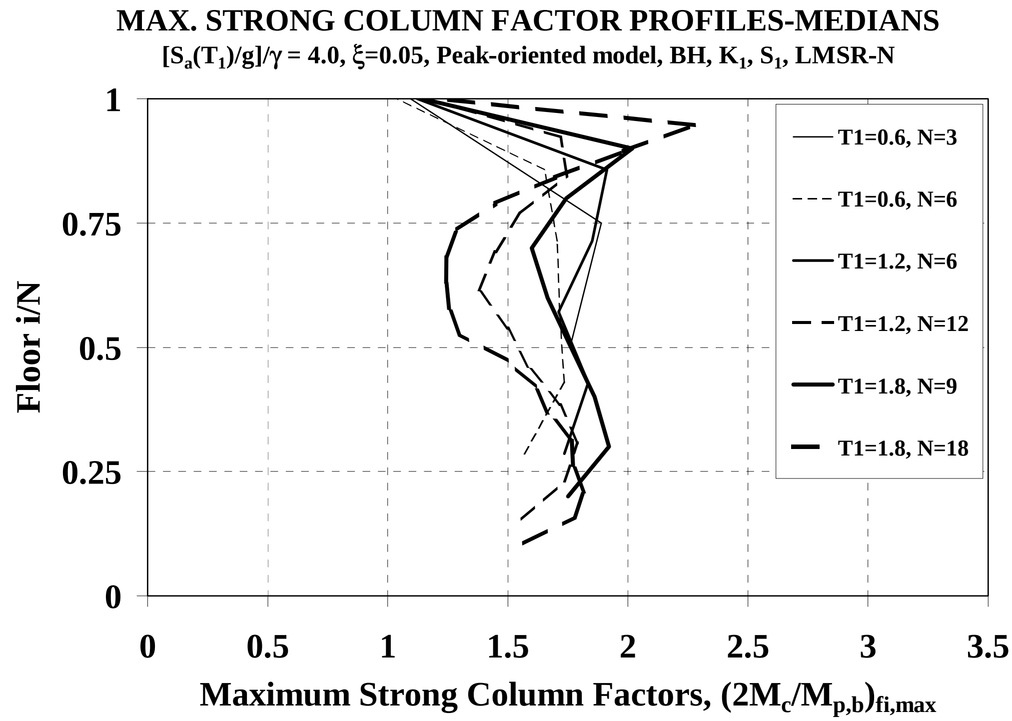

Figure 6.8 Distribution of Maximum Strong Column Factors over the Height, $[S_a(T_1)/g]/\gamma = 4.0$

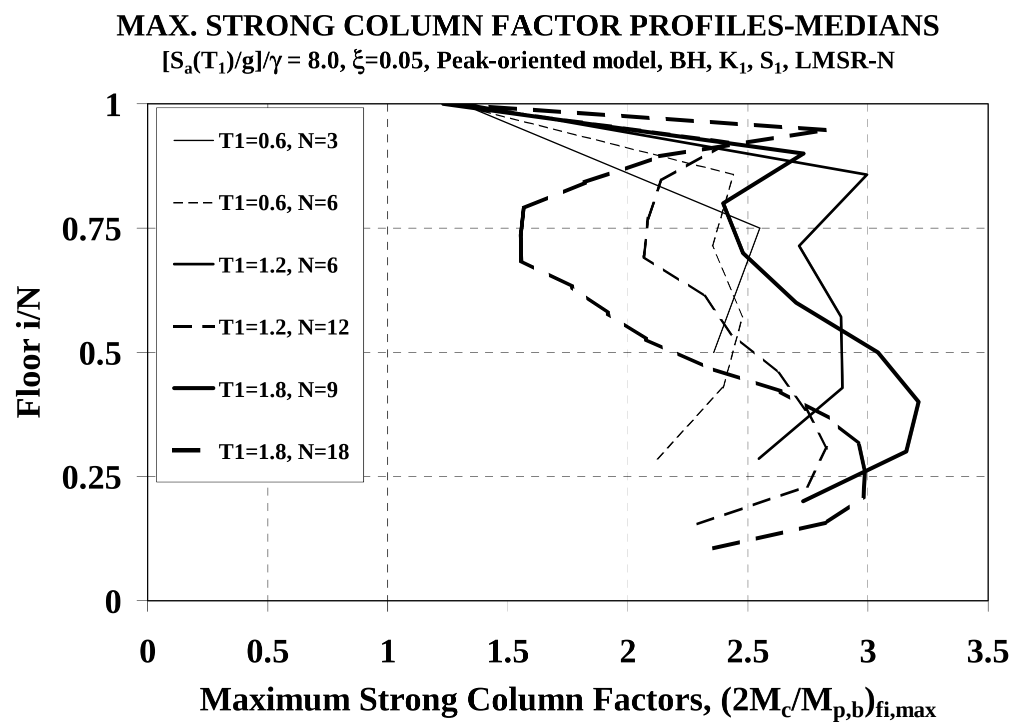

Figure 6.9 Distribution of Maximum Strong Column Factors over the Height, $[S_a(T_1)/g]/\gamma = 8.0$

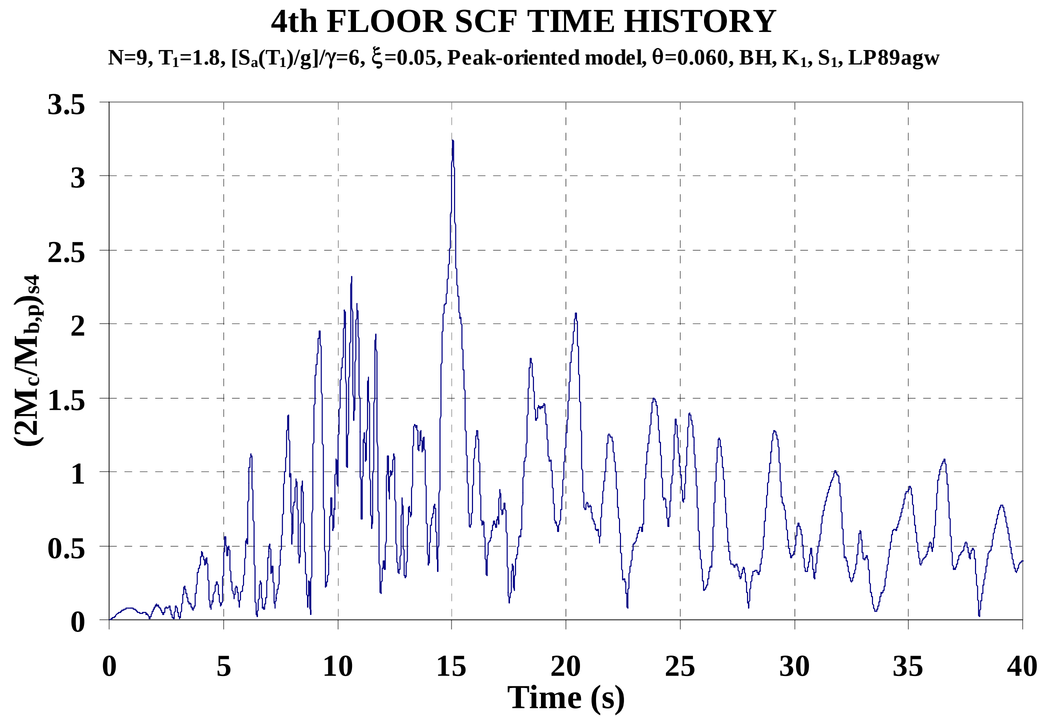

Figure 6.10 4[th] Floor SCF Time History, N = 9, T_1 = 1.8 sec, $[S_a(T_1)/g]/\gamma$ = 6.0, LP89agw

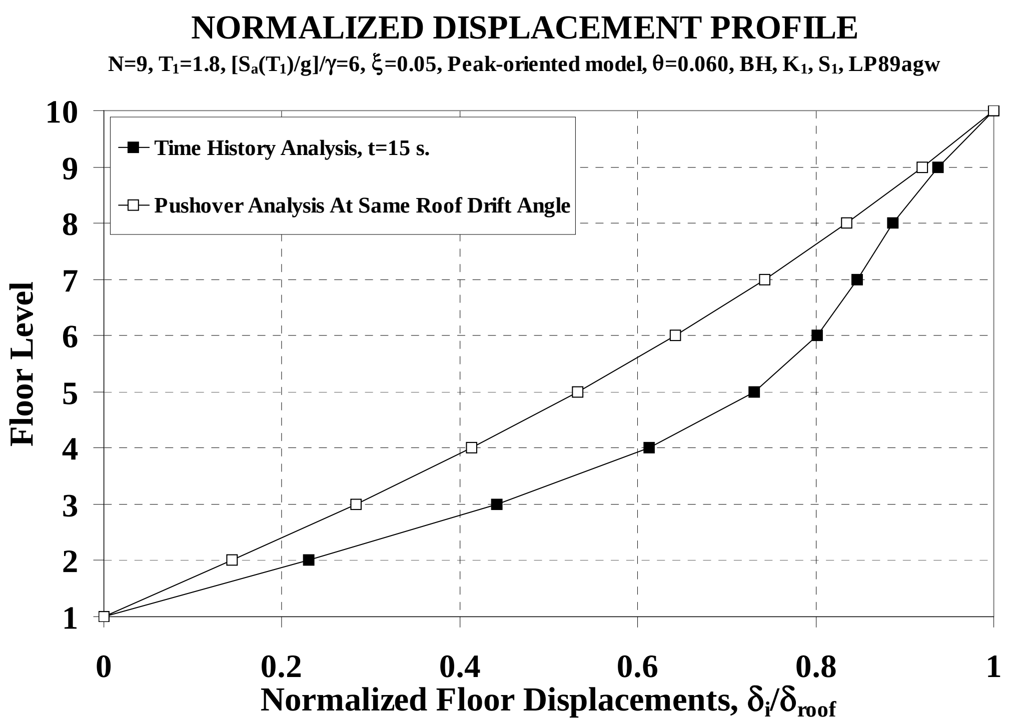

Figure 6.11 Normalized Displacement Profile at t = 15 sec, N = 9, T_1 = 1.8 sec, $[S_a(T_1)/g]/\gamma$ = 6.0, LP89agw

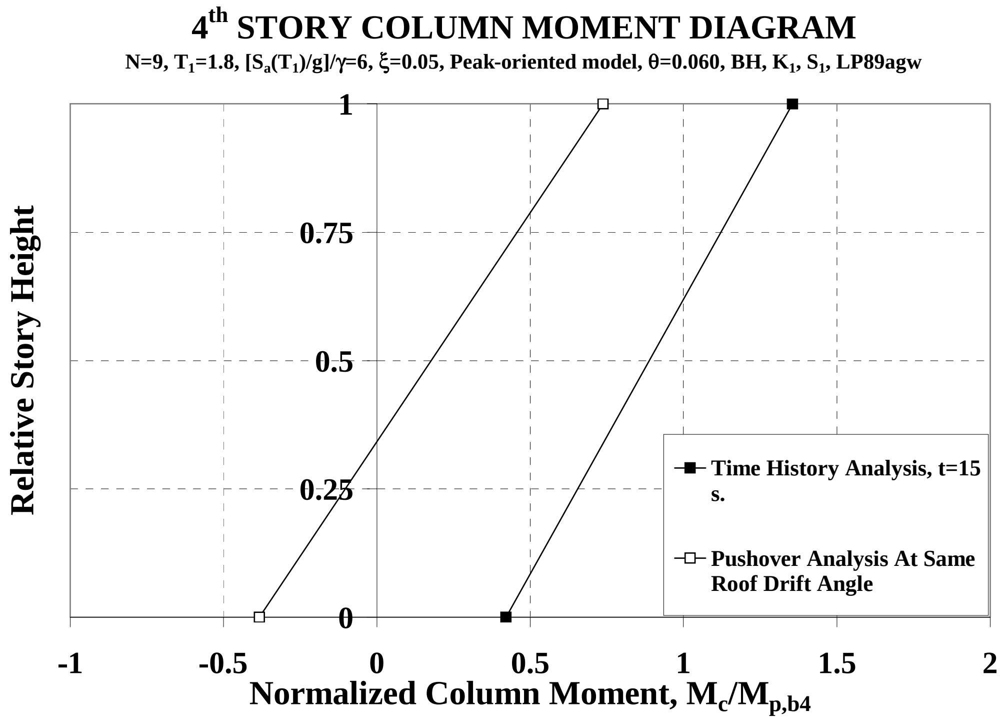

(a) 4th Story Column

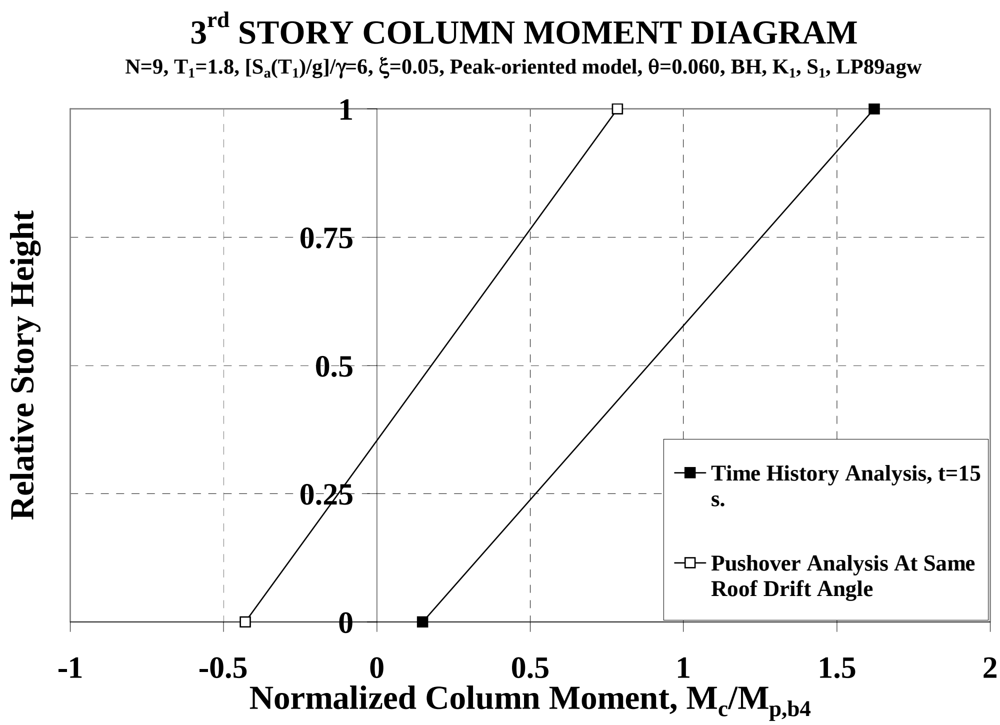

(b) 3rd Story Column

Figure 6.12 Normalized Column Moment Diagrams for a 4th and 3rd Story Column at t = 15 sec, N = 9, T_1 = 1.8 sec, $[S_a(T_1)/g]/\gamma$ = 6.0, LP89agw

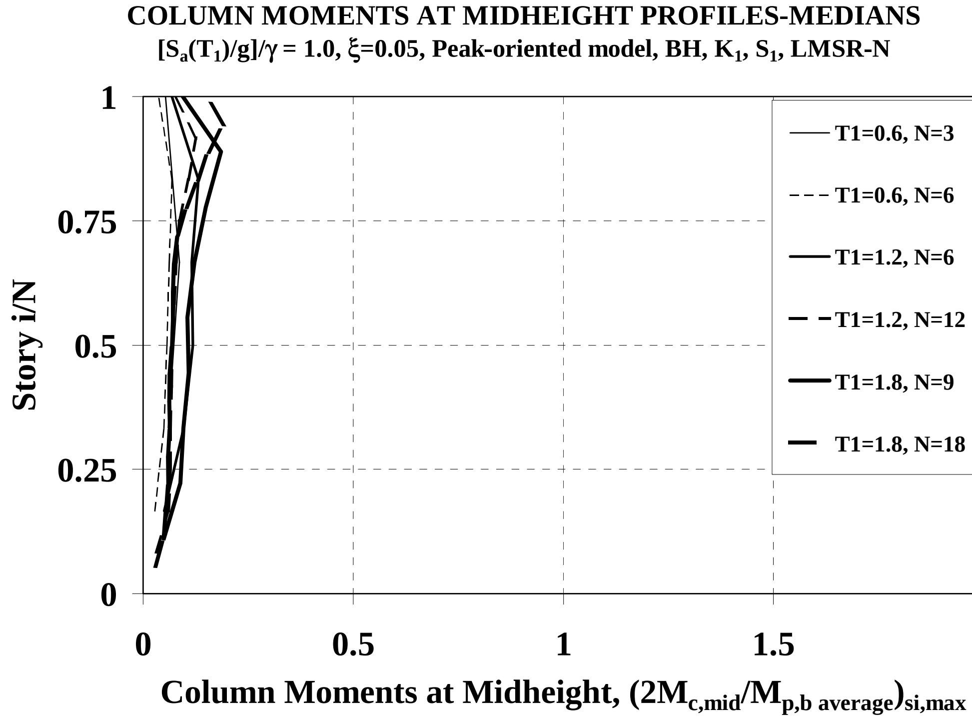

Figure 6.13 Distribution over the Height of Normalized Maximum Column Moments at Midheight, $[S_a(T_1)/g]/\gamma = 1.0$

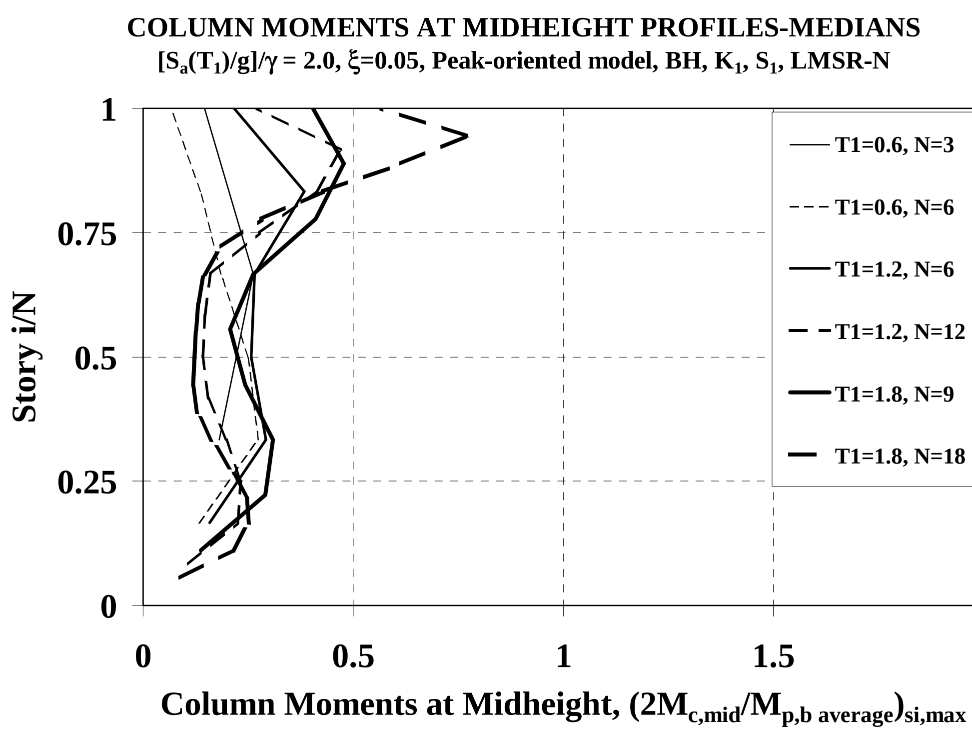

Figure 6.14 Distribution over the Height of Normalized Maximum Column Moments at Midheight, $[S_a(T_1)/g]/\gamma = 2.0$

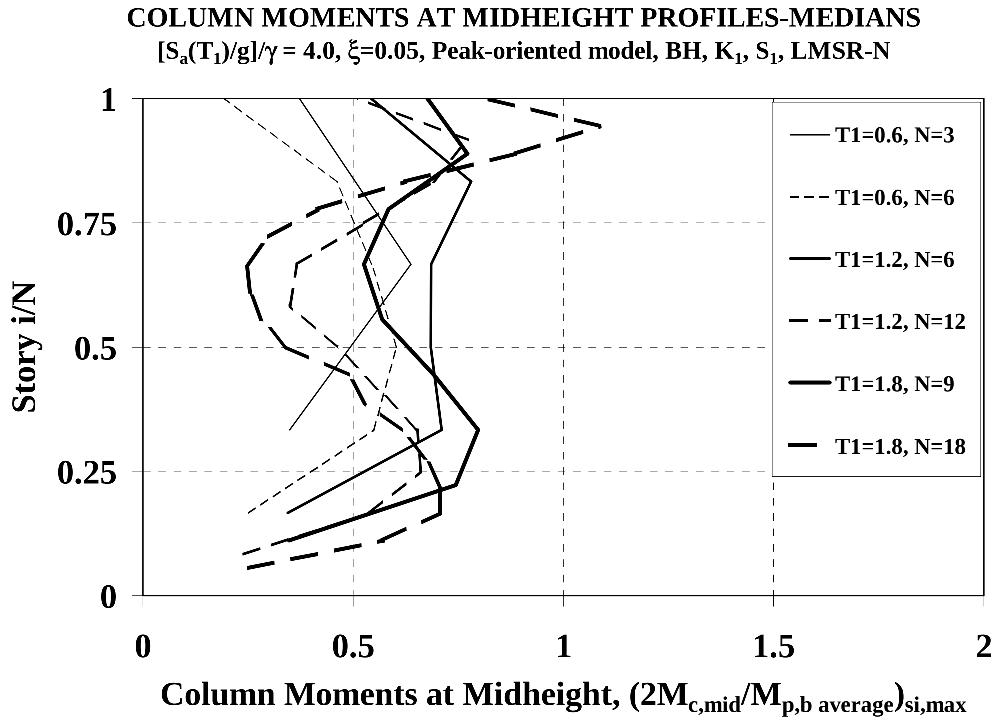

Figure 6.15 Distribution over the Height of Normalized Maximum Column Moments at Midheight, [$S_a(T_1)$/g]/γ = 4.0

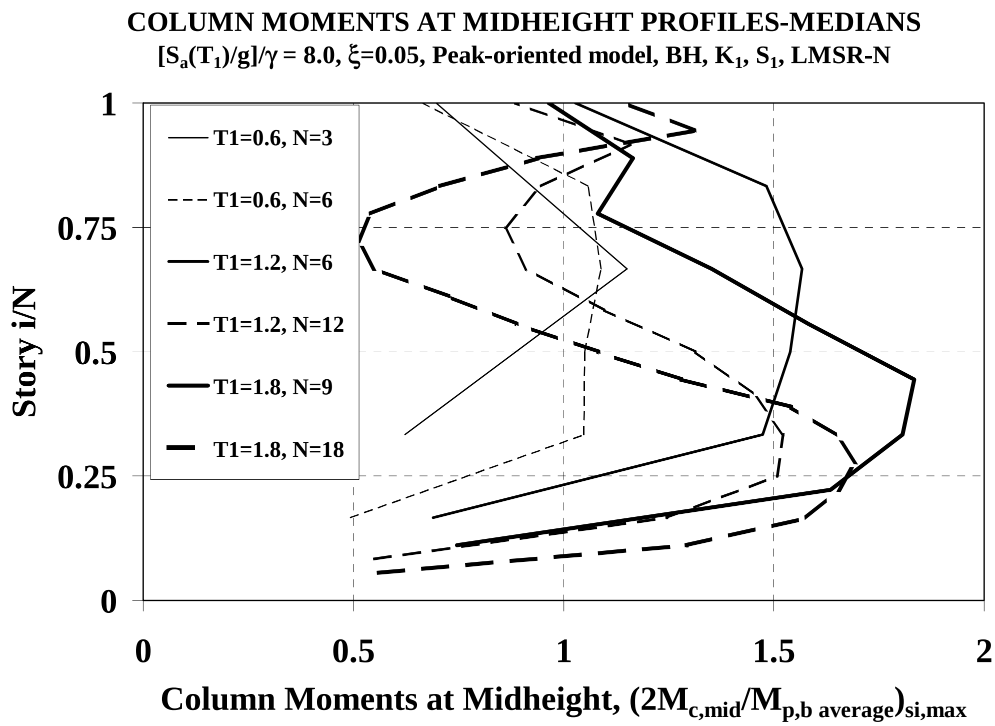

Figure 6.16 Distribution over the Height of Normalized Maximum Column Moments at Midheight, [$S_a(T_1)$/g]/γ = 8.0

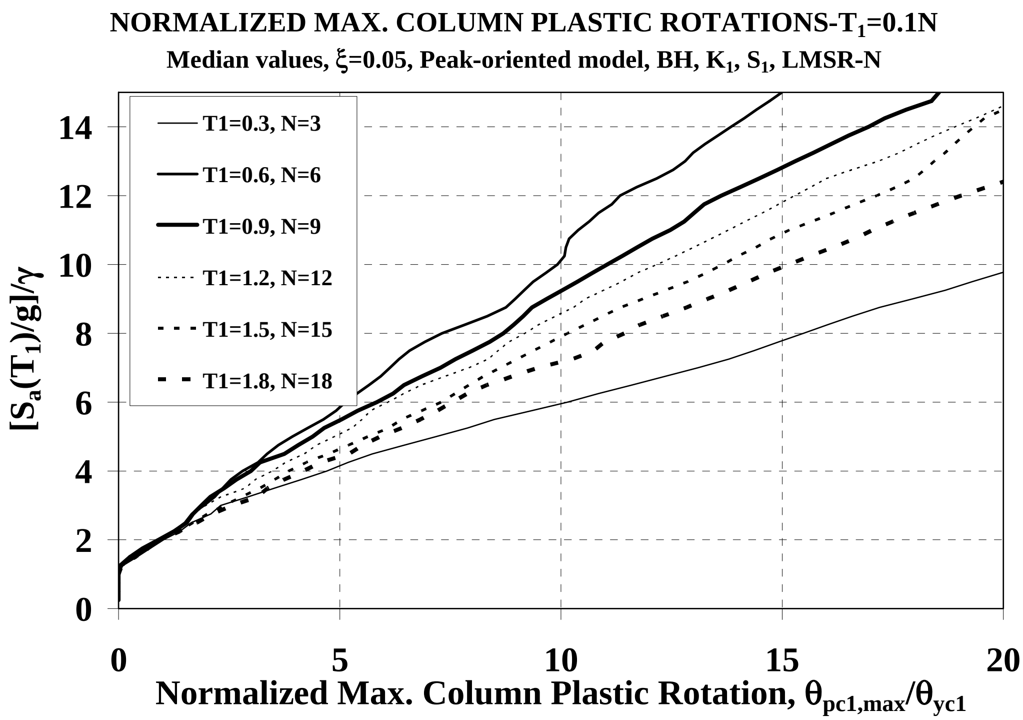

(a) Median Values

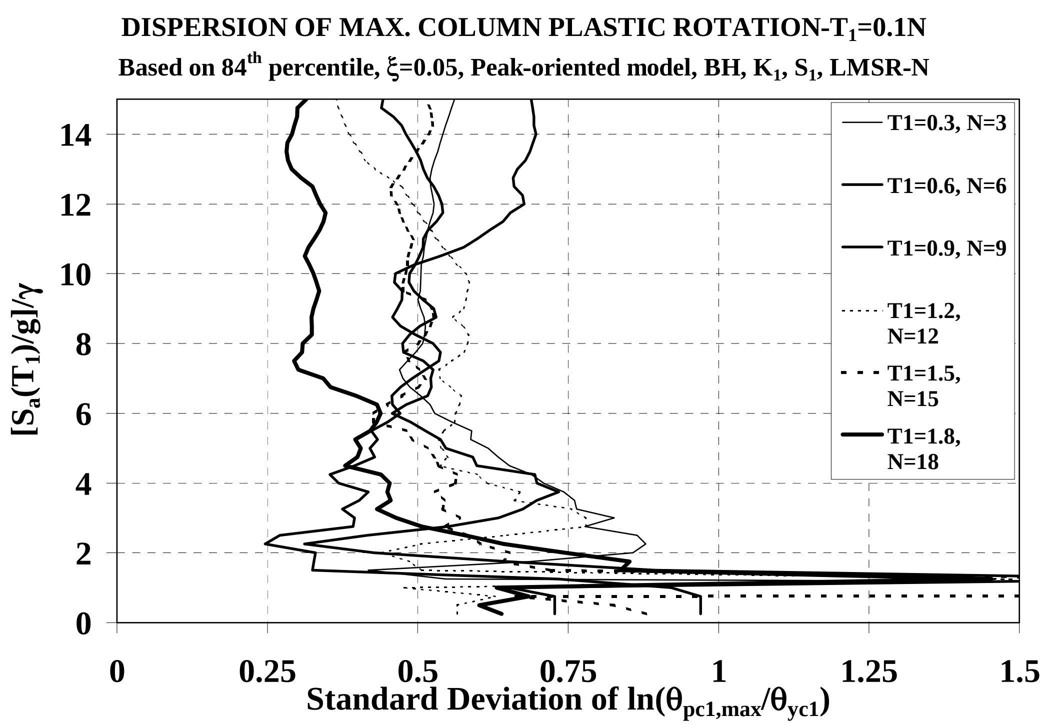

(b) Dispersion

Figure 6.17 Normalized Maximum Column Plastic Rotation, $T_1 = 0.1N$, Various Relative Intensities

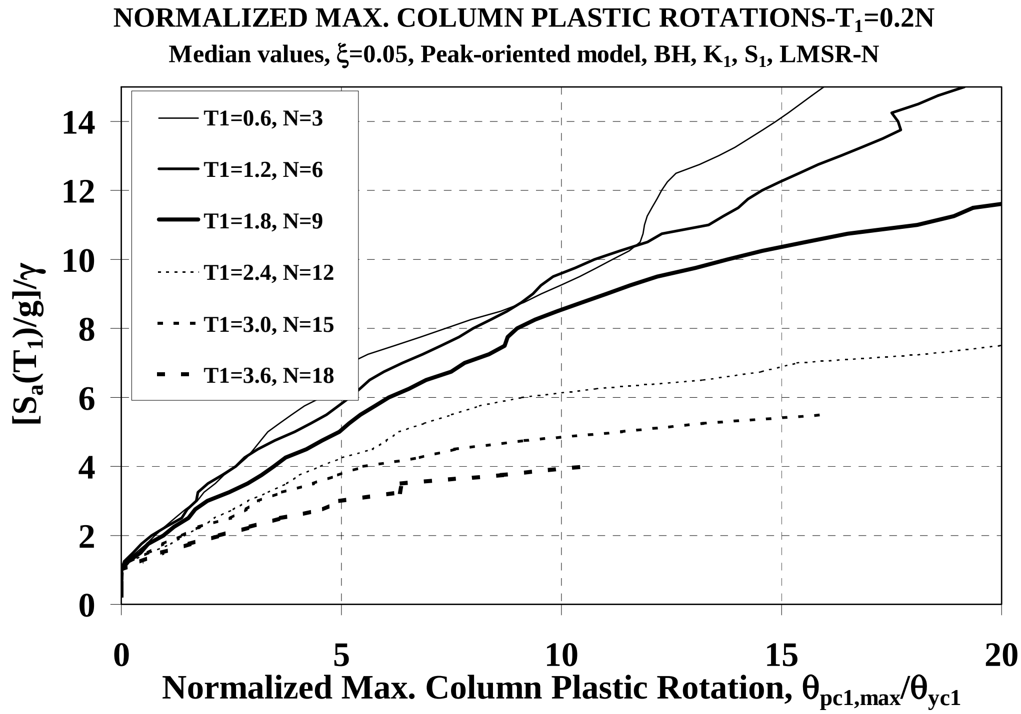

(a) Median Values

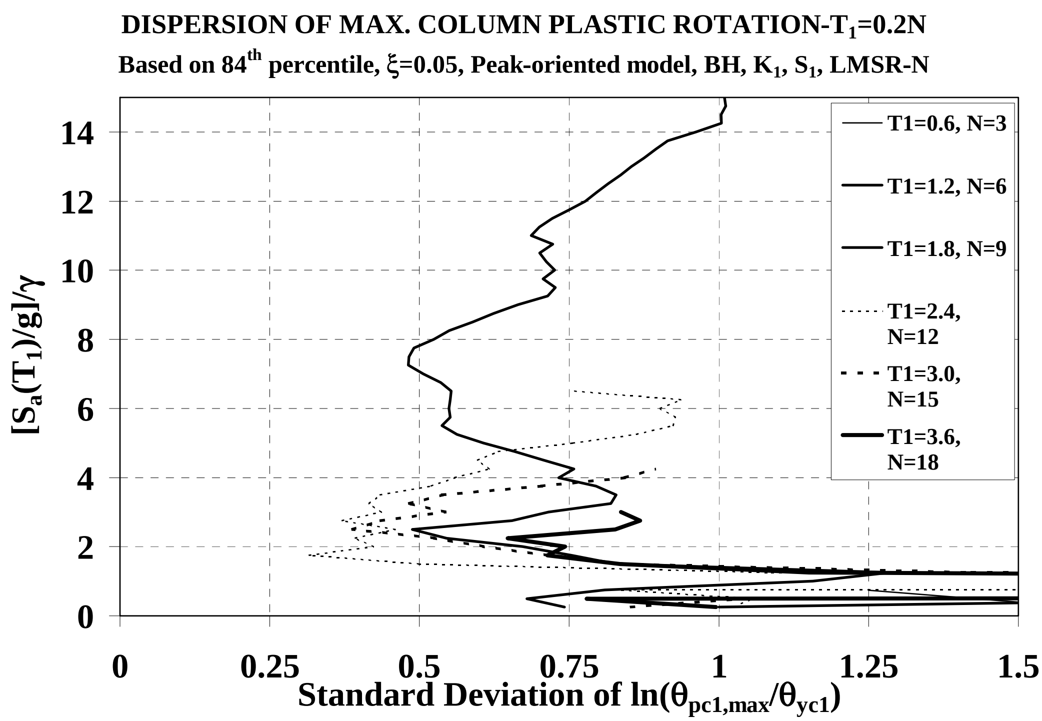

(b) Dispersion

Figure 6.18 Normalized Maximum Column Plastic Rotation, T_1 = 0.2N, Various Relative Intensities

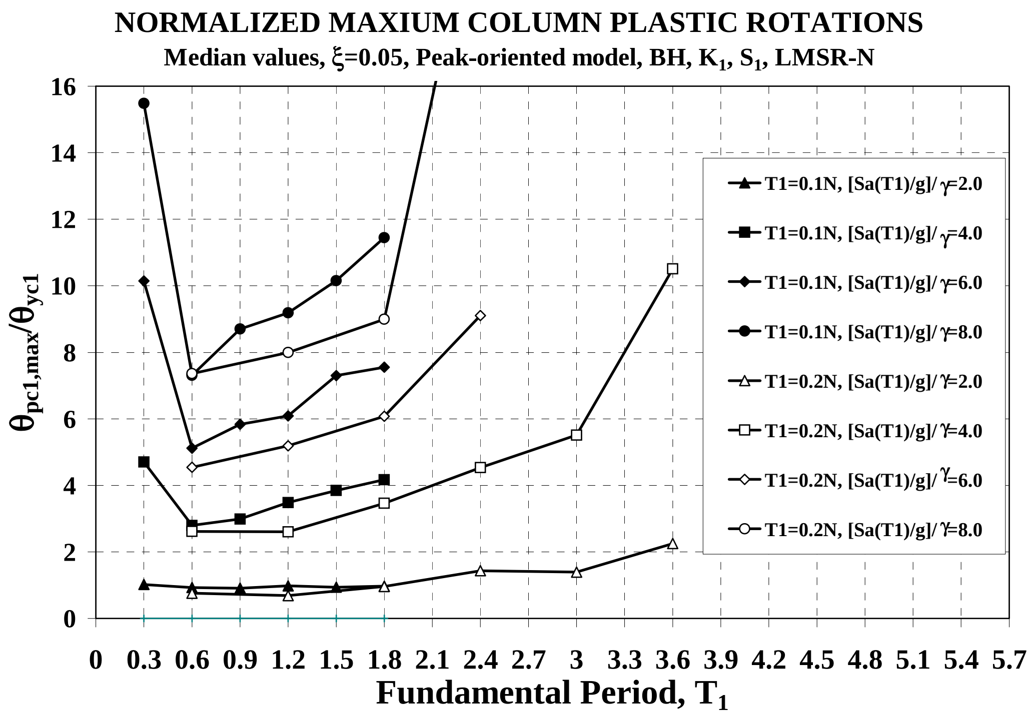

Figure 6.19 Normalized Maximum Column Plastic Rotation at the Base, All Frames, Various Relative Intensities

7 Seismic Demands for Variations in Structural Properties

7.1 INTRODUCTION

Previous chapters deal with the evaluation of seismic demands for the base case family of generic frame structures (see Section 2.4.1) subjected to the LMSR-N set of ordinary ground motions. The objective of this chapter is to study the sensitivity of engineering demand parameters and patterns of behavior to variations in structural properties, with respect to the base case. Emphasis is placed on the 3-, 9- and 18-story generic frames. The structural properties addressed include:

- Hysteretic behavior, e.g., peak-oriented versus pinching and bilinear;
- Strain hardening in the moment-rotation relationship at the component level, e.g., postyield slope equal to 0% versus 3% of the initial slope;
- Structure P-delta effects;
- Additional strength and stiffness provided by elements that do not form part of the moment-resisting frame;
- Story strength distribution based on different design load patterns, e.g., parabolic versus triangular, uniform, and story shear strength including random overstrength;
- Effects of gravity load on the formation of plastic hinges; and
- Mechanism, e.g., beam-hinge models versus column-hinge models

7.2 HYSTERETIC BEHAVIOR

Peak-oriented hysteretic behavior is used to model the moment-rotation relationship at the beam ends and at the bottom of the first-story columns for the base case family of generic frame structures. In this section, the sensitivity of roof drift and maximum story drift angles over the height is studied for two additional types of hysteretic models: pinching and bilinear. The general characteristics of the load-deformation behavior of the peak-oriented, pinching and bilinear models are illustrated in Figure 2.2. Unless otherwise specified, a pinching model with $\kappa_d = \kappa_f = 0.25$ is utilized and is denoted as "pinching" in the graphs (the parameters κ_d and κ_f, which control the amount of stiffness degradation in the pinching model, are also defined in Figure 2.2). A value of 0.25 is chosen because it is representative of severe pinching in the response. Figure 7.1 shows the response of pinching models with $\kappa_d = \kappa_f = 0.25$ and $\kappa_d = \kappa_f = 0.50$. In all three hysteretic models, 3% strain hardening is used.

In general, models with severe pinching ($\kappa_d = \kappa_f = 0.25$) exhibit normalized maximum roof drift demands larger than those observed for the case of models with peak-oriented and bilinear hysteretic behavior, as illustrated in Figures 7.2–7.4. It appears that severe stiffness degradation causes the system to become "softer," and hence, experience larger deformation demands. It is important to note that models with peak-oriented hysteretic behavior, which also has stiffness degradation, exhibit maximum roof drift demands comparable to (and in some cases smaller than) those observed for the bilinear model (except for $T_1 = 0.3$ sec in which demands for the peak-oriented model are larger than those experienced by the bilinear model). These observations indicate that for medium to long-period structures limited stiffness degradation (i.e., peak-oriented case) can in some cases "improve" the seismic behavior of regular frame structures. However, when the amount of stiffness degradation is significant, it becomes detrimental to the behavior of the system.

For the frame structure with $N = 18$ and $T_1 = 3.6$ sec, structure P-delta effects cause the system with bilinear hysteretic behavior to experience dynamic instability at a relative intensity level smaller than that of the systems with peak-oriented and pinching hysteretic behavior (Figure 7.4(b)). This phenomenon is attributed to the fact that the response of the system with bilinear hysteretic behavior spends more time on the envelope of the moment-rotation relationship of its components, which added to the P-delta effect produces an effective negative tangent stiffness in P-delta-sensitive structures.

The variation of the median normalized maximum roof drift demand with the fundamental period of the frame is presented in Figure 7.5 for both the stiff ($T_1 = 0.1N$) and flexible ($T_1 =

0.2N) frames and a relative intensity, $[S_a(T_1)/g]/\gamma = 4.0$. The observations made in the previous paragraphs are applicable for the ranges of period illustrated in the plots. Models with pinching hysteretic behavior exhibit deformation demands larger than those observed for the peak-oriented and bilinear models, especially in the short-period range ($T_1 = 0.3$ sec).

Figure 7.6 presents median ratios of maximum inelastic to elastic displacement for SDOF systems with a strength reduction factor, R, equal to 4.0, 3% strain hardening, and bilinear, peak-oriented and pinching ($\kappa_d = \kappa_f = 0.25$) hysteretic behavior. For the nonlinear time history analyses, the effect of P-delta is modeled by adding a negative slope in parallel to the hysteretic load-deformation response. The absolute value of the P-delta slope is assumed to be given by the elastic first-story stability coefficient of the 0.1N (Figure 7.6(a)) and 0.2N (Figure 7.6(b)) frame structures (values for this coefficient are presented in Figure A.4). A comparison between Figure 7.5 and 7.6 shows that except for $T_1 = 0.3$ sec, the difference in inelastic displacement demands between the pinching model and the other two models are more noticeable in the MDOF domain. For long-period SDOF systems ($T > 1.8$ sec), the response of the bilinear model becomes P-delta sensitive while the response of the peak-oriented and pinching models is stable. Dynamic instability of the bilinear SDOF model occurs at $T = 3.25$ sec, which is close to the period at which instability occurs for the $N = 18$, $T_1 = 3.6$ sec frame structure (see Figure 7.5(b)).

Figure 7.7 illustrates the dependence of median normalized maximum story drift angles over the height on the fundamental period for the stiff and flexible frames. Differences between systems with various types of hysteretic models follow patterns similar to the ones observed for the normalized maximum roof drift angles. Thus, the ratio of the maximum story drift angle over the height to the maximum roof drift angle is only weakly dependent on the type of hysteretic model, except for cases in which the response of frame structures is sensitive to P-delta effects, as can be seen in Figure 7.8.

The results presented in this section suggest that the maximum roof and story drift responses are larger for systems with hysteretic behavior that exhibits severe stiffness degradation such as the pinching model with $\kappa_d = \kappa_f = 0.25$. Unless severe stiffness degradation is assumed, differences between the pinching and peak-oriented models diminish as shown in Figure 7.9. This figure shows representative results for both stiff and flexible frames with hysteretic behavior represented by bilinear, peak-oriented, and pinching ($\kappa_d = \kappa_f = 0.25$) models as well as a pinching model with $\kappa_d = \kappa_f = 0.50$ (denoted in the graphs as "pinching (2)"). The maximum roof drift demands are similar between the pinching (2) (represented by the filled squares in the plot) and peak-oriented models. The presented results are for a relative intensity of $[S_a(T_1)/g]/\gamma = 4.0$, but they are representative of the results obtained for different relative intensities and frame structures with N = 3, 9, and 18 stories.

7.3 STRAIN HARDENING

The base case family of generic structures used in this study has hysteretic behavior represented by a peak-oriented moment-rotation relationships with 3% strain hardening. In this section, results for models that have no strain hardening are compared to base case results to assess the sensitivity to variations in strain hardening. For this purpose, representative results for the 9-story frames with $T_1 = 0.9$ sec and 1.8 sec are discussed.

The effect of strain hardening in the nonlinear static response of the 9-story frames is illustrated in Figure 7.10. Global pushover curves are presented in the normalized domain, using the yield values of the system without P-delta effects for normalization (yield values can be obtained from the information presented in Tables A.11 and A.12). Because of P-delta, the absence of strain hardening in the moment-rotation relationship of components leads to a negative postyield stiffness which is small for the T = 0.9 sec frame (Figure 7.10(a)) and substantial for the T = 1.8 sec frame (Figure 7.10(b)). The postyield behavior of the models presented in Figure 7.10 helps in understanding the nonlinear dynamic response of these systems when subjected to ordinary ground motions, as discussed in the following paragraph.

Median normalized maximum roof drift angles are shown in Figure 7.11 for both the N = 9, T_1 = 0.9 sec, and 1.8 sec frames with and without strain hardening. The general observation is that in both cases the absence of strain hardening does not have a pronounced influence on the behavior of the systems except for highly inelastic systems ($[S_a(T_1)/g]/\gamma > 6.0$). The increase in the absolute value of the negative slope due to the absence of strain hardening (Figure 7.10(b)) causes the nonlinear response of the N = 9, $T_1 = 1.8$ sec frame to approach dynamic instability at a relative intensity of $[S_a(T_1)/g]/\gamma = 9.0$ as opposed to $[S_a(T_1)/g]/\gamma = 14$ for the case of the system with strain hardening.

7.4 STRUCTURE P-DELTA EFFECTS

When P-delta effects cause the nonlinear static response of a system to have a negative postyield slope, amplification of displacements occurs and the potential for dynamic instability exists (Bernal, 1987; Gupta and Krawinkler, 2000). The objective of this section is to quantify the effect of structure P-delta on the nonlinear response of regular frames.

In this study, structure P-delta effects are quantified by the elastic first-story stability coefficient, which is defined as the ratio of the "equivalent P-delta" shear ($P\delta/h$) to the first-order shear in the elastic portion of the response. Values for the elastic first-story stability coefficient of the base case frame structures are given in Figure A.4. A discussion on how these values are obtained is presented in Section A.3.

Figures 7.12 and 7.13 show the global and first-story pushover curves of an 18 story frame with $T_1 = 1.8$ sec and 3.6 sec, respectively. These systems have a first-story elastic stability coefficient of 0.033 and 0.130, respectively. It can be seen in Figure 7.12 that both the global (roof) and first-story nonlinear static responses of the $T_1 = 1.8$ sec frame have a positive postyield stiffness even when structure P-delta effects are included in the analysis. It is important to note that in the first story (Figure 7.12(b)) the postyield slope ($0.009K_i$) is not equal to the slope without P-delta *($0.038K_i$)* minus a slope based on the first-story stability coefficient ($0.033K_i$)**.** This behavior occurs because of the changes in deflected shapes that the system experiences in the postyield portion of the response (Aydinoglu, 2001). The elastic first-story stability coefficient is based on a deflected shape that is close to a straight line, so it is not adequate to accurately estimate the stiffness in the postyield portion of the response if changes in deflected shape occur. The same observation applies for the $T_1 = 3.6$ sec frame (Figure 7.13) with the difference that in this case the P-delta effects are large enough to overcome the strain hardening of the components and cause the postyield stiffness of the pushover curves to be negative.

An understanding of the change in postyield stiffness due to the presence of P-delta effects can be obtained by interpreting the displacement profiles shown in Figure 7.14. For both the T_1 =

1.8 sec and the 3.6 sec frame structures, the elastic deflected shapes are close to a straight line. The T_1 = 1.8 sec frame (Figure 7.14(a)) exhibits changes in deflected shape with an increase in the roof displacement without a concentration of story drifts at any level over the height of the frame structure. On the other hand, for the case of the T_1 = 3.6 sec frame (Figure 7.14(b)), once the structure yields, there is a concentration of maximum story drifts at the bottom stories due to the presence of P-delta effects. As the roof displacement increases, the bottom story drift values increase at a rapid rate until dynamic instability is approached (see curve for δ_r/δ_{yr} = 3.0 in Figure 7.14(b)). At this point the system is no longer able to sustain its own gravity loads. Thus, at the first-story level, the difference in slopes between the cases with and without P-delta should be closer to the elastic first-story stability coefficient for the T_1 = 1.8 sec frame because its deflected shape in the postyield portion of the response is relatively close to a straight line.

The effect of structure P-delta on the nonlinear dynamic response of the18-story frames is illustrated in Figures 7.15 and 7.16. Median values for the normalized maximum roof drift angle and the normalized maximum story drift angle over the height are shown for cases with and without structure P-delta effects. Figures 7.15(a) and 7.16(a) show that the dynamic response of the T_1 = 1.8 sec frame is only weakly dependent on structure P-delta. However, the dynamic behavior of the T_1 = 3.6 sec frame (Figures 7.15(b) and 7.16(b)) is greatly influenced by structure P-delta effects. In this case, when P-delta is included in the analysis, dynamic instability is approached at a relative intensity approximately equal to 4.0. The T_1 = 3.6 sec model without P-delta effects and the T_1 = 1.8 sec models do not experience dynamic instability because the postyield slopes from the pushover analyses are positive. It is important to note that cyclic deterioration effects (which are not addressed in this study) might lead systems to experience global "collapse" even for structures that exhibit a positive postyield slope in the pushover analysis.

Figure 7.17 shows a comparison between the median incremental dynamic analysis curve for the N = 18, T_1 = 3.6 sec structure with a strength of γ = 0.10 and its global pushover curve. In order to compare both curves, the base shear from the global pushover analysis is normalized by 70% of the total mass of the system. This value of mass is close to the effective modal mass corresponding to the first mode, which is equal to 77% of the total mass. In the elastic range the correlation between the normalized base shear and $S_a(T_1)$ is good but not perfect due to factors such as the presence of higher modes in the response. The incremental dynamic analysis curve shows that in the median, the onset of dynamic instability is approached at a maximum roof drift angle that approximately coincides with the roof drift angle at "collapse" given by the global pushover curve. For this case, the global pushover curve adequately identifies the drift level at which dynamic instability will occur.

7.5 ADDITIONAL STRENGTH AND STIFFNESS PROVIDED BY ELEMENTS THAT DO NOT FORM PART OF THE MOMENT-RESISTING FRAME

As discussed in Section 7.4, when structure P-delta effects cause the postyield slope of the global pushover analysis to be negative, there is a potential for dynamic instability in the response. Analytical models, such as those represented by the base case family of generic frame structures used in this study neglect the contribution of "secondary" elements that do not form part of the moment-resisting frame, i.e., staircases, nonstructural components, gravity load frames, and others. The dynamic response of a system is influenced by the contribution of these "secondary" elements, especially for structures that are sensitive to structure P-delta effects.

The effect of elements that are not explicitly modeled as part of the moment-resisting frames is approximately evaluated by adding an *elastic* frame in parallel with the base case frame structure. This additional elastic frame is assumed to have the same relative stiffness distribution as the base case frame in order to permit a direct quantification of the story stiffness added by the elastic frame. Figure 7.18 shows the global pushover curves for three cases:

- The base case, N = 18, T_1 = 3.6 sec model
- A model with an additional elastic frame in which story stiffnesses are equal to 3% of the story stiffnesses of the base case frame
- A model with an additional elastic frame in which story stiffnesses are equal to 6% of the story stiffnesses of the base case frame

Median normalized maximum roof drift angle curves are shown in Figure 7.19. It can be seen that for high levels of inelastic behavior the relatively small increase in stiffness provided by the elastic frame (3% and 6%) improves the nonlinear behavior of the base case frame considerably. The relative intensity, $[S_a(T_1)/g]/\gamma$, at which dynamic instability is approached is approximately equal to 4.0, 5.5, and 13 for the base case model and the models with an elastic frame with 3% and 6% of the story stiffness of the base case, respectively.

Figure 7.19 demonstrates that great benefit can be achieved in P-delta-sensitive structures if a flexible “back-up system” is provided. It is arguable whether most of the elements that are not considered explicitly as part of the moment-resisting frame will maintain their stiffness at large drifts, but some benefit could be derived from their presence. The purpose of this pilot case study is to illustrate the potential benefit of a flexible back-up system and to encourage further exploration of this concept.

7.6 STORY SHEAR STRENGTH DISTRIBUTION

Models that form part of the base case family of generic frame structures used in this study are designed so that simultaneous yielding is attained under a parabolic load pattern. This section presents results on the sensitivity of maximum roof and story drift angle demands to various story shear strength distributions, including those based on triangular and uniform load patterns in addition to the parabolic one (see Figure 7.20). Furthermore, models that include overstrength and story shear strength distributions not tuned to a prescribed load pattern are also considered. This is the case for most frame structures in which constructability and exogenous design decisions influence the distribution of story shear strength over the height.

7.6.1 Story Shear Strength Distribution Based on Parabolic, Triangular, and Uniform Load Patterns

Figure 7.20 shows that for a given base shear strength, the largest story shear strength over the height is associated with a parabolic design load pattern and the smallest story shear strength is associated with a uniform design load pattern. Differences in the story shear strength distribution over the height are reflected in the nonlinear dynamic behavior of the frames as shown in Figures 7.21–7.23. Results for the normalized maximum roof and story drift angles as well as the ratio of the maximum story-angle over the height to the maximum roof drift angle are presented for 9-story frames with T_1 = 0.9 sec and 1.8 sec.

Median normalized maximum roof drifts for models whose story shear strengths are based on parabolic, triangular and uniform load patterns are presented in Figure 7.21. The differences in roof drifts are small, except when P-delta effects become important in the T = 1.8 sec structure, which happens at much smaller relative intensities for systems designed according to a uniform load pattern.

Differences among models designed according to the parabolic, triangular and uniform load patterns are more pronounced for the median normalized maximum story drift angle over the height (see Figure 7.22). For all relative intensities, except very small ones causing only elastic response, the maximum story drift is significantly larger for the structures designed according to the uniform load pattern. The differences are particularly large around $[S_a(T_1)/g]/\gamma = 2$. The reason is that the uniform design load pattern produces very weak top stories that yield early and cause very large story drifts. The relatively weak top stories, as compared to those in real structures, exist already in the base case generic models because of the tuning of story shear strengths to a lateral design load pattern. In Chapter 4 it is shown that the generic models start to yield in the top stories, which creates very large drifts in these stories before the migration of maximum story drifts occurs from top to bottom of the structure. This early yielding and the large top story drifts, which are more pronounced for long-period structures, create the "hump" in the maximum story drift curves observed already in Figures 4.13 and 4.14, and evident again around $[S_a(T_1)/g]/\gamma = 2$ in Figure 7.22(b). For the structure designed according to a uniform load pattern, this hump becomes much larger. The same observations can be made from Figure 7.23, which shows the variation of the ratio of the maximum story drift angle over the height to the maximum roof drift angle with the relative intensity.

The arguments made in the previous paragraph about large top story drifts are underscored by the drift profiles presented in Figures 7.24 and 7.25. In most cases, the maximum story drifts at the top and bottom stories are comparable for the N = 9, T_1 = 0.9 sec base case structure (Figure 7.24(a)). However, for the structure designed with the uniform load pattern the top story drifts are much larger than the bottom story drifts, particularly around $[S_a(T_1)/g]/\gamma = 2$, which causes the large hump in the story drift curve of Figure 7.22(a). For the N = 9, T_1 = 1.8 sec base case structure, the top story drifts are largest around $[S_a(T_1)/g]/\gamma = 2$ (Figure 7.25(a)), which also causes the hump in the story drift curve denoted as "Parabolic Load Pattern" in Figure 7.22(b).

This hump gets much amplified for the uniform load pattern case in which the top story drifts are much larger at all relative intensities (Figure 7.25(c)).

The preceding discussion serves to show that the inelastic response experienced at small relative intensities by the medium to long-period frames used in this study is dominated by weak upper stories. Compared to real structures, whose story shear strength in the upper stories may be controlled by gravity load or constructability considerations, the relatively large maximum story drifts associated with the humps in the relative intensity drift curves (mostly around $[S_a(T_1)/g]/\gamma = 2$) may be exaggerated. This phenomenon is amplified when a triangular or uniform design load pattern is assumed. The latter two load patterns are used primarily to illustrate the sensitivity of the EDPs to story shear strength distributions rather than as representations of realistic shear strength distributions over the height of the structure.

7.6.2 Story Shear Strength Distribution Including Overstrength

In actual structures the story shear strengths are influenced by various decisions involved in the design process. In order to explore the sensitivity of maximum roof and story drifts to a nonuniform story shear strength distribution that includes overstrength, the $N = 9$, $T_1 = 1.8$ sec base case frame is utilized. A model that includes overstrength is generated by assuming a mean overstrength of 50% in the beam moment capacity and randomly varying this capacity at each floor level between maximum and minimum values of 100% and 0% overstrength. The resulting story shear strength distribution is shown in Figure 7.26. The story shear strengths for the structure with overstrength are computed based on the procedure proposed in FEMA 355C (2000), in which the static story shear strength is estimated by summing one half of the floor moment "capacity" of the floors bounding the story and dividing this sum by the story height.

Global pushover curves for the base case model and the model with random overstrength are shown in Figure 7.27. The negative postyield slope in the global pushover curve is attained at a normalized roof drift displacement of $\delta_r/\delta_{yr} = 1$ for the base case model and $\delta_r/\delta_{yr} > 3$ for the model with random overstrength. The model with random overstrength exhibits a negative postyield stiffness at a much larger roof displacement because simultaneous yielding does not occur, since member strengths are not tuned to predefined load pattern. Larger base shear strength and the delay in the formation of a negative postyield stiffness translate into improved behavior in which dynamic instability is approached at a larger relative intensity, as shown in Figure 7.28. Figure 7.28(a) presents the median normalized maximum roof drift angle for the base case model and the model with random overstrength. For $[S_a(T_1)/g]/\gamma < 5$, median roof drift angles are similar between the two models, but the responses tend to diverge with an increase in relative intensity. Median normalized maximum story drift angles over the height are plotted in Figure 7.28(b). The model with random overstrength exhibits a more uniform variation in this EDP with the relative intensity level. Except for a decrease in the hump observed for the response of the base case model at $[S_a(T_1)/g]/\gamma = 2$, no significant improvement is obtained by providing overstrength, except at large levels of inelastic behavior ($[S_a(T_1)/g]/\gamma > 8$) at which the onset of dynamic instability is approached.

The drift profiles presented in Figure 7.29 also show that the effect of random overstrength is small for $[S_a(T_1)/g]/\gamma < 8$. However, a few noticeable differences are present. For instance, the model with random overstrength exhibits smaller upper-story drifts at $[S_a(T_1)/g]/\gamma = 2$ (which explains the absence of a pronounced hump at this intensity level in Figure 7.28(b)). Moreover, at large $S_a(T_1)/g]/\gamma$ values the effect of its relatively small shear strength in stories 2 and 3 (see Figure 7.26) leads to an increase in drift in these stories as compared to the first-story drift.

7.7 BEAM MOMENTS DUE TO GRAVITY LOADS

The effect of gravity loads on the formation of plastic hinges at the beam ends are not considered in the seismic demand evaluation carried out in this study for the base case family of generic frame models. In order to evaluate this effect, gravity loads are added to the beam elements such that the fixed-end gravity moments at the beam ends are equal to 50% of the plastic moment capacity of the beam at a given floor level.

Figure 7.30 shows the global pushover curves for the 9-story frames with T_1 = 0.9 sec and 1.8 sec with and without gravity loads. The presence of gravity moments cause redistribution of moments such that simultaneous yielding is not attained and the displacement at which the postyield slope becomes negative is larger than that of the base case frame model. This behavior implies that differences in the nonlinear time history results of models with and without gravity loads are expected to be more noticeable at roof displacements up to twice the roof yield displacement.

Figures 7.31 and 7.32 show the variation of the median normalized maximum roof drift and of the median normalized maximum story drift over the height with the relative intensity. The general observation is that the models with gravity loads exhibit maximum roof and story drifts that are smaller than those experienced by the base case frame models, except for large relative intensities at which the median responses are almost identical. In particular, the maximum story drifts are smaller for the gravity load models in the range that is assumed to be of primary interest for loss evaluation ($[S_a(T_1)/g]/\gamma$ between 1.0 and 4.0). In this range the story drift profiles corresponding to the gravity load models are slightly more uniform than those of the base cases, as can be seen from Figures 7.33 and 7.34.

The "improved" drift response of the gravity load models for $[S_a(T_1)/g]/\gamma < 4$ is attributed to the second slope of the trilinear global pushover curves (Figure 7.30). While the base case models reach the small (or negative) postyield stiffness once simultaneous yielding occurs, the models with gravity loads reach the same postyield stiffness at larger displacements. This delay in the attainment of the small postyield stiffness decreases the maximum story drifts at small to medium levels of inelastic behavior.

7.8 "FAILURE" MECHANISM

The base case family of generic structures used in this study is designed according to the strong-column, weak-beam philosophy. Plastic hinges develop at the end of beams and at the bottom of the first-story columns (beam-hinge [BH] mechanism). Although code provisions are intended to produce designs that develop a beam-hinge mechanism and avoid plastic hinging in columns, real frame structures do not always behave according to this criterion. It is well established that strict adherence to the strong-column, weak-beam concept is difficult to implement; thus, there is a potential for the formation of undesirable story mechanisms due to plastic hinging in columns. In order to assess the sensitivity of maximum roof and story drift demands to the type of mechanism, the response of 3-, 9-, and 18-story frame structures that develop a beam-hinge and a column-hinge mechanism are compared.

Frames with column-hinge (CH) mechanisms are modeled by using rigid beams and flexible columns. Springs are located at the ends of the flexible columns to model peak-oriented moment-rotation hysteretic behavior. Both beam-hinge and column-hinge models are designed to have a straight-line first-mode shape and attain simultaneous yielding when subjected to a parabolic lateral load pattern.

Figure 7.35 presents the median normalized maximum roof drift angle for beam-hinge and column-hinge frame models with N = 3, 9, and 18. Frames that develop a column-hinge mechanism experience maximum roof drift demands that are smaller than those experienced by frames that develop a beam-hinge mechanism because the global deformation of the CH models is dominated by the first story (see Figure 7.37). This observation regarding maximum roof drift demands applies to cases in which P-delta effects do not cause dynamic instability in the response. If the frames are sensitive to structure P-delta effects, the relative intensity, $[S_a(T_1)/g]/\gamma$, at which the frames approach the onset of dynamic instability is much smaller for the column-hinge models (see Figure 7.35(b)) because of the development of story mechanisms. For instance, the N = 9, T_1 = 1.8 sec frame structure approaches the onset of dynamic instability at $[S_a(T_1)/g]/\gamma > 14$ for the beam-hinge model and $[S_a(T_1)/g]/\gamma < 4$ for the column-hinge model.

The influence of the "failure" mechanism on the potential for dynamic instability is evident already for the N = 18, T_1 = 1.8 sec model, which exhibits no P-delta-sensitive behavior for the beam-hinge model, but dynamic instability around $[S_a(T_1)/g]/\gamma = 7$ for the column-hinge model. At this relative intensity, the CH model experiences P-delta collapse with more than 50% of the ground motions. Global and first-story pushover analyses for both cases are shown in Figure 7.36. For the BH model, both the global and first-story pushover curves have a positive postyield stiffness, whereas both stiffnesses are negative for the CH model. The negative stiffnesses are caused by story mechanisms that are developed in the lower stories in which the negative P-delta stiffness overcomes the strain hardening effect at the plastic hinge locations in the columns. The consequence is the formation of story mechanisms that lead to large amplification of story drifts in the time history response (ratcheting). These large story drifts are evident in the drift profiles shown in Figure 7.37(b). The first-story drift is greatly amplified already at a relative intensity of $[S_a(T_1)/g]/\gamma = 2$, and the first- and second-story drifts grow to very large values at $[S_a(T_1)/g]/\gamma = 6$. For the BH model (Figure 7.37(a)), these amplifications do not occur.

The concentration of story drifts in one or two stories for the CH models, and the corresponding large amplification of maximum story drifts, are evident also in Figure 7.38, which shows the maximum story drifts over the height for the models used in Figure 7.35. Even in cases with no evident sensitivity of the response to P-delta, the maximum story drifts corresponding to the CH models are much larger than those corresponding to the BH models. As discussed before, the opposite behavior is observed for the maximum roof drifts (Figure 7.35). The implication is that for the CH models the ratio of maximum story drift to maximum roof drift consistently is much larger than for the BH models (Figure 7.39).

7.9 SUMMARY

Previous chapters deal with the evaluation of seismic demands for the base case family of generic frame structures subjected to ordinary ground motions. Models that form part of this family of structures have very specific characteristics that influence patterns of behavior and the magnitude of seismic demands. In order to study the sensitivity of drift demands to variations in structural characteristics, the properties of the base case generic frames are modified and a statistical evaluation of drift demand parameters is carried out. Structural properties and characteristics of interest include: hysteretic behavior, strain hardening, structure P-delta, strength and stiffness provided by elements that do not form part of the moment-resisting frames, story shear strength patterns, the effect of gravity load moments, and "failure" mechanisms. Conclusions drawn in this chapter are applicable only within the conditions identified in each section. The main observations and conclusions are as follows:

- Maximum drift demands are moderately sensitive to the amount of stiffness degradation present at the component level. For frame models of all periods, severe stiffness degradation (e.g., pinching hysteretic behavior with $\kappa_d = \kappa_f = 0.25$) causes an amplification of drift demands with respect to system with nondegrading stiffness, i.e., the bilinear model. Medium to long-period frame models with stiffness degradation of the type present in components with peak-oriented hysteretic behavior experience maximum drift demands similar to, and in some cases smaller than, those experienced by nondegrading stiffness models.
- Except for the short-period range, patterns of behavior identified in the previous paragraph for regular frames with severe stiffness degradation are not clearly identified in the SDOF domain.

- The ratio of the maximum story drift angle over the height to the maximum roof drift angle is essentially independent of the amount of stiffness degradation present at the component level.
- Nondeteriorating regular frame structures that are sensitive to structure P-delta effects approach the onset of dynamic instability at smaller relative intensity values when the moment-rotation relationship at the component level does not experience stiffness degradation (bilinear model). This phenomenon is attributed to the fact that the response of the system with bilinear hysteretic behavior spends more time on the envelope of the moment-rotation relationship of its components, which added to the P-delta effect produces an effective negative tangent stiffness in P-delta-sensitive structures.
- Strain hardening in the moment-rotation relationship at the component level is beneficial in order to decrease (and in some cases eliminate) the potential for dynamic instability in the response.
- Structure P-delta effects can lead to the concentration of drift demands in a few stories, and hence, dynamic instability problems. The pushover analysis is a useful tool to identify the potential for dynamic instability. When P-delta effects cause a negative postyield stiffness in the pushover analysis, the potential for dynamic instability exists and increases with the absolute value of the postyield slope. Pushover curves can be used to roughly estimate the maximum drift demand at which dynamic instability is expected to occur.
- Structural and nonstructural elements that contribute to lateral stiffness and strength, but customarily are not modeled as part of a moment frame structure, may be very beneficial in delaying the onset of dynamic instability, particularly if these elements maintain their stiffness far into the inelastic range.
- Maximum story drifts as well as the distribution of maximum drifts over the height of moment-resisting frames are sensitive to the design story shear strength pattern. Patterns that are intended to account for the contribution of higher mode effects, i.e., parabolic load pattern, produce designs with smaller drift demands and a more uniform distribution of maximum story drift angles over the height than the ones obtained with other load patterns, e.g., triangular and uniform.
- The inelastic response experienced at small relative intensities by the medium to long-period frames used in this study is dominated by weak upper stories. Compared to real structures, whose story shear strength in the upper stories may be controlled by gravity load or

constructability considerations, the relatively large maximum story drifts at small relative intensities (mostly around $[S_a(T_1)/g]/\gamma = 2$) may be exaggerated.

- The effect of random overstrength (in this case, with a mean of 50%) on roof and story drifts is relatively small, except for P-delta sensitive structures in which overstrength causes an increase in the relative intensity at which dynamic instability in the response is approached.
- The effect of gravity load moments on the roof drift is negligible. For relatively small relative intensities, gravity load moments reduce the maximum story drifts because the system reaches the small postyield stiffness from the pushover analysis at a larger drift as compared to systems without gravity load moments.
- Plastic hinging in columns should be avoided in order to prevent the formation of story mechanisms that lead to large story drift demands. Story mechanisms cause maximum story drift angles to concentrate in a few stories, increasing the potential for dynamic instability when P-delta effects are considered.

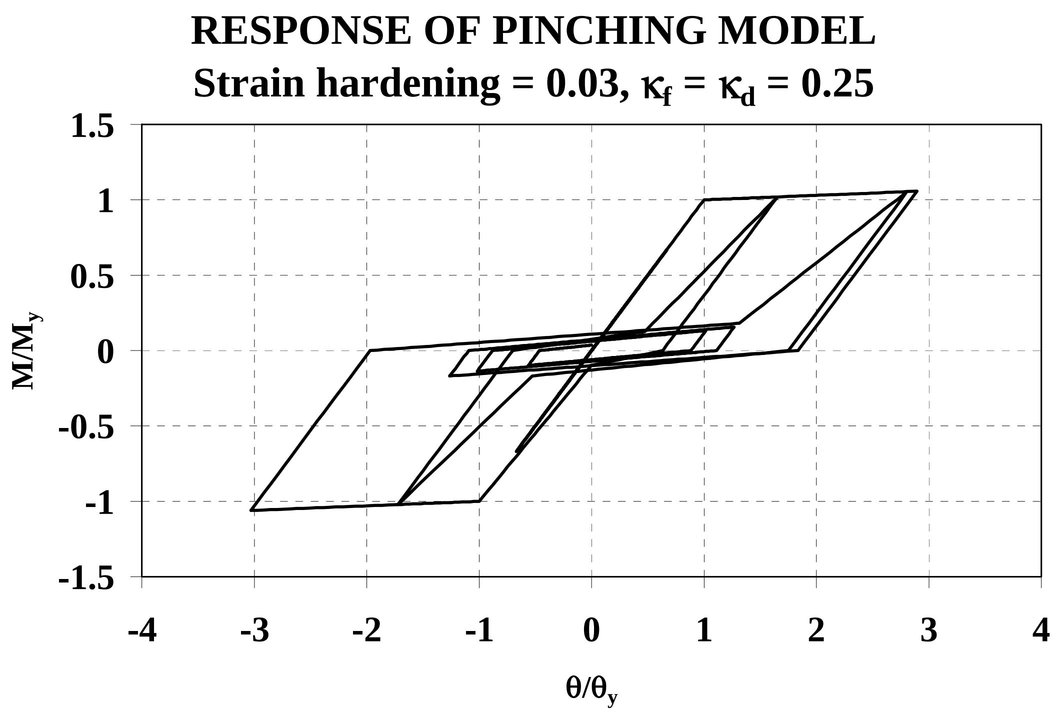

(a) $\kappa_f = \kappa_d = 0.25$

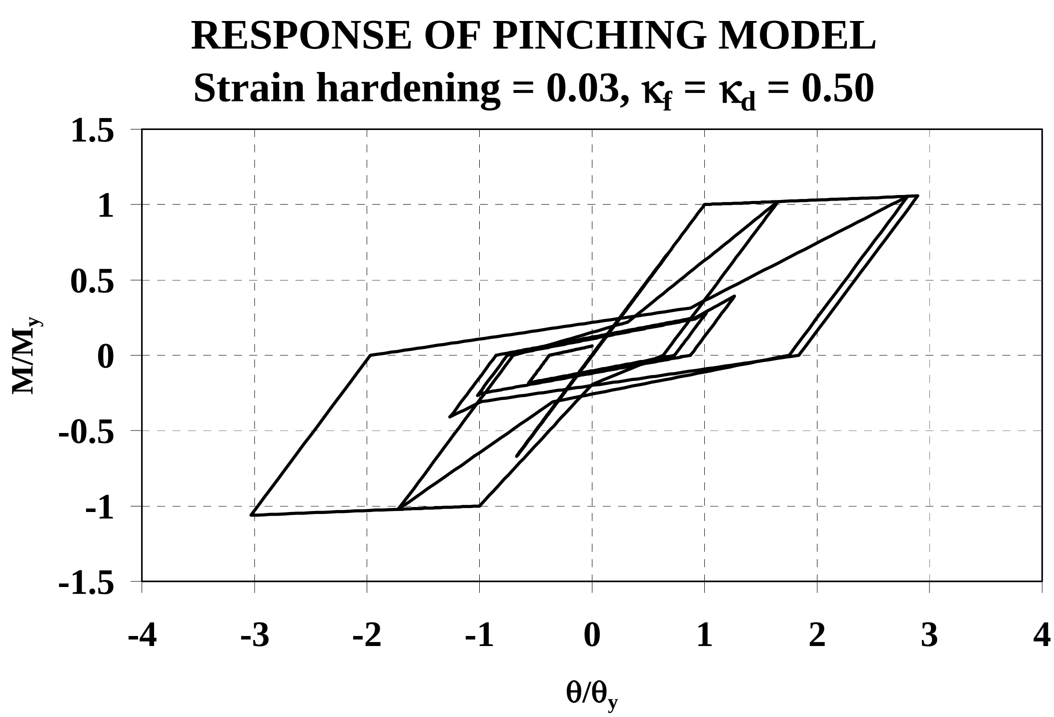

(b) $\kappa_f = \kappa_d = 0.50$

Figure 7.1 Effect of Parameter κ in the Response of the Pinching Hysteretic Model

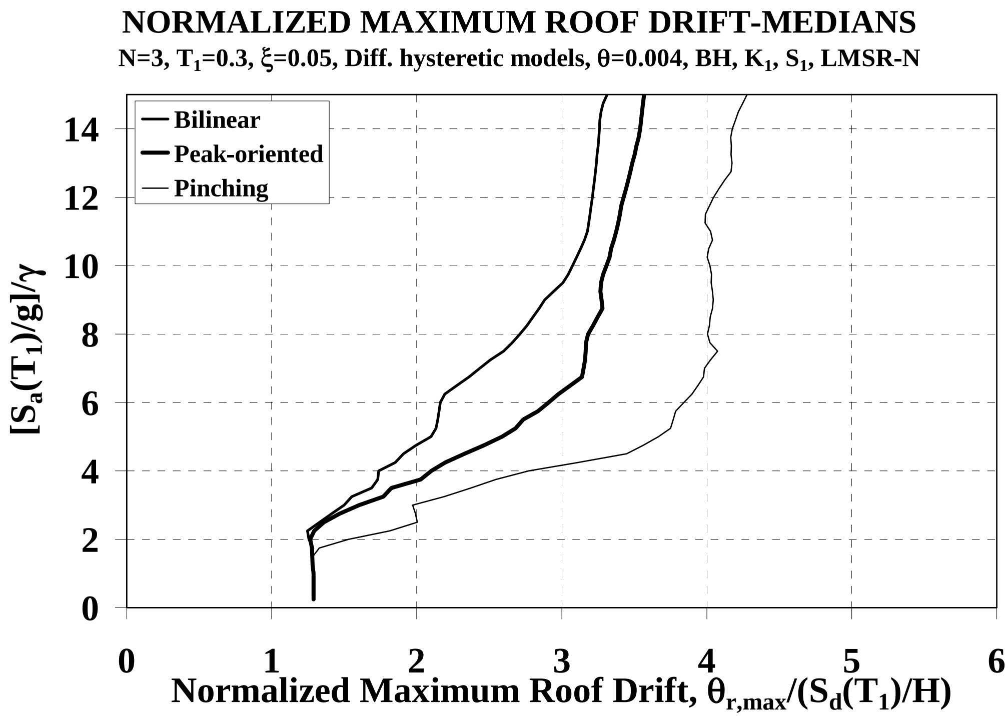

(a) T_1 = 0.3 sec

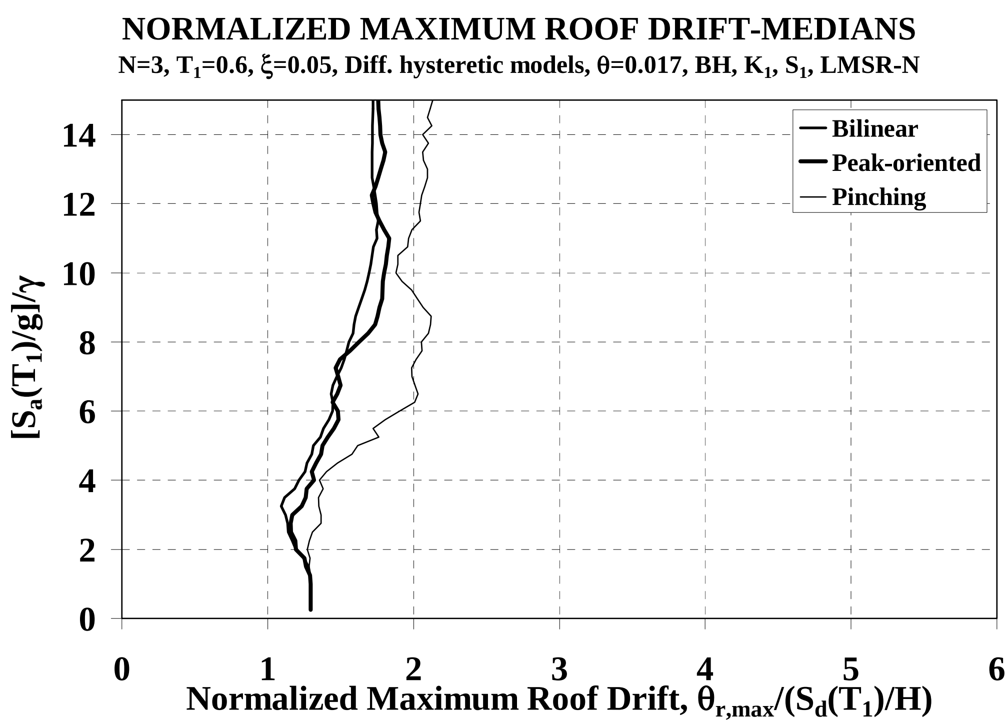

(b) T_1 = 0.6 sec

Figure 7.2 Effect of the Hysteretic Model on the Median Normalized Maximum Roof Drift Demand, N = 3

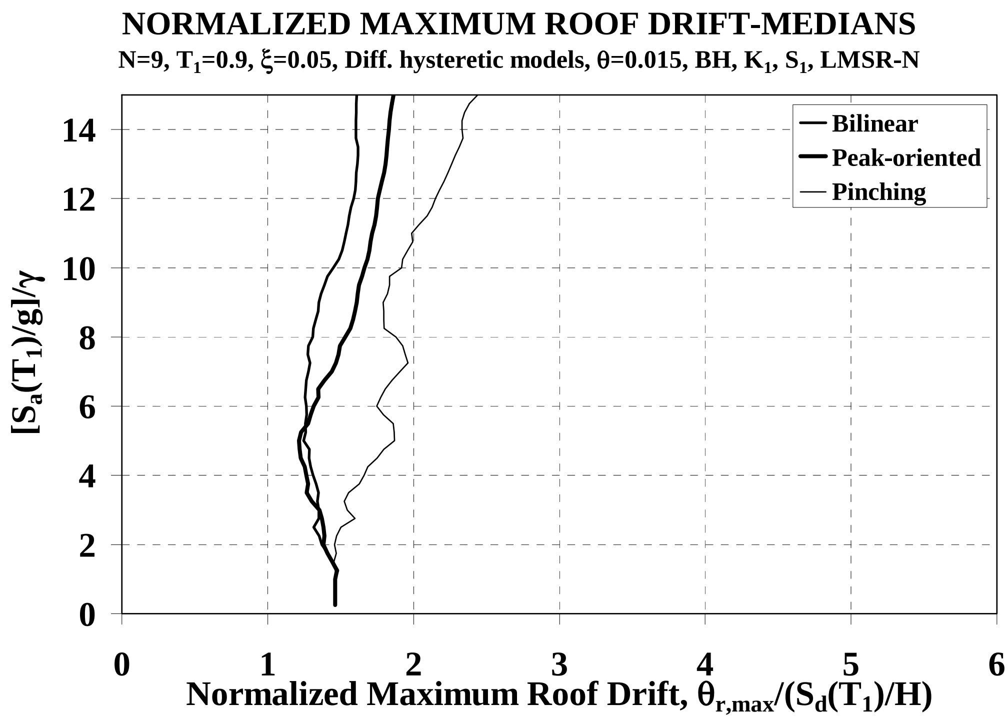

(a) T_1 = 0.9 sec

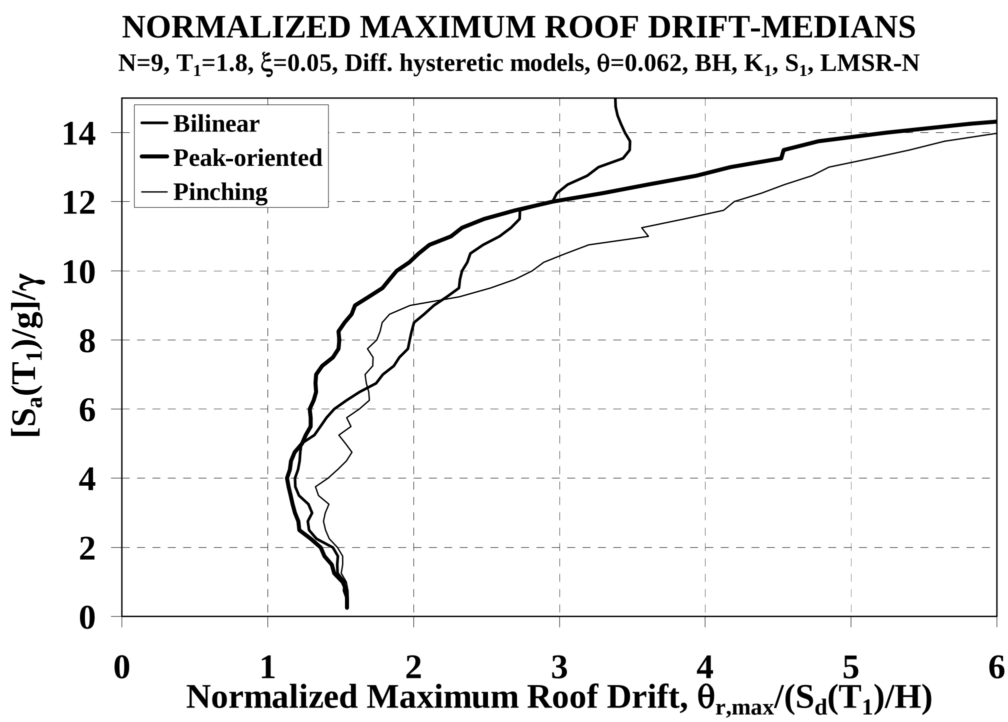

(b) T_1 = 1.8 sec

Figure 7.3 Effect of the Hysteretic Model on the Median Normalized Maximum Roof Drift Demand, N = 9

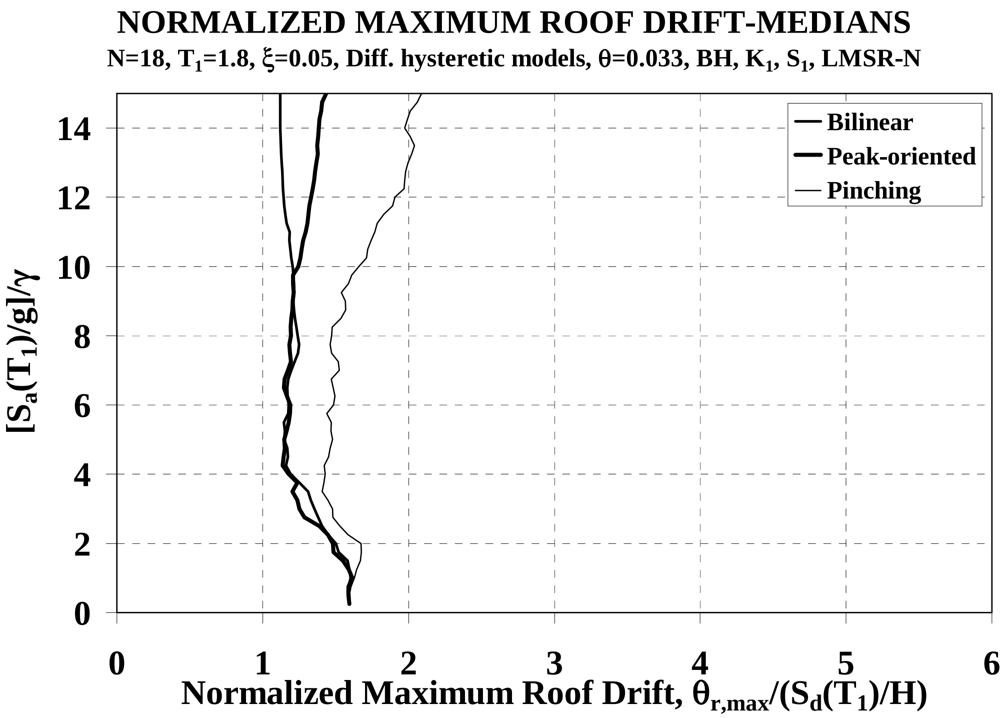

(a) T_1 = 1.8 sec

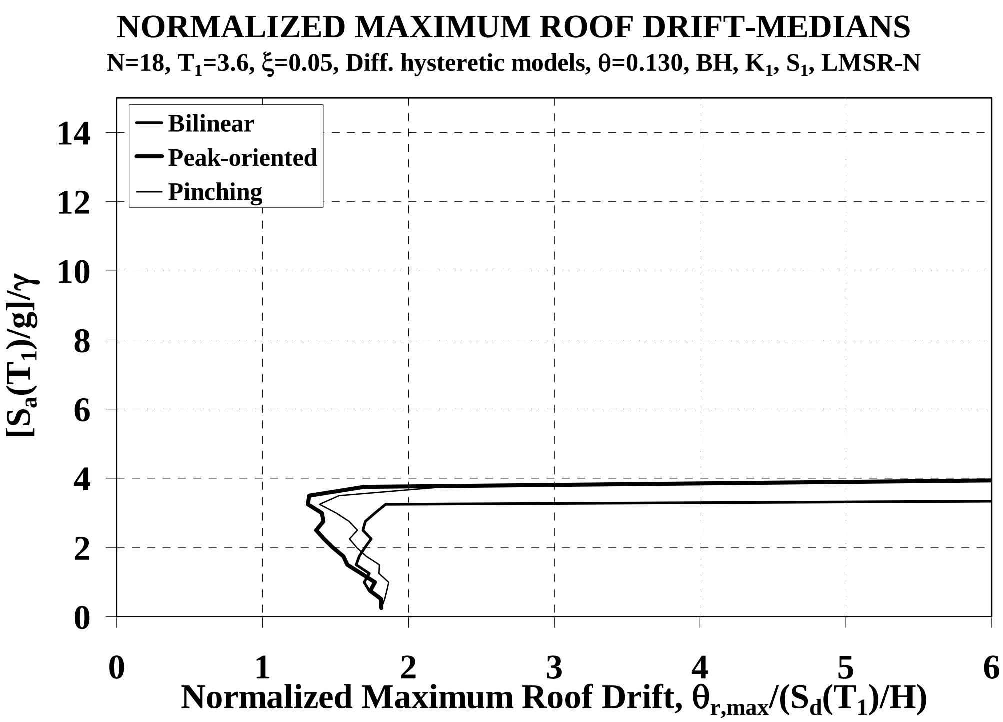

(b) T_1 = 3.6 sec

Figure 7.4 Effect of the Hysteretic Model on the Median Normalized Maximum Roof Drift Demand, N = 18

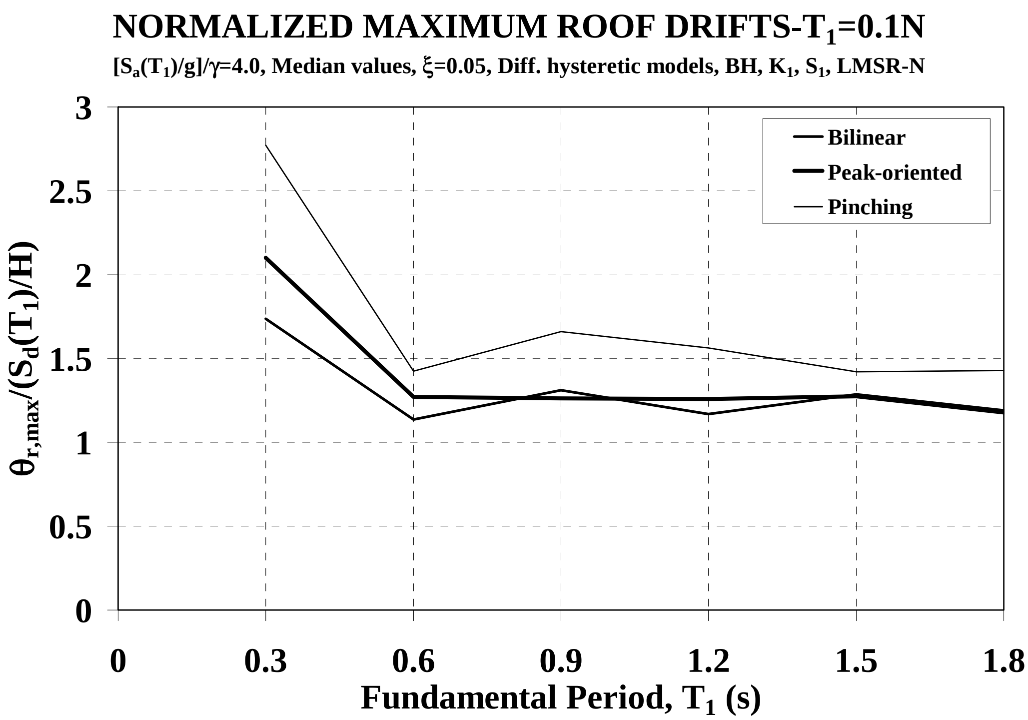

(a) $T_1 = 0.1N$

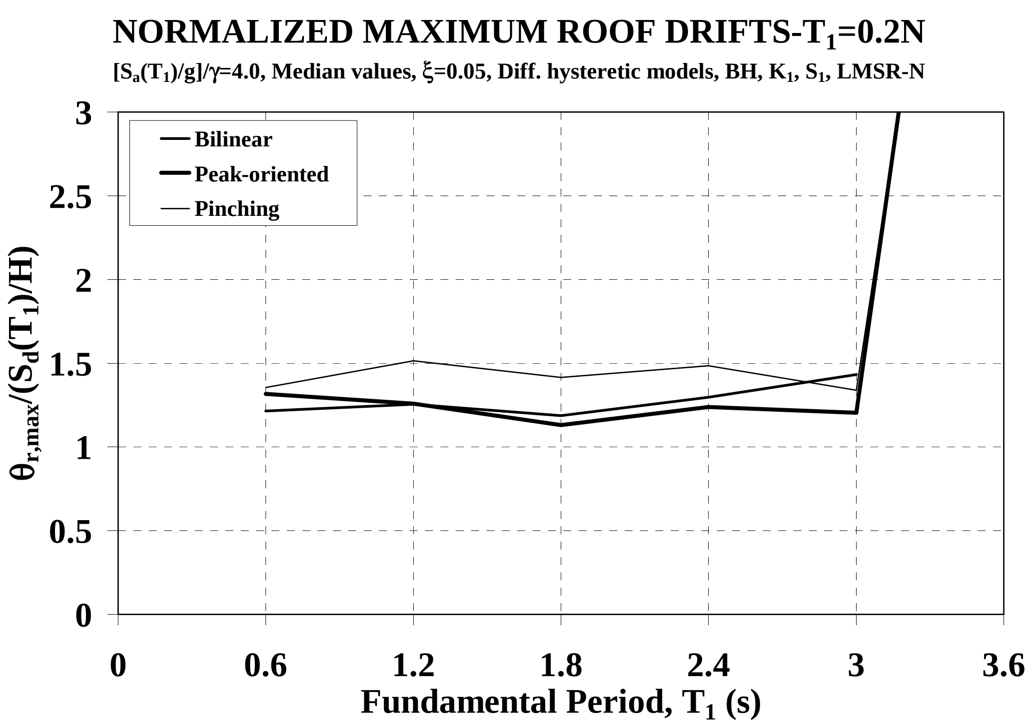

(b) $T_1 = 0.2N$

Figure 7.5 Median Normalized Maximum Roof Drifts, Effect of the Hysteretic Model on Stiff and Flexible Frames, $[S_a(T_1)/g]/\gamma = 4.0$

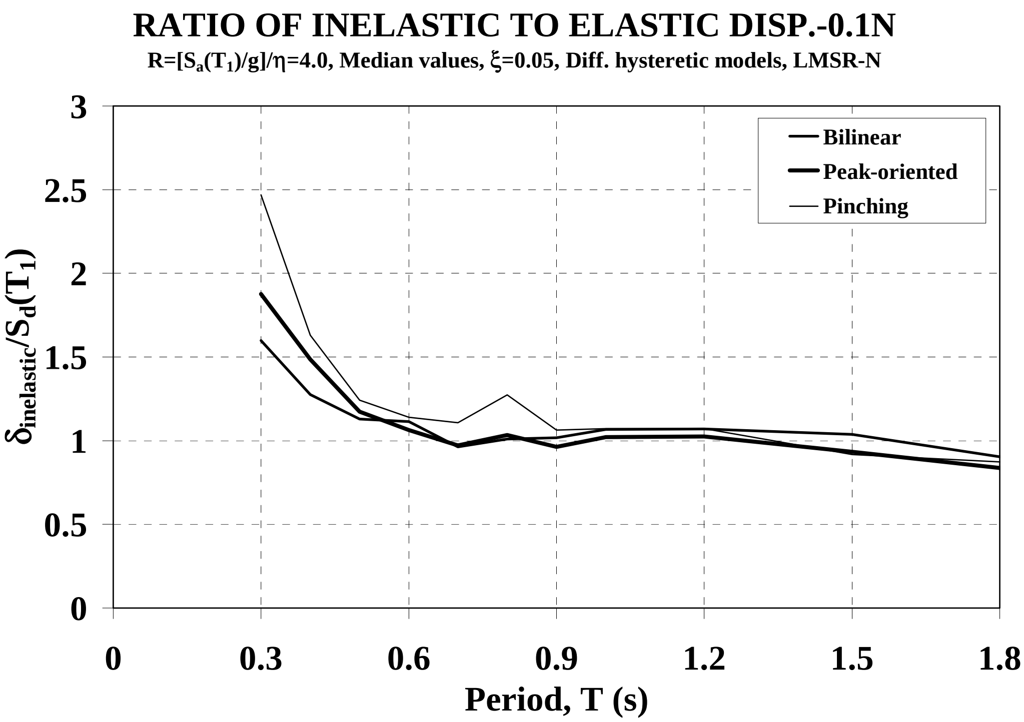

(a) P-delta Slope Equal to the Elastic First-Story Stability Coefficient of the 0.1N Frames

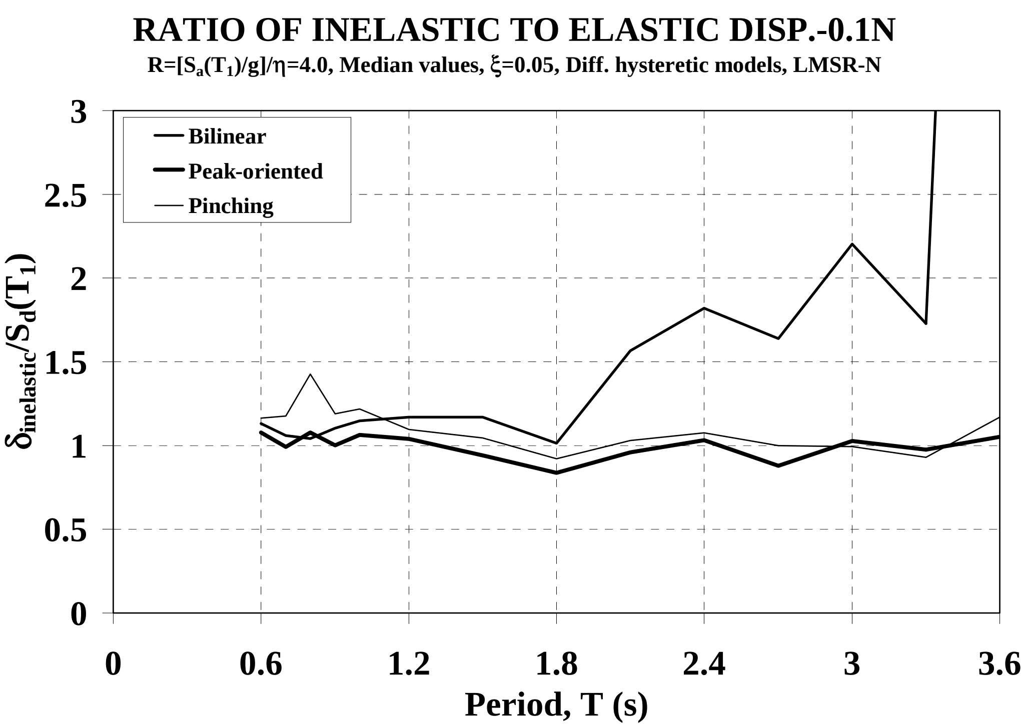

(b) P-delta Slope Equal to the Elastic First-Story Stability Coefficient of the 0.2N Frames

Figure 7.6 Ratio of Inelastic to Elastic Displacement, Effect of the Hysteretic Model on SDOF Systems, R-Factor = $[S_a(T_1)/g]/\eta$ = 4.0

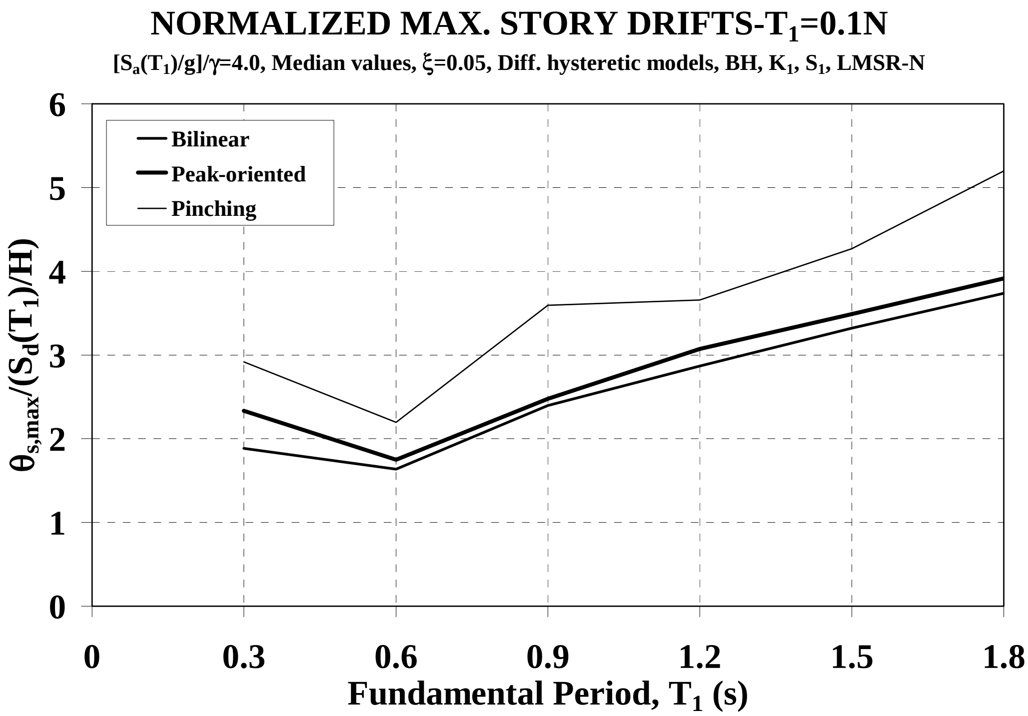

(a) T_1 = 0.1N

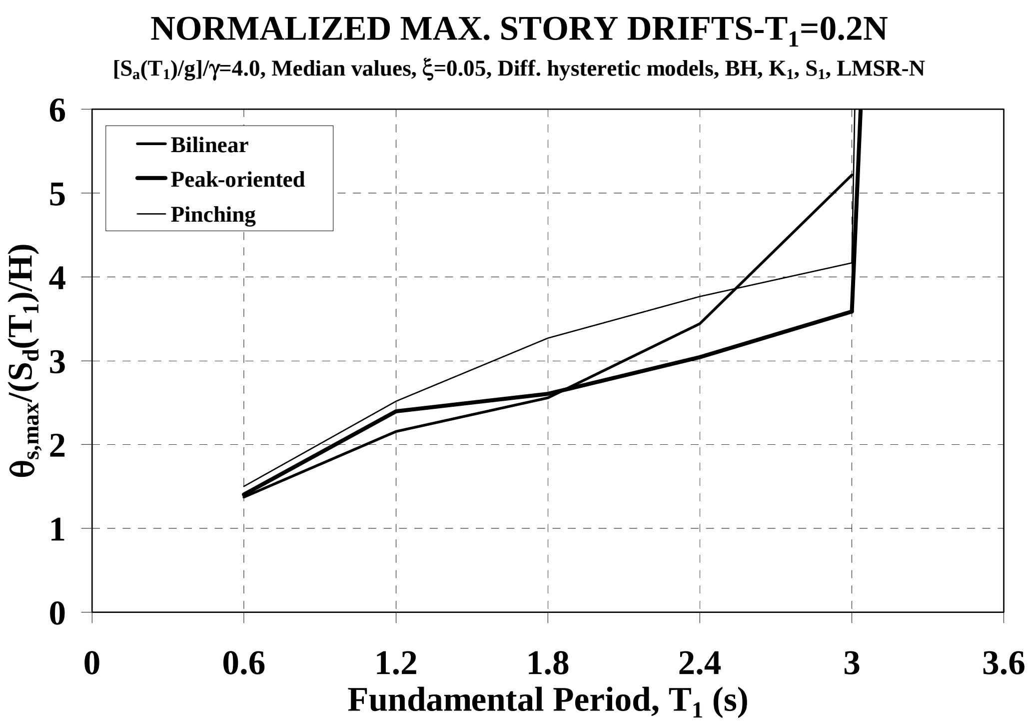

(b) T_1 = 0.2N

Figure 7.7 Median Normalized Maximum Story Drifts over the Height, Effect of the Hysteretic Model on Stiff and Flexible Frames, $[S_a(T_1)/g]/\gamma = 4.0$

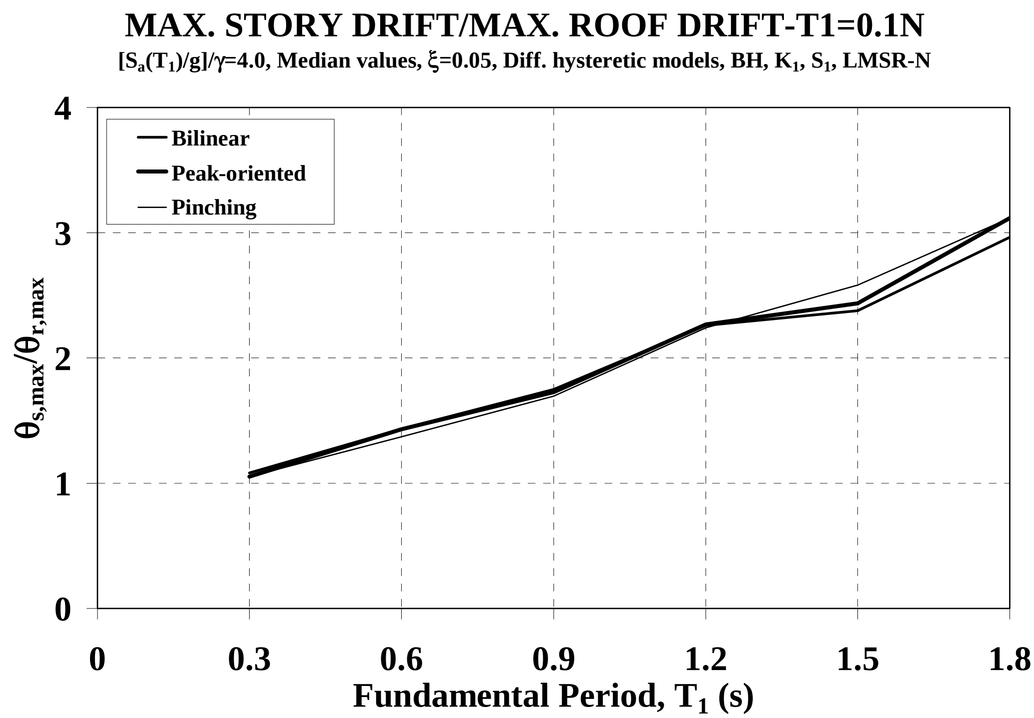

(a) $T_1 = 0.1N$

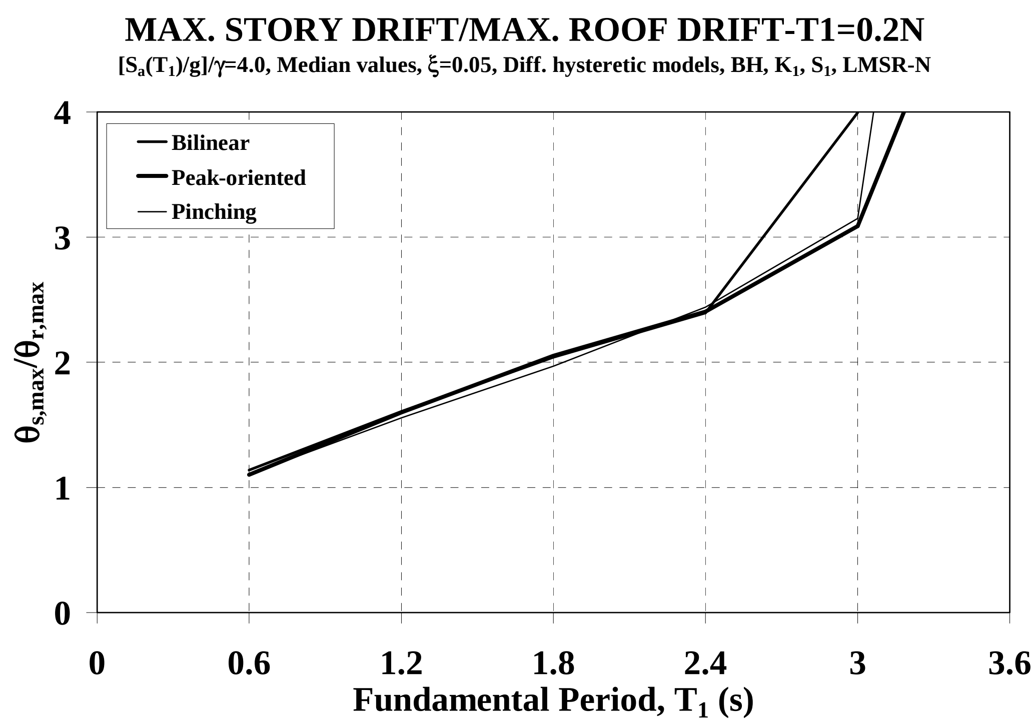

(b) $T_1 = 0.2N$

Figure 7.8 Ratio of the Maximum Story Drift Angle over the Height to the Maximum Roof Drift Angle, Effect of the Hysteretic Model on Stiff and Flexible Frames, $[S_a(T_1)/g]/\gamma = 4.0$

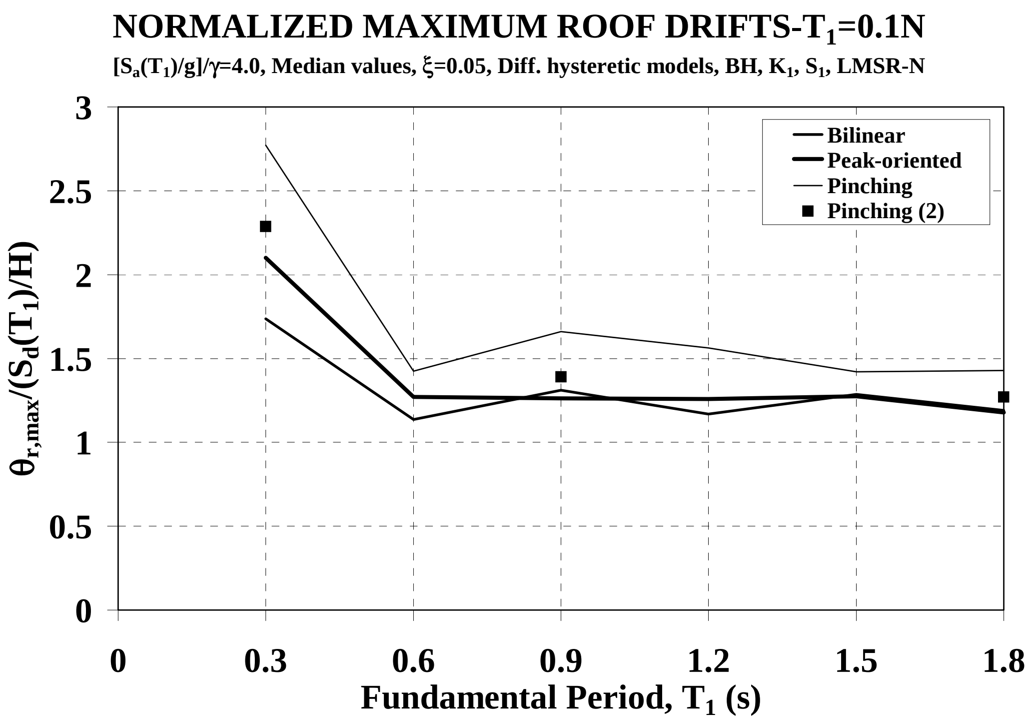

(a) $T_1 = 0.1N$

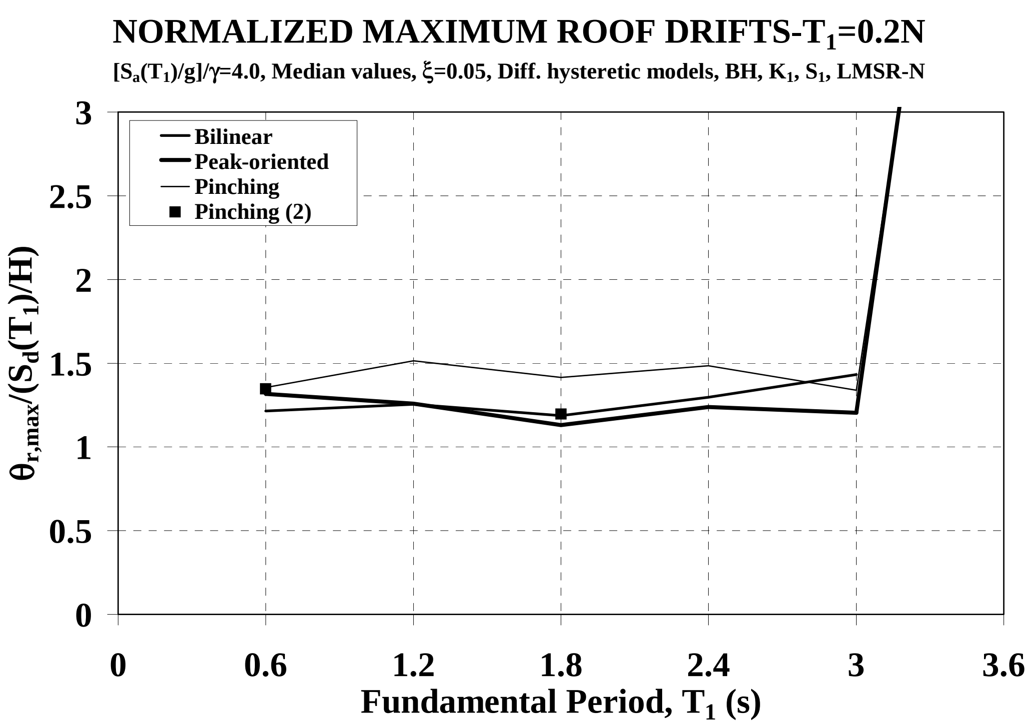

(b) $T_1 = 0.2N$

Figure 7.9 Median Normalized Maximum Roof Drifts, Effect of the Degree of Stiffness Degradation on Various Hysteretic Models, Stiff and Flexible Frames, $[S_a(T_1)/g]/\gamma = 4.0$

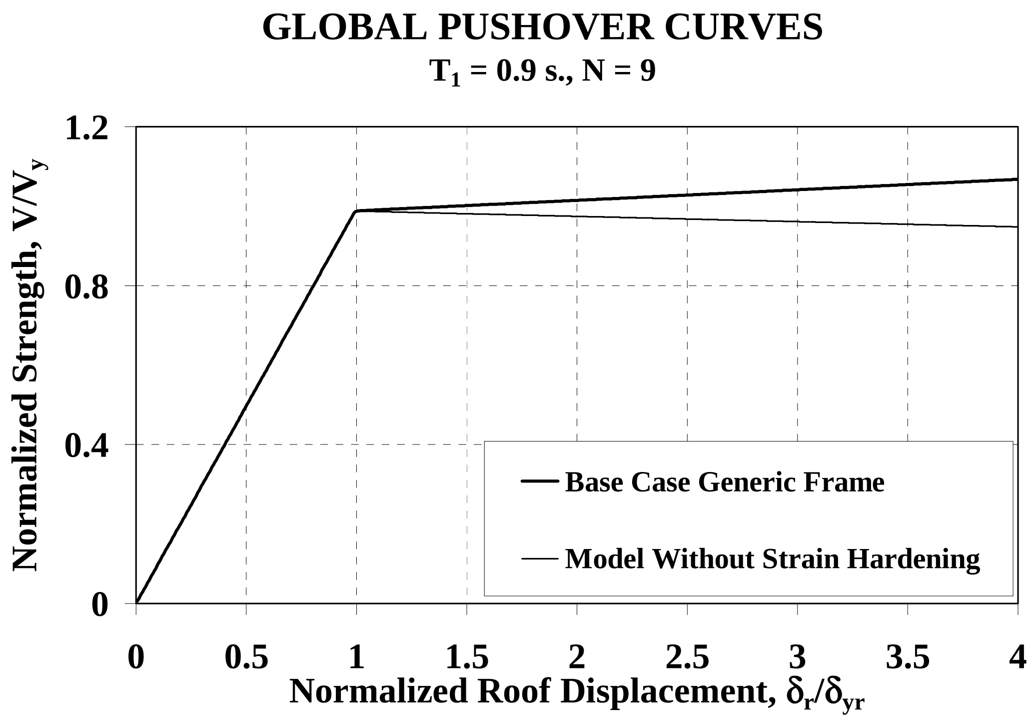

(a) T_1 = 0.9 sec

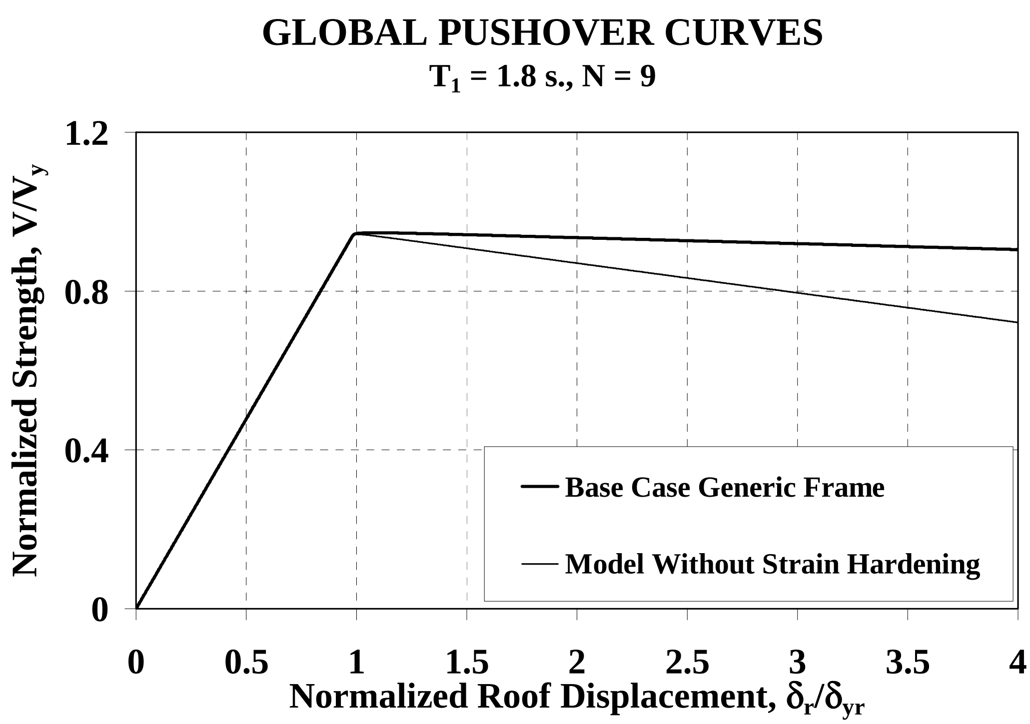

(b) T_1 = 1.8 sec

Figure 7.10 Global Pushover Curves Based on a Parabolic Load Pattern, Base Case Model and Model without Strain Hardening, N = 9, T_1 = 0.9 sec

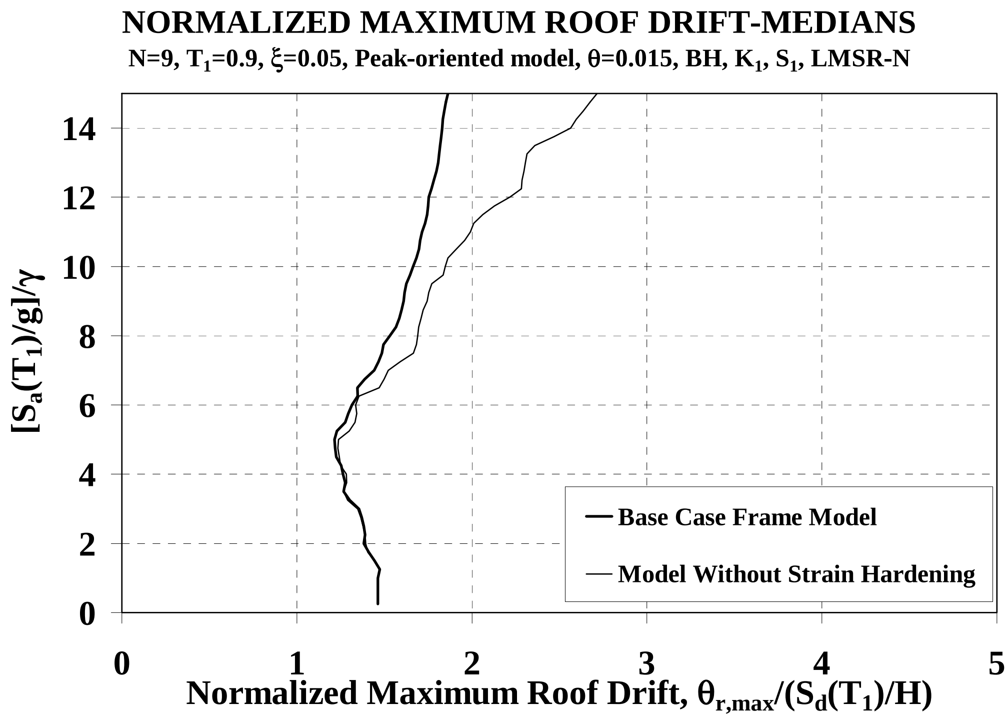

(a) T_1 = 0.9 sec

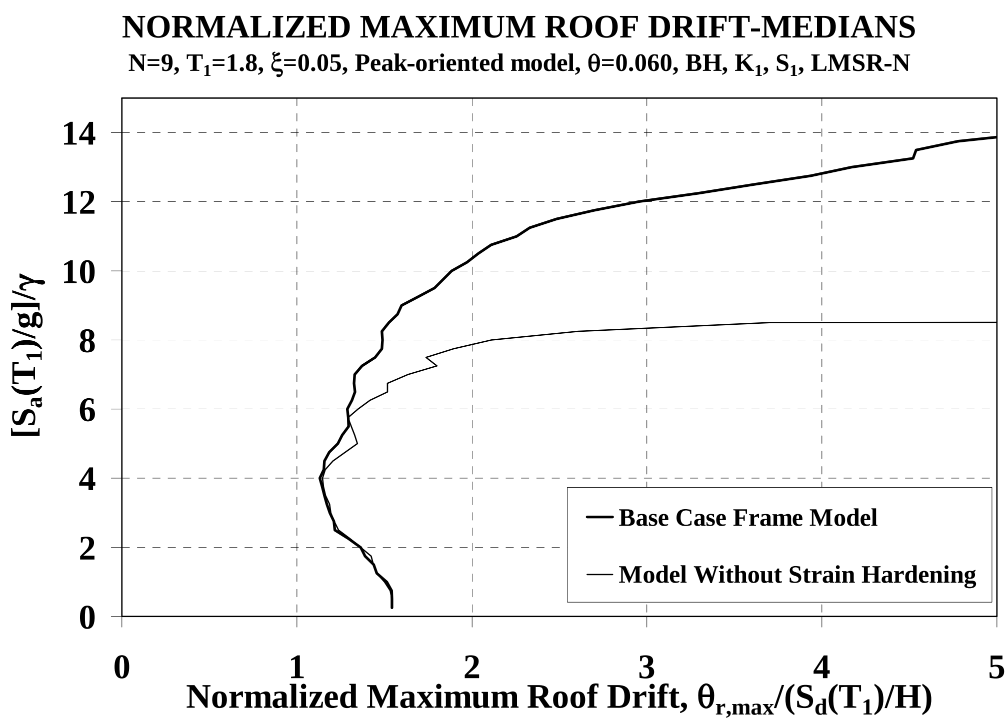

(b) T_1 = 1.8 sec

Figure 7.11 Effect of Strain Hardening on the Median Normalized Maximum Roof Drift Angle, N = 9

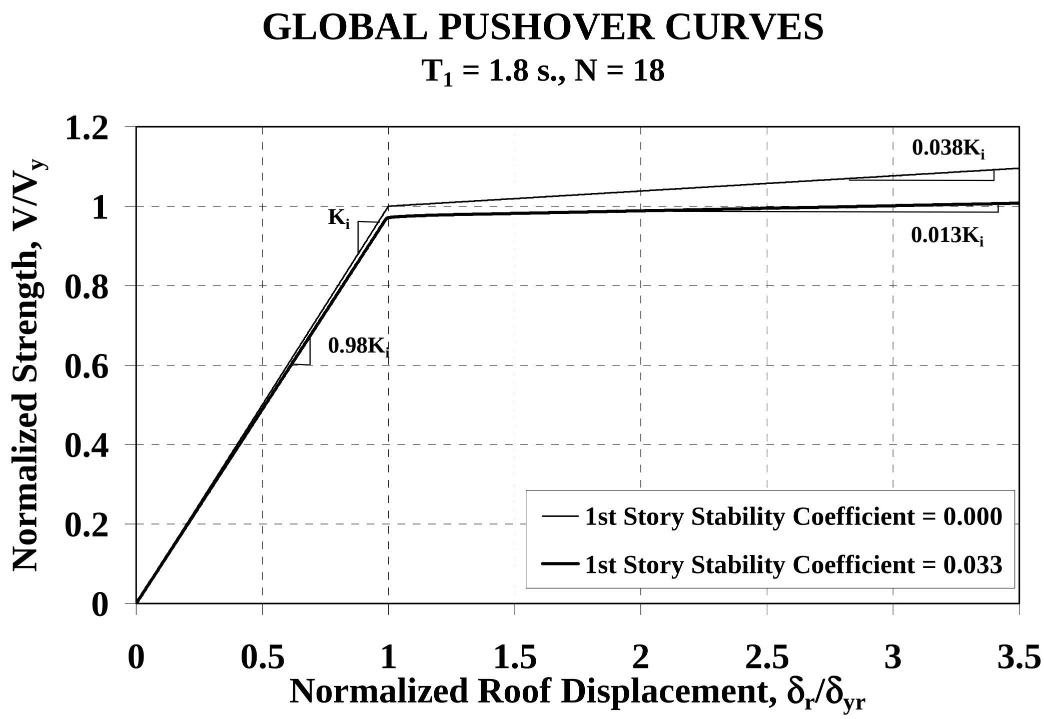

(a) Global Pushover Curves

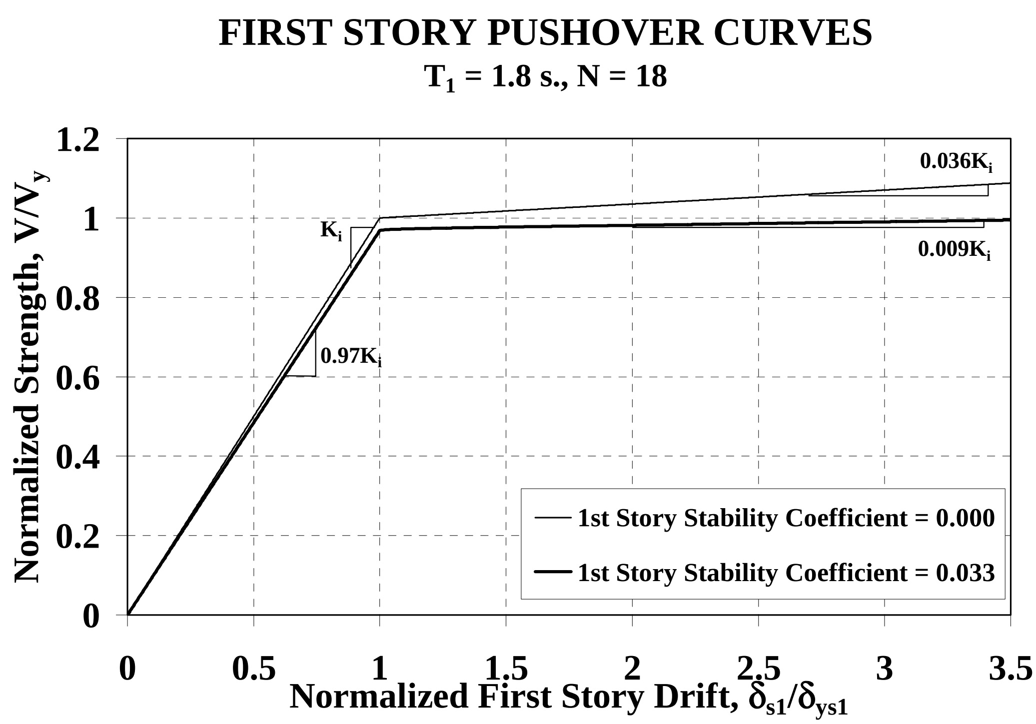

(b) First-Story Pushover Curves

Figure 7.12 Pushover Curves Based on a Parabolic Load Pattern, Base Case Model and Model without P-Delta Effects, N = 18, T_1 = 1.8 sec

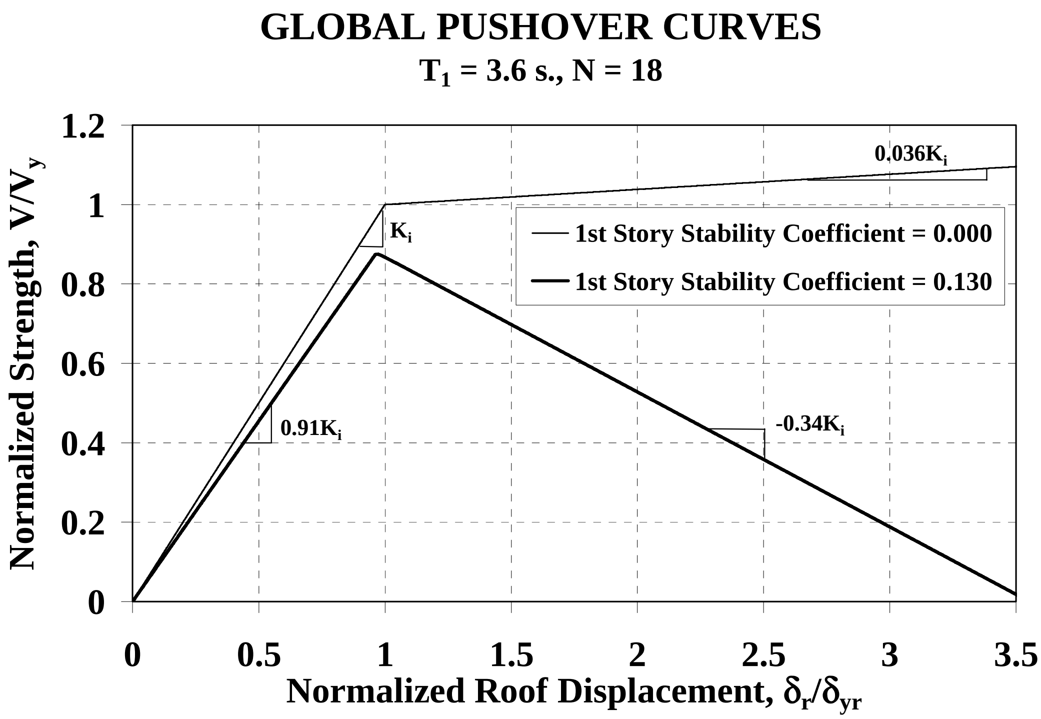

(a) Global Pushover Curves

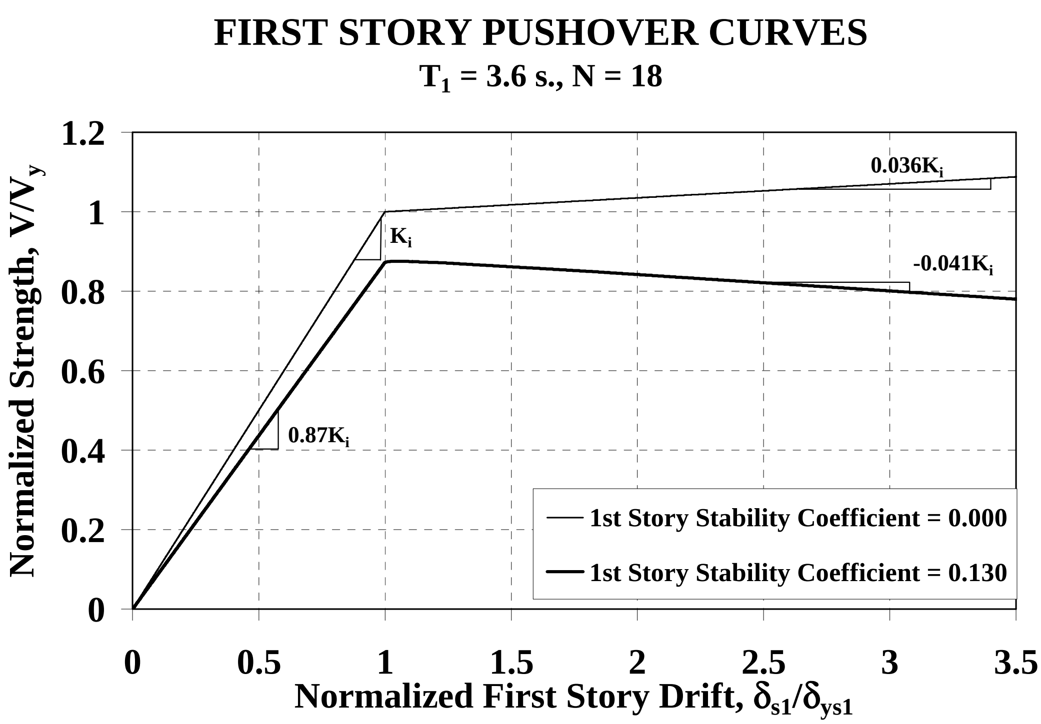

(b) First-Story Pushover Curves

Figure 7.13 Pushover Curves Based on a Parabolic Load Pattern, Base Case Model and Model without P-Delta Effects, N = 18, T_1 = 3.6 sec

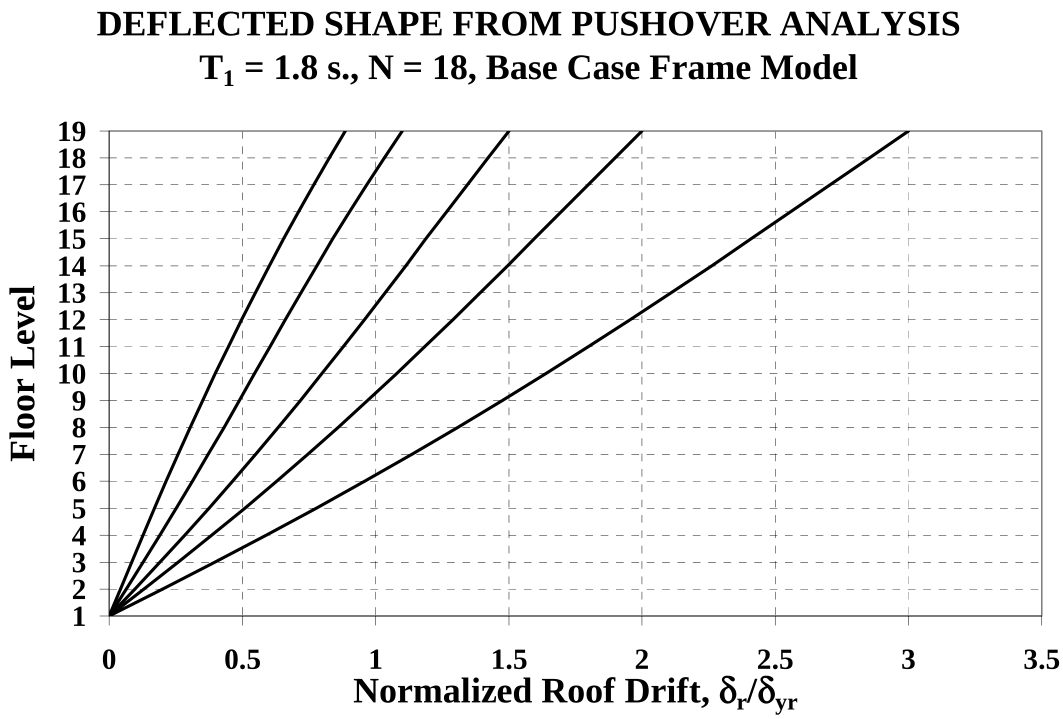

(a) T_1 = 1.8 sec

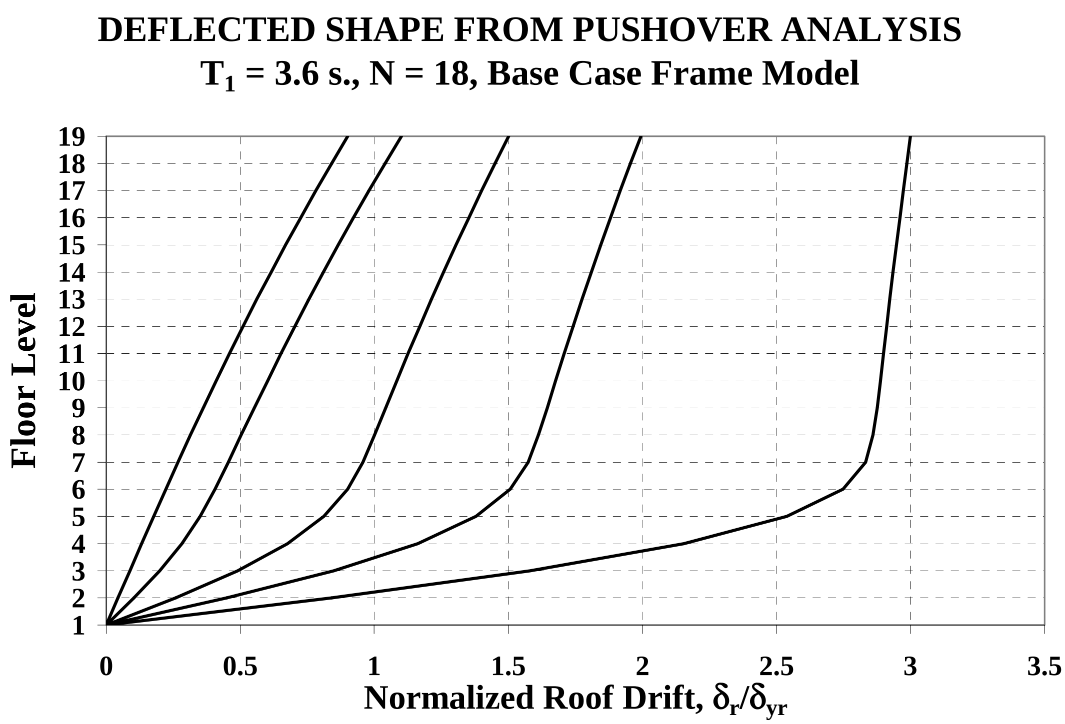

(b) T_1 = 3.6 sec

Figure 7.14 Deflected Shapes from Pushover Analyses, Base Case Frame Models, N = 18

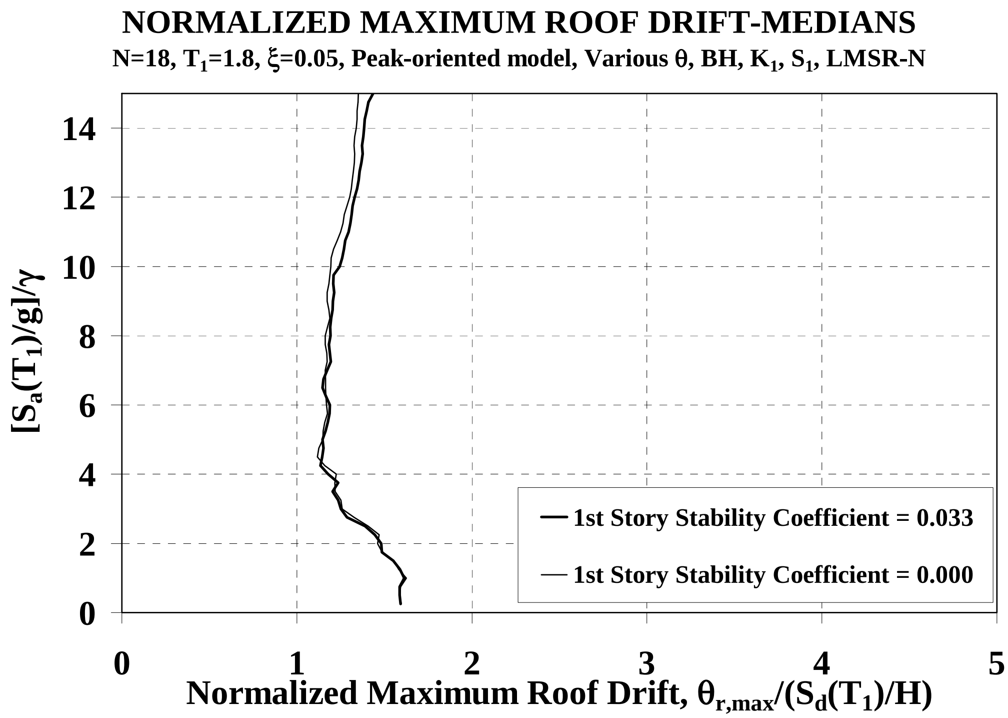

(a) T_1 = 1.8 sec

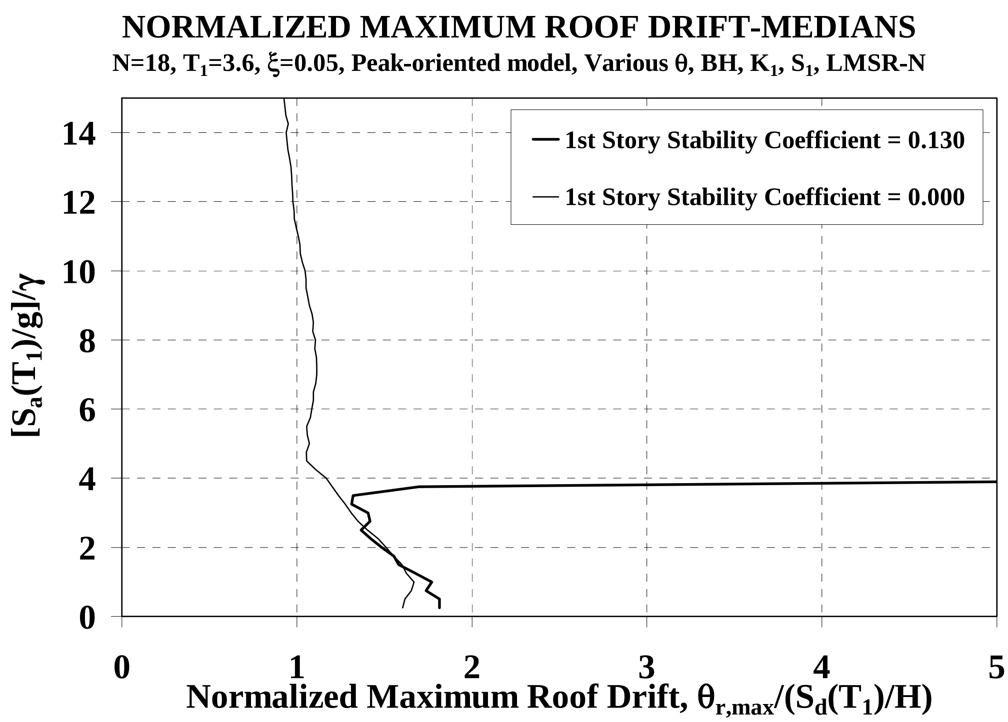

(b) T_1 = 3.6 sec

Figure 7.15 Effect of Structure P-delta on the Median Normalized Maximum Roof Drift Angle, N = 18

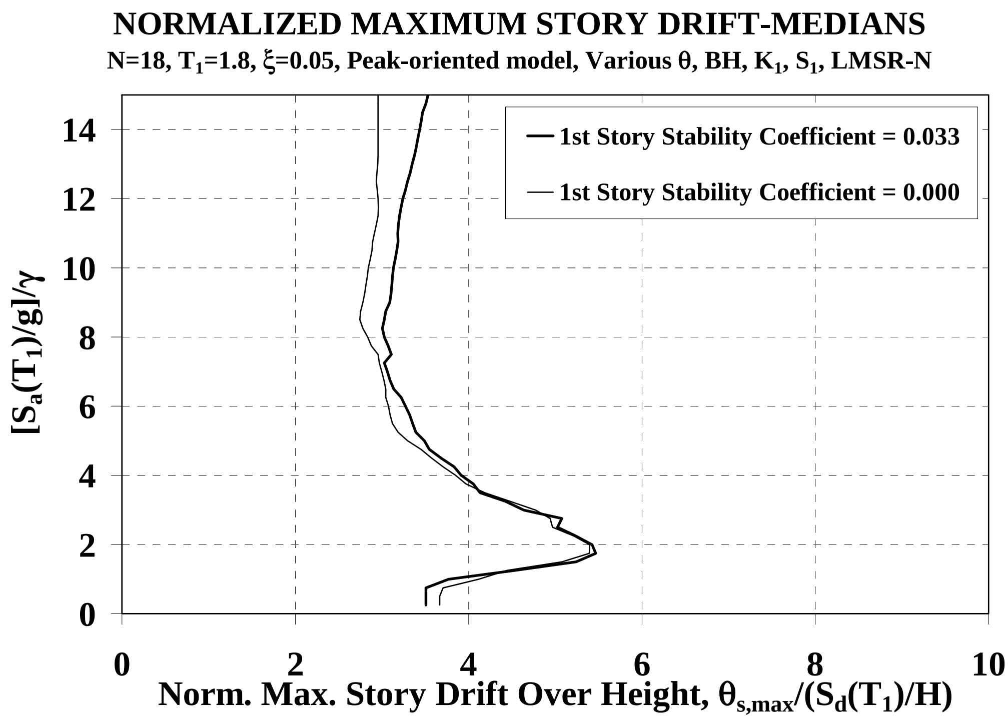

(a) T_1 = 1.8 sec

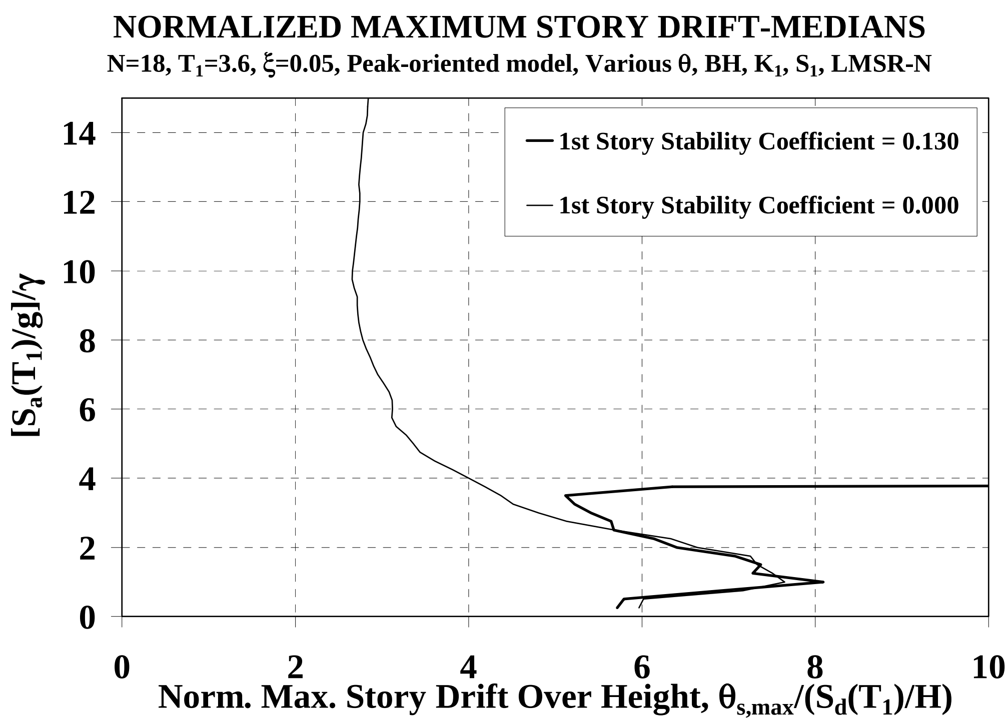

(b) T_1 = 3.6 sec

Figure 7.16 Effect of Structure P-delta on the Median Normalized Maximum Story Drift Angle over the Height, N = 18

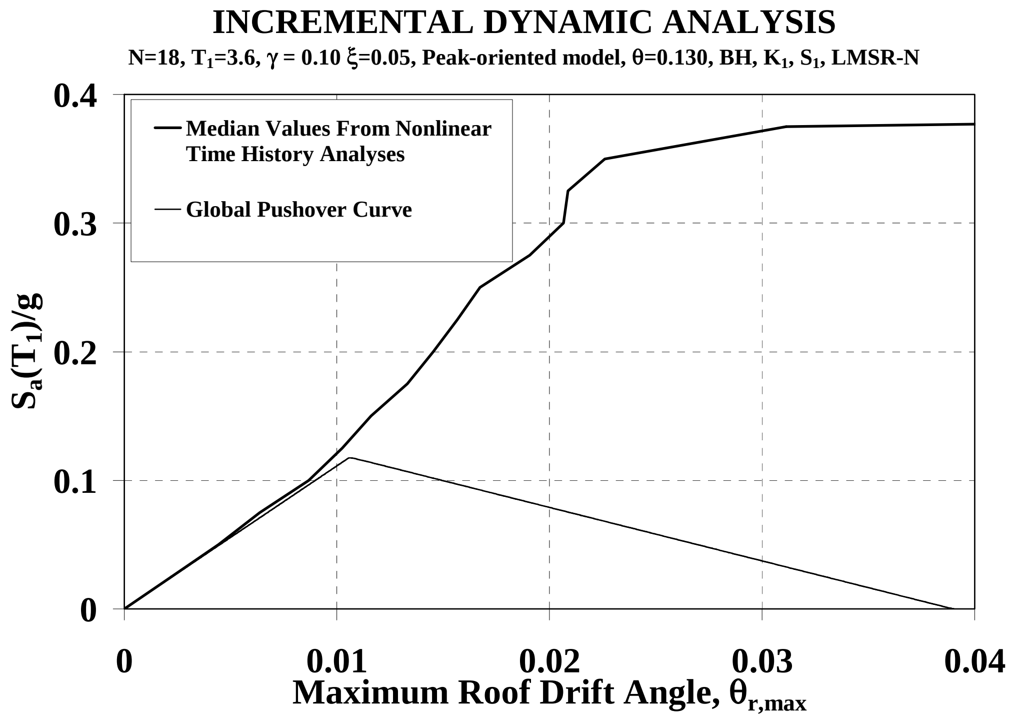

Figure 7.17 Median Incremental Dynamic Analysis Curve and Global Pushover Curve, N = 18, T_1 = 3.6 sec, γ = 0.10

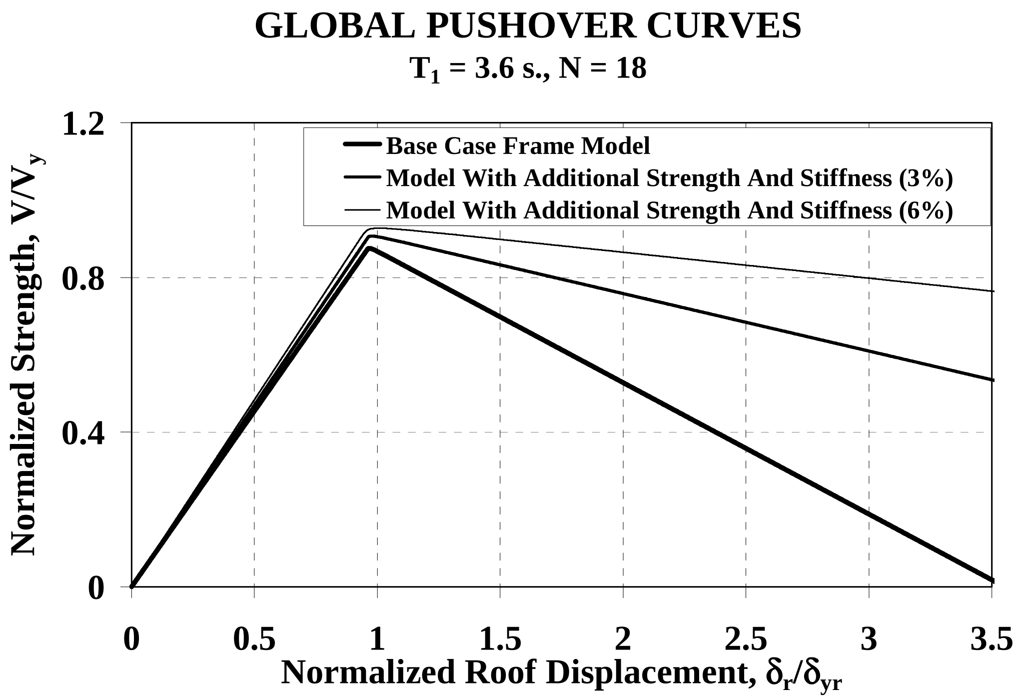

Figure 7.18 Global Pushover Curves Based on a Parabolic Load Pattern, Base Case Frame Model and Models with Additional Strength and Stiffness, N = 18, T_1 = 3.6 sec.

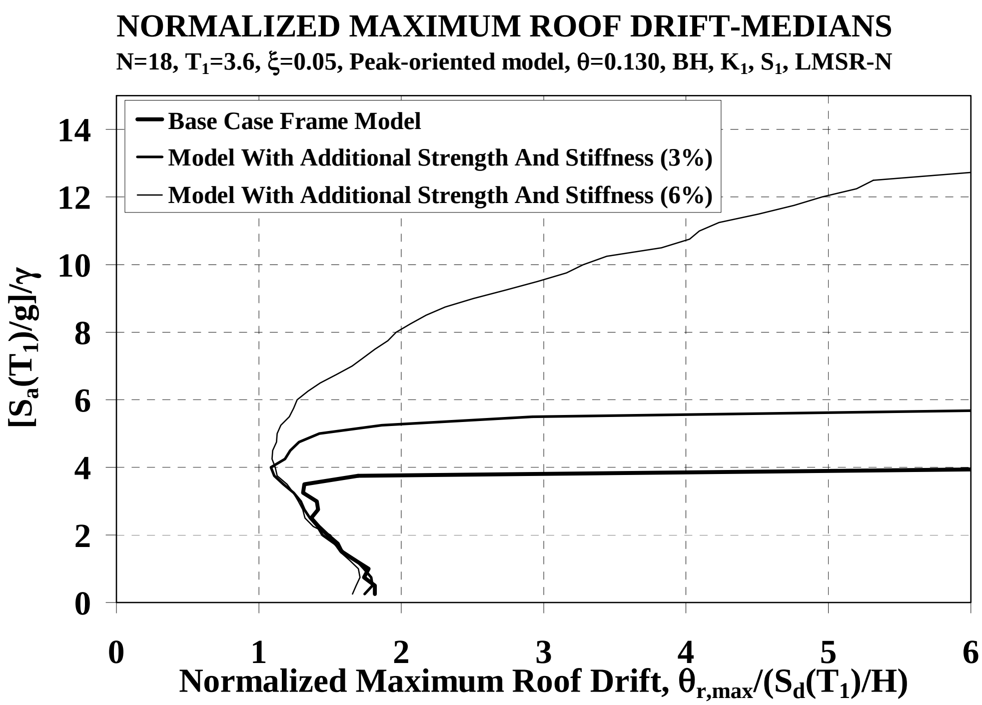

Figure 7.19 Effect of Additional Strength and Stiffness on the Median Normalized Maximum Roof drift Demands, N = 18, T_1 = 3.6 sec.

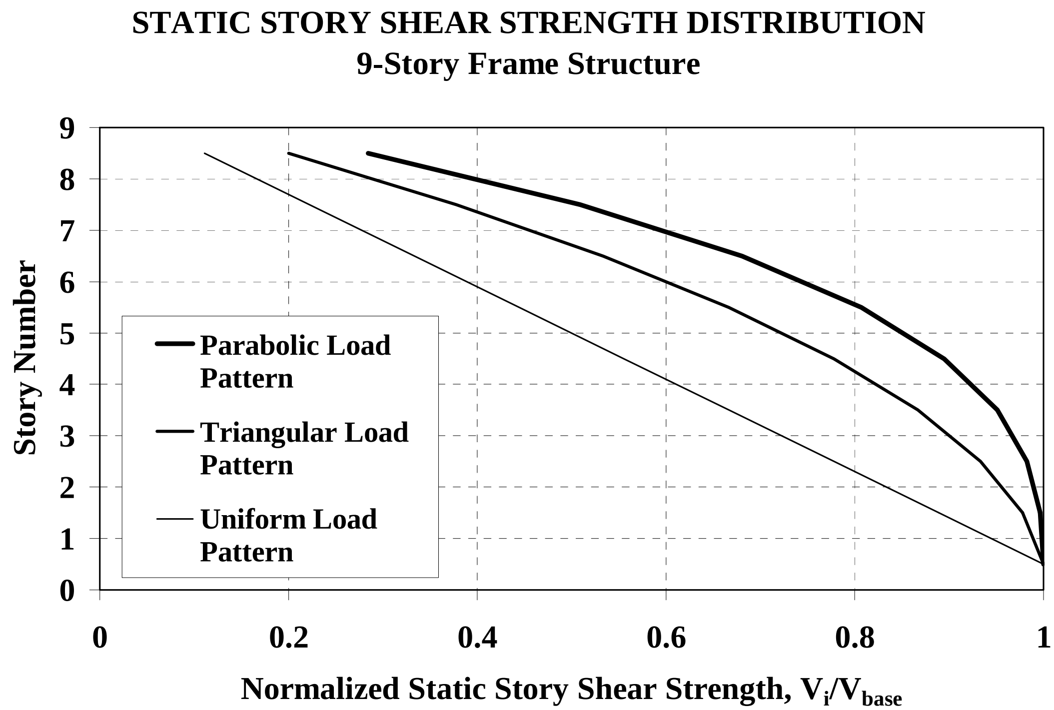

Figure 7.20 Normalized Static Story Shear Strength Distribution, Various Design Load Patterns, N = 18, T_1 = 1.8 sec

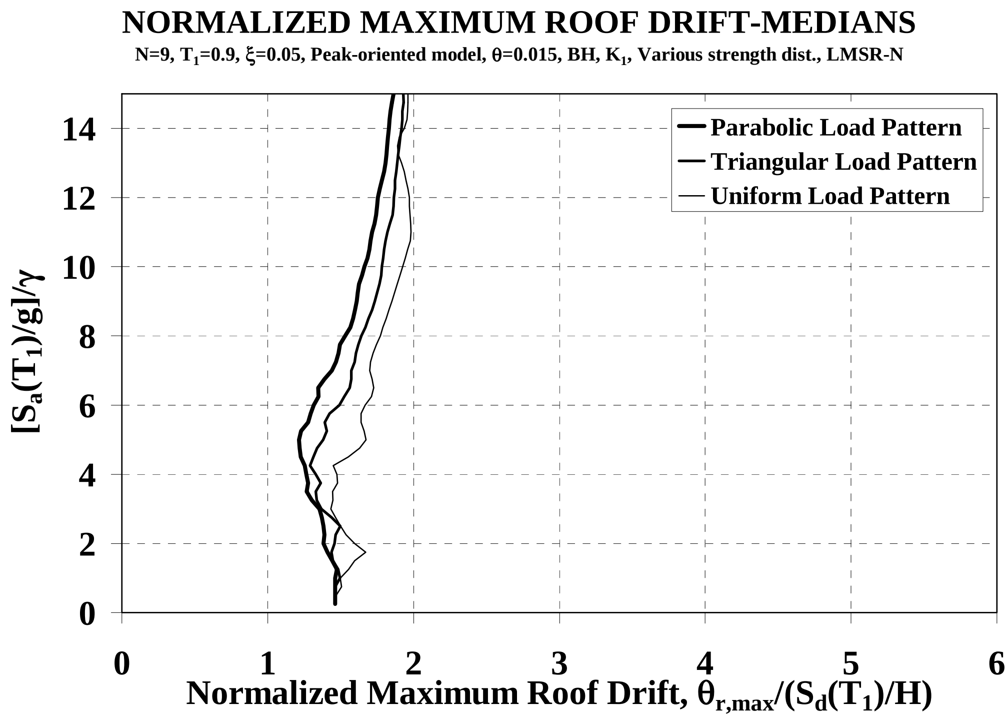

(a) T_1 = 0.9 sec

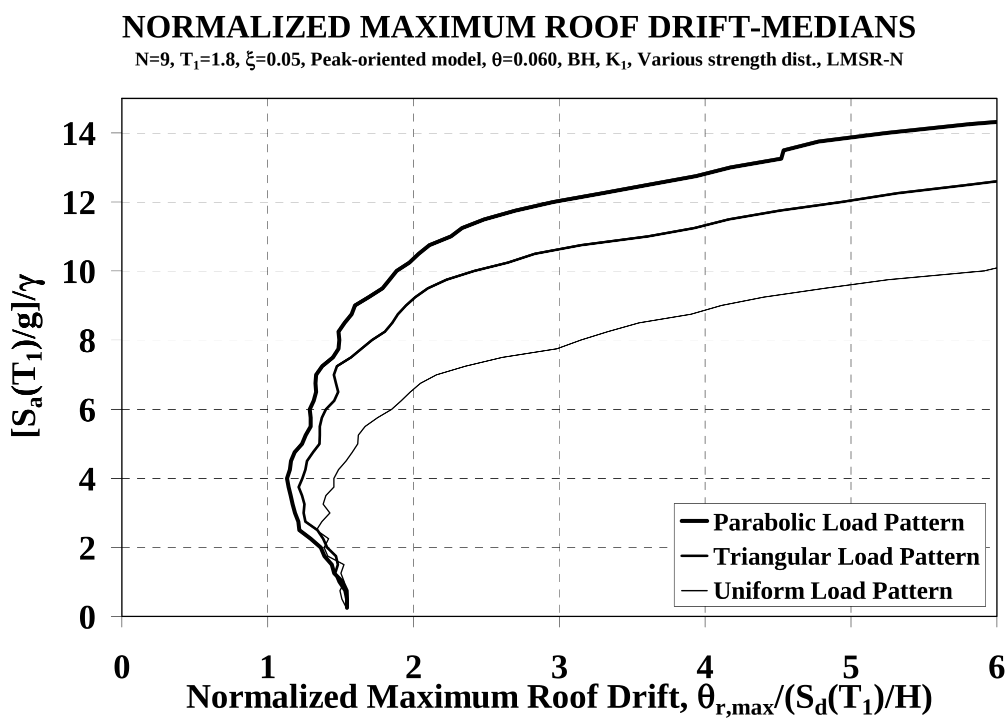

(b) T_1 = 1.8 sec.

Figure 7.21 Effect of Various Story Shear Strength Distributions on the Median Normalized Maximum Roof Drift Demand, N = 9

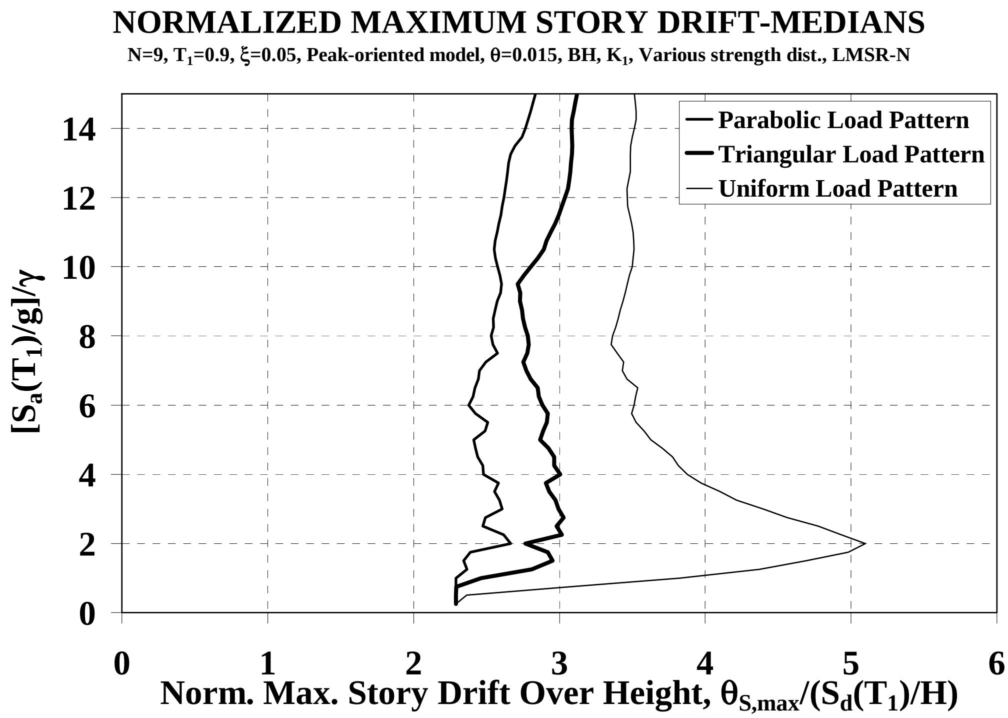

(a) T_1 = 0.9 sec

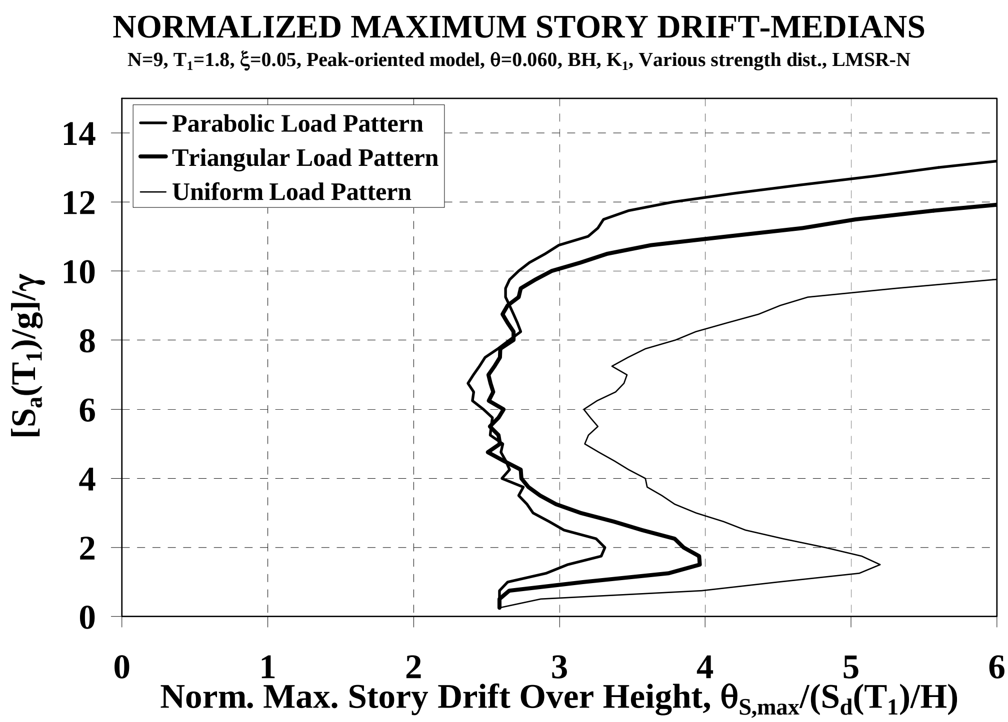

(b) T_1 = 1.8 sec

Figure 7.22 Effect of Various Story Shear Strength Distributions on the Median Normalized Maximum Story Drift Angle over the Height, N = 9

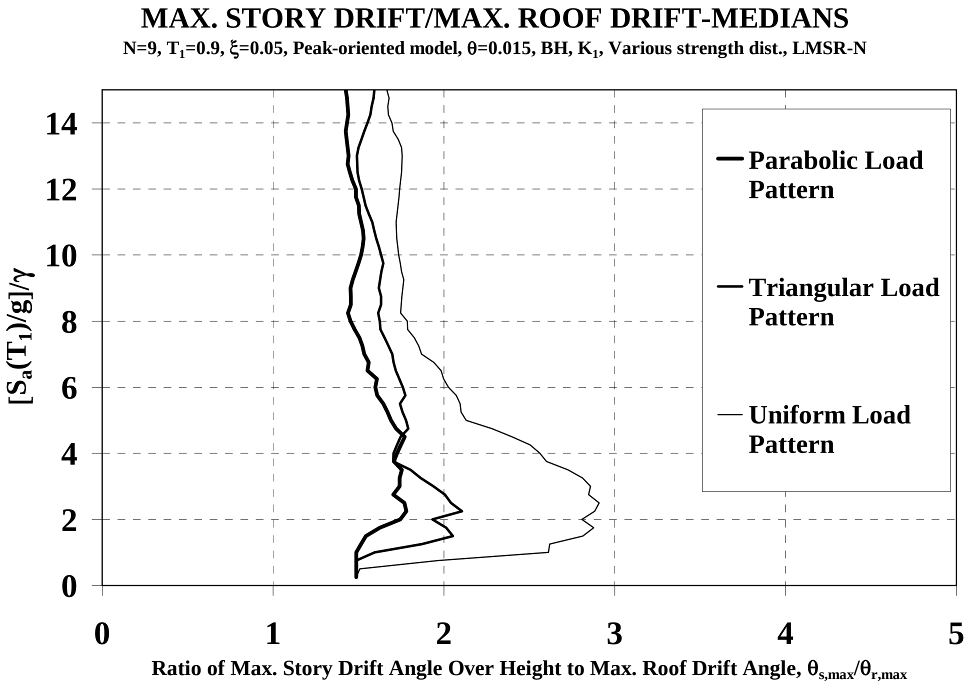

(a) T_1 = 0.9 sec

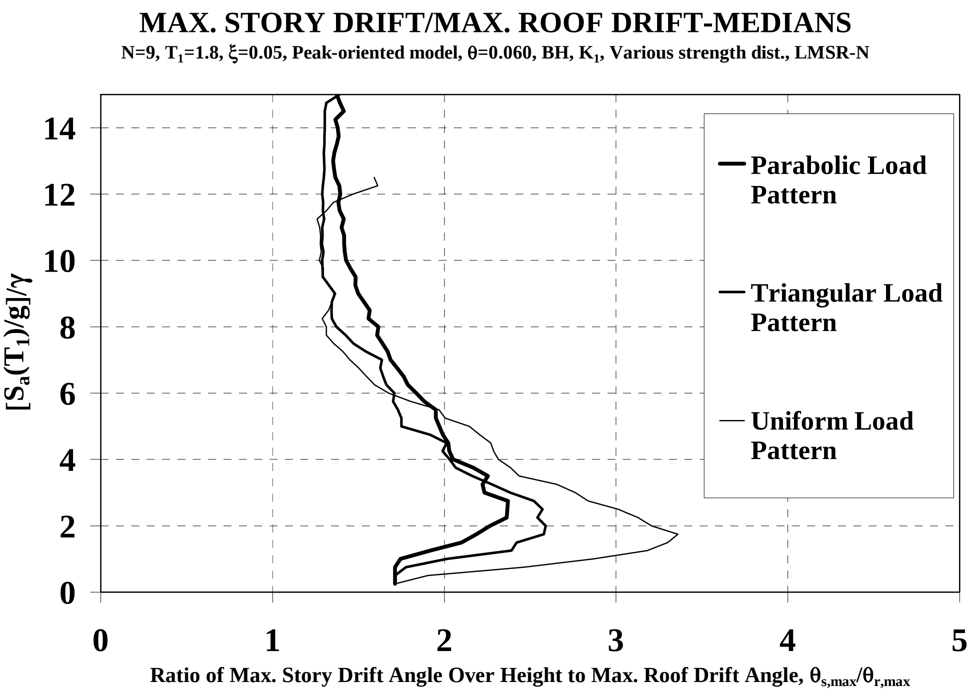

(b) T_1 = 1.8 sec

Figure 7.23 Effect of Various Story Shear Strength Distributions on the Median Ratio of the Maximum Story Drift Angle over the Height to the Maximum Roof Drift Angle, N = 9

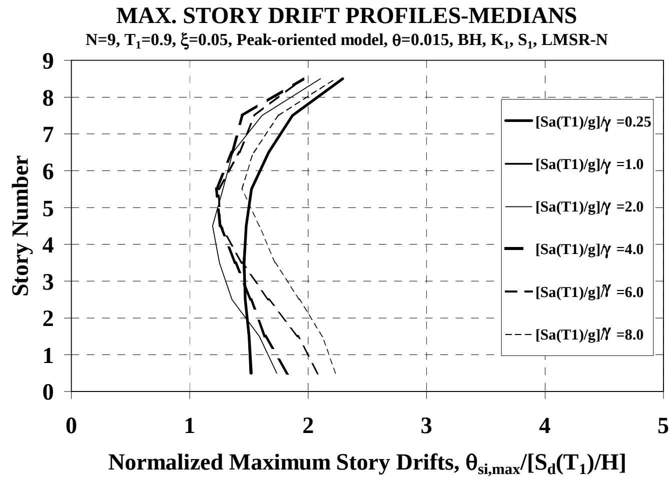

(a) Parabolic Load Pattern

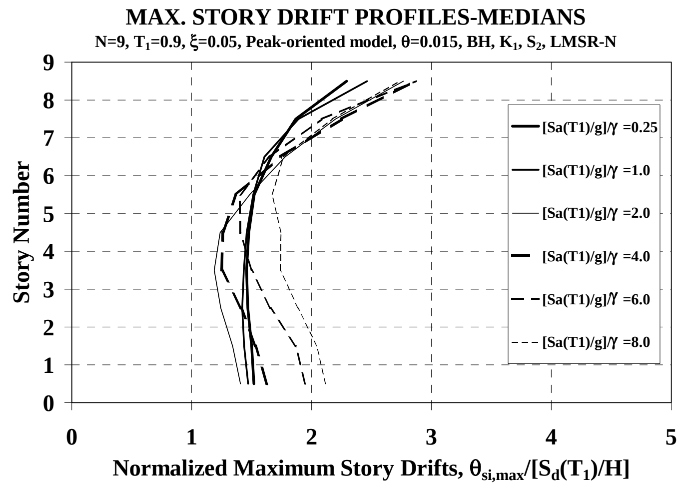

(b) Triangular Load Pattern

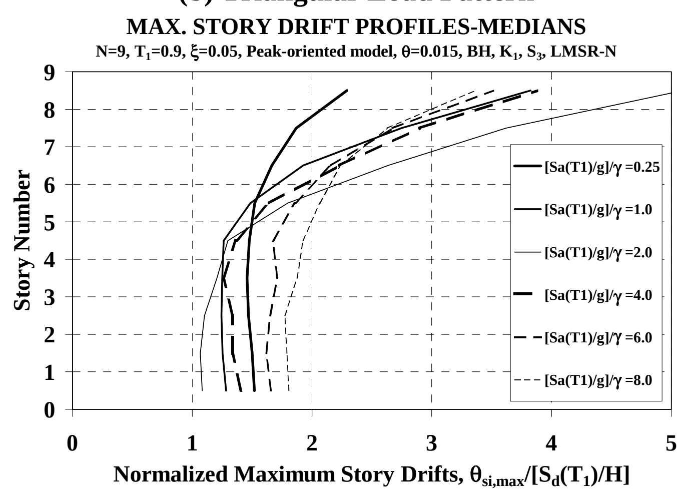

(c) Uniform Load Pattern

Figure 7.24 Effect of Various Story Shear Strength Patterns on the Distribution over the Height of Median Normalized Maximum Story Drift Angles, N = 9, T_1 = 0.9 sec

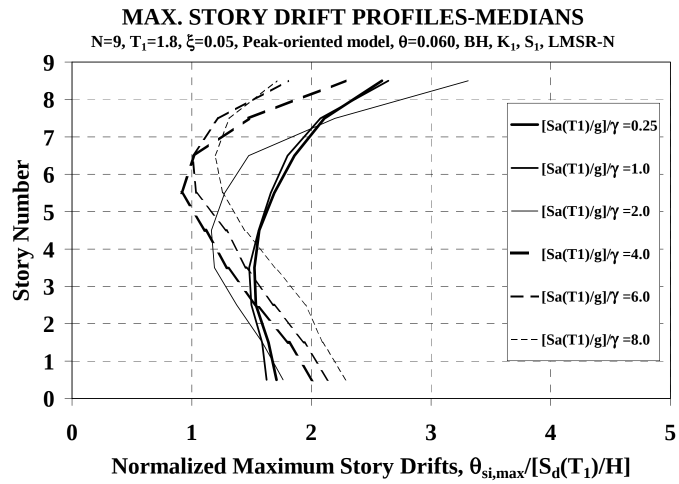

(a) Parabolic Load Pattern

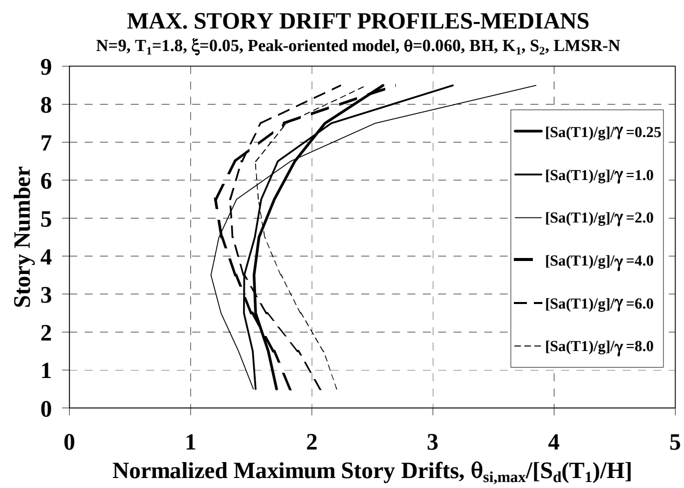

(b) Triangular Load Pattern

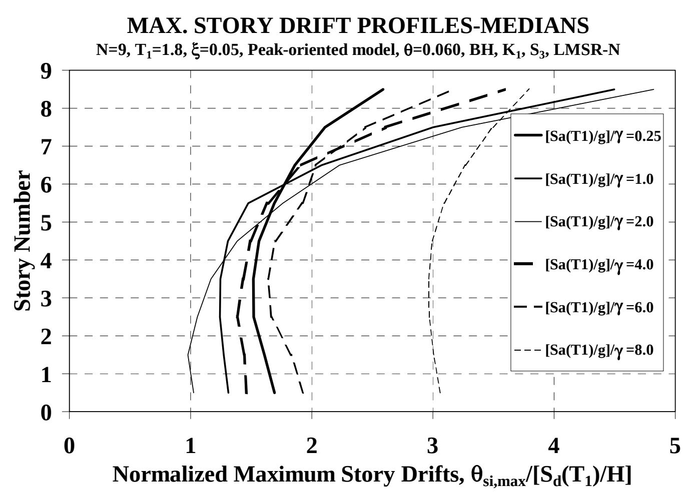

(c) Uniform Load Pattern

Figure 7.25 Effect of Various Story Shear Strength Patterns on the Distribution over the Height of Median Normalized Maximum Story Drift Angles, N = 9, T_1 = 1.8 sec

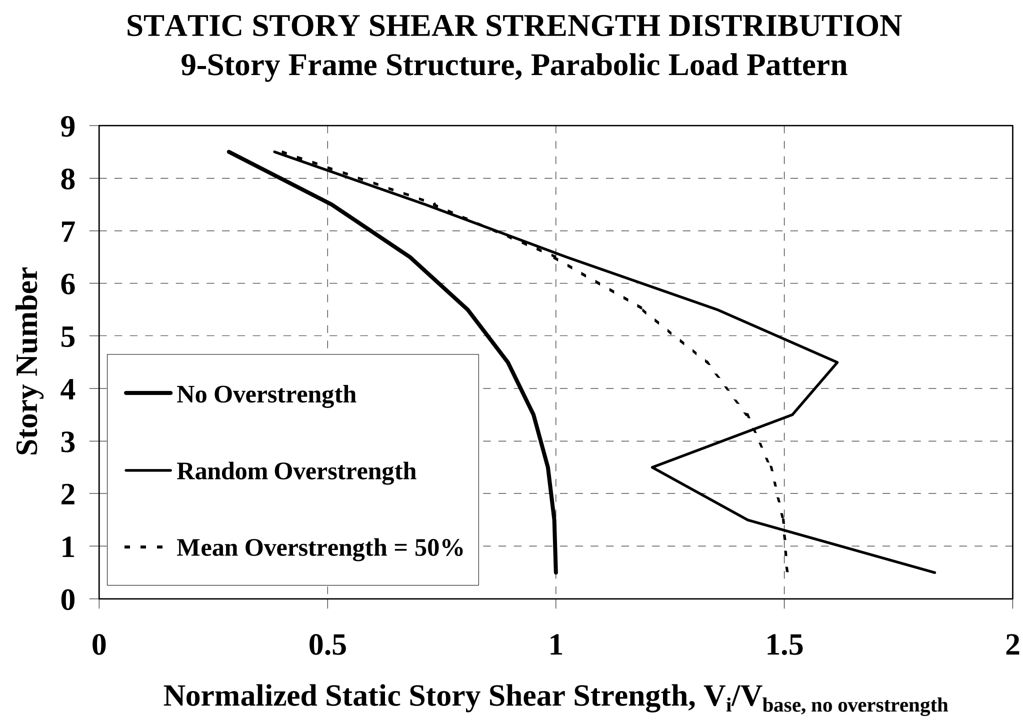

Figure 7.26 Normalized Static Story Shear Strength Distribution, Models with and without Random Overstrength, N = 9

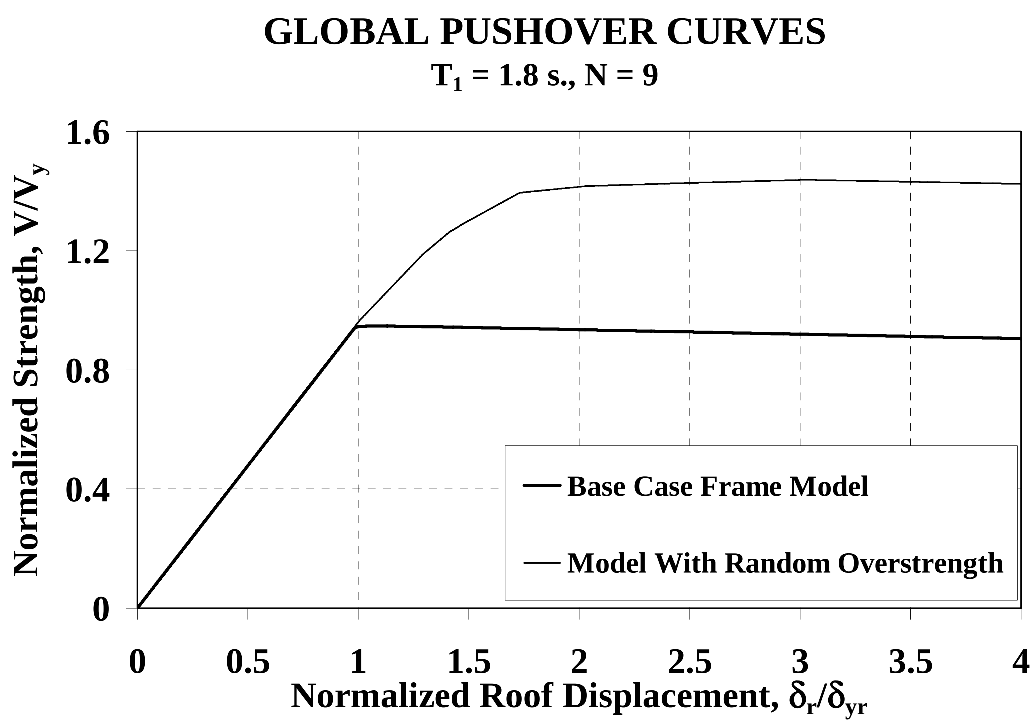

Figure 7.27 Global Pushover Curves Based on a Parabolic Load Pattern, Base Case Frame Model and Model with Random Overstrength, N = 9, T_1 = 1.8 sec

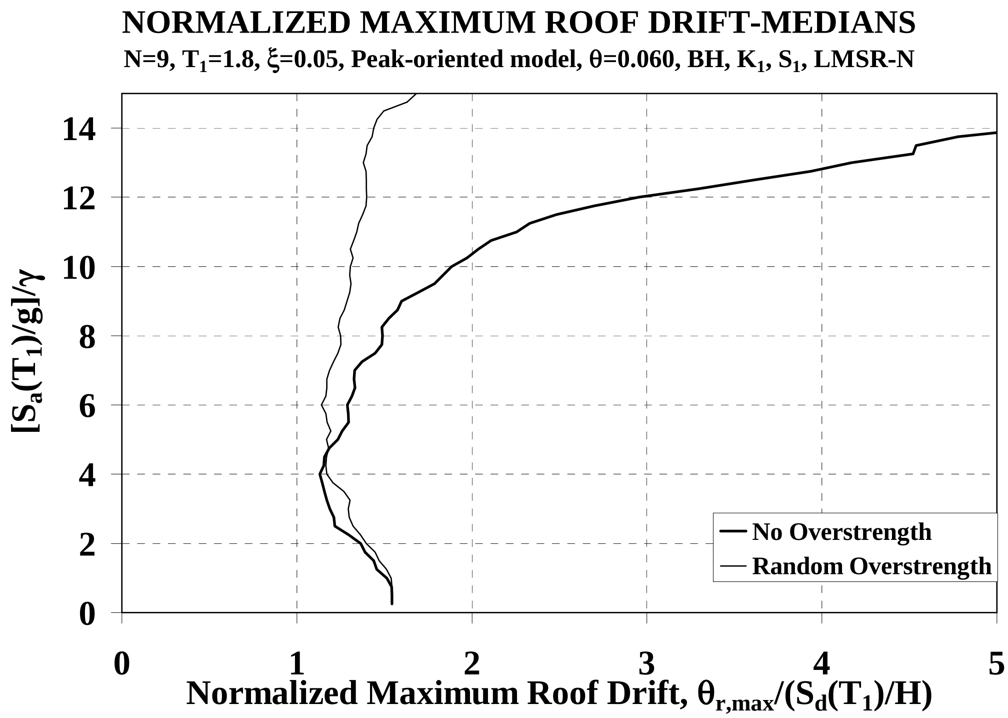

(a) Median Normalized Maximum Roof Drift Angle

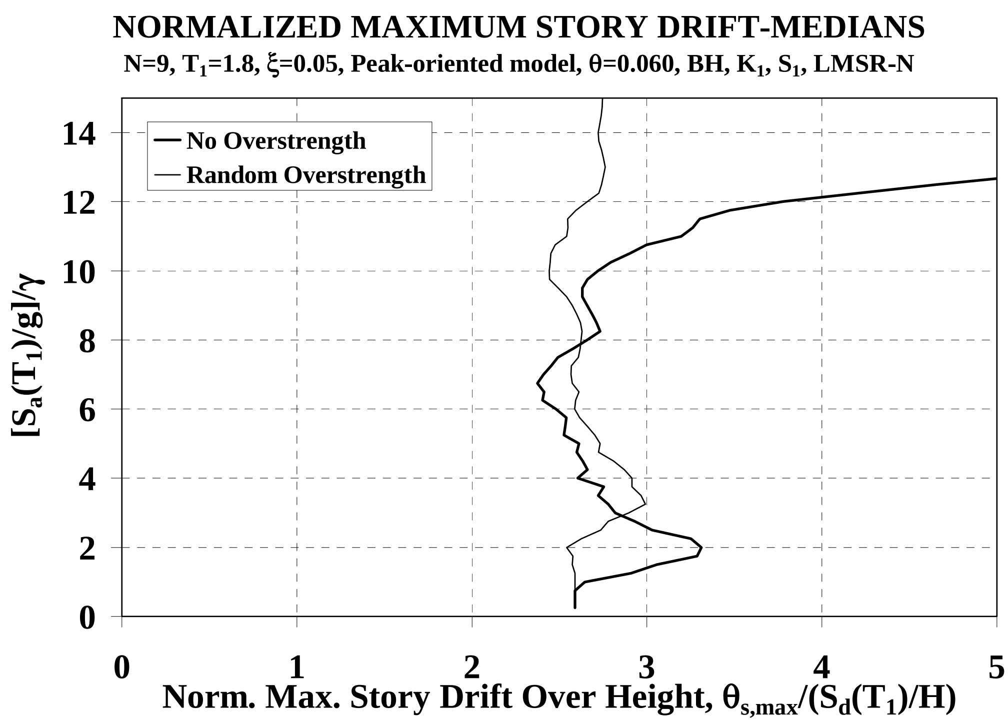

(b) Median Normalized Maximum Story Drift Angle over the Height

Figure 7.28 Effect of Random Overstrength on the Medians of the Maximum Roof Drift and the Maximum Story Drift Angle over the Height, N = 9, T_1 =1.8 sec

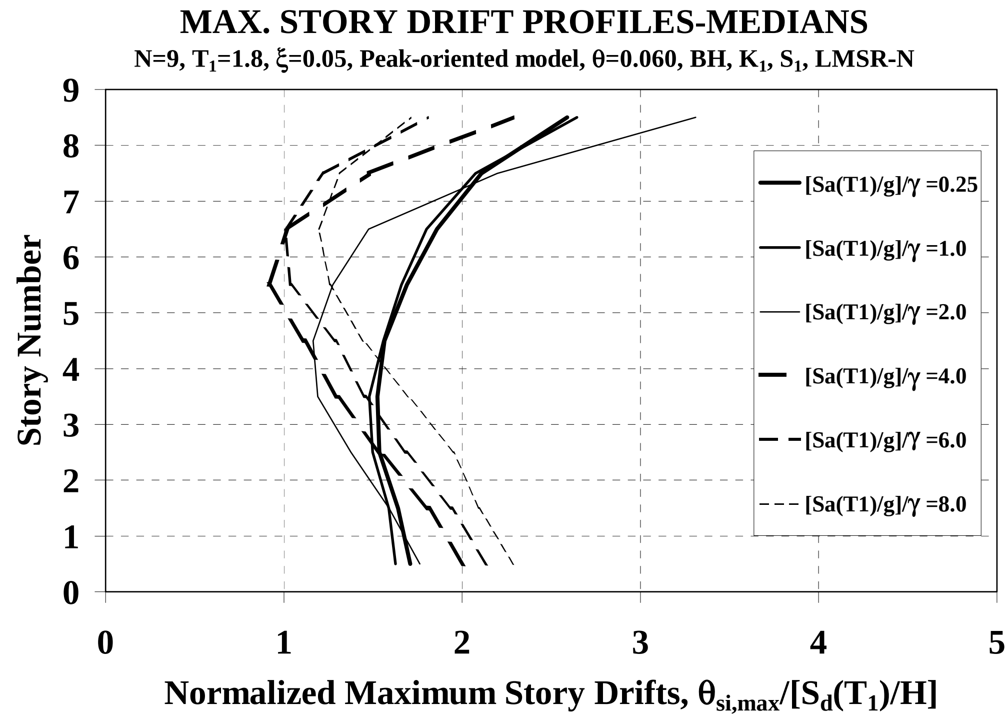

(a) Base Case Frame Model (No Overstrength)

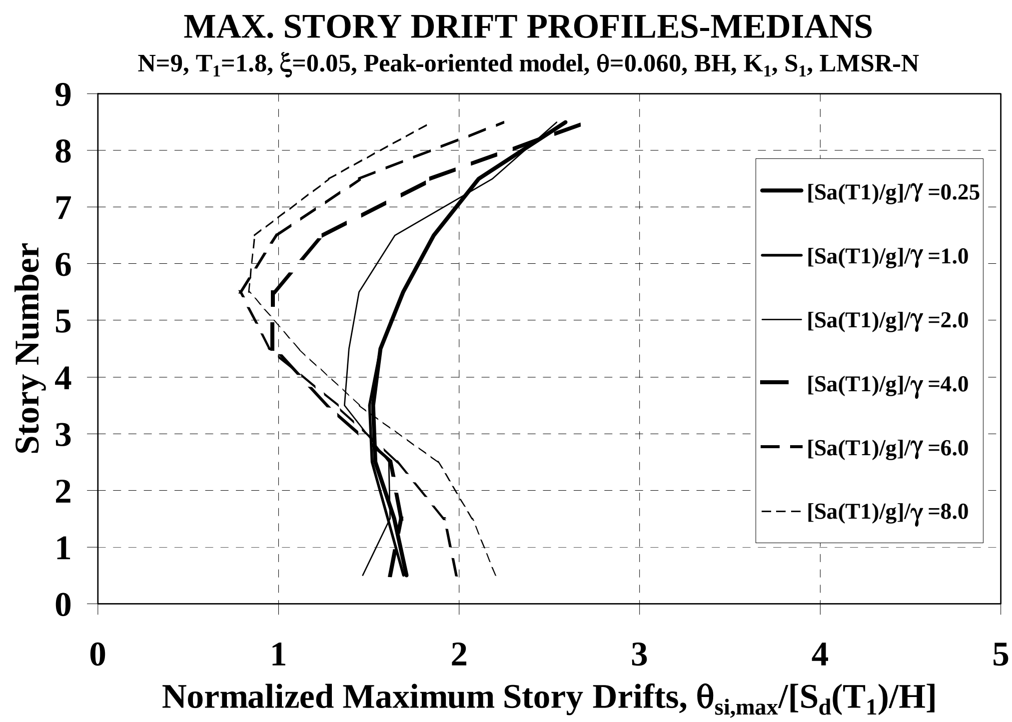

(b) Model with Random Overstrength

Figure 7.29 Effect of Random Overstrength on the Distribution over the Height of Median Normalized Maximum Story Drift angles, N = 9, T_1 = 1.8 sec

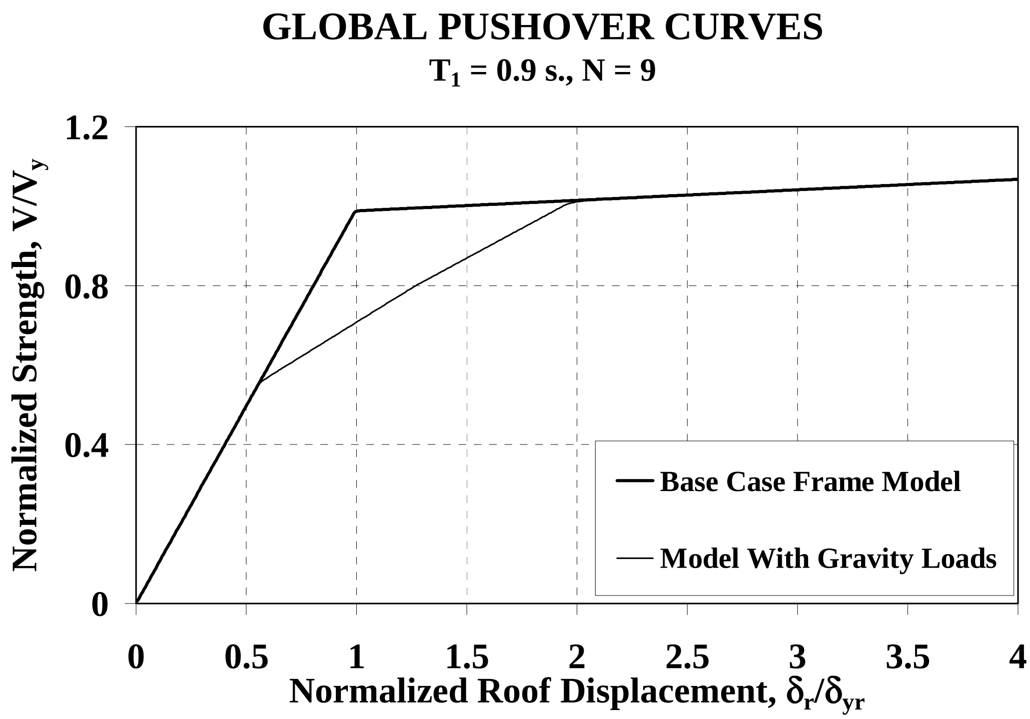

(a) T_1 = 0.9 sec

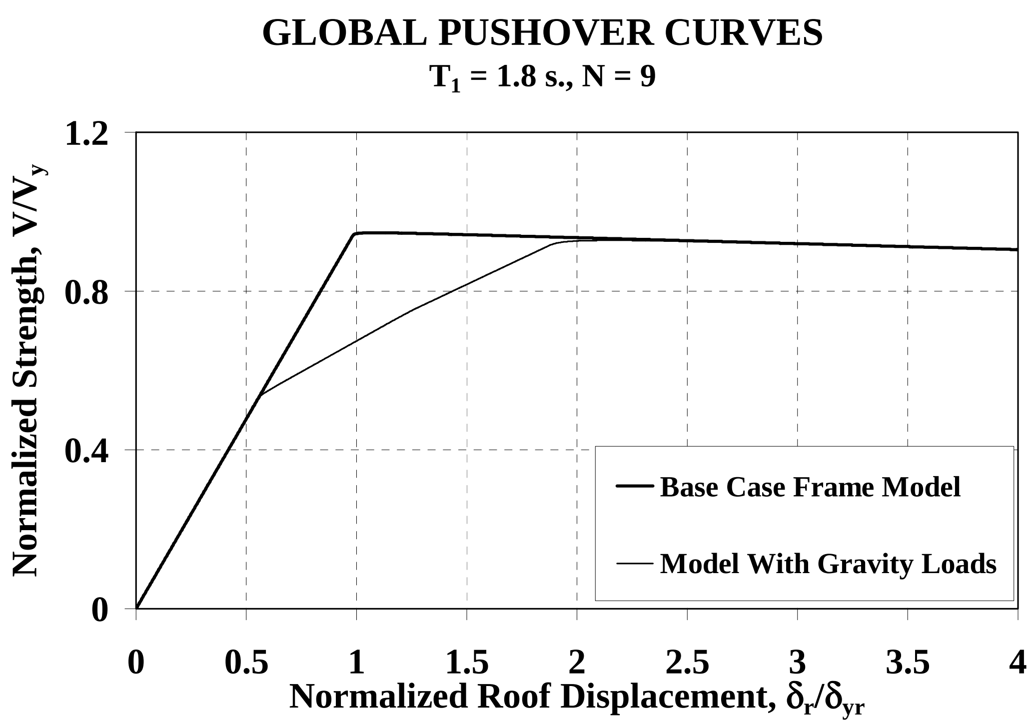

(b) T_1 = 1.8 sec

Figure 7.30 Global Pushover Analyses Based on a Parabolic Load Pattern, Base Case Frame Models and Models with Gravity Load Moments, N = 9

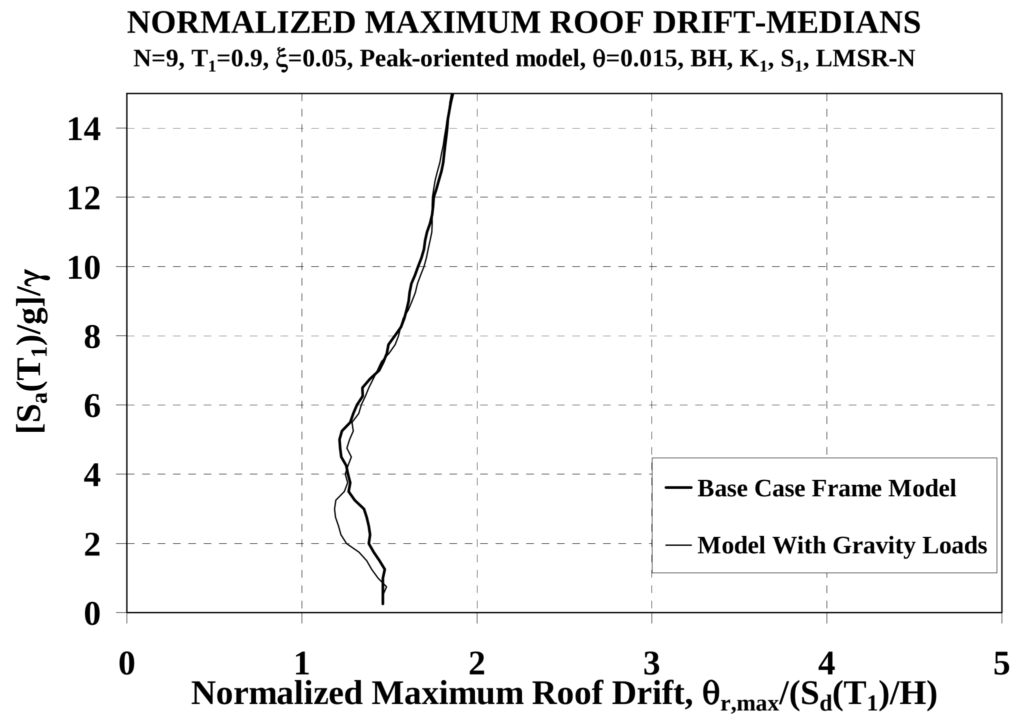

(a) T_1 = 0.9 sec

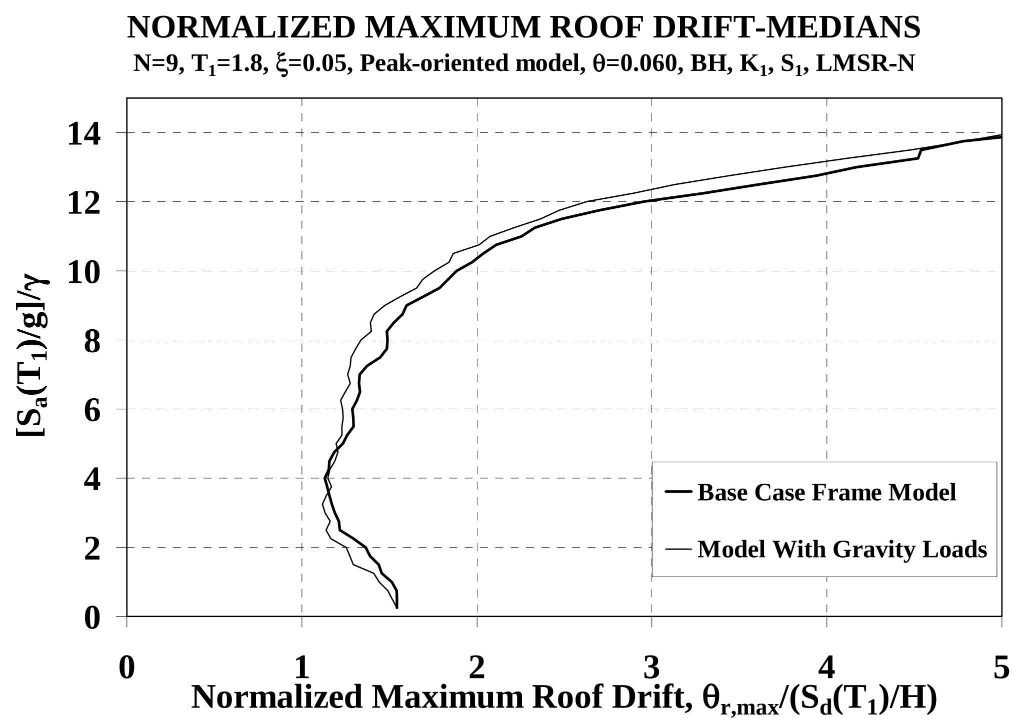

(b) T_1 = 1.8 sec

Figure 7.31 Effect of Gravity Load Moments on the Median Normalized Maximum Roof Drift Angle, N = 9

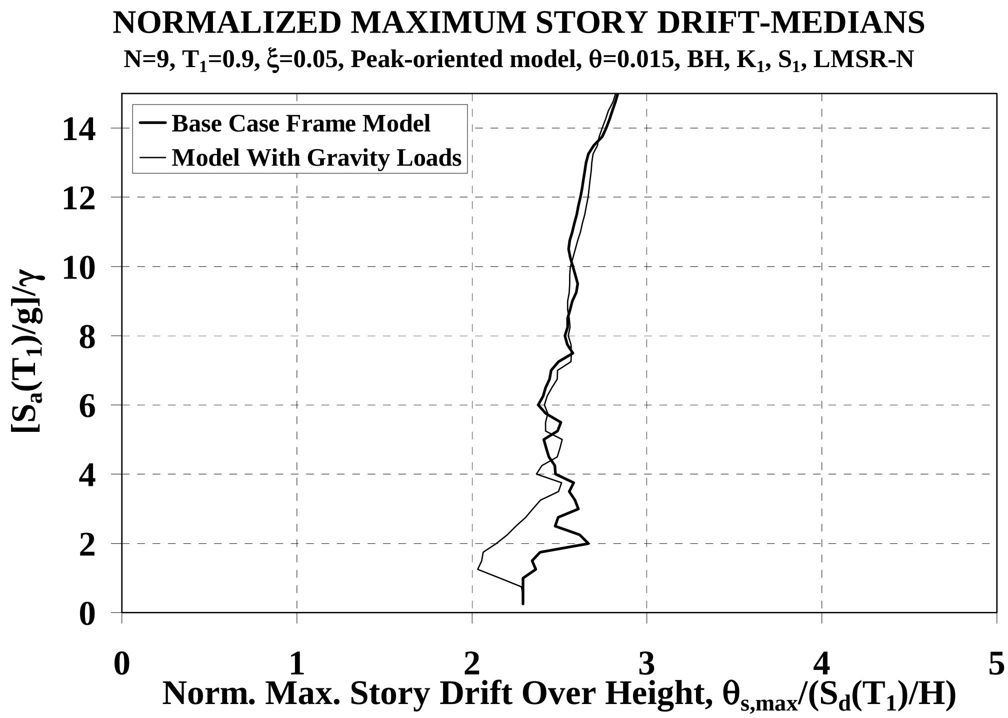

(a) T_1 = 0.9 sec

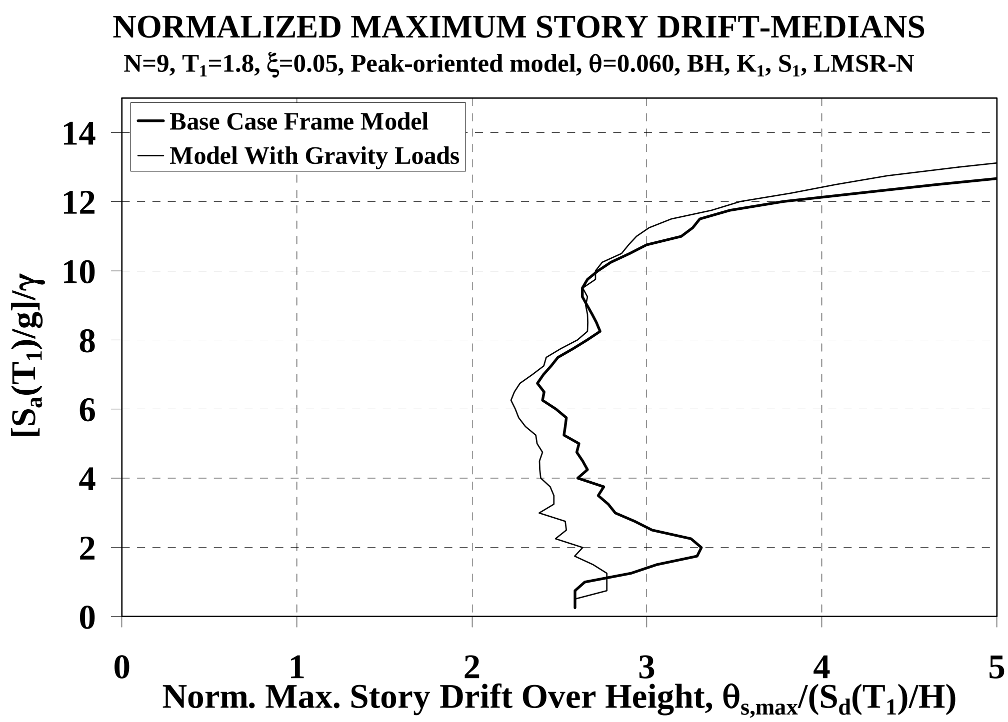

(b) T_1 = 1.8 sec

Figure 7.32 Effect of Gravity Load Moments on the Median Normalized Maximum Story Drift Angle over the Height, N = 9

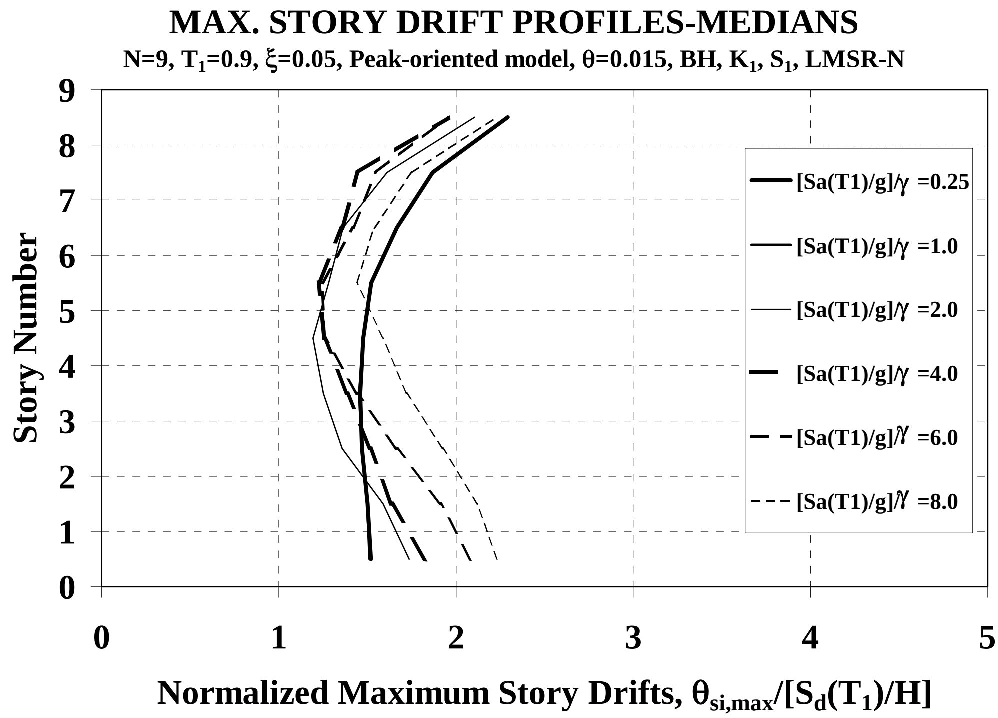

(a) Base Case Frame Model (No Gravity Load Moments)

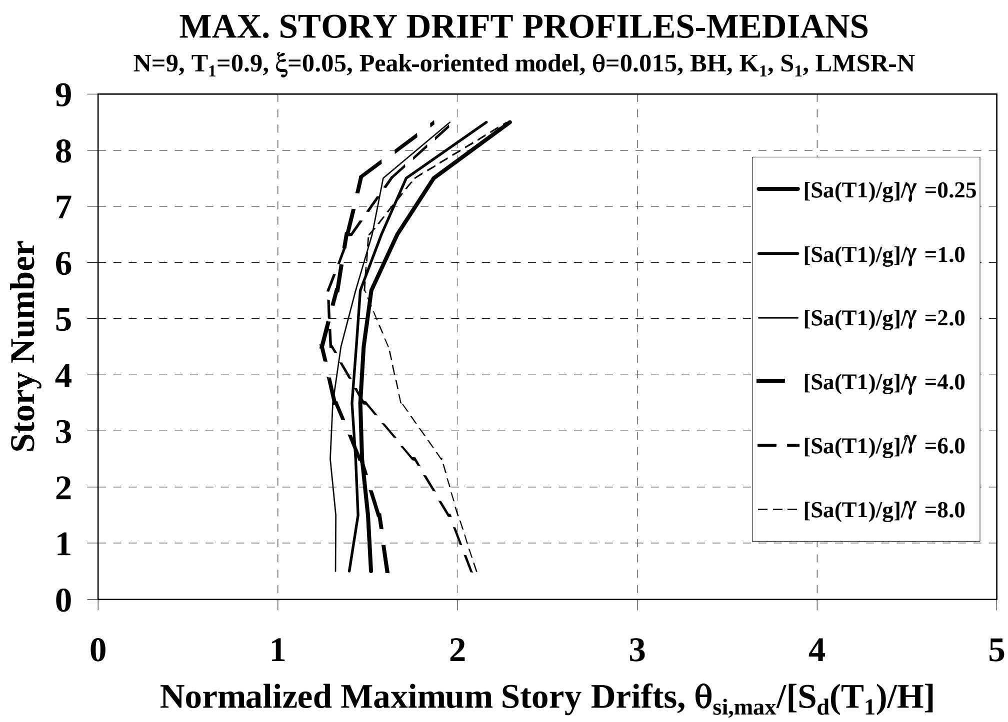

(b) Model that Includes Gravity Load Moments

Figure 7.33 Effect of Gravity Load Moments on the Distribution over the Height of Median Normalized Maximum Story Drift Angles, N = 9, T_1 = 0.9 sec

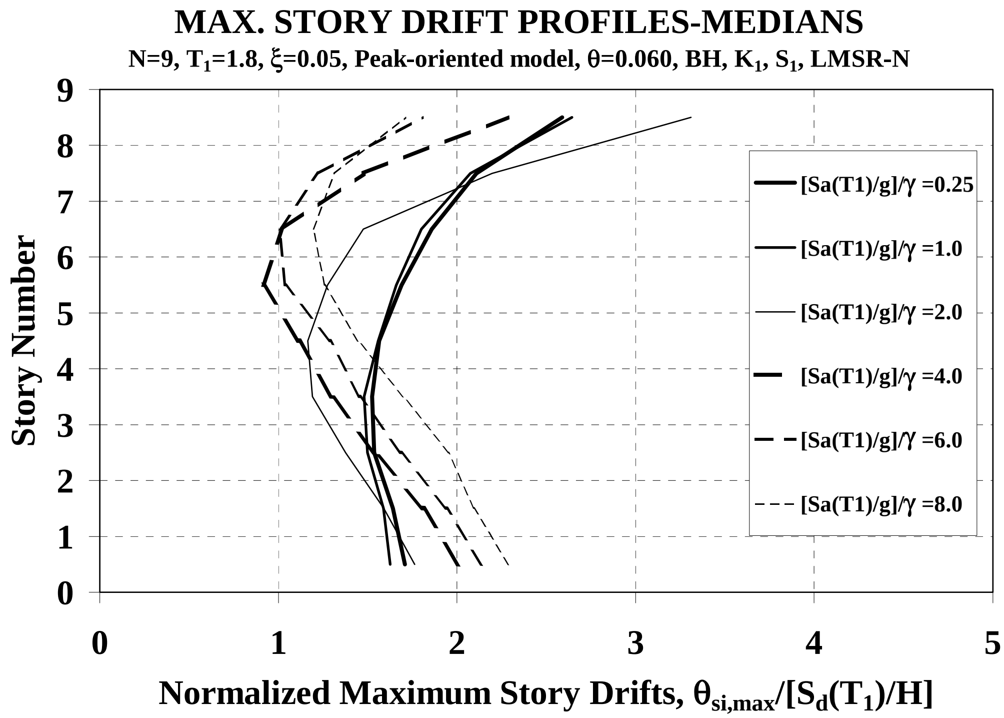

(a) Base Case Frame Model (No Gravity Load Moments)

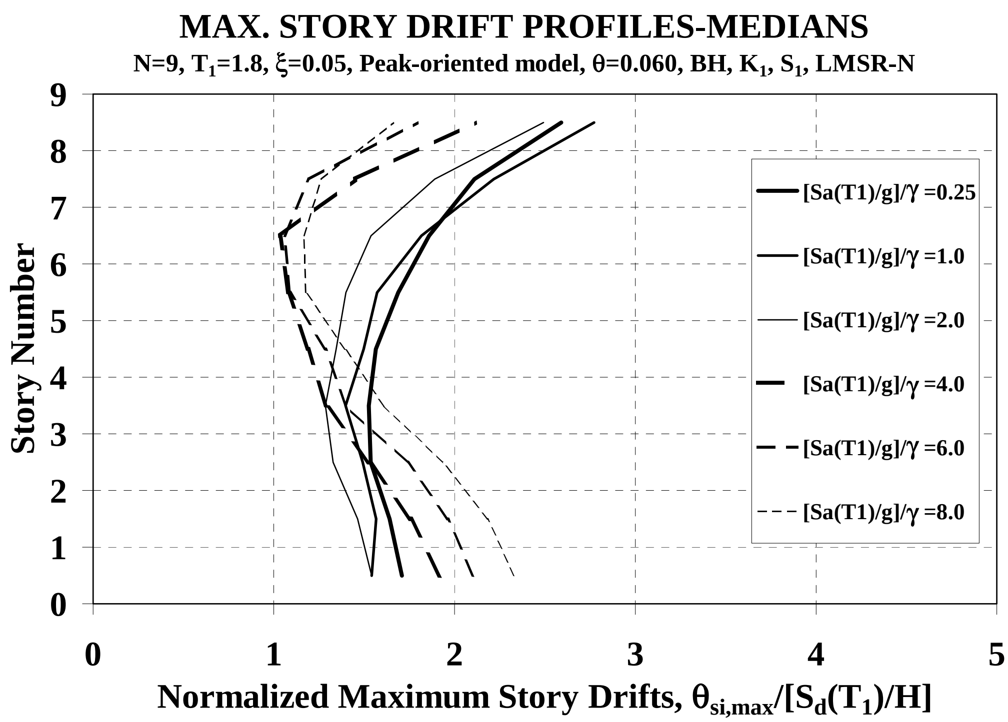

(b) Model that Includes Gravity Load Moments

Figure 7.34 Effect of Gravity Load Moments on the Distribution over the Height of Median Normalized Maximum Story Drift Angles, N = 9, T_1 = 1.8 sec

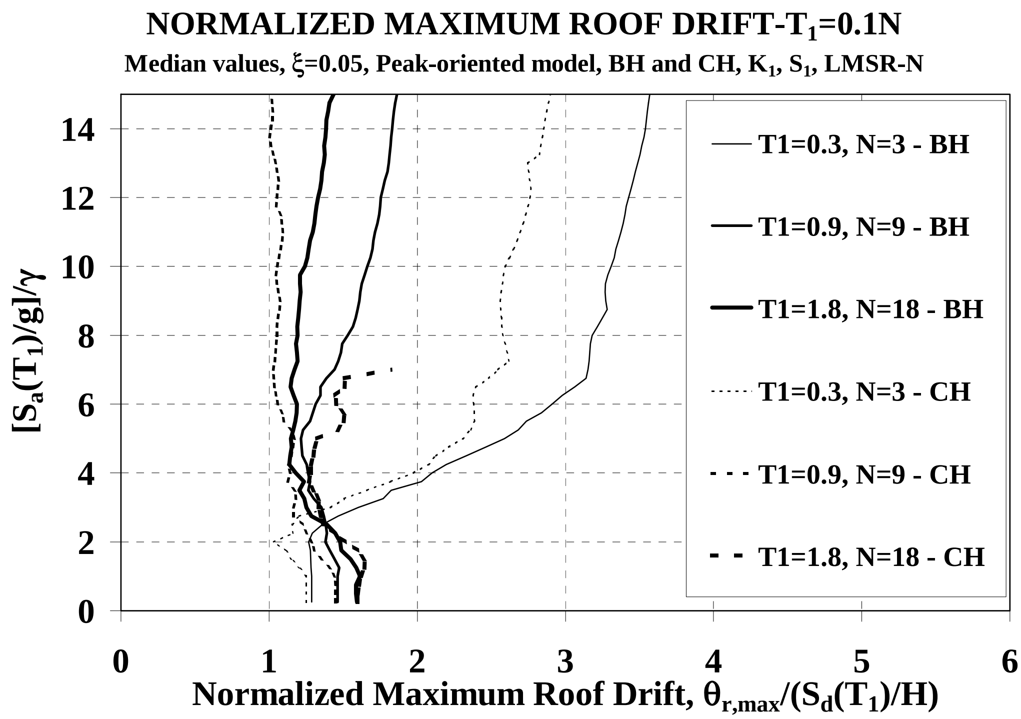

(a) $T_1 = 0.1N$

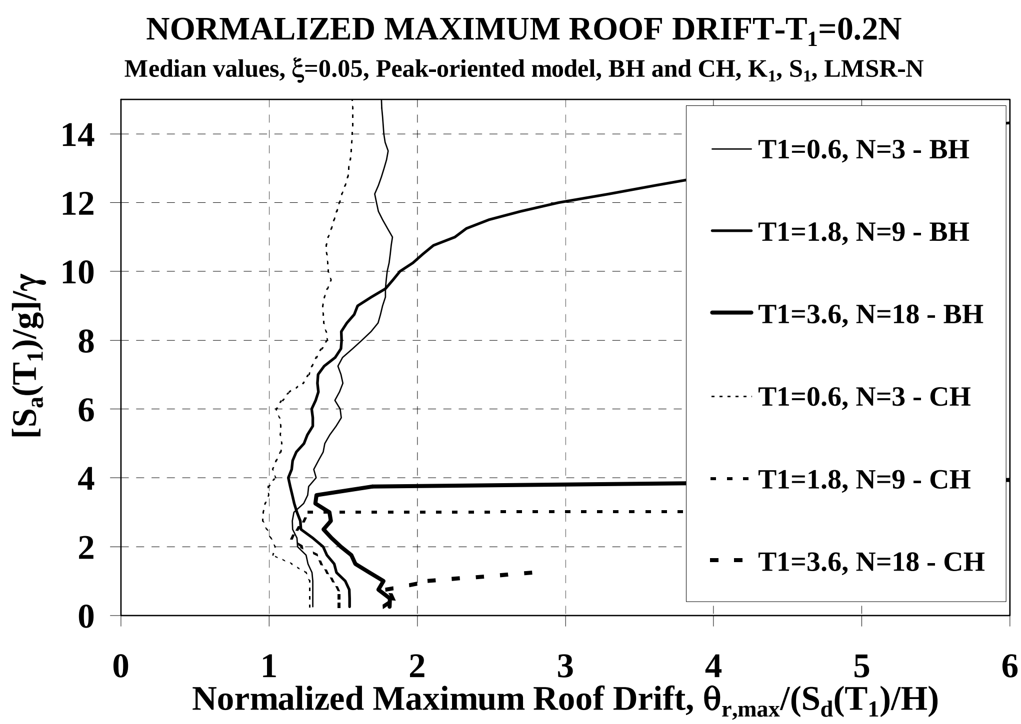

(b) $T_1 = 0.2N$

Figure 7.35 Effect of Various Mechanisms on the Median Normalized Maximum Roof Drift Demand, Stiff and Flexible Frames

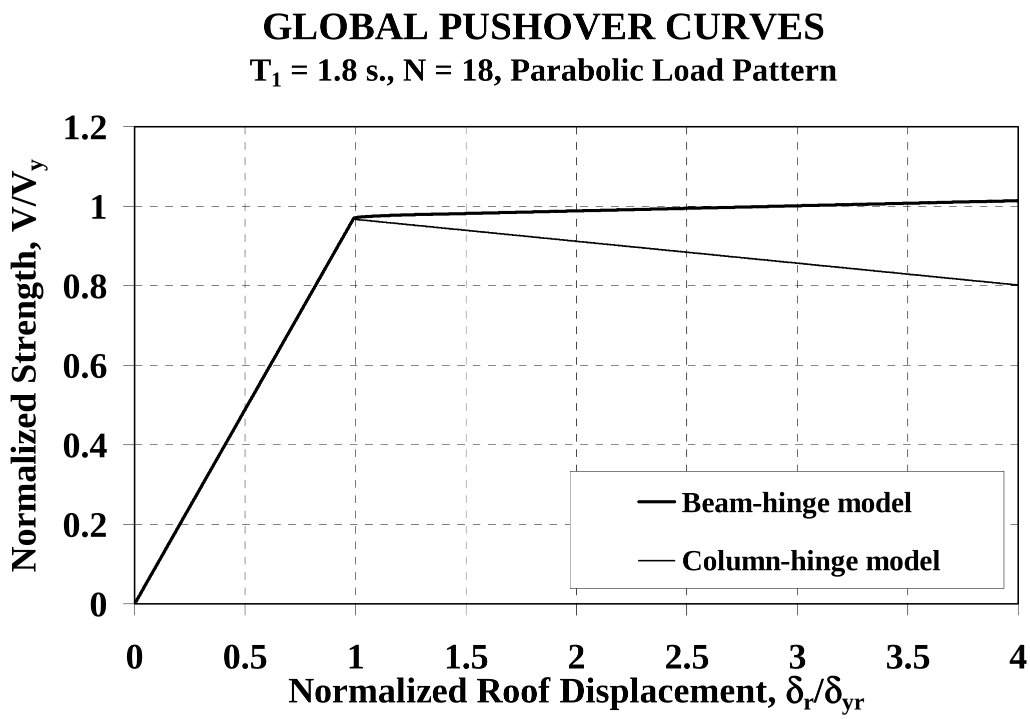

(a) Global Pushover Curves

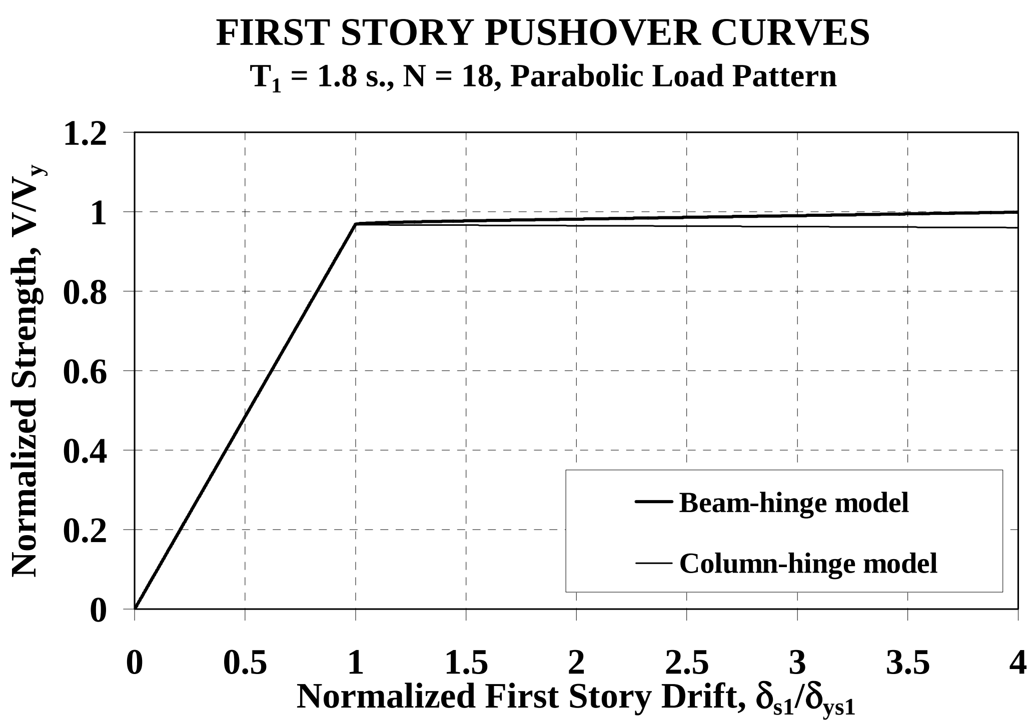

(b) First-Story Pushover Curves

Figure 7.36 Pushover Curves Based on a Parabolic Load Pattern, BH and CH Mechanisms, N = 18, T_1 = 1.8 sec

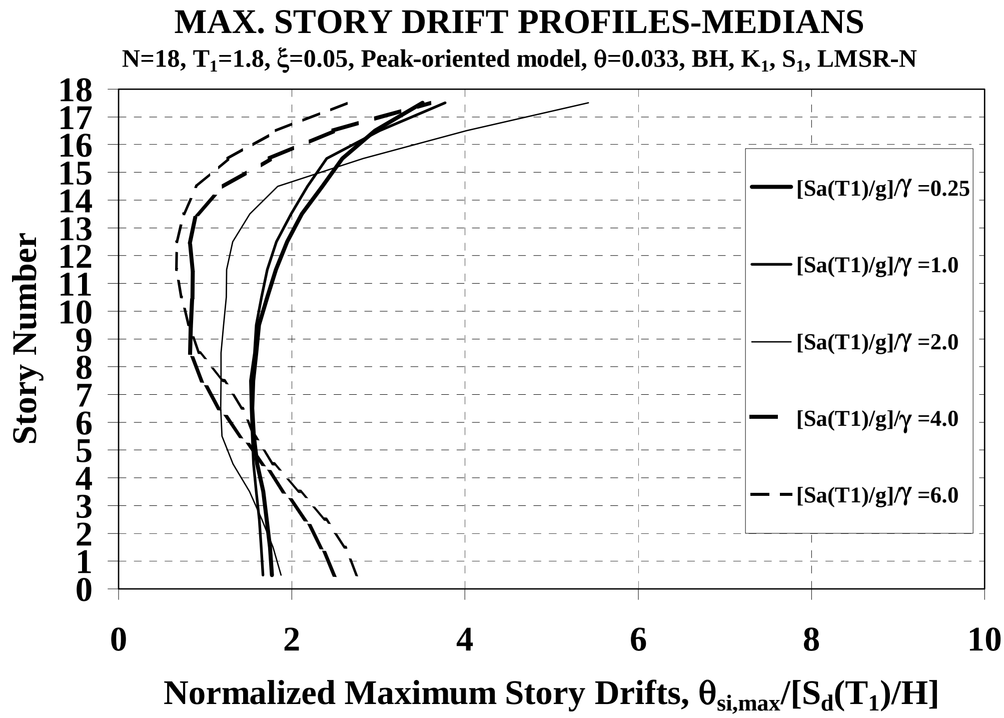

(a) Beam-Hinge Model

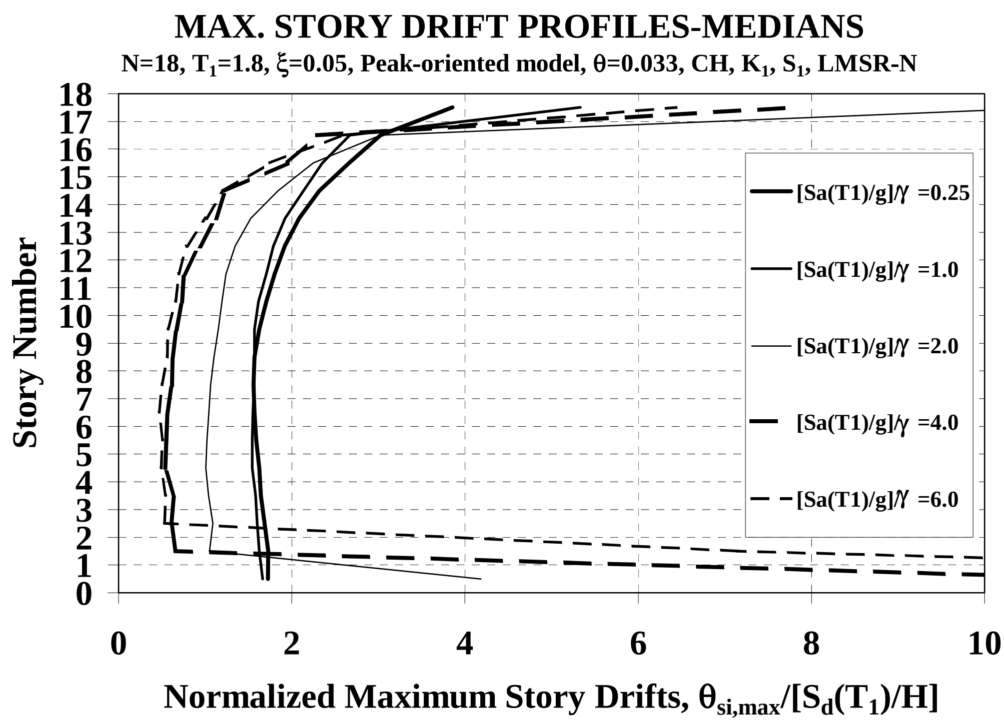

(b) Column-Hinge Model

Figure 7.37 Effect of BH and CH Mechanisms on the Distribution over the Height of Normalized Maximum Story Drift Angles, N = 18, T_1 = 1.8 sec

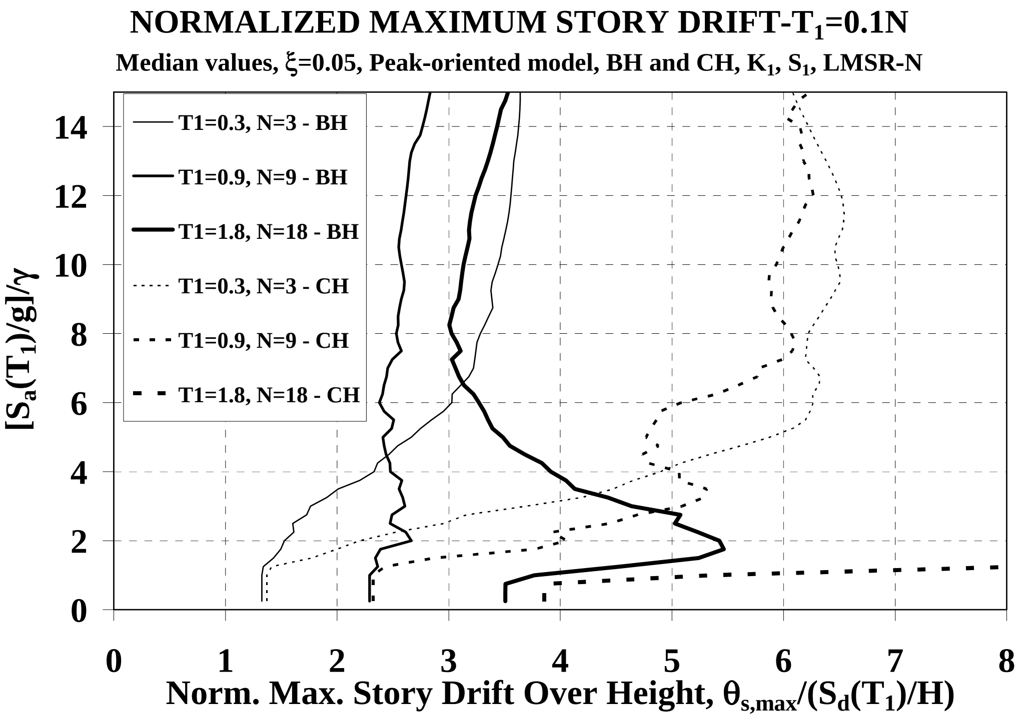

(a) $T_1 = 0.1N$

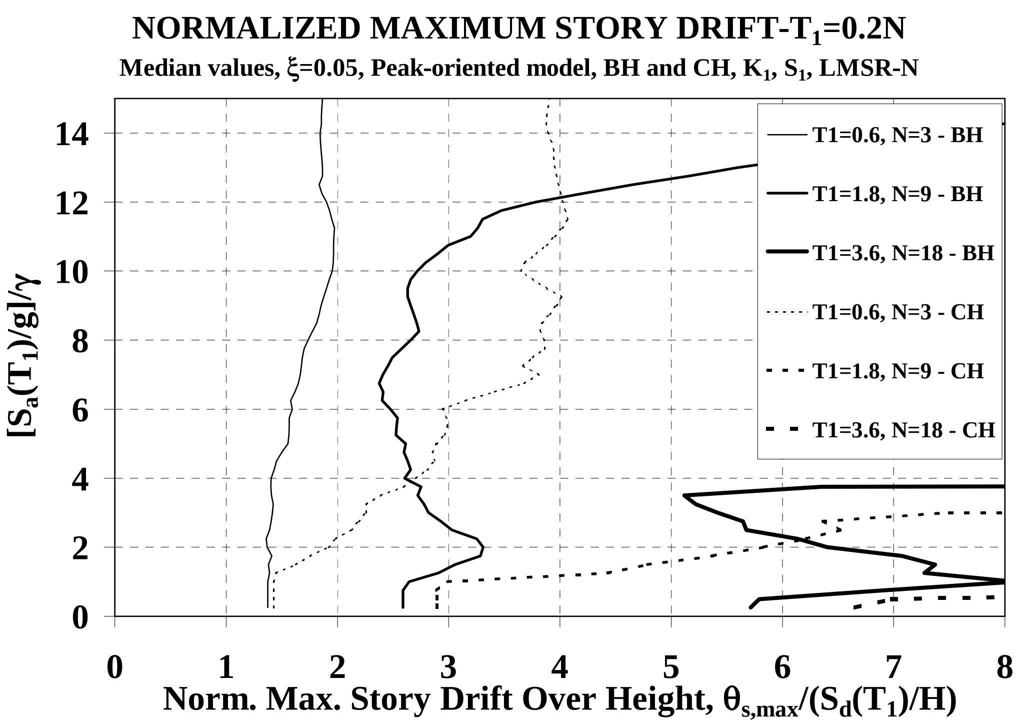

(b) $T_1 = 0.2N$

Figure 7.38 Effect of BH and CH Mechanisms on the Median Normalized Maximum Story Drift over the Height, Stiff and Flexible Frames

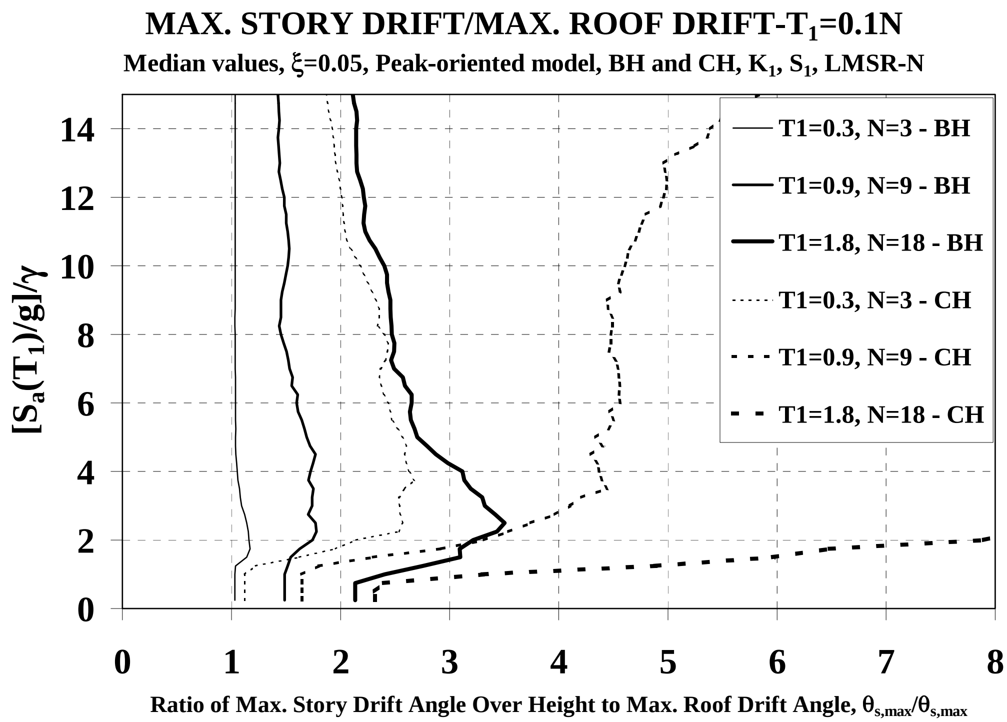

(a) $T_1 = 0.1N$

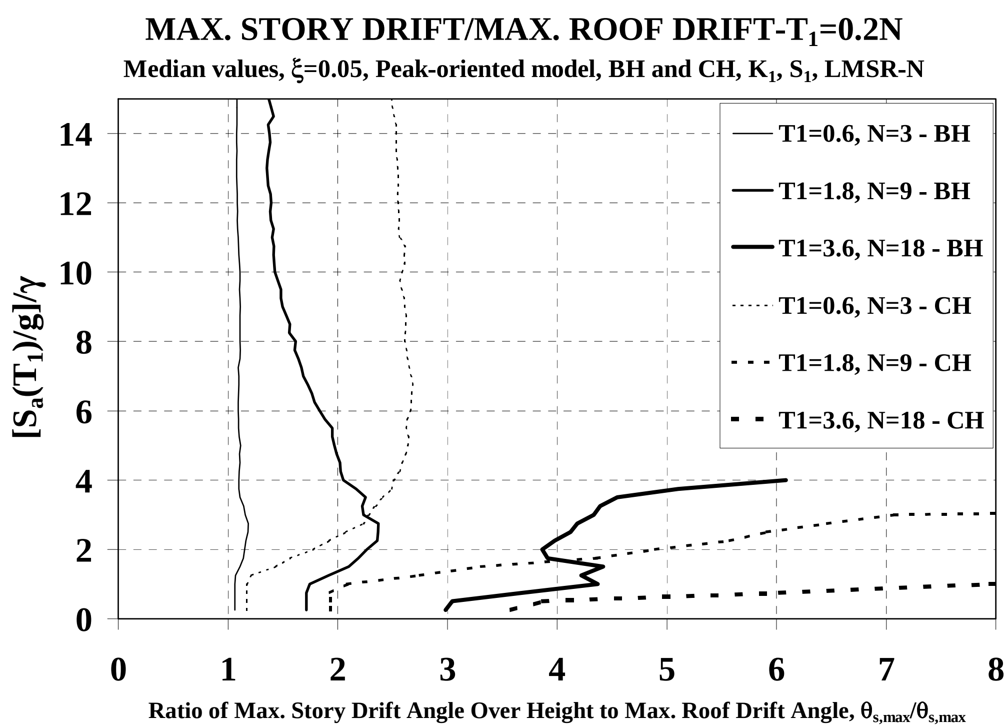

(b) $T_1 = 0.2N$

Figure 7.39 Effect of BH and CH Mechanisms on the Median Ratio of the Maximum Story Drift Angle over the Height to the Maximum Roof Drift Angle, Stiff and Flexible Frames

8 Use of One-Bay Generic Frames for Seismic Demand Evaluation

8.1 INTRODUCTION

Fundamental studies on seismic demand evaluation such as the ones presented in this report have to be carried out on structural systems that most closely resemble actual ones and with analytical tools that permit "sufficiently accurate" prediction of all demand parameters of interest. The term "sufficiently accurate" depends on the context. This study is not concerned with a rigorous demand prediction for a specific structure, in which case all contributing components would have to be represented in the analytical model. It is concerned with an evaluation of patterns and sensitivities to important ground motion and structural characteristics. In this context the term "sufficiently accurate" takes on the meaning of being capable of representing important characteristics, which significantly affect the demands, in a transparent manner that permits interpretation of the results. For instance, for the regular frames and the performance levels of interest in this study (direct losses and downtime) such characteristics have to do with strength, stiffness, deformation capacity (ductility) and geometric nonlinearities such as structure P-delta effects. Thus, accurate modeling of details, even if these would greatly affect the demands for a specific structure, is not considered to be important in this context. The emphasis is on one-bay generic models of regular moment-resisting frame systems whose structural properties can be tuned so that the aforementioned characteristics can be simulated in patterns that facilitate a comprehensive evaluation of demands. It is recognized that in the process reality gets distorted (e.g., no structure has a constant strain hardening of 3%), but this is the compromise that has to be accepted in sensitivity studies.

However, the use of one-bay generic frames assumes that they are able to represent the behavior of more complex regular multi-bay frames. The objective of this chapter is to correlate the seismic response of a ninestory multi-bay steel frame with that of its “equivalent” one-bay frame to assess the adequacy of the one-bay frame to model the behavior of the multi-bay frame.

8.2 SAC LA9-M1 MODEL AND ITS “EQUIVALENT” ONE-BAY FRAME

The SAC LA9-M1 frame model (Gupta and Krawinkler, 1999) is utilized to validate the use of one-bay frames to represent the behavior of regular multi-bay frames. This model, from here on referred to as the “LA9-M1” model, corresponds to one of the steel perimeter moment-resisting frames located in the north-south direction of a standard office building in the Los Angeles area, situated on stiff soil and designed according to the UBC 1994 code. It is based on centerline dimensions; thus, the contribution of the panel zones to the response is neglected. The hysteretic behavior at plastic hinge locations is modeled by using bilinear hysteretic rules with 3% strain hardening. Axial load-bending moment interaction in columns is included as well as second-order structure P-delta effects. Strength properties are based on the expected strength of the material and 2% Rayleigh damping is used at the first mode and at a period of 0.2 sec. Figure 8.1 shows a plan view and elevation of this frame and Table 8.1 presents details of its main structural properties.

A one-bay frame model based on the stiffness and strength properties of the LA9-M1 model was developed according to the following *simplified* assumptions:

- The beam span was assumed to be 24 feet (same beam span as the generic models used in this study).
- Story heights are equal to the story heights of the LA9-M1 model (including the basement).
- Beam stiffness is calculated based upon $\Sigma(I/L)$ of the beams at each floor level.
- Column stiffness is calculated based upon $\Sigma(I/L)$ of the columns at each story level.
- Column areas at each story are estimated as the area needed to provide the same global bending stiffness as the LA9-M1 model, so they are computed based upon $2\Sigma(A_i x_i^2/L^2)$, where A_i is the area of an individual column, x_i is the distance from the center of the column to the centerline of the moment-resisting frame, and L is the span of the one-bay frame (24 feet).
- The beam strength is computed as one half of the sum of the plastic moment capacity of the end of the beams that form part of a moment-resisting connection at that floor level.

- The column strength is computed as one half of the sum of the plastic moment capacity of the corresponding end of the columns at that story level. P-M interaction is ignored.
- For both beams and columns, rotational springs with 3% strain hardening are used to model the hysteretic behavior at plastic hinge locations.
- P-delta loads at each floor level are computed as the sum of the P-delta loads at each floor level of the LA9-M1 model.

8.2.1 Modal Properties

Modal properties of the one-bay LA9-M1 and the LA9-M1 models are presented in Table 8.2. For the one-bay LA9-M1 model, the mass and stiffness proportional factors in the Rayleigh damping formulation are tuned to obtain 2% damping at the first mode and the mode with a period of 0.2 sec so that modal properties are compatible between the two models. In Table 8.2 it can be observed that the basic modal properties are similar. The one-bay LA9-M1 is slightly stiffer than the LA9-M1 model (T_1 = 2.27 vs. 2.34 sec). The mode shapes are also close to identical (a plot with the first-mode shape for both structures is presented in Figure 8.2).

8.2.2 Nonlinear Static Behavior

In order to assess the adequacy of the one-bay LA9-M1 frame in representing the nonlinear behavior of the LA9-M1 model, a pushover analysis with a parabolic load pattern is performed. Figures 8.3 and 8.4 depict the global (roof) and first-story pushover analyses, respectively. It can be observed that the general shape of the pushover curves is similar for the two models, which implies that yielding patterns and sequences are similar. The one-bay LA9-M1 is approximately 6% stiffer and 2% stronger. In view of the information provided by the pushover curves, the behavior of the two models in the inelastic range is expected to be compatible. Whether or not this expectation is met in the nonlinear time history analysis of these models is evaluated in the following section.

8.3 EVALUATION OF THE NONLINEAR DYNAMIC RESPONSE OF THE LA9-M1 AND THE ONE-BAY LA9-M1 MODELS

Time history analyses are performed for both models using the LMSR-N set of ordinary ground motions and the IDA approach, i.e., the intensity of the ground motion is varied while the strength of the structure is kept constant. The IM of interest is the spectral acceleration at the first-mode period; thus, for each analysis the records are scaled to the same $S_a(T_1)$. Similarities and differences in the responses are evaluated based on two EDPs: the maximum roof drift angle and the maximum story drifts over the height.

8.3.1 Maximum Roof Drift Angle

Figure 8.5 presents the statistical evaluation of the maximum roof drift angle for the LA9-M1 and the one-bay LA9-M1 models. It can be observed that behavior of the two models is very similar up to $[S_a(T_1)/g/\gamma] = 4$. For larger levels of inelastic behavior, the one-bay LA9-M1 performs better with the median normalized maximum roof drift angle approaching the onset of dynamic instability at a value of 8.0 as opposed to 6.5 for the LA9-M1 model. Figure 8.6(a) isolates the median curves for both cases, and Figure 8.6(b) depicts the dispersion of the data.

8.3.2 Maximum Story Drift Angles

Figure 8.7 is presented in order to assess how effective the one-bay LA9-M1 model is in representing the response of the LA9-M1 model based on the average of the maximum story drift angles, $\theta_{si,ave}$, and the maximum story drift angle over the height, $\theta_{s,max}$. Similarities in patterns observed for the maximum normalized roof drift angle are also present in Figure 8.7. Both the median values of the EDPs given the IM and the dispersion in the data are very similar for both models up to $[S_a(T_1)/g/\gamma] = 4$. Differences are noticeable at larger relative intensities.

8.3.3 Ratio of the Average of the Maximum Story Drift Angles and the Maximum Story Drift Angle to the Maximum Roof Drift Angle

Figure 8.8 presents the statistical evaluation of the ratios of the average of the maximum story drift angles to the maximum roof drift angle, $\theta_{si,ave}/\theta_{r,max}$, and the maximum story drift angle over the height to the maximum roof drift angle, $\theta_{s,max}/\theta_{r,max}$, for the LA9-M1 and the one-bay LA9-M1 models when subjected to records from the LMSR-N bin. As expected from the results in the previous two sections, the median values for these ratios as well as their dispersions are comparable except in the region where structure P-delta effects take over the response of the systems.

8.3.4 Distribution of Maximum Story Drifts over the Height

Figure 8.9 shows the variation of median normalized maximum story drift angle profiles with the intensity level for both the one-bay LA9-M1 and the LA9-M1 models. For most relative intensity levels, median profiles show very consistent patterns. They have the same general shapes and comparable absolute values. The only important difference can be observed at $[S_a(T_1)/g/\gamma] = 6$ where the LA9-M1 model exhibits a significantly larger amplification of maximum story drift demands in the bottom stories, which is consistent with the observations made in Sections 8.3.1 to 8.3.3.

8.4 SUMMARY

The information presented in this chapter shows that simplified one-bay frames are able to represent the main patterns of behavior exhibited by regular multi-bay frames at different levels of inelasticity.

Table 8.1 Beam and Column Sections for the LA9-M1 Model

PRE-NORTHRIDGE DESIGNS

NS Moment Resisting Frame

9-story Building

Story/Floor	COLUMNS		DOUBLER	GIRDER
	Exterior	Interior	PLATES (in)	
-1/1	W14x370	W14x500	0,0	W36x160
1/2	W14x370	W14x500	0,0	W36x160
2/3	W14x370, W14X370	W14x500, W14x455	0,0	W36x160
3/4	W14x370	W14x455	0,0	W36x135
4/5	W14x370, W14x283	W14x455, W14x370	0,0	W36x135
5/6	W14x283	W14x370	0,0	W36x135
6/7	W14x283, W14x257	W14x370, W14x283	0,0	W36x135
7/8	W14x257	W14x283	0,0	W30x90
8/9	W14x257, W14x233	W14x283, W14x257	0,0	W27x84
9/Roof	W14x233	W14x257	0,0	W24x68

NS Gravity Frames

COLUMNS		BEAMS
Below penthouse	Others	
W14x211	W14x193	W21x44
W14x211	W14x193	W18x35
W14x211, W14x159	W14x193, W14x145	W18x35
W14x159	W14x145	W18x35
W14x159, W14x120	W14x145, W14x109	W18x35
W14x120	W14x109	W18x35
W14x120, W14x90	W14x109, W14x82	W18x35
W14x90	W14x82	W18x35
W14x90, W14x61	W14x82, W14x48	W18x35
W14x61	W14x48	W16x26

Notes:
1. Column line A has exterior column sections oriented about strong axis,
Column line F has exterior column sections oriented about weak axis,
Column lines B, C, D and E have interior column sections.

Table 8.2 Modal Properties, LA9-M1 and One-Bay LA9-M1 Models

Basic Modal Properties

	Mode	Period	P. Factor	Modal Mass	Modal Damp.
LA9-M1					
	1	2.34	1.37	0.84	0.02
	2	0.88	-0.56	0.11	0.01
	3	0.50	0.24	0.04	0.01
One-bay LA9-M1					
	1	2.27	1.37	0.84	0.02
	2	0.85	-0.56	0.11	0.01
	3	0.49	0.23	0.04	0.01

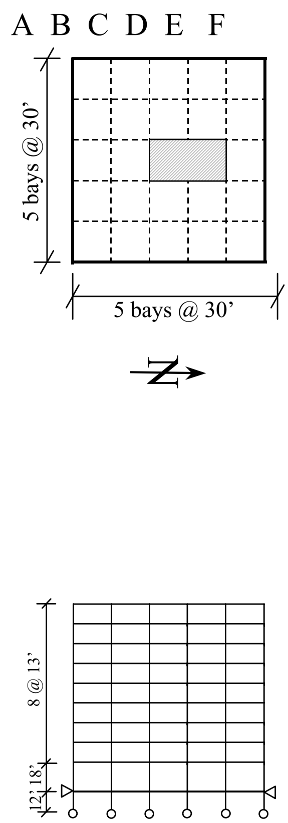

Figure 8.1 Perimeter Moment-Resisting Frame, LA9 -M1 Model

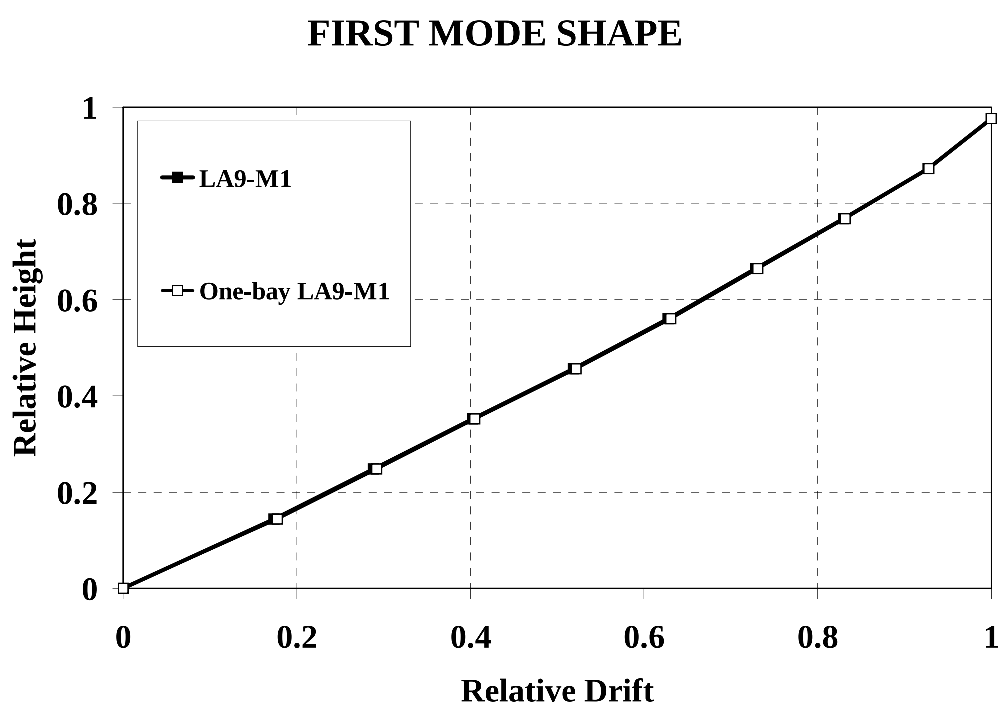

Figure 8.2 First-Mode Shape, LA9-M1 and One-Bay LA9-M1 Models

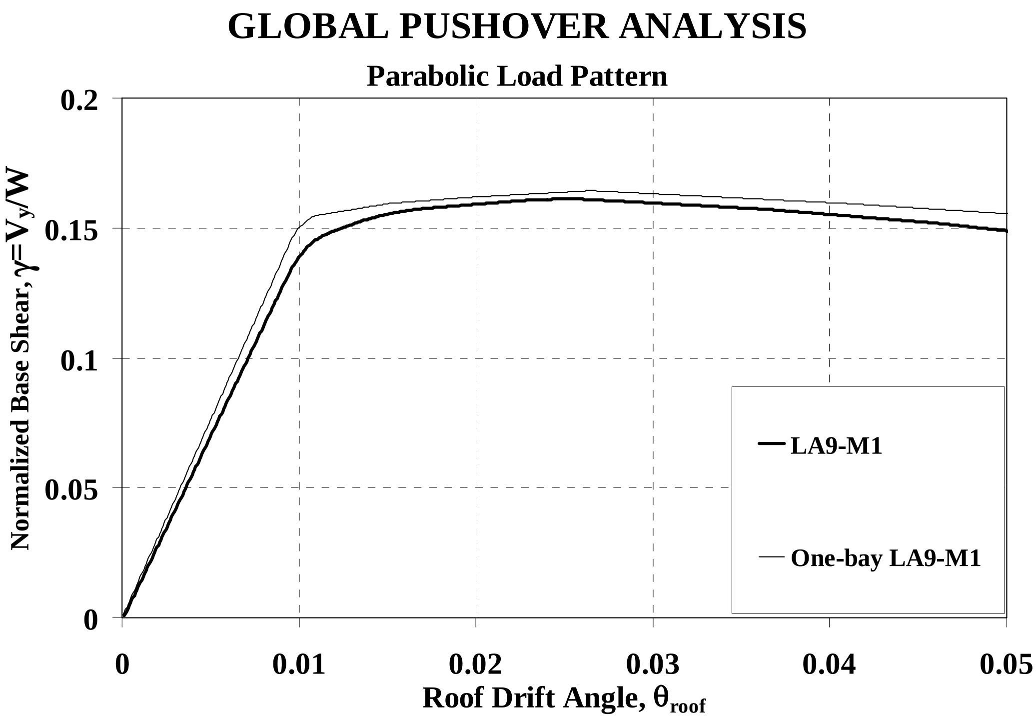

Figure 8.3 Global Pushover Curve, LA9-M1 and One-Bay LA9-M1 Models

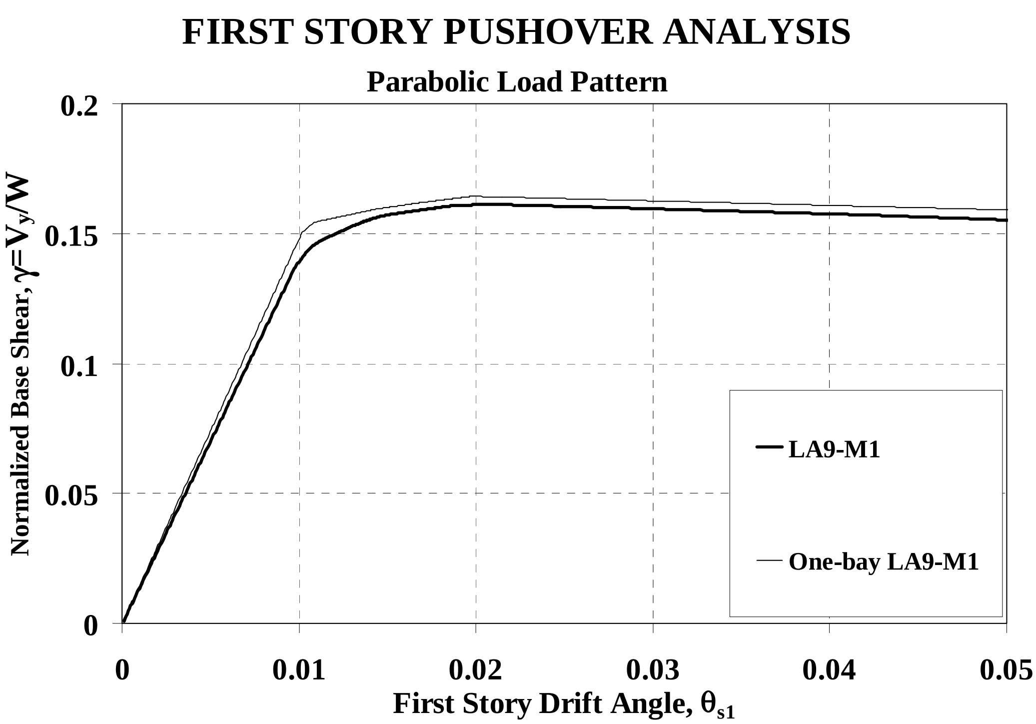

Figure 8.4 First-Story Pushover Curve, LA9-M1 and One-Bay LA9-M1 Models

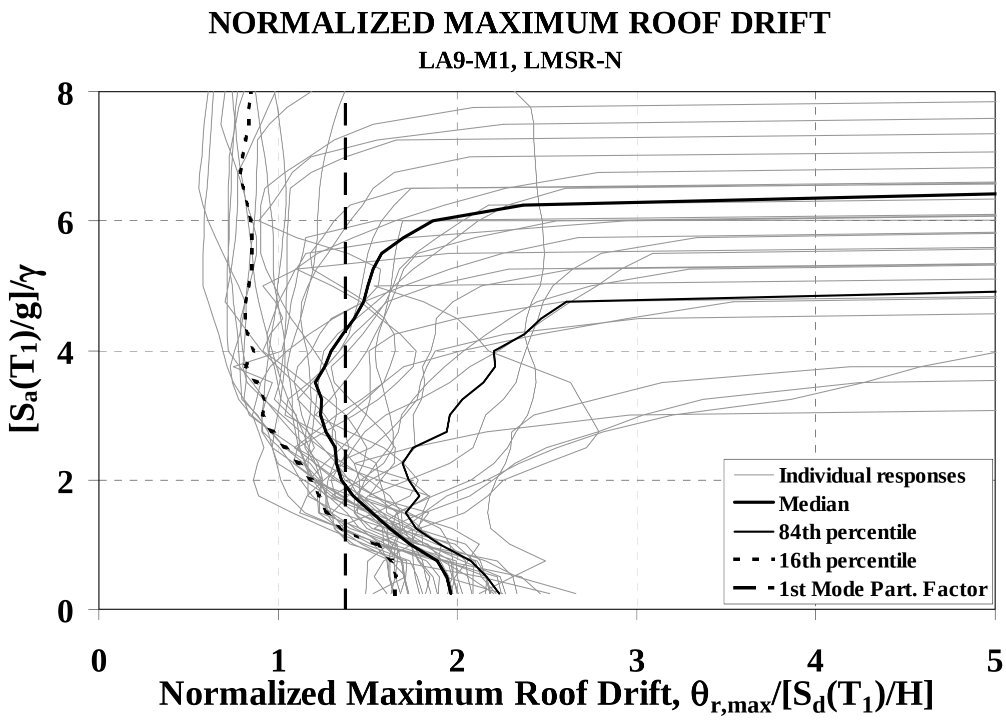

(a) LA9-M1 Model

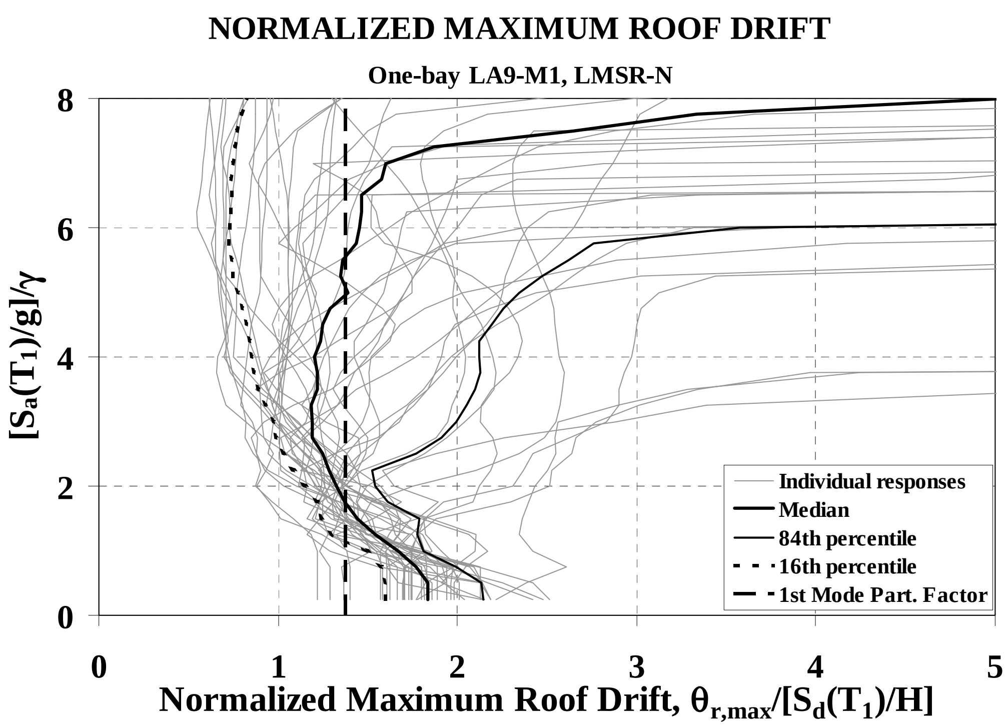

(b) One-Bay LA9-M1 Model

Figure 8.5 Normalized Maximum Roof Drift Data, LA9-M1 and One-Bay LA9-M1 Models

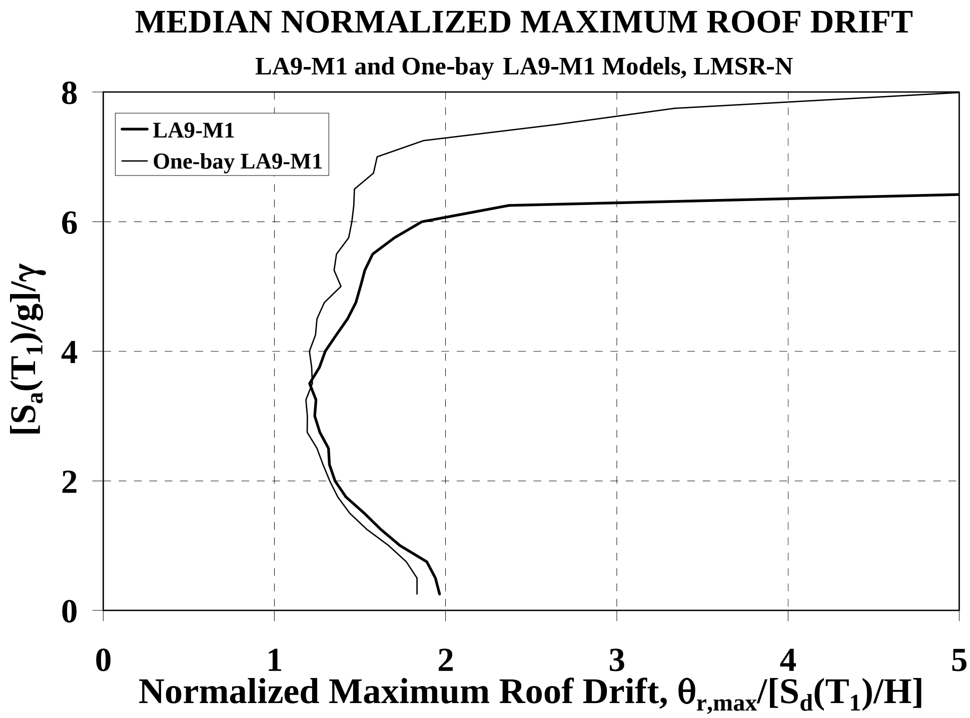

(a) Median Values

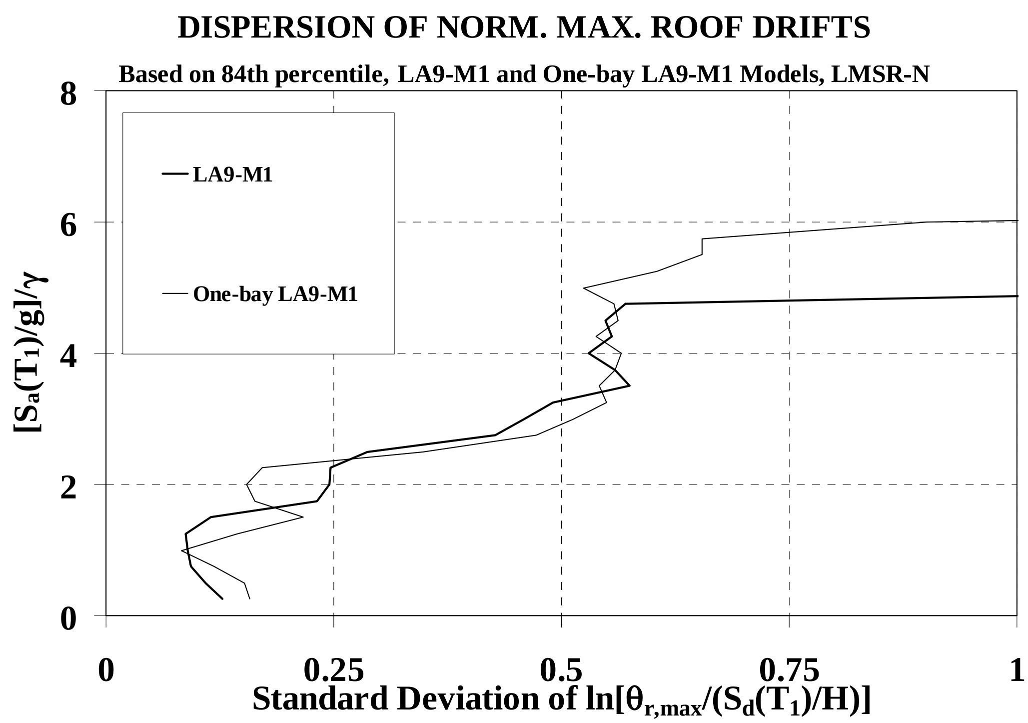

(b) Dispersion

Figure 8.6 Normalized Maximum Roof Drift, LA9-M1, and One-Bay LA9-M1 Models

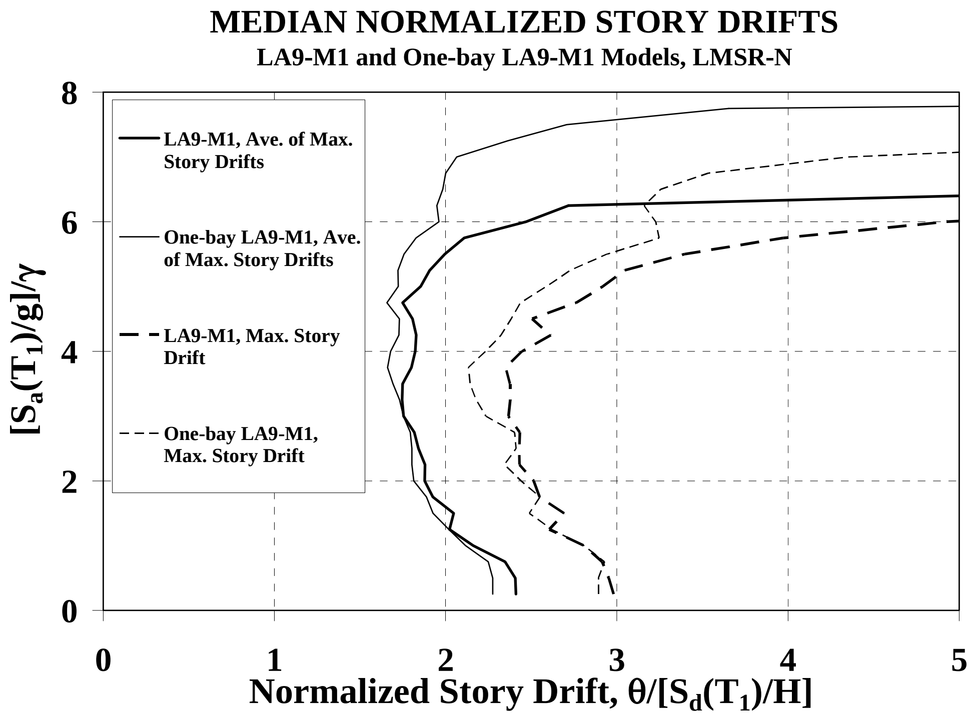

(a) Median Values

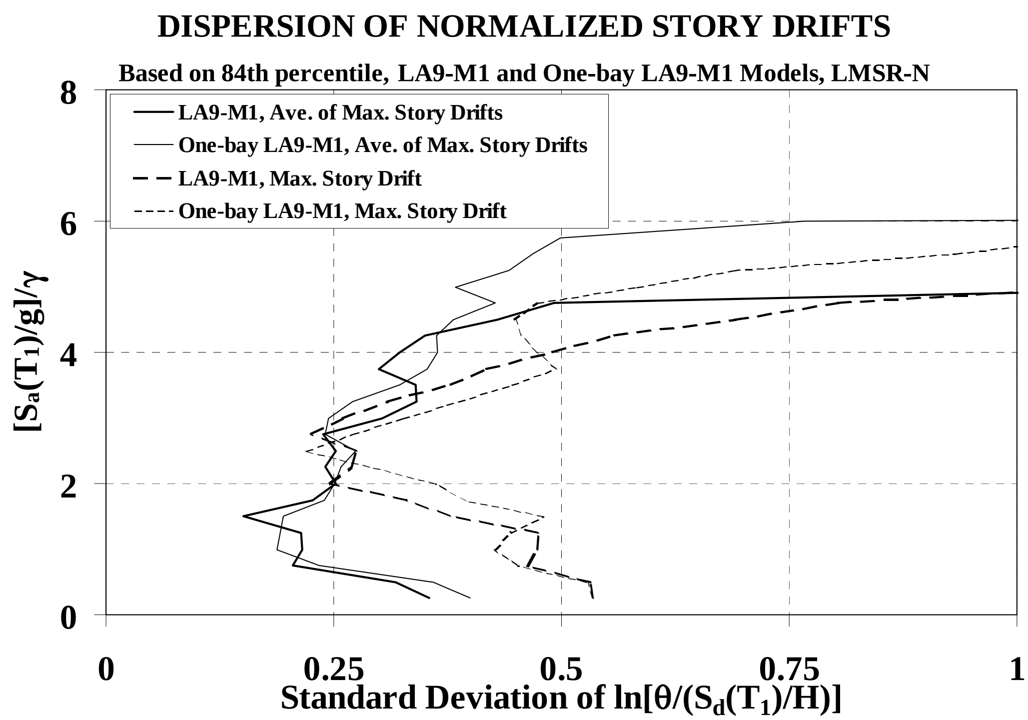

(b) Dispersion

Figure 8.7 Normalized Story Drifts, LA9-M1, and One-Bay LA9-M1 Models

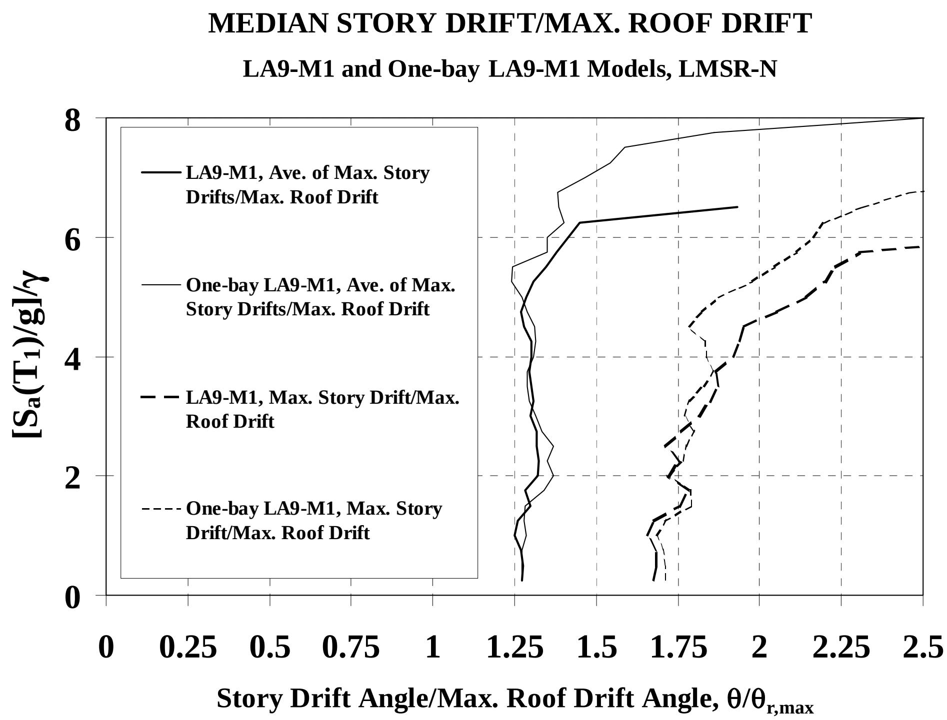

(a) Median Values

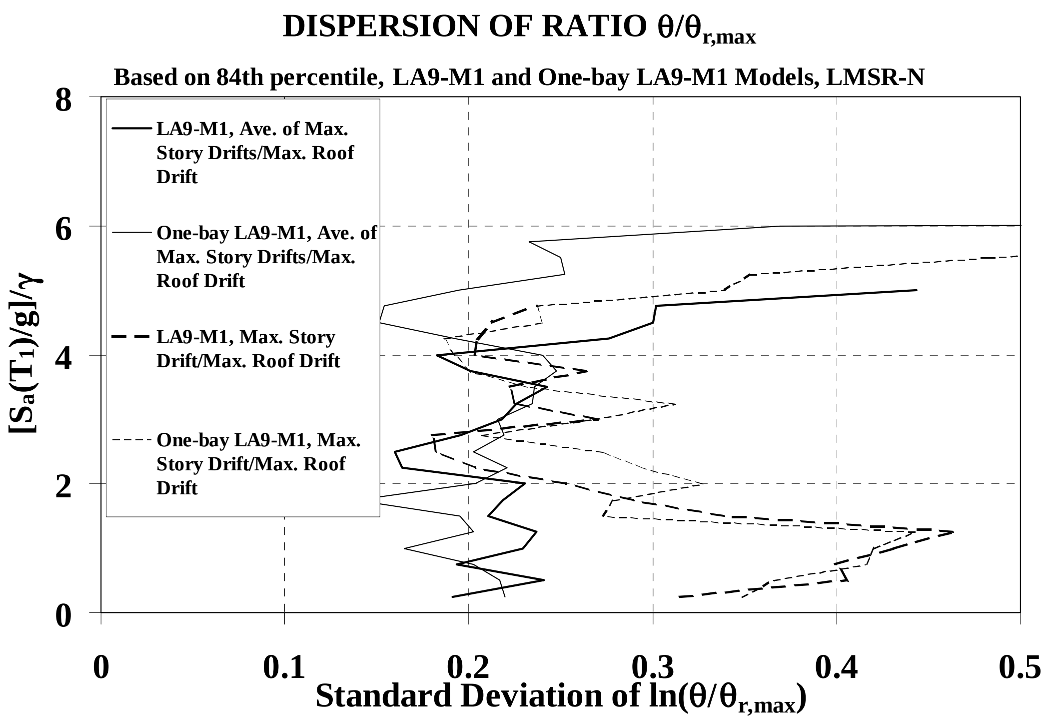

(b) Dispersion

Figure 8.8 Ratio of the Average of the Maximum Story Drift Angles to the Maximum Roof Drift Angle, LA9-M1, and One-Bay LA9-M1 Models

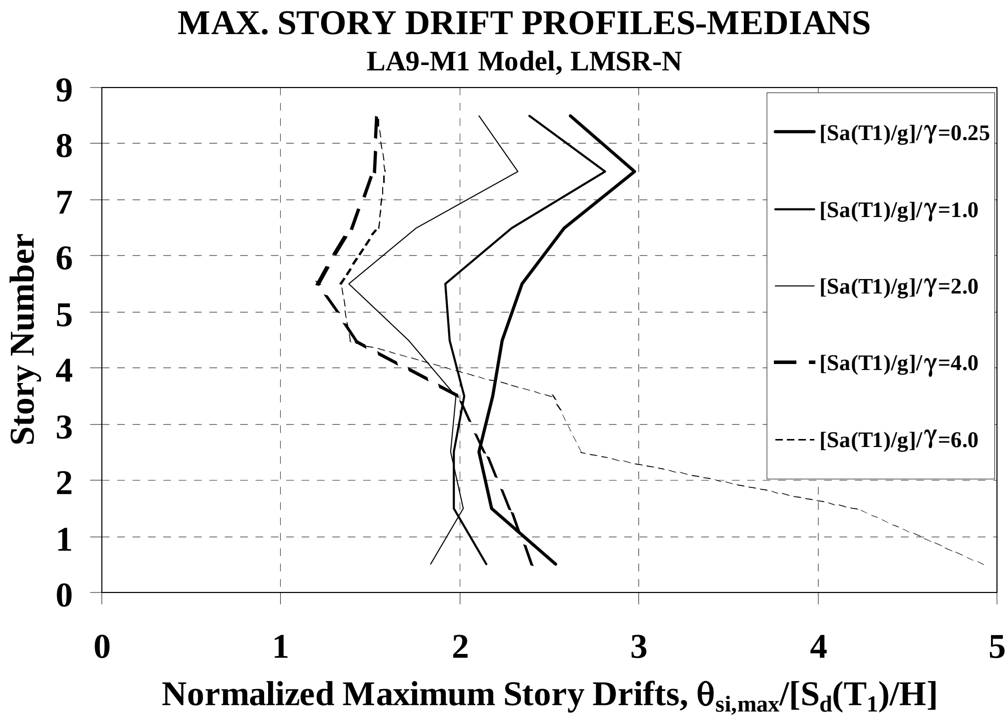

(a) LA9-M1 Model

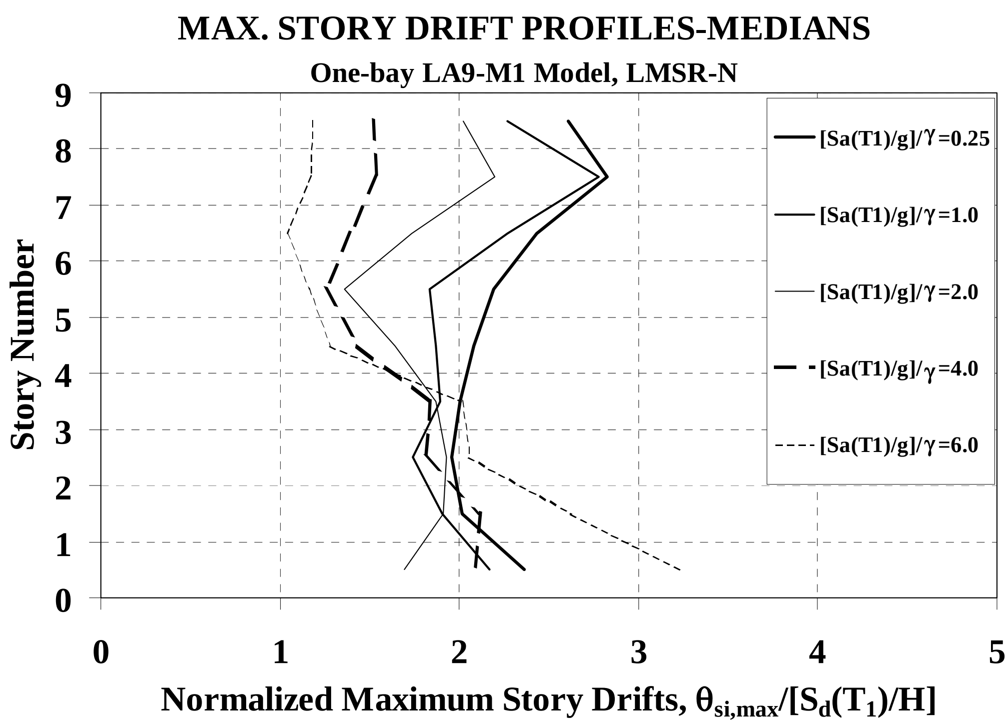

(b) One-Bay LA9-M1 Model

Figure 8.9 Distribution of Median Maximum Story Drift Angles over the Height, LA9-M1, and One-Bay LA9-M1 Models

9 Probabilistic Seismic Performance Assessment

9.1 INTRODUCTION

Performance assessment implies that the structure is given (i.e., $\gamma = V_y/W$, T_1, and other properties are known), and decision variables, such as losses, have to be evaluated. Part of this process is probabilistic seismic demand analysis that includes quantification of a response parameter (EDP) and its associated uncertainties to be used for probabilistic damage assessment. This quantification can be carried out by computing the mean annual frequency of exceedance of the EDP, i.e.,

$$\lambda_{EDP}(y) = \int P[EDP \geq y \mid IM = x] \, | \, d\lambda_{IM}(x) \, | \tag{9.1}$$

where $\lambda_{EDP}(y)$ = mean annual frequency of EDP exceeding the value y

$P[EDP \geq y \mid IM = x]$ = probability of EDP exceeding y given that IM equals x

$\lambda_{IM}(x)$ = mean annual frequency of IM exceeding x (ground motion hazard)

A prerequisite to the implementation of Equation (9.1) is hazard analysis for a single ground motion intensity measure or for a vector of intensity measures. At this time, the spectral acceleration at the first-mode period of the structure, $S_a(T_1)$, is most commonly used as the intensity measure. Similar to the IM hazard, the mean annual frequency of the EDP exceeding a certain value also can be represented in a hazard curve.

Performance assessment also includes the evaluation of the global collapse potential of a structural system. Probabilistic collapse assessment can be carried out according to the following equation:

$$\lambda_f = \int F_{C_{IM}}(x) \, | \, d\lambda_{IM}(x) \, | \qquad (9.2)$$

where λ_f = mean annual frequency of collapse

$F_{CIM}(x)$ = probability of IM capacity exceeding x

$\lambda_{IM}(x)$ = mean annual frequency of IM exceeding x (ground motion hazard)

However, evaluation of collapse requires the utilization of models that are able to incorporate the most important factors that influence the collapse of a system, e.g., component cyclic deterioration. Since this study is based on nondeteriorating regular frames, the only source of global collapse is dynamic instability due to structure P-delta effects.

The work contained in this chapter focuses on an illustration of the development of maximum drift hazard curves that include the aleatory uncertainty inherent in the seismic phenomena and the calculation of the mean annual frequency of collapse due to structure P-delta effects.

9.2 ESTIMATION OF EDP HAZARD CURVES

Evaluation of Equation (9.1) to compute the the EDP hazard (mean annual frequency of the EDP exceeding y, given that $S_a(T_1)$ equals S_a) requires hazard analysis information on $S_a(T_1)$, which represents the term $\lambda_{IM}(x)$ in Equation (9.1) as well as data on EDPs. Since this evaluation is performed for structures of a given strength (γ), it is convenient to represent the EDP data in the conventional IDA form of $S_a(T_1)$ versus EDP, given the strength γ. Representative IDA curves (for individual records as well as median, 16^{th} and 84^{th} percentile), using the maximum roof drift angle, $\theta_{r,max}$, and the maximum story drift angle over the height, $\theta_{s,max}$, as EDPs for a frame with N = 9, T_1 = 1.8 sec, and $\gamma = V_y/W = 0.1$, are shown in Figures 9.1(a) and 9.2(a). Figures 9.1(b) and 9.2(b) show the standard deviation of the log of the EDP given the IM, based on the counted 16^{th} and 84^{th} percentile values.

One alternative for the evaluation of Equation (9.1) is numerical integration using lognormal distributions whose median and dispersion are computed from the EDP data for the discrete hazard levels at which numerical integration is performed. These curves may be viewed as "accurate," but they require numerical procedures. In order to eliminate the numerical effort and provide a closed-form solution, the following procedure, described by Cornell et al. (2002) may be implemented to develop EDP hazard curves:

The IM hazard can be estimated by a curve of the type

$$\lambda_{IM}(x) = P[IM \geq x] = k_o x^{-k}$$

or specifically $$\lambda_{S_a(T_1)}(S_a) = P[S_a(T_1) \geq S_a] = k_o S_a^{\ -k} \quad (9.3)$$

The exponent –k approximates the local slope of the hazard curve (in the log domain) around the return period of interest. The procedure requires the local (around the return period of primary interest) fitting of a median relationship to the EDP-IM data. The convenient form of this relationship is the same as for the hazard curve, i.e.,

$$E\hat{D}P = a(IM)^b \quad (9.4)$$

If the conditional distribution of the EDP for a given IM can be assumed as lognormal, i.e.,

$$P[EDP \geq y \mid IM = x] = 1 - \Phi\left(\ln[y / ax^b] / \sigma_{\ln EDP|IM}\right) \quad (9.5)$$

(Φ is the widely tabulated "standardized" Gaussian distribution function, and the notation $\sigma_{\ln EDP|IM}$ implies that only record-to-record variability is considered), then, assuming that $\sigma_{\ln EDP|IM}$ is constant, the mean annual frequency of exceeding any specified EDP value of y can be calculated in closed analytical form as

$$\lambda_{EDP}(y) = P[EDP \geq y] = \lambda_{IM}(IM_y) \exp\left[\frac{1}{2}\frac{k^2}{b^2}\sigma^2_{\ln EDP|IM}\right] \quad (9.6)$$

where IM_y is defined as the intensity measure corresponding to $E\hat{D}P =$ y (i.e., the inverse of the median relationship between IM and EDP, $IM_y = (y/a)^{1/b}$, see Equation (9.4)). In final form, the EDP hazard curve can be expressed as

$$\lambda_{EDP}(y) = P[EDP \geq y] = k_o \left[(y/a)^{1/b}\right]^{-k} \exp\left[\frac{1}{2}\frac{k^2}{b^2}\sigma^2_{\ln EDP|IM}\right] \quad (9.7)$$

For a given IM hazard, the EDP hazard predicted from this equation depends on a and b, the parameters defining the median relationship between EDP and IM, and the dispersion $\sigma_{\ln EDP|IM}$.

For illustration, and using the data from Figures 9.1 and 9.2, EDP hazard curves are developed based on a $S_a(T_1)$ hazard curve estimated from the equal-hazard response spectra values calculated for Van Nuys, California, (site class NEHRP D) as part of the PEER research effort to develop Performance-Based Earthquake Engineering Methodologies (Somerville and Collins, 2002). Equal-hazard response spectra values are given for the 50/50, 10/50, and 2/50 hazard levels and discrete periods: 0.01, 0.1, 0.2, 0.3, 0.5, 0.8, 1.0, 1.5, and 2.0 sec. Since there are no values for 1.8 sec, they are estimated by linear interpolation between the values corresponding to 1.5 and 2.0 sec as shown in Figure 9.3. Then, Equation (9.3) is used to obtain a $S_a(T_1)$ hazard curve from the interpolated hazard values corresponding to 1.8 sec, yielding the following relationship:

$$\lambda_{S_a(1.8)}(S_a) = P\left[S_a(1.8) \geq S_a\right] = 0.000373 S_a^{-2.4} \tag{9.8}$$

The hazard level of primary interest to develop EDP hazard curves from the data in Figures 9.1 and 9.2 is the 10/50 level, so the exponent k in Equation (9.3) is estimated as the average of the two slopes joining the three discrete mean annual frequency of exceedance values (open squares) shown in Figure 9.3.

EDP hazard curves for the maximum roof drift angle and the maximum story drift angle over the height are shown in Figure 9.4. Predicted drift hazard curves are superimposed on the hazard curves obtained from numerical integration. The curves shown in dashed lines are based on Equation (9.7) and a constant dispersion of $\sigma_{\ln EDP|IM}$ = 0.24 and 0.30 for the maximum roof drift angle and maximum story drift angle, respectively, which are representative of the average dispersion in the range of interest ($0 \leq S_a(T_1) \leq 0.6$g). Values of dispersions used for the drift hazard curves are based on the 16th percentile of the data (see Figures 9.1(b) and 9.2(b). Note that dispersions have to be calculated based on percentiles values since counted statistics are used, see Section 2.7). Fitted curves used to quantify EDP-IM relationships needed for the closed-form solutions are computed in the range corresponding to $0 \leq S_a(T_1) \leq 0.6$g because at $S_a(T_1) > 0.6$g the highly inelastic response most likely will cause strength deterioration, which would affect the data points.

The drift hazard curves shown in Figure 9.4 permit a probabilistic assessment of EDPs, in this case maximum roof and story drift angles, in which the uncertainty in the ground motion hazard and the aleatory uncertainty in the response of the system are incorporated. The presumption is that the frequency content of the ground motion selected for the nonlinear time history analyses is representative of the hazard levels of interest. For the cases summarized in the previous paragraph, the closed-form solution seems to provide a reasonable estimate of the drift hazard obtained from numerical integration, even though the dispersion of the EDPs, given IM, gradually increases as a function of the ground motion intensity level. However, different conclusions might be obtained if a closed-form solution is used with a constant dispersion, when drastic variations in the dispersion of the data as a function of the ground motion intensity are encountered. This issue is discussed next.

Figures 9.5 and 9.6 show drift hazard curves computed using dispersions obtained based on the 16^{th} percentile and the 84^{th} percentile of the data (see Figures 9.1(b) and 9.2(b)). (The objective *is not* to discuss the differences between values of dispersion from counted statistics based on 16^{th} and 84^{th} percentiles; it is to demonstrate that the accuracy of EDP hazard curves obtained by using a closed-form solution and assuming a constant dispersion depends upon the variation of the dispersion of the EDP (given the IM) with the intensity level). For the maximum roof drift angle, results are consistent regardless of whether the dispersion is based on the 16^{th} or the 84^{th} percentile. This result is expected, since Figure 9.1(b) shows that for the range of interest $0 \leq S_a(T_1) \leq 0.6g$ there are no significant differences between the dispersion based on the 16^{th} and the 84^{th} values. However, for the maximum story drift angle over the height, the variation of the dispersion (shown in Figure 9.2(b)) plays an important role in the drift hazard curves. The drift hazard curve from numerical integration using dispersions based on the 84^{th} percentile provides higher values of drift associated with the same hazard level. This result is due to the large values of dispersion observed in the range $S_a(T_1) < 0.2g$, which is also the range where the $S_a(T_1)$ hazard is the highest.

For the maximum story drift angle, the closed-form solution with a constant dispersion that is based on the 84^{th} percentile of the data ($\sigma_{\ln EDP|IM} = 0.35$) is not a good representation of the solution obtained from numerical integration. This value corresponds to the average dispersion in the range of interest ($0 \leq S_a(T_1) \leq 0.6g$). A single $\sigma_{\ln EDP|IM}$ value is not able to accurately capture the effect of the dispersion in the results when the scatter of the data changes radically with the intensity level. In this case, the variation of the dispersion with the level of intensity is attributed to the fact that a few dynamic responses exhibit relatively large drift values at small levels of inelastic behavior. Thus, changes in the dispersion of the EDP given IM play an important role in the estimation of the EDP hazard. Similar conclusions have been obtained by Aslani and Miranda, 2002.

9.3 PROBABILITY OF COLLAPSE

For P-delta-sensitive structures, which have the potential for dynamic instability, relationships between maximum roof drift and relative intensity of the type presented in Chapter 4 can also be utilized to estimate the mean annual frequency of global collapse. The process is illustrated here for a frame with 18 stories, a period of 3.6 sec, and $\gamma = 0.10$. Incremental dynamic analysis results for this frame are presented in Figure 9.7. The values of $S_a(T_1)$ at which the frame approaches the onset of dynamic instability (horizontal lines in Figure 9.7) correspond to the spectral acceleration values at collapse, which can be used to compute a global collapse fragility curve whose median $S_a(T_1)$ is 0.40 and whose $\sigma_{\ln Sa(T1)}$ is 0.38, as shown in Figure 9.8. (In this example, the fragility curve is computed by fitting a lognormal distribution to the $S_a(T_1)$ values at collapse.) This fragility function can be used in conjunction with a $S_a(T_1)$ hazard curve to estimate the mean annual frequency of collapse using Equation (9.2). If for instance, the $S_a(T_1)$ hazard curve is the one developed for Van Nuys, California, for a period of 4.0 sec, as shown in Figure 9.9 (Abrahamson, 2001), then Equation (9.2) can be solved numerically to obtain the mean annual frequency of collapse for the system, which in this case is equal to 1.86e-04.

9.4 SUMMARY

The information presented in this chapter relates to the probabilistic seismic assessment of regular frames subjected to ordinary ground motions. EDP hazard curves are developed to illustrate the process of performing probabilistic evaluation of EDPs. Then, a fragility curve is used to estimate the mean annual frequency of collapse of a long, flexible frame. The main observations presented in this chapter are as follows:

- When the spectral acceleration at the first mode is used as the IM, EDP hazard curves can be developed using available seismic hazard information. This process gives good results provided the frequency content of the ground motions is not very sensitive to magnitude and distance. When different scalar IMs (or a vector of IMs) are needed to adequately describe the seismic hazard, e.g., for the case of near-fault ground motions, the development of EDP hazard curves necessitates the modification of available seismic hazard information and/or the development of new seismic hazard information on selected IMs.

- Closed-form solutions provide a very useful and convenient way of estimating EDP hazard curves. In some cases, the variation of the dispersion of the EDP (given IM) with the intensity level is large. Thus, good judgment must be exercised when using closed-form solutions (based on constant dispersion) to evaluate EDP hazard curves.
- The potential for global collapse of a frame structure can be expressed probabilistically in terms of a mean annual frequency of collapse, using a collapse fragility function based on the IM at which dynamic instability of the structural system occurs. However, results should be obtained with component models that are able to represent the main factors that influence the global collapse of a system, e.g., cyclic deterioration in strength and stiffness.

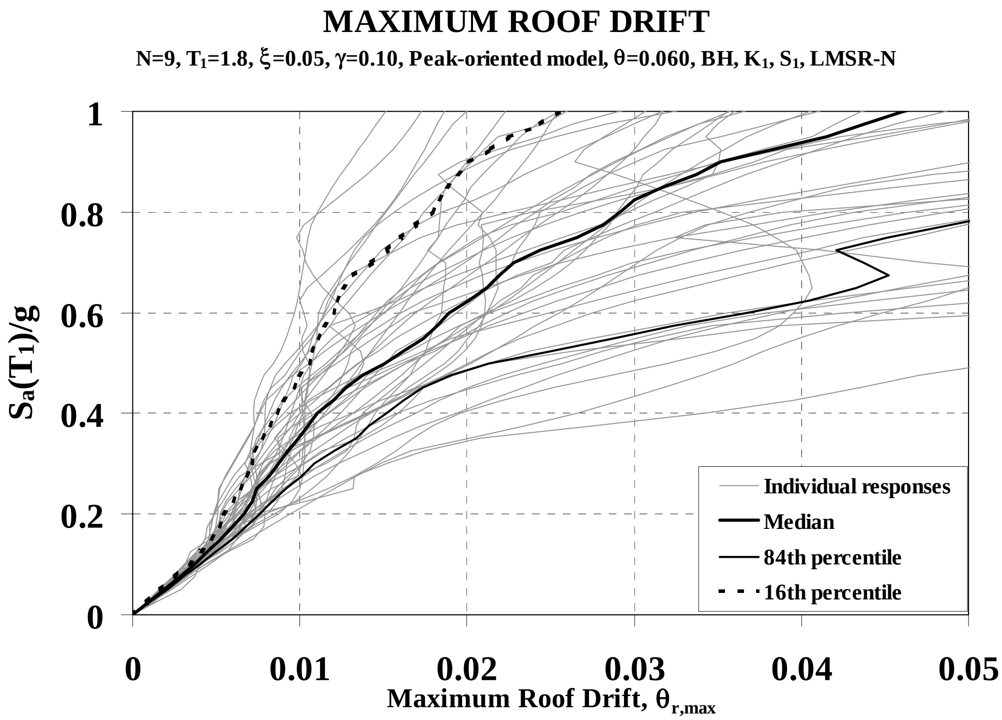

(a) Incremental Dynamic Analysis Curves

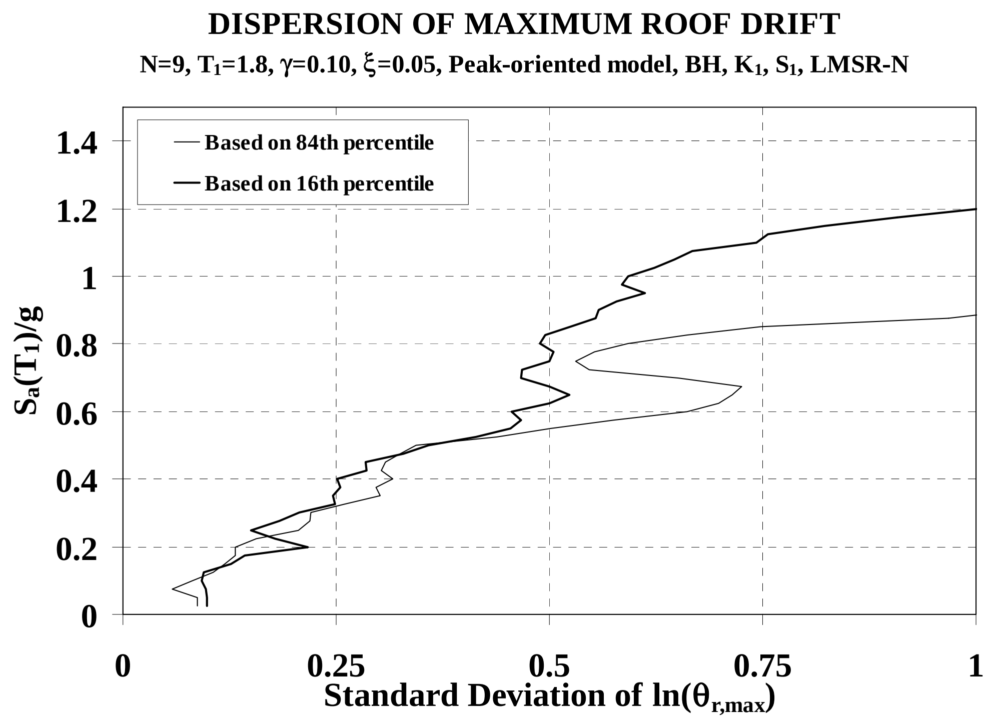

(b) Dispersion

Figure 9.1 Relationship between $S_a(T_1)$ and the Maximum Roof Drift Angle, N = 9, T_1 = 1.8 sec, γ = 0.10

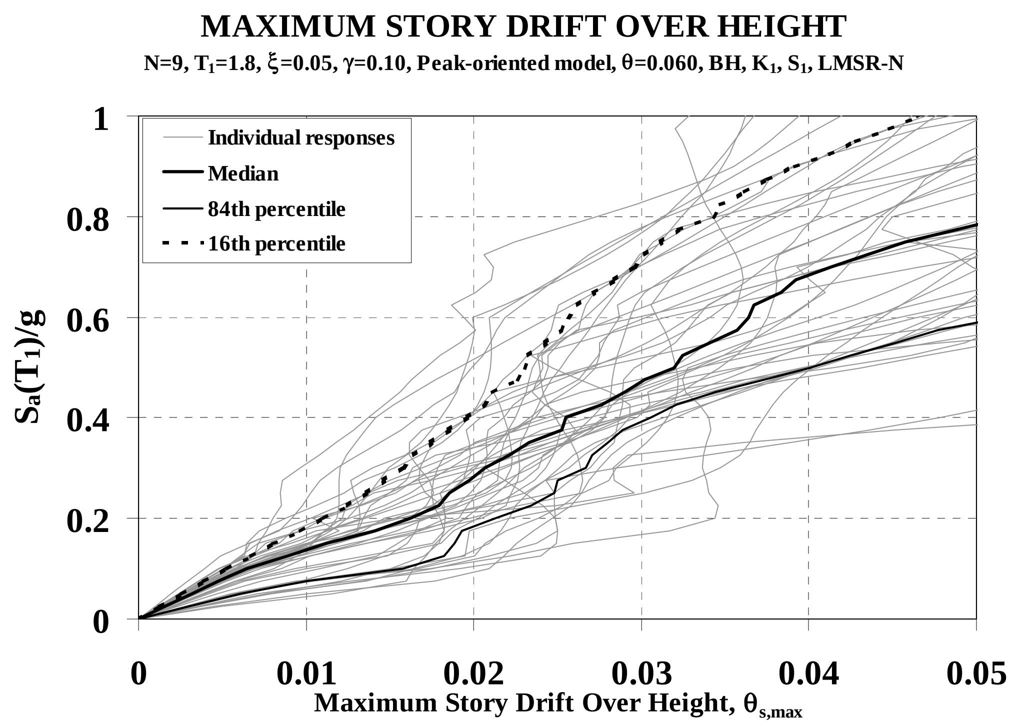

(a) Incremental Dynamic Analysis Curves

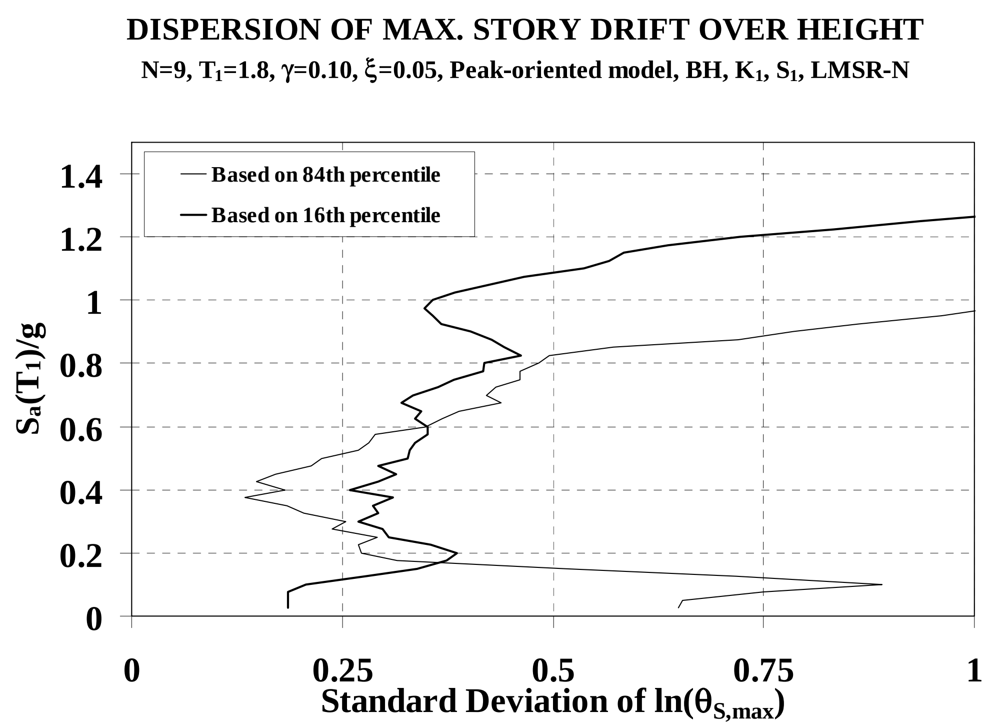

(b) Dispersion

Figure 9.2 Relationship between $S_a(T_1)$ and the Maximum Story Drift Angle over Height, N = 9, T_1 = 1.8 sec, γ = 0.10

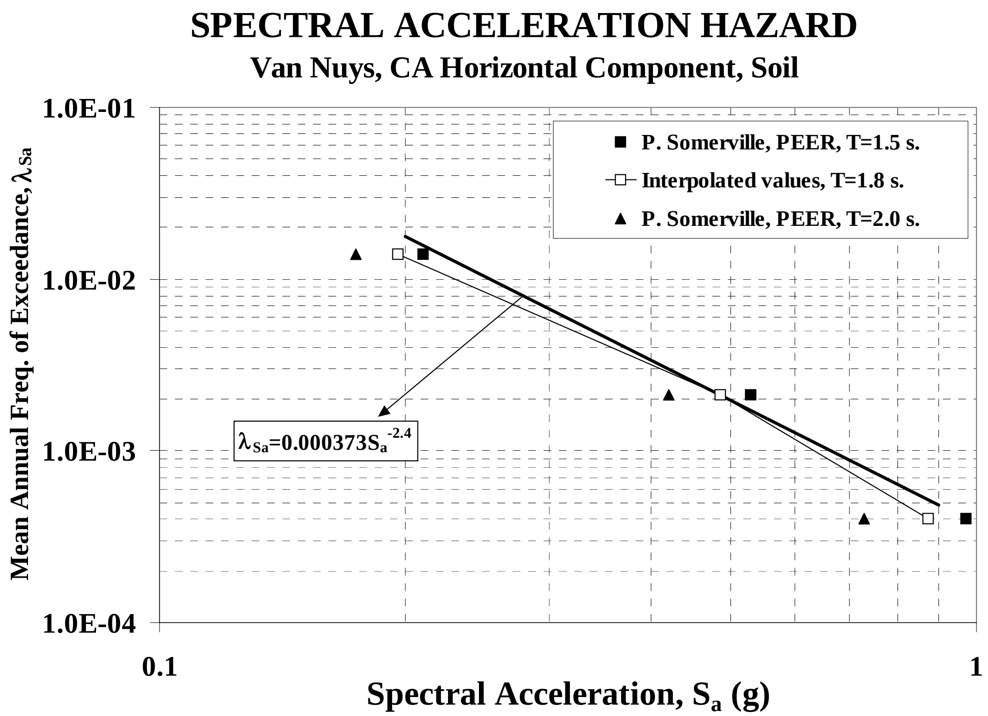

Figure 9.3 Estimated Spectral Acceleration Hazard Curve for T = 1.8 sec.

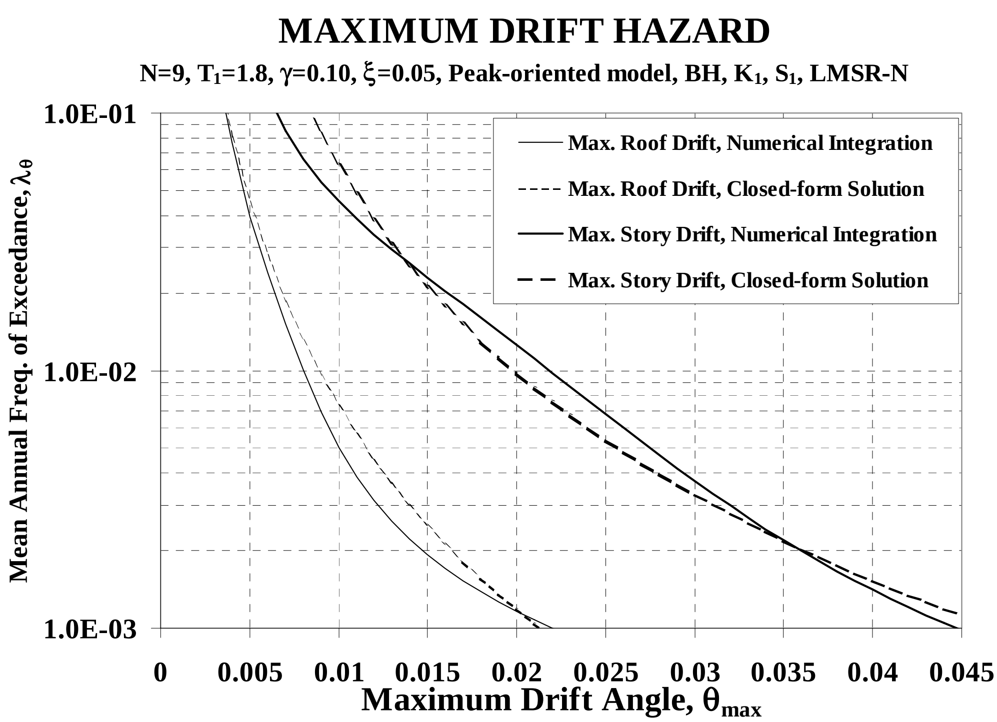

Figure 9.4 Drift Hazard Curves, N = 9, T_1 = 1.8 sec, γ = 0.10

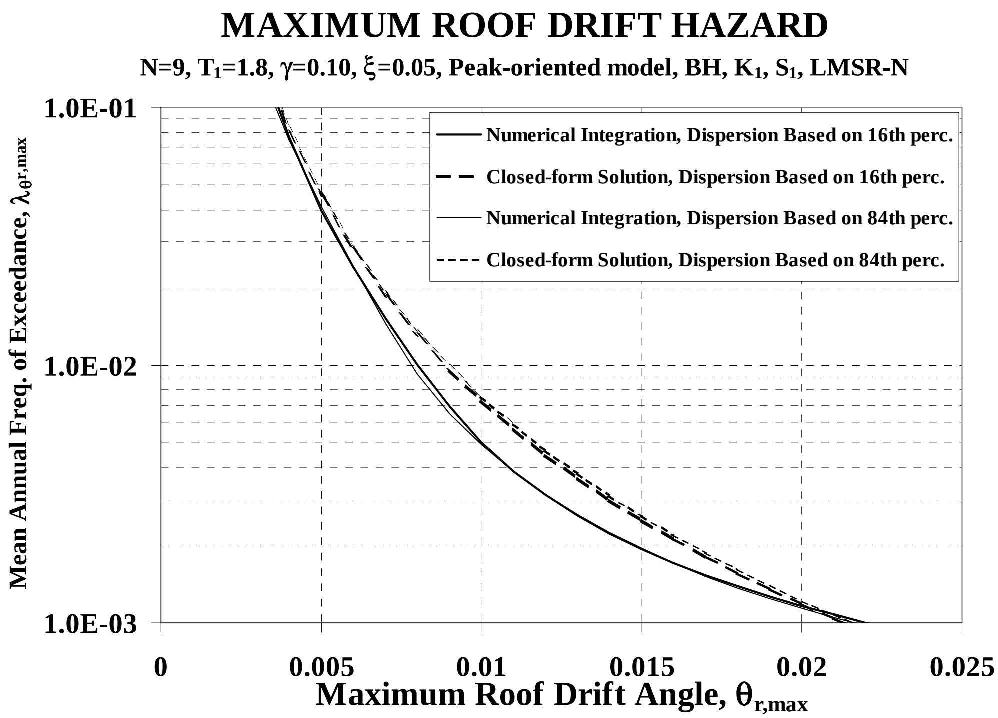

Figure 9.5 Maximum Roof Drift Angle Hazard Curves, N = 9, T_1 = 1.8 sec, γ = 0.10

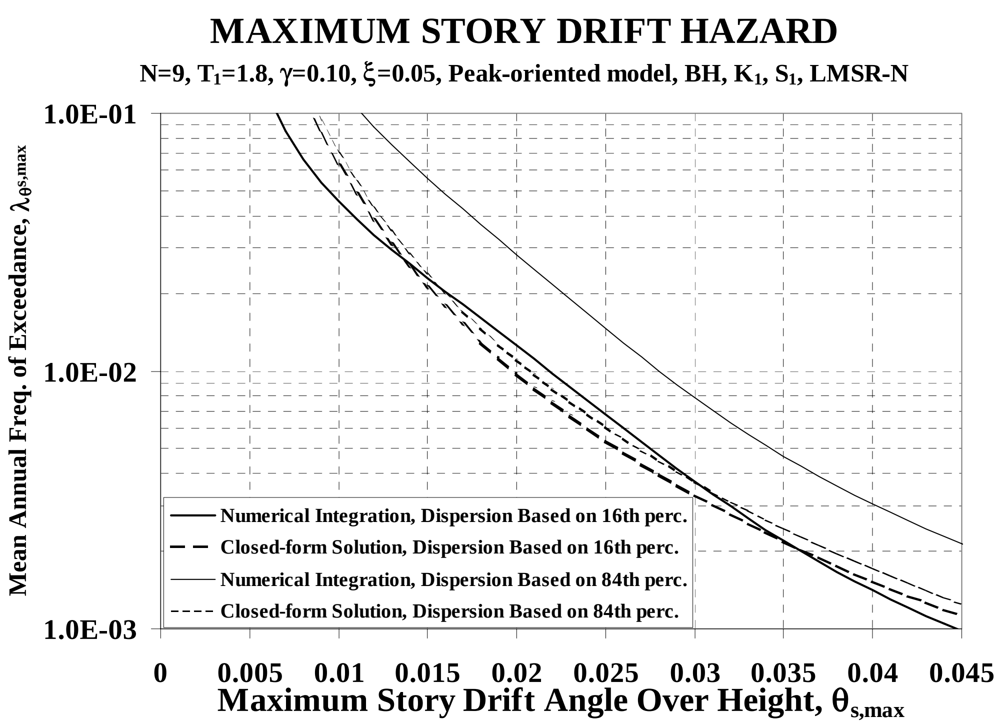

Figure 9.6 Maximum Story Drift Angle Hazard Curves, N = 9, T_1 = 1.8 sec, γ = 0.10

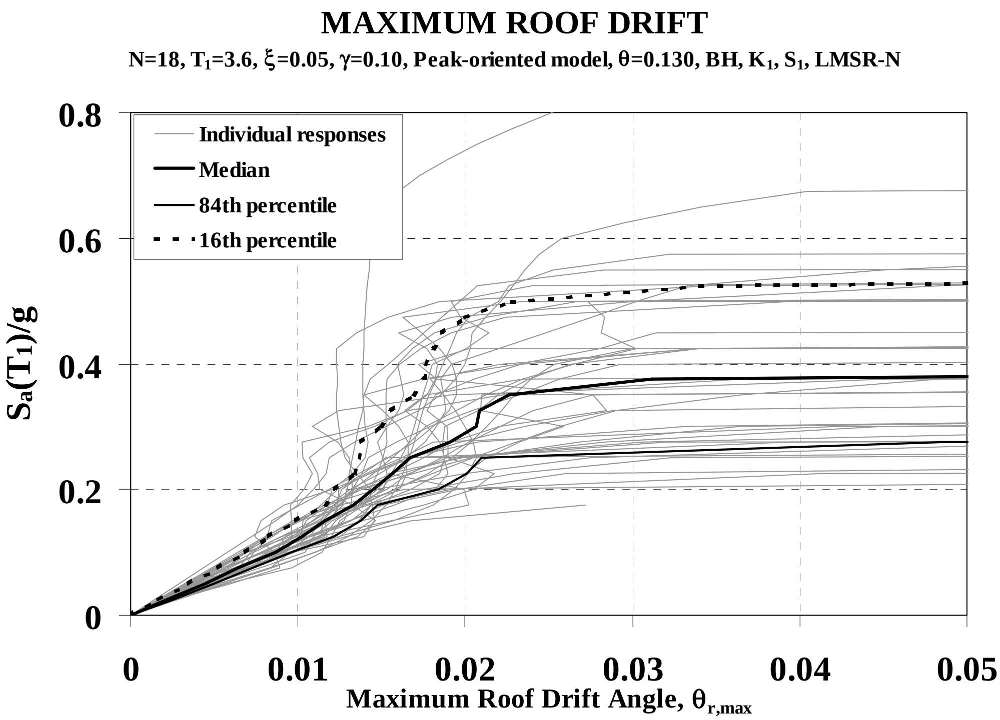

Figure 9.7 Incremental Dynamic Analysis, N = 18, T_1 = 3.6 sec, γ = 0.10

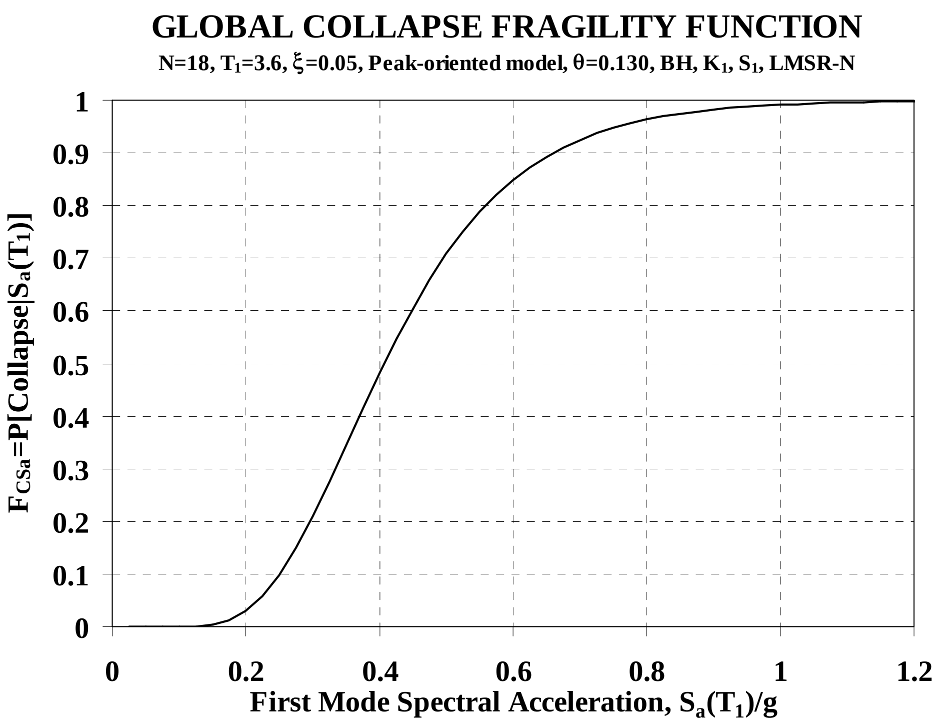

Figure 9.8 Global Collapse Fragility Function, N = 18, T_1 = 3.6 sec, γ = 0.10

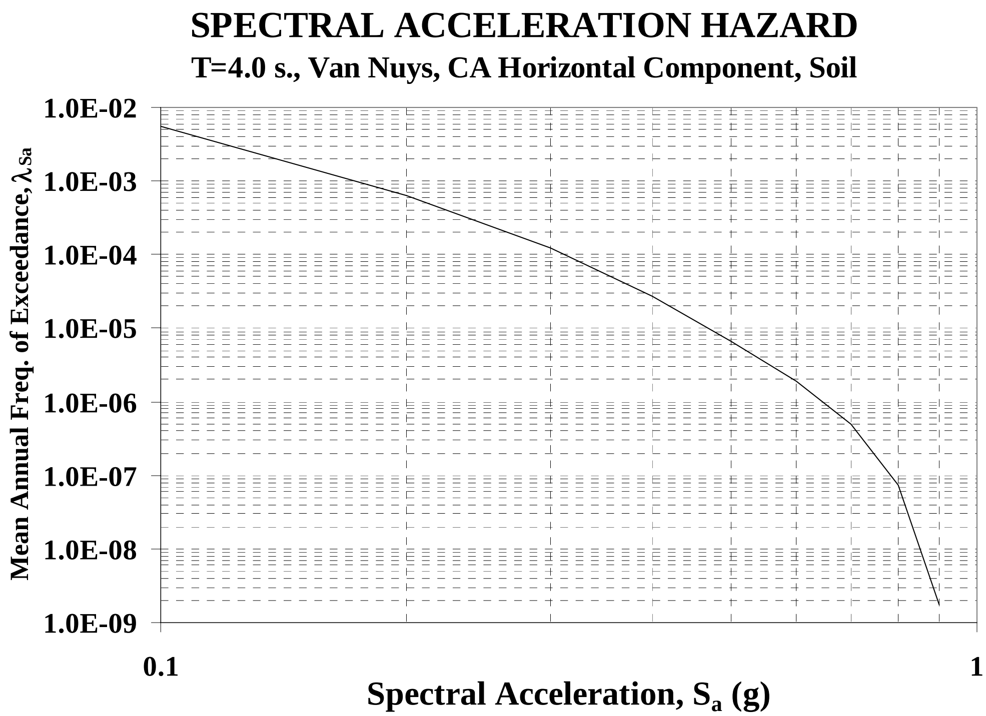

Figure 9.9 Spectral Acceleration Hazard Curve for T = 4.0 sec (Abrahamson, 2001)

10 Summary and Conclusions

The objective of this study is to improve the understanding of behavior patterns and the quantification of seismic demands for nondeteriorationg regular frames subjected to ordinary ground motions. In this study, the term *ordinary* refers to ground motions that are recorded at distances greater than 13 km from the fault rupture, do not exhibit pulse-type characteristics, and are recorded on stiff soil sites. Engineering demand parameters (EDPs) of interest include roof and story drifts, local deformations, absolute floor accelerations and velocities, story shears and overturning moments, and energy terms, which are obtained by means of nonlinear time history analyses. A relational database management system is used to perform a statistical evaluation of seismic demands and establish relationships between structural and ground motion parameters. In the context of the performance assessment methodology discussed in this study, the ground motion input is characterized by an intensity measure, IM. The primary IM used in this project is the spectral acceleration at the first mode of the structure, $S_a(T_1)$. This spectral acceleration is obtained from an elastic SDOF oscillator with 5% critical damping. Since nondeteriorating frames are used, the EDPs of primary interest are those that correlate best with structural, nonstructural and contents damage at performance levels related to direct dollar losses and downtime (loss of function). The emphasis of this study is on quantification of EDPs for performance evaluation, but includes a discussion of issues related to the design of components that need to be protected to avoid brittle failure in the response, e.g., columns in a moment-resisting frame.

The bulk of the analysis is performed by using a set of 40 ordinary ground motions recorded in California at stations corresponding to NEHRP site class D (USGS C), in earthquakes with moment magnitude ranging from 5.8 to 6.9 and at sites with a closest distance to the fault rupture from 13 km to 40 km. A family of two-dimensional, nondeteriorating generic regular frame models is utilized, in which nonlinear behavior is modeled by using a concentrated plasticity approach utilizing nonlinear rotational springs. The dependence of the results on variations in the following structural properties and characteristics is investigated: hysteretic model, strain hardening in the moment-rotation relationship at the component level, additional strength and stiffness provided by elements that do not form part of the moment-resisting frames, story shear strength distribution, overstrength, the effect of gravity load moments, and "failure" mechanism. A correlation between seismic demands obtained using one-bay generic frame models and a model of a "real" structure is discussed to evaluate the effectiveness of generic models in reproducing the global seismic behavior of a "real" moment-resisting frame structure.

An exploration of the probabilistic evaluation of EDPs is summarized, in which EDP hazard curves are developed based on available seismic hazard information. The use of global collapse fragility functions (for a frame in which P-delta causes dynamic instability in the response) along with an IM hazard curve to estimate the mean annual frequency of collapse is also presented.

The main conclusions derived in this report are summarized as follows:

Ground motions and intensity measures

- As part of the seismic performance assessment process, probabilistic expressions for EDPs given an IM need to be established. This necessitates the selection of sets of ground motions on which seismic demand analysis can be based, and which represent the seismic hazard defined by an appropriate IM. The selection of ground motions, which adequately represent the magnitude and distance dependence of the earthquake intensity for an appropriate range of return periods, is a fundamental issue of seismic performance assessment. It is found that, within certain limits, the frequency characteristics (spectral shapes) are statistically not very sensitive to magnitude and distance. The limits tested in this study cover a range of magnitude from 5.8 to 6.9, and a range of distances from 13 to 60 km (a set of 80 ground motion records is used for this purpose). For a given magnitude, the distance dependence is found to be small for the full range of distances investigated, and for a given distance, the magnitude dependence is found to be discernible but not very large for the magnitude range of $6.5 \le M_w \le 6.9$. Thus, for these ranges it is believed that any sufficiently large (and site-class consistent) set of records, together with a single IM, can be used to describe the seismic hazard. For larger magnitudes and smaller distances, near-fault effects may significantly alter the frequency characteristics. Demand evaluation for these conditions is outside the scope of this study.

- The spectral acceleration at the first-mode period of the structure, $S_a(T_1)$, (which is the IM utilized in this study) is one choice of an IM, but its use may result in large dispersions in EDPs, particularly for inelastic systems with significant higher mode or structure P-delta effects. The larger the dispersion, the larger is the number of records necessary to determine statistical measures with sufficient confidence. The alternative is to select a more complex (structure-specific) intensity measure, which may reduce the dispersion but will make the ground motion hazard analysis more complex.

Unless otherwise specified, the following conclusions are drawn from a statistical study with generic single-bay frames with fundamental periods, T_1, equal to 0.1N and 0.2N in which N is the number of stories. Frames with N = 3, 6, 9, 12, 15, and 18 stories are used. The generic frames are designed so that the first mode is a straight line and simultaneous yielding is attained when subjected to a parabolic (NEHRP, k = 2) load pattern. Frames are designed according to the strong-column, weak-beam concept so that a beam-hinge mechanism is developed, i.e., plastic hinges are confined to the beam ends and the base of the first-story columns. A peak-oriented model (Clough model) that includes 3% strain hardening is used to represent the hysteretic behavior at plastic hinge locations (cyclic deterioration effects are neglected). Rayleigh damping is implemented so that 5% damping is obtained at the first mode and at the mode in which the total mass participation exceeds 95%. Global P-delta effects are modeled in all cases. Frames are subjected to the set of 40 LMSR-N bins described in Chapter 3, and basic EDP-IM relationships are studied as a function of a relative intensity measure defined by $[S_a(T_1)/g]/\gamma$, in which γ is the base shear coefficient, V_y/W. The primary range of interest in this study is $[S_a(T_1)/g]/\gamma < 8$ (and in many cases much less than 8 because strength deterioration may set in at much smaller relative intensities).

Behavior issues (base case frame models)

- Short-period frames (T_1 = 0.3 sec) and P-delta-sensitive structures (systems in which the postyield tangent stiffness from a pushover analysis is negative) present patterns of behavior quite distinct from the rest of the systems used in this study:
  - Inelastic short-period frames experience drift demands that are much larger than the elastic ones, which imposes large ductility demands on its components. The dynamic response of short-period structures is mostly dominated by the first mode; thus, the distribution over the height of story drift and ductility demands is rather uniform.
  - P-delta-sensitive frame systems exhibit relative large drift demands due to the formation of a negative tangent stiffness in the response. Because of P-delta, the maximum story drifts concentrate in a few stories at the bottom of the structure, which can lead to dynamic instability problems. Mitigation of potential instability due to P-delta effects can be achieved by creating designs (for new buildings) or retrofit strategies (for existing buildings) in which the formation of a negative postyield slope in the response is delayed. This can be achieved by providing a flexible back-up system. The nonlinear pushover analysis technique is a useful to assess the dynamic instability potential of P-delta-sensitive structures.
- Understanding the relationship between fundamental period and number of stories is important for design and demand evaluation procedures based on SDOF baseline information in which the effect of the number of stories cannot be explicitly represented. The values of fundamental used for this evaluation are T_1 = 0.6 sec, 1.2 sec, and 1.8 sec. *Given the fundamental period and the relative intensity,* the effect of different number of stories is summarized as follows:
  - The effect of higher modes on the drift demands is more noticeable for taller, stiffer frames (T_1 = 0.1N) than for shorter, flexible ones (T_1 = 0.2N). The maximum story drift demand over the height is larger for stiffer frames and a larger number of stories translates into a less uniform distribution of story drifts over the height as compared to frame structures with smaller number of stories. The observations presented in this paragraph are applicable to frame structures that are not P-delta sensitive.

   - For relatively small levels of inelastic behavior, frames with larger number of stories exhibit larger maximum absolute floor accelerations. As the relative intensity increases, maximum absolute floor acceleration demands become weakly dependent on the number of stories.
   - Maximum absolute floor velocity demands are weakly dependent on the number of stories for all relative intensity levels.
- An evaluation of the distribution of damage over the height necessitates the quantification of statistical information on EDPs that correlate with damage, such as maximum story drift angles, maximum absolute floor accelerations and velocities, maximum plastic beam rotations, and normalized hysteretic energy demands. A summary of behavior patterns of the distribution over the height of these EDPs is as follows:
   - For the base case generic frames used in this study, and except for short-period systems, the maximum story drift angle demands concentrate at the top stories for elastic behavior and relatively low levels of inelastic behavior. As the level of inelastic behavior increases, maximum story drift angle demands migrate towards the bottom stories. The large top story drifts at small levels of inelastic deformation are due to the fact that the beam strength at the top floors is tuned to the NEHRP k = 2 load pattern. For real frame structures, in which gravity loads tend to control beam sizes at the top floors, smaller maximum story drifts in the top stories are expected. Thus, the design story shear strength distribution is critical to assess the level of damage over the height of a structure.
   - Except for short-period systems, maximum absolute floor accelerations concentrate at the top floors for elastic systems and systems with relative small levels of inelastic behavior. Maximum absolute floor acceleration demands migrate to the bottom floors with an increase in the relative intensity. For short-period systems, maximum absolute floor accelerations occur at the top floor regardless of the level of inelastic behavior. This information has relevant implications in the design of acceleration-sensitive components because current seismic design guidelines assume amplification of floor accelerations proportional to height regardless of the level of inelastic behavior, fundamental period, and number of stories.
   - Maximum absolute floor velocity demands also tend to concentrate at the top of the structures regardless of the structural period and the level of inelastic behavior.

    - The distribution of maximum beam plastic rotations and normalized hysteretic energy demands (defined as the hysteretic energy dissipated at plastic hinge locations normalized by the yield moment times the yield rotation of the component) follow patterns similar to those observed for the distribution of maximum story drift angles over the height.
- Cumulative damage in structural components is believed to be proportional to the normalized hysteretic energy dissipated in the segment of the response preceding the excursion with the maximum deformation amplitude (prepeak response segment). This issue is particularly important for stiffness-degrading models in which a large amount of energy can be dissipated in small hysteretic loops without inducing significant additional structural damage to the component. If this is the case, energy demand evaluation based on the total energy dissipated by a component may provide a misleading picture of its real damage state. In Chapter 5, a definition of strong motion duration that identifies the interval of the response that is most relevant for demand evaluation and damage assessment is discussed. This strong motion duration tends to increase with fundamental period and relative intensity. A rapid increase is observed for P-delta-sensitive frames.
- For regular frame structures with story shear strengths tuned to a code-specified load pattern, simultaneous yielding in all stories is likely to occur during their nonlinear dynamic response. Thus, a reduction of the story overturning moments based on $\Sigma 2M_{pi}/L$ is not justified, especially at medium and large relative intensity levels.
- Higher modes (particularly the second mode) and dynamic redistribution of forces cause the point of inflection in some columns to move from near the midheight of a column (for elastic behavior) to one of its ends, which in some cases produces a condition of single curvature in a column. This behavior is not appropriately captured by a pushover analysis based on a predefined load pattern, since the effects of higher modes and dynamic redistribution are not incorporated. These changes to the column moment diagram lead to:
    - large moments at the ends of columns, which translate into strong column factors (SCFs) that increase almost linearly with the level of inelastic behavior. Except for the short-period frame, T_1 = 0.3 sec, which exhibits larger SCFs, SCFs increase with increasing fundamental period. Median strong column factors of 3 and larger are observed in the range of intensity levels of interest for nondeteriorating frames. Thus, the potential of plastic hinging in columns is high for regular frames designed according to the strong-column, weak beam requirements of current code provisions, which in the United States

require strong column factors greater than or equal to 1.0 for steel, and 1.2 for reinforced concrete frames.

- large moments at the midheight of columns. Thus, a design based on the assumption of a point of inflection near the midheight of the column is not adequate once the structure experiences large levels of inelastic behavior.

Behavior issues (variations to the base case)

- The amount of stiffness degradation present at the component level can have a noticeable effect on the drift demands of a frame structure. For instance, frames that are not sensitive to P-delta with hysteretic behavior that exhibits "severe" stiffness degradation (significant pinching in the response) tend to experience larger roof and story drift demands than models with less stiffness degradation (peak-oriented model) and models with no stiffness degradation (bilinear models). The effect of severe stiffness degradation in the response of regular frame structures is more noticeable than in the response of SDOF systems. Frame structures that are sensitive to structure P-delta effects approach the onset of dynamic instability at smaller relative intensity values when the moment-rotation relationship at the component level does not experience stiffness degradation (bilinear model). This phenomenon is attributed to the fact that the response of the system with bilinear hysteretic behavior spends more time on the envelope of the moment-rotation relationship of its components, which added to the P-delta effect produces an effective a negative tangent stiffness in P-delta-sensitive structures.
- Strain hardening in the moment-rotation relationship at the component level is beneficial in order to decrease (and in some cases eliminate) the potential for dynamic instability in the response.
- Structural and nonstructural elements that contribute to the lateral stiffness and strength of a moment-frame structure, but customarily are not included in the model of the frame, may be very beneficial in delaying the onset of dynamic instability, particularly if these elements maintain their stiffness far into the inelastic range.
- The magnitude and distribution over the height of maximum story drifts are sensitive to the "static" story shear strength pattern and the presence of overstrength in the response.

- Story shear strength patterns that are intended to account for the contribution of higher mode effects, i.e., parabolic load pattern, produce designs with smaller drift demands and a more uniform distribution of maximum story drift angles over the height than the ones obtained with other load patterns, e.g., triangular and uniform. Story shear strength patterns causing significant strength irregularities over the height may lead to the formation of undesirable story mechanisms and compromise the stability of the system.
- The design of real frame structures may lead to story overstrength values that vary with height. Such overstrength is not always associated with a decrease in story drifts. For P-delta-sensitive frames, the presence of overstrength is beneficial because it reduces the relative intensity at which dynamic instability is approached.

- The effect of gravity load moments on the roof drift is negligible. For relatively small levels of intensity, gravity load moments reduce the maximum story drifts because the system reaches the small postyield stiffness from the pushover analysis at a larger drift as compared to systems without gravity load moments.
- Plastic hinging in columns should be avoided in order to prevent the formation of story mechanisms that lead to large story drift demands. Story mechanisms cause maximum story drift angles to concentrate in a few stories, increasing the potential for dynamic instability when P-delta effects are considered.

Quantification of deformation, acceleration, and velocity demands

In this study, EDPs of interest for damage assessment include the maximum roof drift angle, $\theta_{r,max}$, the average of the maximum story drift angles, $\theta_{si,ave}$, the maximum story drift angle over the height, $\theta_{s,max}$, the maximum absolute floor acceleration over the height, $a_{f,max}$, and the maximum absolute floor velocity over the height, $v_{f,max}$. The statistical evaluation of these EDPs is based on a counted median value (which provides a measure of the central tendency of the EDP given the IM) and a measure of dispersion, which is defined as the standard deviation of the natural log of the data and accounts for record-to-record variability. A summary of the most important aspects regarding the statistical evaluation of the aforementioned EDPs is presented as follows:

- Except for inelastic short-period systems and P-delta-sensitive frames, the median normalized maximum roof drift angle, $\theta_{r,max}/S_d(T_1)$, in which $S_d(T_1)$ is the elastic spectral displacement at the first-mode period, is approximately equal to the first-mode participation factor, PF_1, which implies that both the elastic and inelastic roof displacements are dominated by the first mode (PF_1 is obtained using a first-mode shape which is normalized to be equal to one at the roof level). $\theta_{r,max}/S_d(T_1)$ is a stable quantity associated with a small dispersion especially for the range of relative intensities of interest in this study, $[S_a(T_1)/g]/\gamma < 8$.

- The normalized average of maximum story drift angles, $\theta_{si,ave}/S_d(T_1)$, shows trends similar to that of the maximum roof drift angle. Its dispersion is also comparable to that of the normalized maximum roof drift angle except at low levels of inelastic behavior ($[S_a(T_1)/g]/\gamma < 2$) in which higher modes cause larger dispersions. The ratio $\theta_{si,ave}/\theta_{r,max}$ is a very stable parameter which is weakly dependent on the fundamental period. For a given fundamental period, the median $\theta_{si,ave}/\theta_{r,max}$ is not sensitive to the number of stories. The dispersion associated with this ratio is very small (in the order of 0.15), which implies that this parameter is slightly dependent on the frequency content of the ground motions. A simplified relationship to obtain median estimates of $\theta_{si,ave}/\theta_{r,max}$ as a function of the fundamental period is presented in Chapter 4. This relationship is applicable to the range of relative intensities of interest and structures that are not sensitive to P-delta effects.
- Median normalized maximum story drift angles over the height, $\theta_{s,max}/S_d(T_1)$, exceed the median roof drift by a percentage that increases with period, i.e., the median of the ratio $\theta_{s,max}/\theta_{r,max}$ increases with period. For a given period and relative intensity, higher mode effects cause systems with larger number of stories to experience larger median $\theta_{s,max}/\theta_{r,max}$, and hence, a less uniform distribution of maximum story drift angles over the height. The dispersion of this ratio is relatively small (less than 0.25) except for $[S_a(T_1)/g]/\gamma < 2$ at which higher mode effects cause the dispersion to increase. Simplified relationships to estimate the median $\theta_{s,max}/\theta_{r,max}$ as a function of the fundamental period and the number of stories are also given in Chapter 4. These relationships are applicable to the range of relative intensities of interest and structures that are not sensitive to P-delta effects.
- PGA and PGV are used to normalize floor acceleration and velocity demands because they provide a direct measure of the amplification (or de-amplification) of floor demands relative to the ground floor. Moreover, except for the $T_1 = 0.3$ sec frame, absolute floor acceleration demands correlate better with PGA rather than $S_a(T_1)$ because of inelastic effects and the

influence of higher modes in the response. Except for medium to long-period systems ($T_1 >$ 1.2 sec) and large relative intensities, absolute floor velocity demands are controlled by the first mode; thus, $S_v(T_1)$ is a more efficient ground motion IM for elastic and moderately inelastic systems.

- The amplification of floor accelerations and velocities with respect to maximum ground motion parameters, e.g., PGA and PGV, respectively, decreases with relative intensity until it becomes rather constant with increasing levels of inelastic behavior. This trend is not observed in the SDOF system for which the normalized maximum acceleration demands are approximately inversely proportional to the strength reduction factor, i.e., relative intensity level.
- The amplification of absolute floor acceleration and velocity demands with respect to PGA and PGV, respectively, is slightly dependent on the frequency content of ordinary ground motions, which is demonstrated by their small dispersion as compared to the dispersion observed for the maximum story drift demands.

Probabilistic assessment of EDPs

- Results presented in Chapter 9 demonstrate that when the spectral acceleration at the first mode is used as the IM, EDP hazard curves can be developed using available seismic hazard information. This process gives good results provided the frequency content of the ground motions is not very sensitive to magnitude and distance. When different scalar IMs (or a vector of IMs) are needed to adequately describe the seismic hazard, e.g., for the case of near-fault ground motions, the development of EDP hazard curves necessitates the modification of available seismic hazard information and/or the development of new seismic hazard information on selected IMs.
- Closed-form solutions provide a very useful and convenient way of describing EDP hazard curves. In some cases, the variation in the dispersion of the EDP (given IM) with the intensity level is significant. Thus, good judgment must be exercised when using closed-form solutions (based on constant dispersion) to evaluate EDP hazard curves.
- The potential for global collapse of a frame structure can be expressed probabilistically in terms of a mean annual frequency of collapse, using a fragility function based on the value of the IM that causes global collapse. Rigorous collapse assessment implies that these results

should be obtained with component models that are able to represent the main factors that influence the global collapse of a system, e.g., cyclic deterioration in strength and stiffness.

The conclusions and observations presented in this chapter are based on two-dimensional, nondeteriorating generic regular frame models subjected to ordinary ground motions. Interpretation of these conclusions needs to be made within this context and the conditions identified in each chapter for the structural models and ground motion input.

This research study provides a step, but not yet a complete answer, toward a comprehensive quantification of EDPs. Additional information on seismic behavior and quantification of EDPs and their uncertainties has to be obtained by addressing issues such as:

- Near-fault ground motions
- Additional lateral-load-resisting systems, e.g., structural walls and dual systems
- Axial-moment-shear (P-M-V) interaction
- Soil-foundation-structure interaction
- Cyclic deterioration effects
- Asymmetric hysteretic behavior at the component level, e.g., $M_y^+ \neq |M_y^-|$
- Irregularities in plan and elevation
- Different stiffness distribution over the height

Appendix A: Properties and Static Behavior of Base Case Generic Regular Frame Models

A.1 PROPERTIES OF THE BASE CASE FAMILY OF GENERIC FRAME MODELS

The general characteristics of the base case family of generic frame models used in this study are listed in Section 2.4.1. Modal and structural properties are summarized in more detail in Tables A.1 to A.18. The tables are divided into two major sections:

Table of modal properties (Tables A.1 to A.6)

1. *Modal properties (**first five** modes only, i denotes mode number)*

- Period ratios, T_i / T_1
- Participation factors, PF_i
- Mass participation, MP_i (as a fraction of the total mass)
- Modal damping, ξ_i

2. *Mode shapes (first five modes)*

- Normalized mode shapes, ϕ_i

Table of structural properties (Tables A.7 to A.18)

1. *Stiffness properties (i denotes story or floor)*

- Weight ratio, W_i / W (W = total weight)
- Moment of inertia ratio, I_i / I_1 (I is the same for columns and top beam in a story)
- Story stiffness ratio (load pattern independent), K_{ai} / K_{a1}. The story stiffness is defined here as the load (story shear force) required to produce a unit displacement of a subassembly consisting of a "story" (two columns and the beam above). The columns of the subassembly

are fixed at the base and all three elements (two columns and beam) have the same moment of inertia.

- Floor stiffness ratio (load pattern independent), K_{fi} / K_{f2}. Floor stiffness is defined as the story shear force required producing a unit displacement of a subassembly consisting of a floor beam and half of the length of the columns on top and below the floor level (assuming points of inflection occurs at the midheight of columns). This definition is used at all levels, except for the top floor where the subassembly is composed of the floor beam and half of the length of the columns below it.
- Story stiffness ratio, K_{ki} / K_{k1}, based upon triangular load pattern and K_{si} / K_{s1}, based upon parabolic load pattern. Story stiffness is defined here as the load-pattern-dependent story shear force required to cause a unit story drift in that story.
- Beam stiffness ratio, K_{bi} / K_{b2} (beam stiffness, K_b = 6EI / L)
- Spring stiffness at base, K_c = 3EI / L of the second-floor beam (see Section A.2)

*2. Strength and deformation parameters for a structure designed with a normalized base shear strength $\gamma = V_y / W = 1.0$ and a parabolic design load pattern **without** considering P-Delta effects (i denotes story or floor).*

- Story shear strength ratio, V_i / V_1
- Story overturning moment ratio, M_{OTi} / M_{OT1} (overturning moment based on the axial loads and bending moments at the bottom of the columns in a story)
- Story strain-hardening ratio from pushover analysis, α_{si} (story strain hardening is different from the element strain hardening, since the columns provide additional stiffness after yielding in the beams and at the base occurs).
- Floor beam strength ratio, M_{ybi} / M_{yb2}
- Column strength at base, M_{yc}
- Beam end yield rotation ratio, θ_{ybi} / θ_{yb2}
- Column yield rotation at base, θ_{yc}
- Story drift ratio, δ_{si} / δ_r, where δ_{si} is the story drift in story i, and δ_r is the roof displacement
- Story drift angle ratio, θ_{si} / θ_r (θ_i is defined as δ_{si} / h_i and θ_r as δ_r / H, where h_i is the story height and H the total height)

A.2 ROTATIONAL SPRINGS AT THE BASE

As discussed in Section 2.4.1 the stiffness of the base case generic frames is tuned so that the first mode is a straight line. Relative member stiffnesses are assigned so that for any given story, the columns and the beam above them have the same moment of inertia. In order to obtain a straight-line first mode, when assuming a fixed end condition of the columns at the base, the required moment of inertia of the first-story column should be smaller than the moment of inertia of the second-story columns (and in some cases, smaller than the moment of inertia of a few stories above the first-story level).

A flexible spring is added at the bottom of the first-story columns to obtain a uniform distribution of moments of inertia over the height. The elastic stiffness of the rotational springs is equal to 3EI/L, where I and L are the moment of inertia and span of the second floor beam. The flexible springs are also used to model plastification at the bottom of the first-story columns. For elastic behavior, the point of inflection is near the midheight of the first-story columns due to the presence of the flexible springs with stiffness 3EI/L at the base. Thus, the total elastic stiffness at the rotational degree of freedom at the base is given by:

$$K_T = \frac{K_c K_s}{K_c + K_s} \tag{A.1}$$

where K_c is the rotational stiffness provided by the column (which is approximated by $6EI_{column}/L_{column}$) and K_s is the rotational stiffness provided by the spring ($3EI_{beam}/L_{beam} = 1.5EI_{column}/L_{column}$). Thus,

$$K_T = \frac{6}{5}\frac{EI_{column}}{L_{column}} \tag{A.2}$$

Because the objective is to have a moment-rotation relationship with a post-yield stiffness $K_{T2} = 0.03K_T$ (3% strain hardening) while the column element remains elastic, the post-yield stiffness of the spring is given by $K_{s2} = 0.024145K_s$. With this stiffness value, 3% strain hardening at the base of the first-story columns is approximately obtained if there is no significant change in the moment gradient of the column once the rotational spring at the base has yielded.

In order to assess whether the presence of flexible springs at the base has a significant effect on the dynamic behavior of the frame structures as compared to frame models in which plastification is modeled as part of the element formulation, nonlinear time history analyses are performed with the 18-story frame (T_1 = 3.6 s. and γ = 0.08, bilinear model with 3% strain hardening) subjected to the set of 20 SAC 2/50 ground motions (Somerville, 1997). For the case without flexible springs at the base, plastification at the bottom of the first-story columns is modeled by using the DRAIN-2DX beam-column element, which allows the formation of plastic hinges at the ends of the element (in this case plastic hinging is allowed only at one end, e.g., at the bottom of the first-story columns). Figure A.1 presents statistical results for the distribution of the maximum story drift angles over the height using models with and without flexible springs at the base. It can be seen that both models exhibit a similar response justifying the use of the frame models with flexible springs at the base.

A.3 NONLINEAR STATIC BEHAVIOR AND STRUCTURE P-DELTA EFFECTS

Figures A.2 and A.3 show the nonlinear pushover curves for the base case family of generic frame models used in this study. Global as well as first-story pushover curves are depicted. The curves are plotted in a normalized domain, in which normalization values are those obtained based on a first-order analysis (not considering P-delta effects). When absolute values are of interest, the pushover curves can be "scaled" by using the yield values included in Tables A.7 to A.18.

Some of the pushover curves exhibit a negative postyield stiffness due to structure P-delta effects. In this report, structure P-delta is quantified by using the elastic first-story stability coefficient (FEMA 368, 2000), which is defined here as

$$\theta = \left(\frac{V_1^{'}}{V_1}\right) = \left(\frac{P\delta_1}{V_1 h_1}\right) \qquad \text{(A.3)}$$

where $V^{'}_1$ is the equivalent shear force at the first-story level caused by structure P-delta effects, V_1 is the base shear force, P is the total dead + live load acting at the first-story level, δ_1 is the first-story drift from the elastic portion of the pushover curve, and h_1 is the height of the first story.

This elastic first-story stability coefficient can also be estimated by using the following equation (Aydinoglu, 2001):

$$\theta = \left(\frac{P}{W}\right)\left(\frac{2}{N+1}\right)\left(\frac{g}{h_1}\right)\left(\frac{T_1^2}{4\pi^2}\right) \tag{A.4}$$

where W is the total seismic effective weight, N is the number of stories, g is the acceleration of gravity, and T_1 is the fundamental period of the frame. Equation A.4 assumes equal story heights and masses as well as an elastic straight-line deflected shape, which is a reasonable assumption for the base case family of generic frames used in this study.

Figure A.4 shows the relationship between the fundamental period, number of stories, and elastic first-story stability coefficient. The values of θ used in this study are based on a P/W ratio of 1.4, which implies that the total gravity load acting at the first-story level is computed based on the total dead load plus live load equal to 40% of the dead load. A ratio P/W of 1.4 is considered to be conservative (a value of 1.2 is more representative of average conditions).

A.4 MODELING OF PLASTIC HINGES TO AVOID SPURIOUS DAMPING MOMENTS AT THE JOINTS

In this study, the Rayleigh damping formulation is used based on the following relationship:

$$\underline{C} = \alpha \underline{M} + \beta_o \underline{K_o} \tag{A.5}$$

where $\underline{C}$ is the viscous damping matrix, $\underline{M}$ is the mass matrix, $\underline{K_o}$ is the initial stiffness matrix and α and β_o are the mass and stiffness proportional factors. This formulation is implemented in the DRAIN-2DX computer program.

An alternative viscous damping matrix is given by:

$$\underline{C_t} = \alpha \underline{M} + \beta_t \underline{K_t} \tag{A.6}$$

where $\underline{C_t}$ is the current damping matrix, $\underline{K_t}$ is the tangent (current) stiffness matrix, and β_t is the stiffness proportional factor. Tangent stiffness proportional damping is not an option in DRAIN-2DX.

The authors of DRAIN-2DX implemented a constant damping matrix formulation (Equation A.5) to avoid unbalance of forces during the analysis (which is based on an event-to-event strategy, DRAIN-2DX, 1993). However, a constant damping matrix causes spurious damping moments at the joints once a change of stiffness occurs in nonlinear elements that have stiffness proportional damping based on their initial stiffness (Bernal, 1994). Although dynamic equilibrium is satisfied, spurious damping moments cause static equilibrium to be violated at joints as shown in Figure A.5. This figure shows the beam, column, and spring moments at a joint normalized by the beam plastic moment at the top floor of a one-bay, 18-story frame (elasto-plastic hysteretic behavior is used). Plastification is allowed at the beam end springs and the spring at the bottom of the first-story columns. In this case, the columns are flexible and elastic, the beams are rigid, and the springs are flexible, so stiffness proportional damping based on the initial stiffness is assigned to the columns and springs.

The presence of spurious damping moments can be understood by looking at the dynamic equilibrium equation. For a nonlinear system, Newmark's equation for the average acceleration method is implemented in DRAIN-2DX as:

$$\left[\frac{4}{(\Delta t)^2}\underline{M} + \frac{2}{\Delta t}\underline{C_t} + \underline{K_t}\right]\{\Delta u\} = \{P(t+\Delta t)\} + \underline{M}\left\{\ddot{u}(t) + \frac{4}{\Delta t}\dot{u}(t)\right\} + \{F_{damp}\} - \{F_{elastic}\} \quad \text{(A.7)}$$

where {u} is the vector of nodal deformations, $\{F_{damp}\}$and$\{F_{elastic}\}$are vectors corresponding to the "damping" and the elastic restoring forces (or moments) computed at the element level. For each element, the damping force is calculated as the product of the stiffness proportional factor, β, the initial stiffness of the element, and the current velocity at the degree of freedom of interest. The left-hand side of Equation A.7 includes the damping and stiffness matrices as a function of the current tangent stiffness. The velocities used to calculate $\{F_{damp}\}$ will be "correct" if the damping matrix $\underline{C_t}$ is proportional to the current stiffness matrix. However, if $\underline{C_t}$ is a function of the initial stiffness matrix, $\underline{K_o}$, it will not be modified when nonlinear elements change stiffness. Therefore, if Equation A.7 is used with the damping matrix $\underline{C}$ (which is based on the initial stiffness) as opposed to $\underline{C_t}$, the calculated displacements will not be consistent with the damping forces and static equilibrium is not always satisfied.

In order to obtain a solution that satisfies both static and dynamic equilibrium, three different alternatives are feasible:

- Use mass proportional damping only. This solution enforces static equilibrium at all times, but it is not implemented, since higher modes will be "under-damped,". Moreover, a model that includes damping proportional to both mass and stiffness is considered to be more representative of "real" conditions.

- Use $\underline{K_t}$ in the solution algorithm. This alternative provides an approximate solution, but it is not considered, since the use of $\underline{K_t}$ in the solution of the equation of motion may lead to potential unbalance of forces when an event-to-event strategy is implemented. Moreover, it is not clear how to implement this approach when nonlinear elements have a negative slope (this issue is applicable to elements that include strength deterioration, e.g., elements that model fracture at a connection).
- Model plastic hinging by using nonlinear rotational springs with a rigid initial slope (rigid as compared to the stiffness of the beam attached to them) and flexible beam elements, while assigning zero stiffness proportional damping to the nonlinear springs. This alternative provides an approximate solution to the problem. This is the strategy implemented in the models used in this study (see paragraphs below).

Plastic hinging in beams is modeled by using rotational springs at the beam ends that have a stiffness, K_{spring}, which is equal to 10 times the rotational stiffness of the beam element, K_{ele} (a value greater than 10 may cause numerical problems in the solution). Thus, at each beam end, the total rotational stiffness, K_{rot} is given by:

$$K_{rot} = \frac{K_{spring} K_{ele}}{K_{spring} + K_{ele}} \tag{A.8}$$

the modified element stiffness, K_{ele}, is computed from $K_{rot} = 6EI/L$ (I is the moment of inertia at that floor (or story) level, L is the beam span), and $K_{spring} = 10K_{ele}$.

In order to obtain 3% strain hardening in the moment-rotation relationship at the ends of the beams, the post-yield rotational spring stiffness is equal to $0.002804K_{spring}$.

Because no stiffness proportional damping is assigned to the nonlinear rotational springs, the β (stiffness proportional) factor for the beam element needs to be multiplied by 1.1 to compensate for the lack of stiffness proportional damping provided by the rotational springs. A factor of 1.1 is needed, since $K_{ele} = 1.1K_{rot.}$ For the generic frames, zero stiffness proportional damping is also assigned to the rotational spring at the base (see Section A.2), so the β value for the first-story column elements needs to be increased by a factor of 2.5, since $K_s = 0.25K_c = 1.25K_T$ and the spring is located only at one end of the column.

The models discussed in the previous paragraph, which are the ones used in this study, satisfy both dynamic and static equilibrium at each joint, as it is shown in Figure A.6. In this case, columns and beams are elastic and flexible and the springs have an initial stiffness equal to 10 times $6EI_{ele}/L_{ele}$ of the flexible beams, so stiffness proportional damping based on the initial stiffness is assigned to the columns and beams only.

Figure A.7 shows statistical values for the normalized maximum story drift angle over the height corresponding to a frame with 9 stories and a fundamental period of 0.9 sec. Results for the generic model used in this study (in which static equilibrium is satisfied) and a model in which beams are rigid and all the flexibility is concentrated in the rotational springs at the beam ends are presented. For the second model, in which static equilibrium is not satisfied, the displacements are smaller in the inelastic range. This behavior occurs because the element damping forces are based on their initial stiffness; thus, additional damping is present in the system once the rotational springs enter the nonlinear range.

Table A.1 Modal Properties, N = 3, T_1 = 0.3 sec, and 0.6 sec

Modal Properties					***Story/Floor***	***Mode Shapes***		
Mode	T_i / T_1	PF_i	MP_i	ξ_i		ϕ_1	ϕ_2	ϕ_3
1	1.000	1.286	0.857	0.050	0/1	0.000	0.000	0.000
2	0.335	-0.353	0.115	0.052	1/2	0.333	-1.000	1.000
3	0.156	0.218	0.028	0.104	2/3	0.667	-0.927	-0.844
					3/4	1.000	0.951	0.229

Table A.2 Modal Properties, N = 6, T_1 = 0.6 sec, and 1.2 sec

Modal Properties					***Story/Floor***	***Mode Shapes***				
Mode	T_i / T_1	PF_i	MP_i	ξ_i		ϕ_1	ϕ_2	ϕ_3	ϕ_4	ϕ_5
1	1.000	1.385	0.808	0.050	0/1	0.000	0.000	0.000	0.000	0.000
2	0.380	0.536	0.119	0.038	1/2	0.167	0.392	0.753	0.876	0.893
3	0.209	0.267	0.043	0.051	2/3	0.333	0.678	0.913	0.401	-0.401
4	0.130	0.194	0.019	0.076	3/4	0.500	0.758	0.270	-0.775	-0.697
5	0.088	0.136	0.008	0.114	4/5	0.667	0.542	-0.735	-0.591	1.000
					5/6	0.833	-0.038	-1.000	1.000	-0.533
					6/7	1.000	-1.000	0.758	-0.331	0.111

Table A.3 Modal Properties, N = 9, T_1 = 0.9 sec, and 1.8 sec

Modal Properties					***Story/Floor***	***Mode Shapes***				
Mode	T_i / T_1	PF_i	MP_i	ξ_i		ϕ_1	ϕ_2	ϕ_3	ϕ_4	ϕ_5
1	1.000	1.421	0.789	0.050	0/1	0.000	0.000	0.000	0.000	0.000
2	0.394	0.626	0.117	0.040	1/2	0.111	0.229	-0.491	-0.624	-0.773
3	0.230	-0.298	0.045	0.050	2/3	0.222	0.431	-0.809	-0.806	-0.631
4	0.152	-0.226	0.022	0.068	3/4	0.333	0.579	-0.828	-0.386	0.295
5	0.107	-0.165	0.012	0.094	4/5	0.444	0.645	-0.506	0.362	0.875
					5/6	0.556	0.606	0.072	0.851	0.262
					6/7	0.667	0.437	0.686	0.558	-0.808
					7/8	0.778	0.119	0.982	-0.424	-0.544
					8/9	0.889	-0.361	0.533	-1.000	1.000
					9/10	1.000	-1.000	-1.000	0.590	-0.334

Table A.4 Modal Properties, N = 12, T_1 = 1.2 sec, and 2.4 sec

Modal Properties					***Story/Floor***	***Mode Shapes***				
Mode	T_i / T_1	PF_i	MP_i	ξ_i		ϕ_1	ϕ_2	ϕ_3	ϕ_4	ϕ_5
1	1.000	1.440	0.780	0.050	0/1	0.000	0.000	0.000	0.000	0.000
2	0.399	0.677	0.115	0.035	1/2	0.083	0.160	-0.309	-0.561	-0.568
3	0.240	-0.361	0.045	0.039	2/3	0.167	0.308	-0.557	-0.898	-0.753
4	0.163	-0.201	0.023	0.050	3/4	0.250	0.436	-0.692	-0.867	-0.417
5	0.119	-0.192	0.013	0.065	4/5	0.333	0.532	-0.679	-0.460	0.230
					5/6	0.417	0.585	-0.507	0.174	0.728
					6/7	0.500	0.585	-0.196	0.761	0.669
					7/8	0.583	0.523	0.196	0.991	0.029
					8/9	0.667	0.389	0.573	0.660	-0.691
					9/10	0.750	0.175	0.799	-0.163	-0.741
					10/11	0.833	-0.127	0.714	-1.000	0.162
					11/12	0.917	-0.520	0.150	-0.962	1.000
					12/13	1.000	-1.000	-1.000	0.933	-0.489

Table A.5 Modal Properties, N = 15, T_1 = 1.5 sec, and 3.0 sec

Modal Properties					*Story/Floor*	*Mode Shapes*				
Mode	T_i / T_1	PF_i	MP_i	ξ_i		ϕ_1	ϕ_2	ϕ_3	ϕ_4	ϕ_5
1	1.000	1.452	0.774	0.050	0/1	0.000	0.000	0.000	0.000	0.000
2	0.402	-0.711	0.114	0.035	1/2	0.067	-0.122	-0.220	-0.391	-0.491
3	0.245	-0.406	0.045	0.040	2/3	0.133	-0.238	-0.412	-0.684	-0.771
4	0.170	-0.234	0.024	0.050	3/4	0.200	-0.344	-0.551	-0.801	-0.715
5	0.126	-0.186	0.014	0.063	4/5	0.267	-0.435	-0.618	-0.704	-0.334
					5/6	0.333	-0.504	-0.599	-0.408	0.212
					6/7	0.400	-0.548	-0.489	0.018	0.674
					7/8	0.467	-0.560	-0.296	0.459	0.814
					8/9	0.533	-0.537	-0.040	0.777	0.522
					9/10	0.600	-0.472	0.245	0.843	-0.094
					10/11	0.667	-0.362	0.510	0.585	-0.699
					11/12	0.733	-0.201	0.689	0.037	-0.865
					12/13	0.800	0.013	0.707	-0.613	-0.335
					13/14	0.867	0.285	0.478	-1.000	0.627
					14/15	0.933	0.615	-0.077	-0.623	1.000
					15/16	1.000	1.000	-1.000	0.980	-0.683

Table A.6 Modal Properties, N = 18, T_1 = 1.8 sec, and 3.6 sec

Modal Properties					*Story/Floor*	*Mode Shapes*				
Mode	T_i / T_1	PF_i	MP_i	ξ_i		ϕ_1	ϕ_2	ϕ_3	ϕ_4	ϕ_5
1	1.000	1.459	0.770	0.050	0/1	0.000	0.000	0.000	0.000	0.000
2	0.404	-0.735	0.113	0.035	1/2	0.056	-0.098	-0.168	-0.291	0.463
3	0.248	-0.440	0.045	0.040	2/3	0.111	-0.193	-0.322	-0.531	0.789
4	0.174	-0.263	0.024	0.050	3/4	0.167	-0.283	-0.447	-0.678	0.880
5	0.131	0.167	0.014	0.062	4/5	0.222	-0.363	-0.532	-0.702	0.701
					5/6	0.278	-0.432	-0.568	-0.595	0.299
					6/7	0.333	-0.486	-0.548	-0.370	-0.211
					7/8	0.389	-0.523	-0.470	-0.063	-0.666
					8/9	0.444	-0.539	-0.338	0.271	-0.906
					9/10	0.500	-0.532	-0.160	0.561	-0.824
					10/11	0.556	-0.499	0.049	0.736	-0.417
					11/12	0.611	-0.437	0.269	0.737	0.191
					12/13	0.667	-0.344	0.469	0.532	0.759
					13/14	0.722	-0.216	0.616	0.140	0.996
					14/15	0.778	-0.052	0.667	-0.353	0.690
					15/16	0.833	0.151	0.575	-0.777	-0.124
					16/17	0.889	0.394	0.291	-0.884	-0.993
					17/18	0.944	0.678	-0.228	-0.372	-1.000
					18/19	1.000	1.000	-1.000	1.000	0.929

Table A.7 Structural Properties, N = 3, T_1 = 0.3 sec

Story/Floor	*Stiffness Properties*								*$\gamma = V_y / W$ = 1.0, Parabolic Design Load Pattern*								
	W_i / W	I_i / I_1	K_{ai} / K_{a1}	K_{fi} / K_{f2}	K_{ki} / K_{k1}	K_{si} / K_{s1}	K_{bi} / K_{b2}	K_c	V_i / V_1	M_{OTi} / M_{OT1}	α_{si}	M_{ybi} / M_{yb2}	M_{yc}	$\theta_{ybi} / \theta_{yb2}$	θ_{yc}	δ_{si} / δ_r	θ_{si} / θ_r
0/1								8458858					21450		0.003		
1/2	0.333	1.000	1.000	1.000	1.000	1.000	1.000		1.000	1.000	0.037	1.000		1.000		0.307	0.920
2/3	0.333	0.731	0.731	0.681	0.929	0.864	0.731		0.929	0.611	0.039	0.775		1.061		0.330	0.989
3/4	0.333	0.344	0.344	0.595	0.643	0.542	0.344		0.643	0.250	0.043	0.337		0.978		0.364	1.091
	W	I_1	K_{a1}	K_{f2}	K_{k1}	K_{s1}	K_{b2}		V_1	M_{OT1}		M_{yb2}		θ_{yb2}		δ_r	θ_r
	(k)	(in^4)	(k/in)	(k/in)	(k/in)	(k/in)	(k-in)	(k-in)	(k)	(k-in)		(k-in)	(k-in)	(rad)	(rad)	(in)	(rad)
	600	28002	3730	630	1364	1313	16917715		600	222171		42440		0.003		1.490	0.003

Table A.8 Structural Properties, N = 3, T_1 = 0.6 sec

Story/Floor	*Stiffness Properties*								*$\gamma = V_y / W$ = 1.0, Parabolic Design Load Pattern*								
	W_i / W	I_i / I_1	K_{ai} / K_{a1}	K_{fi} / K_{f2}	K_{ki} / K_{k1}	K_{si} / K_{s1}	K_{bi} / K_{b2}	K_c	V_i / V_1	M_{OTi} / M_{OT1}	α_{si}	M_{ybi} / M_{yb2}	M_{yc}	$\theta_{ybi} / \theta_{yb2}$	θ_{yc}	δ_{si} / δ_r	θ_{si} / θ_r
0/1								2114714					21450		0.010		
1/2	0.333	1.000	1.000	1.000	1.000	1.000	1.000		1.000	1.000	0.035	1.000		1.000		0.307	0.920
2/3	0.333	0.731	0.731	0.681	0.929	0.864	0.731		0.929	0.611	0.037	0.775		1.061		0.330	0.989
3/4	0.333	0.344	0.344	0.595	0.643	0.542	0.344		0.643	0.250	0.041	0.337		0.978		0.364	1.091
	W	I_1	K_{a1}	K_{f2}	K_{k1}	K_{s1}	K_{b2}		V_1	M_{OT1}		M_{yb2}		θ_{yb2}		δ_r	θ_r
	(k)	(in^4)	(k/in)	(k/in)	(k/in)	(k/in)	(k-in)	(k-in)	(k)	(k-in)		(k-in)	(k-in)	(rad)	(rad)	(in)	(rad)
	600	7000	932	157	341	329	4229429		600	222171		42440		0.010		5.940	0.014

Table A.9 Structural Properties, N = 6, T_1 = 0.6 sec

Story/Floor	*Stiffness Properties*								*$\gamma = V_y / W$ = 1.0, Parabolic Design Load Pattern*								
	W_i / W	I_i / I_1	K_{ai} / K_{a1}	K_{fi} / K_{f2}	K_{ki} / K_{k1}	K_{si} / K_{s1}	K_{bi} / K_{b2}	K_c	V_i / V_1	M_{OTi} / M_{OT1}	α_{si}	M_{ybi} / M_{yb2}	M_{yc}	$\theta_{ybi} / \theta_{yb2}$	θ_{yc}	δ_{si} / δ_r	θ_{si} / θ_r
0/1								7635208					43310		0.006		
1/2	0.167	1.000	1.000	1.000	1.000	1.000	1.000		1.000	1.000	0.035	1.000		1.000		0.146	0.876
2/3	0.167	0.924	0.924	0.919	0.989	0.958	0.924		0.989	0.794	0.036	0.963		1.041		0.151	0.904
3/4	0.167	0.812	0.812	0.799	0.945	0.868	0.812		0.945	0.590	0.038	0.888		1.094		0.159	0.954
4/5	0.167	0.648	0.648	0.623	0.846	0.729	0.648		0.846	0.395	0.040	0.746		1.152		0.170	1.017
5/6	0.167	0.437	0.437	0.390	0.670	0.539	0.437		0.670	0.220	0.042	0.518		1.185		0.182	1.089
6/7	0.167	0.189	0.189	0.318	0.396	0.299	0.189		0.396	0.082	0.045	0.203		1.076		0.193	1.160
	W	I_1	K_{a1}	K_{f2}	K_{k1}	K_{s1}	K_{b2}		V_1	M_{OT1}		M_{yb2}		θ_{yb2}		δ_r	θ_r
	(k)	(in^4)	(k/in)	(k/in)	(k/in)	(k/in)	(k-in)	(k-in)	(k)	(k-in)		(k-in)	(k-in)	(rad)	(rad)	(in)	(rad)
	1200	25275	3366	584	1200	1174	15270416		1200	837415		86930		0.006		7.000	0.008

Table A.10 Structural Properties, N = 6, T_1 = 1.2 sec

Story/Floor	*Stiffness Properties*								*$\gamma = V_y / W$ = 1.0, Parabolic Design Load Pattern*								
	W_i / W	I_i / I_1	K_{ai} / K_{a1}	K_{fi} / K_{f2}	K_{ki} / K_{k1}	K_{si} / K_{s1}	K_{bi} / K_{b2}	K_c	V_i / V_1	M_{OTi} / M_{OT1}	α_{si}	M_{ybi} / M_{yb2}	M_{yc}	$\theta_{ybi} / \theta_{yb2}$	θ_{yc}	δ_{si} / δ_r	θ_{si} / θ_r
0/1								1908802					43310		0.023		
1/2	0.167	1.000	1.000	1.000	1.000	1.000	1.000		1.000	1.000	0.035	1.000		1.000		0.146	0.876
2/3	0.167	0.924	0.924	0.919	0.989	0.958	0.924		0.989	0.794	0.036	0.963		1.041		0.151	0.904
3/4	0.167	0.812	0.812	0.799	0.945	0.868	0.812		0.945	0.590	0.038	0.888		1.094		0.159	0.954
4/5	0.167	0.648	0.648	0.623	0.846	0.729	0.648		0.846	0.395	0.040	0.746		1.152		0.170	1.017
5/6	0.167	0.437	0.437	0.390	0.670	0.539	0.437		0.670	0.220	0.042	0.518		1.185		0.182	1.089
6/7	0.167	0.189	0.189	0.318	0.396	0.299	0.189		0.396	0.082	0.045	0.203		1.076		0.193	1.160
	W	I_1	K_{a1}	K_{f2}	K_{k1}	K_{s1}	K_{b2}		V_1	M_{OT1}		M_{yb2}		θ_{yb2}		δ_r	θ_r
	(k)	(in^4)	(k/in)	(k/in)	(k/in)	(k/in)	(k-in)	(k-in)	(k)	(k-in)		(k-in)	(k-in)	(rad)	(rad)	(in)	(rad)
	1200	6319	842	146	299	294	3817604		1200	837415		86930		0.023		28.000	0.032

Table A.11 Structural Properties, N = 9, T_1 = 0.9 sec

Story/Floor	*Stiffness Properties*								*γ = V_y / W = 1.0, Parabolic Design Load Pattern*								
	W_i / W	I_i / I_1	K_{ai} / K_{a1}	K_{fi} / K_{f2}	K_{ki} / K_{k1}	K_{si} / K_{s1}	K_{bi} / K_{b2}	K_c	V_i / V_1	M_{OTi} / M_{OT1}	α_{si}	M_{ybi} / M_{yb2}	M_{yc}	$\theta_{ybi} / \theta_{yb2}$	θ_{yc}	δ_{si} / δ_r	θ_{si} / θ_r
0/1								7316974					64920		0.009		
1/2	0.111	1.000	1.000	1.000	1.000	1.000	1.000		1.000	1.000	0.036	1.000		1.000		0.096	0.861
2/3	0.111	0.965	0.965	0.963	0.996	0.980	0.965		0.996	0.859	0.036	0.988		1.024		0.097	0.875
3/4	0.111	0.913	0.913	0.908	0.982	0.937	0.913		0.982	0.719	0.037	0.964		1.056		0.100	0.902
4/5	0.111	0.836	0.836	0.829	0.951	0.872	0.836		0.951	0.581	0.038	0.919		1.098		0.104	0.938
5/6	0.111	0.739	0.739	0.727	0.895	0.785	0.739		0.895	0.447	0.039	0.846		1.145		0.109	0.981
6/7	0.111	0.618	0.618	0.602	0.807	0.674	0.618		0.807	0.321	0.040	0.737		1.193		0.115	1.031
7/8	0.111	0.475	0.475	0.453	0.681	0.541	0.475		0.681	0.207	0.042	0.587		1.234		0.120	1.084
8/9	0.111	0.311	0.311	0.275	0.509	0.385	0.311		0.509	0.112	0.043	0.388		1.247		0.126	1.138
9/10	0.111	0.131	0.131	0.500	0.284	0.206	0.131		0.284	0.040	0.045	0.147		1.120		0.132	1.189
	W	I_1	K_{a1}	K_{f2}	K_{k1}	K_{s1}	K_{b2}		V_1	M_{OT1}		M_{yb2}		θ_{yb2}		δ_r	θ_r
	(k)	(in^4)	(k/in)	(k/in)	(k/in)	(k/in)	(k-in)	(k-in)	(k)	(k-in)		(k-in)	(k-in)	(rad)	(rad)	(in)	(rad)
	1800	24222	3226	562	1141	1120	14633949		1800	1841684		130200		0.009		16.800	0.013

Table A.12 Structural Properties, N = 9, T_1 = 1.8 sec

Story/Floor	*Stiffness Properties*								*γ = V_y / W = 1.0, Parabolic Design Load Pattern*								
	W_i / W	I_i / I_1	K_{ai} / K_{a1}	K_{fi} / K_{f2}	K_{ki} / K_{k1}	K_{si} / K_{s1}	K_{bi} / K_{b2}	K_c	V_i / V_1	M_{OTi} / M_{OT1}	α_{si}	M_{ybi} / M_{yb2}	M_{yc}	$\theta_{ybi} / \theta_{yb2}$	θ_{yc}	δ_{si} / δ_r	θ_{si} / θ_r
0/1								1829244					64920		0.035		
1/2	0.111	1.000	1.000	1.000	1.000	1.000	1.000		1.000	1.000	0.036	1.000		1.000		0.096	0.861
2/3	0.111	0.965	0.965	0.963	0.996	0.980	0.965		0.996	0.859	0.036	0.988		1.024		0.097	0.876
3/4	0.111	0.913	0.913	0.908	0.982	0.938	0.913		0.982	0.719	0.037	0.964		1.056		0.100	0.902
4/5	0.111	0.836	0.836	0.829	0.951	0.873	0.836		0.951	0.581	0.038	0.919		1.098		0.104	0.938
5/6	0.111	0.739	0.739	0.727	0.895	0.785	0.739		0.895	0.447	0.039	0.846		1.145		0.109	0.981
6/7	0.111	0.618	0.618	0.602	0.807	0.674	0.618		0.807	0.321	0.040	0.737		1.193		0.115	1.031
7/8	0.111	0.475	0.475	0.453	0.681	0.541	0.475		0.681	0.207	0.042	0.587		1.234		0.120	1.084
8/9	0.111	0.311	0.311	0.275	0.509	0.385	0.311		0.509	0.112	0.043	0.388		1.247		0.126	1.138
9/10	0.111	0.131	0.131	0.220	0.284	0.206	0.131		0.284	0.040	0.045	0.147		1.120		0.132	1.190
	W	I_1	K_{a1}	K_{f2}	K_{k1}	K_{s1}	K_{b2}		V_1	M_{OT1}		M_{yb2}		θ_{yb2}		δ_r	θ_r
	(k)	(in^4)	(k/in)	(k/in)	(k/in)	(k/in)	(k-in)	(k-in)	(k)	(k-in)		(k-in)	(k-in)	(rad)	(rad)	(in)	(rad)
	1800	6055	807	141	284	281	3658487		1800	1841684		130200		0.036		66.900	0.052

Table A.13 Structural Properties, N = 12, T_1 = 1.2 sec

Story/Floor	*Stiffness Properties*								*γ = V_y / W = 1.0, Parabolic Design Load Pattern*								
	W_i / W	I_i / I_1	K_{ai} / K_{a1}	K_{fi} / K_{f2}	K_{ki} / K_{k1}	K_{si} / K_{s1}	K_{bi} / K_{b2}	K_c	V_i / V_1	M_{OTi} / M_{OT1}	α_{si}	M_{ybi} / M_{yb2}	M_{yc}	$\theta_{ybi} / \theta_{yb2}$	θ_{yc}	δ_{si} / δ_r	θ_{si} / θ_r
0/1								7150259					86520		0.012		
1/2	0.083	1.000	1.000	1.000	1.000	1.000	1.000		1.000	1.000	0.037	1.000		1.000		0.071	0.854
2/3	0.083	0.980	0.980	0.979	0.998	0.988	0.980		0.998	0.894	0.038	0.994		1.014		0.072	0.864
3/4	0.083	0.950	0.950	0.948	0.992	0.963	0.950		0.992	0.789	0.038	0.984		1.036		0.073	0.880
4/5	0.083	0.906	0.906	0.902	0.978	0.925	0.906		0.978	0.684	0.038	0.964		1.064		0.075	0.903
5/6	0.083	0.849	0.849	0.844	0.954	0.874	0.849		0.954	0.580	0.039	0.931		1.096		0.078	0.932
6/7	0.083	0.780	0.780	0.773	0.915	0.811	0.780		0.915	0.480	0.040	0.884		1.133		0.080	0.964
7/8	0.083	0.698	0.698	0.689	0.860	0.735	0.698		0.860	0.383	0.041	0.818		1.173		0.083	1.000
8/9	0.083	0.603	0.603	0.591	0.785	0.646	0.603		0.785	0.292	0.041	0.731		1.213		0.086	1.038
9/10	0.083	0.495	0.495	0.481	0.785	0.622	0.495		0.785	0.209	0.042	0.619		1.251		0.090	1.078
10/11	0.083	0.374	0.374	0.356	0.562	0.428	0.374		0.562	0.126	0.043	0.479		1.280		0.093	1.120
11/12	0.083	0.241	0.241	0.212	0.408	0.299	0.241		0.408	0.067	0.045	0.309		1.281		0.097	1.163
12/13	0.083	0.101	0.101	0.168	0.222	0.157	0.101		0.222	0.023	0.046	0.115		1.143		0.100	1.203
	W	I_1	K_{a1}	K_{f2}	K_{k1}	K_{s1}	K_{b2}		V_1	M_{OT1}		M_{yb2}		θ_{yb2}		δ_r	θ_r
	(k)	(in^4)	(k/in)	(k/in)	(k/in)	(k/in)	(k-in)	(k-in)	(k)	(k-in)		(k-in)	(k-in)	(rad)	(rad)	(in)	(rad)
	2400	23670	3153	550	1108	1098	14300519		2400	3268844		173400		0.012		30.700	0.018

Table A.14 Structural Properties, N = 12, T_1 = 2.4 sec

Story/Floor	*Stiffness Properties*								*γ = V_y / W = 1.0, Parabolic Design Load Pattern*								
	W_i / W	I_i / I_1	K_{ai} / K_{a1}	K_{fi} / K_{f2}	K_{ki} / K_{k1}	K_{si} / K_{s1}	K_{bi} / K_{b2}	K_c	V_i / V_1	M_{OTi} / M_{OT1}	α_{si}	M_{ybi} / M_{yb2}	M_{yc}	$\theta_{ybi} / \theta_{yb2}$	θ_{yc}	δ_{si} / δ_r	θ_{si} / θ_r
0/1								1787565					86520		0.048		
1/2	0.083	1.000	1.000	1.000	1.000	1.000	1.000		1.000	1.000	0.037	1.000		1.000		0.071	0.854
2/3	0.083	0.980	0.980	0.979	0.998	0.988	0.980		0.998	0.894	0.038	0.994		1.014		0.072	0.863
3/4	0.083	0.950	0.950	0.948	0.992	0.963	0.950		0.992	0.789	0.038	0.984		1.036		0.073	0.880
4/5	0.083	0.906	0.906	0.902	0.978	0.925	0.906		0.978	0.684	0.038	0.964		1.064		0.075	0.903
5/6	0.083	0.849	0.849	0.844	0.954	0.875	0.849		0.954	0.580	0.039	0.931		1.096		0.078	0.931
6/7	0.083	0.780	0.780	0.773	0.915	0.811	0.780		0.915	0.480	0.040	0.884		1.133		0.080	0.964
7/8	0.083	0.698	0.698	0.689	0.860	0.735	0.698		0.860	0.383	0.041	0.818		1.173		0.083	1.000
8/9	0.083	0.603	0.603	0.591	0.785	0.646	0.603		0.785	0.292	0.041	0.731		1.213		0.086	1.038
9/10	0.083	0.495	0.495	0.481	0.785	0.621	0.495		0.785	0.209	0.042	0.619		1.251		0.090	1.079
10/11	0.083	0.374	0.374	0.356	0.562	0.428	0.374		0.562	0.126	0.043	0.479		1.280		0.093	1.121
11/12	0.083	0.241	0.241	0.212	0.408	0.299	0.241		0.408	0.067	0.045	0.309		1.281		0.097	1.164
12/13	0.083	0.101	0.101	0.168	0.222	0.157	0.101		0.222	0.023	0.046	0.115		1.143		0.100	1.203
	W	I_1	K_{a1}	K_{f2}	K_{k1}	K_{s1}	K_{b2}		V_1	M_{OT1}		M_{yb2}		θ_{yb2}		δ_r	θ_r
	(k)	(in^4)	(k/in)	(k/in)	(k/in)	(k/in)	(k-in)	(k-in)	(k)	(k-in)		(k-in)	(k-in)	(rad)	(rad)	(in)	(rad)
	2400	5917	788	138	277	275	3575129		2400	3268844		173400		0.049		122.600	0.071

Table A.15 Structural Properties, N = 15, T_1 = 1.5 sec

Story/Floor	***Stiffness Properties***								***$\gamma = V_y / W$ = 1.0, Parabolic Design Load Pattern***								
	W_i / W	I_i / I_1	K_{ai} / K_{a1}	K_{fi} / K_{f2}	K_{ki} / K_{k1}	K_{si} / K_{s1}	K_{bi} / K_{b2}	K_c	V_i / V_1	M_{OTi} / M_{OT1}	α_{si}	M_{ybi} / M_{yb2}	M_{yc}	$\theta_{ybi} / \theta_{yb2}$	θ_{yc}	δ_{si} / δ_r	θ_{si} / θ_r
0/1								7048071					108100		0.015		
1/2	0.067	1.000	1.000	1.000	1.000	1.000	1.000		1.000	1.000	0.038	1.000		1.000		0.057	0.850
2/3	0.067	0.987	0.987	0.986	0.999	0.992	0.987		0.999	0.914	0.038	0.997		1.010		0.057	0.856
3/4	0.067	0.967	0.967	0.965	0.996	0.976	0.967		0.996	0.828	0.038	0.992		1.025		0.058	0.867
4/5	0.067	0.939	0.939	0.936	0.989	0.952	0.939		0.989	0.742	0.038	0.981		1.045		0.059	0.883
5/6	0.067	0.902	0.902	0.898	0.976	0.918	0.902		0.976	0.657	0.040	0.964		1.068		0.060	0.903
6/7	0.067	0.857	0.857	0.853	0.956	0.877	0.857		0.956	0.573	0.040	0.939		1.096		0.062	0.926
7/8	0.067	0.804	0.804	0.798	0.927	0.827	0.804		0.927	0.491	0.039	0.905		1.126		0.063	0.952
8/9	0.067	0.742	0.742	0.735	0.887	0.769	0.742		0.887	0.411	0.040	0.859		1.157		0.065	0.981
9/10	0.067	0.672	0.672	0.664	0.835	0.702	0.672		0.835	0.334	0.040	0.800		1.191		0.067	1.012
10/11	0.067	0.593	0.593	0.584	0.770	0.627	0.593		0.770	0.263	0.041	0.727		1.225		0.070	1.043
11/12	0.067	0.507	0.507	0.496	0.690	0.544	0.507		0.690	0.196	0.042	0.638		1.259		0.072	1.076
12/13	0.067	0.412	0.412	0.399	0.592	0.453	0.412		0.592	0.137	0.042	0.531		1.289		0.074	1.111
13/14	0.067	0.308	0.308	0.292	0.476	0.353	0.308		0.476	0.086	0.043	0.404		1.310		0.076	1.146
14/15	0.067	0.197	0.197	0.173	0.340	0.244	0.197		0.340	0.045	0.045	0.256		1.302		0.079	1.181
15/16	0.067	0.082	0.082	0.136	0.181	0.127	0.082		0.181	0.016	0.045	0.094		1.156		0.081	1.213
	W	I_1	K_{a1}	K_{f2}	K_{k1}	K_{s1}	K_{b2}		V_1	M_{OT1}		M_{yb2}		θ_{yb2}		δ_r	θ_r
	(k)	(in^4)	(k/in)	(k/in)	(k/in)	(k/in)	(k-in)	(k-in)	(k)	(k-in)		(k-in)	(k-in)	(rad)	(rad)	(in)	(rad)
	3000	23332	3108	543	1092	1085	14096141		3000	5016774		216500		0.015		48.800	0.023

Table A.16 Structural Properties, N = 15, T_1 = 3.0 sec

Story/Floor	***Stiffness Properties***								***$\gamma = V_y / W$ = 1.0, Parabolic Design Load Pattern***								
	W_i / W	I_i / I_1	K_{ai} / K_{a1}	K_{fi} / K_{f2}	K_{ki} / K_{k1}	K_{si} / K_{s1}	K_{bi} / K_{b2}	K_c	V_i / V_1	M_{OTi} / M_{OT1}	α_{si}	M_{ybi} / M_{yb2}	M_{yc}	$\theta_{ybi} / \theta_{yb2}$	θ_{yc}	δ_{si} / δ_r	θ_{si} / θ_r
0/1								1762018					108100		0.061		
1/2	0.067	1.000	1.000	1.000	1.000	1.000	1.000		1.000	1.000	0.038	1.000		1.000		0.057	0.850
2/3	0.067	0.987	0.987	0.986	0.999	0.992	0.987		0.999	0.914	0.038	0.997		1.010		0.057	0.856
3/4	0.067	0.967	0.967	0.965	0.996	0.976	0.967		0.996	0.828	0.038	0.992		1.025		0.058	0.867
4/5	0.067	0.939	0.939	0.936	0.989	0.952	0.939		0.989	0.742	0.038	0.981		1.045		0.059	0.883
5/6	0.067	0.902	0.902	0.898	0.976	0.918	0.902		0.976	0.657	0.040	0.964		1.068		0.060	0.903
6/7	0.067	0.857	0.857	0.853	0.956	0.877	0.857		0.956	0.573	0.040	0.939		1.096		0.062	0.926
7/8	0.067	0.804	0.804	0.798	0.927	0.827	0.804		0.927	0.491	0.039	0.905		1.126		0.063	0.952
8/9	0.067	0.742	0.742	0.735	0.887	0.769	0.742		0.887	0.411	0.040	0.859		1.157		0.065	0.981
9/10	0.067	0.672	0.672	0.664	0.835	0.702	0.672		0.835	0.334	0.040	0.800		1.191		0.067	1.012
10/11	0.067	0.593	0.593	0.584	0.770	0.627	0.593		0.770	0.263	0.041	0.727		1.225		0.070	1.043
11/12	0.067	0.507	0.507	0.496	0.690	0.544	0.507		0.690	0.196	0.042	0.638		1.259		0.072	1.076
12/13	0.067	0.412	0.412	0.399	0.592	0.453	0.412		0.592	0.137	0.042	0.531		1.289		0.074	1.111
13/14	0.067	0.308	0.308	0.292	0.476	0.353	0.308		0.476	0.086	0.043	0.404		1.310		0.076	1.146
14/15	0.067	0.197	0.197	0.173	0.340	0.244	0.197		0.340	0.045	0.045	0.256		1.302		0.079	1.181
15/16	0.067	0.082	0.082	0.136	0.181	0.127	0.082		0.181	0.016	0.045	0.094		1.156		0.081	1.213
	W	I_1	K_{a1}	K_{f2}	K_{k1}	K_{s1}	K_{b2}		V_1	M_{OT1}		M_{yb2}		θ_{yb2}		δ_r	θ_r
	(k)	(in^4)	(k/in)	(k/in)	(k/in)	(k/in)	(k-in)	(k-in)	(k)	(k-in)		(k-in)	(k-in)	(rad)	(rad)	(in)	(rad)
	3000	5833	777	136	273	271	3524035		3000	5016774		216500		0.061		195.200	0.090

Table A.17 Structural Properties, N = 18, T_1 = 1.8 sec

Story/Floor	*Stiffness Properties*								*$\gamma = V_y / W = 1.0$, Parabolic Design Load Pattern*								
	W_i / W	I_i / I_1	K_{ai} / K_{a1}	K_{fi} / K_{f2}	K_{ki} / K_{k1}	K_{si} / K_{s1}	K_{bi} / K_{b2}	K_c	V_i / V_1	M_{OTi} / M_{OT1}	α_{si}	M_{ybi} / M_{yb2}	M_{yc}	$\theta_{ybi} / \theta_{yb2}$	θ_{yc}	δ_{si} / δ_r	θ_{si} / θ_r
0/1								6978823					129700		0.019		
1/2	0.056	1.000	1.000	1.000	1.000	1.000	1.000		1.000	1.000	0.036	1.000		1.000		0.047	0.847
2/3	0.056	0.991	0.991	0.990	1.000	0.994	0.991		1.000	0.928	0.036	0.998		1.007		0.047	0.852
3/4	0.056	0.977	0.977	0.976	0.998	0.982	0.977		0.998	0.856	0.036	0.995		1.018		0.048	0.861
4/5	0.056	0.957	0.957	0.955	0.993	0.965	0.957		0.993	0.784	0.036	0.988		1.033		0.048	0.872
5/6	0.056	0.931	0.931	0.929	0.986	0.942	0.931		0.986	0.712	0.036	0.978		1.050		0.049	0.887
6/7	0.056	0.900	0.900	0.897	0.974	0.913	0.900		0.974	0.641	0.037	0.964		1.071		0.050	0.904
7/8	0.056	0.862	0.862	0.859	0.957	0.879	0.862		0.957	0.571	0.037	0.944		1.094		0.051	0.923
8/9	0.056	0.819	0.819	0.815	0.934	0.838	0.819		0.934	0.502	0.037	0.917		1.119		0.052	0.944
9/10	0.056	0.770	0.770	0.764	0.903	0.792	0.770		0.903	0.434	0.038	0.882		1.146		0.054	0.967
10/11	0.056	0.715	0.715	0.709	0.865	0.739	0.715		0.865	0.369	0.038	0.839		1.174		0.055	0.992
11/12	0.056	0.654	0.654	0.647	0.817	0.680	0.654		0.817	0.307	0.038	0.787		1.203		0.057	1.018
12/13	0.056	0.587	0.587	0.580	0.760	0.616	0.587		0.760	0.248	0.038	0.724		1.233		0.058	1.045
13/14	0.056	0.515	0.515	0.506	0.692	0.546	0.515		0.692	0.193	0.039	0.650		1.262		0.060	1.074
14/15	0.056	0.436	0.436	0.427	0.612	0.470	0.436		0.612	0.143	0.039	0.563		1.290		0.061	1.103
15/16	0.056	0.352	0.352	0.341	0.519	0.388	0.352		0.519	0.099	0.040	0.463		1.314		0.063	1.133
16/17	0.056	0.262	0.262	0.248	0.412	0.300	0.262		0.412	0.062	0.041	0.349		1.330		0.065	1.164
17/18	0.056	0.167	0.167	0.146	0.291	0.206	0.167		0.291	0.032	0.041	0.219		1.315		0.066	1.193
18/19	0.056	0.069	0.069	0.114	0.154	0.107	0.069		0.154	0.011	0.042	0.080		1.166		0.068	1.221
	W	I_1	K_{a1}	K_{f2}	K_{k1}	K_{s1}	K_{b2}		V_1	M_{OT1}		M_{yb2}		θ_{yb2}		δ_r	θ_r
	(k)	(in^4)	(k/in)	(k/in)	(k/in)	(k/in)	(k-in)	(k-in)	(k)	(k-in)		(k-in)	(k-in)	(rad)	(rad)	(in)	(rad)
	3600	23102	3077	538	1080	1075	13957647		3600	7187546		259700		0.019		71.100	0.027

Table A.18 Structural Properties, N = 18, T_1 = 3.6 sec

Story/Floor	*Stiffness Properties*								*$\gamma = V_y / W = 1.0$, Parabolic Design Load Pattern*								
	W_i / W	I_i / I_1	K_{ai} / K_{a1}	K_{fi} / K_{f2}	K_{ki} / K_{k1}	K_{si} / K_{s1}	K_{bi} / K_{b2}	K_c	V_i / V_1	M_{OTi} / M_{OT1}	α_{si}	M_{ybi} / M_{yb2}	M_{yc}	$\theta_{ybi} / \theta_{yb2}$	θ_{yc}	δ_{si} / δ_r	θ_{si} / θ_r
0/1								1744706					129700		0.074		
1/2	0.056	1.000	1.000	1.000	1.000	1.000	1.000		1.000	1.000	0.036	1.000		1.000		0.047	0.848
2/3	0.056	0.991	0.991	0.990	1.000	0.994	0.991		1.000	0.928	0.036	0.998		1.007		0.047	0.852
3/4	0.056	0.977	0.977	0.976	0.998	0.983	0.977		0.998	0.856	0.036	0.995		1.018		0.048	0.861
4/5	0.056	0.957	0.957	0.955	0.993	0.965	0.957		0.993	0.784	0.036	0.988		1.033		0.048	0.872
5/6	0.056	0.931	0.931	0.929	0.986	0.942	0.931		0.986	0.712	0.036	0.978		1.050		0.049	0.887
6/7	0.056	0.900	0.900	0.897	0.974	0.913	0.900		0.974	0.641	0.037	0.964		1.071		0.050	0.904
7/8	0.056	0.862	0.862	0.859	0.957	0.879	0.862		0.957	0.571	0.037	0.944		1.094		0.051	0.923
8/9	0.056	0.819	0.819	0.815	0.934	0.838	0.819		0.934	0.502	0.037	0.917		1.119		0.052	0.944
9/10	0.056	0.770	0.770	0.764	0.903	0.792	0.770		0.903	0.434	0.038	0.882		1.146		0.054	0.967
10/11	0.056	0.715	0.715	0.709	0.865	0.739	0.715		0.865	0.369	0.038	0.839		1.174		0.055	0.992
11/12	0.056	0.654	0.654	0.647	0.817	0.680	0.654		0.817	0.307	0.038	0.787		1.203		0.057	1.018
12/13	0.056	0.587	0.587	0.580	0.760	0.616	0.587		0.760	0.248	0.038	0.724		1.233		0.058	1.045
13/14	0.056	0.515	0.515	0.506	0.692	0.546	0.515		0.692	0.193	0.039	0.650		1.262		0.060	1.074
14/15	0.056	0.436	0.436	0.427	0.612	0.470	0.436		0.612	0.143	0.039	0.563		1.290		0.061	1.103
15/16	0.056	0.352	0.352	0.341	0.519	0.388	0.352		0.519	0.099	0.040	0.463		1.314		0.063	1.133
16/17	0.056	0.262	0.262	0.248	0.412	0.300	0.262		0.412	0.062	0.041	0.349		1.330		0.065	1.164
17/18	0.056	0.167	0.167	0.146	0.291	0.206	0.167		0.291	0.032	0.041	0.219		1.315		0.066	1.193
18/19	0.056	0.069	0.069	0.114	0.154	0.107	0.069		0.154	0.011	0.042	0.080		1.166		0.068	1.221
	W	I_1	K_{a1}	K_{f2}	K_{k1}	K_{s1}	K_{b2}		V_1	M_{OT1}		M_{yb2}		θ_{yb2}		δ_r	θ_r
	(k)	(in^4)	(k/in)	(k/in)	(k/in)	(k/in)	(k-in)	(k-in)	(k)	(k-in)		(k-in)	(k-in)	(rad)	(rad)	(in)	(rad)
	3600	5776	769	135	270	269	3489412		3600	7187546		259700		0.074		284.400	0.110

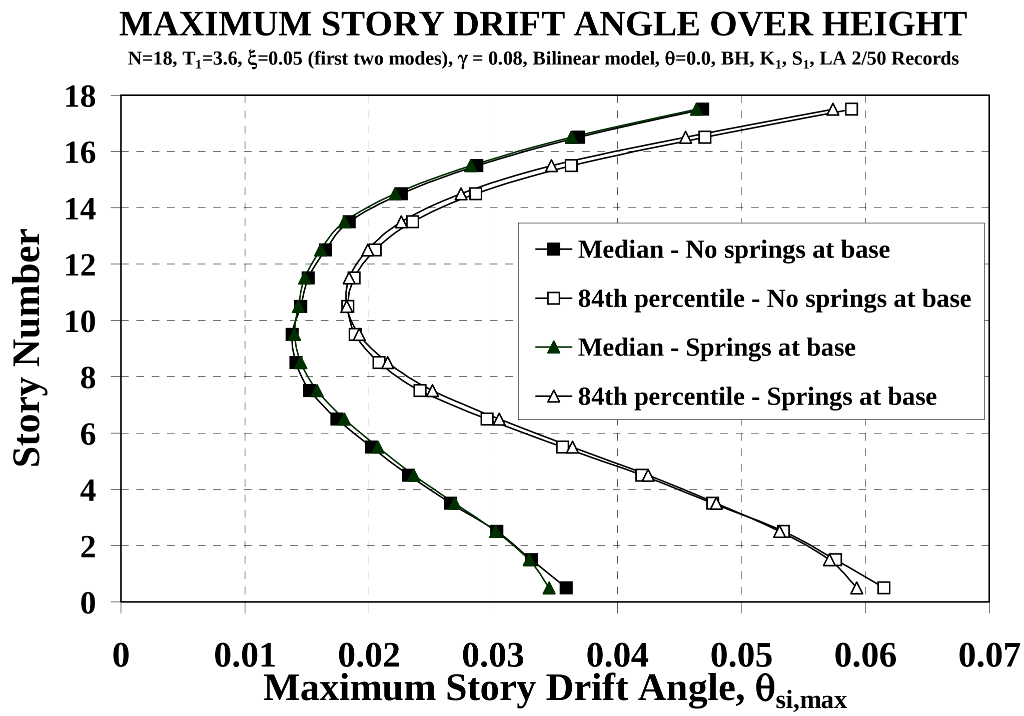

Figure A.1 Story Drift Profiles from Nonlinear Time History Analyses, N = 18, T_1 = 3.6 sec, γ = 0.08 (Models with and without Flexible Springs at the Base of the First-Story Columns)

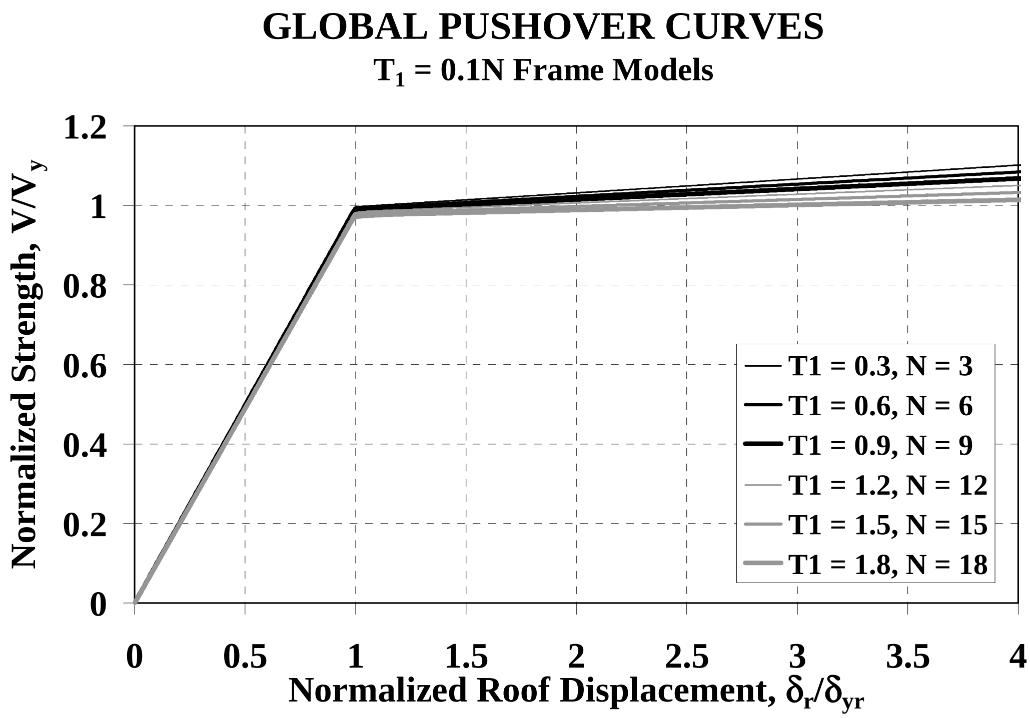

(a) $T_1 = 0.1N$

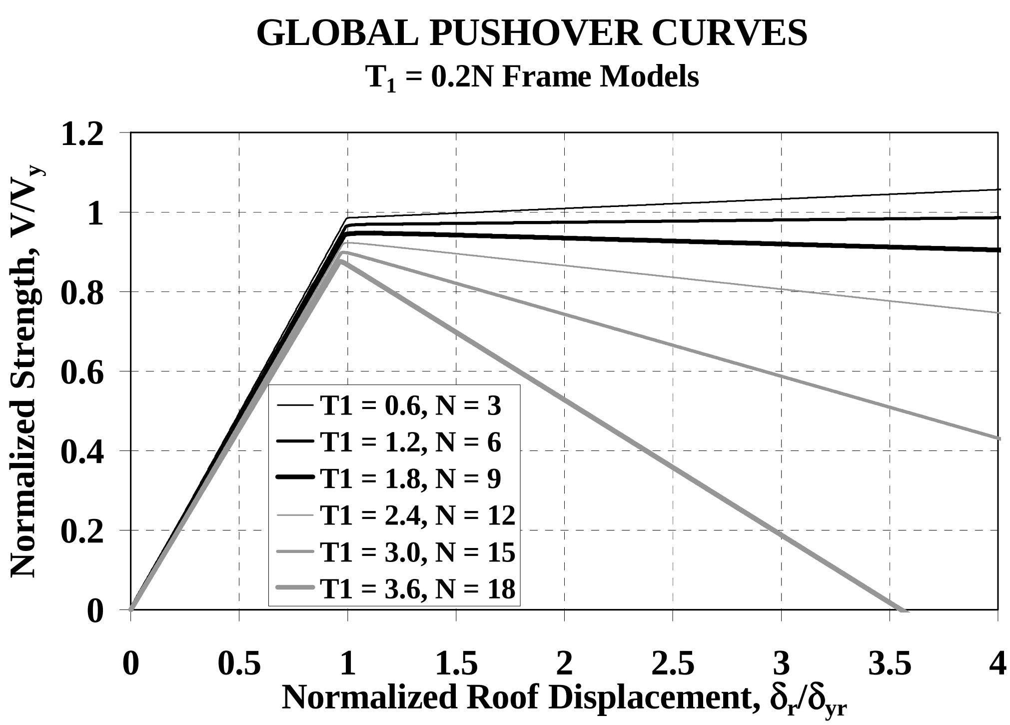

(b) $T_1 = 0.2N$

Figure A.2 Global Pushover Curves, Base Case Family of Generic Frames

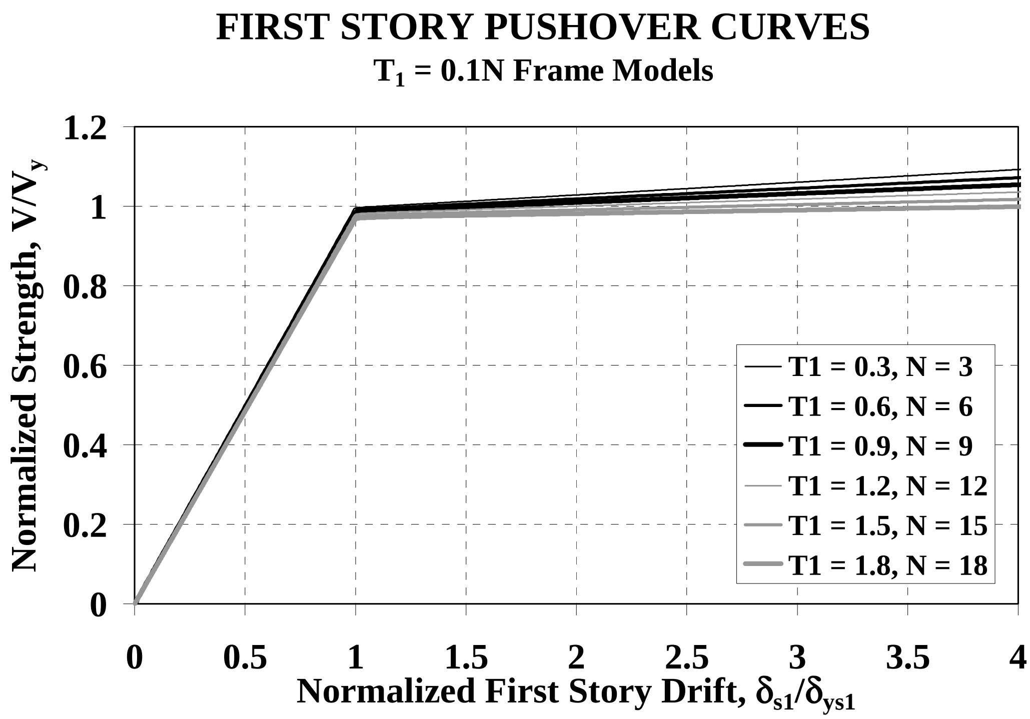

(a) T_1 = 0.1N

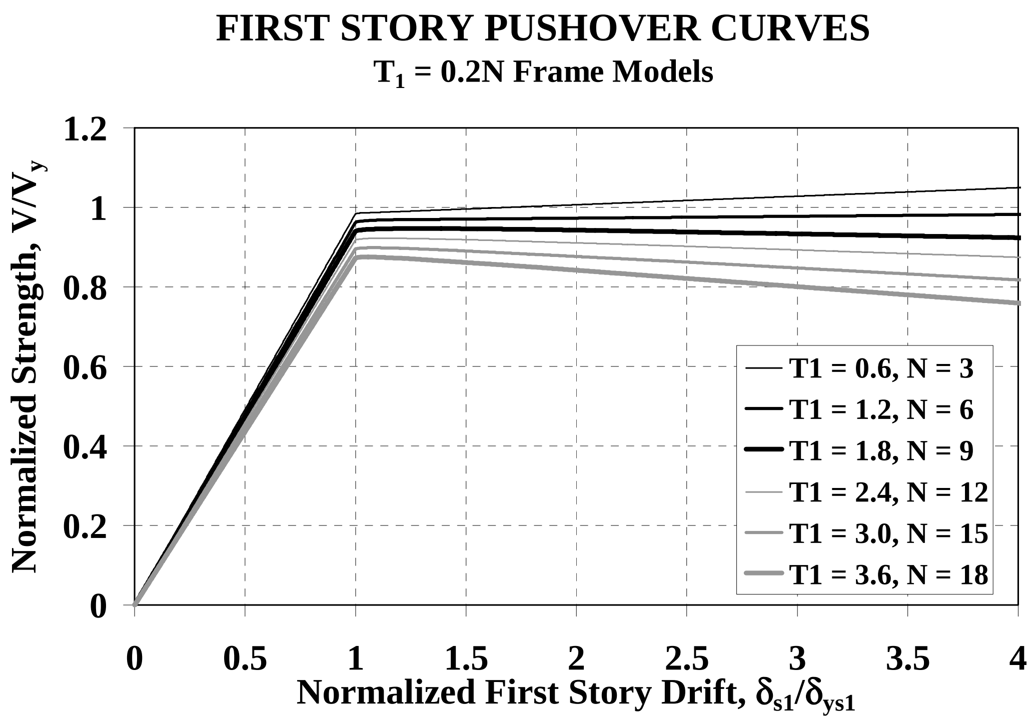

(b) T_1 = 0.2N

Figure A.3 First-Story Pushover Curves, Base Case Family of Generic Frames

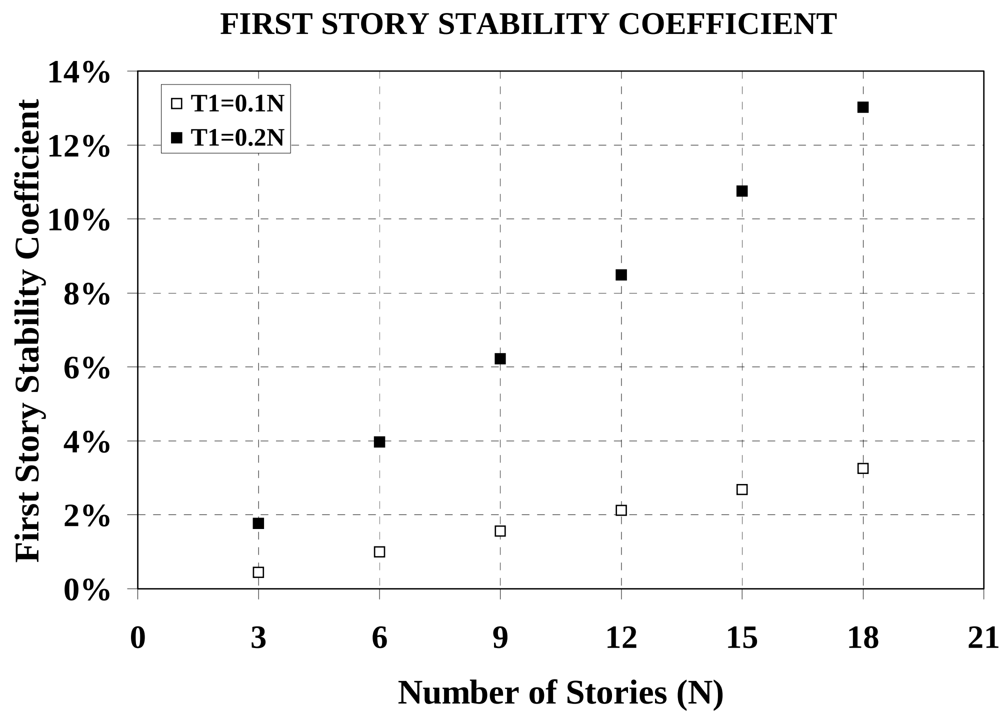

Figure A.4 First-Story Stability Coefficients, Base Case Family of Generic Frames

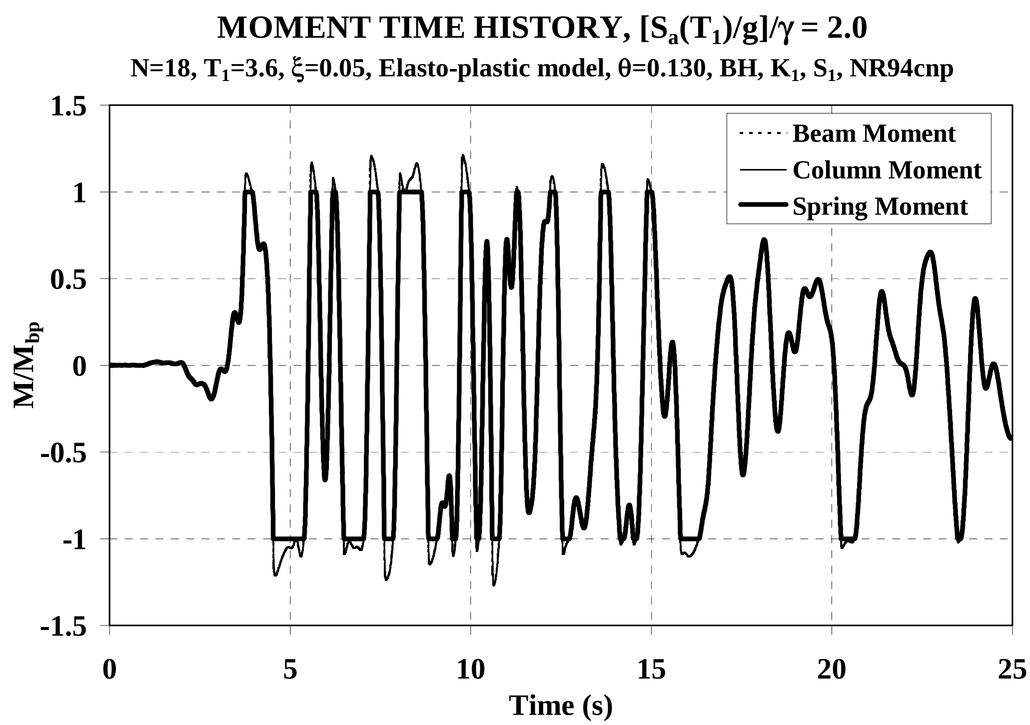

Figure A.5 Time History of Normalized Beam, Column, and Spring Moments at a Joint at the Top Floor, N = 18, T_1 = 3.6 sec, Model That Does Not Satisfy Static Equilibrium in the Response

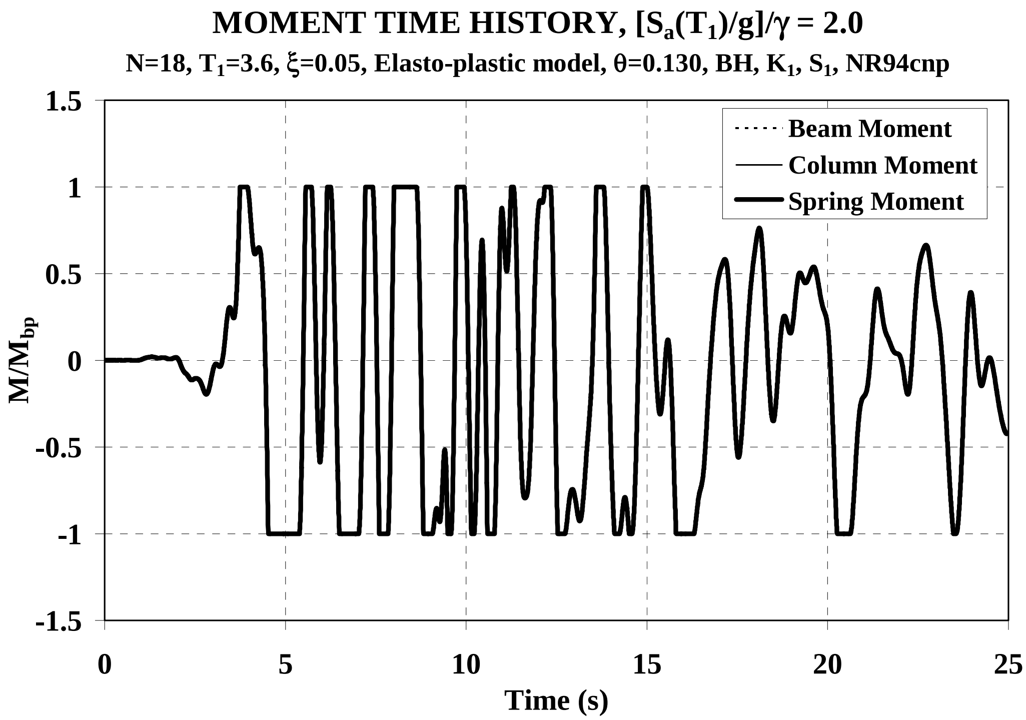

Figure A.6 Time History of Normalized Beam, Column and Spring Moments at a Joint at the Top Floor, N = 18, T_1 = 3.6 sec, Model Used in This Study

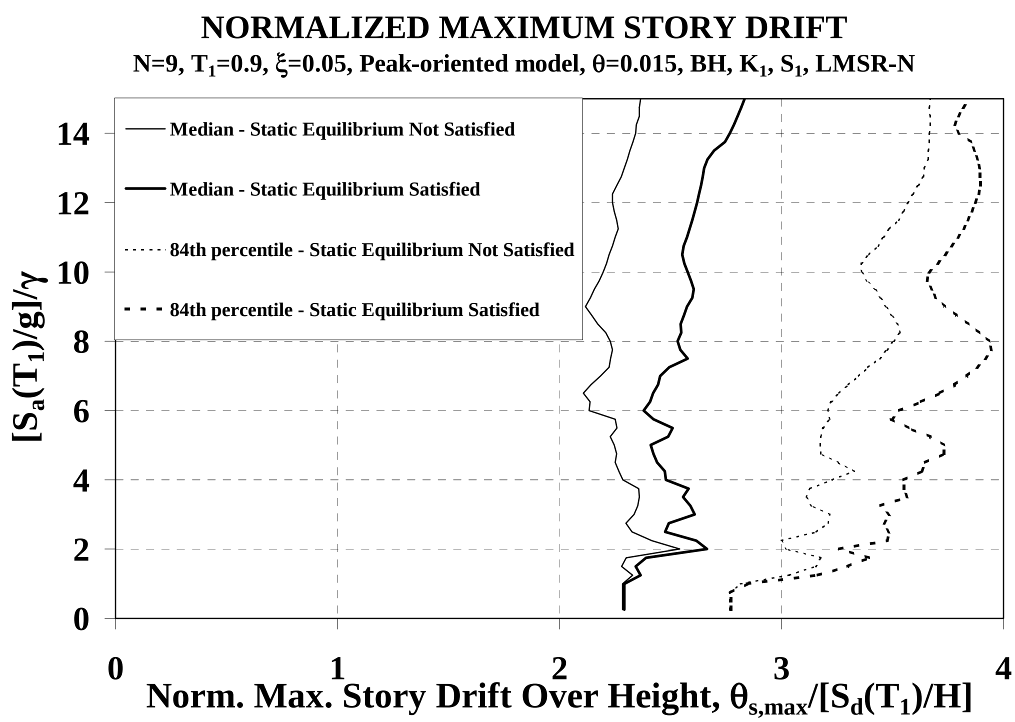

Figure A.7 Normalized Maximum Story Drift Angle over the Height, N = 9, T_1 = 0.9 sec, Model Used in This Study (for Which Static Equilibrium is Satisfied) and Model in Which Static Equilibrium Is Not Satisfied

Appendix B: EDPs for Regular Frame Structures

The following EDPs are obtained from nonlinear time history analyses of generic frame structures and are stored in the relational database:

Global EDPs

Global Deformation Demands:

- Maximum positive and negative floor displacements, $\delta^{+}_{fi,max}$ and $\delta^{-}_{fi,max}$
- Maximum positive and negative story drift angles, $\theta_{si}{}^{+}{}_{,max}$ and $\theta_{si}{}^{-}{}_{,max}$
- Residual floor displacements, $\delta_{fi,res}$
- Residual story drift angles, $\theta_{si,res}$
- Positive and negative story ductilities, $\mu_{si}{}^{+}$ and $\mu_{si}{}^{-}$

Global Strength Demands:

- Maximum positive and negative story shear force demand (first-order shear force, i.e., not including equivalent shear force from structure P-delta effects), $V_{si}{}^{+}{}_{,max}$ and $V_{si}{}^{-}{}_{,max}$
- Maximum story overturning moment demand obtained from the axial loads in columns, $M_{OTi,max}$ (column bending moments are ignored). Axial loads are computed in global coordinates.
- Maximum positive and negative total story overturning moment demand, $M_{totalOTi}{}^{+}{}_{,max}$ and $M_{totalOTi}{}^{-}{}_{,max}$ (first + second-order story overturning moments). Axial loads are computed in global coordinates.

- First-order (not including P-delta effects) story overturning moment demand at the instant of time when the maximum demand defined in the previous bullet point occurs, $M'_{1OTi}{}^{+}{}_{,max}$ and $M'_{1OTi}{}^{-}{}_{,max}$
- Equivalent height of the resultant of the lateral floor loads (story overturning moment normalized by first-order story shear force) corresponding to the overturning moments shown in the previous two bullet points, h_{eq1i}, h_{eq2i}
- Maximum positive and negative first-order (not including P-delta effects) story overturning moment demand, $M_{1OTi}{}^{+}{}_{,max}$ and $M_{lOTi}{}^{-}{}_{,max}$. Axial loads are computed in global coordinates.
- Total story overturning moment demand at the instant of time when the maximum demand shown in the previous bullet point occurs, $M'_{totalOTi}{}^{+}{}_{,max}$ and $M'_{totalOTi}{}^{-}{}_{,max}$
- Equivalent height of resultant of the lateral floor loads (story overturning moment normalized by first-order story shear force) corresponding to the overturning moments shown in the previous two bullet points, h_{eq3i}, h_{eq4i}
- Maximum positive and negative absolute floor accelerations, $a_{fi}{}^{+}{}_{,max}$, $a_{fi}{}^{-}{}_{,max}$
- Maximum positive and negative absolute floor velocities, $v_{fi}{}^{+}{}_{,max}$, $v_{fi}{}^{-}{}_{,max}$

Global Energy Demands:

- Total damping energy dissipated, DE
- Input energy at the end of record, IE_{end}

<u>Local EDPs</u>

Rotational Spring Demands (for rotational springs in both the beam-hinge and column-hinge models):

- Maximum spring rotation in the positive and negative directions, $\theta^{+}_{spr,max}$ and $\theta^{-}_{spr,max}$
- Maximum spring plastic rotation in the positive and negative directions, $\theta^{+}_{pspr,max}$ and $\theta^{-}_{pspr,max}$

- Cumulative spring plastic rotation ranges in the positive and negative directions, $\Sigma\Delta\theta_{pspr}^{+}$ and $\Sigma\Delta\theta_{pspr}^{-}$
- Cumulative spring plastic rotation ranges in the positive and negative directions during the pre-peak interval of the response (definition of pre-peak interval of the response is presented in Section 5.4), $\Sigma\Delta\theta_{pp,pspr}^{+}$ and $\Sigma\Delta\theta_{pp,pspr}^{-}$
- Maximum spring moments in the positive and negative directions, $M^{+}_{spr,max}$, $M^{-}_{spr,max}$
- Spring residual rotation, $\theta_{spr,res}$
- Number of positive and negative inelastic excursions, N_{spr}^{+} and N_{spr}^{-}
- Number of positive and negative inelastic excursions in the prepeak interval of the response, $N_{pp,spr}^{+}$, and $N_{pp,spr}^{-}$
- Time of first yielding, $t_{y,spr}$ (see Section 5.4)
- Duration of prepeak interval of the response, $t_{pp,spr}$ (see Section 5.4)
- Hysteretic energy dissipated in the springs (positive and negative directions), HE_{spr}^{+} and HE_{spr}^{-}
- Hysteretic energy dissipated in the springs during the prepeak period of the response (positive and negative directions), $HE_{pp,spr}^{+}$ and $HE_{pp,spr}^{-}$
- Total normalized hysteretic energy dissipated in the springs, $NHE_{spr} = HE_{spr} / (M_{yspr} * \theta_{yspr})$

Column Element Demands:

- Maximum positive and negative moments at the top and bottom of columns, $M_{ct}^{+}{}_{,max}$, $M_{ct}^{-}{}_{,max}$, $M_{cb}^{+}{}_{,max}$, $M_{cb}^{-}{}_{,max}$
- Moments at the opposite end of a column at the instant of time when the maximum moment demand defined in the previous bullet point occurs (to obtain the moment gradient when the maximum moment demand occurs), $M'_{ct}{}^{+}{}_{,max}$, $M'_{ct}{}^{-}{}_{,max}$, $M'_{cb}{}^{+}{}_{,max}$, $M'_{cb}{}^{-}{}_{,max}$
- Maximum positive and negative moment at the column midheight, $M_{cm}^{+}{}_{,max}$, $M_{cm}^{-}{}_{,max}$
- Maximum column shear force, $V_{c,max}$ (including second-order effects, i.e. $P\Delta/L$ [which is the actual shear perpendicular to the chord of the member when P-Δ is included]).

- Maximum column axial force in tension and compression, $P_{ct,max}$, $P_{cc,max}$ (including gravity loads; however, the axial loads due to dynamic action can be obtained, since the gravity loads are constant). Axial loads are computed in global coordinates.

REFERENCES

Abrahamson, N.A., Hazard Code, Version 30, PG&E, May 2001 (Draft).

Abrahamson, N.A. and Silva, W.J. (1997), "Empirical response spectral attenuation relations for shallow crustal earthquakes", *Seismological Research Letters*, Vol. 68, No. 1, 94-127.

ACI Committee 318 (1999), "Building code requirements for structural concrete (ACI 318-99) and commentary (ACI 318R-99)", *American Concrete Institute*, Farmington Hills, MI.

Adam, C., and Krawinker, H.. (2003). "Large deflections of elastic-plastic frames exposed to pulse-type ground motions", *Conference on the Response of Structures to Extreme Loading*, Elsevier Science, August 3-6, Toronto, Canada.

AISC (1997) – American Institute of Steel Construction, Inc., "Seismic provisions for structural steel buildings, load and resistance factor design", 2nd Edition, Chicago, Illinois.

Aslani, H. and Miranda, E. (2002), "Probabilistic building response analysis for loss estimation", *Seventh US National Conference on Earthquake Engineering* (7NCEE), *Urban Earthquake Risk*, July 21-25, Boston, Massachusetts, USA.

Aydinoglu, M. N. (2001), "Inelastic seismic response analysis based on story pushover curves including P-Delta effects", *Report No. 2001/1, KOERI, Department of Earthquake Engineering*, Bogazici University, Istanbul, Turkey.

Bernal, D. (1994), "Viscous damping in inelastic structural response", *Journal of Structural Engineering*, 120, 4, April, pages 1240-1254.

Bernal, D. (1987), "Amplification factors for inelastic dynamic P-delta effects in earthquake analysis", *Earthquake Engineering & Structural Dynamics*, 15, 5, July, pages 635-651.

Bertero. V. V. and Teran-Gilmore, A. (1993), "Use of energy concepts in earthquake-resistant analysis and design: issues and future directions", Published in *Primeras Jornadas Andinas de Ingenieria Estructural*, Memorias del VIII Seminario Latinoamericano de Ingenieria Sismo-Resistente 5 al 8 de Julio, Merida, Venezuela.

Bondy, K.D. (1996). "A more rational approach to capacity design of seismic moment frame columns", *Earthquake Spectra*, 12, 3, August, pages 395-406.

Bray, J., et. al.(2001). "Identification and prediction of performance-related ground motion parameters", *Pacific Earthquake Engineering Research Center*, Project No. 2242001.

Chai, Y. H. and Fajfar, P. (2000), "A procedure for estimating input energy spectra for seismic design", *Journal of Earthquake Engineering*, 4, 4, October, pages 539-561.

Cordova, P., et. al.(2000). "Development of a two-parameter seismic intensity measure and probabilistic assessment procedure", *PEER-2000/10, The Second U.S.-Japan Workshop on Performance-Based Earthquake Engineering Methodology for Reinforced Concrete Building Structures*, September 11-13.

Cornell, C. A. et. al. (2002), "Probabilistic basis for 2000 SAC Federal Emergency Management Agency steel moment frame guidelines", *ASCE Journal of Structural Engineering*, Vol. 128, No. 4, April, pages 526-534.

DRAIN-2DX (1993), "DRAIN-2DX: basic program description and user guide", *Report No. UCB/SEMM-93/17*, by Prakash, V., Powell, G. H., and Campbell, S., University of California, Berkeley, CA.

Fajfar, P. (2000), "A nonlinear analysis method for performance-based seismic design", *Earthquake Spectra*, 16, 3, August, pages 573-592.

FEMA 355C (2000), "State of the art report on systems performance of steel moment frames subject to earthquake ground shaking", *SAC Joint Venture*, September.

FEMA 356 (2000), "Prestandard and commentary for the seismic rehabilitation of buildings", *Federal Emergency Management Agency*, Washington D.C.

FEMA 368 (2000), "NEHRP recommended provisions for seismic regulations for new buildings and other structures", *Building Seismic Safety Council*, Washington D.C.

Goel, R. K. and Chopra, A. K. (1997), "Period formulas for moment-resisting frame buildings", *Journal of Structural Engineering*, 123, 11, November, pages 1454-1461.

Gupta, A. and Krawinkler H. (2000), "Dynamic P-delta effects for flexible inelastic steel structures", [Special Issue: Steel Moment Frames after Northridge--Part I], *Journal of Structural Engineering*, 126, 1, January, pages 145-154.

Gupta, A., and Krawinkler, H.. (1999). "Prediction of seismic demands for SMRFs with ductile connections and elements", *SAC Background Document, Report No. SAC/BD-99/06*.

Gupta, A., and Krawinkler, H.. (1998). "Quantitative performance assessment for steel moment frame structures under seismic loading", *Proceedings of the 11th European Conference on Earthquake Engineering*, A. A. Balkema, Rotterdam.

Ibarra, L., Medina, R., and Krawinkler, H. (2002) "Collapse assessment of deteriorating SDOF systems", *Proceedings of the 12th European Conference on Earthquake Engineering*, Paper Ref. 665, Elsevier Science Ltd., September 9-13, London, UK.

Krawinkler, H. (2002), "A general approach to seismic performance assessment," *Proceedings, International Conference on Advances and New Challenges in Earthquake Engineering Research*, ICANCEER 2002, August 19-20, Hong Kong.

Krawinkler, H., Parisi, F., Ibarra, L., Ayoub, A. and Medina, R. (2000). "Development of a testing protocol for woodframe structures", *CUREE Publication* No. W-02.

Krawinkler, H., Medina, R., Miranda, M. and Ayoub, A. (1999). "Seismic demands for performance-based design", *Proceedings of the U.S.-Japan Workshop on Performance-Based Earthquake Engineering Methodology for Reinforced Concrete Building Structures*, PEER Report 1999/10, September 13, Maui, Hawaii.

Krawinkler, H., and Zohrei, M. (1983). "Cumulative damage in steel structures subjected to earthquake ground motions", *Journal on Computers and Structures,* Vol. 16, No. 1-4.

Luco, N. and Cornell, C. Allin, (2002). ”Structure-specific scalar intensity measures for near-source and ordinary earthquake ground motions,” Accepted for Publication: *Earthquake Spectra*.

Miranda, E.. (1999). “Approximate seismic lateral deformation demands in multistory buildings”, *Journal of Structural Engineering*, 125, 4, April, pages 417-425.

Miranda, E. (1998), “Simplified method to estimate maximum seismic interstory drift demands in multi-story buildings”, *Proceedings, Sixth U.S. National Conference on Earthquake Engineering*, Earthquake Engineering Research Inst., Oakland, California.

Nakashima, M. and Sawaizumi, S. (2000), “Column-to-beam strength ratio required for ensuring beam-collapse mechanisms in earthquake responses of steel moment frames”, *12th World Conference on Earthquake Engineering*, New Zealand Society for Earthquake Engineering, Paper No. 1109, Upper Hutt, New Zealand.

Nassar, A.A. and H. Krawinkler (1991). “Seismic demands for SDOF and MDOF systems”, *John A. Blume Earthquake Engineering. Center Report No. 95*, Department of Civil Engineering, Stanford University.

OpenSees (2002), Open System for Earthquake Engineering Simulation, Pacific Earthquake Engineering Research Center.

Rodriguez, M. E., et. al. (2002), “Earthquake-induced floor horizontal accelerations in buildings”, *Earthquake Engineering & Structural Dynamics*, 31, 3, March, pages 693-718.

Seneviratna, G.D.P.K., and Krawinkler, H.. (1997). “Evaluation of inelastic MDOF effects for seismic design”, *John A. Blume Earthquake Engineering Center Report No. 120*, Department of Civil Engineering, Stanford University.

Shome, N. and Cornell A.. (1999). “Probabilistic seismic demand analysis of nonlinear structures”, *Report No. RMS-35*, Department of Civil Engineering, Stanford University.

Somerville, P. and Collins, N. (2002), “Ground motion time histories for the Van Nuys building”, *PEER Methodology Testbeds Project,* URS Corporation, March 7, Pasadena, CA.

Somerville, P., Smith, N., Punyamurthula, S., and Sun, J. (1997). “Development of ground motion time histories for phase 2 of the FEMA/SAC steel project,” *SAC Background Document, Report No. SAC/BD-97/04.*

Trifunac, M. D. and Brady, A. G. (1975), “A study of the duration of strong earthquake ground motion”, *Bulletin of the Seismological Society of America*, Vol. 65, 581-626.

Uang, C. M., Bertero V.V. (1988), “Use of energy as a design criterion in earthquake-resistant design”, UCB/EERC-88/18, Berkeley: *Earthquake Engineering Research Center*, University of California, November, 46 pages.

UBC (1997). “Uniform Building Code”, *International Conference on Building Officials*, Whittier, CA.

Vamvatsikos, D., and Cornell, C. A.. (2002), “Incremental dynamic analysis”, *Earthquake Engineering & Structural Dynamics*, 31, 3, March, pages 491-514.

PEER REPORTS

PEER reports are available from the National Information Service for Earthquake Engineering (NISEE). To order PEER reports, please contact the Pacific Earthquake Engineering Research Center, 1301 South 46th Street, Richmond, California 94804-4698. Tel.: (510) 231-9468; Fax: (510) 231-9461.

PEER 2003/16 *Seismic Demands for Performance-Based Design of Bridges.* Kevin Mackie and Božidar Stojadinović. August 2003.

PEER 2003/15 *Seismic Demands for Nondeteriorating Frame Structures and Their Dependence on Ground Motions.* Ricardo Antonio Medina and Helmut Krawinkler. May 2004.

PEER 2003/14 *Finite Element Reliability and Sensitivity Methods for Performance-Based Earthquake Engineering.* Terje Haukaas and Armen Der Kiureghian. April 2004.

PEER 2003/13 *Effects of Connection Hysteretic Degradation on the Seismic Behavior of Steel Moment-Resisting Frames.* Janise E. Rodgers and Stephen A. Mahin. March 2004.

PEER 2003/12 *Implementation Manual for the Seismic Protection of Laboratory Contents: Format and Case Studies.* William T. Holmes and Mary C. Comerio. October 2003.

PEER 2003/11 *Fifth U.S.-Japan Workshop on Performance-Based Earthquake Engineering Methodology for Reinforced Concrete Building Structures.* February 2004.

PEER 2003/10 *A Beam-Column Joint Model for Simulating the Earthquake Response of Reinforced Concrete Frames.* Laura N. Lowes, Nilanjan Mitra, and Arash Altoontash. February 2004.

PEER 2003/09 *Sequencing Repairs after an Earthquake: An Economic Approach.* Marco Casari and Simon J. Wilkie. April 2004.

PEER 2003/08 *A Technical Framework for Probability-Based Demand and Capacity Factor Design (DCFD) Seismic Formats*. Fatemeh Jalayer and C. Allin Cornell. November 2003.

PEER 2003/07 *Uncertainty Specification and Propagation for Loss Estimation Using FOSM Methods.* Jack W. Baker and C. Allin Cornell. September 2003.

PEER 2003/06 *Performance of Circular Reinforced Concrete Bridge Columns under Bidirectional Earthquake Loading*. Mahmoud M. Hachem, Stephen A. Mahin, and Jack P. Moehle. February 2003.

PEER 2003/05 *Response Assessment for Building-Specific Loss Estimation.* Eduardo Miranda and Shahram Taghavi. September 2003.

PEER 2003/04 *Experimental Assessment of Columns with Short Lap Splices Subjected to Cyclic Loads*. Murat Melek, John W. Wallace, and Joel Conte. April 2003.

PEER 2003/03 *Probabilistic Response Assessment for Building-Specific Loss Estimation.* Eduardo Miranda and Hesameddin Aslani. September 2003.

PEER 2003/02 *Software Framework for Collaborative Development of Nonlinear Dynamic Analysis Program.* Jun Peng and Kincho H. Law. September 2003.

PEER 2003/01 *Shake Table Tests and Analytical Studies on the Gravity Load Collapse of Reinforced Concrete Frames.* Kenneth John Elwood and Jack P. Moehle. November 2003

PEER 2002/24 *Performance of Beam to Column Bridge Joints Subjected to a Large Velocity Pulse.* Natalie Gibson, André Filiatrault, and Scott A. Ashford. April 2002.

PEER 2002/23 *Effects of Large Velocity Pulses on Reinforced Concrete Bridge Columns.* Greg L. Orozco and Scott A. Ashford. April 2002.

PEER 2002/22 *Characterization of Large Velocity Pulses for Laboratory Testing.* Kenneth E. Cox and Scott A. Ashford. April 2002.

PEER 2002/21 *Fourth U.S.-Japan Workshop on Performance-Based Earthquake Engineering Methodology for Reinforced Concrete Building Structures*. December 2002.

PEER 2002/20 *Barriers to Adoption and Implementation of PBEE Innovations.* Peter J. May. August 2002.

PEER 2002/19 *Economic-Engineered Integrated Models for Earthquakes: Socioeconomic Impacts.* Peter Gordon, James E. Moore II, and Harry W. Richardson. July 2002.

PEER 2002/18 *Assessment of Reinforced Concrete Building Exterior Joints with Substandard Details.* Chris P. Pantelides, Jon Hansen, Justin Nadauld, and Lawrence D. Reaveley. May 2002.

PEER 2002/17 *Structural Characterization and Seismic Response Analysis of a Highway Overcrossing Equipped with Elastomeric Bearings and Fluid Dampers: A Case Study.* Nicos Makris and Jian Zhang. November 2002.

PEER 2002/16 *Estimation of Uncertainty in Geotechnical Properties for Performance-Based Earthquake Engineering.* Allen L. Jones, Steven L. Kramer, and Pedro Arduino. December 2002.

PEER 2002/15 *Seismic Behavior of Bridge Columns Subjected to Various Loading Patterns.* Asadollah Esmaeily-Gh. and Yan Xiao. December 2002.

PEER 2002/14 *Inelastic Seismic Response of Extended Pile Shaft Supported Bridge Structures.* T.C. Hutchinson, R.W. Boulanger, Y.H. Chai, and I.M. Idriss. December 2002.

PEER 2002/13 *Probabilistic Models and Fragility Estimates for Bridge Components and Systems.* Paolo Gardoni, Armen Der Kiureghian, and Khalid M. Mosalam. June 2002.

PEER 2002/12 *Effects of Fault Dip and Slip Rake on Near-Source Ground Motions: Why Chi-Chi Was a Relatively Mild M7.6 Earthquake.* Brad T. Aagaard, John F. Hall, and Thomas H. Heaton. December 2002.

PEER 2002/11 *Analytical and Experimental Study of Fiber-Reinforced Strip Isolators*. James M. Kelly and Shakhzod M. Takhirov. September 2002.

PEER 2002/10 *Centrifuge Modeling of Settlement and Lateral Spreading with Comparisons to Numerical Analyses***.** Sivapalan Gajan and Bruce L. Kutter. January 2003.

PEER 2002/09 *Documentation and Analysis of Field Case Histories of Seismic Compression during the 1994 Northridge, California, Earthquake.* Jonathan P. Stewart, Patrick M. Smith, Daniel H. Whang, and Jonathan D. Bray. October 2002.

PEER 2002/08 *Component Testing, Stability Analysis and Characterization of Buckling-Restrained Unbonded Braces^{TM}.* Cameron Black, Nicos Makris, and Ian Aiken. September 2002.

PEER 2002/07 *Seismic Performance of Pile-Wharf Connections.* Charles W. Roeder, Robert Graff, Jennifer Soderstrom, and Jun Han Yoo. December 2001.

PEER 2002/06 *The Use of Benefit-Cost Analysis for Evaluation of Performance-Based Earthquake Engineering Decisions*. Richard O. Zerbe and Anthony Falit-Baiamonte. September 2001.

PEER 2002/05 *Guidelines, Specifications, and Seismic Performance Characterization of Nonstructural Building Components and Equipment*. André Filiatrault, Constantin Christopoulos, and Christopher Stearns. September 2001.

PEER 2002/04 *Consortium of Organizations for Strong-Motion Observation Systems and the Pacific Earthquake Engineering Research Center Lifelines Program: Invited Workshop on Archiving and Web Dissemination of Geotechnical Data, 4–5 October 2001*. September 2002.

PEER 2002/03 *Investigation of Sensitivity of Building Loss Estimates to Major Uncertain Variables for the Van Nuys Testbed.* Keith A. Porter, James L. Beck, and Rustem V. Shaikhutdinov. August 2002.

PEER 2002/02 *The Third U.S.-Japan Workshop on Performance-Based Earthquake Engineering Methodology for Reinforced Concrete Building Structures*. July 2002.

PEER 2002/01 *Nonstructural Loss Estimation: The UC Berkeley Case Study.* Mary C. Comerio and John C. Stallmeyer. December 2001.

PEER 2001/16 *Statistics of SDF-System Estimate of Roof Displacement for Pushover Analysis of Buildings.* Anil K. Chopra, Rakesh K. Goel, and Chatpan Chintanapakdee. December 2001.

PEER 2001/15 *Damage to Bridges during the 2001 Nisqually Earthquake.* R. Tyler Ranf, Marc O. Eberhard, and Michael P. Berry. November 2001.

PEER 2001/14 *Rocking Response of Equipment Anchored to a Base Foundation.* Nicos Makris and Cameron J. Black. September 2001.

PEER 2001/13 *Modeling Soil Liquefaction Hazards for Performance-Based Earthquake Engineering.* Steven L. Kramer and Ahmed-W. Elgamal. February 2001.

PEER 2001/12 *Development of Geotechnical Capabilities in OpenSees.* Boris Jeremic. September 2001.

PEER 2001/11 *Analytical and Experimental Study of Fiber-Reinforced Elastomeric Isolators*. James M. Kelly and Shakhzod M. Takhirov. September 2001.

PEER 2001/10 *Amplification Factors for Spectral Acceleration in Active Regions.* Jonathan P. Stewart, Andrew H. Liu, Yoojoong Choi, and Mehmet B. Baturay. December 2001.

PEER 2001/09 *Ground Motion Evaluation Procedures for Performance-Based Design.* Jonathan P. Stewart, Shyh-Jeng Chiou, Jonathan D. Bray, Robert W. Graves, Paul G. Somerville, and Norman A. Abrahamson. September 2001.

PEER 2001/08 *Experimental and Computational Evaluation of Reinforced Concrete Bridge Beam-Column Connections for Seismic Performance*. Clay J. Naito, Jack P. Moehle, and Khalid M. Mosalam. November 2001.

PEER 2001/07 *The Rocking Spectrum and the Shortcomings of Design Guidelines.* Nicos Makris and Dimitrios Konstantinidis. August 2001.

PEER 2001/06 *Development of an Electrical Substation Equipment Performance Database for Evaluation of Equipment Fragilities*. Thalia Agnanos. April 1999.

PEER 2001/05 *Stiffness Analysis of Fiber-Reinforced Elastomeric Isolators.* Hsiang-Chuan Tsai and James M. Kelly. May 2001.

PEER 2001/04 *Organizational and Societal Considerations for Performance-Based Earthquake Engineering.* Peter J. May. April 2001.

PEER 2001/03 *A Modal Pushover Analysis Procedure to Estimate Seismic Demands for Buildings: Theory and Preliminary Evaluation.* Anil K. Chopra and Rakesh K. Goel. January 2001.

PEER 2001/02 *Seismic Response Analysis of Highway Overcrossings Including Soil-Structure Interaction.* Jian Zhang and Nicos Makris. March 2001.

PEER 2001/01 *Experimental Study of Large Seismic Steel Beam-to-Column Connections.* Egor P. Popov and Shakhzod M. Takhirov. November 2000.

PEER 2000/10 *The Second U.S.-Japan Workshop on Performance-Based Earthquake Engineering Methodology for Reinforced Concrete Building Structures.* March 2000.

PEER 2000/09 *Structural Engineering Reconnaissance of the August 17, 1999 Earthquake: Kocaeli (Izmit), Turkey.* Halil Sezen, Kenneth J. Elwood, Andrew S. Whittaker, Khalid Mosalam, John J. Wallace, and John F. Stanton. December 2000.

PEER 2000/08 *Behavior of Reinforced Concrete Bridge Columns Having Varying Aspect Ratios and Varying Lengths of Confinement.* Anthony J. Calderone, Dawn E. Lehman, and Jack P. Moehle. January 2001.

PEER 2000/07 *Cover-Plate and Flange-Plate Reinforced Steel Moment-Resisting Connections.* Taejin Kim, Andrew S. Whittaker, Amir S. Gilani, Vitelmo V. Bertero, and Shakhzod M. Takhirov. September 2000.

PEER 2000/06 *Seismic Evaluation and Analysis of 230-kV Disconnect Switches.* Amir S. J. Gilani, Andrew S. Whittaker, Gregory L. Fenves, Chun-Hao Chen, Henry Ho, and Eric Fujisaki. July 2000.

PEER 2000/05 *Performance-Based Evaluation of Exterior Reinforced Concrete Building Joints for Seismic Excitation.* Chandra Clyde, Chris P. Pantelides, and Lawrence D. Reaveley. July 2000.

PEER 2000/04 *An Evaluation of Seismic Energy Demand: An Attenuation Approach.* Chung-Che Chou and Chia-Ming Uang. July 1999.

PEER 2000/03 *Framing Earthquake Retrofitting Decisions: The Case of Hillside Homes in Los Angeles.* Detlof von Winterfeldt, Nels Roselund, and Alicia Kitsuse. March 2000.

PEER 2000/02 *U.S.-Japan Workshop on the Effects of Near-Field Earthquake Shaking.* Andrew Whittaker, ed. July 2000.

PEER 2000/01 *Further Studies on Seismic Interaction in Interconnected Electrical Substation Equipment.* Armen Der Kiureghian, Kee-Jeung Hong, and Jerome L. Sackman. November 1999.

PEER 1999/14 *Seismic Evaluation and Retrofit of 230-kV Porcelain Transformer Bushings*. Amir S. Gilani, Andrew S. Whittaker, Gregory L. Fenves, and Eric Fujisaki. December 1999.

PEER 1999/13 *Building Vulnerability Studies: Modeling and Evaluation of Tilt-up and Steel Reinforced Concrete Buildings.* John W. Wallace, Jonathan P. Stewart, and Andrew S. Whittaker, editors. December 1999.

PEER 1999/12 *Rehabilitation of Nonductile RC Frame Building Using Encasement Plates and Energy-Dissipating Devices.* Mehrdad Sasani, Vitelmo V. Bertero, James C. Anderson. December 1999.

PEER 1999/11 *Performance Evaluation Database for Concrete Bridge Components and Systems under Simulated Seismic Loads.* Yael D. Hose and Frieder Seible. November 1999.

PEER 1999/10 *U.S.-Japan Workshop on Performance-Based Earthquake Engineering Methodology for Reinforced Concrete Building Structures.* December 1999.

PEER 1999/09 *Performance Improvement of Long Period Building Structures Subjected to Severe Pulse-Type Ground Motions*. James C. Anderson, Vitelmo V. Bertero, and Raul Bertero. October 1999.

PEER 1999/08 *Envelopes for Seismic Response Vectors.* Charles Menun and Armen Der Kiureghian. July 1999.

PEER 1999/07 *Documentation of Strengths and Weaknesses of Current Computer Analysis Methods for Seismic Performance of Reinforced Concrete Members.* William F. Cofer. November 1999.

PEER 1999/06 *Rocking Response and Overturning of Anchored Equipment under Seismic Excitations.* Nicos Makris and Jian Zhang. November 1999.

PEER 1999/05 *Seismic Evaluation of 550 kV Porcelain Transformer Bushings.* Amir S. Gilani, Andrew S. Whittaker, Gregory L. Fenves, and Eric Fujisaki. October 1999.

PEER 1999/04 *Adoption and Enforcement of Earthquake Risk-Reduction Measures.* Peter J. May, Raymond J. Burby, T. Jens Feeley, and Robert Wood.

PEER 1999/03 *Task 3 Characterization of Site Response General Site Categories*. Adrian Rodriguez-Marek, Jonathan D. Bray, and Norman Abrahamson. February 1999.

PEER 1999/02 *Capacity-Demand-Diagram Methods for Estimating Seismic Deformation of Inelastic Structures: SDF Systems*. Anil K. Chopra and Rakesh Goel. April 1999.

PEER 1999/01 *Interaction in Interconnected Electrical Substation Equipment Subjected to Earthquake Ground Motions.* Armen Der Kiureghian, Jerome L. Sackman, and Kee-Jeung Hong. February 1999.

PEER 1998/08 *Behavior and Failure Analysis of a Multiple-Frame Highway Bridge in the 1994 Northridge Earthquake.* Gregory L. Fenves and Michael Ellery. December 1998.

PEER 1998/07 *Empirical Evaluation of Inertial Soil-Structure Interaction Effects.* Jonathan P. Stewart, Raymond B. Seed, and Gregory L. Fenves. November 1998.

PEER 1998/06 *Effect of Damping Mechanisms on the Response of Seismic Isolated Structures.* Nicos Makris and Shih-Po Chang. November 1998.

PEER 1998/05 *Rocking Response and Overturning of Equipment under Horizontal Pulse-Type Motions.* Nicos Makris and Yiannis Roussos. October 1998.

PEER 1998/04 *Pacific Earthquake Engineering Research Invitational Workshop Proceedings, May 14–15, 1998: Defining the Links between Planning, Policy Analysis, Economics and Earthquake Engineering.* Mary Comerio and Peter Gordon. September 1998.

PEER 1998/03 *Repair/Upgrade Procedures for Welded Beam to Column Connections.* James C. Anderson and Xiaojing Duan. May 1998.

PEER 1998/02 *Seismic Evaluation of 196 kV Porcelain Transformer Bushings.* Amir S. Gilani, Juan W. Chavez, Gregory L. Fenves, and Andrew S. Whittaker. May 1998.

PEER 1998/01 *Seismic Performance of Well-Confined Concrete Bridge Columns.* Dawn E. Lehman and Jack P. Moehle. December 2000.